The University of Sheffield

Department of Mechanical Engineering

3D Cellular Automata Finite Element modelling of cleavage and ductile fracture

A thesis submitted for the degree of Doctor of Philosophy

(December 2008)

by

Rubén Cuamatzi Meléndez

Acknowledgments

I would like to acknowledge my academic supervisors Professor John Yates and Professor Ian Howard for supervising this research project in all experimental, numerical simulations and modelling, for their constructive suggestions, and their mind–stimulating discussions.

I also like to acknowledge my sponsor "The National Council of Science and Technology, CONACYT Mexico" for support my PhD studies at The University of Sheffield.

I want to thanks to my wife Ericka Vega Lazcano for her love and encouragement that she gave me to finish this project and for her patience.

I also would like to sincerely acknowledge my Mom Rosa Meléndez Bello and my Dad Tiburcio Cuamatzi Maldonado, and my brothers Alfredo and Fernando, for their encouragement in this research project and for their special support.

The author is grateful to Dr. Anton Shterenlikht for his pioneering work in the subject area.

I appreciate the assistance of the department staff for their suggestions in some stages of the experimental work.

Summary

In the present research work, a three-dimensional Cellular Automata Finite Element (CAFE) multi-scale model was developed to simulate, ductile fracture, cleavage and the ductile–brittle transition in a structural steel.

For the simulation of the ductile–brittle fracture, at least two Cellular Automata arrays are needed, one to represent the ductile material properties and the other one to account for the brittle fracture process. The cell sizes in both arrays are independent of each other and of the finite element size. The cell sizes in each Cellular Automata array are related to the microstructural process of each fracture mechanism. The finite elements size is chosen to represent the macro strain gradients accurately. The model was implemented through the user define material behavior subroutine VUMAT in the finite element program ABAQUS Explicit Version 5.6. In the CAFE model, the material information is moved from the structural response of finite elements and stored in the appropriated number of Cellular Automata (CA) arrays.

In the present CAFE model, the Rousselier ductile damage model was applied to each ductile cell. The critical value of the maximum principal stress was used to assess the failure of each brittle cell. In the brittle CA arrays, four different cleavage fracture nucleation micromechanisms, found experimentally at test temperatures down to –196°C in a ferritic–pearlitic Grade A ship plate steel were included in the model. This was done in order to simulate the real micro-features nucleating cleavage in ferritic steels.

In this model, the physical damage parameters of the ductile and brittle parts were calibrated separately. After calibration the CAFE model simulated the experimentally measured distribution of brittle microcracks generated in the notch region of blunt four point double–notch bend tests performed at test temperatures from 25°C to –196°C. The ductile part of the CAFE model was calibrated with the simulation of tensile and impact Charpy tests performed at room temperature. Subsequently the model was applied to simulate the ductile–brittle transition of Grade A ship plate steel. When numerical against experimental data was obtained, the parameters were considered true material model parameters of the steel under analysis.

Nomenclature

σ_F	Fracture stress.
σ_1	Maximum principal stress.
σ_{yy}	General yield stress.
P_F	Fracture load.
P_{GY}	General yield load fracture.
ε	Logarithmic plastic strain.
E	Young's modulus.
$f_{o(R)}$	Initial void volume fraction (Rousselier damage model).
f_o	Initial void volume fraction (Gurson's-Tvergaard-Needleman model).
f_c	Critical void volume fraction (threshold of stress carrying capacity).
$\dot{f}$	Void volume fraction rate.
$\dot{f}_g$	Rate of growth of existing voids.
$\dot{f}_n$	Void nucleation rate.
f_ε	Void nucleation intensity.
$f^*(f)$	Void coalescence function
f_f	Void volume fraction at final fracture
ε_{ij}^p	Plastic strain rate.
I_{ij}	Second-order unit tensor.
ν	Poisson's ratio.
ε_{yy}	Maximum normal strain.
ρ	Notch root.
γ	Effective surface energy
γ_{cf}	Effective surface energy of a carbide-ferrite interface
γ_{pp}	Effective surface energy of particles in lamellar pearlite.

γ_{pf}	Effective surface energy of pearlite-ferrite interface.
γ_{ff}	Effective surface energy of a ferrite-ferrite interface
d_g	Grain size.
d_c	Carbide size
C_o	Diameter of the penny-shaped microcrack
σ_F	Fracture stress
σ_F^{cf}	Fracture stress of a carbide-ferrite interface
σ_F^{ff}	Fracture stress of a ferrite-ferrite interface
σ_F^{pp}	Fracture stress of the lamellar particles microstructure
D	Rousselier damage model parameter.
σ_1	Rousselier damage model parameter.
σ_{eq}	Effective von Mises equivalent stress.
$\frac{d\eta_{zb}}{d\varepsilon_{eq}}$	Damage rate of McClintok model.
ε_{eq}	Equivalent strain.
ε_{eq}^p	Equivalent plastic strain.
F_{zb}^f	Critical value of the relative growth factor.
n	Hardening exponent.
σ_a and σ_o	The two principal stresses at infinite.
q_1, q_2, q_3	Material damage model parameters.
σ_o	Flow stress.
β	Scalar damage variable of Rousselier damage model
B	Damage function of Rousselier damage model
$H\left(\varepsilon_{eq}^p\right)$	Term describing the hardening properties of materials in Rousselier damage model
σ_m^e	Elastic mean stress
ε_m^p	Plastic mean strain

K	Strength coefficient
σ_{eq}^{e}	Elastic effective von Mises equivalent stress
t_i	Time increment
$\vec{n}$	Normal vector
S	Area of intersection of voids
$D(\vec{n})$	Damage variable
A and n	Material properties of the Ramberg-Osgood hardening law
S_o and s_o	Parameters in the damage evolution law of Ramberg-Osgood law
σ_n	Normal stress
a	Notch deep length
σ_1 and σ_2	First and second principal stresses
$g(\theta)$	Angular distribution of microcracks with respect to the principal loading direction.
P_{nF}	Probability of non failure
τ	Shear stress
σ_1	Maximum principal stress
V_o	Reference volume
σ_u	Scale parameter of Weibull stress.
σ_{th}	Threshold stress parameter of Beremin model required to propagate the largest microcrack
Φ	Yield potential function
σ_w	Weibull stress
ε_{pc}	Critical plastic strain
ε_p	Plastic strain
l_c	Inter-inclusion spacing
L_D	Ductile cell size
N_v	Average number of inclusions per unit volume
d_x, d_y, d_z	Average inclusion sizes in three perpendicular dimensions

$\dot{\varepsilon}$	Strain rate
σ_T	True stress
ε_T	True strain
P	Load applied
l_i	Instantaneous gauge length of tensile specimens
l_o	Original gauge length of tensile specimens
L_F	Gauge length at fracture
A_o	Initial cross section
A_F	Cross-sectional area at fracture
σ_{UTS}	Ultimate tensile strength
f_v	Volume fraction of void nucleating particles
r	Relative density
M	Bending moment
b	Width of specimens
$s(t)$	Hammer displacement as a function of time
$v(t)$	Instantaneous velocity of hammer during impact
v_o	Initial hammer velocity
m	Mass of hammer
$E(s)$	Charpy fracture energy absorbed under the force-displacement data
B	Specimen Breadth
$S_{\max}$, $S_{\min}$	Maximum and minimum inner loading points
$g(\theta)$	Angular distribution of microcracks
$\beta(t_{i+1})$	Damage variable at time increment
θ	Misorientation angle
$(\theta_a - \theta_b)$	Misorientation angle between two cells
θ_F	Misorientation threshold
D_{ijkl}	Stiffness matrix

$N^P(\xi_k)$	Interpolation function
ε_{kl}	The logarithmic or true strain tensor
u_{ij}^p	Displacement tensor
p	Finite element node
k	Parametric coordinated tensor
$u_{ij}(\xi_k)$	Displacement tensor at point ξ_k
r	Gaussian or material point
R	Total number of integration points per finite element
α	Grain orientation angle
Γ	Cell solution-dependent variable
$\Delta_{\sqcup}$	Change in variable $\sqcup$ during one time increment
δ_{ij}	Kronecker delta
ε_{ij}^e	Elastic strain tensor
ε_{ij}^p	Plastic strain tensor, $\varepsilon_{ij}^p = e_{ij}^p + \varepsilon_m^p \delta_{ij}$
e_{ij}^p	Plastic strain deviatory
ε_m^p	Mean plastic strain, $\varepsilon_m^p = \frac{1}{3}\varepsilon_{ii}$
ε_{eq}^p	Equivalent plastic strain, $\varepsilon_{eq}^p = \sqrt{\frac{2}{3} e_{ij}^p e_{ij}^p}$
η	Fraction of the brittle CA cells which have a grain boundary carbide
Λ	Cell property
Ξ	CA to FE transition function
σ_{ij}	Stress tensor, $\sigma_{ij} = S_{ij} + \sigma_m \delta_{ij}$
σ_m	Mean stress, $\sigma_m = \frac{1}{3}\sigma_{ii}$
σ_{eq}	Equivalent stress, $\sigma_{eq} = \sqrt{\frac{3}{2} S_{ij} S_{ij}}$
σ_Y	Yield stress
σ_{Yo}	First yield stress

Υ	Cell state
Ω	Cell transition rule
A	Total number of state variables per FE integration point
C_v	The total energy absorbed in the Charpy V-notch impact test
c_D	Concentration factor for a ductile CA array
c_B	Concentration factor for a brittle CA array
d_k	Direction cosines
E_{ijkl}	Isotropic elastic modulus, $E_{ijkl} = 2G\delta_{ik}\delta_{jl} + \left(K - \frac{2}{3}G\right)\delta_{ij}\delta_{kl}$
f	Probability density function
G	Shear modulus, $G = \frac{E}{2(1+\nu)}$
K	Compression modulus, $K = \frac{E}{3(1-2\nu)}$
L	Damage cell size
L_{FE}	Finite element size
$\mathbb{M}$	Mapping function
M	Total number of cells per CA
$\mathbb{N}$	The set of natural numbers
N	Total number of cell properties
Q	Total number of cell state variables
R	Total number of integration points per FE
S_{ij}	Stress deviator
t	Time
W_β	Shape parameter of Weibull distribution
W_γ	Location parameter of Weibull distribution
W_η	Scale parameter of Weibull distribution
$X^{\max}$	The maximum number of dead cells allowed per CA
Y	Finite element solution-dependent variable

Contents

Chapter I

Background

The analysis of the fracture behaviour of "Grade A" ship plate steels used for the construction of the hulls of merchant ships is of paramount importance. These structures withstand severe loads resulting from harsh environmental conditions. Recent failures in merchant ships constructed with this steel show the importance of the concern where cracks of the order of 6 metres long were developed on the port side of the hull of a ship while navigating in icy water (Transportation Safety Board of Canada, 2002). In this failure the crew members noticed water entering on the port side of the hold. Analyses of the cracks led to increasing concern about the susceptibility of the steel to brittle fracture. This in turn led to more detailed analysis of the steel in order to give recommendations about its use for the construction of the hull of merchant ships, especially when the intention is to navigate in cold water.

1.1 Review of some recent failures in ship structures and problem definition.

Ships play a vital role in the transportation of products and people in the world and at the same time, they are essential for the development of the economy. The integrity of ship structures is an area of great interest as the world depends on such structures to transport products to consumers. Recent ship failures (Transportation Safety Board of Canada, 2002) illustrates the importance of the concern of cleavage fracture analysis which is characteristic of Grade A ship plate steels. An example of a casualty occurred in a merchant ship constructed with a Grade A plate steel was the Lake Carling, when the ship was navigating in icy water in the Gulf of St. Lawrence in Quebec Canada, the hatch cover of No. 4 hold was opened for routine maintenance. Crew members discovered water entering on the port side of the hold, the air and water temperature were –6ºC and 0ºC respectively. At the same time, historical data reported a wave from 1.5 to 2.5 m high, with a wavelength of approximately 56 m, which caused the development of the fractures. Figure 1.1 shows the ship where fractures were discovered.

Figure 1.1 – Lake Carling stopped in ice, 22 March 2002.

Further inspections revealed that the principal fracture was six-metre long and had developed on the port side shell as shown in figure 1.2. The principal side shell fracture (figure 1.2) was on the port side extending upwards and forward from the toe of the weld at the base of the side shell frame. The examination indicated that the principal fracture originated at the toe of the weld. Fracture origin was located $1.3m$ below the neutral axis of the vessel. Five similar cracks were found in No. 4 hold; on the port side. All cracks appeared to originate near the base of the frame at the toe of the weld; all of these cracks were rusted and had probably been present for some time.

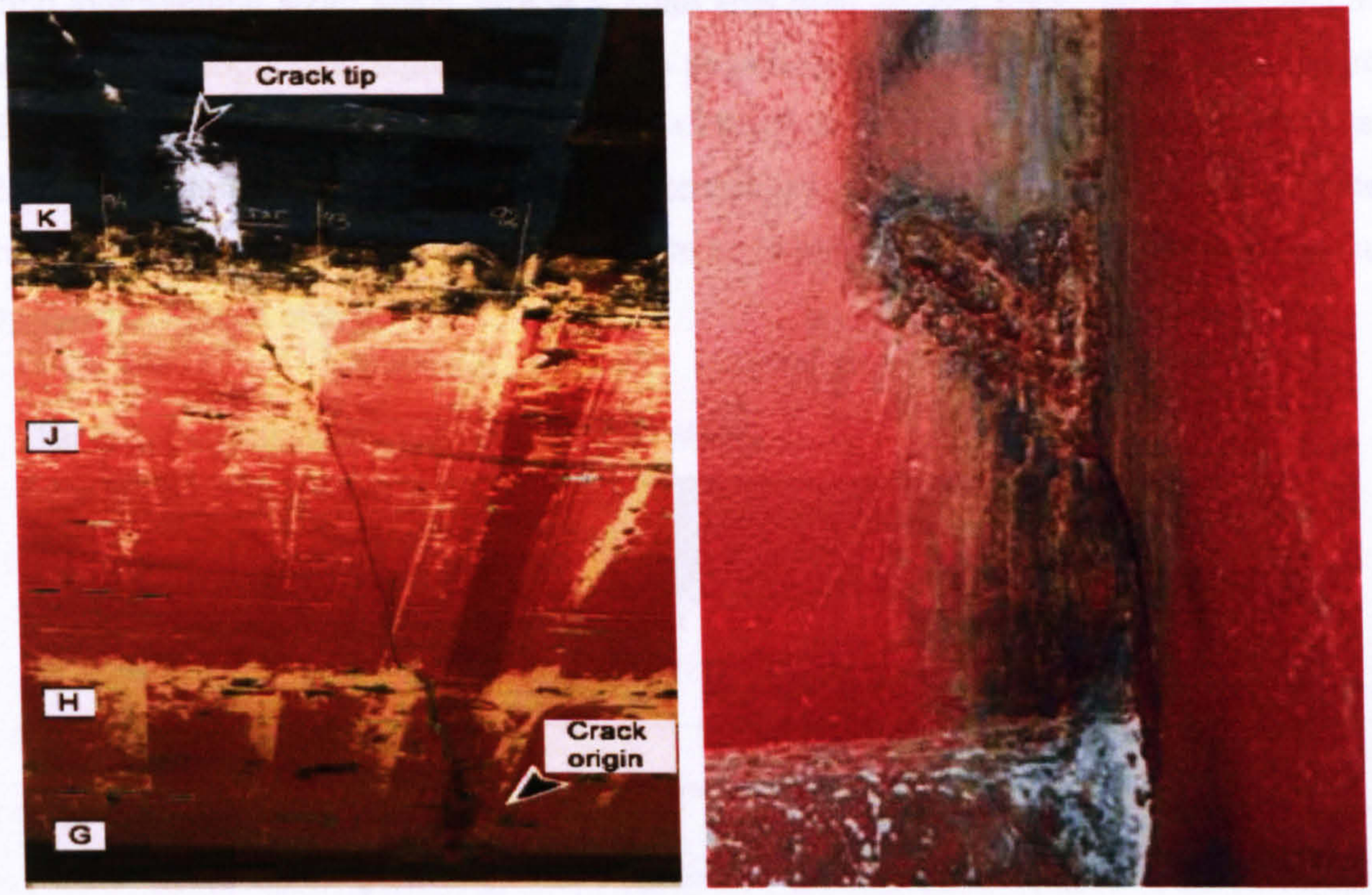

Figure 1.2 – The principal fracture and a fracture from which water ingress was observed.

Suspected factors that caused these fractures (Transportation Safety Board of Canada, 2002) were: abnormal forces in the ship structure, presence of flaws or notches in the structure where fractures originated, unsatisfactory welding procedures and inadequate mechanical properties of structural steel at service temperatures. Other ships built with Grade A ship plate steel that incurred similar failures are: the "Herald of Free Enterprise", and "The Estonia" (Meftah, 1994) with a large number of casualties. In this work, the author will focus on the last point of the suspected factors that cause failure in merchant ships built with Grade A plate steel: inadequate mechanical properties of structural steel at service temperature. It has been reported as well that the risk of failure due to fracture increases rapidly after the vessel has been in service for approximately 8 years (British Steel plc for the Health and Safety Executive, 1997) this may be due to the significant development of fracture initiation sites.

Specifications for the construction of bulk carriers, (IACS, 1979-2, Randerson and Morrison, 1989, Lloyds Register, 1997), developed a classification of grade of plate steels for the construction of merchant ships in terms of Charpy impact energy values which is based on: the dimensions of ships, the operating temperature, and stress concentration zones for most of the plates. Table 1.1 shows the classification of graded plate steels used for the construction of merchant bulk carriers. From table 1.1, it is clearly shown that Grade A plate steels have no minimum specifications in terms of Charpy impact energy values for the constructions of merchant ships, even when the proportion of Grade A plate steel for the construction of such structures is large (Randerson and Morrison, 1989): from 80 to 85% in large vessels and 95% in

small and intermediate sized ships. Grade A plate less than 25 mm thick can be supplied and used without any toughness requirement, so it is possible to construct the hull of a ship entirely from Grade A steel provided the plate is less than 25 mm thick and the length of the ship is less than 250 m (Randerson and Morrison, 1989). According to IACS (IACS, 1979-2), Grade A steel less than 50 mm thick (and Grade B less or equal to 25 mm thick) does not require a minimum Charpy V-notch impact energy.

Table 1.1 – Classification of graded ship steels.

GRADE	TEMPERATURE (°C)	CVN (Joules) Longitudinal / Transverse	
A	None required	None Required	
B	0	27[(a)]	20
D	–10	27	20
E	–40	27	20
CVN tests are generally not required for grade B steel with a thickness of 25 mm or less.			

Recently Lloyds Register (Lloyds Register, 1997) included a Charpy impact energy requirement for Grade A plates of 27J in the longitudinal direction and 20J in the transverse direction at room temperature (+25°C). According to a survey by British Steel plc for the Health and Safety Executive (British Steel plc for the Health and Safety Executive, 1997) most ships operate in sea water at temperatures below +25°C. This survey also reports that ships operate at 0°C and above for 97% of their life, so 0°C is therefore commonly the accepted design temperature. (British Steel plc for the Health and Safety Executive, 1997). Ships for Arctic seas are exposed to lower temperatures, but 0°C is usually taken as the design temperature and the steels used for such conditions need to fulfil a Charpy energy value. It can be shown that the possibility of cleavage initiating brittle fracture in ships fabricated with Grade A plate steel is therefore a real possibility as such structures fabricated with this steel may be subjected to low temperature conditions. This shows the increasing concern about the susceptibility of Grade A ship steel plate to brittle fracture.

1.2 Fracture toughness requirement of steels to prevent fracture in merchant ship structures.

Charpy tests results, reported in Marine Investigation Reports (Welding, 1979-2, Sumpter and Caudrey, 1995, Sumpter, 1991, British Steel plc for the Health and Safety Executive, 1997,

British Steel Limited Swinden Technology Centre Health and Safety Executive, 2000-2001, Transportation Safety Board of Canada, 2002) showed that the average of CVN impact energy of Grade A steel available worldwide is often quite high. Sometimes it behaves in a brittle fracture manner, rather than ductile fracture, even if the grain size of these steels is relatively small, around $10\,\mu m$ (British Steel Limited Swinden Technology Centre Health and Safety Executive, 2000-2001, British Steel plc for the Health and Safety Executive, 1997, Materials Laboratory, 1997). Based on the high values of CVN impact energy, ship constructors, and on classification societies expect and depend upon Grade A plate steel having a fracture toughness that is sufficient for all operational conditions, but without specifications, we cannot ensure adequate fracture toughness and damage tolerance cannot be ensured in the plate.

Some researchers have proposed a minimum fracture toughness value for Grade A plate steel to sustain structural integrity in ships. The maximum nominal stress in the shell side of the vessels is typically $100N/mm^2$ (Sumpter, 1991) but can reach yield due to the presence of stress concentrations or dynamic loading. Maximum stress intensity factors, including applied and residual stress, are typically $125MPa\sqrt{m}$ which according to Sumpter (Sumpter and Caudrey, 1995) assure structural integrity. The strain rates in such structures are typically from 10^{-2} to 10^{-3} s^{-1}, but dynamic fracture toughness tests have much higher strain rates, the strain rate in Charpy tests is about $\dot{\varepsilon} = 10^3 s^{-1}$.

The effect of the strain rate for the nucleation of cleavage fracture may affect the microstructures for cleavage fracture nucelation. The analysis of the microstructure for cleavage fracture, along with the development of modern models for fracture analysis are needed for a better understanding of the fracture process of this steel, especially at micro level where all the conditions prior to failure take place. Sumpter (Sumpter and Caudrey, 1995) proposed a minimum toughness of $125MPa\sqrt{m}$ for a temperature of 0ºC and a loading rate of $10^4 MPa\sqrt{\mathrm{m}}\, s^{-1}$ to guarantee structural integrity given the applied and residual stress levels likely to be present in a normal ship. Fracture toughness results of (Sumpter and Caudrey, 1995) provided very reasonable results for Grade A but as mentioned above, even when the material shows reasonably high toughness values, the susceptibility of the steel to brittle fracture is high. Further investigations at micro-level of the fracture process of Grade A are proposed in this work in order to understand the fracture process of Grade A ship plate steels in the transition region and the microstructures leading to ductile and brittle fracture.

The examples of cracks developed in merchant ships (section 1.1), show the need for the development of physically based models to study the susceptibility of the material to cleavage

fracture. Between the techniques available to the date to study cleavage, the finite element method has been extensively used for modelling cleavage of a huge variety of materials. But conventional finite element methods are still limited for combined modelling ductile and cleavage fracture. Therefore, for effective modelling of fracture, the development of modern models which address the micromechanics of ductile and brittle fracture in a single model is needed. Consequently a model which can include the micromechanics of ductile and cleavage fracture is needed to study the fracture response of steels used for the construction of merchant ships.

Any novel modelling strategy must be physically based on the damage mechanics for each fracture process. It is well established that MnS inclusions nucleate microvoids in the ductile fracture process (Franklin, 1969). But different microstructures have been associated for the nucleation of microcracks (Gibson et al., 1991, Druce et al., 1992, Zhang and Knott, 2000, Rosenfield et al., 1983, Rosenfield and Shetty, 1973, Tanguy et al., 2005),(Smith, 1968, Smith, 1996, Curry, 1980, Valiente et al., 2005, Liu, 1982). Therefore it can be seen that it is vital to perform research work to investigate the microstructures for the nucleation of microcracks in order to develop a more realistic model which includes the microstructures for the nucleation of microcracks of the steel under analysis. Therefore one of the main aims of the present research work is to investigate the microstructures associated with the nucleation of cleavage fracture for the Grade A ship steel under analysis. This will be done by performing extensive metallographic work of the appropriate laboratory specimens tested in the ductile–brittle transition region of the steel.

Recently an hybrid modelling strategy based on a combination of cellular automata and finite element analysis (CAFE model) has been proposed by Shterenlikht (Shterenlikht, 2003) for the simulation of the ductile–brittle transition in steels. This model has incorporated the micromechanics of ductile and brittle fracture via two cellular automata arrays in a single model. The two cellular automata arrays were created inside the structure of the finite elements to carry on all the material information of interest. But this CAFE model can be extended to incorporate all the microstructures which play a vital role in the development of fracture in engineering structures at micro–cellular level. The microstructural response of the material can be visualized at cellular level by the use of a visualization program. This gives a great tool for the visualization of the response of the model not only at finite element level but also at micro structural level. This property is very important because now it is possible to simulate and visualize distributions of microvoids and microcracks at micro–cellular level which is essential in order to validate the numerical results with experimental data at cellular and finite element level. Consequently, because of the described advantage of the CAFE model, this model will be extended for the modelling of cleavage and ductile fracture of a Grade A ship plate steel. This in order to give

some recommendations about the use of Grade A ship plate steels for the construction of merchant ships, specially when the intention is to navigate in cold water.

1.3 Conclusions.

It can be concluded that some Grade A Ship plates steel appear to have insufficient toughness to sustain structural integrity when navigating in cold water. The present sections also show the importance for studying the development of fracture initiation sites in order to understand the toughness properties of Grade A ship plates steel.

1.4 References.

BRITISH STEEL LIMITED SWINDEN TECHNOLOGY CENTRE HEALTH AND SAFETY EXECUTIVE (2000-2001) Offshore Technology Report OTO-2000 001.

BRITISH STEEL PLC FOR THE HEALTH AND SAFETY EXECUTIVE (1997) Literature Review of the Fracture Properties of Grade A Ship Plate: OTH 95 489.

CURRY, D. A. (1980) Cleavage micromechanisms of craks extesion in steels. *Metal Science,* 14, 319-326.

DRUCE, S., GIBSON, G. & CAPEL, M. (1992) Micromechanical control of cleavage fracture in an A508 steel class 3 pressure vessel steel. *In: Ernst H, Saxena A, McDowell D, editors. Fracture Mechanics: Twenty Second Symposium, vol. I. ASTM STP 1131.*, 682-706.

GIBSON, G., CAPEL, M. & DRUCE, S. (1991) Effect of heat tratment on the fracture toughness transition properties of an A508 Class 3 steel. *In: Blauel J, Schwalbe K - H, editors. Defect assessment in components - fundamentals and applications, ESIS/EGF9. Mechanical Engineering Publications.*, 587-611.

IACS (1979-2) Requirements for Normal and High Strength Hull Structural Steel.

LIU, Z. (1982) Cleavage fracture initiated by pearlite packets. *Iron Steel,* 17, 12.

LLOYDS REGISTER (1997) Rules and Regulations for the Classification of Ships.

MATERIALS LABORATORY, E. S. N. R., CROYDON, CR0 2DS (1997) Investigation of Toughness Properties of Grade A Ship Plate. 97-3353.

MEFTAH, M. M. (1994) Fatigue crack propagation in A-Grade ship plate material. *Mastery thesis, University of Sheffield.*

RANDERSON, K. & MORRISON, W. B. (1989) Materials for Ships, British Steel Technical, Swinden Laboratories.

ROSENFIELD, A. & SHETTY, D. (1973) Cleavage fracture of steel in the upper ductile-brittle transition region. *Engng Fract Mech,* 17(5), 461-470.

ROSENFIELD, A., SHETTY, D. & SKIDMORE, A. (1983) A fractographic observations of cleavage initiation in the ductile-brittle transition regions of a reactore-pressure-vessel steel. *Met Trans,* 14, 1934-1937.

SHTERENLIKHT, A. (2003) 3D CAFE modelling of transitional ductile-brittle fracture in steels. *Ph.D Thesis, Department of Mechanical Engineering, University of Sheffield.*

SMITH, E. (1968) Cleavage fracture in mild steel. *The International Journal of Fracture Mechanics,* 4, 131-145.

SMITH, H. (1996) The nucleation and growth of cleavage microcracks in mild steels. *Proc. Conf. Physical Basis of Yield and Fracture, Inst. Phys. and Phys. Soc., London*, 36.

SUMPTER, J. D. G. (1991) Fracture Avoidance in Submarines and Ships, Advances in Marine Structures - 2. *Proceeding of International Conference, Elsevier Applied Science.*

SUMPTER, J. D. G. & CAUDREY, A. J. (1995) Recommended fracture toughness for ship hull steel and weld. *Marine Structures,* 8, 345-357.

TANGUY, B., BESSON, J., PIQUES, R. & PINEAU, A. (2005) Ductile to brittle transition of an A508 steel characterized by Charpy impact test. Part I: experimental results. *Engineering Fracure Mechanics,* 72, 49-72.

TRANSPORTATION SAFETY BOARD OF CANADA (2002) Marine Investigation Report, Report Number M02L0021, Hull Fracture Bulk Carrier Lake Carling Gulf of St. Lawrence, Quebec.

VALIENTE, A., RUIZ, J. & ELICES, M. (2005) A probabilistic model for the pearlite-induced cleavage of a plain carbon structural steel. *Engineering Fracure Mechanics,* 72, 709-728.

WELDING, I. W. P. O. M. A. (1979-2) IACS Requirements for Normal and High Strength Hull Structural Steel, IACS.

ZHANG, X. & KNOTT, J. (2000) The statistical modelling of brittle fracture in homogeneous and heterogeneous steel microstructures. *Acta Mater,* 48, 2135-2146.

Chapter II

Literature review

Fracture propagation models have been developed in the last decades to characterize the ductile and brittle fracture process. Most of these models use the local approach, which takes into account only a small volume ahead of the crack tip, the most loaded regions, and the physical fracture models corresponding to the fracture mechanisms. The most used failure models for ductile fracture analysis are the Rousselier and Gurson's damage models. Beremin weakest link statistical model and the local fracture stress are the most used models for cleavage fracture. In these fracture models microstructural and damage parameters of materials are needed as they are material based models.

2.1 The local approach.

In the local approach only a small volume of material ahead of the crack tip or the region of interest is taken. In this region all the micromechanisms for fracture initiation and propagation are developed. This volume of material must be included in the plastic region of the crack tip. This makes this technique very appropriate for modelling fracture (Rousselier, 1987, Mudry, 1987, Bordet et al., 2005a, Bordet et al., 2005b, Wu and Knott, 2004, Eripret and Rousselier, 1994). This approach, for fracture characterization (Jacques and Steven, 1998) is generally defined by the computation of the combination of stresses and deformations in the most loaded regions of mechanical structures. Therefore this technique is very appropriate for modelling fracture initiation and propagation in materials (Kotrenchko et al., 2007, Knott, 2008). The local approach is geometry–independent as opposed to the single and two parameter methods of fracture mechanics from which the toughness value depends on a geometric factor characteristic of the geometry of the specimens. Other advantage of the local approach is that different fracture mechanisms such as ductile fracture, brittle fracture, creep, fatigue, corrosion can be modelled with the local approach. Because in the present work the author is dealing with ductile and brittle fracture, the literature review will be focused on ductile and brittle fracture.

In ductile fracture, many material failure models have been proposed. The most used are the Gurson (Gurson, 1977a) and the Rousselier damage models (Rousselier, 1987). Gurson damage model was developed based on a micromechanical description of the porosity in materials. Rousselier damage model was derived from thermodynamic considerations (Bilby et. al., 1995 and Besson et. al., 2001). A single scalar damage parameter is used in both damage models to simulate the initiation and growth of microvoids to characterize the evolution of porosity.

In cleavage fracture the proper definition of the microstructures for the nucleation of cleavage are essential in the derivation of the local approach. The local approach was derived from Weibull statistics, this means that it is needed a state of stress intensification on a local level in order to produce cleavage. These high stresses must be located in a distance around the peak position of the normal tensile stress located in the high stressed volume of a material. This region of is usually considered the active zone for cleavage fracture initiation because the stresses are high enough to nucleate microcracks which can propagate along the notch plane (Wang and Chen, 2000, Tanguy et al., 2003, Griffiths and Owen, 1971, Ritchie et al., 1973, Lin et al., 1986). In the local approach, once identified the micromechanical damage model parameters with laboratory specimens, which are considered material constants, for ductile or brittle fracture, they are transferable to real or large structures. Therefore such damage model parameters can be used to predict the fracture response of real engineering structures.

2.2 Ductile fracture analysis and modelling.

The porosity observed on ductile fracture surfaces on tensile specimens, Charpy tests, and in general in fracture toughness tests, has been associated with the distribution of hard particles in the matrix of materials (Tipper, 1949, Puttick, 1959, Rogers, 1960, Beachem, 1963, Gurland and Plateau, 1963, Bluhm and Morrissey, 1966, Liu and Gurland, 1968, Hayden and Floreen, 1969, Gladman et al., 1970, Gladman et al., 1971, Gurland, 1972, Goods and Brown, 1979). Advance in the understanding of the ductile fracture process has lead to the conclusions that ductile fracture process involves the following steps: nucleation and growth of microvoids (McClintock, 1968); internal necking of cavities (Thomason, 1968) that is caused by the large growth and coalescence of microscopic voids (Rice and Tracey, 1969). Then it was concluded that fracture propagation is via the nucleation and growth of voids (Gurson, 1977a). From these observations it was concluded that ductile fracture involves three related stages: microvoids nucleation, microvoids growth and microvoids coalescence (Bates, 1984, Thomason, 1990, Gladman, 1997, Thomason, 1998).

The growth of microvoids can be volumetric or by the change of their shape. In this process the triaxiality states of stresses influence strongly on the shape of microvoids, this consequently affects the strain to fracture. In tensile tests for example, microvoids generally grow in the direction of tensile stress prior to necking, but the onset of necking changes the uniaxial stress state to triaxial state (Bridgman, 1952) causing volumetric growth (Gladman, 1997, Thomason, 1998) and consequently the strain to rupture will be smaller. The process of microvoids coalescence involves internal necking of microvoids in the volume of material with internal porosity (Thomason, 1981, Puttick, 1959, Rhines, 1961, Bluhm and Morrissey, 1964). The ultimate stage in fracture propagation is the failure of the submicron intervoid ligament by shearing along crystallographic planes.

The development of physically based models for modelling ductile fracture has been slow due to the different stages of ductile fracture described above. This is because each stage of ductile fracture requires a separate physical model. Therefore such models must take into account the size, shape and spacing of the voids which are the result of the whole history of strain in engineering structures (McClintock, 1968). The plastic strain and the hydrostatic stress are the main factors that lead to failure; therefore ductile fracture model must incorporate the whole history of these main factors. Between the ductile damage models available in the literature, the most used physical constitutive damage model which defines an initial void volume fraction are: Gurson–Tvergaard–Needleman (Gurson, 1977a) and Rousselier (Rousselier, 1981, Rousselier, 1986) damage models. These two models can be modified according to the physical behaviour

of mechanical structures. A review of some of the most used models for ductile fracture modelling is described below.

2.2.1 McClintock model.

McClintock developed a physical model for the growth of microvoids (McClintock, 1968). He considered a three–dimensional array of cylindrical voids with an elliptical cross–section in a material. In this array of voids, the main axes of the voids are parallel to the principal stress axes. The condition for fracture propagation was by the contact of neighbouring voids. In the three–dimensional array of voids, the voids have their cylindrical axes parallel to the z direction. The two semi axes were designated as a and b. If the microvoids growth in the b direction, then the formulation for the onset of fracture is expressed in the following form:

$$\frac{d\eta_{zb}}{d\varepsilon_{eq}} = \frac{1}{\ln F_{zb}^{f}}\left[\frac{\sqrt{3}}{2(1-n)}\sinh\left(\frac{\sqrt{3}(1-n)}{2}\frac{\sigma_a+\sigma_b}{\sigma_{eq}}\right)+\frac{3}{4}\frac{\sigma_a+\sigma_b}{\sigma_{eq}}\right] \qquad 2.1$$

where $\frac{d\eta_{zb}}{d\varepsilon_{eq}}$ is the damage rate, ε_{eq} = equivalent strain, $d\eta_{zb}$ = damage increment, F_{zb}^{f} is a critical value of the relative growth factor, n is a hardening exponent, σ_a and σ_b are the two principal stresses at infinity and σ_{eq} is the equivalent stress. It can be seen that according to this model, void growth is a smooth process until final rupture, but as pointed out by Thomason, Liu, Gurland, Hayden and Floreen (Thomason, 1968, Thomason, 1981, Thomason, 1998, Liu and Gurland, 1968, Hayden and Floreen, 1969); the onset of failure by void coalescence is essentially due to a loss of stability. Therefore this model does not properly simulate the growth of microvoids because the stress history over the porous region and the rate of microvoids growth are not included. This makes the model limited for the true modelling of void growth. The major contribution of this model is that it demonstrates that fast decrease of failure is caused by the increase of stress triaxiality.

2.2.2 Rice–Tracey model.

Rice and Tracey (Rice and Tracey, 1969) considered the growth of an isolated spherical microvoid in infinite space under uniform stress state. Their equation for the growth of the microvoid under a high triaxiality stress state is:

$$D = 0.283 \cdot \exp\left(1.5\frac{\sigma_m}{\sigma_{eq}}\right) \qquad 2.2$$

In this model, D is the ratio of the strain rate on the surface of a void to the strain rate at infinity, σ_m is the mean stress and σ_{eq} is the equivalent stress. It can be seen that, as the previous model (equation 2.1), Rice and Tracey model does not takes into account void interaction in any way. The equation cannot predict the strain at fracture because it does not record the stress history over the region of the void. In equation 2.2, if $\sigma_m = 0$, then the void acts only as a constant stress concentrator. As in previous model, this model does not include the distortion of the voids. According to Liu, Gurland, Hayden and Floreen (Liu and Gurland, 1968, Hayden and Floreen, 1969), the distortion of the voids must be included in ductile models because it has a big contribution in the process of void growth. Therefore the use of equation 2.2 is limited for the simulation of damage in ductile fracture.

2.2.3 Lemaitre model.

Lemaitre (Lemaitre, 1985, Lemaitre, 1996) formulated a thermodynamically damage model to account for porosity or other forms of damage. Lemaitre assumed a small volume of material containing defects (microvoids or microcracks). If the intersection of this volume of material with a plane defined by a normal vector $\vec{n}$, and S is the area of intersection of voids and cracks of the volume by this plane is $S_D(\vec{n})$, then the damage variable is defined as:

$$D(\vec{n}) = \frac{S_D(\vec{n})}{S} \qquad 2.3$$

Since $0 \le S_D(\vec{n}) \le S$ then $0 \le D(\vec{n}) \le 1$. If $D = 0$, it means that the material has no load–bearing capacity, therefore fracture propagation occurs. If D does not depend on $\vec{n}$ then the damage is considered isotropic and the damage variable is $D = \frac{S_D}{S}$. In this case the damage variable models and effective density of microdefects. It can be seen that in Lemaitre's model, any strain constitutive equation for a damage material can be derived in the same way as for an undamaged material by replacing the usual stress by the effective stress (Lemaitre, 1996). Based on this principle Lemaitre derived an equation for isotropic damage, this equation has the following form:

$$\dot{D} = \left[\frac{A^2}{2ES_o} \left(\frac{2}{3}(1-\upsilon) + 3(1-2\upsilon)\left(\frac{\sigma_m}{\sigma_{eq}} \right)^2 \right) \left(\varepsilon_{eq}^p \right)^{2/n} \right]^{s_o} \varepsilon_{eq}^p \qquad 2.4$$

where A and n are material properties in the Ramberg–Osgood hardening law expressed by:

$\varepsilon^P = \left(\vec{\sigma} / A \right)^n$, S_o and s_o are parameters in the damage evolution law:

$$\dot{D} = \left(\frac{-y}{S_o} \right)^{s_o+1} \dot{\varepsilon}_{eq}^p \qquad 2.5$$

In equation 2.5, the term $-y$ is called the damage strain energy release rate (Lemaitre, 1985). The above formulation shows that Lemaitre's damage model is fundamentally a continuum softening theory where defects are introduced via the damage variable D. But the use of this approach for modelling ductile damage is then very questionable. This is because the model does not takes into account the void volume fraction growth rate and the micromechanical process of joining microvoids which are the micromechanism for controlling damage. From the ductile damage models described up to know, it can be seen that none of them incorporates a function to describe the rapid loss of stress–carrying capacity which account the process of void coalescence. The models which incorporate such function are the Gurson and Rosselier ductile damage models, both models are described in the following sections.

2.2.4 Gurson–Tvergaard–Needleman model.

Gurson (Gurson, 1977a) developed a methodology to obtain an approximate yield surface for a material containing microvoids which is based on the idea of Berg (Berg, 1970) who pointed out that localisation occurs when the hardening behaviour of the matrix material is overweighed by softening due to the dilation of voids. The theory describes the mechanisms to characterize the process of void growth and coalescence driving the material failure. For spherical voids the yield function is originally expressed in the form of the yield potential:

$$\Phi = \left(\frac{\sigma_{eq}}{\sigma_y} \right)^2 + 2f \cdot \cosh\left(\frac{3\sigma_m}{2\sigma_y} \right) - 1 - f^2 = 0 \qquad 2.6$$

where σ_{eq} is the macroscopic effective von Mises equivalent stress; σ_y is the macroscopic material yield strength; σ_m is the mean stress, f is the void volume fraction. This condition is reduced to the classical von Mises yield criteria if $f = 0$. It can be seen that equation 2.6 modifies the von Misses yield condition by the incorporation of damage via the void volume fraction parameter. The change in void volume fraction is described as:

$$\dot{f} = \dot{f}_g + \dot{f}_n \qquad 2.7$$

where $\dot{f}$ is the rate of release of void volume fraction, $\dot{f}_g$ is the rate of growth of existing voids, $\dot{f}_n$ is the void nucleation rate. For the growth of voids Gurson (Gurson, 1977b) proposed only dilation in the following form:

$$f_o = (1-f)\varepsilon_{ij}^p I_{ij} \qquad 2.8$$

where ε_{ij}^p is a plastic strain rate, I_{ij} is the second–order unit tensor. A variety of nucleation models have been proposed by Gurson (Gurson, 1977b):

$$\dot{f}_n = f_\varepsilon\left(\varepsilon_{eq}^p\right)\dot{\varepsilon}_{eq}^p \qquad 2.9$$

where f_ε is the void nucleation intensity, ε_{eq}^p is the equivalent plastic strain. It is well accepted that microvoids nucleate from large MnS inclusions at the beginning of plastic deformation. Therefore it can be assumed that microvoids are nucleated as soon as plasticity begins. The amount of microvoids is expressed by the initial void volume fraction, f_o, (Zhang et al., 2000).

When most microvoids are nucleated from smaller particles, for example carbides, a continuous nucleation mechanism is more suitable (HKS, 2001, Brocks et al., 196, Guennouni and Francois, 1989, Lautridou and Pineau, 1981, Besson et al., 2001).

When Yamamoto (Yamamoto, 1978) applied equation 2.6 to the analysis of a shear band developed on the fracture surfaces of fracture toughness specimens, he found that for a material without defects, equation 2.6 predicts unrealistically large strains at localisation. Therefore he concluded that defects must be included in the model in order to achieve

localisation at reasonable strains. This idea was explored by Tvergaard (Tvergaard, 1982a, Tvergaard, 1982b), Tvergaard introduced two adjustable parameters in equation 2.6, q_1 and q_2, resulting the following equation:

$$\Phi = \left(\frac{\sigma_{eq}}{\sigma_y}\right)^2 + 2q_1 f \cdot \cosh\left(\frac{3q_2\sigma_m}{2\sigma_y}\right) - [1 + q_1 f^2] = 0 \qquad 2.10$$

Tvergaard (Tvergaard, 1981, Tvergaard, 1982b) applied equation 2.10 to model the experimental results of Gladman (Gladman et al., 1970, Gladman et al., 1971). Tvergaard found that with $q_1 = 1.5$ and $q_2 = 1$ it was possible to improve about 50% the simulation results of notch tensile specimens. In order to improve numerical results with the use of equation 2.10, some authors introduced another q parameter (HKS, 2001) resulting the following equation:

$$\Phi = \left(\frac{\sigma_{eq}}{\sigma_y}\right)^2 + 2q_1 f \cdot \cosh\left(\frac{3q_2\sigma_m}{2\sigma_y}\right) - [1 + q_3 f^2] = 0 \qquad 2.11$$

q_1, q_2 and q_3 have been considered as true material constants of the material under simulation with equation 2.11 (Tvergaard, 1982b, Tvergaard, 1990, HKS, 2001). But experimental evidences have shown that they depend on the triaxiality level (Pardoen and Hutchinson, 2000, Andrews et al., 2002). The q parameters are generally set to the following values: $q_1 = 1.5,\ q_2 = 1,\ q_3 = q_1^2$ for ferritic steels (Tvergaard, 1981, Tvergaard and Needleman, 1984). One of the main advantages of equation 2.11 it that the q parameters can be adjusted to fit experimental data.

From the original formulation of Gurson's model, it can be seen that the model can only simulate microvoids nucleation and dilation. But the model does not takes into account the coalescence process. Tvergaard introduce the function $f^*(f)$ to model the rapid loos of stress–carrying capacity in an attempt to account for void coalescence (Tvergaard and Needleman, 1984). The $f^*(f)$ function has the form:

$$f^*(f) = \begin{cases} f & \text{for } f \le f_c \\ f_c - \dfrac{f_u^* - f_c}{f_f - f_c}(f - f_c) & \text{for } f > f_c \end{cases} \qquad 2.12$$

where f_c is a critical value of void volume fraction, the value at which a rapid loss of load–bearing capacity begins; f_f is void volume fraction at final fracture and $f_u^* = 1/q_1$. For a ferritic steel, the typical values f_c and f_f are: $f_c = 0.15$ and $f_f = 0.25$ (Tvergaard and Needleman, 1984).

Gurson's model includes a total number of nine parameters; three parameters (ε_n, f_n, s_n) are used to model void nucleation, three parameters (f_0, f_c, f_f) describe the evolution of void growth up to coalescence and final failure and the three remaining parameters (q_1, q_2, q_3) characterize the yield behaviour of the material (Bernaur and Brocks, 2001).

The physically based damage model described above is generally called Gurson–Tvergaard–Needleman (GTN) model. Good correlation between numerical and experimental data has been obtained with this model (chapter IV). The limitation of the model is that it predicts strain to fracture that is much higher than that observed in experiments. Thomason and Zhang (Thomason, 1981, Thomason, 1985a, Zhang et al., 2000) pointed out that the excessive strain to fracture is due to the fact that the model takes into account only the homogeneous deformation. In this model it can be noted that the voids were effectively substituted by a continuous porosity field. Therefore the effect of voids in this model is through the pressure–dependent yield surface.

In Gurson's model, fracture propagates when the damage parameter reaches its critical value designated by f_c (threshold of rapid loss of stress carrying capacity). The evolution of the void volume fraction is partly due to the growth of existing voids and partly due to the nucleation of new voids. The latter is suggested to follow a Gaussian law as suggested by Chu and Needleman (Chu and Needleman, 1980) and approved by Kwon and Asaro (Kwon and Asaro, 1990):

$$\dot{f} = (1-f)\,\dot{\varepsilon}_{ij}^{pl}\,\delta_{ij} + \frac{f_N}{S_N\sqrt{2\pi}}\exp\left[-\frac{1}{2}\left(\frac{\varepsilon_M^{pl}-\varepsilon_N}{S_N}\right)^2\right]\dot{\varepsilon}_M^{pl} \qquad 2.13$$

where: $\dot{\varepsilon}_{ij}^{pl}$ is the plastic part of the macroscopic strain increment, δ_{ij} the Kronecker delta, $\dot{\varepsilon}_M^{pl}$ the equivalent plastic strain increment in the matrix, f_N is the volume fraction of void nucleating particles, ε_N the mean strain for nucleation, S_N the corresponding standard deviation. The

final void volume fraction at total failure is represented by f_f, the damage parameters are commonly regarded as material constants.

Another parameter is the cell size, L_c, which represents the spacing of large inclusions in the steel. These parameters should be determined to perform damage simulations. The initial void volume fraction can be measured with fractography analysis on the fracture zone of tensile tests with scanning electron microscopy by measuring the distance between voids. It can also be calculated from Franklin's formula (Franklin, 1969) with knowledge of the percent of sulphur (S) and manganese (MnS) content in the steel, Franklin's formula has the form:

$$f_o = f_v \frac{(d_x d_y)^{1/2}}{d_z} \qquad 2.14$$

$$f_0 = 0.054\left(S\% - \frac{0.001}{Mn\%}\right) \qquad 2.15$$

where: d_x, d_y and d_z are the average dimensions of the inclusions. Assuming spherical inclusions, equation 2.14 gives $f_o = f_v$. The relative density (ratio of solid volume to total volume of material) can be obtained with next equation:

$$r = 1 - f_o \qquad 2.16$$

In a program of simulations performed for a European numerical round robin using different damage models implemented in different finite element programs (Bernaur and Brocks, 2001) the authors applied Franklin's formula to obtain the initial void volume fraction, f_o, it was shown that this value was too small in order to obtain experimental vs numerical correlation. The authors had to fit this parameter by trial and error to a higher value of the initial void volume fraction which was very different to that obtained with Franklin's formula. Hashemi showed the same trend (Hashemi, 2004) when applying Franklin's formula to obtain the f_o in a high toughness pipeline steel. These examples show that Franklin's formula gives only an initial value of f_o to start the simulations but finally this value must be fitted by trial and error in order to obtain numerical vs experimental correlation in finite element simulations of fracture propagation. The application of this material damage model for ductile material is now well documented (Steglich and Brocks, 1997, Besson et al., 2001, Besson et al., 2003) for simulation

of ductile fracture propagation. Yamamoto (Yamamoto, 1978) showed that Gurson model gives realistic critical strains only after significant changes in void volume fractions.

2.2.5 Rousselier model.

Rousselier proposed a thermodynamically consistent ductile damage model for modelling the growth and coalescence of microvoids (Rousselier, 1981). The plastic potential of Rousselier's damage model is described in the following equations. In equation 2.17 it can be seen that the von Misses equivalent stress is modified by the incorporation of the damage variable β.

$$\frac{\sigma_{eq}}{\rho} - H\left(\varepsilon_{eq}^{p}\right) + B(\beta) D \exp\left(\frac{\sigma_m}{\rho\sigma_1}\right) = 0 \qquad 2.17$$

where:

$$\dot{\beta} = \dot{\varepsilon}_{eq}^{p} D \exp\left(\frac{\sigma_m}{\rho\sigma_1}\right) \qquad 2.18$$

$$\rho(\beta) = \frac{1}{1 - f_o + f_o \exp\beta} \qquad 2.19$$

$$B(\beta) = \frac{\sigma_1 f_o \exp\beta}{1 - f_o + f_o \exp\beta} \qquad 2.20$$

$$\sigma_m = \sigma_m^e - 3K\Delta\varepsilon_m^p \qquad 2.21$$

$$\sigma_{eq} = \sigma_{eq}^e - 3G\Delta\varepsilon_{eq}^p \qquad 2.22$$

$$\sigma_m^e = \frac{1}{3}\sigma_{ij}^e \qquad 2.23$$

$$\sigma_{eq}^e = \sqrt{\frac{3}{2} S_{ij}^e S_{ij}^e} \qquad 2.24$$

$$S_{ij}^{e} = \sigma_{ij}^{e} - \sigma_{m}^{e}\delta_{ij} \qquad 2.25$$

$$\sigma_{ij}^{e} = E_{ijkl}\varepsilon_{kl} \qquad 2.26$$

$$\varepsilon_{kl} = \varepsilon_{ij}^{e}(t_i) + \Delta\varepsilon_{ij} \qquad 2.27$$

$$\varepsilon_{eq}^{p} = \varepsilon_{eq}^{p}(t_i) + \Delta\varepsilon_{eq}^{p} \qquad 2.28$$

$$\beta = \beta(t_i) + \Delta\beta \qquad 2.29$$

In the model, β is a scalar damage variable and its evolution is determined by equation 2.18. If the material is in the elastic limit then $\beta = 0$; B is the damage function; ρ is a dimensionless density. From equation 2.19 it can be seen that ρ decreases with increasing β; D and σ_1 are considered material constants; f_o is the initial void volume fraction; $H(\varepsilon_{eq}^{p})$ is a term describing the hardening properties of material, in general this is equal to the yield stress of the undamaged material, $H(\varepsilon_{eq}^{p}) = \sigma_Y(\varepsilon_{eq}^{p})$.

The ductile damage model parameters of the damage models described above have to be calibrated in order to be considered true material properties of the material under analysis. In Gurson model, the parameters q_1, q_2 and q_3 are tuned to predict the same void growth as the model of a discrete spherical cavity (Faleskog et al., 1998). The next stage is to tune the critical and final fracture values of the void volume fraction, f_c and f_f, using coalescence mechanics (Faleskog and Shih, 1997). The last step is to tune the finite element cell size, L_D, and the initial void volume fraction, f_o, to reproduce experimental data of fracture tests. The initial value of L_D can be calculated with the used the empirical equations: $L_D = 2N_v^{-1/3}$ (Rousselier, 1987) or $L_D = 5N_v^{-1/3}$ (Rousselier et al., 1989), where N_v is the average number of inclusions per unit volume. Generally Franklin formula (Franklin, 1969), is used to calculate the initial void volume fraction, f_o, which is based on the Mn and S contents of a steel. The Rousselier model, σ_1 is measured with the use of notch tensile specimens with different notch radius (Batisse et al., 1987).

2.3 Modelling cleavage fracture and microanalysis.

There are two types of brittle fracture, intergranular and transgranular. The first is characterized by the crack travelling along the grain boundaries of the microstructures and usually occurs when the phase in the grain boundary is weak and brittle (cementite in iron grain boundaries), figure 2.1a for example. In the latter a crack travels through the grains of the material, the crack changes direction from grain to grain due to the different misorientation angle of grains. When the crack reaches a new grain it may have to find a new path or plane of atoms to travel on.

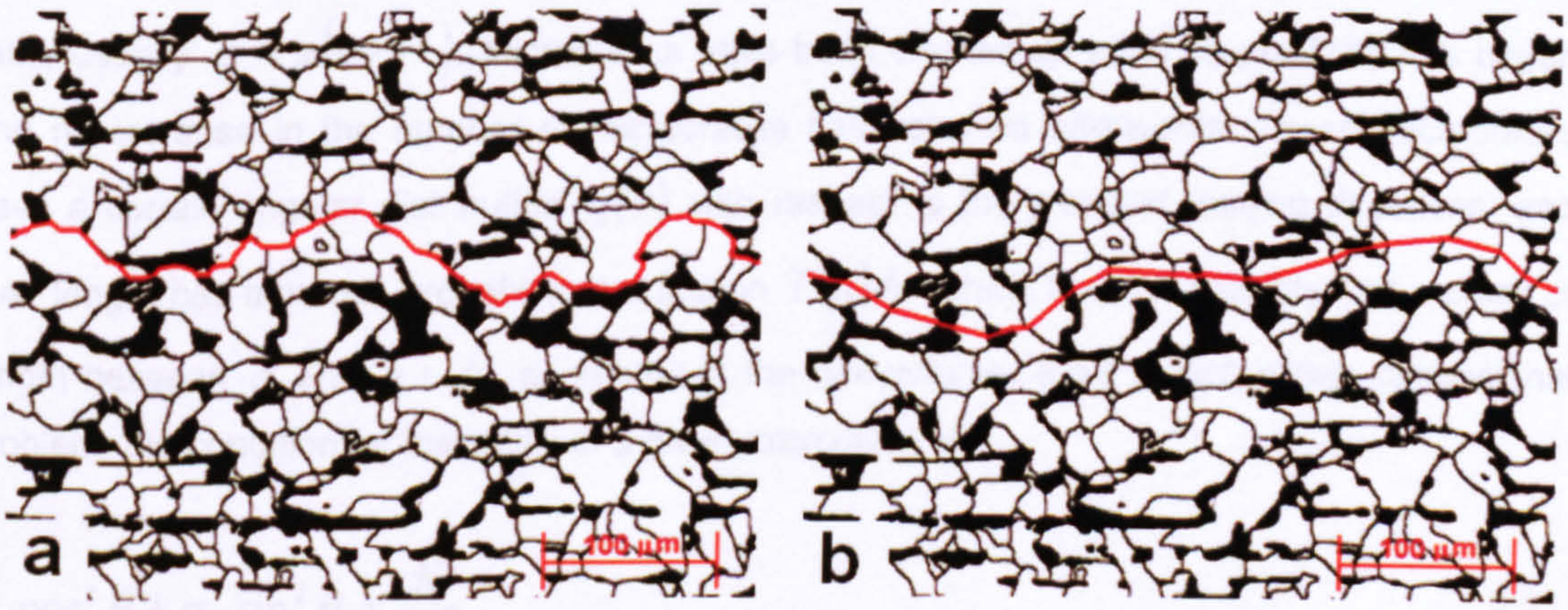

Figure 2.1 – Intergranular fracture (a) and transgranular or cleavage fracture (b).

In most ferritic steels, brittle fracture occurs by either transgranular or intergranular cleavage cracking along well–defined, low index crystallographic planes (Hahn et al., 1960, Knott, 1973). Low strength materials fail by catastrophic brittle fracture as their microstructure do not have the ability to arrest potential microcracks nucleated by grain boundary cracked carbides distributed in the microstructure. Since the work of Griffith (Griffith, 1921, Griffith, 1924), the mechanisms inducing brittle fracture has been the concern of much research work (Averbach et al., 1959, Knott, 1973, Hahn et al., 1960, Hahn, 1984, Thompson and Knott, 1993, Young-Roc Im, 2004, Wang and Chen, 1998). Then it was concluded that an intensification of stresses on a very local region is needed to initiate cleavage. The models incorporating such intensification of stresses are based on the broken of non–metallic inclusions due to the incompatible dislocation gliding in the adjacent crystal, grain boundary cracked carbides, accumulation of dislocations on a sessile plane, twin interactions, incompatible grain boundary sliding, etc. In all these models the generated microcracks are not necessary unstable. The stability is possible if the work required to propagate such microcracks is higher than the work of the stress normal to the microcrack. Mudry (Mudry, 1987) proposed that microcracks are created as soon as plasticity begins, conversely no microcracks exist out of the plastic zone, this criterion has been used extensively for many local approach models. The second step will be the instability of a microcrack, the

instability occurs as soon as microcracks become unstable when the normal stress to the microcracks plane reaches a critical value given by equation 2.30.

$$\sigma_n \approx \frac{k}{\sqrt{a}} \qquad 2.30$$

where $k = \sqrt{E\gamma/\alpha}$ and can be considered as a material constant, a is the size of the microcracks, E is Young's modulus, γ is the energy per unit area required for separation of cleavage plane, α is a numerical constant depending on the exact geometry and Poisson's ratio, usually $\alpha = \pi\left(1-\nu^2\right)$. Microcracks have been created as soon as plasticity has begun and no increase in the number of microcracks has occurred afterwards. These microcracks have a certain angular distribution $g(\theta)$ with respect to the principal loading directions; and their length has a certain probability distribution $P(a)da$ which is the probability that a crack of length between a and $a+da$ is present in the unit volume. If we sketch a two–dimensional problem, the condition for instability of a given microcrack is:

$$\sigma_1 \cos^2\theta + \sigma_2 \sin^2\theta = \frac{K}{\sqrt{A}} \qquad 2.31$$

where σ_1 and σ_2 are the first and second principal stresses. Therefore, the probability of non failure of a unit volume will be given by the following formula:

$$p_{nF} = \iint_{S(\sigma_1,\sigma_2)} P(a)g(\theta)dad\theta, \qquad 2.32$$

where $S(\sigma_1,\sigma_2)$ is the area in the (θ,a) plane such that $\left(\sigma_1 \cos^2\theta + \sigma_2 \sin^2\theta\right)\sqrt{a} < k$. Mudry (Mudry, 1987) explained the influence of the second principal stress σ_2 where the angular distribution $g(\theta)$ will depend on the mechanism creating the microcracks. In bcc metals, there are three different cleavage planes. Therefore, almost no microcracks will exist for $\theta > \pi/4$ as shown in figure 2.2. $g(\theta)$ will depend on the mechanism creating the microcracks. In Smith's model (Smith, 1966) where microcracks are nucleated in carbides, most microcrack were around $\theta = 0$.

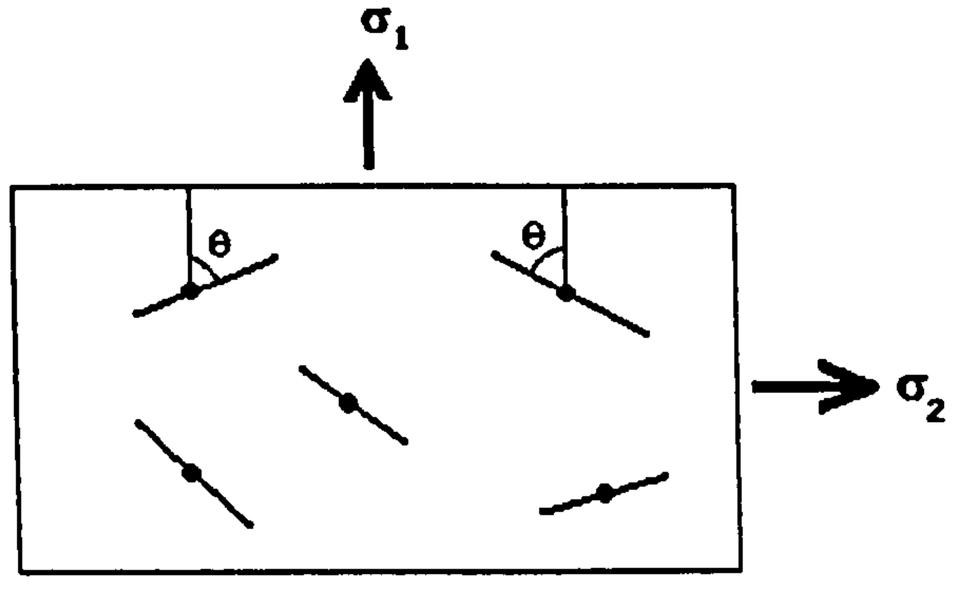

Figure 2.2 – Angular distribution of microcracks.

In these cases, the error involved in neglecting the effect of the angular distribution will be negligible. The probability of non failure will approximately be given by:

$$P_{nF}(\sigma_1) = \int_0^{(k/\sigma_1)^2} P(a)da \qquad 2.33$$

It is only dependent on the maximum principal stress σ_1. No evidence has shown any effect of the second principal stress on the cleavage fracture strength.

2.3.1 Microcrack initiation models.

Cleavage fracture is initiated by a local discontinuity in the most stressed volume of material. A dislocation pile–up at an obstacle, such as a grain carbide, can cleave the boundary of a grain and thus nucleate a microcrack (McMahon and Cohen, 1965, Lin et al., 1987a, Thompson and Knott, 1993). Thus inhomogeneous plastic deformation in the microstructure is always necessary to produce the very high stresses needed to fracture a neighbouring carbide and therefore nucleated microcracks (Smith, 1968, Lin et al., 1987a). The stresses required to generate a microcrack (Hahn et al., 1959) is expressed as follows:

$$\tau = 4.4\frac{\gamma}{na} \qquad 2.34$$

$$\sigma = K\frac{\gamma}{na} \qquad 2.35$$

where τ and σ are the shear and normal stresses accordingly, γ is an effective surface energy, n is the number of dislocations piled up against a grain boundary, a is the atomic

spacing and K is a coefficient depending on the arrangement of the dislocation pile–up. The number of microcracks increases with the applied strain and the number and intensity of dislocation pile–up increases with plastic straining (Gurland, 1972). It is generally accepted that a microcrack can growth if the following condition is satisfied:

$$\sigma_n \geq \sigma_F \qquad 2.36$$

where σ_n is a normal stress acting across the grain–carbide interface and σ_F is the fracture stress (Smith, 1966, Smith, 1968). Smith developed the theory for the fracture stress of a carbide–ferrite particle interface. Then based on Smith's model, Lin (Lin et al., 1987a) derived a similar model to compute the fracture stress for a ferrite–ferrite particle interface. The equations are shown below:

$$\sigma_F^{cf} = \sqrt{\frac{\pi E \gamma_{cf}}{(1-\nu^2)d_c}} \qquad 2.37$$

$$\sigma_F^{ff} = \sqrt{\frac{\pi E \gamma_{ff}}{(1-\nu^2)d_g}} \qquad 2.38$$

where σ_F^{cf} and σ_F^{ff} are the fracture stresses of a carbide–ferrite and a ferrite–ferrite interfaces, γ_{cf} and γ_{ff} are the effective surface energies of a carbide–ferrite and a ferrite–ferrite interfaces, d_c and d_g are carbide and ferrite grain sizes, E is the elasticity modulus and ν is the Poisson's ratio. Ritchie (Ritchie et al., 1973) suggested that equation 2.37 must be satisfied in a distance of the size of two ferrite grain size ahead of the crack tip for cleavage propagation.

2.3.2 Weakest link model.

Beremin (Beremin, 1983) developed the concept of weakest link statistics to provide a frame work for quantifying the relationship between micro and macro scales driving forces to cleavage fracture. Beremin's model considers a small volume of material, V, ahead of the crack tip which is included in the plastic zone. This volume of material contains a distribution of microcracks of different lengths. Catastrophic failure occurs when a microcrack of critical size is found in this volume of material. This microcrack is the weakest link for cleavage fracture to

occur. Therefore the probability of failure is the probability of finding such microcrack. The volume of material, V, can be divided into smaller volumes V_o, but they must be big enough to met the condition of finding a microcrack of critical size. Careful must be paid in the choice of V_o because this volume must be subjected to homogeneous stress state. V_o generally include several grains. Beremin's failure probability has the following form:

$$\Phi = 1 - \exp\left[- \int_0^V \frac{1}{V_o} \int_0^\sigma g(S) dS \right] \qquad 2.39$$

where $g(S)dS$ is the number of microcracks per volume V_o, stresses are required to propagate them between S and $S + dS$. Generally a three–parameter Weibull probability distribution function (Weibull, 1951) is used to express, $g(S)dS$:

$$\int_0^\sigma g(S) dS = \left(\frac{\sigma_1 - \sigma_{th}}{\sigma_u} \right)^m \qquad 2.40$$

in equation 2.40, σ_1 is a maximum principal stress in V_o, m is a shape parameter, σ_u is a scale parameter and σ_{th} is the threshold stress required to propagate a microcrack of critical size. Substituting equation 2.40 into 2.39, the following equation is obtained:

$$\Phi = 1 - \exp\left[- \left(\frac{\sigma_w}{\sigma_u} \right)^m \right] \qquad 2.41$$

where:

$$\sigma_w = \left[\frac{1}{V_o} \int_0^V (\sigma_1 - \sigma_{th}) dV \right]^{1/m} \qquad 2.42$$

Equation 2.42 is usually called the Weibull stress (Beremin, 1983). The Weibull stress model enables scaling of fracture toughness values between crack configuration exhibiting different constraint levels based on equal probabilities of fracture (Gao et al., 2001). Beremin model has been extensively used in the analysis of brittle fracture since its creation (Beremin, 1983, Bernauer et al., 1999, Petti and Dodds, 2003, Xiaosheng and Dodds, 2005).

2.3.3 Crack arrest.

Crack arrest has not been investigated profoundly because in many cases the arrest of brittle cracks does not occur. An example can be seen in the structure of the hull of the merchant ship shown in figure 1.2 of section 1.2. In this figure a crack of 6 metre long was developed on the port side of the shell. The poor properties of crack arrest of the plate and the high level of stresses developed in the local area of the ship structure promoted the development of such a big crack. In some cases a brittle crack would not stop until it reaches the end of the structure producing catastrophic failures. A running crack can arrest if the following conditions are satisfied: if the applied stresses decrease with increasing crack length, if the crack hits an area of fine grains or if the crack encounters a region of high mis–oriented grains.

According to equation 2.37 the fracture stress of a ferrite–ferrite interface is inversely related to the grain size, so fine grains may stop or retard the advance of a crack. There is experimental evidence that support this idea (Malik et al., 1996), (Jang et al., 2003). There is also experimental evidence that a high–angle misorientation boundary can act as a crack arrester for microcracks or at least retard the propagation of a crack (Zikry and Kao, 1996, Nohava et al., 2002).

2.3.4 Grain misorientation angle.

The local microstructural variation characterized in terms of the misorientation angle of grains has a profound effect on the fracture behaviour of polycrystalline materials. The physical strengthening effect of the grain boundaries is related to their operation as strong obstacles for dislocation motion. Until slip can proceed through the grain boundary, a pile–up of several dislocations has to be formed. The pile–up results in the multiplication of the shear stress acting on the first dislocation, which aids the slip to proceed to the adjacent grain. If the grain is small, generation of the large dislocation pile–ups is more difficult, and thus, higher external stress is needed to carry on the plastic deformation.

The misorientation angle has become one of the major concerns for the study of cleavage fracture propagation in steels. Shehata and Boyd (Shehata and Boyd, 1981) found that varying amounts of acicular ferrite in a TMCR steel (a steel composed of bands of fine and coarse polygonal ferrite grains in a bimodal distribution), the relationship between low temperature toughness and microstructure was inconsistent. They concluded that low temperature toughness depended basically on the detailed constitution of ferrite such as its subgrain and the dislocation structure, and not just on the optically resolvable microstructure. One of the major

factors that make up the constitution of ferrite grains, other than its size is its orientation with respect to their neighbouring grains. The distribution of misorientation angles between grain boundaries can be quantified using electron back scattered diffraction (EBSD) patterns (Randle, 1990, Cizek et al., 2006). In this analysis an alternative method is proposed which is based on the misorientation of cleavage facets for the characterization of cleavage fracture propagation in ferritic steel. It is well known that the overall properties of a polycrystalline material are governed by the contribution from all the grain boundaries rather than a specific individual boundary (Flewitt and Wild, 2001).

Kim (Kim et al., 2000) used 3–point bend pre–cracked Charpy specimens tested at –100°C to analyze the facets size in the fractured surfaces, he considered a flat surface as a facet. The size of the facets was calculated using the linear intercept method which is generally used in calculating the grain size. He compared the effective grain and its average size D_m, the effective grain can be defined by the ability of its boundary to act as the barrier to the deformation or crack propagation and its ability can be explained in relation to the misorientation boundaries. The average of the effective grain size was also measured with EBSD analysis in terms of the misorientation angle for a tolerance–angle set to 15° and 20°. With this method he obtained a value of 11.9 μm and 12.8 μm respectively. The average of the measured facets size that he obtained was 12.7 μm. This value was very similar to $D_m = 11.9 \mu m$ and 12.8 μm obtained with EBSD analysis, then it was concluded that the size of facet is closely related to the effective grain size and less resistance to cleavage fracture is promoted by low misorientation angles. This would be reflected in the fracture surfaces and in fracture toughness values. Reed–Hill and Abbaschian (Reed-Hill and Abbaschian, 1992) compared high–angle boundaries with low–angle boundary misorientation. They found that the high–angle boundaries exhibit higher surface energy, typically in the range from $0.43 J/m^2$ to $0.5 J/m^2$ for ferrite grains. Furthermore, unlike in the low–angle boundaries, where the boundary energy is related to the misorientation angle, and thus, to the number of dislocations involved in the boundary, the energy of high–angle boundary is independent of the misorientation angle. The energy of the high–angle boundaries does not directly depend on the geometry of the boundary. The simplest boundary is a tilt boundary where the rotation axis is parallel to the boundary plane as shown in figure 2.3a. This boundary can be conceived as forming from a single, contiguous crystalline or grain which is gradually bent by some external force. The energy associated with the elastic bending of the lattice can be reduced by inserting a dislocation, which is essentially a half–plane of atoms that act like a wedge, creating a permanent misorientation between the two sides.

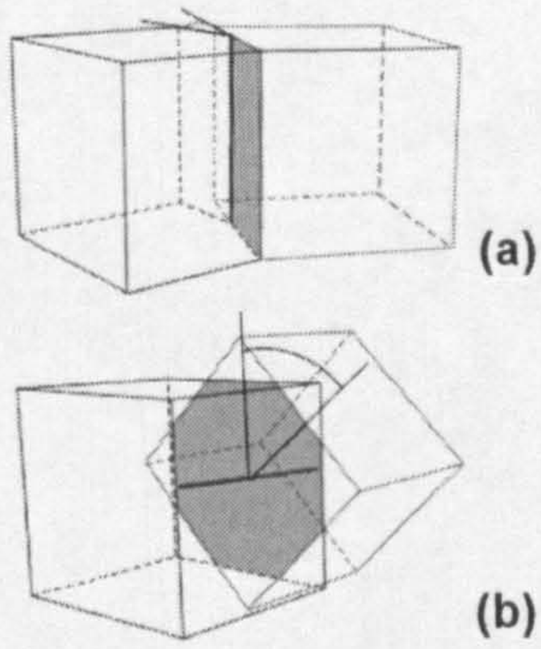

Figure 2.3 – Two typical misorientation angle definitions, (a) tilt misorientation angle, (b) twist misorientation angle.

As the grains bend further, more and more dislocations must be introduced to accommodate the deformation resulting in a growing wall of dislocations (low angle boundary). The grain can now be considered to have split into two sub–grains of related crystallography but notably different orientations.

An alternative is a twist boundary (figure 2.3b) where the misorientation occurs around an axis that is perpendicular to the boundary plane. This type of boundary incorporates two sets of screw dislocations. If the Burgers vectors of the dislocations are orthogonal then the dislocations do not strongly interact and form a square network. In other cases the dislocations may interact to form a more complex hexagonal structure. These concepts of tilt and twist boundaries represent somewhat idealised cases.

The majority of boundaries are of a mixed type, containing dislocations of different types and Burgers vector, in order to create the best fit between the neighbouring grains. While the dislocations in the boundary remain isolated and distinct the boundary can be considered to be low–angle. If deformation continues the density of dislocations will increase and so reduce the spacing between neighbouring dislocations. Eventually, the cores of the dislocations will begin to overlap and the ordered nature of the boundary will begin to breakdown. At this point the boundary can be considered to be high–angle and the original grain to have separated into two entirely separate grains. High–angle boundaries are considerably more disordered with large areas of poor fit and a comparatively open structure. It is well accepted that a boundary consists of structural units which depend on both the misorientation of the two grains and on the plane of the interference. The types of structural unit that exist can be related to the concept of the coincidence site lattice where regions of poor fit occur between points where the two lattices happen to fit together.

2.3.5 Critical stress theory and the local fracture stress σ_F.

It is well known that cleavage fracture in ferritic steels is controlled by the critical tensile stress $\sigma_{yy} \geq \sigma_F$ (Knott, 1966, Wang et al., 2005, Tetelman et al., 1968, Ritchie et al., 1973). This critical value generally exhibits some experimental scatter and small size dependence in the following form $\sigma_c^m \cdot V$. The critical fracture stress was introduced by Orowan (Orowan, 1948) and Knott (Knott, 1969). The critical local cleavage fracture stress, σ_F, (Lin et al., 1987b) can be determined by different methods: plotting the maximum principal stress calculated by the finite element analysis of appropriate specimens against the cleavage initiation distance from the notch root, the intersection between these two values is the fracture stress σ_F; with the use of the grain size in Lin's equation (Lin et al., 1987a, Wang and Chen, 2000)and the values of the effective fracture surface energy (γ); with values of fracture load measured experimentally in combination with finite element results of the stress–strain distributions ahead of the notch root under plane strain conditions (Wu and Knott, 2000, Wu et al., 2005). This parameter is considered the most stable cleavage fracture parameter and consequently a toughness parameter. Generally it exhibits some scatter (Wu and Knott, 2004, Wang et al., 2004, Wang et al., 2003, Yahya et al., 1998, Wang and Chen, 2000). This parameter is not sensitive to temperature, loading rate, notch size and location of notch in the specimens (Wang and Chen, 2000). In a recent publication (Wu and Knott, 2004), it was demonstrated that the σ_F values are almost independent of test temperature when the temperature is relatively low. For higher temperatures the σ_F values decrease slightly as temperature increases. This may be related to the plastic zone size developed ahead of the notch root, which becomes larger at higher temperature. The probability of sampling a particularly large inclusion in a high stress region is then also higher. It is assumed that the largest maximum principal stress corresponding to the failure load of the specimen is the critical local fracture stress (Wu and Knott, 2004).

According to Chen, and co–workers (Chen et al., 1990, Chen and Yang, 1992, Wang and Chen, 1996, Wang and Chen, 1999, Chen et al., 1996, Chen et al., 1997c, Yang et al., 1993), the scattered values of σ_F and the critical plastic strain ε_{pc} are caused by the different size distribution of ferrite grains and second phase particles. In consequence the scatter of fracture loads $\left(P_F / P_y\right)$ is caused by the combined effects of the scatter of σ_F and ε_{pc} and the location of the critical distance X_F of the weakest link constituent relative to the notch root. Wang and Chen (Wang and Chen, 2000) reported that increasing the applied load $\left(P_F / P_{gy}\right)$, the normal

tensile stress and strain increase, thus the probability of failure will increase, the authors also reported that the length of the active zone is limited to the distance segment in which the dual criterion for cleavage fracture $\varepsilon_p \geq \varepsilon_{pc}$ and $\sigma_{yy} \geq \sigma_F$ is simultaneously satisfied.

2.3.6 Micromechanisms inducing cleavage fracture.

Most of the mechanisms proposed to explain the fracture modes are often based on dislocation interaction involving complex slip and crystallographic relationships. The mechanisms for cleavage fracture can change in the same steel after being exposed to irradiation or after a period of time subjected to load conditions (Wu and Knott, 2004) changing from transgranular cleavage fracture to intergranular fracture or vice versa.

Based on the Griffith expression for fracture stress, as interpreted by Curry, Knott and Tweed (Curry and Knott, 1978, Curry and Knott, 1979) and (Tweed and Knott, 1987), cleavage fracture initiated at inclusions occurs at a critical local fracture stress, σ_F, for a penny–shaped microcrack, given by:

$$\sigma_F = \left[\frac{\pi E \gamma_p}{(1-\nu^2)C_o}\right]^{1/2} \qquad 2.43$$

where γ_p is the effective surface energy, E is the Young's modulus, ν is the Poisson's ratio and C_o is the diameter of the penny–shaped microcrack. It is clearly shown that a larger value of C_o will result in a lower value of σ_F. The inclusions initiating cleavage in the highly stressed test volume may vary from specimen to specimen so a degree of scatter in σ_F values could be expected at any given temperature.

For pre–strained specimens, different σ_F values are obtained in comparison to non–prestrained specimens, (Groom and Knott, 1975). Wu (Wu and Knott, 2004) obtained different σ_F values for an as–degraded and as–received C–Mn steel, for transgranular cleavage fracture in wrought mild steel. They showed that σ_F and γ_p values increased with the amount of prestrain, the authors also pointed out that the largest maximum principal stress corresponding to the failure load of the specimen is the critical local fracture stress σ_F (Wu and Knott, 2004).

2.3.7 Statistical models for cleavage fracture.

Many statistical models have been developed to describe the distribution of measured scatter values and evaluate fracture toughness parameters for cleavage fracture such as K_{Ic}, J_{Ic}, $CTOD$ and various notch toughness parameters using pre–cracked specimens (Curry and Knott, 1979, Pineau, 1981, Bermin, 1983, Wallin et al., 1984, Tsann Lin et al., 1986, Godse and Gurland, 1989, Martin et al., 1994) and notched specimens (Hendrickson, 1998, Knott, 1966, Lewandowski and Thompsom, 1986, Thompson and Knott, 1993, Wang and Chen, 1998, Bordet et al., 2004b), notches produce elastic and plastic constraint and then a triaxial state of stress in plane strain conditions, making it easy for cleavage to occur.

Most statistical models are based on the weakest link theory where the whole specimen fails at the moment when the normal stress (σ_{yy}) exceeds the local fracture stress (σ_F) and propagates a cleavage crack. Cleavage fracture initiates in an active zone determined by a dual criterion ahead of a notch (Wang and Chen, 2000, Tsann Lin et al., 1986). Other models are based on a recently suggested physical model and the concept of an active zone which is limited by three criteria for cleavage fracture (Wang and Chen, 2000), namely a critical plastic strain $(\varepsilon_p \geq \varepsilon_{pc})$ for nucleating a crack nucleus, a critical stress triaxiality $(\sigma_m / \sigma \geq T_c)$ for preventing the induced crack nucleus from blunting, and a critical normal stress $(\sigma_{yy} \geq \sigma_F)$ for propagating the crack through the boundary between a second phase particle and a ferrite grain, and takes account of the effect of the preceding loading processes. Cleavage fracture is propagation controlled and the fracture criteria is that a local cleavage fracture stress σ_F is exceeded by the maximum principal tensile stress ahead of the notch root $(\sigma_{yy} \geq \sigma_F)$. Cleavage fracture in ferritic steels involves three stages:

1. Local plastic flow, either by movement of dislocations or twins, is necessary to produce crack nuclei in a second phase particle or in the phase boundary.
2. The local tensile stress composed of the applied normal stress and that produced by the dislocation piling–up must be sufficient for the initiated microcrack to propagate through the boundary between the particle and ferrite grain.
3. The local tensile stress caused the ferrite grain–size crack propagating through the boundary of the ferrite grains.

In these three stages the fracture is propagation controlled and the fracture criterion is that a local cleavage fracture stress σ_F is exceeded by the maximum principal tensile stress σ_{yy}

ahead of notch root $\sigma_{yy} \geq \sigma_F$ (Hendrickson, 1998, Knott, 1966, Lewandowski and Thompsom, 1986, Thompson and Knott, 1993, Cottrell, 1959). Recent studies (Wallin, 1984, Wall et al., 1994, Madan et al., 1996, Chen et al., 1997b) have suggested that a critical level of plastic strain in addition to the critical level of stress to be exceeded is also required for the brittle fracture of a toughness specimen. This implies that the final cleavage fracture is controlled by the critical combination of plastic strain and tensile stress.

Studies on the mechanism of cleavage fracture in notched specimens of C–Mn steel and weld metal (Chen et al., 1990, Chen and Yang, 1992, Wang and Chen, 1996, Wang and Chen, 1999, Chen et al., 1996, Chen et al., 1997a, Chen et al., 1997b, Chen et al., 1997c, Yang et al., 1993) in four point double–notch bend tests at low temperatures led to the conclusion that the critical event for cleavage fracture is the propagation of a microcrack of the critical size.

Plane strain specimens deformed in the temperature range were completely broken, and they showed that cleavage cracks occurs after appreciable plastic strain in the work–hardening region of the stress–strain curve, whereas twining is restricted to the Lüders region (Lindley et al., 1970). Although the twins might form sub–microscopic cracks which subsequently propagate, such cracks are more likely to be blunted by the ensuing deformation, and it is considered that the observed cracks are produced as direct result of the slip bands forming in the work hardening region. Smith (Smith, 1968) proposed that plastic deformation always precedes fracture, and that cleavage crack formation is directly associated with the inhomogeneous nature of plastic flow, cracks form at the tips of both slip and twin bands.

Bordet (Bordet et al., 2004a) proposed a new statistical local criterion for cleavage, the model is based on the same fundamental assumption as the Beremin model with the difference that the local criterion accounts for both the nucleation and propagation stages of cleavage, the model expresses the necessity of maintaining a dynamic connectivity between microcracks nucleation and unstable propagation for cleavage fracture.

2.4 Ductile–brittle transition in steels.

The Charpy impact test, originally proposed by Russell and Charpy (Russell, 1898, Charpy, 1901) is one of the most cost effective material control tests. In the Charpy test, a V–notched specimen is placed on an anvil and hit in its mid–span by a heavy swinging pendulum, released from a known height. The height difference before and after the impact is a measure of energy losses during the fracture event.

One of the principal advantages of the Charpy test is that the toughness can easily be measured over a range of temperatures. Specimens can be heated or cooled to the specified temperature and then placed in the Charpy machine and broken quickly enough so that its temperature change is negligible. Charpy specimens are largely used to characterize the ductile–brittle transition of steels over a wide range of temperatures, usually from room temperature to liquid nitrogen temperature. More complete analysis include the different microstructures for nucleation of ductile and/or cleavage fracture.

The main issue in conventional impact tests is that only one output; the overall fracture energy can be obtained from the machine. Over the last few decades, extensive effort has been made to develop new test methods to obtain as much failure information as possible from the impact test; this was motivated mostly by the nuclear industry. Currently research work with Charpy tests on steels used for the construction of nuclear vessels still continues, some work has been oriented towards setting up instruments on the striker, anvils or the specimen itself or by setting an interferometer laser to measure displacement in addition to the load–line displacements derived from the load signal (Tronskar et al., 2002) in order to obtain as much failure information as possible from Charpy tests. Figure 2.4 shows the set up of Charpy tests.

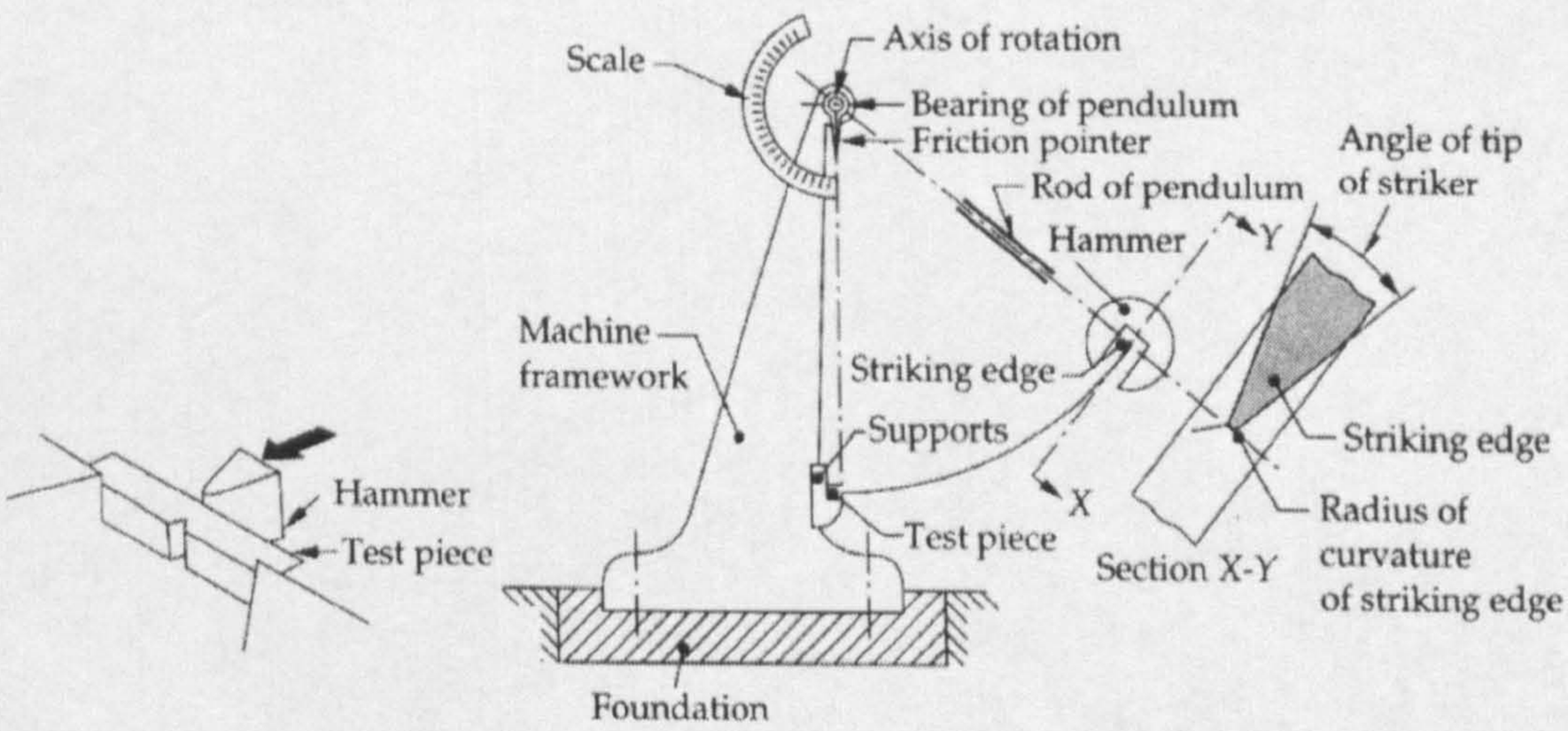

Figure 2.4 – Schematic of Charpy tests.

Materials specifications for the marine industry construction generally include chemical composition limits, minimum tensile yield strength and Charpy V–notch impact energy values (British Steel Limited Swinden Technology Centre Health and Safety Executive, 2000-2001, British Steel plc for the Health and Safety Executive, 1997). But analysis on the microstructure affecting fracture nucleation needs to be done for a better understanding of the fracture process of such steels.

2.5 The problem of simulations with the Finite Element method.

As shown above, ductile initiation occurs at inclusions and second–phase particles, either by interfacial decohesion or by failure of inclusions. Cleavage is generally nucleated by the cracking of grain boundary carbides. It can be seen that the size of the described micro–features is very small for structural integrity assessment. In fracture propagation simulation, the finite elements size ideally must be related to the size of such micro–features or to the micro fracture process for each type of fracture. In these cases, the finite elements mesh size must be very small and it has to be extended far enough ahead of the crack tip to allow the modelling of crack propagation. This will result in finite element models built with tens or hundreds of thousands of finite elements, especially in 3D models. In such models the analysis takes weeks or months and the analysis becomes very unstable due to ill–conditioned stiffness matrices.

The microstructure is another problem because of the different size of the grains and the micro features distributed in the matrix of the material. For example, grains size is tens of times larger than grain boundary carbides and tens of times smaller than a lath packet. It can be seen that the nature of microstructures influence extremely the rules of mesh size designed to analyze ductile or brittle fracture. The space between microvoids or large inclusions is closely related to the sensitive steps in ductile fracture. Therefore the mesh size has to be chosen based in the distance between large or medium microvoids. The grains size, cleavage facets, lath packets or groups of grains with small misorientation angles must be taken to choose the finite element size for the brittle fracture propagation.

As mentioned above, fracture grows in sensitive steps; the steps for ductile fracture are related to the distance between microvoids or large inclusions, therefore the mesh size has to be chosen based in the distance between large or medium microvoids. In brittle fracture, the grain size, cleavage facets, lath packets or groups of grains with small misorientation angles are taken to choose the finite element size for fracture propagation. The present analysis shows that the size of finite elements for ductile and brittle is different as the sensitive steps for ductile and brittle fracture are different. Therefore in order to satisfy the conflict of the different size of the sensitive steps described above is by the used of a single finite elements size. But the accuracy of the solution is questionable. This problem exists because with the conventional finite element method, a finite element is material and structural unit simultaneously fused into an inseparable entity. This approach may be good enough for the simulation of ductile or brittle fracture. But for the simulation of the ductile–brittle transition, were at least two different sizes of finite elements are needed for each type of fracture, a compromise approach of a single size finite element is incorrect.

As suggested by Shterenlikht (Shterenlikht, 2003), the Cellular Automata technique coupled into Finite Elements (CAFE model), can simulate better the ductile–brittle transition than the conventional finite element method. In this model, the material properties are moved away from finite elements and distributed in the appropriate cellular automata arrays. Finite elements are designed only to represent the macro strain gradients adequately which are now a solely structural entity.

A model where a number of cellular automata arrays in which the size of cells and their number can be chosen independently gives the possibility to analyze the material properties at each size scale separately. CAFE model can accommodate as many size scales as necessary to address the material properties of steels and the ductile and brittle fracture simultaneously micro–cellular level. The model also allows the implementation of the micro features of materials as they play a vital role in their fracture properties because they nucleate fracture.

2.6 Coupling modelling for ductile–brittle fracture simulation.

Many combinations of ductile and brittle fracture models, previously described, can be used to simulate the ductile–brittle transition of steels; the most popular are the Gurson Tvergaard Needleman model + Beremin model (Xia and Shih, 1996, Xia and Cheng, 1997, Koppenhoefer and Dodds, 1998) and the Rousselier model + Beremin model (Eripret et al., 1996, Sherry et al., 1998, Burstow, 1998, Howard et al., 2000, Shterenlikht, 2003). The last combination assumes loss of stability associated with rapid loss of stiffness in the damage zone as the onset of the catastrophic brittle fracture. In above models we have to chose the damage cell (finite element) size, l_c, which is the space between inclusions.

In the coupling of the ductile–brittle fracture, we have to use the same finite element size in the region of interest. In the CAFE model, the ductile and brittle fracture processes are addressed by a cellular automata array for each type of fracture (Shterenlikht, 2003). Therefore, now we have to choose the appropriate finite element size, l_c, along with the ductile and brittle cells size. As pointed out by Rousselier (Rousselier et al., 1989) the size of l_c must be related to the distance between large voids, in the CAFE model this distance is associated with the ductile cells size. Therefore now the chose of the finite elements size must be chosen in order to accommodate the ductile cells in a finite element with the right size for a proper compute of the stress and strain gradients. The easiest way is by trial en error up to correlate numerical vs experimental data of the appropriate toughness tests. For the case of the brittle fracture

process, the size of the grain size or groups of grains with small misorientation angles, as mentioned above, can be taken to choose the appropriate brittle cells size.

The described damage cells are used to introduce the related microstructurally significant size scales into the local approach for the analysis of fracture. Damage cell sizes reported in the literature for ductile damage are $0.1-0.5mm$ (Sherry et al., 1998, Burstow, 1998, Howard et al., 2000) and $0.005-0.05mm$ for brittle fracture Burstow and Howard (Sherry et al., 1998, Burstow, 1998, Howard et al., 2000). It can be seen that In the conventional FE method, it is difficult to accommodate both damage cell sizes in a single finite element model.

Generally, with the conventional finite element method, the ductile–brittle transition simulation involves a post processing method (Tanguy et al., 2005a), where the ductile part is evaluated using a damage model first, then the previous calculations are postprocessed using the Beremin model (Beremin, 1983) to evaluate the brittle part in the transition region. But in order to simulate better the ductile–brittle transition, both fracture processes must be implemented in the same finite element model. The typical finite element model cannot address with this point. As explained above, the problem exists because in conventional finite element analysis, a finite element is a material and structural unit simultaneously. The structure and material are thus merged into an inseparable entity. This method can give not reliable results (Tanguy et al., 2001, Shterenlikht and Howard, 2004, Wu et al., 2005, Tanguy et al., 2005a). A better approximation can be obtained with a combination of the Cellular Automata technique and the Finite Element method. In this approach arrays of cells for the ductile and brittle fracture process are implemented into finite elements to handle the ductile and brittle fracture processes in the same finite element (Shterenlikht, 2003). The following sections explain this approach.

2.6.1 Cellular automata.

Since the introduction by Von Newmann (Von Newmann, 1966), cellular automata have been used for image processing (Preston and Duff, 1894, Rosenfeld, 1983, Sternberg, 1980), visual pattern recognition (Preston et al., 1979, Rosenfeld, 1979), simulation of recrystallization (Raabe, 2002), for the simulation of nucleation and growth of ferrite grains for low–carbon steels (Zhang et al., 2002), for the prediction of dendritic grain structures formed during solidification with a 3D model (Gandin et al., 1999), and oxide scale failure on hot rolling simulations (Das, 2002), among other applications.

Cellular Automata is made of certain number of cellular automatons (a finite state machine) which are composed of cells. The result is a space filled with cells, each of those cells

containing a finite state machine. Usually the space is divided into a grid or lattice structure, a two dimensional cellular space looks like a piece of graph–paper. Cellular spaces can have any number of dimensions; the most commonly used ones have 1, 2 or 3 dimensions as shown in figure 2.5.

In the cellular space, all the cells go from their current state to some next state according to the "local rule", the switching rule of their state machine. The input for the local rule is the neighbourhood of cells. All the cells use the same local rule. The cells switch from their current state to the next state. The space is synchronous. These simple rules allow complex behaviour to emerge; the resulting complexity is what makes cellular automata so interesting.

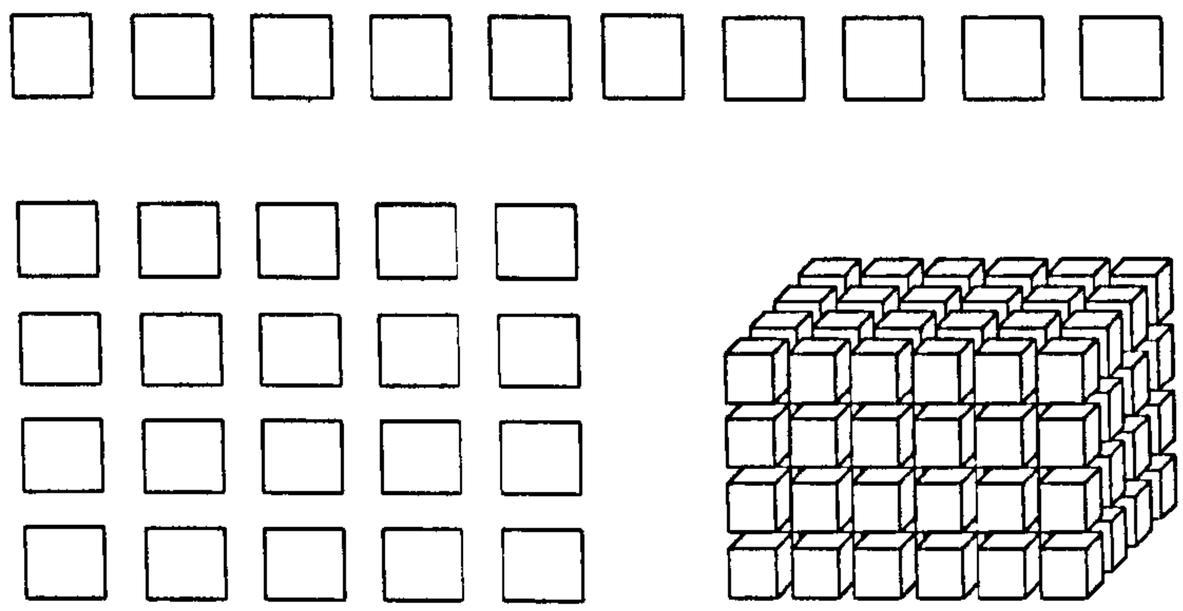

Figure 2.5 – Examples of cellular spaces in one, two and three dimensions.

The implementation of cellular automata into finite element programs has showed the advantage of this model for better characterization and/or simulations of mechanical processes; fracture propagation simulation, rolling process simulation, etc. A combination of cellular automata and finite elements, Cellular Automata Finite Element Model (CAFE), was first proposed by Beynon (Beynon et al., 2002). The CAFE model has then been applied successfully for solidification, (Gandin et al., 1999, Vandyoussefi and Greer, 2002), static recrystallization (Raabe and Becker, 2000) and oxide scale failure (Das, 2002).

2.6.2 The Cellular Automata Finite Element (CAFE) approach.

In the fracture mechanics field, to simulate fracture initiation and propagation in an engineering structure with the finite element method, finite elements size must be related to micromechanical damage mechanisms (section 2.5). These mechanisms are measured on the fractured surfaces of fracture toughness specimens, the critical void volume fraction for ductile fracture (section 2.2) and the facets size for cleavage fracture (section 2.3). As the size of these

physical micro features are in the order of μm, very small finite elements in the region extending ahead of the crack path are necessary, therefore finite element models with meshes with tens of thousands of finite elements are very common, especially in 3D models. As mentioned before, the analysis of such finite element models takes weeks or months. Therefore the need for the development of novel models which incorporate the microstructures and the sensitive steps for each type of fracture is needed. Recently a novel cellular automata finite element model (Shterenlikht, 2003) has been proposed to simulate the ductile–brittle transition in a single finite element model. This multi–scale model was developed to include the micro features initiating ductile and brittle fracture and the micro mechanics characteristics of each type of fracture.

The CAFE model integrates the cellular automata technique into the finite element method. As described in section 2.5, at least two different cells arrays are needed to simulate the ductile–brittle transition of steels. The size of the cell arrays is related to the sensitive fracture steps for each type of fracture as described above. The flow of information between finite elements and cellular automata arrays is shown in figure 2.6 (Shterenlikht, 2003). In CAFE model, the number of cellular automata arrays and size of cells can be chosen independently. This means that one can create as many size scales as necessary to carry on all material information of interest. As mentioned before, in the simulation of the ductile–brittle transition, at least two independent cellular automata arrays are necessary called the ductile and brittle CA arrays. The cells size in the ductile and brittle CA is related to the damage scale characteristic of ductile and brittle fracture: the distance between large microvoids for ductile fracture and cleavage facets size of large grains or groups of grains with small misorientation angle that behaved as a single facet for brittle fracture

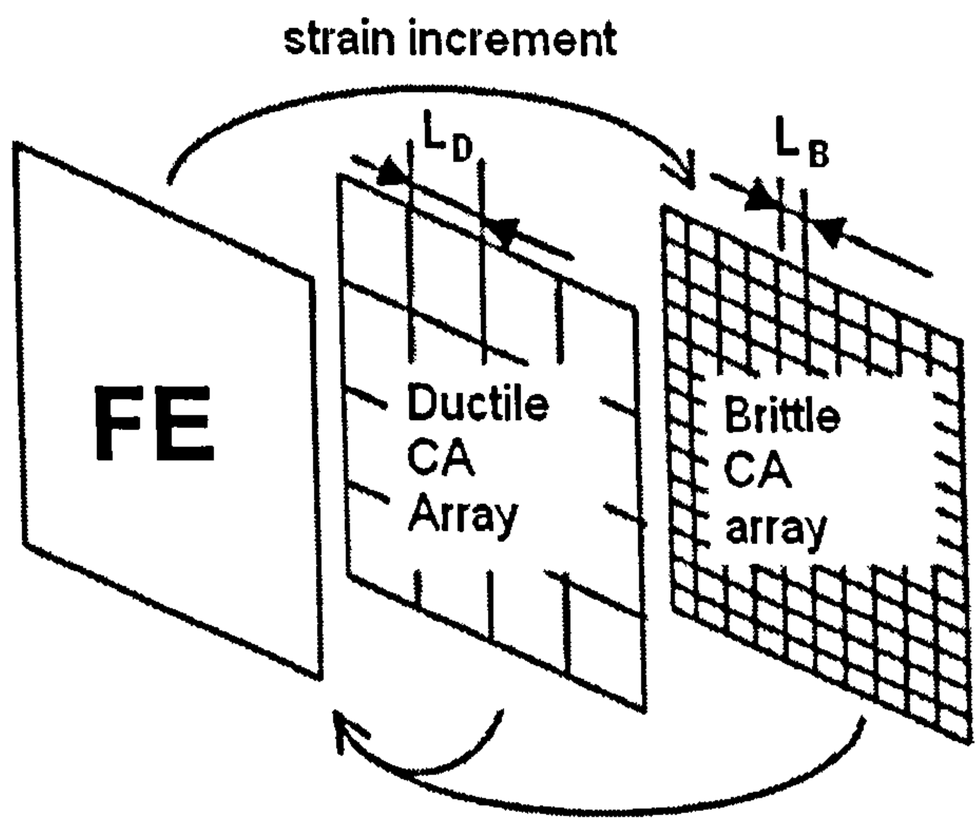

Figure 2.6 – Flow of information between Finite Elements and Cellular Automata (Shterenlikht, 2003).

The CAFE model combines mathematical techniques of cellular automata and finite elements to accomplish integration of the metallurgical structures of steels. The model allows the user to input as many features of metals as needed in order to perform more real fracture propagation simulations. CAFE model evaluates the field variables that can cause elements to fail. The model links the CA (microstructure definition) within the framework of the FE solver. CAFE modelling involves the next main steps:

- Defining the metallurgical structure using CA.
- Connecting the continuum with microstructure and adapting the FE input deck.
- Linking CA and FE.
- Approximating the strain space within CA.
- Physical averaging to FE
- Updating CA using the transformation matrix.

As mentioned above, CAFE model separates the structure from the material so separate independent entities are used to carry structural and material information. The following paragraphs will explain the framework of the model.

Opposite to the conventional finite element method, CAFE model separates the material component from the structural response of finite elements to carry the structural en material information separately. It is well know that a finite element is completely defined by its stiffness matrix, D_{ijkl}, and the interpolation function $N^p(\xi_k)$.

$$D_{ijkl} = \frac{\partial \sigma_{ij}}{\partial \varepsilon_{kl}} \qquad 2.44$$

$$u_{ij}(\xi_k) = N^p(\xi_k) u_{ij}^p \qquad 2.45$$

where σ_{ij} is the Cauchy (or true) stress tensor, ε_{kl} is the logarithmic (or true) strain tensor, u_{ij}^p is the displacement tensor at the finite element node p, $p = 1...P$, P is the total number of nodes in a finite element, ξ_k is the finite element parametric coordinates tensor, $k = 1,2,3$, $\xi_k = [-1...+1]$, $u_{ij}(\xi_k)$ is the displacement tensor at point ξ_k of a finite element (HKS, 2001). The material behaviour at an integration (or Gaussian point) point r is described by a constitutive equation of the form:

$$\dot{\sigma}_{ij}^{r} = f\left(\dot{\varepsilon}_{ij}^{r}\right) \qquad 2.46$$

where $\dot{\sigma}_{ij}^{r}$ and $\dot{\varepsilon}_{ij}^{r}$ are stress and strain rate tensors respectively at an integration point r, $r = 1...R$, R is the total number of integration points per finite element. The way to separate the material information from the structural response of finite elements was done as shown schematically in figure 2.7. In this figure it can be seen that the material unit is addressed in CAFE model via the stress tensor of the material integration points.

The combination of cellular automata en finite elements is shown schematically in figure 2.7. This figure shows that the material information has been moved from the conventional finite element and given to an appropriate number of cellular automata. Therefore finite element models are used only to represent macro strain gradients adequately and the metallurgical structure of the material is defined in the appropriate CA array which results in the definition of a microstructure model coupled to the structure of finite elements as shown in figure 2.7.

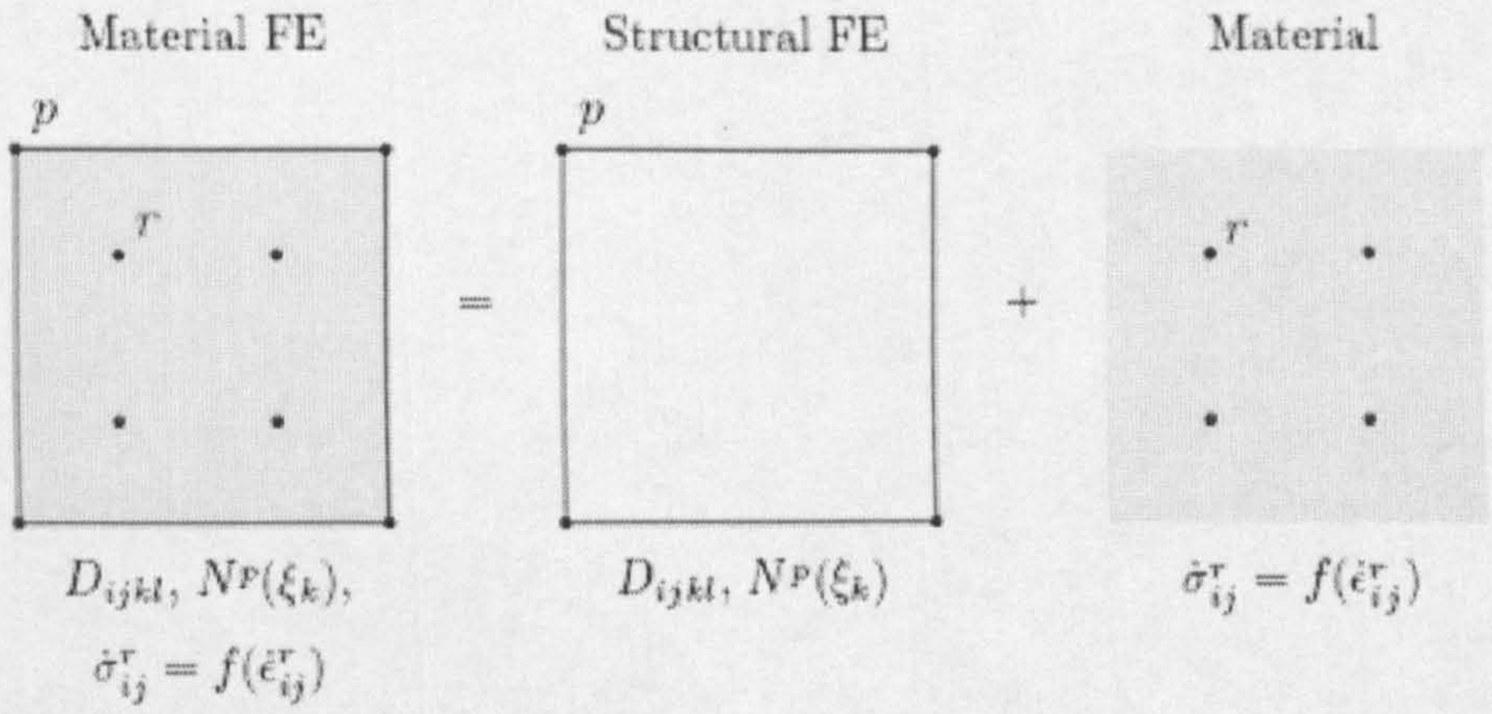

Figure 2.7 – A finite element as a structural and a material unit.

As mentioned in section 2.6.1, a cellular automata is a discrete time entity composed of a finite number of cells which in the present case represent a volume of material as shown schematically in figure 2.6. In Von Newman cellular automata formulation (Von Newmann, 1966), the state of each cell Υ_m at time t_{i+1} is completely defined by the current state of this cell and the state of the neighbouring cells at time t_1:

$$\Upsilon_m(t_{i+1}) = \Omega\left(\Upsilon_m(t_i), \Upsilon_l^m(t_i)\right) \qquad 2.47$$

Where $\Upsilon_l^m(t_t)$ is the state of cell l from the neighbourhood of cell m at t_t, $l=1...L$, L is the number of cells in the neighbourhood of the cell m, $m=1...M$, M is the total number of cells in the CA array; Ω is the transition rule. In the CAFE model (Shterenlikht, 2003), a cellular automata is totally defined by the initial state of each cell, by the transition rules for each cell and by the neighbourhood state of each cell. Typically the same transition rules and neighbourhood conditions are applied to all cells in a CA array.

CA arrays are non–spatial entity (Von Newmann, 1966), this means that the cells do not need to have any size, shape or location in physical space for the successful performance of a CA. Furthermore, whatever the spatial meaning given to cells, it will be no effect on the CA performance. In CAFE model, a spatial meaning was given to the cells because the purpose of the use of the cellular automata technique is to represent material behaviour where the size scale is very important in fracture simulation. It was shown in section 2.6 that the microstructurally significant size scales related to the ductile and brittle fracture are different. Therefore materials have to be modelled with damage cells of two distinctly CA of different sizes.

Two independent CA arrays, *the brittle CA array* and *the ductile CA array*, has been created (Shterenlikht, 2003) to address the mechanics for each type of fracture. In CAFE model, the cubic shape of CA cells was adopted by analogy with cubic damage cells usually used in the conventional finite element modelling of fracture propagation (Xia and Shih, 1996; Howard et al., 2000). A 26–cell neighbourhood has been adopted in CAFE model for each cell. If we imagine a $3\times3\times3=27$ cell cube then the 26 cells lying around the central one are its neighbourhood. 6 cells of this neighbourhood have a common side with the central cell; 12 cells have a common edge and 8 cells have a common corner. The properties of this 26–cell neighbourhood are shown in figure 2.8 (Shterenlikht, 2003). Each neighbourhood has three characteristics:

1. Direction cosines.
2. The coordinates of the cells which must be related to the central cell.
3. The number of each cell in a CA array.

These characteristics are shown in each neighbourhood cell in figure 2.8. From this figure it can be seen that due to the central symmetry only 13 of the 26 neighbourhood cells have unique combination of direction cosines. Their symmetrical partners cells have the same number but with a bar on the top (Shterenlikht, 2003).

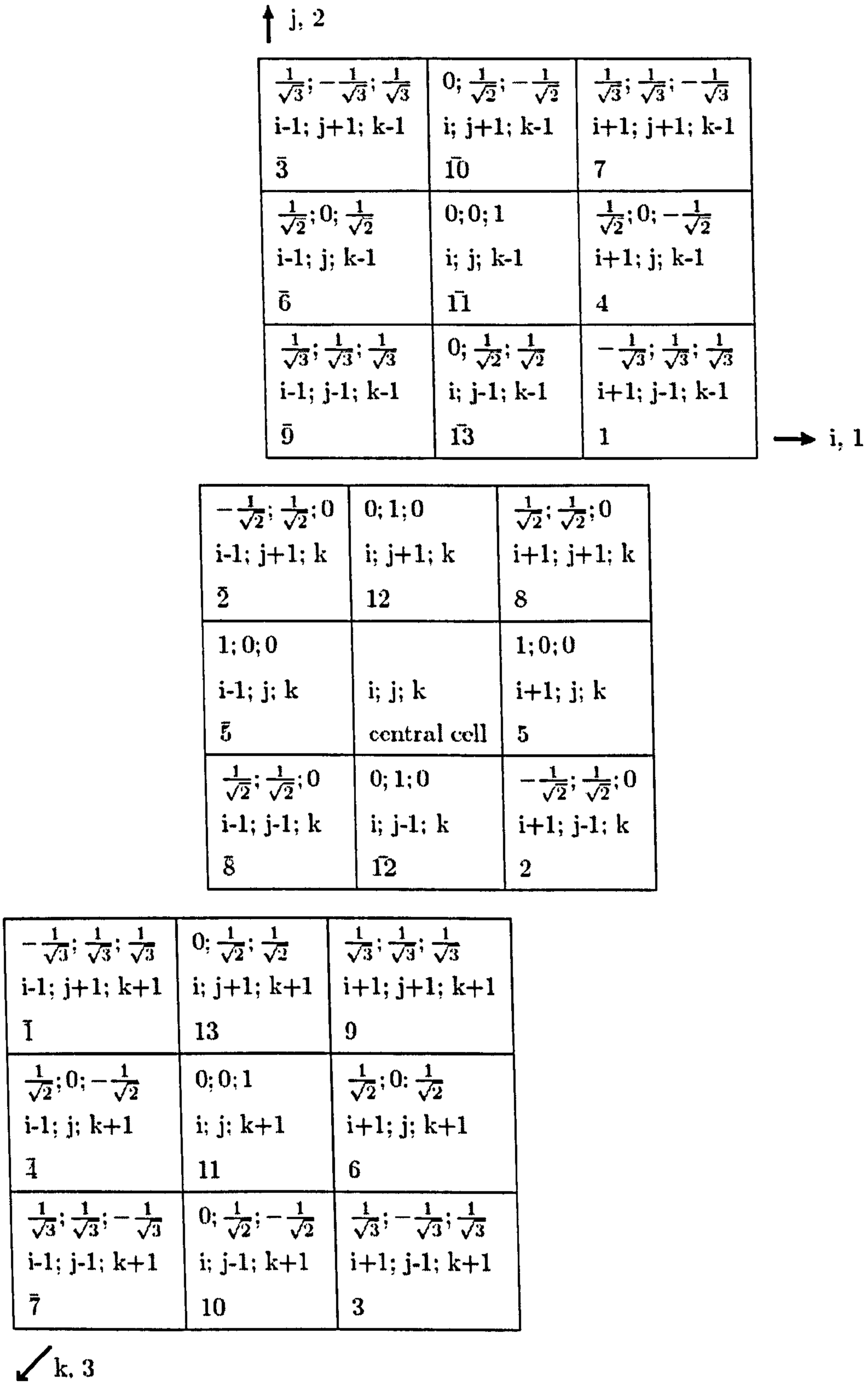

Figure 2.8 – Neighbouring cell numbering convention.

A CA have self–closing boundary conditions because each cell has the same 26–cell neighbourhood, which means that for a cell lying at the edge of a CA the corresponding cells of the opposite edge are considered adjacent. So a 26–cell neighbourhood of an edge cell

consists of cells located at opposite CA edges. The 26–cell neighbourhood of a corner cell is shown in figure 2.9 (Shterenlikht, 2003).

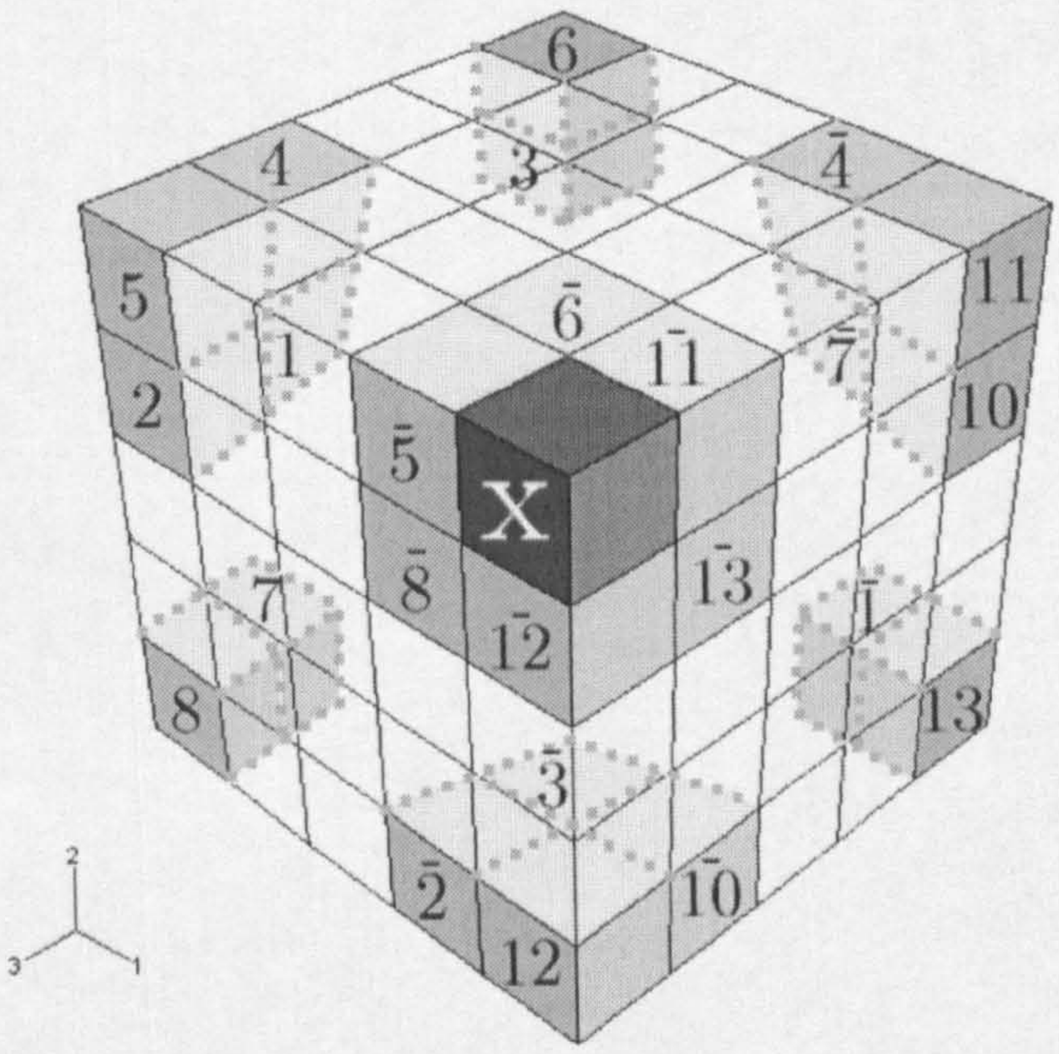

Figure 2.9 – A 26–cell neighbourhood of a corner cell in a CA with self–closing boundary conditions.

In figure 2.9, a corner cell, X, is located at a corner of a three–dimensional cubic CA. This corner is an intersection of three CA edges. The numbers of the neighbouring cells are shown according to the convention given by Shterenlikht (Shterenlikht, 2003). In the projection shown in figure 2.9 the neighbouring cells 9 and $\bar{9}$ are located exactly behind cell X and are therefore not visible. Cell $\bar{9}$ is situated directly behind cell X, and cell 9 occupies the corner of CA opposite to cell X. In each cell of a CA arrays, a set of properties has to be given at the beginning of the simulation and they must remain constant throughout the analysis. In order to fed to each CA array the state of the cells at each time increment time–dependent state variables were introduced to the CAFE model. By incorporating the cell properties and state variables to the right part of equation 2.47, the following equation was obtained:

$$\Upsilon_m(t_{i+1}) = \Omega\,(\Upsilon_m(t_i),\ \Upsilon_l^m(t_i),\ \Lambda_m^n,\ \Lambda_l^n,\ \Gamma_m^q(t_i)) \qquad 2.48$$

where Λ_m^n is property n of cell m, $n=1...N$, N is the total number of properties of each cell; Λ_l^n is property n of a neighbouring cell l, $\Gamma_m^q(t_i)$ is a state variable q of cell m at time (t_i), $q=1...Q$, Q is the total number of state variables defined at each CA cell. All cells of a

CA have the same N and the same Q, this in order to process all cells of a CA according to a unified algorithm. The cell properties, Λ_m^n, of both CA arrays are used to store all material information of interest throughout the analysis. The state variables $\Gamma_m^q(t_i)$ come from the solution of material constitutive equations at time t_i.

In CAFE model, the ductile and brittle CA arrays occupy the same physical space. Consequently the state of cell m of one CA array will depend on the state of a group of S cells of the other CA array in order to make sure that any loss of material integrity, ductile or brittle, is accounted in both CA arrays. The cell states in the ductile CA array are affected by the states of cells in the brittle CA array and vice versa. The full transfer rules for both CA arrays consequently have the following form (Shterenlikht, 2003):

$$\Upsilon_{m(D)}(t_{i+1}) = \Omega_D(\Upsilon_{m(D)}(t_i), \Upsilon_{l(D)}^m(t_i), \Lambda_{m(D)}^n, \Lambda_{l(D)}^n, \Gamma_{m(D)}^q(t_i), \Upsilon_{s(B)}(t_{i+1})) \quad 2.49$$

$$\Upsilon_{m(B)}(t_{i+1}) = \Omega_B(\Upsilon_{m(B)}(t_i), \Upsilon_{l(B)}^m(t_i), \Lambda_{m(B)}^n, \Lambda_{l(B)}^n, \Gamma_{m(B)}^q(t_i), \Upsilon_{s(D)}(t_{i+1})) \quad 2.50$$

where subscripts D and B refer to cells from the ductile and the brittle CA arrays accordingly, cell s belongs to the group of S cells of one CA array, the states of which will have an influence on cell m of the other CA array, $s = 1...S$, $1 \le S \le M$. The number of cells S of one CA array which will affect the state of cell m of the other CA array is difficult to establish exactly. As will be shown later S depends on the total number of cells in each array, M_D and M_B.

As mentioned before, the ductile and brittle CA arrays are totally independent of each other as far as their construction is related, this means that the number and the types of cells states, $\Upsilon_{m(D)}$ and $\Upsilon_{m(B)}$, the total numbers of cells in these arrays, M_D and M_B, the total numbers and types of cell properties, N_D and N_B, and state variables, Q_D and Q_B, and finally the transfer functions, Ω_D and Ω_B can be chosen for each array independently. This gives to the user of the CAFE model high freedom in order to incorporate all the material properties of interest through the CA arrays.

In the same way it was introduced to the CAFE model time–dependent state variables in each CA cell, $\Gamma_m^q(t_i)$, It was introduced solution solution–dependent state variables Υ_a^r to link the state of each cell with the solution of material constitutive equations at each finite element integration point r linked to the states of both CA arrays:

$$\Upsilon_a^r(t_{i+1}) = \Xi(\Upsilon_{m(D)}(t_{i+1}), \Upsilon_{m(B)}(t_{i+1})) \qquad 2.51$$

where $\Upsilon_a^r(t_{i+1})$ is state variable a at time (t_{i+1}) and integration point r, $a = 1...A$, A is the total number of state variables per integration point, Ξ is the CA to FE transfer function. The same transfer function is used for all material points.

The general principles of the CA arrays have been described up until now. The link between the FE and the CA parts of the CAFE model depends on the exact technical realisation of a CAFE generalisation. This means that a CAFE model can be developed as simple as possible where only the more important properties of a material are introduced via the CA arrays. Or a CAFE model can be very complicated where not only the principal microstructures nucleating fractures are introduced in the model but also all the real microstructures of a material can be incorporated in a CAFE model.

In the present CAFE model, the constitutive ductile Rousselier damage model (section 2.2.5) was used to represent the development of ductile fracture. The Rousselier model is integrated at the finite element integration points generating the new FE stress tensor $\sigma_{ij}(t_{i+1})$, and the new damage variable, $\beta(t_{i+1})$. The new damage variable is distributed across all ductile CA cells according to the local strain concentration associated with any dead cells. A ductile CA cell dies when its damage variable exceeds the critical value of the damage variable β_F for this cell. Therefore the analysis of ductile cells consists of checking all ductile cells against this fracture criterion.

For the case of cleavage fracture, the maximum principal stress is distributed across all brittle CA cells according to the local strain concentration, microcracks nucleates if the maximum principal stress exceeds its fractures stress limit. Propagation from a dead brittle a cell to a neighbouring cell b occurs if the misorientation angle between these two cells $|\theta_a - \theta_b|$ is smaller that the misorientation threshold θ_F (Nohava et al., 2002).

As mentioned above, in the CAFE model the number of cellular automata arrays and size of cells can be chosen independently (Shterenlikht, 2003). As a result it is possible to accommodate as many size scales as necessary to carry on all material information of interest. However, to model the ductile–brittle transition, at least two independent ductile and brittle CA arrays are necessary. The cells size in the ductile and brittle CA is related to the damage scale characteristic of ductile and brittle fracture: the distance between large microvoids for ductile fracture and cleavage facets size of large grains or groups of grains with small misorientation

angle that behaved as a single facet for brittle fracture. From the present section it can be seen that the mathematical formulation of the CAFE approach shows that it is possible to simulate simultaneously the ductile and the brittle fracture process in the same finite element model. This is done by the definition of the two different cells arrays, the ductile and the brittle CA arrays to distribute into them the micromechanisms of each fracture process and material properties. Further chapters will explain how the model was developed.

2.7 Statement of work that needs doing.

In the simulation of the ductile–brittle transition it is very important to define correctly the ductile and brittle fracture microstructures for fracture initiation. The ductile fracture micro features for ferritic steels is now well documented. It is well known that MnS inclusions are the most important factors controlling ductile fracture nucleation (Druce et al., 1992, Zhang and Knott, 2000, Rosenfield et al., 1983, Tanguy et al., 2005b, Bernaur and Brocks, 2001, Franklin, 1969).

Cleavage in structural steels is commonly considered to be initiated by dislocation pile–up or by cracked carbides. Little evidence has been found on the role of different microstructures for cleavage fracture nucleation. Experimental work has shown MnS inclusions as cleavage fracture nucleation (Tanguy et al., 2005a, Tweed and Knott, 1983, Tweed and Knott, 1987, Druce et al., 1992, Zhang and Knott, 2000, Rosenfield et al., 1983). Recently, apart from cracked carbides and MnS inclusions different cleavage fracture nucleation microstructures have been discovered:

- Iron based carbides or carbides colonies (Gibson et al., 1991, Druce et al., 1992, Zhang and Knott, 2000).
- Small round manganese sulfides (MnS) inclusions (Druce et al., 1992, Zhang and Knott, 2000, Rosenfield et al., 1983).
- Grain boundary inclusions (Rosenfield and Shetty, 1973).
- TiC particles (Gibson et al., 1991, Druce et al., 1992, Tanguy et al., 2005b).
- Twin and slip bands for grains boundary particles of manganese (Smith, 1968).
- Grain boundary carbide (Smith, 1996, Curry, 1980).
- Pearlite–induced cleavage (Valiente et al., 2005, Liu, 1982).

It can be seen that with time, different triggering cleavage fracture microstructures have been discovered. But most of the work done on the identification of cleavage fracture nucleation microstructures has been performed on fracture surfaces of fracture toughness specimens tested at low temperatures. Little work has been done on the identification of those micro

features in notched specimens experiencing all the critical conditions prior to failure. No further work has been done as well on the identification of different cleavage microstructures in ferritic steels and in the analysis of the competition of different microstructures for cleavage fracture nucleation.

Research work is also needed on the implementation of different microstructures in finite element models for the simulation of the ductile–brittle transition. In ductile–brittle transition modelling, it is very important as well to properly simulate the distribution of cleavage fracture initiation points with respect to the notch root. Their position and thickness of particles nucleating microcracks will affect the fracture toughness parameter, σ_F, because this parameter is dependent on the position of cleavage nucleation points and of the effective fracture surface energy which depend on the size of particles nucleating cleavage fracture. From the present analysis it can be seen that the correct simulation of those points with respect to the notch root is very important in order to obtain reliable results. Wrong simulation and/or or definition of the microstructures for cleavage fracture nucleation will result in an overestimation or under estimation of fracture toughness values such as the impact Charpy energy and consequently poor simulation of the ductile–brittle transition. The correct measurement of the particles triggering cleavage fracture and their correct position with respect to the notch root may help to explain the high scatter in terms of impact Charpy energy values in the transition region of ferritic steels.

Due to the fact that merchant ships are built with Grade A plate steel (Chapter I), it is extremely important to perform analysis at micro level as all the conditions for fracture initiation and propagation are developed in the microstructure of the material. Most of the research work on Grade A plate steels has been directed at the measurement of fracture toughness values without taking into account the microstructures for fracture initiation (Sumpter and Caudrey, 1995, Sumpter, 1991, British Steel plc for the Health and Safety Executive, 1997). Although in some of the empirical equations developed in such research work, the authors associated the grain size with fracture toughness values, these approaches did not include the microstructures for cleavage fracture. Little information about different microstructures nucleating cleavage fracture is available in the literature so more research work is needed for the proper development of models to simulate the ductile–brittle transition in steels.

The Cellular Automata Finite Element (CAFE) approach, used in this work, offers a solution to the implementation of different cleavage fracture nucleation microstructures of the steel under analysis and the simulation of the distribution of cleavage fracture initiation points in the notch region of Charpy specimens and four point double–notch bend tests. Research work is needed in order to correctly implement the physical distribution of microstructures nucleating cleavage

because in previous models only one micromechanism for cleavage fracture was implemented (Wu et al., 2005) and no further work has been done on the possibility to include different micromechanisms for cleavage fracture nucleation in steels.

2.8 Hypothesis.

Most cleavage fracture nucleation analysis are based on the statement that cracked carbides are the principal controlling microstructure for cleavage nucleation in a huge variety of steels. But apart from cracked carbides as mentioned above, different cleavage fracture nucleation microstructures have been discovered in ferritic steels. In mild steels, which are composed of the ferrite matrix with bands of pearlite following the rolling direction and lands of pearlite of distributed randomly in the transverse direction, the lands of pearlite may have a strong influence on the fracture properties of such steels. Due to the fact that the pearlite microstructure is a composition of ferrite and cementite forming layers, which is hard, the lands of pearlite may have a strong influence in the nucleation of cleavage fracture. The inter–lamellar spacing between the nano–scale layers of pearlite may be potential sites for cleavage fracture nucleation as non–metallic inclusions have been found in the inter–spacing of the layers of pearlite (Taleff et al., 2002). This suggests that such particles can nucleate cleavage fracture in mild steels.

The boundary between ferrite grains and lands of pearlite can be another cleavage fracture microstructure because the hard layers of pearlite can break when ferrite grains are being deformed creating microcracks in the loading process. If this is true, apart from grain boundary carbides, MnS inclusions (Druce et al., 1992, Zhang and Knott, 2000, Rosenfield et al., 1983), Grain boundaries (Rosenfield and Shetty, 1973), TiC paricles (Gibson et al., 1991, Druce et al., 1992), Iron based carbides or carbides colonies (Gibson et al., 1991, Druce et al., 1992, Zhang and Knott, 2000) another two cleavage fracture microstructures will nucleate cleavage in the present steel.

The literature has shown MnS inclusions as a cleavage fracture microstructure in ferritic steels. Mild steels are ferritic steels and certainly has MnS inclusions. Grain boundary cracked carbides are well established as the main cleavage microstructure in most steels, including ferritic steels, so this microstructure will certainly be present in mild steels (Smith, 1968, Bernauer et al., 1999). This suggests that a competition of four different cleavage fracture nucleation microstructures may be present in mild steels as Grade A plate steel. The procedure to identify the cleavage fracture nucleation microstructures is by the use of four point double–notch bend specimens, which will be tested in the ductile–brittle transition region of the plate

steel. This hypothesis will be tested with experimental work on the identification of cleavage fracture nucleation microstructures using the notched specimens mentioned above and extensive fractography analysis of the notch region of blunt four point double–notch bend specimens. In these specimens, if loaded symmetrically, when a crack is developed in one notch, the crack will propagate in that notch, but the surviving notch will reveal all the critical conditions prior to failure. The surviving notch will be sectioned, polished and etched to reveal the microstructure and the micro features for cleavage fracture nucleation in Grade A ship plate steel.

One of the main objectives of the present research work is to simulate the distributions of microcracks in the surviving notch of blunt four point double–notch bend tests. In the CAFE model it is possible to implement the different microstructures for cleavage fracture nucleation. The distribution of those cleavage fracture initiation points can be as well simulated with the CAFE model at micro–cellular level. The incorporation of the distributions of the initiation points (microcracks) can help to simulate better the ductile–brittle transition as the fracture toughness values of Charpy specimens depend strongly on the correct simulation of those triggering initiation points. To validate the hypothesis, numerical results will be compared with experimental work. Once correlation between numerical against experimental data is obtained, and the parameters of the damage models are calibrated, the model will be applied to simulate the typical scatter in terms of impact Charpy energy values in the transition region. As explained above, the correct simulation of the cleavage fracture nucleation points will result in better simulation of the ductile–brittle transition in terms of impact Charpy energy values.

2.9 Conclusions.

From the present section, the most used ductile and brittle fracture models for fracture initiation and propagation were explained. Many attempts have taken place to couple ductile and brittle fracture models to simulate the ductile–brittle transition in steels. From literature, it can be seen that little work has been achieved on coupling ductile and brittle models for simulation of the ductile–brittle transition. The present section showed the theoretical structure of a novel Cellular Automata Finite Element model to simulate the ductile–brittle transition in a multi–scale framework; such approach has been proposed in the present work to investigate the toughness properties of a Grade A ship plate steel.

It has been mentioned as well that research work still needs doing for a better understanding of the fracture process in Grade A ship plate steels. Finally a hypothesis was described based on literature work and on earlier experimental work performed in the present research project.

2.10 References.

ANDREWS, R. M., HOWARD, I. C., SHTERENLIKHT, A. & YATES, J. R. (2002) The effective resistence of pipeline steels to running ductile fracture, Modelling of laboratory test data. *in A. Neimitz, I. V. Rokach, D. Kocańda and K. Golоś, ed., "ECF14. Fracture Mechanics Beyond 2000", EMAS Publications, Sheffield, UK.*, 65-72.

AVERBACH, B. L., FELBECK, G. T., HAHN, G. T. & THOMAS, D. A. (1959) Fracture. *Proceedings of an International Conference on the Atomic Mechanisms of Fracture held in Swampscott, Massachusetts, April 1959, The Technology Press of Massachusetts Institute of Technology and John Wyley & Sons, New York.*

BATES, R. C. (1984) Modelling of ductile fracture by microvoid coalescence for the prediction of fracture toughness *in J. M. Wells and J. D. Landes, eds, "Fracture: Interactions of Microstructure, Mechanisms and Mechanics", The Metallurgica Society of AIME*, 117-155.

BATISSE, R., BETHMONT, G., DEVESA, G. & ROUSSELIER, G. (1987) Ductile fracture of a 508 Cl 3 steel in relation with inclusion content: The benefit of the local approach of fracture and continuum damage mechanics. *Nuclear Engineering and Design,* 105, 113-120.

BEACHEM, C. D. (1963) An electron fractography study of the influence of plastic strain conditions upon ductile rupture proecesses in metals. *Transactions of the ASM,* 56, 318-326.

BEREMIN, F. M. (1983) A local criterion for cleavage fracture of a nuclear pressure vessel steel. *Metallurgical Transactions,* 14A, 2277-2287.

BERG, C. A. (1970) Plastic dilatation and void interactoin. *M. F. Khanninen, ed. Inelastic Behavior of Solids. McGraw-Hill*, 171-209.

BERMIN, F. M. (1983) A local criterion for cleavage fracture of a nuclear pressure vessel steel. *Metall. Trans,* 14A, 2277-2287.

BERNAUER, G., BROCKS, W. & SCHMITT, W. (1999) Modifications on the Beremin model for cleavage fracture in the transition region of a ferritic steel. *Engineering Fracture Mechanics,* 64, 305-325.

BERNAUR, G. & BROCKS, W. (2001) Micro-mechanical modelling of ductile damage and tearing - results of an European numerical round robin. *Fatigue Fract Engng Mater Struct,* 25, 363-384.

BESSON, J., STEGLICH, D. & BROCKS, W. (2001) Modeling of crack growth in round bars and plane strain specimens. *International Journal of Solids.*, 38, 8259-8284.

BESSON, J., STEGLICH, D. & BROCKS, W. (2003) Modelign of plane strain ductile rupture. *International journal of Plasticity,* 19, 1517-1541.

BEYNON, J. H., DAS, S., HOWARD, I. C., PALMIERE, E. J. & CHTERENLIKHT, A. (2002) The combination of Cellular Automata and Finite Elements for the study of fracture; the CAFE Model of Fracture. *A. Neimitz, I. V. Rokach, D. Kocanda and K. Gotos, eds, "ECF14, Fracture Mechanics Beyond 2000, EMAS Publucations, Sheffield, UK*, 241-248.

BLUHM, J. I. & MORRISSEY, R. J. (1964) Preliminary investigation of the fracture mechanism in a tensile specimen. *US Army Research Agency, Watertown, Massachusetts, USA.*

BLUHM, J. I. & MORRISSEY, R. J. (1966) Fracture in a tensile specimen. *in Proceeding of First Internationl Conference on Fracture, Vol. 3. Japanese Society for Strength and Fracture of Materials, Sendai, Japan*, 1739-1780.

BORDET, S. R., KARSTENSEN, A. D., KNOWLES, D. M. & WIESNER, C. S. (2004a) A new statistical local criterion for cleavage fracture in steel. Part I: model presentation. *Engineering Fracture Mechanics,* 72, 435-452.

BORDET, S. R., KARSTENSEN, A. D., KNOWLES, D. M. & WIESNER, C. S. (2004b) A new statistical local criterion for cleavage fracture in steel. Part II: application to an offshore structural steel. *Engineering Fracture Mechanics,* 72, 453-474.

BORDET, S. R., KARSTENSEN, A. D., KNOWLES, D. M. & WIESNER, C. S. (2005a) A new statistical local criterion for cleavage fracture in steel. Part I: model presentation. *Engineering Fracture Mechanics,* 72, 435-452.

BORDET, S. R., KARSTENSEN, A. D., KNOWLES, D. M. & WIESNER, C. S. (2005b) A new statistical local criterion for cleavage fracture in steel. Part II: application to an offshore structural steel. *Engineering Fracture Mechanics,* 72, 453-474.

BRIDGMAN, L. M. (1952) Studies in Large Plastic Flow and Fracture. *Metallurgica Engineering Series, 1 edn, McGraw-Hill.*

BRITISH STEEL LIMITED SWINDEN TECHNOLOGY CENTRE HEALTH AND SAFETY EXECUTIVE (2000-2001) Offshore Technology Report OTO-2000 001.

BRITISH STEEL PLC FOR THE HEALTH AND SAFETY EXECUTIVE (1997) Literature Review of the Fracture Properties of Grade A Ship Plate: OTH 95 489.

BROCKS, W., SUN, D.-Z. & HONIG, A. (196) Verification of micromechanical models for ductile fracture by cell model calculations. *Computational Materials Science,* 7, 235-241.

BURSTOW, M. C. (1998) Local approach analysis of fracture in the transition region, Technical report, Department of Mechanical Engineering, The University of Sheffield.

CHARPY, A. G. A. (1901) Essay on the metals impact bend test of notched bars (translated from the original french by E. Lucon), reprinted in: T*he pendulum impact testing*: A Century of Progress, 2000. *Eds. T. A. Siewert and S. Manahan, ASTM STP 1380, West Conshohoken.*

CHEN, J. H., HU, X. J. & WANG, G. Z. (1996) The local fracture stress as a fracture toughness parameter to characterize an heterogeneous weld zone. *Fatigue Fract. Engng Mater. struct.,* 19, 68-80.

CHEN, J. H., WANG, G. Z., YANG, C., MA, H. & L., S. (1997a) Advances in the mechanism of cleavage fracture of low alloy steel at low temperature: Part I: critical event. *International Journal of Fracture,* 83, 105-120.

CHEN, J. H., WANG, G. Z., YANG, C., MA, H. & ZHU, L. (1997b) Advances in the mechanism of cleavage fracture of low alloy steel at low temperature. Part II: fracture model. *Int. J. Fract.,* 83, 121-138.

CHEN, J. H., WANG, G. Z., YANG, C., MA, H. & ZHU, L. (1997c) Advances in the mechanism of cleavage fracture of low alloy steel at low temperature. Part III. Local fracture stress: σf. *Int. J. Fract.,* 83, 139-157.

CHEN, J. H. & YANG, C. (1992) A comparison of toughness of C-Mn weld steel with different grain sizes. *Metallurg. Trans.* , 23A, 2549-2556.

CHEN, J. H., ZHU, L. & MA, H. (1990) On the scattering of the local fracture stress. *Acta Metall,* 38, 2527-2535.

CHU, C. & NEEDLEMAN, A. (1980) Void nucleation effects in biaxially stretched sheets. *Journal of Engineering Materials and Technology,* 102, 249-256.

CIZEK, P., WYNNE, B. P. & RAINFORTH, W. M. (2006) EBSD investigation of the microstructure and texture characteristics of hot deformed duplex stainless steel. *Journal of Microscopy,* 222, 85-96.

COTTRELL, A. H. (1959) Theory of brittle fracture in steel and similar metals. *Proceedings of swampscott Conference on Fracture. (Edited by B. L. Averbach) Wiley, New York*, 20-53.

CURRY, D. A. (1980) Cleavage micromechanisms of craks extesion in steels. *Metal Science,* 14, 319-326.

CURRY, D. A. & KNOTT, J. F. (1978) Effects of microstructure on cleavage fracture stress in steel. *Metal Sci.,* 12, 511-514.

CURRY, D. A. & KNOTT, J. F. (1979) Effect of microstructure on cleavage fracture toughness of quenched and tempered steels. *Metall. Sci*, 341-345.

DAS, S. (2002) The effect of boundary conditions and material data representation on the simulation of deformation during hot rolling. *Department of Engineering Materials, University of Sheffield, Ph. D. Thesis.*

DRUCE, S., GIBSON, G. & CAPEL, M. (1992) Micromechanical control of cleavage fracture in an A508 steel class 3 pressure vessel steel. *In: Ernst H, Saxena A, McDowell D, editors. Fracture Mechanics: Twenty Second Symposium, vol. I. ASTM STP 1131.*, 682-706.

ERIPRET, C., LIDBURY, D. P. G., SHERRY, A. H. & HOWARD, I. C. (1996) Prediction of fracture in the transition regime: application to an A533B pressure vessel steel. *Journal of Physique IV,* 6(C6), 315-323.

ERIPRET, C. & ROUSSELIER, G. (1994) First spinning cylinder test analysis using a local approach to fracture. *Nuclear Engineering and Design,* 152, 11-18.

FALESKOG, J., GAO, X. & SHIH, C. F. (1998) Cell model for nonlinear fracture analysis - I. Micromechanics calibration. *international Journal of Fracture,* 89, 355-373.

FALESKOG, J. & SHIH, C. F. (1997) Micromechanics of coalescence - I. Synergetic effects of elasticity, plastic yielding and multi-size-scale voids. *Journal of the Mechanics and Physics of Solids,* 45, 21-50.

FLEWITT, P. E. J. & WILD, R. K. (2001) Grain boundaries, their Microstrucutre and Chemistry. *Wiley.*

FRANKLIN, A. G. (1969) Comparison between a Quantitave Microscopic and Chemical Methods for Assessment of Nonmetallic Inclusions. *J. Iron and Steel Institute,* 207, 181-186.

GANDIN, C. A., DESBIOLLES, J. L., RAPPAZ, M. & THEVOZ, P. (1999) A three-dimensional Cellular Automaton - finite element model for the prediction of solidification grain structures. *Metallurgical and Materials Transactions,* 30A, 3153-3165.

GAO, X., DODDS, R. H., TREGONING, R. L. & JOYCE, J. A. (2001) Weibull stress model for cleavage fracture under high-rate loading. *Fatigue Fract Engng Mater Struct,* 24, 551-564.

GIBSON, G., CAPEL, M. & DRUCE, S. (1991) Effect of heat tratment on the fracture toughness transition properties of an A508 Class 3 steel. *In: Blauel J, Schwalbe K - H, editors. Defect assessment in components - fundamentals and applications, ESIS/EGF9. Mechanical Engineering Publications.*, 587-611.

GLADMAN, T. (1997) The physical metalluergy of microalloyed steels. *London, the Institute of Materials* 154.

GLADMAN, T., HOLMES, B. & MCIVOR, I. D. (1971) Effects of Second Phase Particles on the Mechanical Properties of Steels. *Iron and Steel Institute, London.*

GLADMAN, T., HOLMES, B. & PICKERING, F. B. (1970) Work hardening of low carbon steels. *Journal of the Iron and Steel Institute,* 208, 172-183.

GODSE, R. & GURLAND, J. (1989) A statistical mode for low temperature cleavage fracture in mild steel. *Acta Metall,* 37, 541-548.

GOODS, S. H. & BROWN, L. M. (1979) The nucleation of cavities by plastic deformation. *Acta Metallurgica,* 27, 1-15.

GRIFFITH, A. A. (1921) The phenomena of fracture and flow in solids. *Philosophical Transactions of the Royal Society of London,* Series A 221 163-198.

GRIFFITH, A. A. (1924) The theory of rupture. *in, Proceedings of the first international congress for applied mechanics, Delft*, 55-63.

GRIFFITHS, J. R. & OWEN, D. R. J. (1971) An elastic-plastic stress analysis for a nothed bar in plane strain bending. *J. Mech. Physics Solids,* 19, 419-431.

GROOM, J. D. G. & KNOTT, J. F. (1975) Cleavage fracture in prestrained mild steel. *Metal Sci.,* 9, 390-400.

GUENNOUNI, T. & FRANCOIS, D. (1989) Influence of secondary void damage in the matrix material around voids. *Fatigue and Fracture of Engineering Materials and Structures,* 12, 105-122.

GURLAND, J. (1972) Observations on the fracture of cementite particles in a spheroidized 1.05%C steel deformed at room temperature. *Acta Metall,* 20, 197-210.

GURLAND, J. & PLATEAU, J. (1963) The mechanism of ductile rupture of metals containing inclusions. *Transactions of the ASM,* 56, 443-454.

GURSON, A. L. (1977a) Continuum theory of ductile rupture by void nucleation and growtn: Part I - Yield criteria and flow rules for porous ductile media. *Eng. Mat. Tech.,* Vol. 99, 2-15.

GURSON, A. L. (1977b) Porous rigid-plastic materials containing rigid inclusions: Part II - Yield function, plastic potential and void nucleation. *D. M. R. Taplin, ed., Proceedings of the international conference of fracture. Vol 2A, Pergamon Press*, 357-364.

HAHN, G. T. (1984) The influence of microstructure on brittle fracture toughness. *Metallurgical Transactions,* A 15, 947-959.

HAHN, G. T., AVERBACH, B. L., OWEN, W. S. & COHEN, M. (1959) Initiation of cleavage microcracks in polycrystalline iron and steel. *in Averbach et al.*, 91-116.

HAHN, G. T., OWEN, W. S., ABERBACH, B. L. & COHEN, M. (1960) Micromechanism of brittle fracture in a low-carbon steel. *Welding Journal,* 3, 367-376.

HASHEMI, S. H. (2004) Assessment of the fracure bahaviour of high grade steel for gas pipelines. *A thesis submited for the degree of Doctor of Philosophy, Department of Mechanial Engineering, The University of Sheffield.*

HAYDEN, H. W. & FLOREEN, S. (1969) Observations of localised deformation during ductile fracture. *Acta Metallurgica,* 17, 213-214.

HENDRICKSON, J. A., WOOD, D. S. AND CLARKE, D. S. (1998) The cleavage fracture of mild steel. *Transation ASM*, 656-676.

HKS, H., KARLSSONN & SORENSEN (2001) Abaqus Theory Manual. *Inc., Providence, Rhode Island, USA.*

HOWARD, I. C., LI, Z. H. & SHEIKH, M. A. (2000) Modeling the ductile to cleavage transition in steels and structures. *in P. C. Paris and K. L. Jerina, eds, "Fatigue and Fracture Mechanics: 30th Volume, ASTM STP 1360" American Society for Testing and Materials, West Conshohocken, PA, USA.*, 152-168.

JACQUES, H. G. & STEVEN, W. K. (1998) Using the local approach to evaluate scaling effects in ductile fracture.

JANG, J. L., LEE, B. W., JU, J. B., KWON, D. & KIM, W. S. (2003) "Experimental analysis of the practical LBZ effects on the brittle fracture performance of cryogenic steel HAZs with respect to crack arrest toughness near fusion line". *Engineering Fracure Mechanics,* 70(10), 1245-1257.

KIM, M.-C., YONG, J. O. & JUNG, H. H. (2000) Characterization of boundaries and determination of effective grain size in Mn-Mo-Ni low alloy steel from the view of misorientation. *Scripta Materialia,* 43, 205-211.

KNOTT, J. F. (1966) Some effects of hydrostatic tension on the fracture behavior of mild steel. *Iron steel institute*, 104-111.

KNOTT, J. F. (1969) On stress intensification in specimens of Charpy geometry prior to general yield. *J. Mech. Phys. Solids,* 15, 97.

KNOTT, J. F. (1973) Fundamentals of fracture mechanics, Butterworths London.

KNOTT, J. F. (2008) Local approach concepts and the microstructures of steels. *Engineering Fracture Mechanics,* 75, 3560-3569.

KOPPENHOEFER, C. & DODDS, R. H. (1998) Ductile crack growth in precracked CVN specimens: numerical studies. *Nuclear Engineering and Design,* 180(3), 185-289.

KOTRENCHKO, S., STRNADEL, B. & DLOUHY, I. (2007) Fracture toughness of cast ferritic steel applying local approach. *Theoretical and Applied Fracture Mechanics,* 47, 171-181.

KWON, D. & ASARO, R. (1990) A study of void nucleation, growth, and coalescence in spheroidized 1518 steel. *Metallurgical Transactions* 21A, 117-134.

LAUTRIDOU, J. C. & PINEAU, A. (1981) Crack initiation and stable growth resistance in A508 steels in relation to inclusion distribution. *Engng Fract Mech,* 15, 5-71.

LEMAITRE, J. (1985) A continuum damage mechanics model for ductile fracture. *Journal of Engineering Materials and Technology,* 107, 83-89.

LEMAITRE, J. (1996) A Course of Damage Mechanics. *2 end. Springer.*

LEWANDOWSKI, J. J. & THOMPSOM, A. W. (1986) Microstructural effect on the cleavage fracture stress of fully pearlitic eutectoid steel. *Metallurg Trans.*

LIN, T., EVANS, A. G. & RITCHIE, R. O. (1986) A statistical model for brittle fracture by transgranular cleavage. *J. Mech. Phys. Solids,* 35, 477-497.

LIN, T., EVANS, A. G. & RITCHIE, R. O. (1987a) Stochastic modeling of the independent roles of particle size and grain size in transgranular cleavage fracture. *Metalluergical Transactions,* 18(4), 641-651.

LIN, T., EVANS, A. G. & RITCHIE, R. O. (1987b) Stochastic modeling of the independent roles of particle size and grain size in transgranular cleavage fracture. *Metalluurgical and Materials Transactions A,* 18A, 641-651.

LINDLEY, T. C., OATES, G. & RICHARDS, C. E. (1970) A critical appraisal of carbide cracking mechanisms in ferride/carbide aggregates *Acta Metall,* 18, 1127-1136.

LIU, C. T. & GURLAND, J. (1968) The fracture behaviour of spheroidized carbon steels. *Transactions of the ASM,* 61, 157-167.

LIU, Z. (1982) Cleavage fracture initiated by pearlite packets. *Iron Steel,* 17, 12.

MADAN, G., MENDIRATTA, ROBERT GOETZ, L. & DENNIS DIMIDUK, M. (1996) Notch fracture in γ-titanium aluminides. *Metallurg Mater. Trans,* 27A, 3903-3912.

MALIK, L., PESSEGODA, B. A., GRAVILLE, B. A. & TYSON, W. R. (1996) Crack arrest toughness of a heat-affected zone containing local brittle zones. *Journal of Offshore Mechanics and Artic Engineering, Transactions of the ASME,* 118, 292-200.

MARTIN, A. M., OCANA ARRISCORRETA, J., GIL, S. & M., F. P. (1994) Modelling cleavage fracture of bainitic steel. *Acta Metall,* 42, 2057-2068.

MCCLINTOCK, F. A. (1968) A Critetion for Ductile Fracture by the Growth of voids. *Journal of Applied Mechanics,* 35, 363-371.

MCMAHON, C. J. & COHEN, M. (1965) Initiation of cleavage in polycrystalline iron. *Acta Metall,* 13, 591-604.

MUDRY, F. (1987) A local approach to cleavage fracture. *Nuclear Engineering and Design,* 105, 65-76.

NOHAVA, J., HAUSILD, J. P., KARLÍK, M. & BOMPARD, P. (2002) Electron backscatering diffraction analysis of secondary cleavage cracks in a reactor pressure vessel steel. *Materials Characterization,* 49 (3), 211-217.

OROWAN, E. (1948) Fracture and strength of solids. *Report on Progress in Physics,* 12, 185.

PARDOEN, T. & HUTCHINSON, J. W. (2000) An extended model for void growth and coalescence. *Journal of the Mechanics and Physics of Solids,* 48, 2467-2512.

PETTI, J. P. & DODDS, R. H. (2003) Couppling of the Weibull stress model and macroscale models to predict cleavage fracture. *Engineering fracture mechanics,* 71, 2079-2103.

PINEAU, A. (1981) Review of fracture micromechanism and a local approach to predicting crack resistance in low strength steels. *Proccedings* ICF5 Canes France, Pergamon Press, Oxford, 553-557.

PRESTON, K. & DUFF, M. J. B. (1894) Modern Cellular Automata Theory and applications. *Plenum Press.*

PRESTON, K., DUFF, M. J. B., NORGREN, P. E. & TORIWAKI, J. L. (1979) Basic of Cellular Logic with Some Applications in Medical Image. *Proc. IEEE 67.*

PUTTICK, K. E. (1959) Ductile fracture in metals. *Phylosophical Magazine, Series 8,* 4(44), 964-969.

RAABE, D. (2002) Cellular automata in materials science with particular reference to recrystallization simulation. *Annu. Rev. Mater. Res,* 32, 53-76.

RAABE, D. & BECKER, R. C. (2000) Coupling of a crystal plasticity finite-element model with a probabilistic cellular automaton for simulating primary static recrystallization in aluminium. *Modelling and Simulation in Materials Science and Engineering,* 8, 445-462.

RANDLE, V. (1990) Representation of grain misorientations (mesotexture) in Rodrigues-Frank space. *Proc. R. Soc. Lond. A.,* 431, 61-69.

REED-HILL, R. E. & ABBASCHIAN, R. (1992) Physical metallurgy principles. *Third edition. PWS-Kent Publishing Company, Boston, USA,* 926.

RHINES, W. J. (1961) Ductile fracture by the growth of pores. *Master's thesis, MIT, Department of Mechanical Engineering.*

RICE, J. R. & TRACEY, D. M. (1969) On the ductile enlargement of voids in triaxiality stress fields. *Journal of the Mechanics and Physics and Solids,* 17, 201-217.

RITCHIE, R. O., KNOTT, J. F. & RICE, J. R. (1973) On the relationship between critical tensile stress and fracture toughness in mild steel. *J. Mech. Phys. Solids,* 21, 395-410.

ROGERS, H. C. (1960) Tensile fracture in ductile metals. *Transactions of the Metallurgical Society of AIME,* 218, 498-506.

ROSENFELD, A. (1979) Picture Languages. *Academic Press.*

ROSENFELD, A. (1983) Parallel Image Processing using Cellular Arrays. *Computer,* 16, 14-20.

ROSENFIELD, A. & SHETTY, D. (1973) Cleavage fracture of steel in the upper ductile-brittle transition region. *Engng Fract Mech,* 17(5), 461-470.

ROSENFIELD, A., SHETTY, D. & SKIDMORE, A. (1983) A fractographic observations of cleavage initiation in the ductile-brittle transition regions of a reactore-pressure-vessel steel. *Met Trans,* 14, 1934-1937.

ROUSSELIER, G. (1981) Finite deformation constitutive relations including ductile fracture damage. *In: Three Dimensional Constitutive Relations and Ductile Fracture (Edited by S. Nemat-Nasser). Amsterdam North-Holland*, 331-355.

ROUSSELIER, G. (1986) Ductile fracture models and their potential in local approach of fracture. *Nuclear Engineering and Design,* 105, 97-111.

ROUSSELIER, G. (1987) Ductile fracture models and their potential in local approach of fracture. *Nuclear Engineering and Design,* 105, 97-111.

ROUSSELIER, G., DEVAUX, J. C., MOTTEL, G. & DEVESA, G. (1989) A methodology of ductile fracture analysis based on damage mechanics: an illustration of a local approach of fracture, in J. D. Landes, A. Saxena and J. G. Merkle, eds. Nonlinear fracture mechanics: Volume II - Elastic-Plastic Fracture, ASTM STP 995, Philadelphia., 332-354.

RUSSELL, S. B. (1898) Experiments with a new machine for testing materials by impact. *American Society of Civil Engineers,* 39, 237-250 (reprinted in: *The Pendulum Impact Testing*: A Century of Progress, Eds. T. A. Siewert and S. Manahan, 2000: 17-45, ASTM STP 1380, West Conshohoken, Pennsylvania.

SHEHATA, M. T. & BOYD, J. D. (1981) Advances in Physical Metallurgy and Applications of Steels, Proc. Conf. University of Liverpool, Uk. *The Metals Society*, 229.

SHERRY, A. H., BEARDSMORE, D. W., LIDBURY, D. P. G., SHEIKH, M. A. & HOWARD, I. C. (1998) Remanent life assessment using the local approach - a prediction of the outcome of the NESC experiment. *in "Remanent Life Prediction - IMechE Seminar, London, 26 November 1997", Mechanical Engineering Publishing, Bury St Edmuns, UK*, 87-103.

SHTERENLIKHT, A. (2003) 3D CAFE modelling of transitional ductile-brittle fracture in steels. *Ph.D Thesis, Department of Mechanical Engineering, University of Sheffield.*

SHTERENLIKHT, A. & HOWARD, I. C. (2004) Cellular automata finite element (CAFE) modelling of transitional ductile-brittle fracture in steel. *Proceedings of The 15th European Conference of Fracture (ECF15)*.

SMITH, E. (1966) Proceddings of the Conference on the Physical Basis of Yield and Fracture, Inst. Phys. Soc. Oxford. *Oxford University Press*, 591.

SMITH, E. (1968) Cleavage fracture in mild steel. *The International Journal of Fracture Mechanics*, 4, 131-145.

SMITH, H. (1996) The nucleation and growth of cleavage microcracks in mild steels. *Proc. Conf. Physical Basis of Yield and Fracture, Inst. Phys. and Phys. Soc., London*, 36.

STEGLICH, D. & BROCKS, W. (1997) Micromechanical modeling of the behavior of ductile materials including particles. *Computational Materials Science*, 9, 7-17.

STERNBERG, S. (1980) Language and Architecture for Parallel Image Processing. *Pro. Conf. in Patern Recognition and Practice. Ed. Gelesman E. S. and Kanal L. N.*

SUMPTER, J. D. G. (1991) Fracture Avoidance in Submarines and Ships, Advances in Marine Structures - 2. *Proceeding of International Conference, Elsevier Applied Science*.

SUMPTER, J. D. G. & CAUDREY, A. J. (1995) Recommended fracture toughness for ship hull steel and weld. *Marine Structures*, 8, 345-357.

TALEFF, E. M., LEWANDOWSKI, J. J. & POURLADIAN, B. (2002) Microstructure-Property Relationships in Pearlitic Eutectoid and Hypereutectoid Carbon Steels. *JOM*, 25-30.

TANGUY, B., BESSON, J. & PINEAU, A. (2003) Comment on Effect of carbide distribution on the fracture toughness in the transition temperature region of a SA 508 steel. *Scripta Materialia*, 49, 191-197.

TANGUY, B., BESSON, J., PIQUES, R. & PINEAU, A. (2001) Numerical modeling of Charpy V-notch tests. *European Structural Integrity Society ESIS, Charpy Centenay Conference*, 2, 737-744.

TANGUY, B., BESSON, J., PIQUES, R. & PINEAU, A. (2005a) Ductile to brittle transition of an A508 steel characterized by Charpy impact test Part II: modeling of the Charpy transition curve. *Engineering Fracure Mechanics*, 72, 413-434.

TANGUY, B., BESSON, J., PIQUES, R. & PINEAU, A. (2005b) Ductile to brittle transition of an A508 steel characterized by Charpy impact test. Part I: experimental results. *Engineering Fracure Mechanics*, 72, 49-72.

TETELMAN, A. S., WILSHAW, T. R. & RAU JR, C. A. (1968) The critical tensile stress criterion for cleavage. *international Journal of Fracture*, 4, 147-157.

THOMASON, P. F. (1968) A theory for ductile fracture by internal necking of cavities. *Journal of the Institute of Metals* 96, 360-365.

THOMASON, P. F. (1981) Ductile fracture and the stability of incompressible plasticity in the presence of microvoids. *Acta Metallurgica*, 29, 763-777.

THOMASON, P. F. (1985a) Three-dimensional models for the plastic limit-loads at incipient failure of the intervoid matrix in ductile porous solids. *Acta Metallurgica*, 33, 1079-1085.

THOMASON, P. F. (1990) Ductile Fracture of Metals. *Pergamon Press.*

THOMASON, P. F. (1998) A view on ductile-fracture modelling. *Fatigue and Fracture of Engineering Materials and Structures,* 21, 1105-1122.

THOMPSON, A. W. & KNOTT, J. F. (1993) Micromechanisms of brittle fracture. *Metallurg Trans,* 24A, 523-534.

TIPPER, C. F. (1949) The fracture of metals. *Metallurgica* 39, 133-137.

TRONSKAR, J. P., MANNAN, M. A. & LAI, M. O. (2002) Measurement of fracture initiation toughness and crack resistance in instrumented Charpy impact testing. *Engineering Fracture Mechanics,* 69, 321-338.

TSANN LIN, A. G., EVANS & RITCHIE, R. O. (1986) A statistical model of brittle fracture by transgranular cleavage. *J. Mech. Phys. Solids* 34, 477-497.

TVERGAARD, V. (1981) Influence of voids on shear band instabilities under plane strain conditions *International Journal of Fracture,* Vol.17, 381-388.

TVERGAARD, V. (1982a) On localization in ductile materials containing spherical voids. *International Journal of Fracture,* 18, 237-252.

TVERGAARD, V. (1982b) On localization in ductile materials containing spherical voids. *International Journal of Fracture,* 18(4), 237-252.

TVERGAARD, V. (1990) Material failure by void growth to coalescence. *Advances in Applied Mechanics,* 27, 83-151.

TVERGAARD, V. & NEEDLEMAN, A. (1984) Analysis of the cup-cone fracture in a round tensile bar. *Acta Matallurgica,* 32, 157-169.

TWEED, J. & KNOTT, J. (1983) Effect of reheating on microstructure and toughness of C-Mn weld metal. *Metal Science,* 17, 45-54.

TWEED, J. H. & KNOTT, J. F. (1987) Micromechanisms of failure in C-Mn weld metals. *Acta Metall.,* 35, 1401-1414.

VALIENTE, A., RUIZ, J. & ELICES, M. (2005) A probabilistic model for the pearlite-induced cleavage of a plain carbon structural steel. *Engineering Fracure Mechanics,* 72, 709-728.

VANDYOUSSEFI, M. & GREER, A. L. (2002) Application of cellular automaton-finite element model to the grain refinement of directionally solidified Al-4.5 wt% Mg alloys. *Acta Materialia,* 50, 1693-1705.

VON NEWMANN, J. (1966) Theory of Self-Reproducing Automata. *University of Illinois Press, Edited and Completed by A. W. Burks.*

WALL, M., LANE, C. E. & HIPPSLEY, C. A. (1994) Fracture criteria for hydrogen and temper embrittlement in 9Cr1Mo steel. *Acta Metal. Mater.,* 42, 1295-1309.

WALLIN, K. (1984) The scatter in Klc result. *Engng Fract. Mech.,* 19, 1085-1093.

WALLIN, K., SAARIO, T. & TORRONEEN, K. (1984) Statistical model for carbide-induced brittile fracture in steel. *Metall. Sci,* 13-16.

WANG, G. Z. & CHEN, J. H. (1996) A comparison of fracture behavior of low alloy steel with different sizes of carbide particles. *Metallurg. Trans.* , 27A, 1909-1917.

WANG, G. Z. & CHEN, J. H. (1998) Cleavage fracture criterion of low alloy steel and weld metal in notched specimens *Int. J Fract.,* 89, 269-284.

WANG, G. Z. & CHEN, J. H. (1999) Effect of notch geometry on the local cleavage fracture stress. *Fatigue Fract. Engng Mater. Struct.,* 22, 849-858.

WANG, G. Z. & CHEN, J. H. (2000) A statistical model for cleavage fracture in notched specimens of C-Mn steel. *Fatigue Fract Engng Mater Struct,* 24, 451-459.

WANG, G. Z., LIU, Y. G. & CHEN, J. H. (2004) Investigation of cleavage fracture initiation in notched specimens of a C-Mn steel with carbides and inclusions. *Materials Science and Engineering,* A369, 181-191.

WANG, G. Z., WANG, J. G. & CHEN, J. H. (2003) Effects of geometery of notched specimens on the local cleavage fracture stress of C-Mn steel.

WANG, G. Z., WANG, Y. L. & CHEN, J. H. (2005) Effects of loading rate on the local cleavage fracture stress σf in notched specimens. *Engineering Fracture Mechanics,* 72, 675-689.

WEIBULL, W. (1951) A statistical distribution function of wide applicability. *Journal of Applied Mechanics,* 18, 293-297.

WU, S. J., DAVIS, C. L., SHTERENLIKHT, A. & HOWARD, I. C. (2005) Modeling the ductile-brittle transition behavior in thermomechanically controlled rolled steels. *Metallurgical and Materials Transactions A,* 36A, 989-997.

WU, S. J. & KNOTT, J. F. (2000) Proc. Conf. on Structural Integirty in the 21st Century, J. Edwards et al., EMAS Publishing. 247-255.

WU, S. J. & KNOTT, J. F. (2004) On the statistical analysis of local fracture stresses in notched bars. *Journal of the Mechanics and Physics of Solids,* 52, 907-924.

XIA, L. & CHENG, L. (1997) Transition from ductile tearing to cleavage fracture: A cell-model approach. *International Journal of Fracture,* 87(3), 289-306.

XIA, L. & SHIH, F. S. (1996) Ductile crack growth - III. transition to cleavage fracture incorporating statistics. *Journal of the Mechanics and Physics of Solids,* 44(4), 603-639.

XIAOSHENG, G. & DODDS, R. H. (2005) Loading rate effects on parameters of the Weibull stress model for ferritic steels. *Engineering fracture mechanics,* 72, 2416-2425.

YAHYA, O. M. L., BORIT, F., PIQUES, R. & PINEAU, A. (1998) Statistical modeling of intergranular brittle fracture in a low alloy steel. *Fatigue and Fracture of Engineering Materials and Structures,* 21, 1485,1502.

YAMAMOTO, H. (1978) Conditions for Shear Localization in the Ductile Fracture of Void-Containig Materials. *International Journal of Fracture,* 14, 347-365.

YANG, C., CHEN, J. H., SUN, J. & WANG, Z. (1993) Critical assessment of the local cleavage stress in notched specimens of C-Mn steel. *Metallurg. Trans.*, 24A, 1381-1389.

YOUNG-ROC IM, B.-J. L., YONG JUN OH, JUN HWA HONG, HU-CHUL LEE (2004) Effect of microstructure on the cleavage fracture strength of low carbon Mn-Ni-Mo bainitic steels. *Journal of Nuclear Materials,* 324, 33-40.

ZHANG, L., ZHANG, C. B., WANG, Y. M., LIU, X. H. & WANG, G. D. (2002) Cellular automaton model to simulate nucleation and growth of ferrite grains for low-carbon steels. *J. Mater. Res. (Materials Research Society),* 17, 2251-2259.

ZHANG, X. & KNOTT, J. (2000) The statistical modelling of brittle fracture in homogeneous and heterogeneous steel microstructures. *Acta Mater,* 48, 2135-2146.

ZHANG, Z. L., THAULOW, C. & ØDEGÅRD, J. (2000) A complete Gurson model approach for ductile fracture. *Engineering Fracure Mechanics,* 67(2), 155-168.

ZIKRY, M. A. & KAO, M. (1996) Inelastic microstructural failure mechanisms in crystalline materials with high angle grain boundaries. *Journal of the Mechanics and Physics of Solids,* 44(11), 1765-1798.

Chapter III

Experimental work

Smooth and notched tests with different constraint level were performed in this section to measure the mechanical properties of the steel under analysis and to characterize its fracture performance. The true stress-strain curve, measured with tensile tests, will be used in further finite element simulations. The notched tensile tests will be used to calibrate the micro damage model parameters to simulate softening behaviour of the steel and fracture propagation. The present section also shows the experimental analysis of the ductile-brittle transition of the steel performed with instrumented Charpy specimens tested from the upper to the lower shelf. Finally, experimental work for the identification of the different micromechanisms nucleating cleavage fracture over the ductile-brittle transition region using blunt four point double-notch bend tests is presented. Distributions of microcracks in the notch region of specimens at different temperatures are also presented in this chapter

3.1 Smooth tensile tests in the rolling and transverse direction.

The mechanical properties of Grade A plates steel along with the chemical composition of Grade A plates of producers of different countries are reported in managements summary reports (Materials Laboratory, 1997, British Steel plc for the Health and Safety Executive, 1997). But these reports and literature reviews did not report the true stress strain data for this steel. This is probably due to fact that, as mentioned in previous chapter, this steel does not require a minimum Charpy impact energy; consequently no deep research work has been done on this type of steels. As shown in this section, the stress–strain curve will be used in finite element models to calibrate damage model parameters and to analyze the fracture process in tensile tests. Therefore we need to measure true stress–strain curves of Grade A plate steel. A comparison of the mechanical properties of the present steel will be made with that reported in literature review. The steel used in the present research work is a commercially available Grade A ship plate steel purchased from a stockholder (Lloyds Register of Shipping). The chemical composition is given in table 1. The microstructure is composed of the ferrite matrix and bands of pearlite.

Table 3.1 – Chemical composition of Grade A ship plate steel, 20 mm plate (in wt %).

C	Si	Mn	P	S	Cr	Ni	Mo	Al	V	Nb	Cu	Ti
0.13	0.24	0.66	0.015	0.016	<0.04	<0.02	<0.005	0.006	<0.005	<0.005	<0/02	<0.005

In the present work, uniaxial tensile tests were performed to measure the mechanical properties of the steel and to characterize the fracture performance of the steel in both, the rolling and the transverse direction of the material. The geometry of test sample is shown in figure 3.1, all dimensions are in mm. Figure 3.2 shows a set of four tensile specimens tested in each direction of the material, each end of the specimens were machined flattened for a better grip by the hydraulic grips. The cylindrical specimens had $40\,mm$ gauge length and $10\,mm$ of diameter. Figure 3.3 shows the instrumentation set up of a tensile test. The figure also shows the axial and transverse extensometers mounted on a smooth tensile specimen, and the hydraulic grips of the Instron test machine:

The tests were performed under displacement control of $0.05\,mm/s$ on a servo–hydraulic Instron 8501 test machine with hydraulic grips. The load, displacement, diametral contraction and axial elongation evolutions were recorded for each test. The load and displacement were recorded automatically from the Instron machine. An Instron Strain Gauge Extensometer model $2620-604$ was used to capture the axial elongation and an Epsilon Extensometer model $3575-100-ST$ was used to obtain the diametral contraction. These extensometers were calibrated and connected to the acquisition system data. Special attention was taken to the

transverse extensometer in order to capture with high accuracy the contraction of the material on the necking zone.

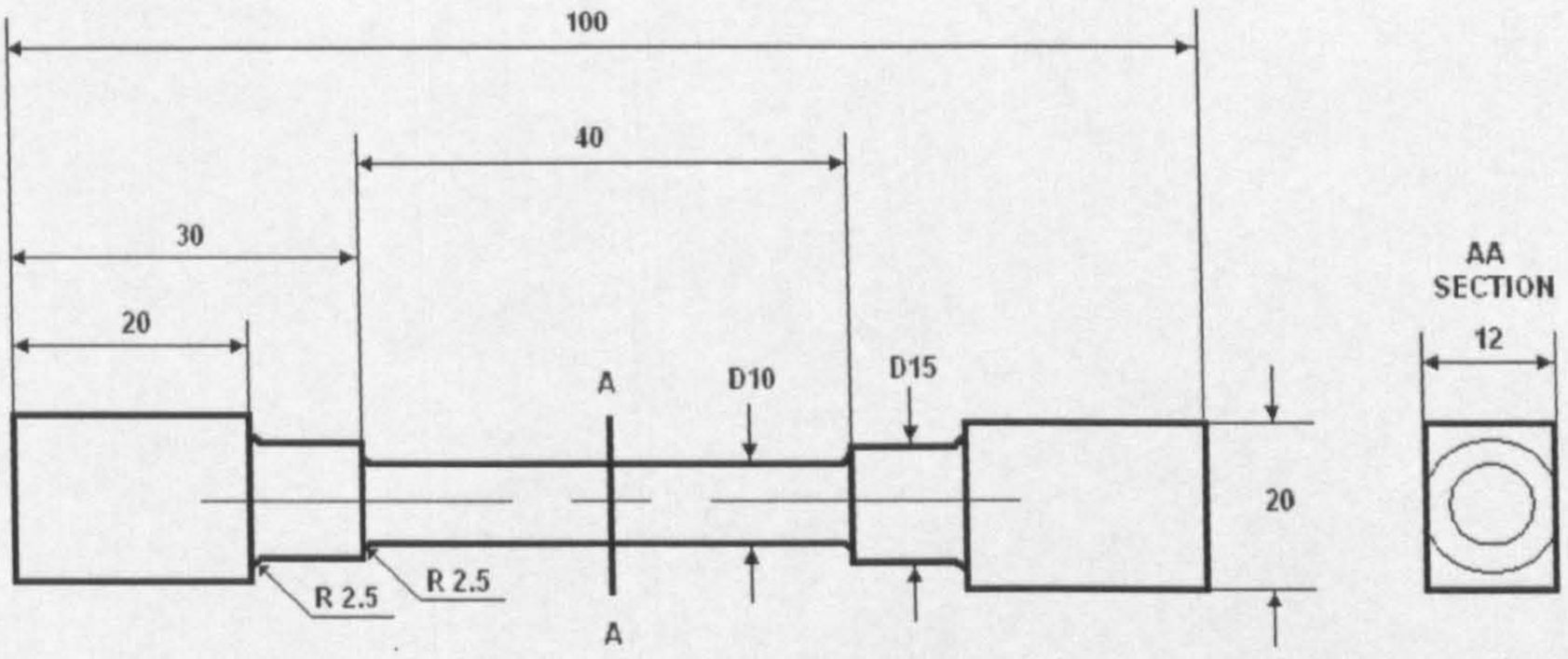

Figure 3.1 – Geometry of plain bar tensile specimen

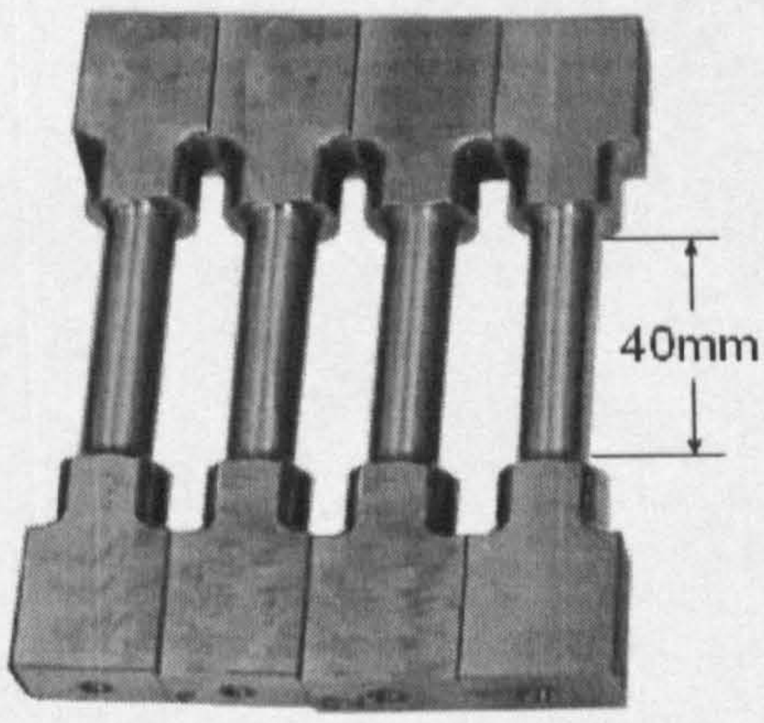

Figure 3.2 – Smooth round bar tensile specimens.

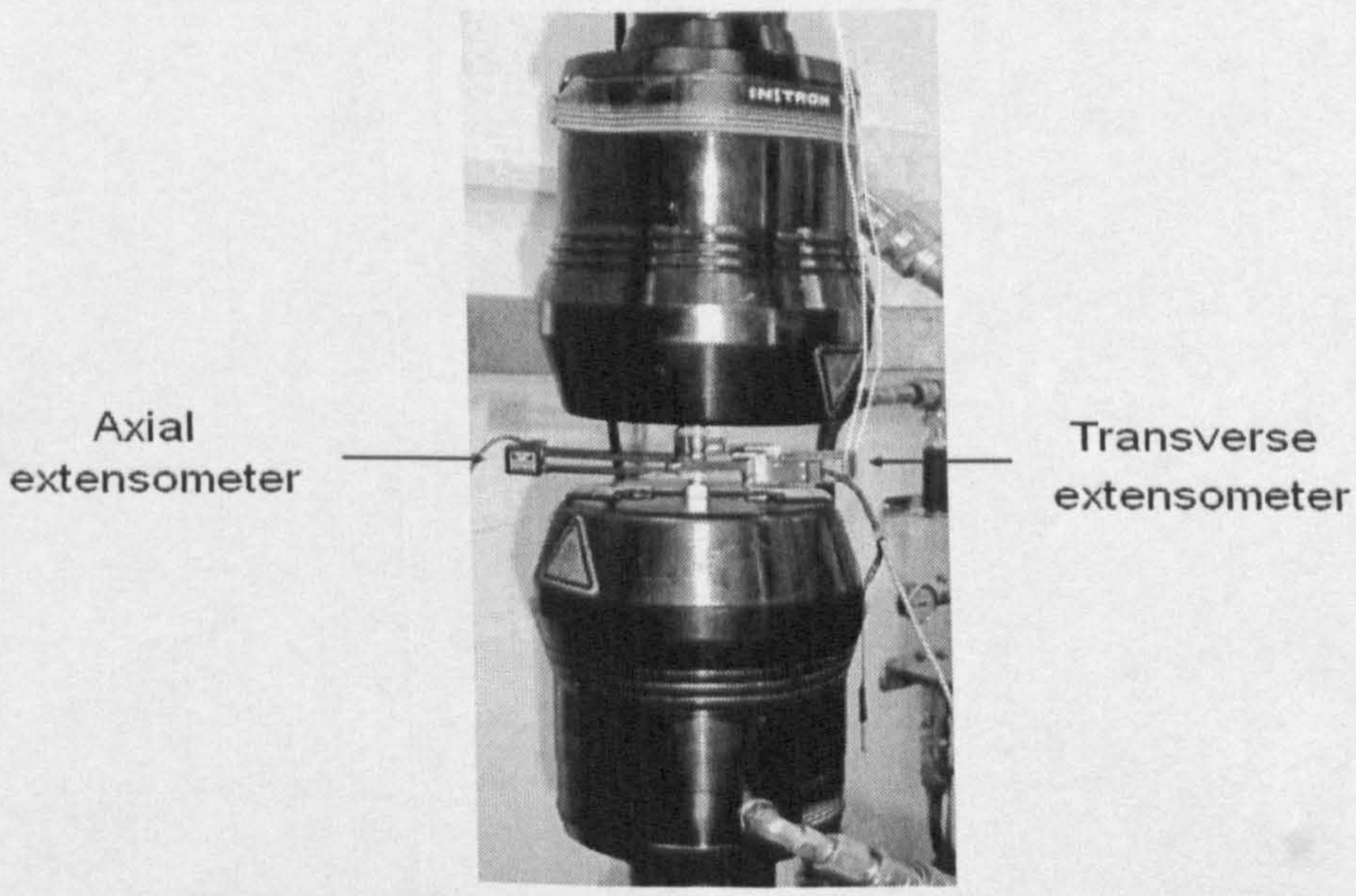

Figure 3.3 – Set up of a tensile test showing the axial and transverse extensometer.

3.1.1 Material characterization.

Figure 3.4 and 3.5 shows the experimentally obtained load vs diametral contraction from two sets of 4 plain tensile experiments for the rolling and the transverse directions of the plate steel respectively. The applied strain rate $\dot{\varepsilon}$ to the tensile tests in both directions of the material was$16.5\times10^{-4}\ s^{-1}$, the stress–strain response of the material obeys the power–hardening relation:

$$\sigma = E\varepsilon; \quad \sigma < \sigma_y \tag{3.1}$$

$$\sigma = K\varepsilon^n; \quad \sigma \geq \sigma_y \tag{3.2}$$

The true stress–stain curve was derived assuming a power law strain hardening for the experimental data between the yield stress and the tensile strength using the equation:

$$Log(10)\sigma_T = Log(10)K + nLog(10)\varepsilon_T \tag{3.3}$$

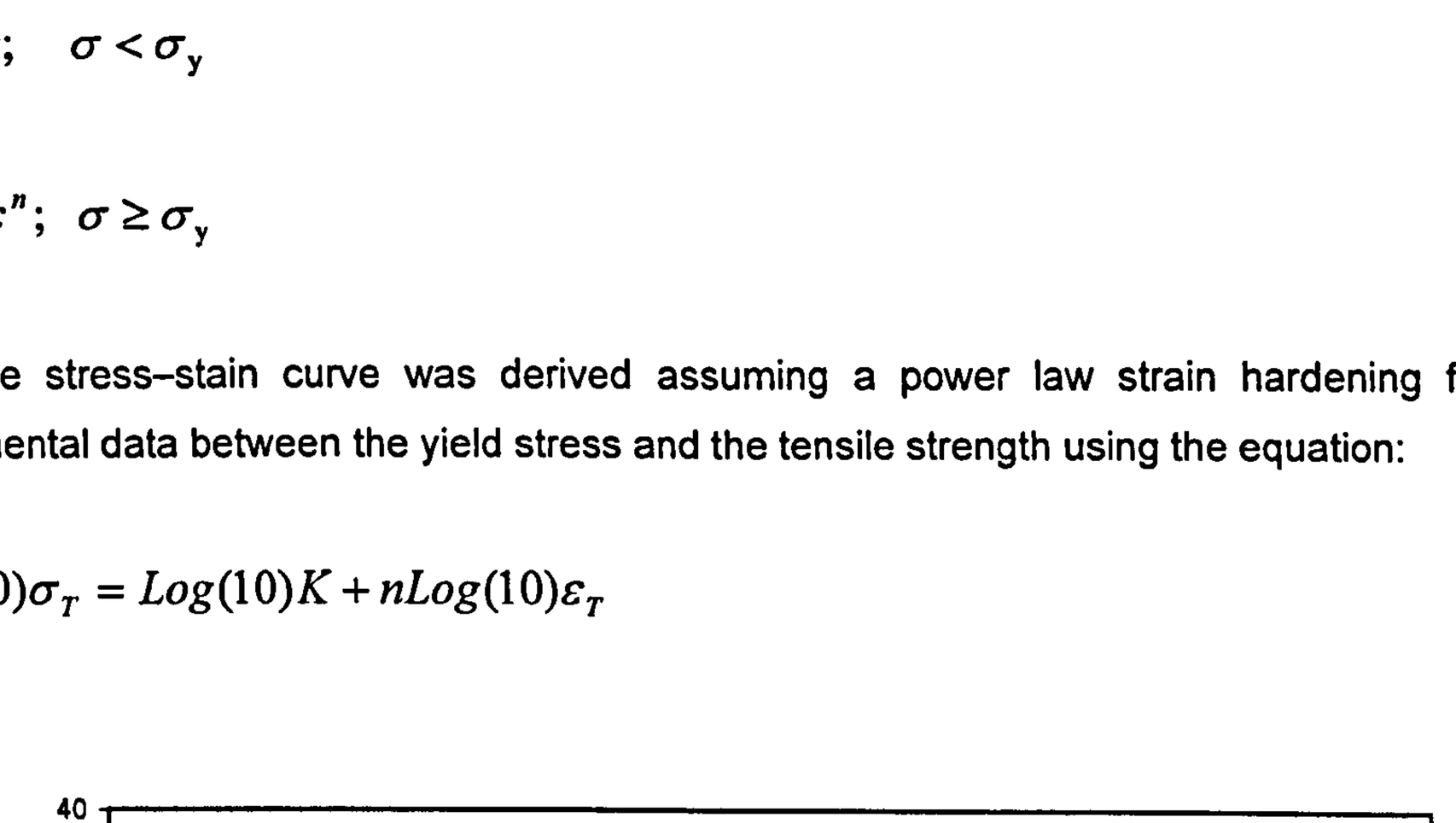

Figure 3.4 – Load–diametral contraction for the set of smooth tensile bars taken from the rolling direction of the plate

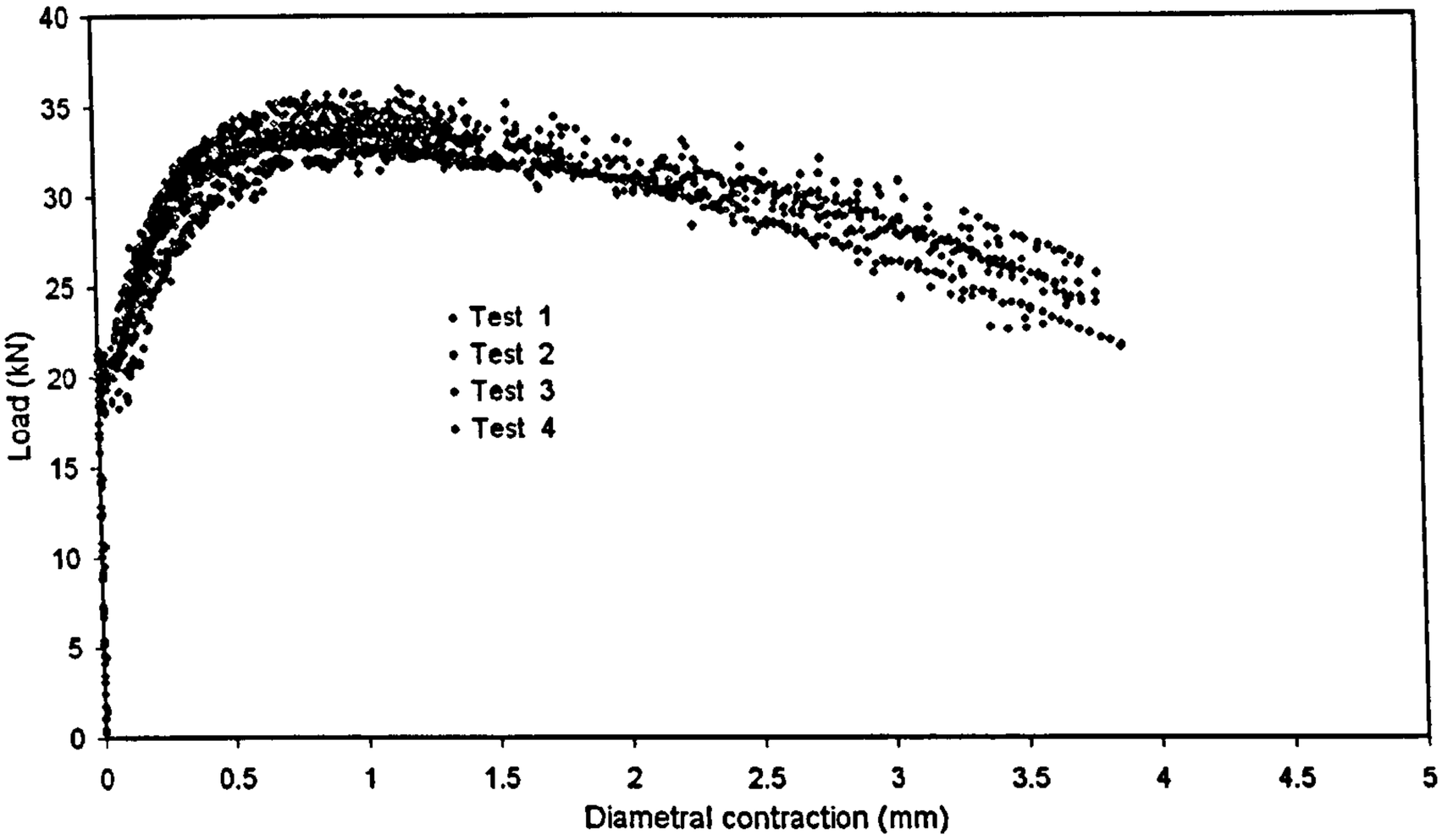

Figure 3.5 – Load–diametral contraction for the set of smooth tensile bars taken from the transverse direction of the plate

where σ_T and ε_T are the true stress and true strain respectively. To estimate the true stress–strain values before the necking of the tensile specimens, the following relationships were used:

$$\sigma_T = \frac{P}{A_T} \tag{3.4}$$

$$\varepsilon_T = \ln\left(\frac{l_i}{l_o}\right) \tag{3.5}$$

where P is the load, A_T is the true value of the cross–sectional area, l_i is the instantaneous length, l_o is the original gauge length of tensile specimens. To estimate the real area of the tensile specimens, the thickness and axial strains were calculated from the circumferential strains using:

$$\varepsilon_{thickness} = \varepsilon_{axial} = -\nu\varepsilon_{circumferential} \tag{3.6}$$

where ν is the Poisson's ratio with values of 0.3 and 0.5 in elastic and plastic regions respectively. The percent of elongation is simply defined as:

$$\%_{Elong}\frac{(L_f - L_o)}{L_o}\times 100\% \qquad 3.7$$

where L_o is the initial gauge length and L_f is the length of the gauge section at fracture. The percent of reduction of area at fracture is defined as:

$$\% = \frac{(A_o - A_f)}{A_o}\times 100\% \qquad 3.8$$

where A_o is the initial cross–sectional area and A_f is the cross–sectional area at fracture. The measured properties of the material are reported in table 3.2 and 3.3 for the rolling and transverse direction of the material respectively. The last row of the tables shows the average value of the measured parameters of the four tested specimens.

Table 3.2 – Mechanical properties obtained for the plate steel in the rolling direction.

Test	σ_Y (0.2% proof strees) MPa	σ_{UTS} MPa	$\frac{\sigma_Y}{\sigma_{UTS}}$	E GPa	Elongation %	Reduction of area %	$\sigma_T = K\varepsilon_T{}^n$ n	K MPa
1	259	540	0.4796	210	30.78	69.75	0.2021	677
2	263	566	0.4646	210	30.50	69.70	0.2050	680
3	268	560	0.4785	210	31.50	70.10	0.2000	673
4	253	570	0.4669	210	30.50	70.00	0.2030	670
Average	261	559	0.4724	210	30.82	69.88	0.2025	675

Table 3.3 – Mechanical properties obtained for the plate steel in the transverse direction.

Test	σ_Y (0.2% proof strees) MPa	σ_{UTS} MPa	$\frac{\sigma_Y}{\sigma_{UTS}}$	E GPa	Elongation %	Reduction of area %	$\sigma_T = K\varepsilon_T{}^n$ n	K MPa
1	258	532	0.4849	210	31.37	61.37	0.175	650
2	270	545	0.4954	210	35.57	60.65	0.172	645
3	262	552	0.4746	210	31.37	62.34	0.175	650
4	267	525	0.5184	210	33.03	63.50	0.177	640
Average	264	536	0.4933	210	32.835	61.96	0.174	646

The mechanical properties reported in tables 3.2 and 3.3 are in the range of the reported values in management summary reports (British Steel Limited Swinden Technology Centre Health and Safety Executive, 2000-2001, British Steel plc for the Health and Safety Executive, 1997). The fitted true stress–strain curves using equation 3.2 for the rolling direction and transverse direction are shown in figure 3.6 and 3.7 respectively. The hardening constitutive relationship of the material already derived was used to extrapolate the true stress–strain data from the yield stress to the tensile strength in the rolling and transverse direction. The hardening exponent n and the strength coefficient K, reported in tables 3.2 and 3.3 were obtained by a log–log plot of the experimentally measured stress vs the plastic strain. The K value is the intercept at true plastic strain equal to 1 $(\varepsilon = 1)$ as shown in figure 3.8. The slope of the straight line of figure 3.8 is the hardening exponent (n).

The mechanical properties reported in table 3.2 and 3.3 along with the true stress–strain curves, in the rolling and transverse direction, obtained in this section, will be used for further finite element simulations to study the mechanical behaviour of the material response and to obtain the material damage value parameters of the damage model used in the present project.

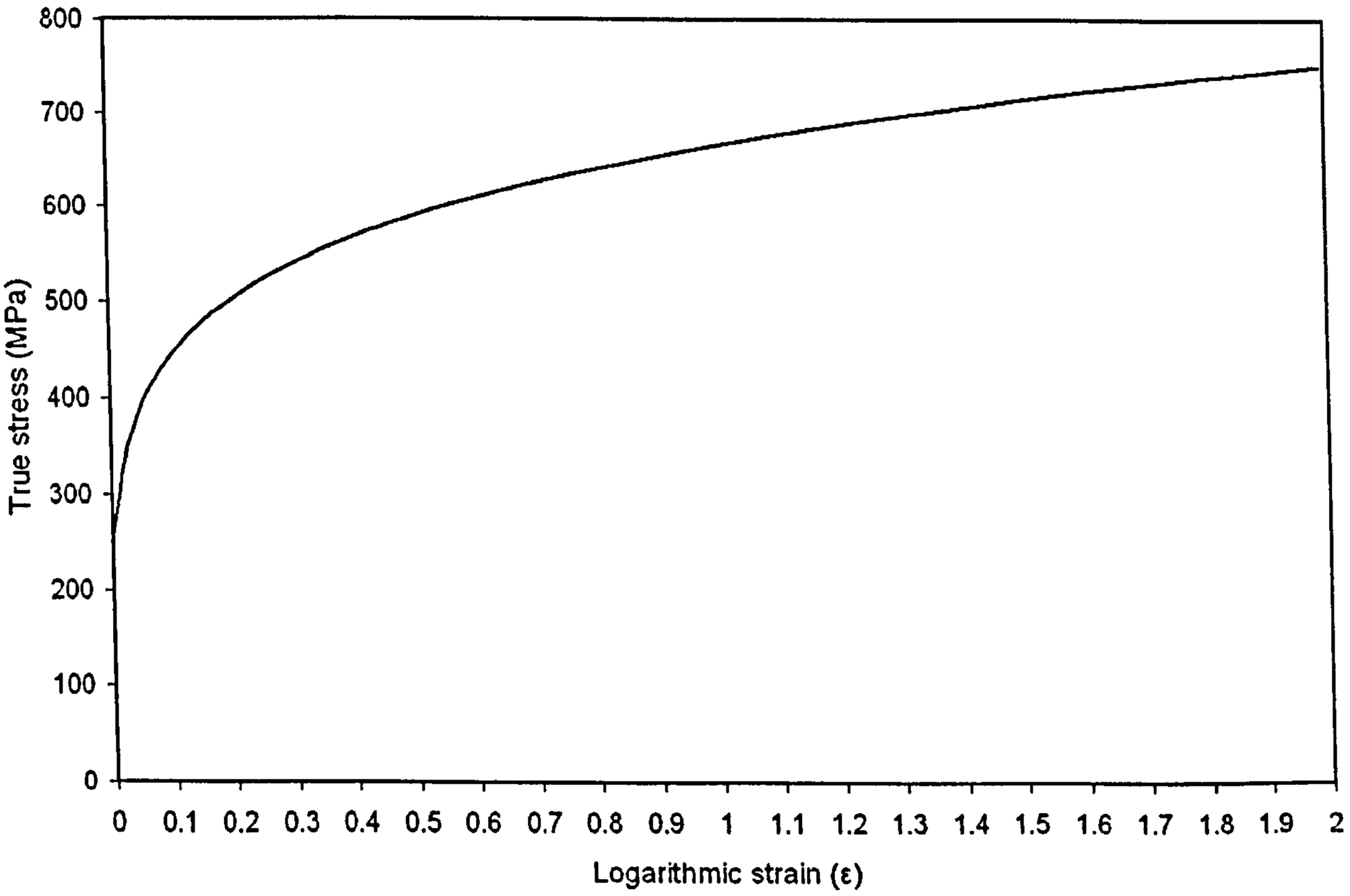

Figure 3.6 – True stress curve as a function of the true strain in the rolling direction.

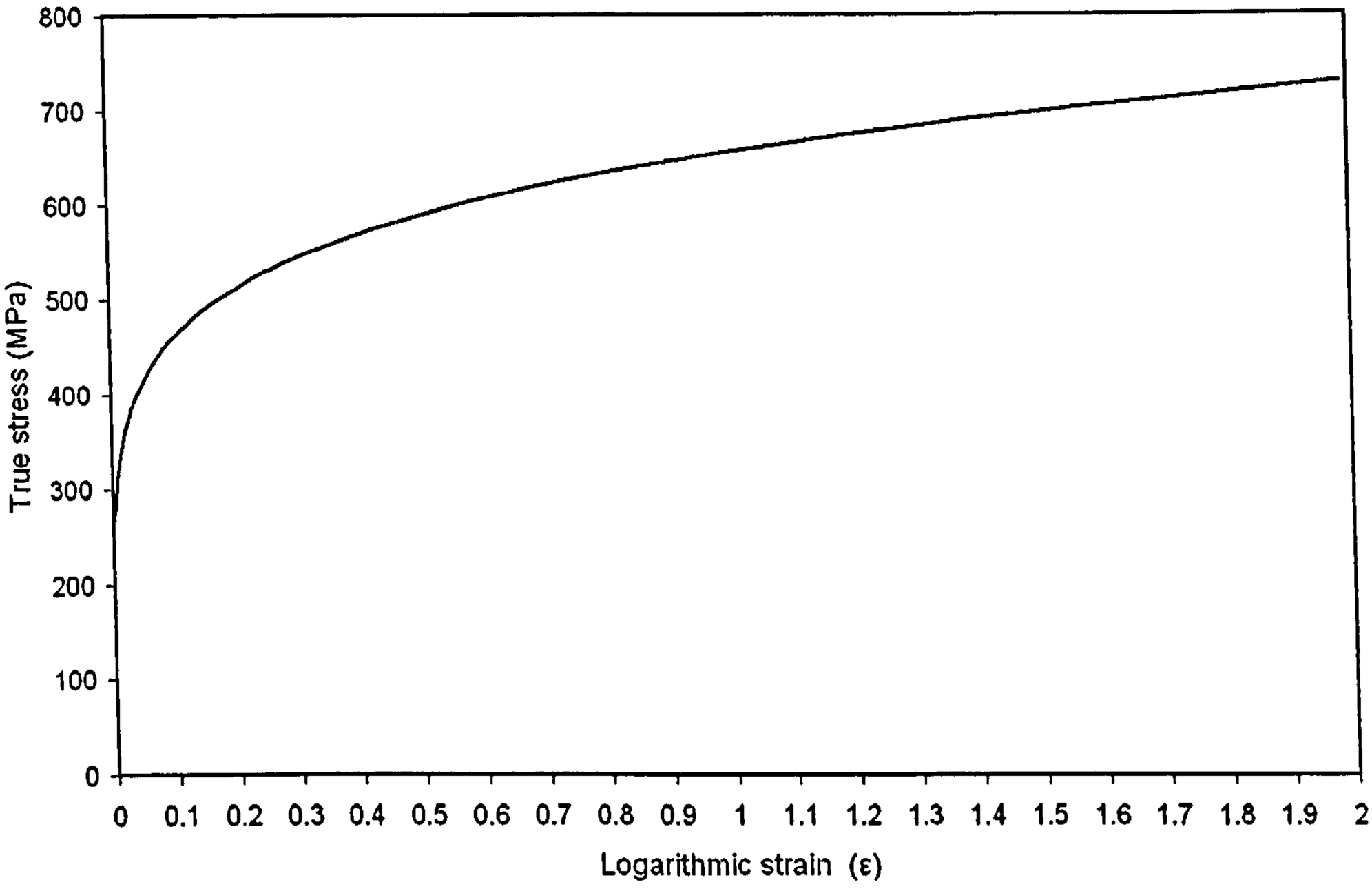

Figure 3.7 – True stress curve as a function of the true strain in the transverse direction.

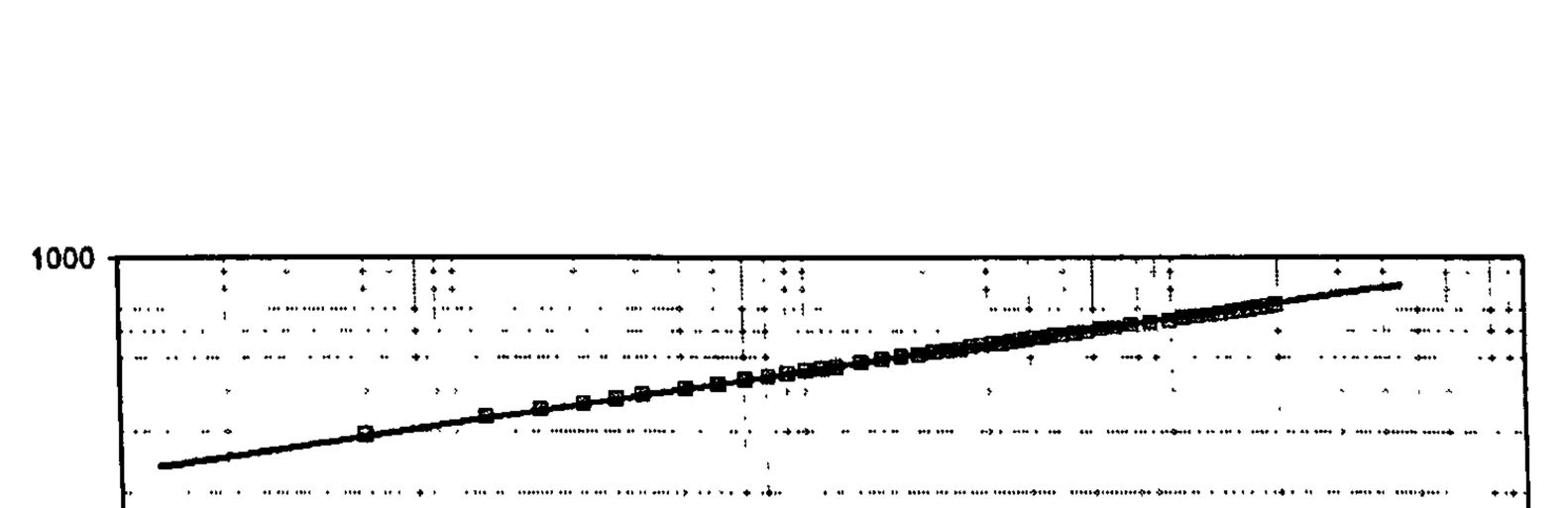

Figure 3.8 – Log–log plot of true stress vs true plastic strain in the rolling direction.

3.2 Notch tensile tests and failure analysis in notched bars.

The purpose of testing notch specimens, in the present research work, was to capture experimental data with different constraint levels to calibrate damage model parameters of the damage models used in the present work to simulate softening on various sets of specimens with different levels of stress triaxiality. Two sets of notch tensile bar specimens with different gauge diameter and notch acuity were tested. Each set had four specimens, the specifications of test samples are shown in figures 3.9 and 3.10 for notch radius of $6\,mm$ and $2\,mm$ respectively. Figure 3.11 and figure 3.12 show two sets of three notch tensile bars specimens used in this work.

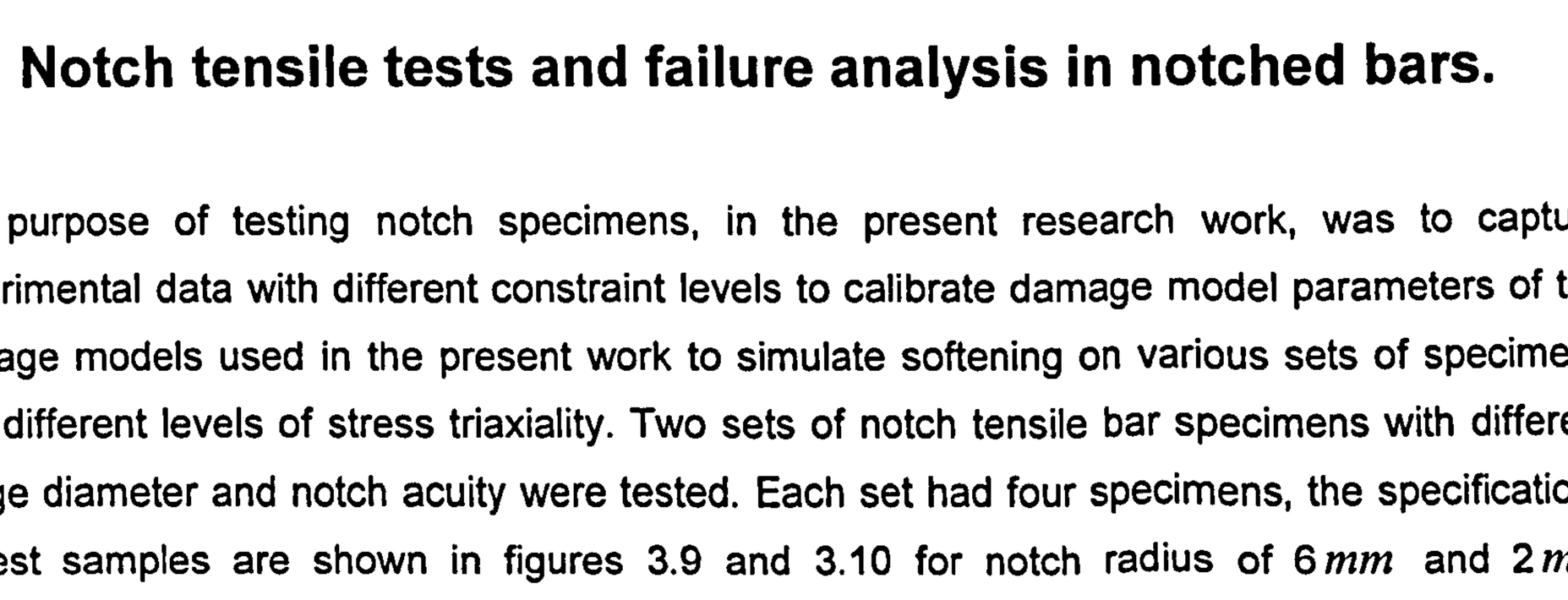

Figure 3.9 – Geometry of notch bar tensile specimen with a notch radio of 6mm, all the dimensions are in mm.

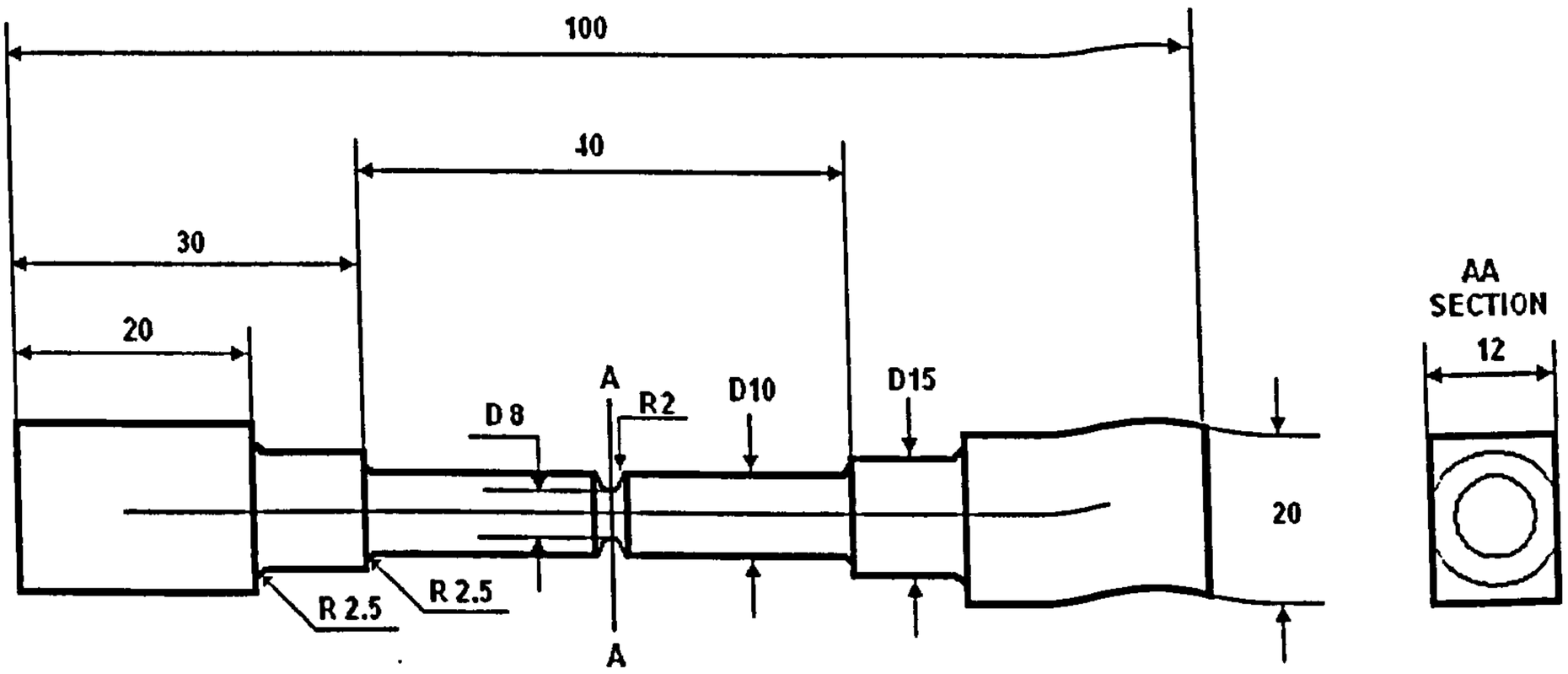

Figure 3.10 – Geometry of notch bar tensile specimen with a notch radio of 2mm, all the dimensions are in mm.

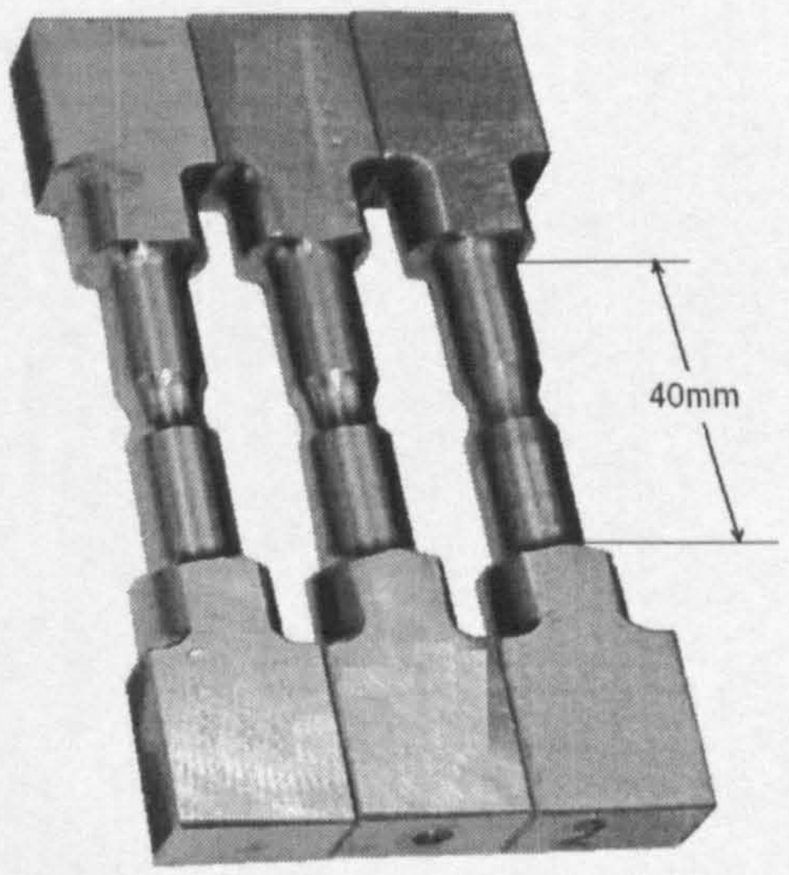

Figure 3.11 – 6mm notch tensile specimens.

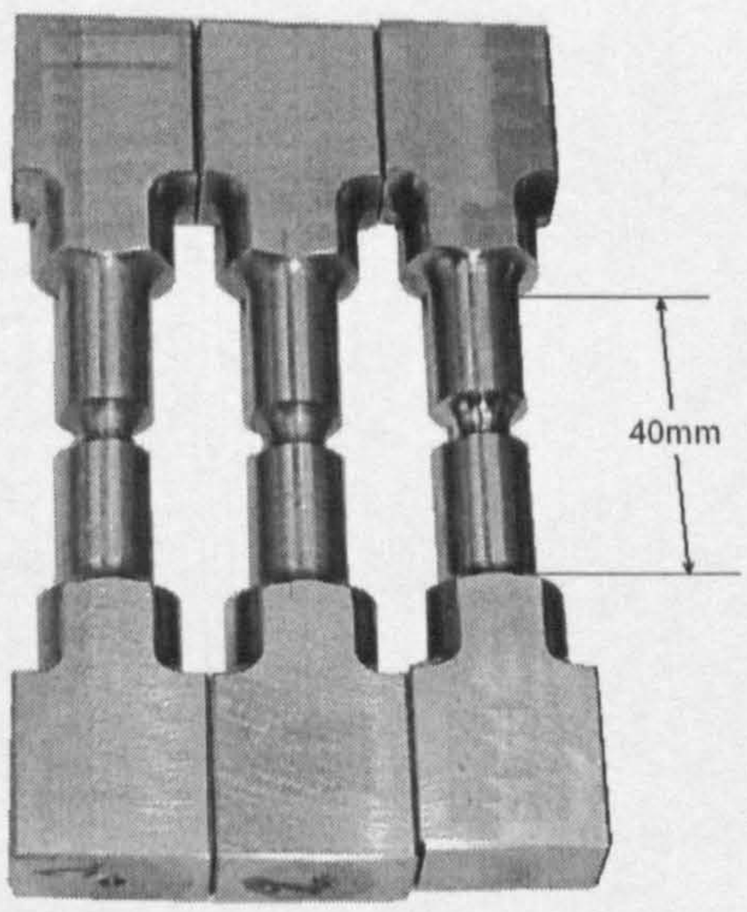

Figure 3.12 – 2mm notch tensile specimens.

The tests were performed under displacement control of $0.05\,mm/s$ on a servo–hydraulic Instron 8501 test machine with hydraulic grips (fig. 3.3). As in the smooth tensile tests, the load and displacement were recorded from the Instron machine. An Instron Strain Gauge Extensometer model $2620-604$ was used to capture the axial elongation and an Epsilon Extensometer model $3575-100-ST$ was used to obtain the diametral contraction. These extensometers were calibrated and connected to the data acquisition system. Special attention was taken to the transverse extensometer in order to capture with high accuracy the contraction of the material in the necking zone. The plot of load vs diametral contraction for the two sets of notch tensile bars of $6mm$ and $2mm$ for the rolling and transverse direction is shown in figures 3.13 and 3.14 respectively.

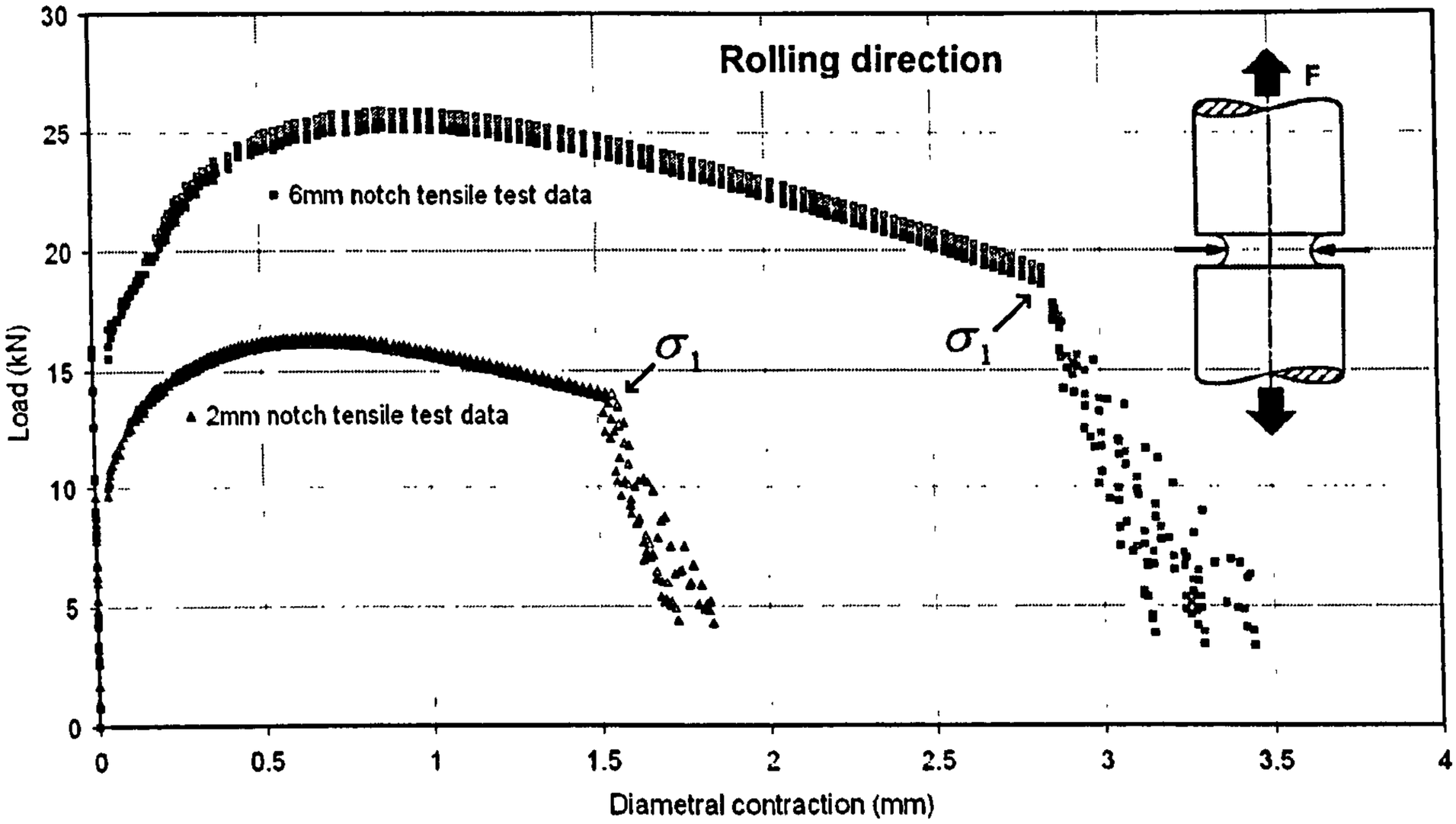

Figure 3.13 – Rousselier damage model parameter σ_1 in the rolling direction.

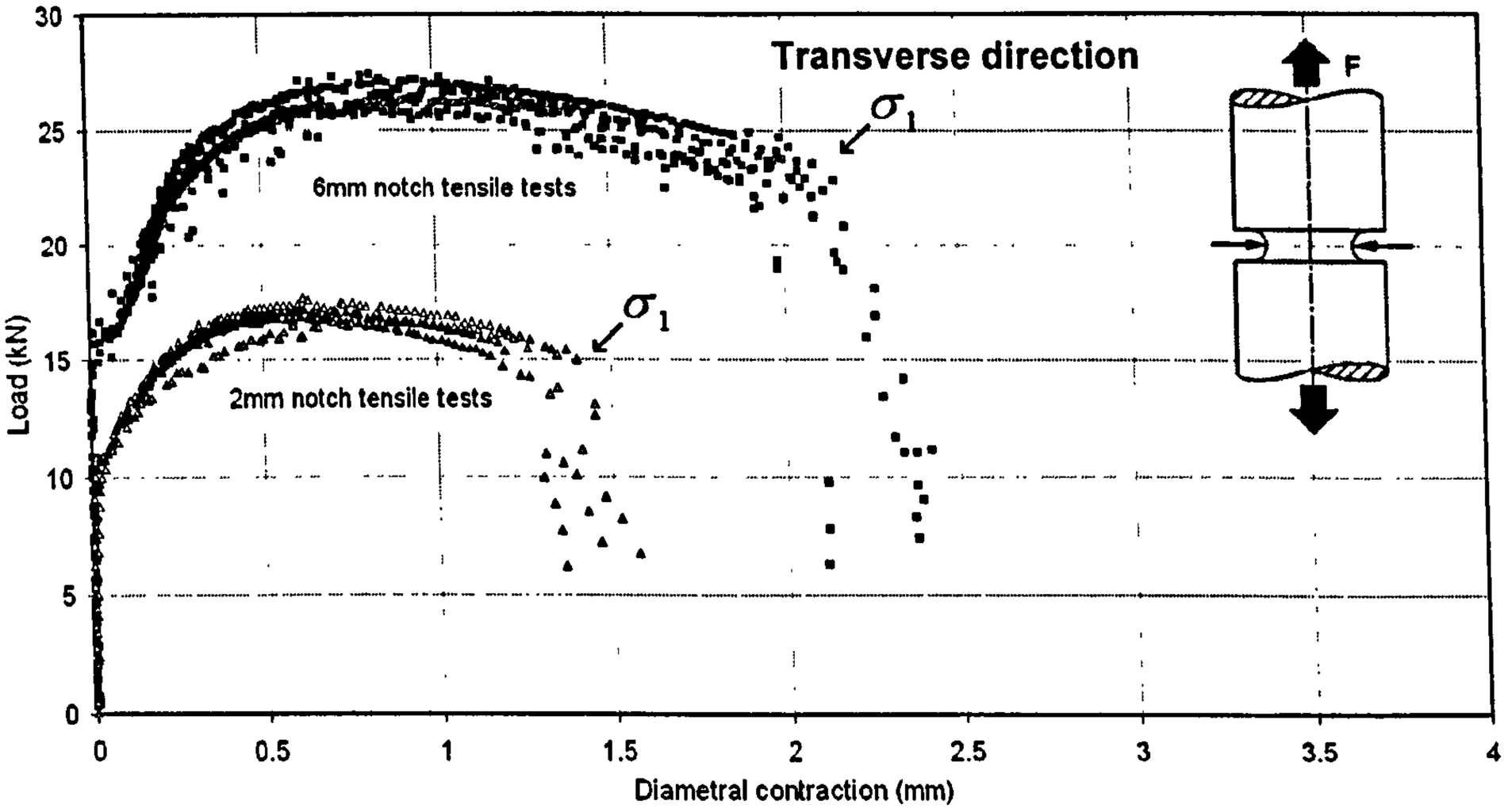

Figure 3.14 – Rousselier damage model parameter σ_1 in the transverse direction.

Figures 3.13 and 3.14 show the data of two sets of notch tensile tests with different notch radii radius, these figures also show the position from where the Rousselier damage model parameter σ_1 is measured. As mentioned above, the present tests were performed mainly to obtain this parameter which will be used in further finite element simulations.

The experimental data of previous figures shows scatters in the data points, this may be attributed to noise induced by the testing machine into the acquisition system during the loading

process. But it is important to mention that Hashemi (Hashemi et al., 2004) and more recently Ayvar (Ayvar et al., 2006) tested tensile specimens of a high–toughness bainitic steel ($X100$ pipe line steel) in the same machine and under the same conditions of displacement as that of Grade A plate steel. Ayvar obtained the experimental result without any evidence of scatter in data points. In order to investigate possible wrong calibration, the author repeated the tests by testing each sample after Ayvar finished his testing with the same results, but in all notch and smooth tensile tests the results presented scatter in data points. No further investigation took place about this phenomenon in the present work as the main purpose of the work is not the investigation of this phenomenon.

3.3 Four point bend tests to measure the mechanical properties of the plate steel at –60°C.

Four point bending is used to measure the mechanical properties of materials that behave in a brittle manner. This method can be applied to obtain the stress–strain curve of metals at low temperatures by measuring the deformation in the elastic region using strain gauges and applying the theoretical relationship between strains and bending moment. Young's modulus and the yield stress value are obtained. With the use of the hardening exponent for low temperatures (n), the stress–strain curve are obtained with equation 3.11. This procedure was used to obtain the true stress–strain curve of a Grade A plate steel for a test temperature of –60°C. At this temperature, laboratory Charpy and double–notch fourpoint bend tests specimens showed 100% of cleavage fracture in the broken surfaces. In this work, a combination of instrumented four–point–bend tests and finite element simulations of those specimens was applied to measure the mechanical properties of the steel at –60°C.

The first step was to measure the mechanical properties of the steel at room temperature on a servo hydraulic Instron tensile test machine under displacement control of $0.05\,mm/s$. As already mentioned in Chapter III, two extensometers were used to capture the displacement in the axial and transverse direction of smooth tensile specimens. From the axial direction, the true strain was obtained with next formula: $\varepsilon = \ln\left[(l_o + \Delta l)/l_o\right]$, where ε is the true strain, l_o is the original gauge length of the specimen, Δl is the increment of the displacement at each point increment up to the rupture of the specimen.

The four point bend specimens (plates) were instrumented with two strain gauges along the longitudinal axis, one on the top and the other one on the bottom as illustrated by figure 3.15. A special container was designed to test the specimens at low temperatures; the container was

insulated completely with polystyrene to help to keep the temperature inside the bath as constant as possible. Liquid nitrogen was used to cool the samples, to control the temperature of the specimens; a thermocouple was inserted in the specimens on the position marked by the arrow in figure 3.15. Careful attention was taken in order to maintain the temperature as constant as possible during testing, this was done by using a special wool fiber in the bottom of the container which absorbed the liquid nitrogen and released cold gas to cool the specimens. A variation of $\pm$ 1ºC was obtained inside the chamber.

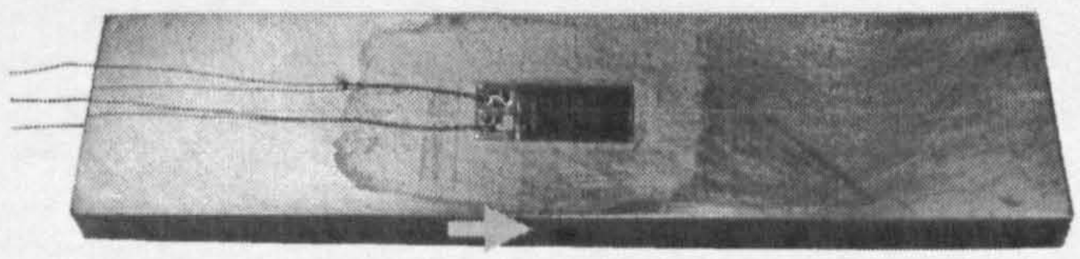

Figure 3.15 – Instrumented four point bend specimen.

The two strain gauges were connected into a half Wheatstone bridge arrangement to increase the strain measurement sensitivity (Willian et al., 2002), each strain gauge was connected in a Vishay Measurement Group's $P3500$ Strain Indicator. Figure 3.16 shows the two strain–indicator boxes where the strain gauges were connected, the output signal of strain indicators were transferred to two Schlumberger 7150 Plus Digital Multimeter as shown in figure 3.16 which were connected to the acquisition system data of the Instron machine.

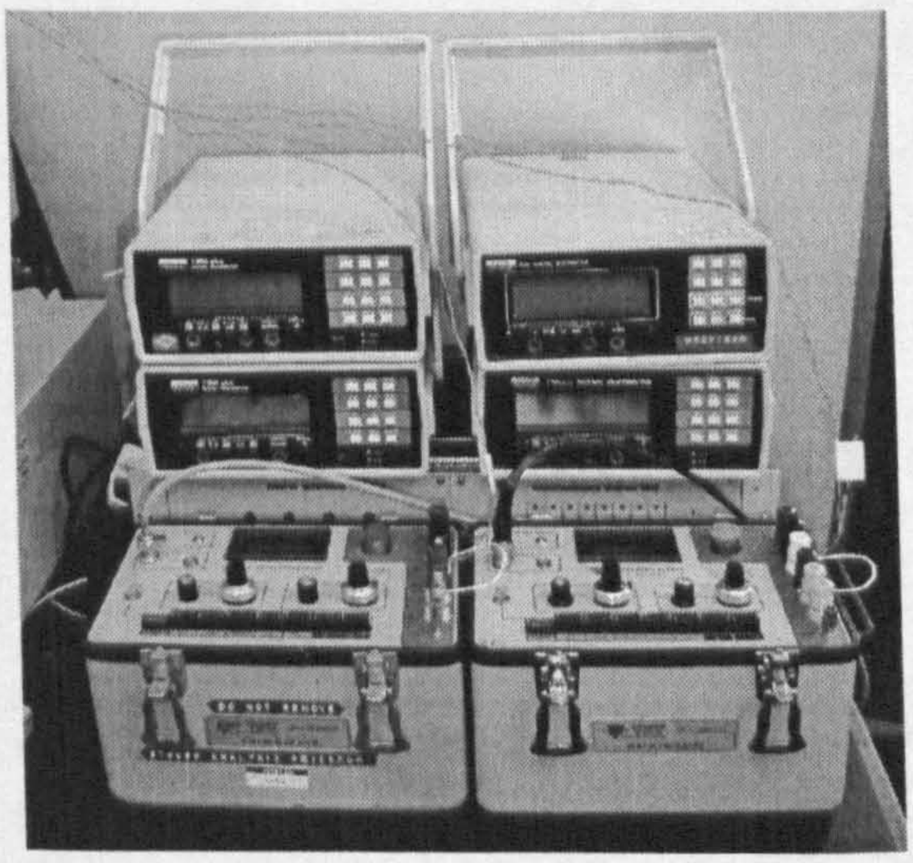

Figure 3.16 – Strain–indictor (yellow boxes) and digital multimeters (white boxes) to acquire the microstrain $(\mu\varepsilon)$ of the strain gauges connected to the specimens.

For the strain gauges used in this work, the Measurement Division (Micro-Measurement Division) specify a gauge factor for the strain gauges under loading conditions at room temperature test (+24ºC) of 2.086. At this temperature the strain gauges do not need any

correction factor, but when the temperature is different, a correction factor must be applied in order to obtain reliable results. Figure 3.17 shows temperature compensation to the gauge factor of the strain gauges used in the present work.

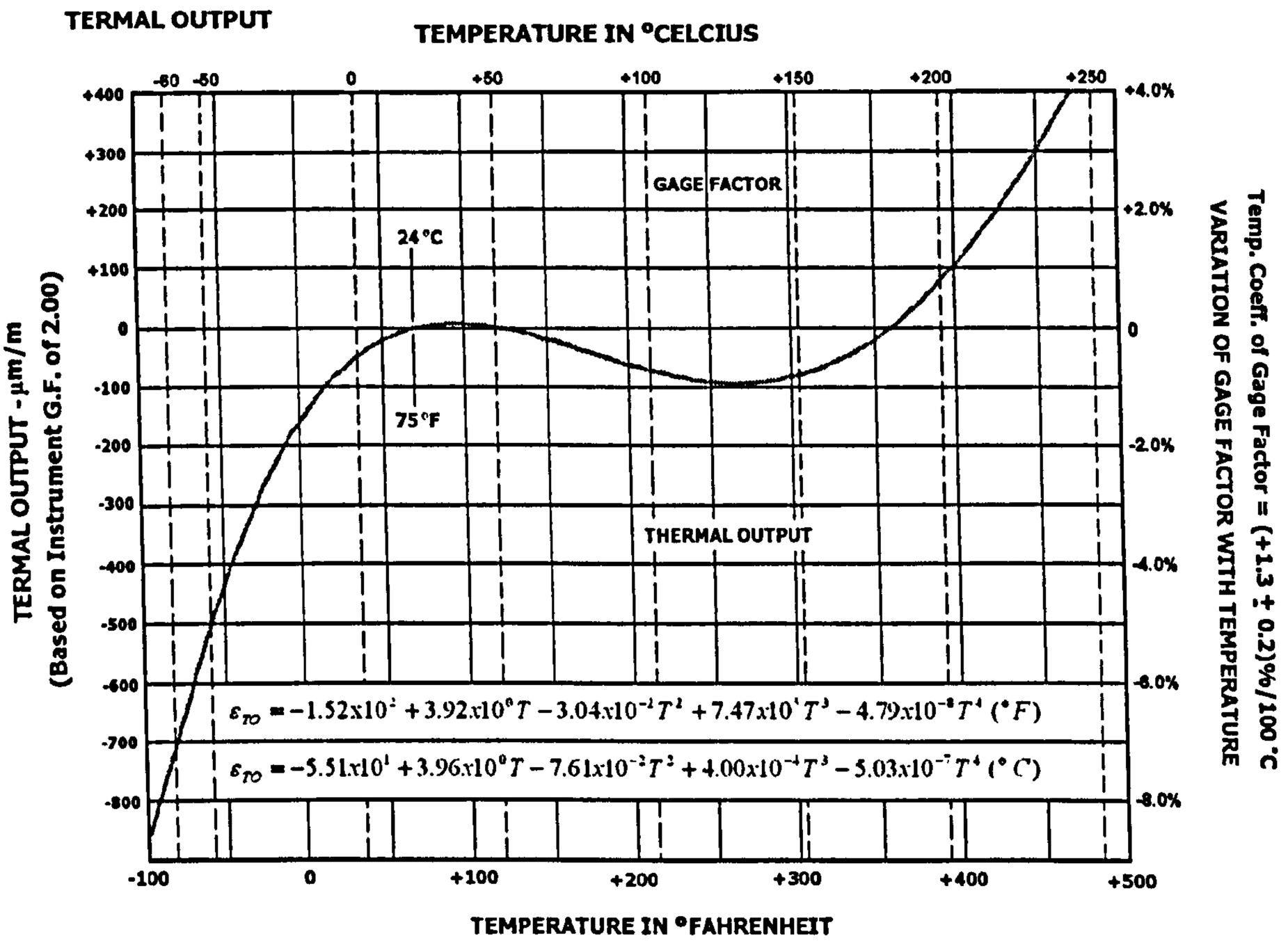

Figure 3.17 – Strain gages self–temperature compensation.

The following procedure was used for temperature compensation: the gauge factor of the strain gauges was set for room temperature and the specimens were tested at –60°C, then to the obtained data a correction factor was applied for this temperature. According to figure 3.17, for test temperature of –60°C, a correction factor of –720 $\mu\varepsilon$ must be subtracted to the measured data (microstrain, $\mu\varepsilon$) in order to apply temperature compensation.

The specimens were loaded in bending with a servo hydraulic Instron test machine under displacement control of $0.05mm/s$. The load arrangement is shown schematically in figure 3.18. The figure shows as well how the strain gauges were attached to the specimens. Three sets of data were measured: load–deflection, load–strain for the strain gauges loaded to tension and load–strain for the strain gauges loaded to compression. The results of strains measured were $2500\mu\varepsilon$ and $2000\mu\varepsilon$ for the strain gauges subjected to tension and compression respectively. The measured $\mu\varepsilon$ values for tension and compression were added and divided by 2, this with the purpose to account, in the analysis, the strains in tension and compression,

the resulted value is 2250 $\mu\varepsilon$. The correction factor for compensation temperature according to figure 3.17 for the strains gauges used in the present work correspond to –720 $\mu\varepsilon$ for –60ºC. Applying the correction factor to the measured $\mu\varepsilon$ values we obtain the following value: 2250 $\mu\varepsilon$ – 720 $\mu\varepsilon$ = 1530 $\mu\varepsilon$, this value corresponds to the corrected $\mu\varepsilon$ for –60ºC.

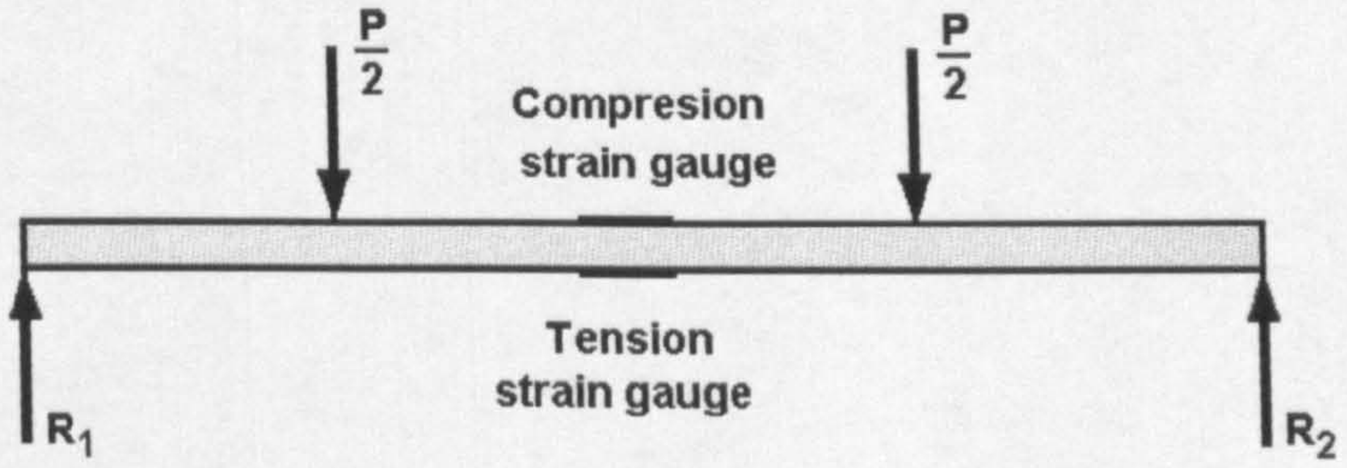

Figure 3.18 – Schematic of four point bend tests loading

3.3.1 Four point bend tests theory and analysis.

The stress–strain relationship is utilized to develop the theoretical parametric relationship between strain ε, bending moment M, tensile modulus E, width b and height h. The relationship between these parameters is expressed by equation 3.9 (Willian et al., 2002).

$$\varepsilon = \frac{6M}{Ebh^2} \qquad 3.9$$

Applying equation 3.9 and solving for Young's modulus E, with the value of strain obtained experimentally $(\varepsilon = 1530\mu\varepsilon)$, the value of the maximum bending moment of the plates is 34.29kN·mm. The width of the specimens is $b = 20mm$ and the thickness of specimens is $h = 5mm$, then a value of $E = 203GPa$ is obtained with equation 3.9. The same value was reported by Dowling (Dowling Norman, 2007) for structural mild steel. This can imply that the technique used in this work to measure the elastic strain at –60ºC was done properly. In order to obtain the yield stress at –60ºC, William (William, 2005) described an equation for four–point bending which has the following form:

$$\sigma_y = \frac{2FL}{wt^2} \qquad 3.10$$

where F is the load applied up to the start of the plastic region measured experimentally, L is the distance between the reaction force and the applied load, w is the width of the specimen and t is the thickness of specimens. By substituting the values $F = 6.5kN$, $L = 12.7mm$, $w = 20mm$, $t = 5mm$ into equation 3.10 we obtain the values of the yield stress $\sigma_y = 330MPa$, for –60°C.

The mechanical properties of Grade A plate steel at room temperature are: $\sigma_y = 260MPa$, $n = 0.20$, $k = 700MPa$, $E = 205GPa$. It can be seen that the yield stress at room temperature of Grade A steel is very similar to the value of $255MPa$ reported by Xiangqiao and Weisheng (Xiangqiao and Weisheng, 1993). The value of yield stress, $\sigma_y = 330MPa$ also correlate with the yield stress reported by Xiangqiao and Weisheng for –60°C (Xiangqiao and Weisheng, 1993). Those values are shown in figure 3.19. In that work, the authors reported the yield stress in terms of test temperatures in the transition region of a mild steel with the chemical composition very similar to Grade A plate steel. The authors tested the steel at different strain rates as shown in figure 3.19.

The strain rate applied to Grade A plate steel, as already mentioned in previous section is $\dot{\varepsilon} = 0.00165s^{-1}$. Interpolation between both strain rates, $\dot{\varepsilon}$, reported by Xiangqiao and Weisheng (Xiangqiao and Weisheng, 1993) and for the strain rate applied to Grade A plate steel took place at room temperature. From figure 3.19 we see that that the interpolated values fall in the curve for the strain rate equal to $\dot{\varepsilon} = 0.000555s^{-1}$. The interpolated curve between both strain rates is shown in figure 3.19. In this figure we see that the interpolated curve is very similar to that measured with a strain rate equal to $\dot{\varepsilon} = 0.000555s^{-1}$. Therefore we can observe that the values of yield stress (σ_y) measured at room temperature and –60°C fall on the curve reported by Xiangqiao and Weisheng (Xiangqiao and Weisheng, 1993) for the strain rate equal to $\dot{\varepsilon} = 0.000555s^{-1}$ and the interpolated data is also very close to the data measured with that strain rate. Based on this analysis and on the fact that the interpolated data is very close to the values reported by Xiangqiao and Weisheng (Xiangqiao and Weisheng, 1993), it can be concluded that the interpolated curve correlated with reported data for a mild steel in the transition region. The obtained curve is shown in figure 3.19, the black curve corresponds to the interpolated data and this curve will be used as yield stress temperature dependence for numerical simulations in the present work.

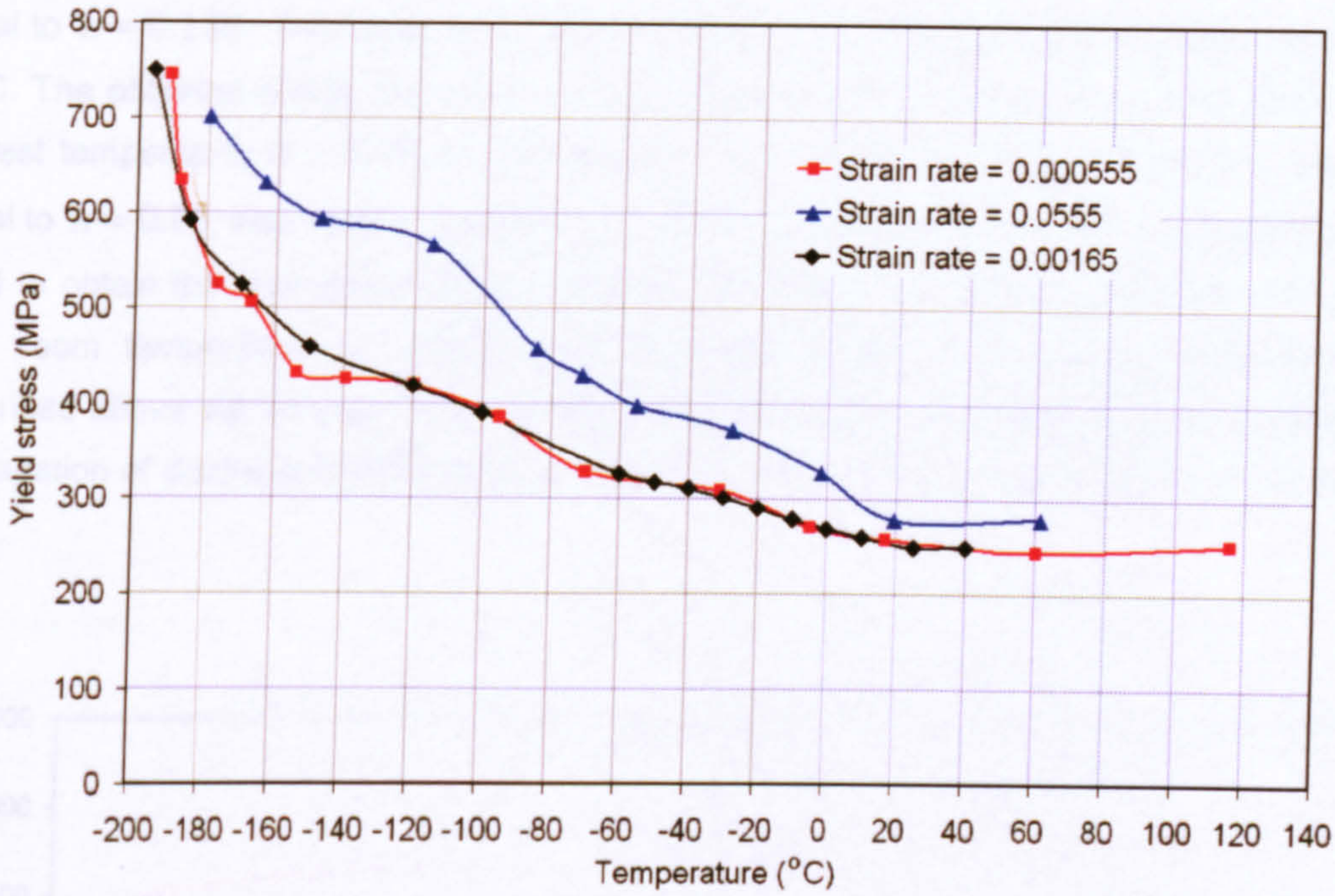

Figure 3.19 – Yield stress in function of test temperature of a steel similar to Grade A plate steel (Xiangqiao and Weisheng, 1993).

The value of Young's modulus (E) and Poisson's ratio ($v = -\varepsilon_{tranversal} / \varepsilon_{longitudinal}$) are temperature invariant (Bogdan et al., 2006) which imply that the same values for E and v were reported by (Xiangqiao and Weisheng, 1993). The flow curve of any metals in the region of uniform plastic deformation can be expressed by the simple power curve relation:

$$\sigma = K\varepsilon^{n} \qquad 3.11$$

Curry (Curry, 1981) reported the mechanical properties of a ferritic mild steel for two different test temperatures (+25°C and –150ºC). His steel had regions of pearlite, grain boundary carbides and numerous sulphide inclusions, as in the steel under analysis. The chemical composition of that steel was very similar to Grade A plate steels. In his work he reported a value of hardening exponent equal to $n = 0.075$ for –150°C. The yield stress of his steel for +25°C and –150ºC fall in the curves of figure 3.19, the yield stress at 150ºC is equal to $\sigma_y = 460MPa$. With the value of the hardening exponent equal to $n = 0.075$ measured by Curry (Curry, 1981) using equation 3.11 for –150ºC, and the value of yield stress equal to $\sigma_y = 460MPa$ and the deformation (ε) of figure 3.20 used for room test temperature we obtain the true stress–strain curve for –150ºC for Grade A plate steel using equation 3.11 and fitting the parameter K on equation 3.11. Taking the hardening exponents measured at room temperature and –150°C and interpolating for –60ºC we obtain a value of hardening exponent

equal to $n = 0.139$. This value was used in equation 3.11 to obtain the true stress–strain for –60°C. The obtained curves are shown in figure 3.20. In this figure the true stress–strain curve for test temperature of –196°C is also obtained. For –196°C, a value of hardening exponent equal to $n = 0.03$ was used in equation 3.11. From the data of figure 3.20, interpolation can be used to obtain the true stress–strain curves for the desired temperatures between the ranges from room temperature to –196°C. The hardening curves of the range of temperatures described above will be used in further finite element models to simulate fracture initiation and propagation of ductile and brittle fracture and to predict the ductile–brittle transition of the plate steel.

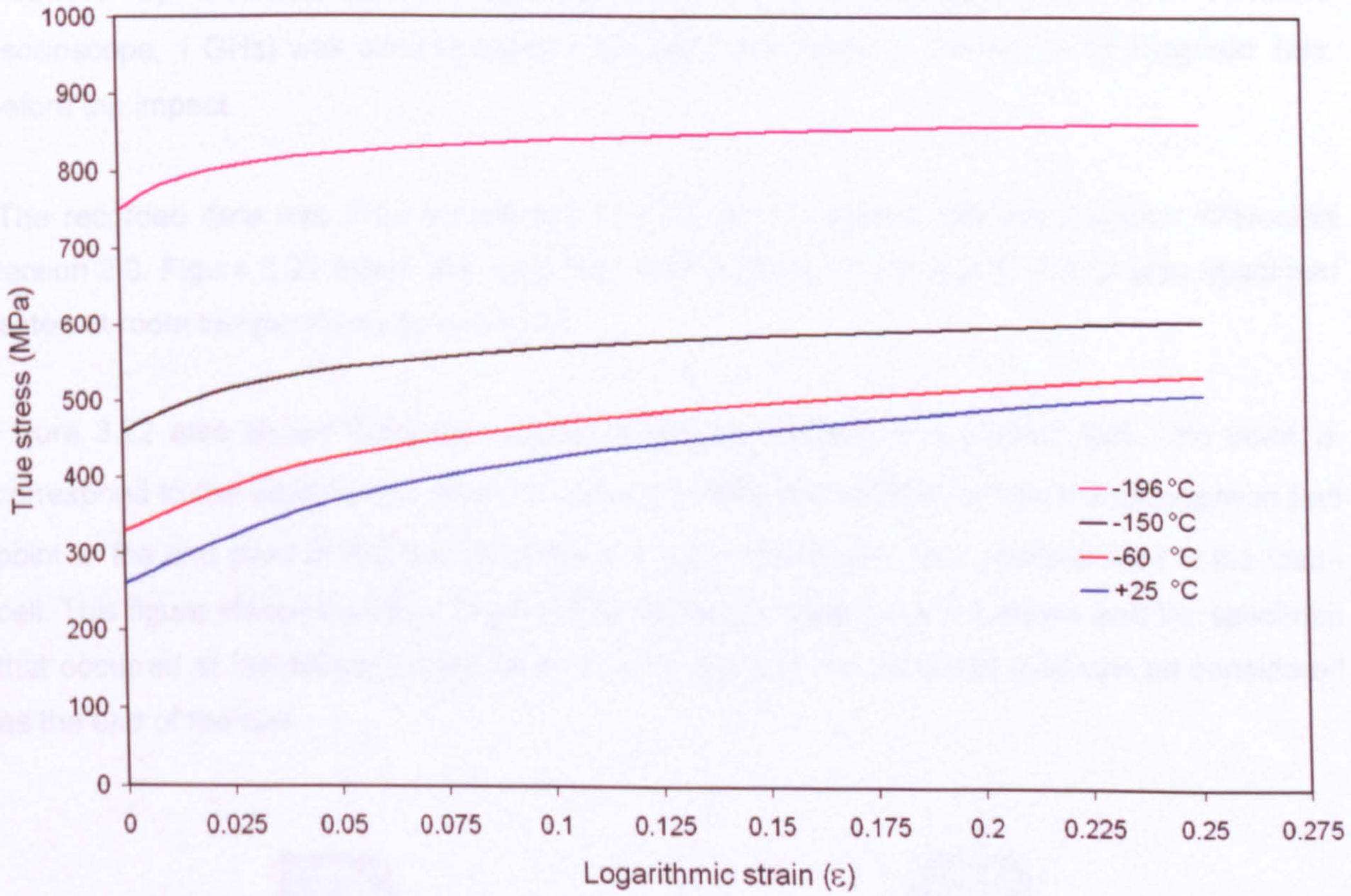

Figure 3.20 – True stress–strain curves for +25°C, –60°C, –150°C and –196°C.

3.4 Experimental work on Charpy tests.

One of the main objectives of capturing the load–displacement data from instrumented Charpy tests is that the data will be used in further sections to calibrate damage model parameters in multi–scale modelling of the ductile–brittle transition of the Grade A plate steel. For correct calibration of the micromechanical damage model parameters, it is very important to correlate the experimental curves with numerical data. With finite element simulations it is possible to

obtain the impact Charpy energy values obtained experimentally but the shape of the curve of numerical results may be different to that of experimental work (Shterenlikht et al., 2005), resulting in wrong numerical simulations.

Instrumented Charpy tests were performed in the present work, strain gauges were used to monitor the elastic deformation of the Charpy striker as being representative of the corresponding contact pressure between the striker and specimen. The instrumentation was conducted according to the recommendation of EN ISO 14556:200 (EN ISO 14556:200 British Standards, 1987). A strain gauge load–cell was attached to the Charpy striker close to the impact point (Shterenlikht et al., 2005) as schematically shown in figure 3.21. The striker is also shown in this figure. A strain indicator (Vishay – P3500) was used to monitor the strain produced by the load–cell. A high frequency digital oscilloscope (TDS 210 Tektronix oscilloscope, 1 GHz) was used to capture the data acquisition. It was set to be triggered $1ms$ before the impact.

The recorded data was then transferred to a PC and analysed with the program Wavestart version 2.0. Figure 3.22 shows the load–time history of the impact test of one Charpy specimen tested at room temperature (around 25°C).

Figure 3.22 also shows the three stages of fracture process in a Charpy test. The point a correspond to the elastic point, point b corresponds to the initiation of fracture propagation and point c the end point of the test. After the end point, there was $1kN$ residual load in the load–cell. This figure showed the final stage of the interaction between the hammer and the specimen that occurred at low hammer velocity, hence the point of the minimum load can be considered as the end of the test.

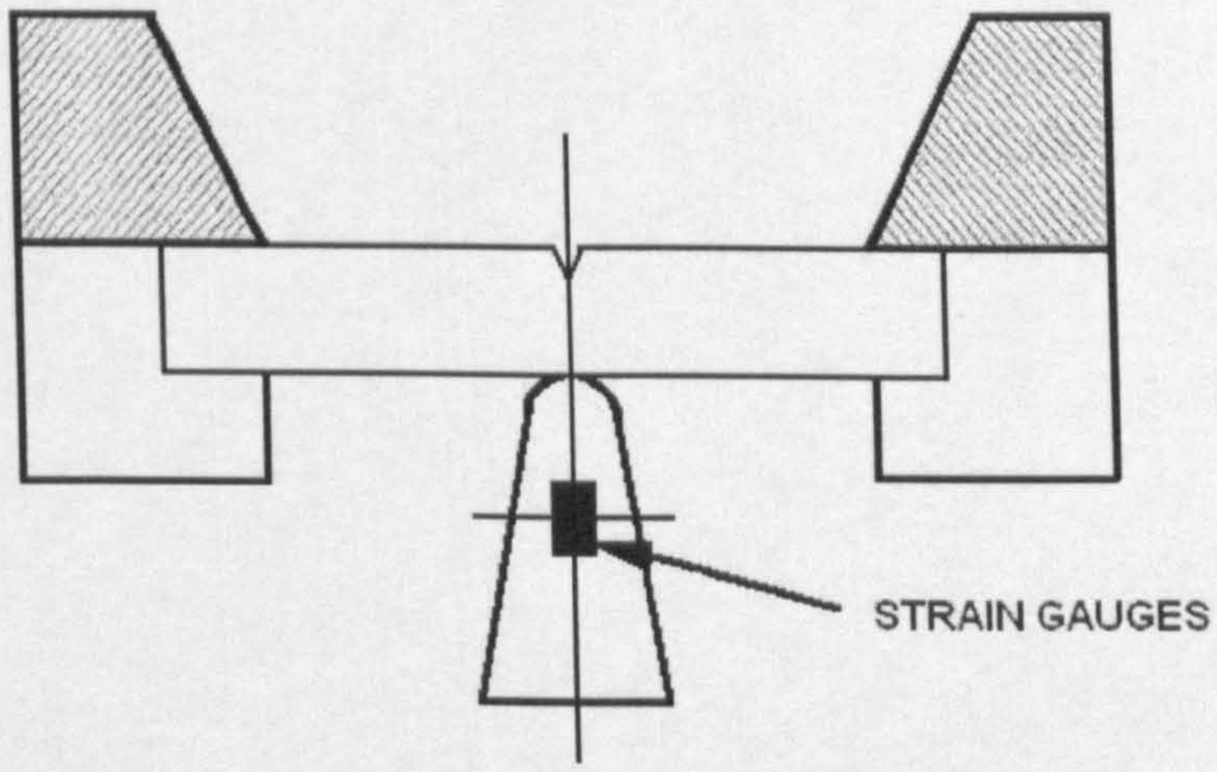

Figure 3.21 – Schematic of Charpy striker, specimen and anvils

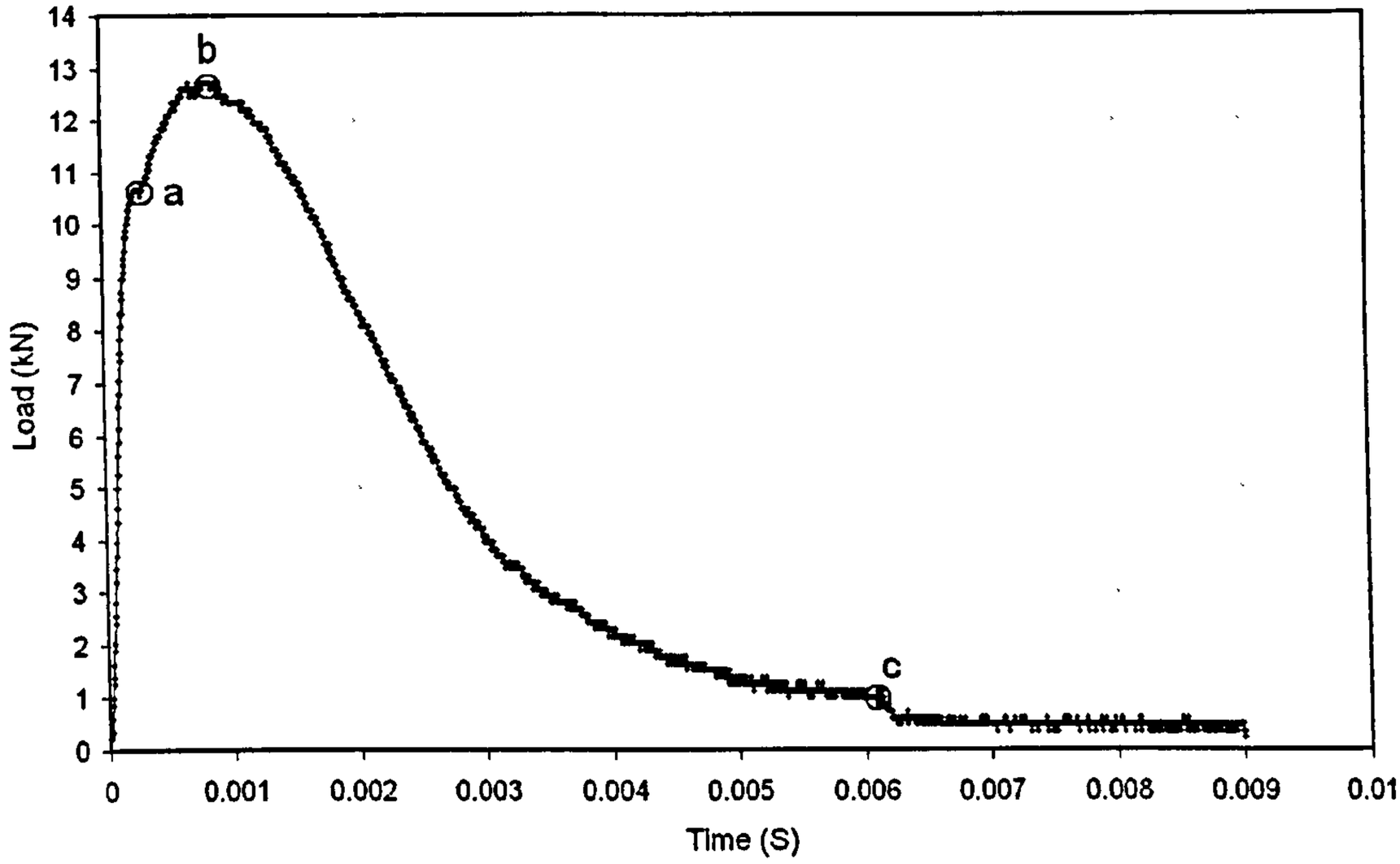

Figure 3.22 – Load–history from an instrumented Charpy test of Grade A ship plate steel tested at room temperature.

3.4.1 Calculation of the absorbed fracture energy.

Full failure information of this material was obtained from the instrumented Charpy impact tests by double integration of the test load–history; fracture energy was calculated as a function of hammer displacement. From this the crack initiation and propagation energy was estimated. The hammer displacement as a function of the time, $s(t)$, can be calculated by double integration of the load–time data with following equations:

$$v(t) = v_o - \frac{1}{m}\int_0^t f(t)dt \qquad 3.12$$

$$s(t) = \int_0^t v(t)dt \qquad 3.13$$

where v_o is the initial hammer velocity, m is the effective mass of the striker, $f(t)$ is the instantaneous contact force obtained from the cell and $v(t)$ is the instantaneous velocity during the impact. The values for the parameters described by equations 3.12 and 3.13 are: $v_o = 5.5\,m/s$ and $m = 19\,kg$. By applying these values in the equations described above we obtain the displacement of the hammer during the fracture process of Charpy impact tests.

Figure 3.23 shows the plot of the load–displacement of a Charpy specimen tested at room temperature.

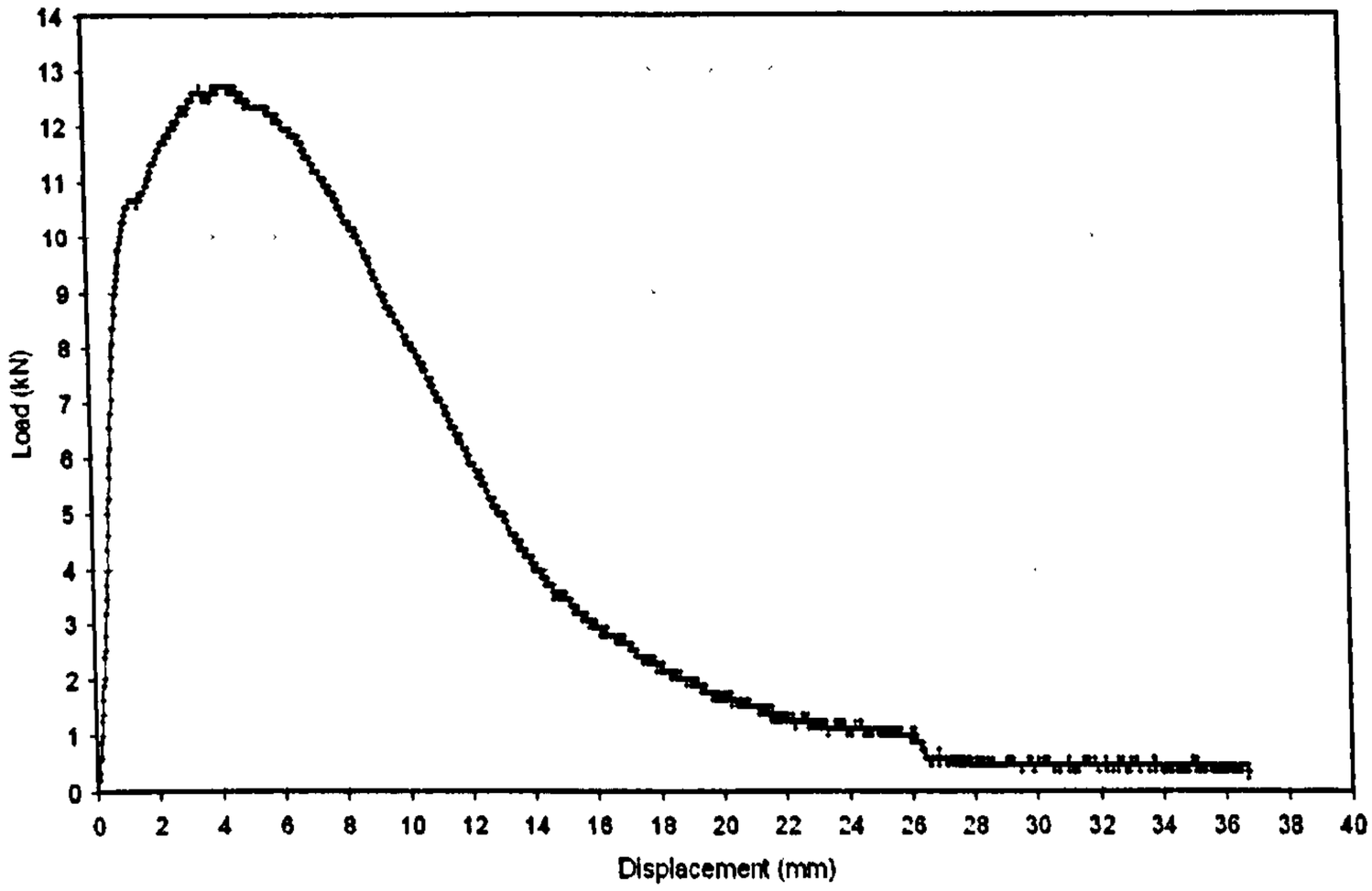

Figure 3.23 – Load–displacement history from an instrumented Charpy test.

The total absorbed fracture energy is estimated from the area under the force–displacement curve with next equation:

$$E(s) = \int_0^s f(s)ds \qquad 3.14$$

Figure 3.24 shows the energy absorbed by a Charpy specimen tested at room temperature. The vertical red line corresponds to point c on figure 3.22 which is considered the end of the test.

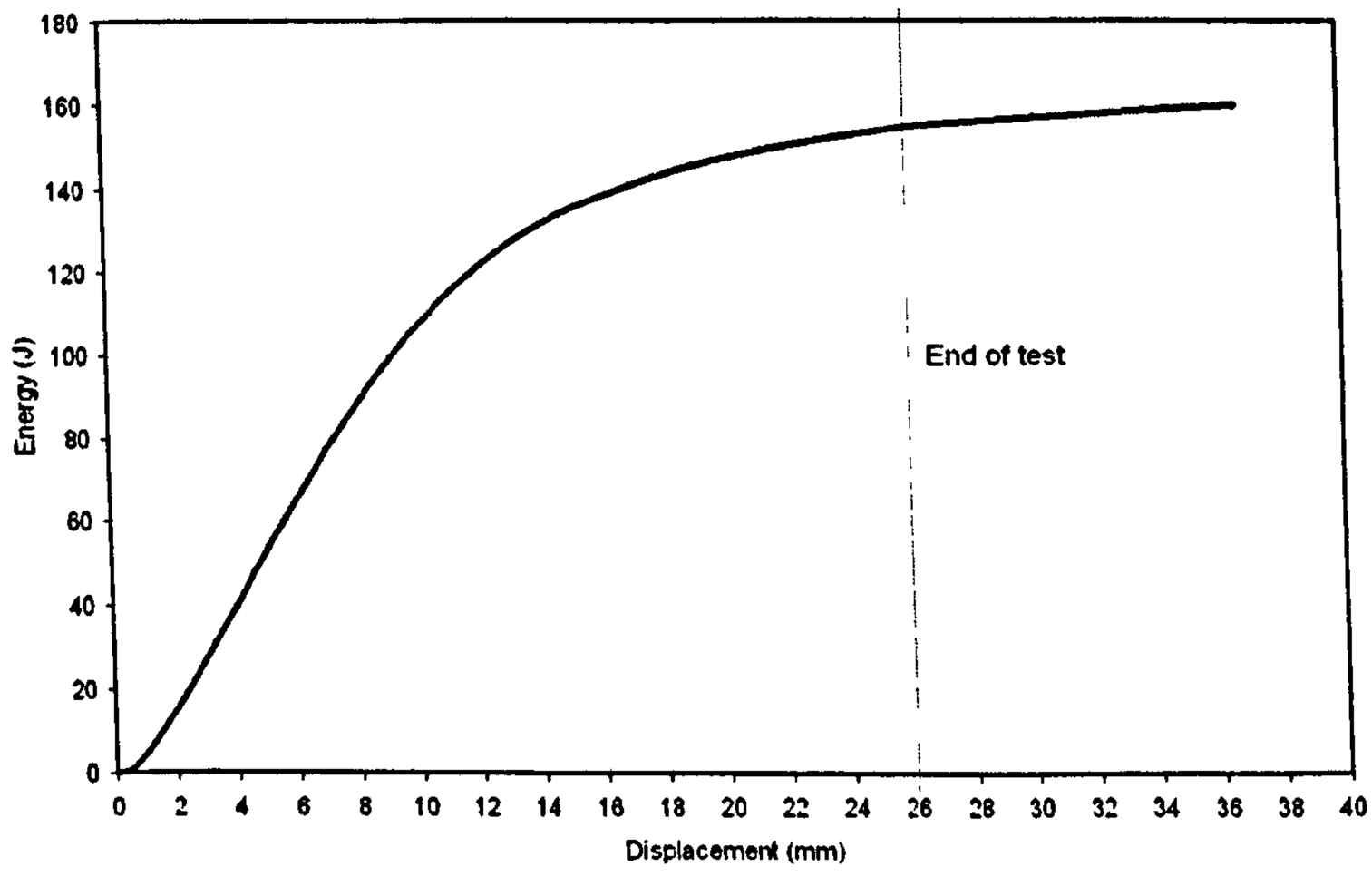

Figure 3.24 – Energy history from an instrumented Charpy test.

The computed data obtained with the double integration method gives a value of $155J$ which is very close to the value of $159J$ obtained in the dial of the Charpy machine. It is clear that very good correlation was obtained within experimental vs the analytical method. From the present analysis it can be concluded that the load–time data obtained experimentally and the application of the double integration method to the experimental data gave the impact Charpy energy value very similar to the values measured by the dial of the of the Charpy machine. This implies that the calibration of strain gauges used in the striker was done appropriately.

3.4.2 Fracture process in Charpy tests and fractography analysis.

For a better understanding of the fracture process in any particular steel, fractography analysis of fracture surfaces of Charpy specimens gives very important information about the micromechanics for fracture. At the same time it provides the micromechanisms for fracture initiation. In ductile fracture, the onset of ductile fracture is initiated by void nucleation around non–metallic inclusions and second–phase particles distributed in the matrix of the metal. They are subjected to plastic strain under the influence of external loading.

The size of the second phase particles and non–metallic inclusions in engineering alloys may vary significantly. Their shape varies from spherical to irregular forms, depending on the size, shape and quantity of these particles. Several models have been developed that account for the micro mechanisms of void nucleation. All models have something in common, which is that void nucleates when the so–called critical stress within inclusion or at inclusion–matrix interface has been exceeded. This depends on the type of the prevailing inclusions as well as on their shapes. It is important to mention as well that the test direction cannot be neglected because it can influence the fracture initiation mechanism. The inclusions will either separate from the matrix due to their incapability to follow plastic deformation or break.

Visual inspection of the fracture surfaces of Charpy specimens tested at room temperature revealed small lands of brightness as shown in figure 3.25. In this figure the points showing brightness are marked by blue arrows in a set of three fracture surfaces of three Charpy specimens. It can be seen that such lands appeared in the three specimens and they are located not only in the region close to the notch root but also quite far from the notch root as clearly shown in figure 3.25. In order to clearly identify and analyze those lands of brightness, fractographic analysis of the Charpy fracture surfaces was done with a Scanning Electron Microscope CAMSCAN model MK2. Lands of cleavage fracture were observed in the fracture surfaces of Charpy specimens tested at room temperature. Those lands are marked by the

arrows in figure 3.25. Figures 3.26, 3.27 and 3.28 show micrographs of the lands of cleavage fracture in Charpy surfaces of figure 3.25.

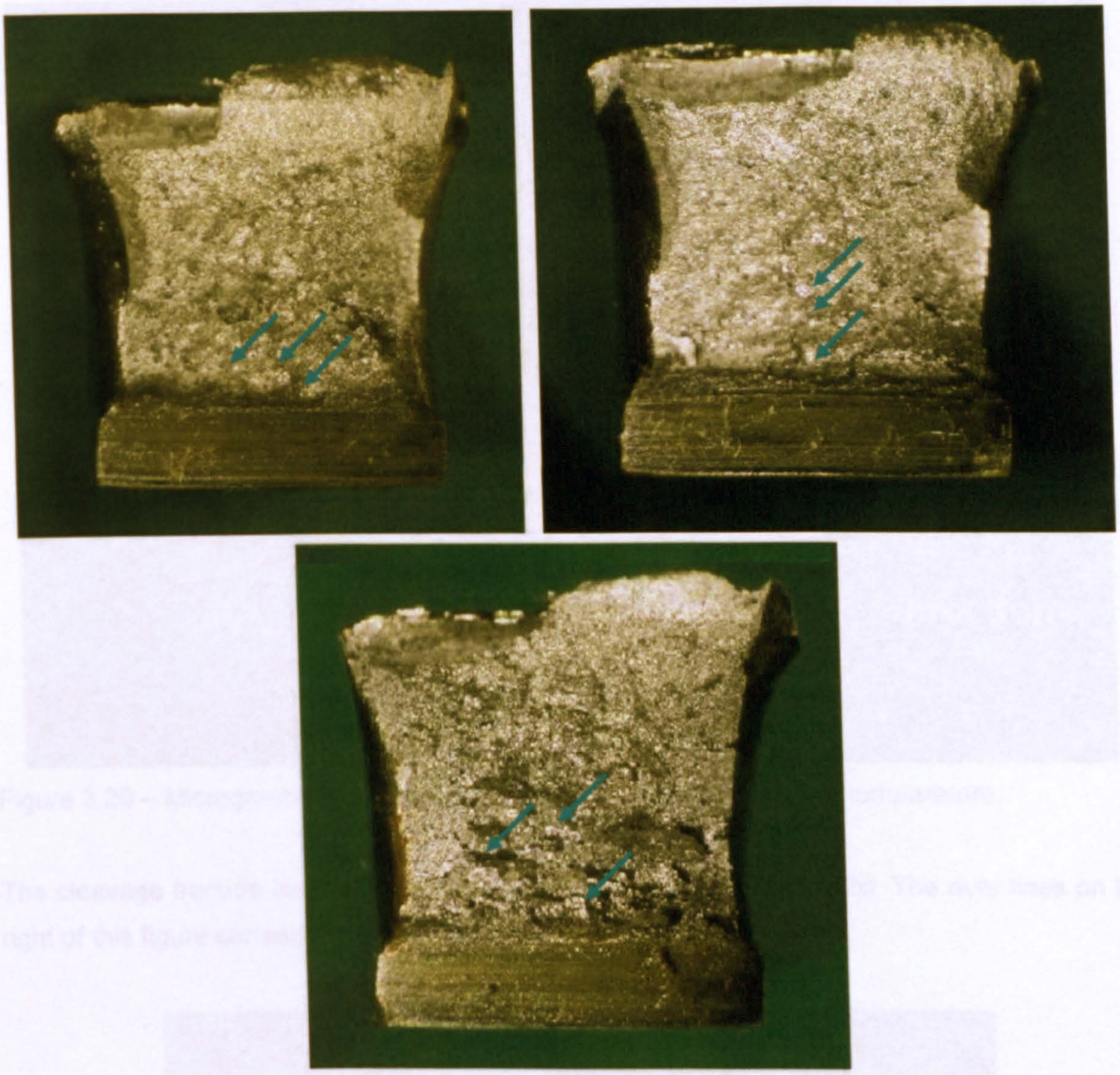

Figure 3.25 – Charpy surfaces tested at room temperature.

The micrographs were taken in a region very close to the notch root. The notch root is marked with an arrow in figure 3.26. The cleavage lands are located at about $200\mu m$ from the notch root. It was mentioned (Transportation Safety Board of Canada, 2002, Materials Laboratory, 1997) that the mean grain size in a huge variety of Grade A ship plate steels is about $10\mu m$. The grain size of the present Grade A plate steel is $19.5\mu m$. Consequently the position of the closest dots of brightness is about the size of 10 ferrite grains of the present steel and 20 ferrite grains of the steels reported in literature. The size of the cleavage fracture lands of figure 3.26 are of about $150\mu m$ which means that those lands are composed of several grains.

Further investigation of the microstructures and the position of the triggering cleavage points was done in this research work and will be explained in the following sections.

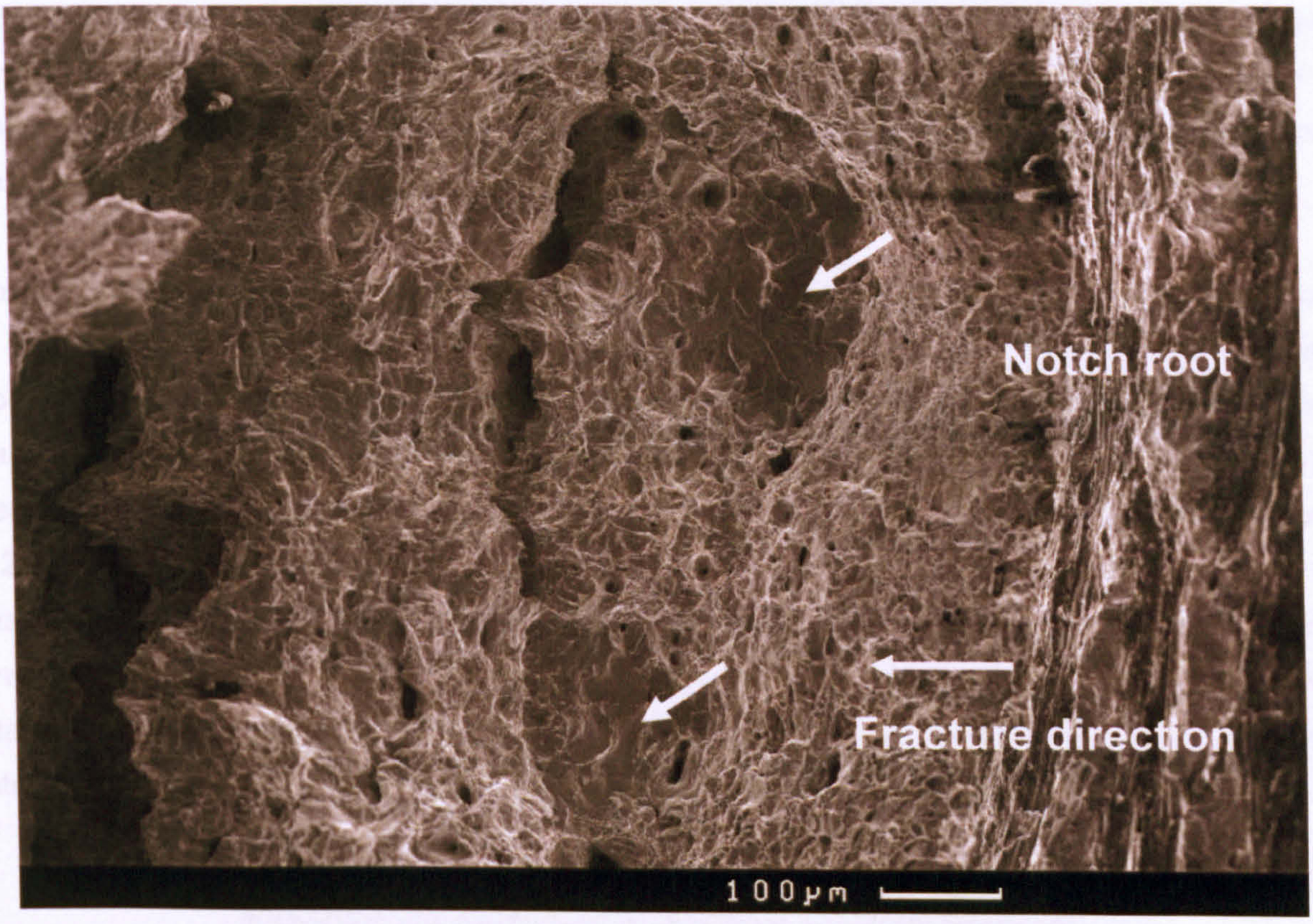

Figure 3.26 – Micrograph of a broken Charpy specimen tested at room temperature.

The cleavage fracture lands are those marked with arrows in figure 3.26. The river lines on the right of this figure correspond to the notch root of Charpy specimens.

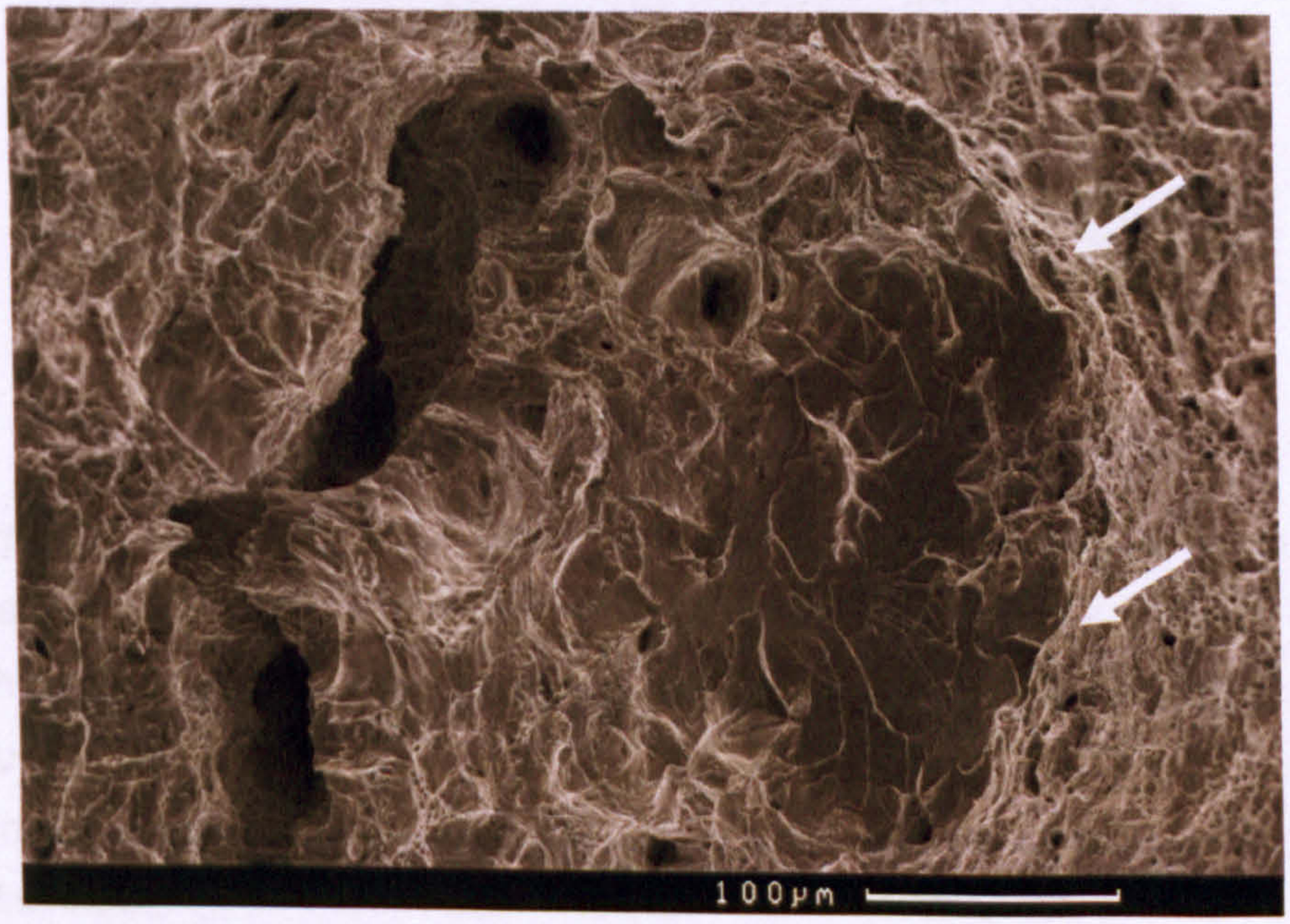

Figure 3.27 – Close view of a land of cleavage fracture of figure 3.32.

Figure 3.27 shows a land of cleavage fracture of figure 3.26 with higher magnification. In this figure, it can be seen that the cleavage region is surrounded apparently by a land of pearlite. The apparent pearlite microstructure is marked by arrows as shown in figure 3.27. In section 3.6.6 it was shown that regions of material with very small microvoids can be related to the pearlite microstructure. Even when it is difficult to identify properly the lands of pearlite on fracture surfaces of toughness specimens, it is more difficult to identify cleavage initiated on pearlite colony boundaries on fracture surfaces of toughness specimens.

Strnadel (Strnadel and Hausild, 2008) analyzed the micromechanisms controlling the formation of fracture surfaces in a pearlitic steel. Strnadel showed microcracks initiated on pearlite colony boundaries and microcracks triggered by stress concentrations around cracked second phase particles. The micrographs in Strnadel's research work, show lands of cleavage and colonies of pearlite around such cleavage lands. Those colonies of pearlite are very similar to that of figure 3.26 and 3.27. This suggests that the boundary of the cleavage land of figures 3.26 and 3.27 is really a colony of pearlite. Figure 3.28 shows the origin of the land of brittle fracture by the black arrow of figure 3.27, the white arrow shows a particle which may debonded from the ferrite matrix. Further investigation about this competition of ductile and brittle fracture is discussed later.

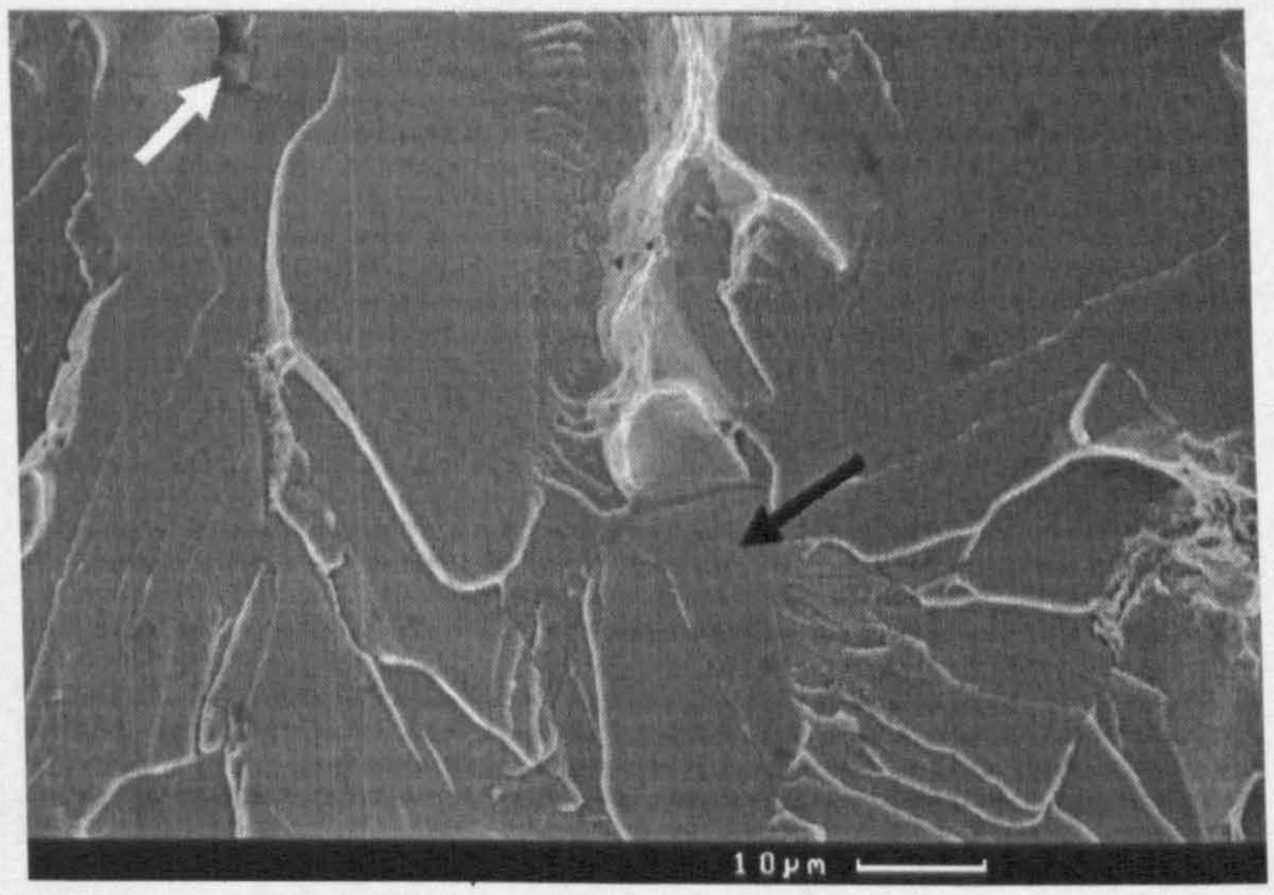

Figure 3.28 – Close view of a land of cleavage fracture of figure 3.27.

Broken Charpy surfaces allowed the identification of the microstructures that nucleated ductile and brittle fracture in the notch root. But in order to be easily identified, the use of four point double–notch bend tests does however allow easier identification of each microstructure clearly. This technique will be explained in next section. Ductile fracture is shown by micrographs taken in broken Charpy specimens, figures 3.29 and 3.30 show distribution of inclusions in large microvoids distributed in the matrix of the metal.

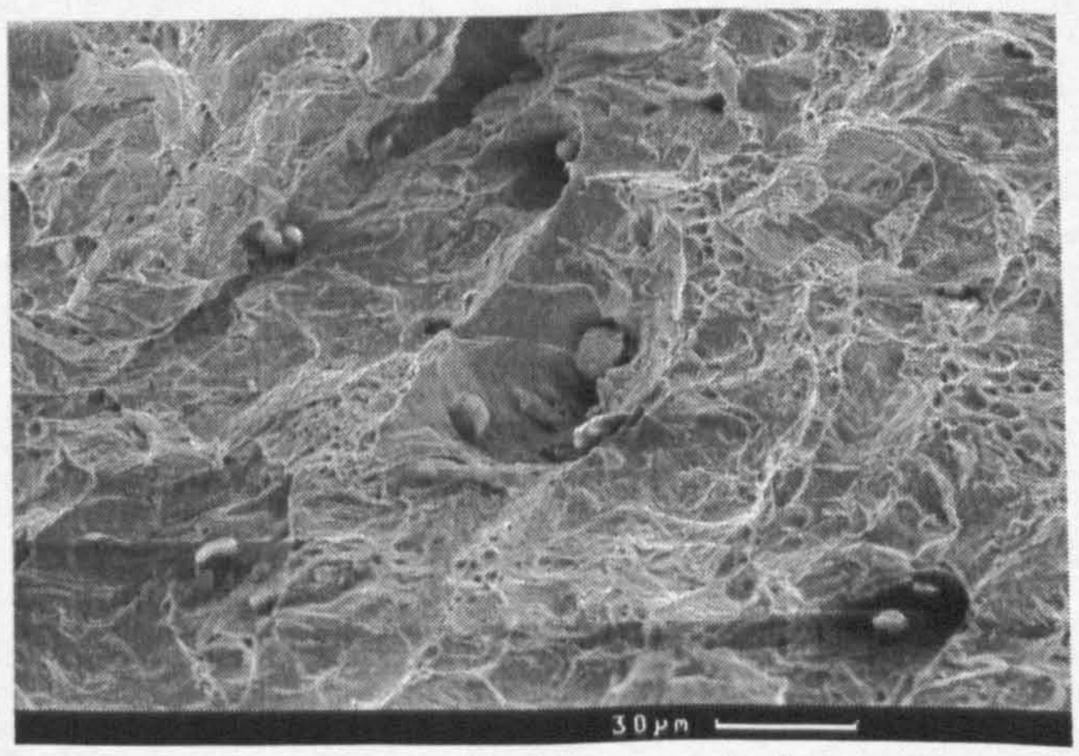

Figure 3.29 – Micrographs of ductile fracture in Charpy surfaces of samples tested +20°C.

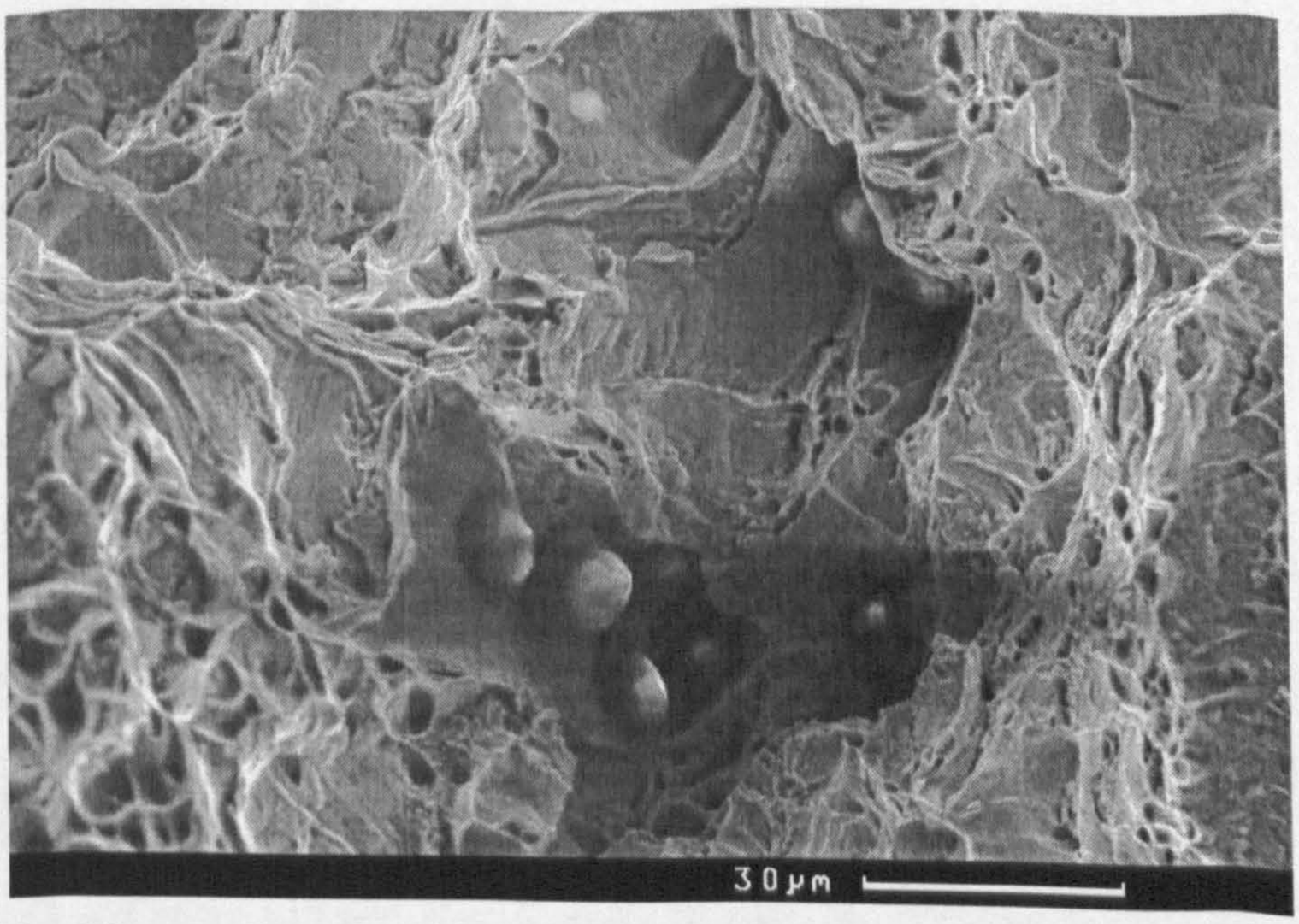

Figure 3.30 – Micrographs of ductile fracture in Charpy surfaces of samples tested at +20°C.

Figures 3.29 and 3.30 (taken in a region close to the notch root) show non–metallic manganese sulphide inclusions in large microvoids which suggest that they are the nucleating microstructures for ductile fracture in Charpy tests at room temperature. Extensive works have been published to investigate the microstructures that lead to ductile fracture, most of them reported the same microstructures for ductile fracture from MnS inclusions, as shown in figures 3.29 and 3.30.

It is well known that in ductile fracture, the size of the dimples is governed by the number and distribution of microvoids that are nucleated. The distribution of the microvoid nucleation sites can significantly influence the fracture surface appearance. Dimple shape is governed by the state of stress within the material as the microvoid forms, grows and coalescence. The analysis of large dimples in ductile fracture took place in order to define the mechanics for the formation

and deformation of dimples walls for a better understanding of dimple rupture. As the material undergoes considerable plastic deformation, it develops large dimples. They generally contain deformation marking on the dimple walls. Most of the mechanisms proposed to explain the various fracture modes are based on dislocation interaction involving complex slip and crystallographic relationships. The discussion of mechanisms in this section will not include detailed dislocation models or complex mathematical treatment, but will present the mechanisms in more general terms in order to impart practical understanding to describe this fracture mode.

As mentioned above, microvoids nucleate at regions of localized strain discontinuity, such as that associated with second–phase particles, inclusions, grain boundaries and dislocations pile–ups. As the strain in the material increases the microvoids grow, coalescence and eventually form a continuous fracture surface. This type of fracture exhibits numerous cuplike depressions, the cuplike depressions are referred as dimples. The size and number of dimples on a fracture surface is governed by the number and distribution of microvoids that are nucleated (ASM International, 1987).

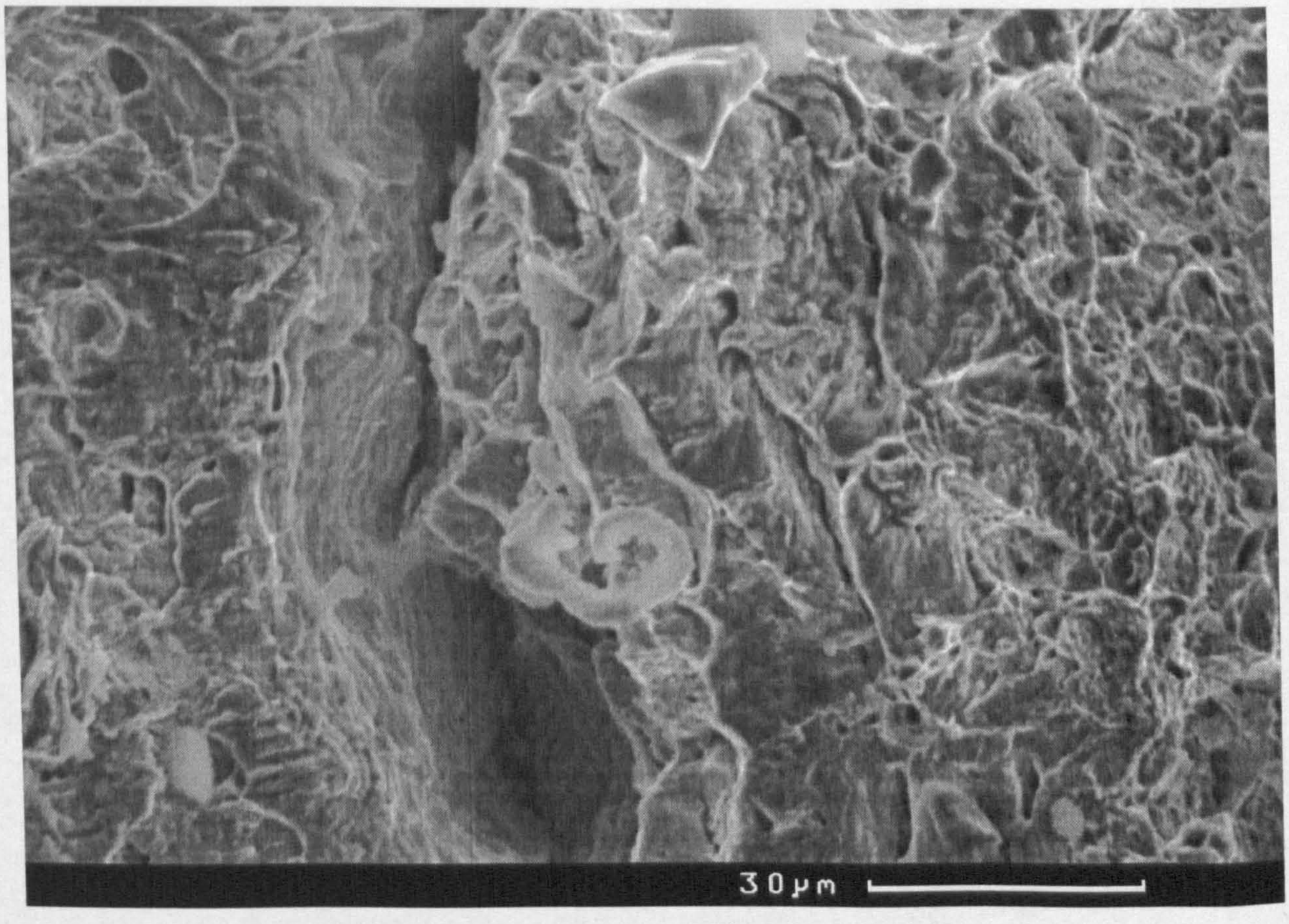

Figure 3.31 – Formation of large dimples in Charpy tests at room temperature.

When the nucleation sites are small and widely spaced, in most clean steels, the microvoids grow to a large size before coalescence and the result is a fracture surface that contains large dimples. Small dimples are formed when numerous nucleating sites are activated and adjacent microvoids join (coalescence) before they have an opportunity to grow to a larger size as those shown in figures 3.29 and 3.30. Dimple shape is governed by the state of stress within the material as the microvoids form and coalescence. Figure 3.31 shows a typical dimple found in a Charpy specimen tested at room temperature.

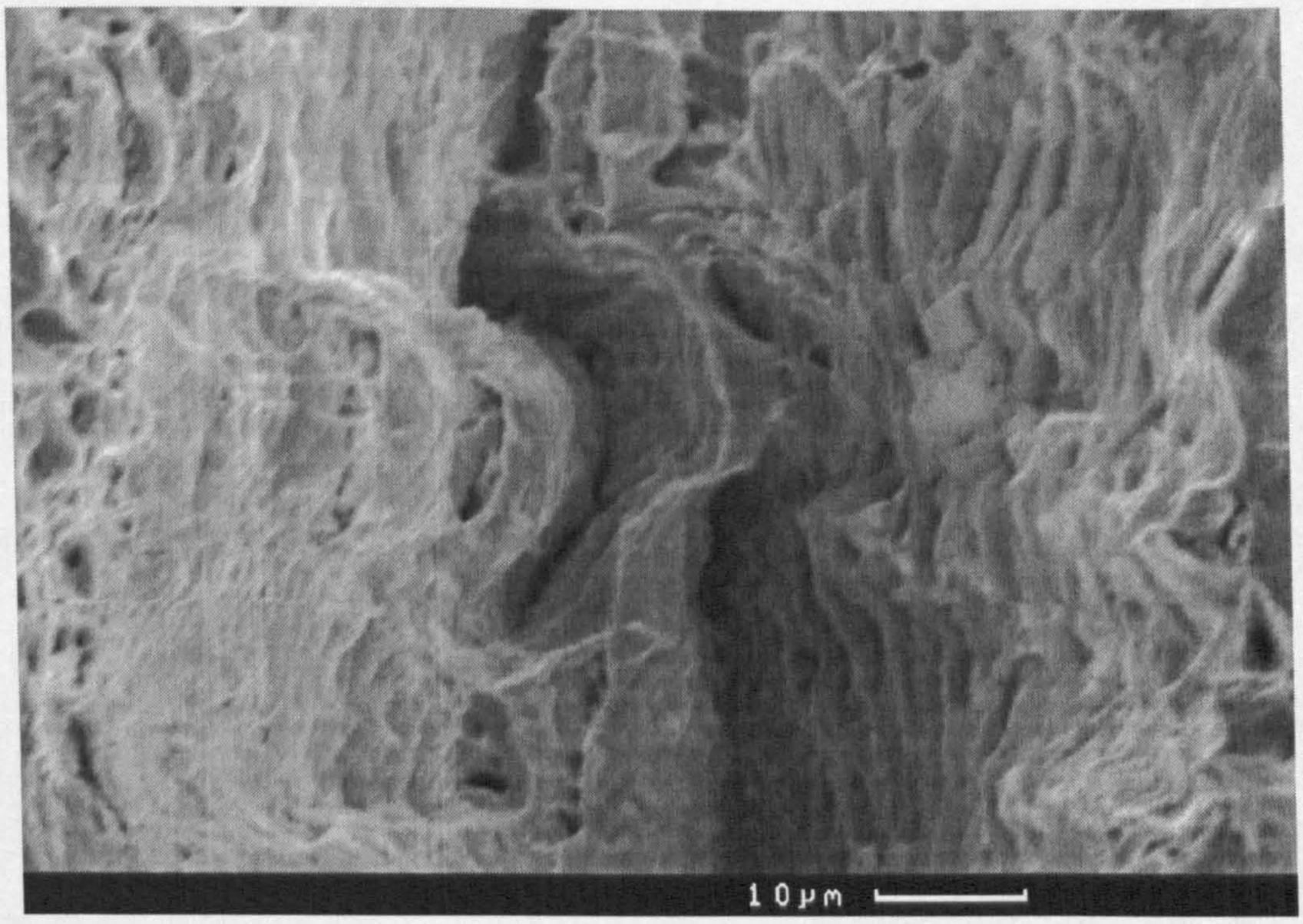

Figure 3.32 – Close view of the formation of markings in large dimples of figure 3.37.

The markings occur when slip–planes at the surface of the dimples are favourably oriented to the major stress direction. The continuous straining of the free surfaces of the dimples due to enlargement of microvoids produces slip–plane displacement at the surface of the dimples (ASM International, 1987). When first formed, the slip traces are sharp, well defined and form a serpentine glide as shown in figure 3.32. As the slip procedure proceeds, the initial sharp slip traces become smooth, resulting in a surface structure that sometimes is referred to as ripples. Due to time constraint and to the fact that the main objective of the project is to analyze the microstructures for fracture initiation, no further research work directed to the formation of ripples in the free surfaces of dimples was done.

Another major concern is the propagating control of brittle fracture which generally occurs by cleavage fracture. This fracture process occurs by a rapid run of cracks through a stressed material, with very little plastic deformation before failure occurs. In most cases, this is the worst type of fracture because one can not repair visible damage in a part or structure before it

breaks. In brittle fracture, the cracks run close to perpendicular to the applied stress. This perpendicular fracture leaves a relatively flat surface at the break. Besides having a nearly flat fracture surface, brittle materials usually contain a pattern on their fracture surfaces. Some brittle materials have lines and ridges beginning at the origin of the crack and spreading out across the crack surface. Fractography examination was carried out to investigate the damage processes in the brittle regime. In this case the nature and location of the cleavage triggering sites were studied and any modification in the DBT range was investigated.

Examinations for the identification of the triggering sites for cleavage fracture were the second step in the fractography study. This analysis was performed using 4PB double notch specimens, where the initiation points were quantified. The distances of the cleavage triggering site with respect to the notch root were measured. The fracture initiation sites analysis is performed in the following section.

3.5 The ductile–brittle transition.

The aim of the measurements of the ductile–brittle transition in the damage zone of Charpy specimens is to provide a wide experimental database and microstructural observation to supply, calibrate and validate models used in the local approach methodology. Charpy tests provide toughness values which are required to assess structural integrity. These tests are mainly used to ensure that the steel of a structure has sufficient toughness to arrest the propagation of any potential fracture under severe conditions of load.

To characterize the ductile–brittle transition of a metal, Charpy specimens are tested over a range of temperature by varying the temperature of the material from very low to high temperatures, this to find the temperature at which the material changes from ductile to brittle fracture. Notched specimens are used because the notch induces a triaxial state field used for fracture mechanics measurements. The presence of notches reduces the ductility due to the presence of a triaxial state field and stress gradients.

Sets of 5 Charpy specimens were tested at a range of temperatures from –196°C to room temperature (+25°C). The transition ductile–brittle experimental results in the rolling direction of the plate steel are shown in figure 3.33. These values are recorded from the dial of the Charpy machine. The Charpy experiments were carried out on a 300 Joules Losenhausenwerk impact machine whose pendulum impact velocity at the maximum working capacity was $5.5m/s$ and a hammer of $19kg$.

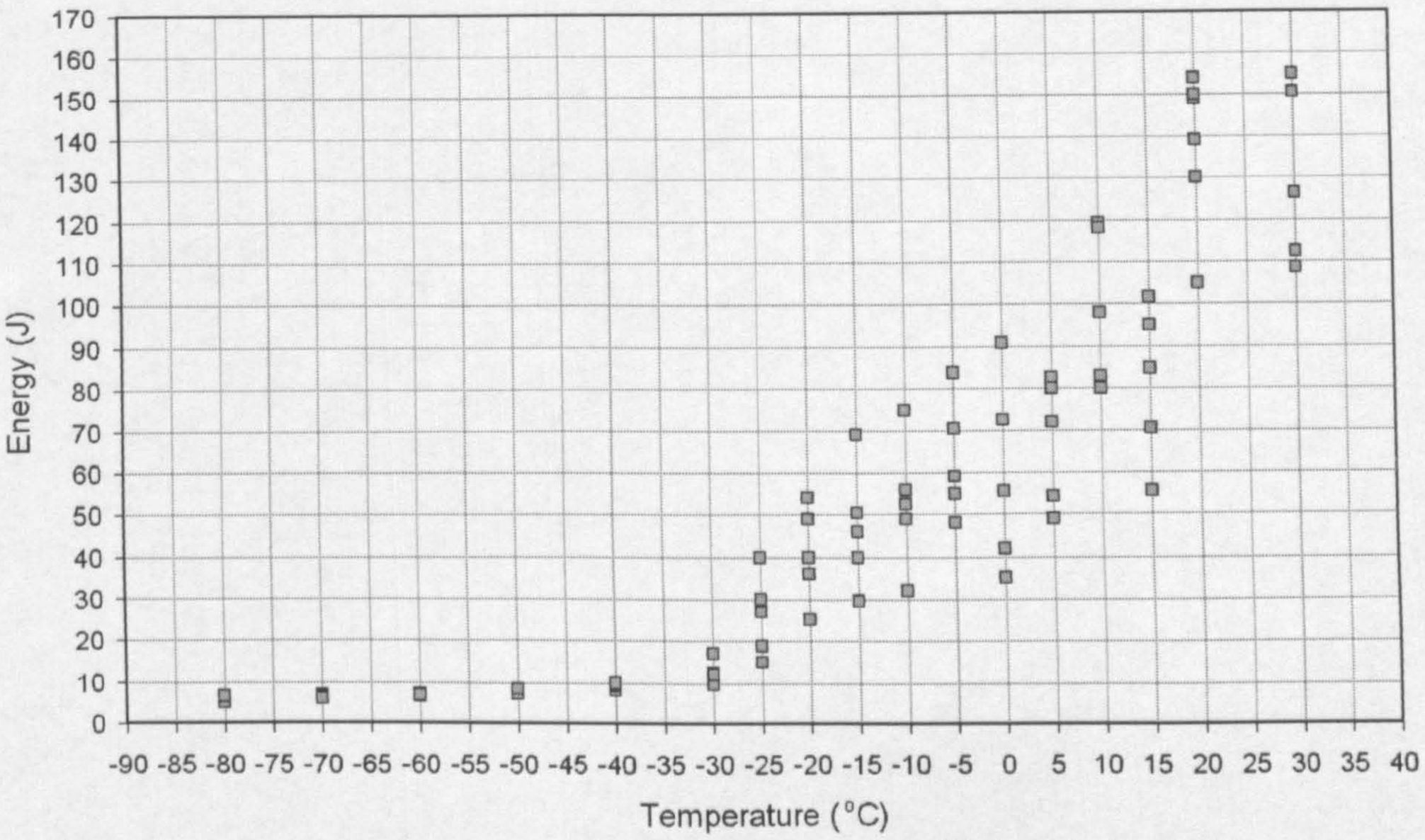

Figure 3.33 – Transition ductile–brittle of instrumented Charpy test in the rolling direction of the plate steel.

For a more precise assessment, a better understanding of the Charpy tests and of the microstructures involved in the fracture process of the transition ductile–brittle is needed. This is the first step to establish a non–empirical micromechanically based relationship between the Charpy energy and the fracture toughness in the ductile–brittle transition. In Charpy broken specimens, each fracture surface is generally classified in 3 main failure mode categories: fully brittle, ductile–brittle and fully ductile. The ductile–brittle surfaces in the specimens correspond to the beginning of stable ductile tearing which can be followed by unstable fracture by cleavage. A major concern for the use of materials is the control of propagating ductile fracture or brittle fracture by cleavage.

Fractography analysis of each region of the Charpy surface took place to investigate the brittle and ductile fracture processes. In the first case, the nature and location of the cleavage triggering sites were studied. In the second case, nucleation of microvoids around second phase particles was investigated. This examination was carried out in a Scanning Electron Microscope CAMSCAN model MK2. A common measurement obtained from the Charpy test results from the examination is to determine whether the fracture is fibrous (shear fracture), granular (cleavage fracture) or a mixture of both. The ductile process of Charpy specimens was explained in previous section, the following section will explain the brittle fracture process of Grade A plate steel.

One of the main objects of the present research work is to model the ductile–brittle transition curve of the steel under analysis, therefore the data of figure 3.33 is needed to validate the proposed model (Chapter V) in the present research work for the prediction of the ductile–brittle transition of steels.

3.6 Experimental work on the identification of the micro features initiating cleavage fracture.

Four point double–notch bend specimens with root radius $\rho = 0.20mm$ and *notch depth* equal to $4.25mm$ (Griffiths and Owen, 1971) were tested in the transition zone, at test temperatures of –196°C, –60°C, 0°C and room temperature (+25°C) to study and identify the cleavage fracture nucleation microstructures of a Grade A plate steel. The notches of the specimens were machined with wire cutting electric discharge machine. The explanation of choosing this range of temperatures is described as follows: fracture surfaces of Charpy specimens tested at 25°C, as showed in section 3.4.2, showed lands of cleavage fracture, therefore cleavage fracture must be investigated from room test temperature to lower temperatures.

The choice of 0°C is based on OTH 65 489 Offshore Technology Report (British Steel plc for the Health and Safety Executive, 1997) where the authors report the proportion of the life of ships navigating at different temperatures. Ships operate at temperature less than 0°C for only 3% of their life. Arctic service may give rise to lower temperature but 0°C is usually taken as the design temperature for conventional ships. This shows the importance for studying cleavage fracture at 0°C. At –60°C, fracture surfaces of Charpy specimens showed 100% of cleavage fracture. This temperature is in the lower shelf test temperature where cleavage is the mechanism that controls fracture. At –196°C all the conditions for cleavage fracture to occur are ensured. Figure 3.34 shows the geometry and loading configuration of 4PB specimens.

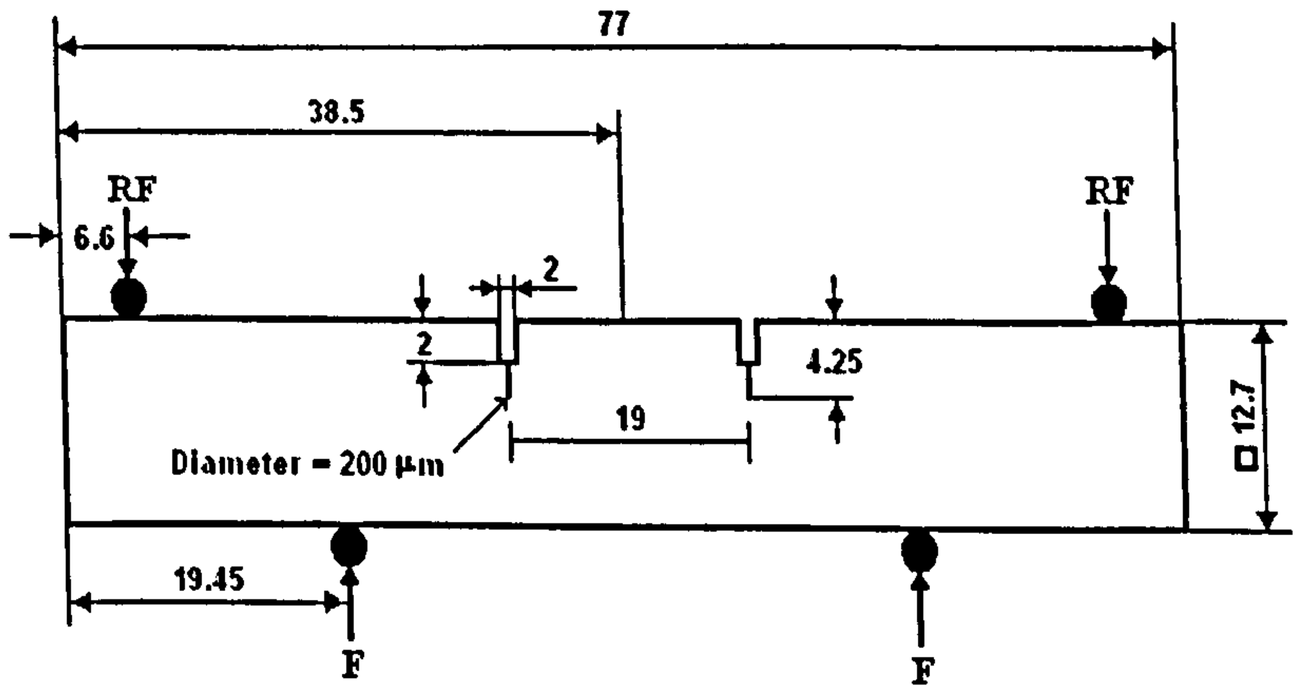

Figure 3.34 – Four point double–notch bend specimen showing the load configuration.

In four point double–notch bend specimens, when loaded symmetrically, both notches are subjected to the same state of stresses and strains. When cleavage fracture initiates in one notch, and consequently fracture occurs, the crack will certainly propagate from that notch but the surviving notch must have been very close to the critical state of stress and strain condition developed in the failed notch. The surviving notch will reveal the micro and macro mechanical states just prior to fracture.

Four point double–notch bend tests were carried out in a servo hydraulic Instron 8501 test machine under displacement control of $0.05mm/s$. The load–displacement curves were recorded automatically for each test temperature. A special bath and grips were designed to perform the tests at low temperatures, the grips were welded to the bath, the bath was built from stainless steel to avoid corrosion and insulated with polystyrene to keep the temperature as constant as possible. Pins fabricated from recrystallised alumina solid rod of $10\,mm$ diameter were used to isolate the specimens from the grips and to ensure minimal thermal transfer from the test machine and grips to the specimens. Special fiber was allocated at the bottom of the bath to absorb liquid nitrogen and liberate cold gas to chill the specimens. The container was insulated. In the top a small hole was placed in the cover to allow the addition of small amounts of liquid nitrogen to maintain the desired temperature. To control the temperature, a thermocouple was inserted in the opposite side of the notches in a hole of 5mm deep. Figure 3.35 shows the experimental set up of 4PB test, this figure also shows the Instron test machine, the special bath and the thermometer used to control the test temperature is also shown in figure 3.35.

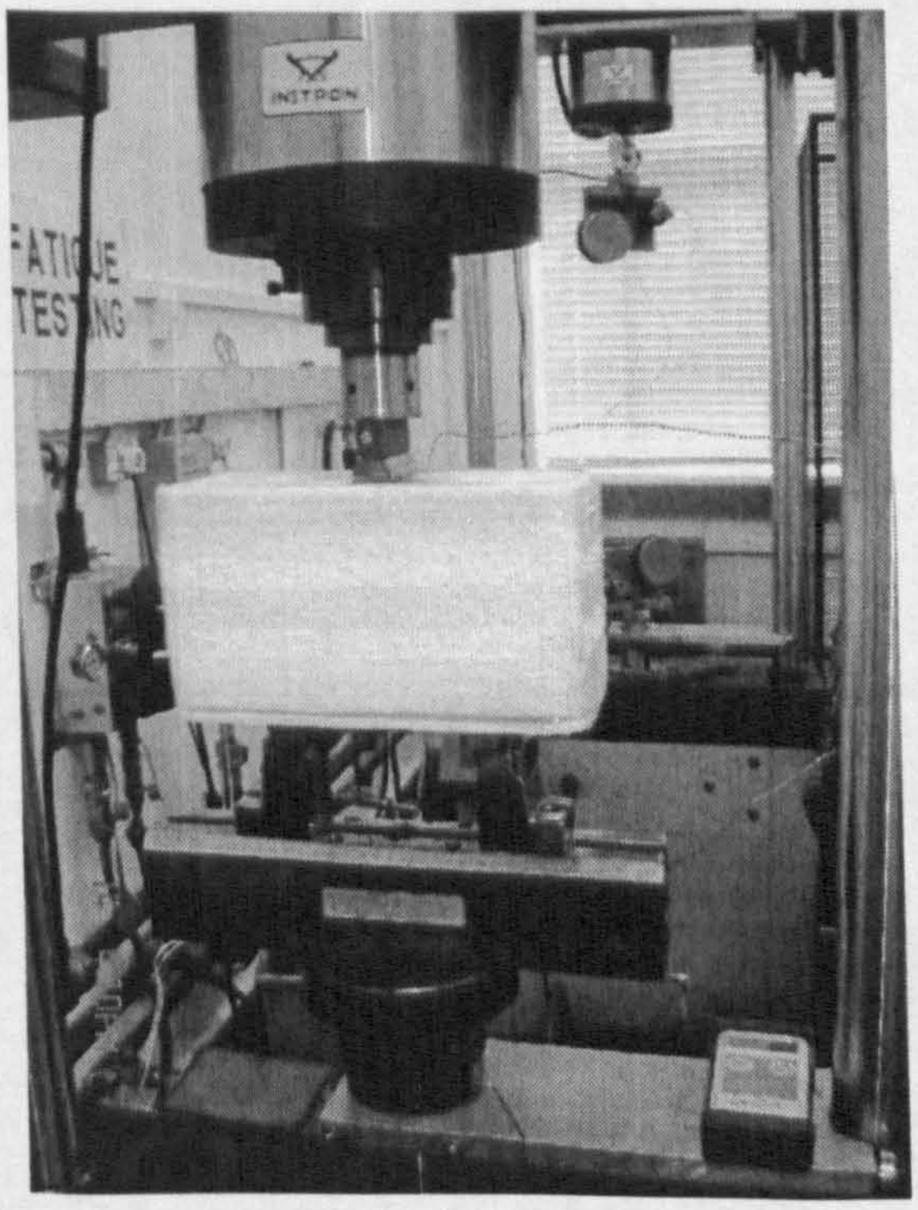

Figure 3.35 – Experimental set–up of four point double–notch bend tests.

When the desired temperature was controlled, the specimens were maintained at that temperature for 30 minutes and then the loading process started. The displacement rate applied to 4PB specimens was the same as that of quasi–static tensile tests ($0.05mm/s$). Figure 3.36 shows a set of three 4PB specimens machined in the rolling direction of the plate steel used in this research work. The automatically recorded load–deflection data of 4PB tests are shown in the following two sections for the rolling and transverse direction of the plate steel as well the surviving and failed notch in such specimens.

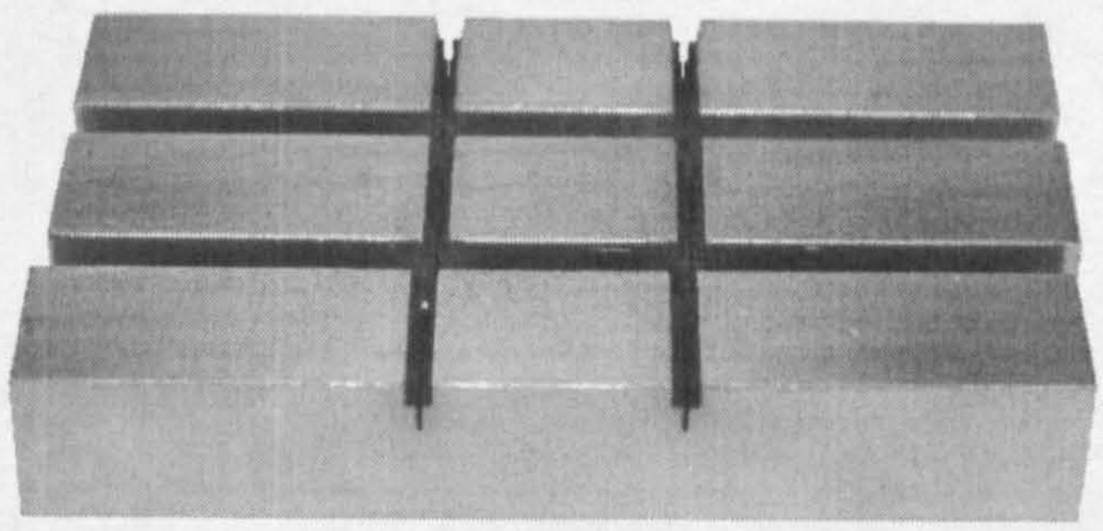

Figure 3.36 – Set of four point double–notch bend specimens.

The fracture load P_F in 4PB double–notch tests can be obtained directly from the load–displacement curve, the general yield load P_{gy} is calculated based on the upper bound solution to the bending moment M for notched specimens (Knott, 1973):

$$2M = 0.63B(W-a)^2\sigma_y = P_{gy}S \qquad 3.15$$

where B is the specimen breadth; $(W-a)$ is the specimen depth below the notch; S is the moment arm, $S = 0.5(S_{\max} - S_{\min})$, $S_{\max}$ and $S_{\min}$ represent the span between the two outer and the two inner loading points.

3.6.1 Experimental data of four point double–notch bend tests in the rolling direction.

The load–deflection curves of blunt four point double–notch bend tests in the rolling direction of the plate steel and the tested specimens which show the surviving and failed notch are shown in the following figures.

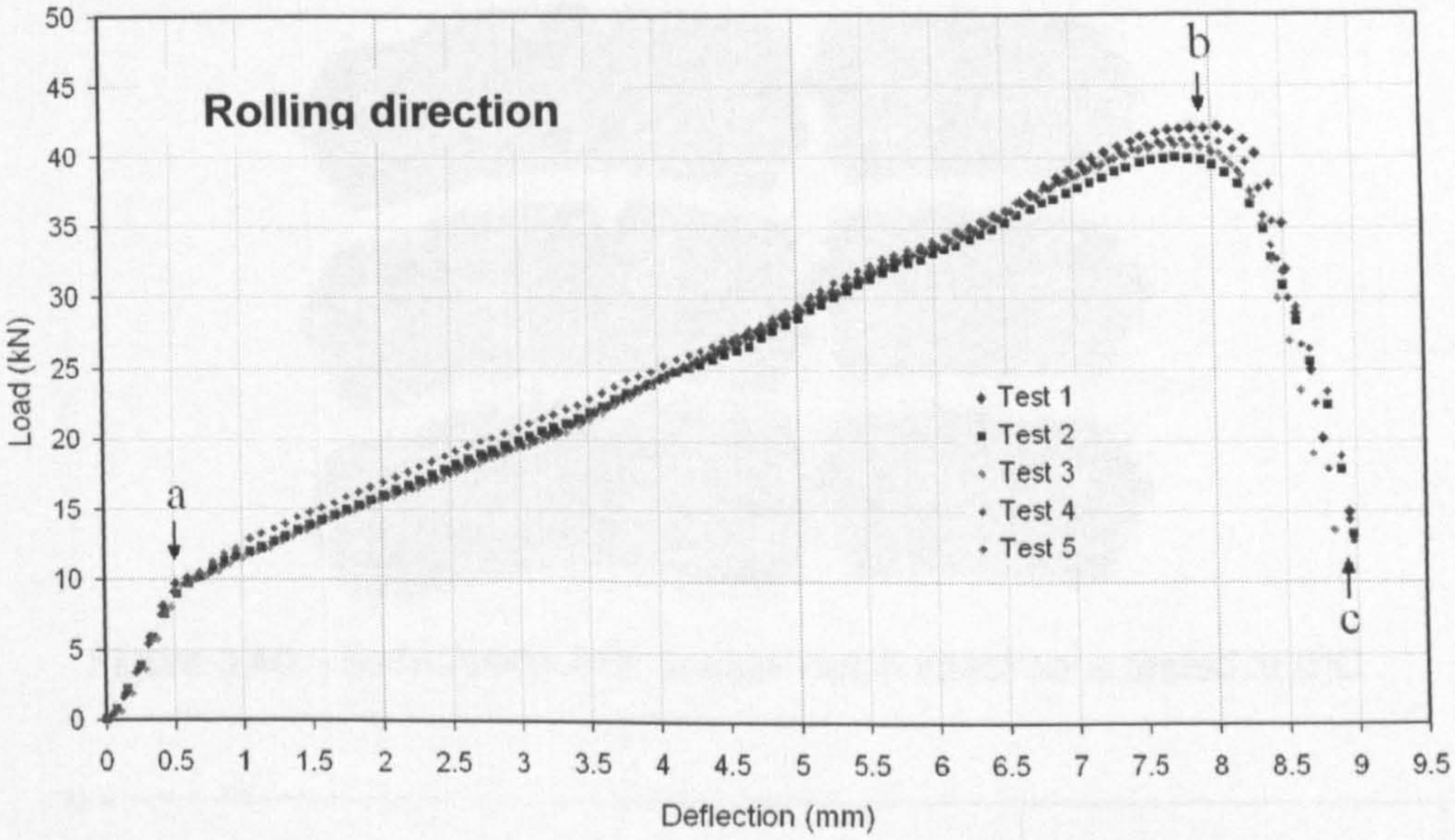

Figure 3.37 – Experimental data of 4PBT at +25ºC.

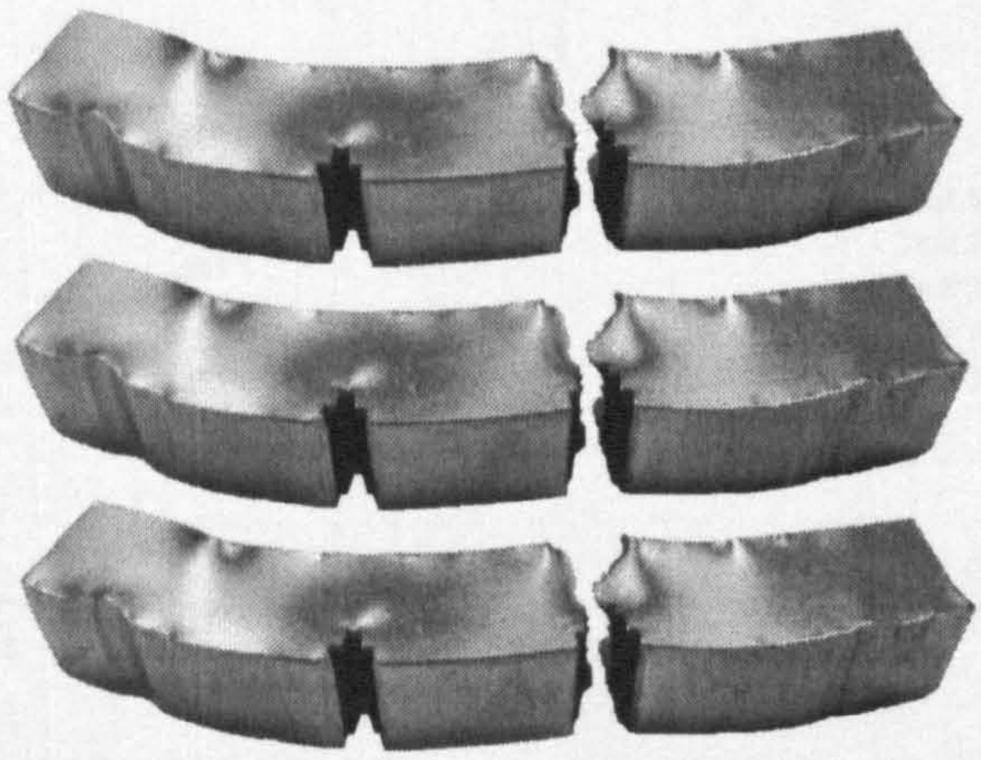

Figure 3.38 – Set of three 4PB double–notch specimens tested at +25ºC.

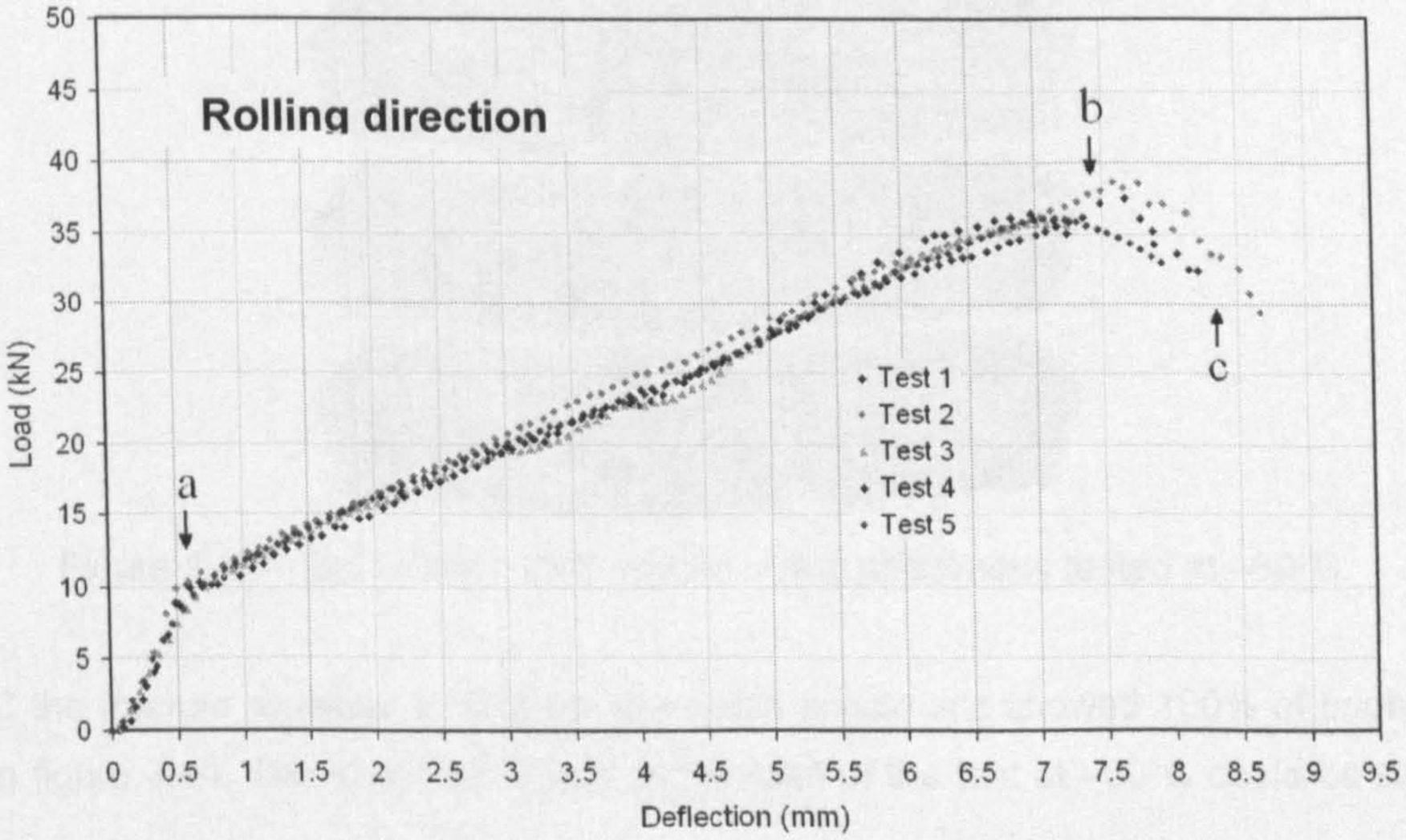

Figure 3.39 – Experimental data of 4PBT at 0ºC.

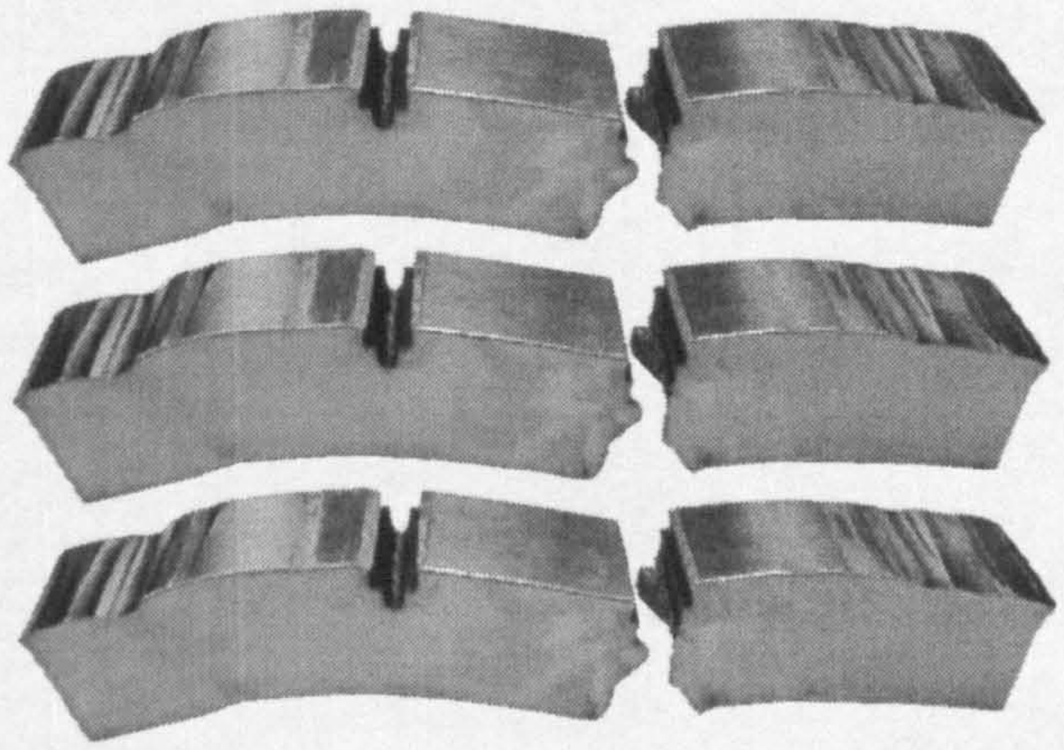

Figure 3.40 – Set of three 4PB double–notch specimens tested at 0ºC.

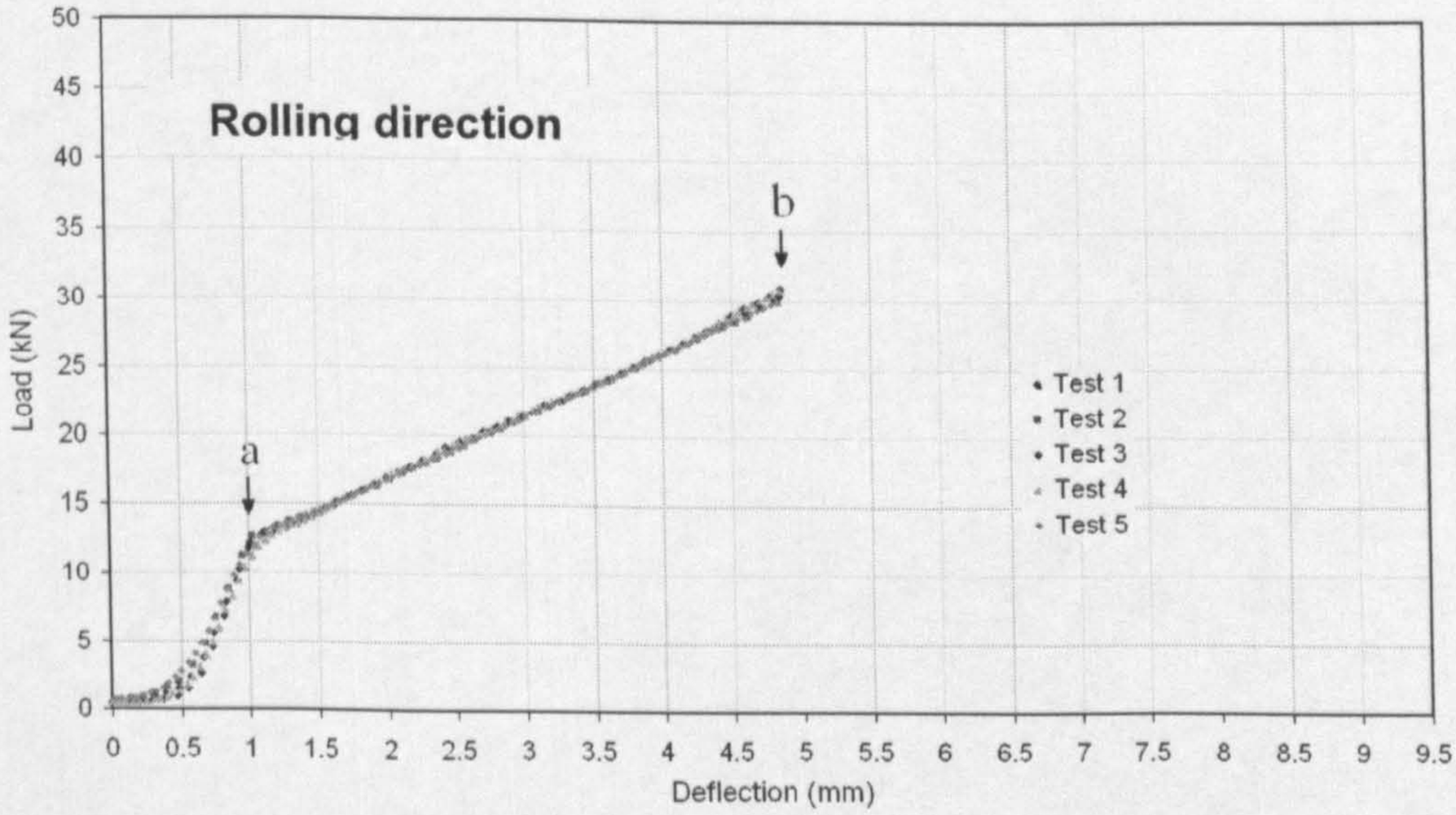

Figure 3.41 – Experimental data of 4PBT at –60ºC.

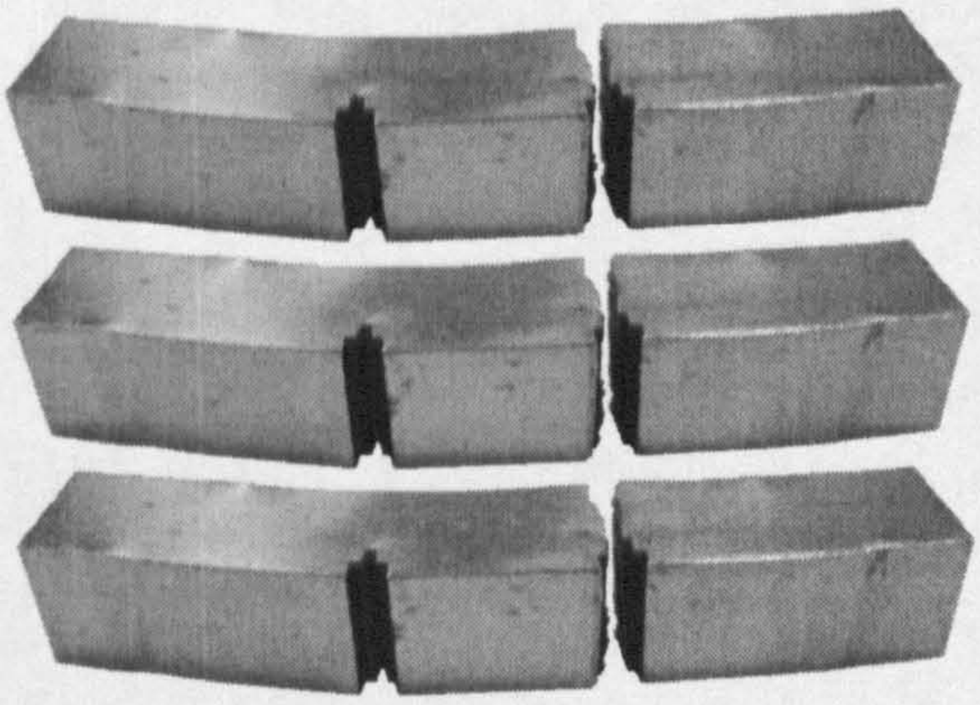

Figure 3.42 – Set of three 4PB double–notch specimens tested at –60ºC.

At –60ºC the fracture surfaces of 4PB double–notch specimens showed 100% of brightness as shown in figure 3.44. The slow rise in load at the start of the test at –60°C could be caused by

sliding of the specimens on the pins during the loading process. The same effect occurred on the curves of the test temperatures at –196°C.

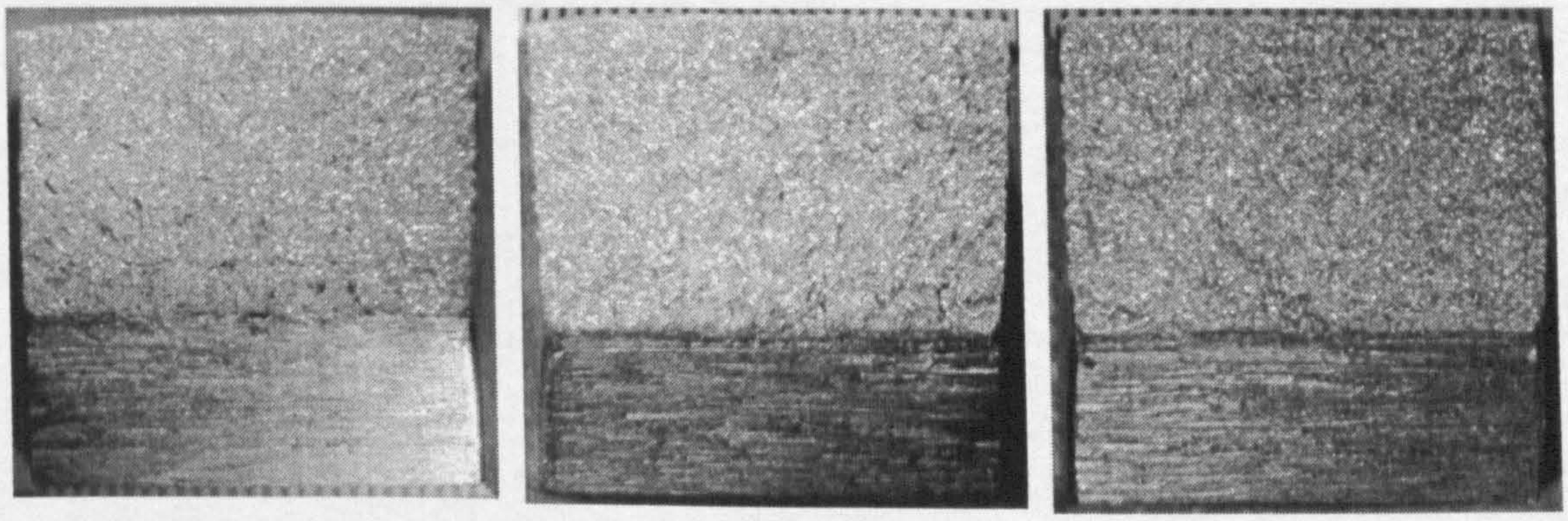

Figure 3.43 – Fracture surfaces of 4PB specimens tested at –60ºC.

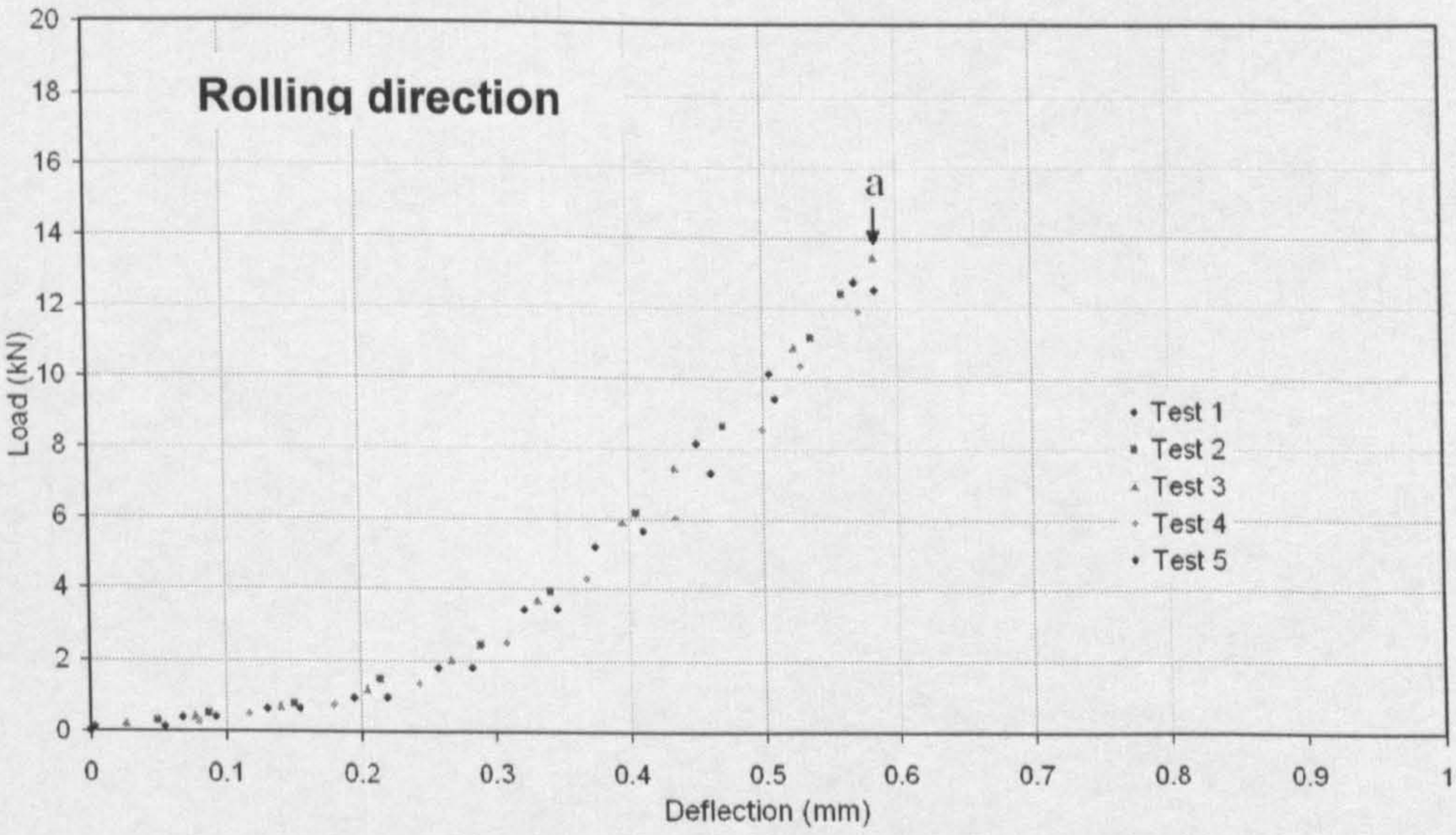

Figure 3.44 – Experimental data of 4PBT –196ºC.

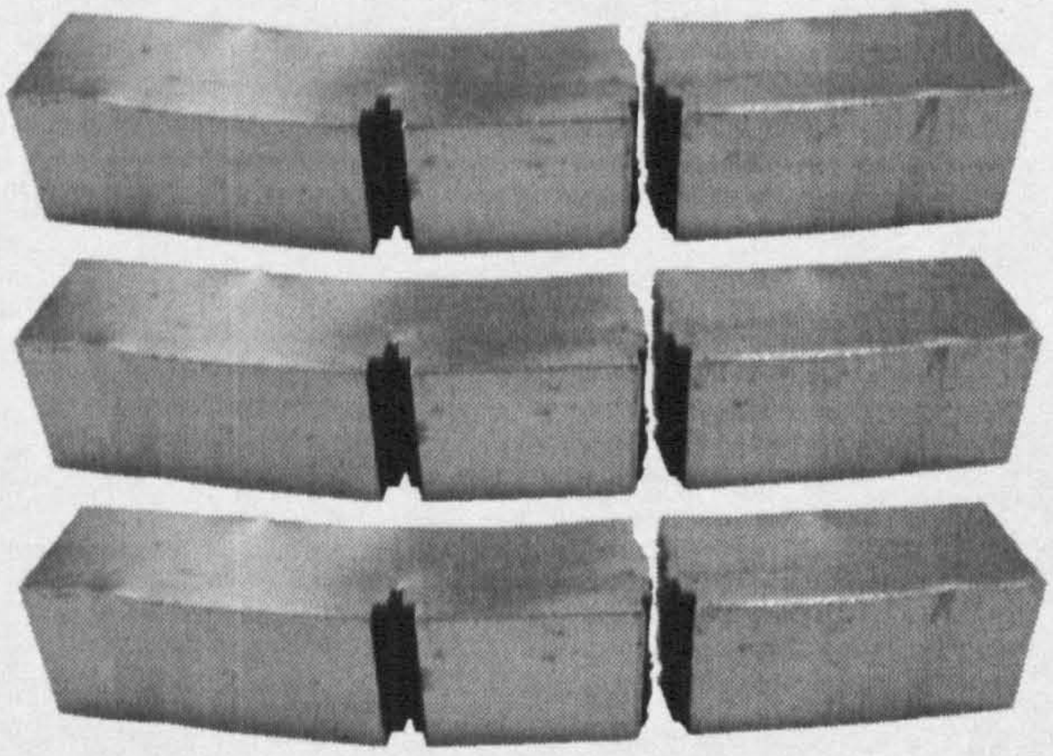

Figure 3.45 – Set of three 4PB double–notch specimens tested at –196ºC.

From the experimental curves of figures 3.37, 3.39, 3.41 and 3.44 of 4PB double–notch tests it can be seen that both notches, in all temperatures, supported almost the same load of about $12kN$ in the elastic region of the load–deflection curve as marked by the letter a. The stage between point a and b is the hardening part of the curves. In this loading step both notches are subjected to the same state of stress and strain and consequently in this stage all the micromechanisms for nucleating microcracks are developed. At this stage the critical plastic strain $\left(\varepsilon_p \geq \varepsilon_{pc}\right)$ for nucleating a crack nucleus, and the critical stress triaxiality $\left(\sigma_m / \sigma \geq T_c\right)$ for preventing the inducing crack nucleus from blunting are satisfied (Wang and Chen, 2000).

The stage between points b and c is the stage of fracture propagation of the notch that developed the critical normal stress $\left(\sigma_{yy} \geq \sigma_F\right)$ criterion for fracture for propagating the microcrack through the boundary between a second phase particle and a ferrite grain.

For low temperatures, (–60°C and –196°C) the stage between points b and c is almost imperceptable as brittle fracture propagation is a rapid run of cracks through the stressed material. Some degree of deformation was observed in the surviving notches of 4PB double notch specimens at –60°C.

But at –196°C the specimens broke immediately in the elastic limit region of the material, as clearly showed in graph 3.44. At this temperature, the three criterion for cleavage fracture described above are developed in the elastic regime. Very little deformation is needed to nucleate microcrack nucleus in front of the notches and once these microcracks nucleate they run very quickly. At this temperature microcracks can be developed not only in front of the notch root but in positions very far away from the notch root (at positions close to the edge opposite to the notch), this phenomenon will be shown in section 3.6.4 for this test temperature. It can be seen clearly that as soon as the critical conditions for cleavage fracture occur in one of the two notches (Wang and Chen, 2000), the fracture propagated very quickly.

3.6.2 Experimental data of four point double–notch bend tests in the transverse direction.

The load–deflection curves of blunt four point double–notch bend tests in the transverse direction of the plate steel and the tested specimens which show the surviving and failed notch are shown in the following images for the transition region.

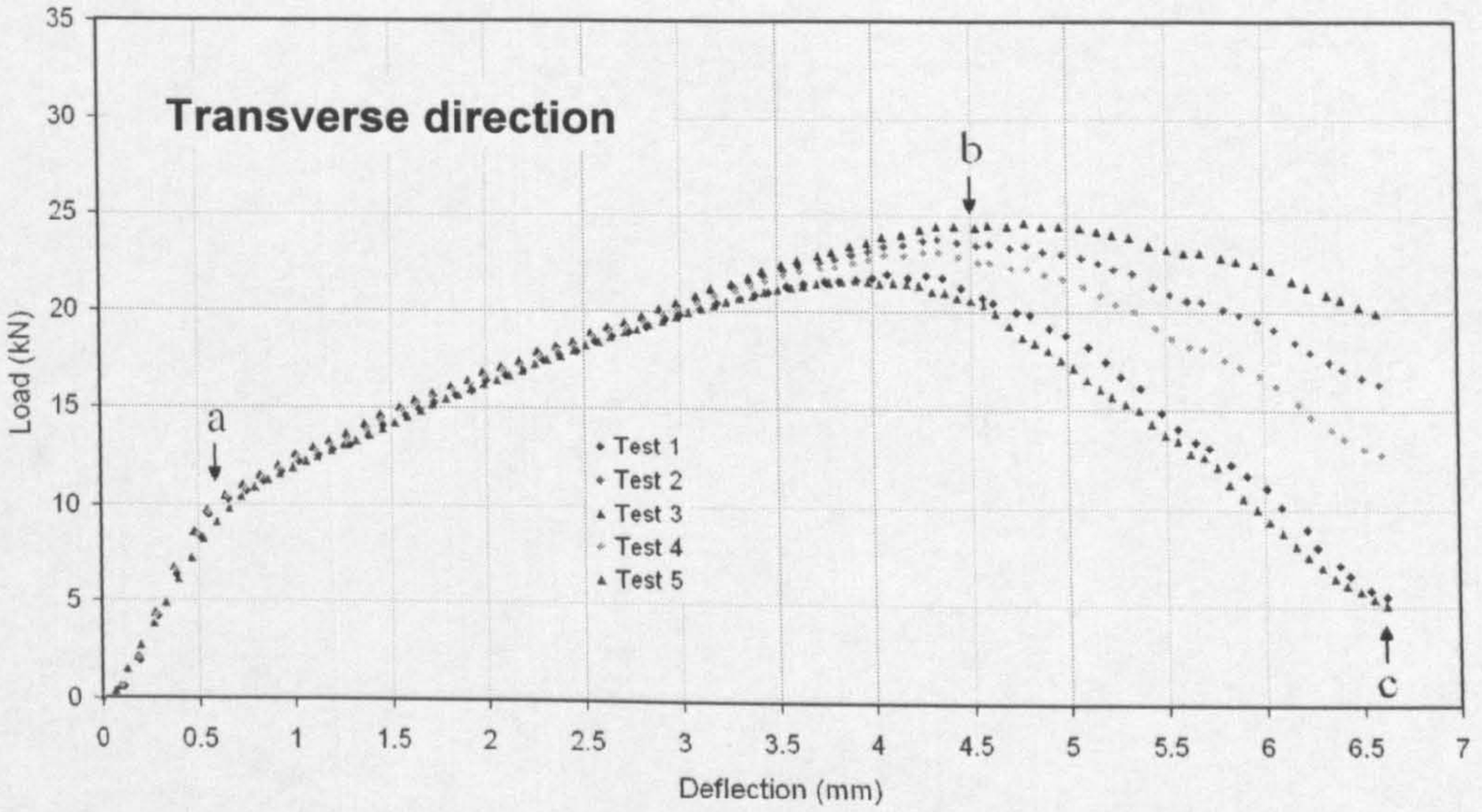

Figure 3.46 – Experimental data of 4PBT at room temperature (+25ºC).

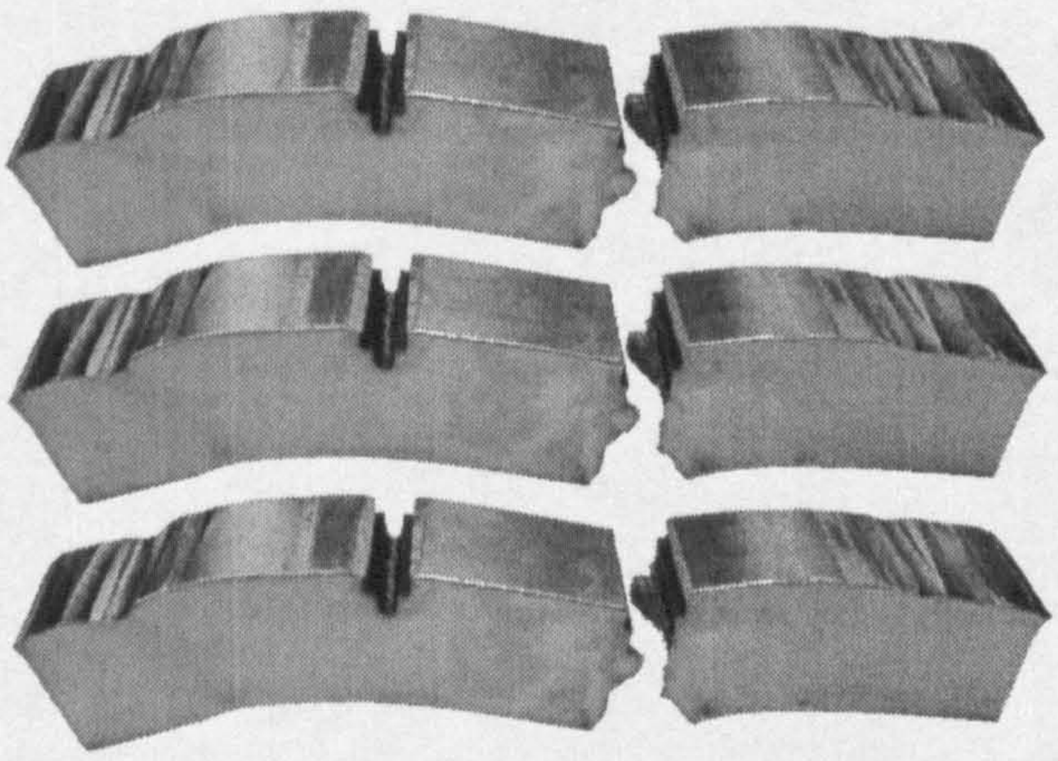

Figure 3.47 – Set of three 4PB double–notch specimens tested at room temperature (+25ºC.)

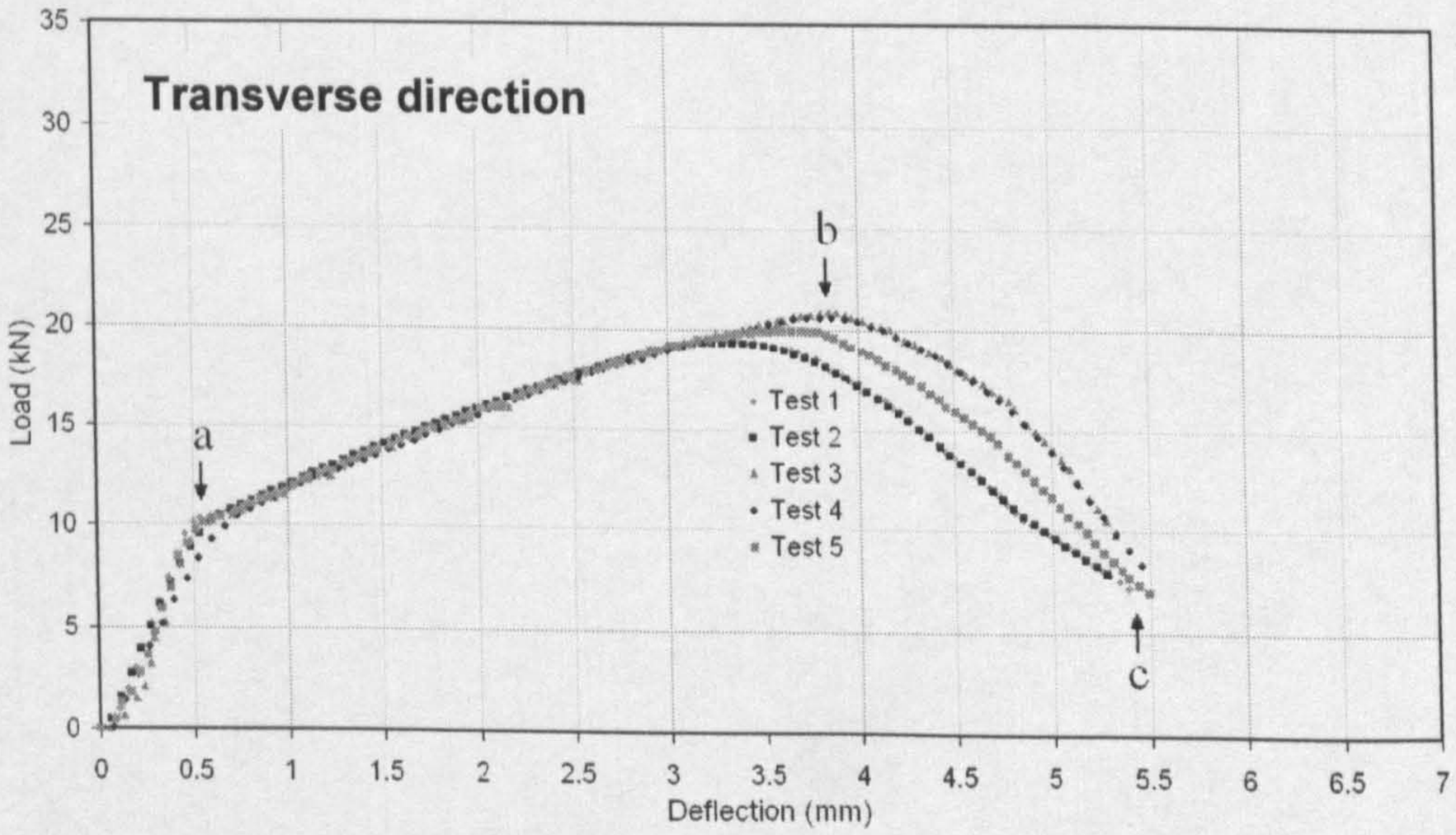

Figure 3.48 – 4PBT experimental data at room temperature (0ºC)

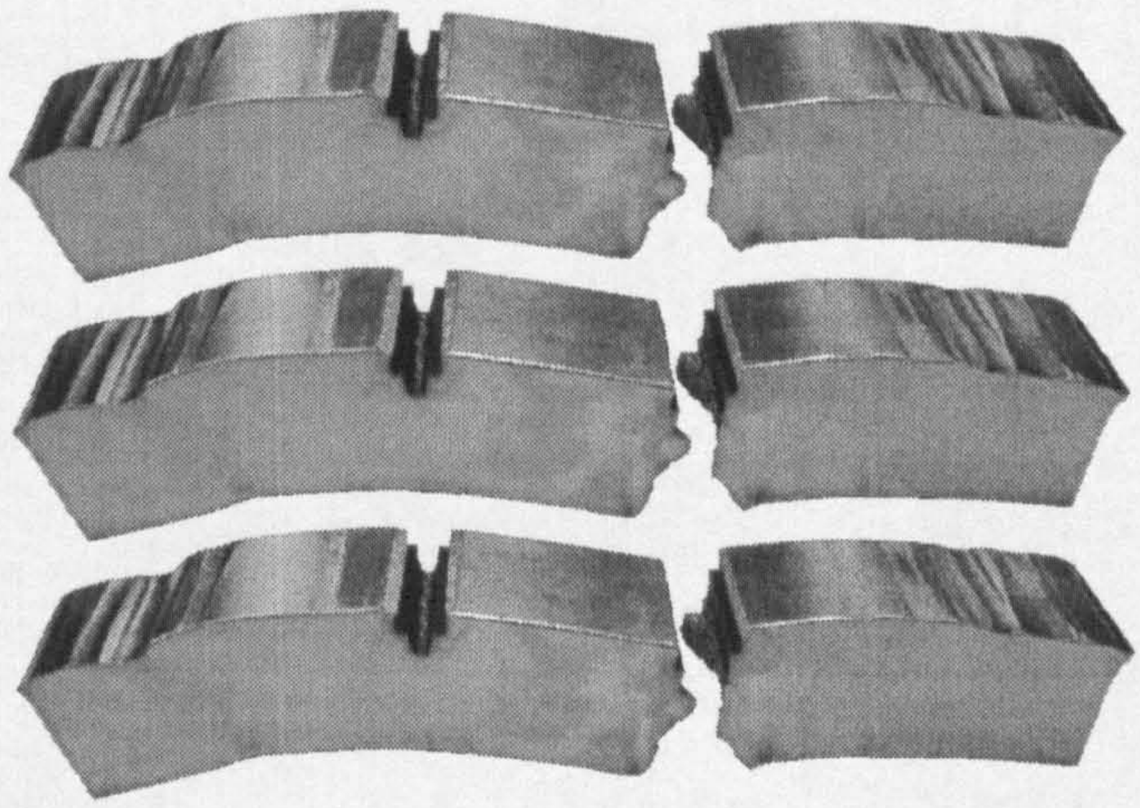

Figure 3.49 – Set of three 4PB double–notch specimens tested at 0ºC.

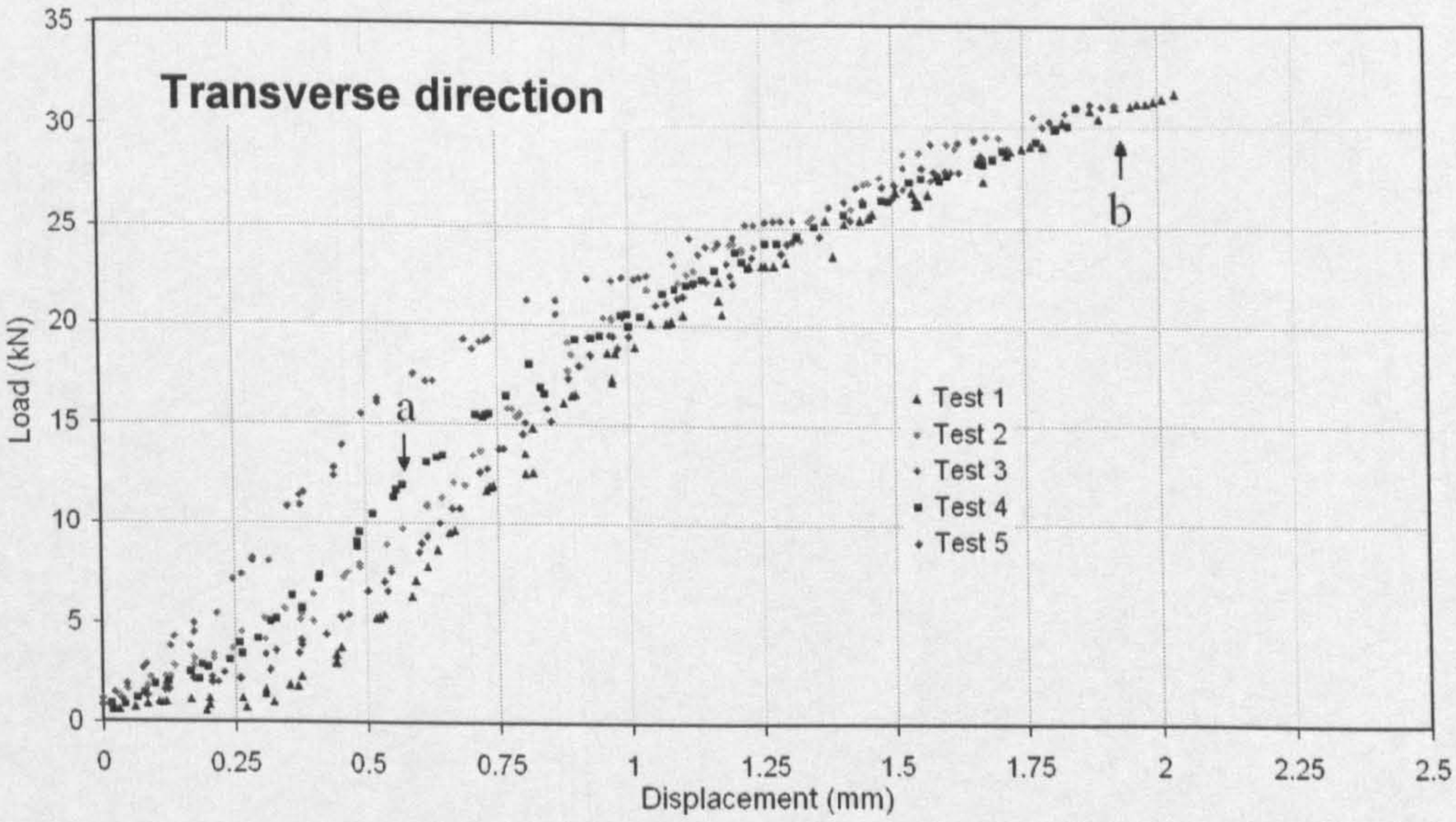

Figure 3.50 – 4PBT experimental data at room temperature (–60ºC).

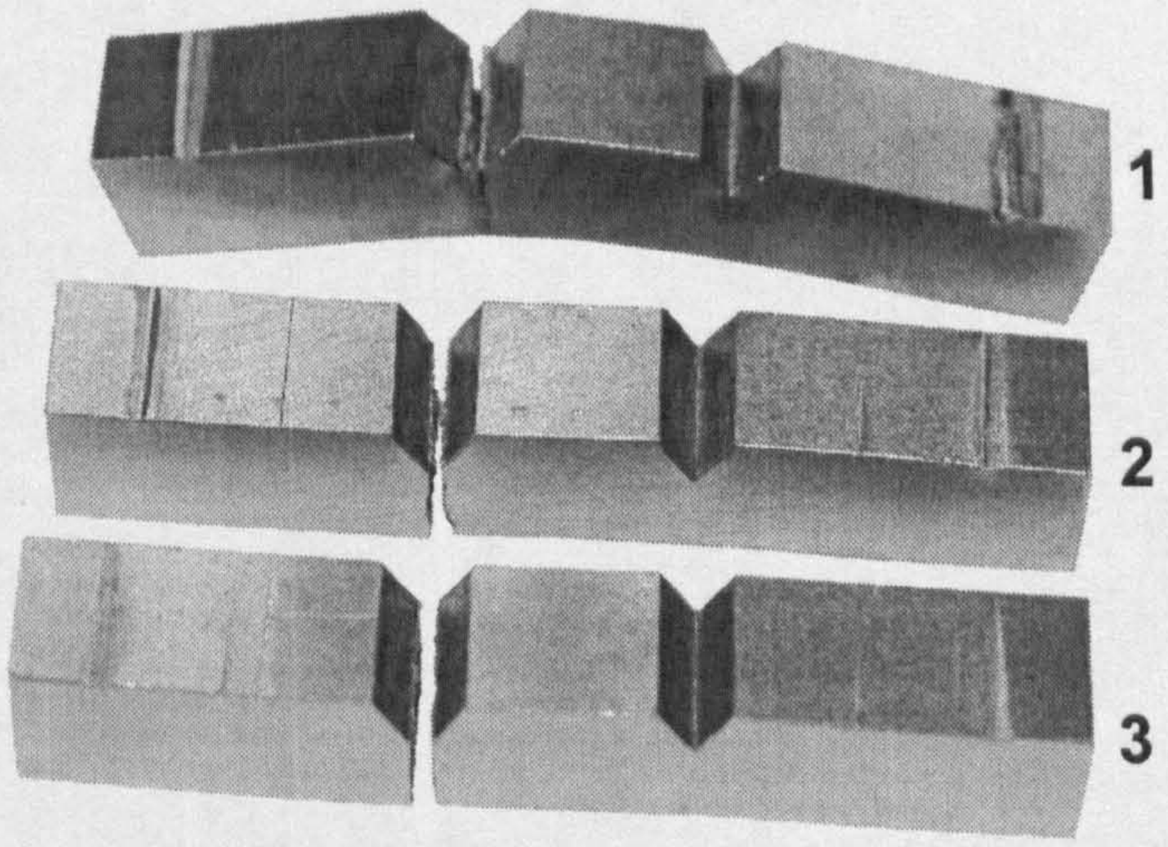

Figure 3.51 – Set of three 4PB double–notch specimens tested at –60ºC.

It is important to observe that for the transverse direction, at –60°C, it was observed scatter at low load in the data of figure 3.50 for each test. This could be due to the statistical distribution of particles of critical size in the notch region and to the random distribution of lands of pearlite with random size (contrary to the rolling direction where the lands are oriented according to the rolling direction). Pearlite colonies of critical size nucleate cleavage, and due to the fact that the pearlite microstructure is the dominant microstructure nucleating microcracks at this test temperature (sections 3.6.4 and 3.6.7). Therefore each specimen may sample lands of pearlite and particles of different size which can result in the scatter observed in figure 3.50.

From the experimental curves of figures 3.46, 3.48 and 3.50 it can be seen that both notches experienced almost the same load of about $10kN$ in the elastic region of the load–deflection curve as marked by point a. At –60ºC the specimens showed 100% of brightness in the fracture surfaces of 4PB double–notch as for the rolling direction and at the same temperature. Figure 3.52 shows a set of 3 broken specimens tested at –60ºC. Test 1 shows high local plasticity in the survived notch and the site where the thermocouple was inserted in all specimens tested at all test temperatures in the transverse and rolling direction. The failed notch did not break totally when the crack advanced. This is probably due to the high misorientation angle that the crack found in it's path or may be to some physical micro features that stopped the crack. This phenomenon is explained in section 5.8.5.

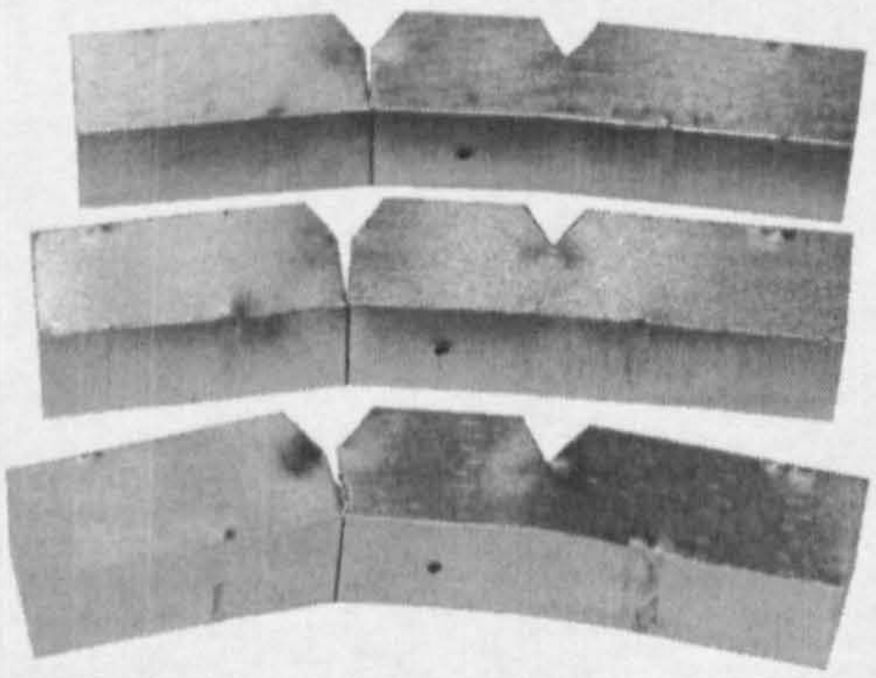

Figure 3.52 – Set of three four point double–notch bend specimens tested at –60°C.

3.6.3 Experimental technique for the identification of the cleavage fracture initiation points.

As already mentioned, in blunt four point double–notch bend tests when one notch fractures, the surviving notch will reveal the critical condition prior to fracture as both notches are subjected to the same state of stresses and strains in the loading process (Chen et al., 2003,

Wang et al., 2004a, Wang and Chen, 1999, Wang et al., 2003c, Bordet et al., 2005, Young-Roc Im, 2004, Wang et al., 2004b, Wang et al., 2005b, Chen et al., 2001, Chen et al., 1997). In order to analyze the physical fracture process mechanisms prior to the critical event, the surviving notches were sectioned, polished and etched to reveal the microstructure and consequently the micro features that nucleate fracture. Figure 3.53 shows how the surviving notches were sectioned.

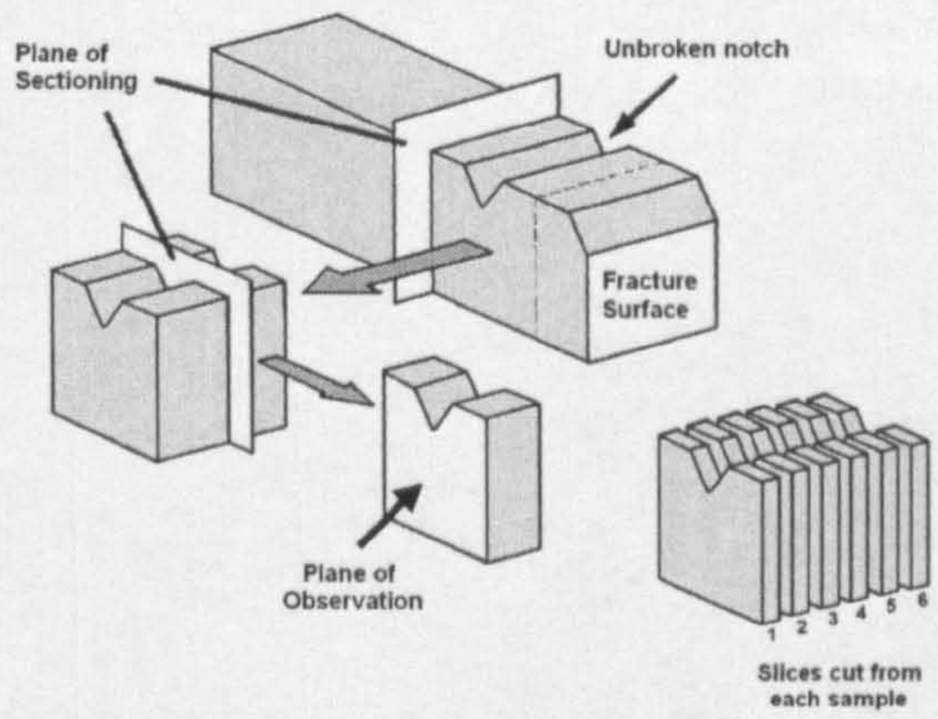

Figure 3.53 – Schematic of the sections for analysis of four point double–notch bend test.

Six slices were cut from the surviving notches, each section was mounted in bakelite and polished with water based monocrystalline diamond suspension of 9 micron, 3 micron, 1 micron and finally 0.25 micron to obtain very flat surfaces without scratches. The samples were etched with a mixture of nital at 5% with small amounts of picral in order to reveal better the ferrite and pearlite microstructure and the triggering micro features for fracture nucleation. Figure 3.54 shows the machine used to polish the samples with a set of 6 samples ready for polishing.

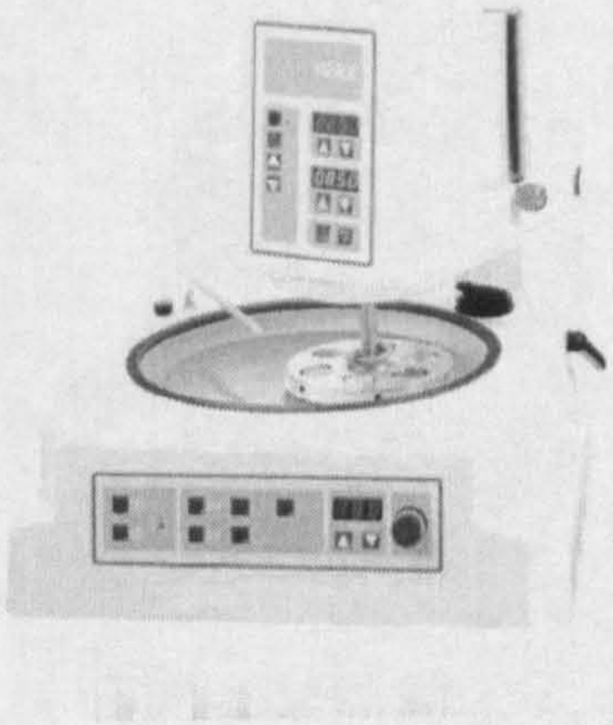

Figure 3.54 – Polishing machine

3.6.4 SEM analysis of the sectioned slices of 4PB double–notch specimens in the rolling (RD) and transverse (TD) directions.

Once the samples were polished and etched, they were examined in a Scanning Electron Microscope CAMSCAN model MK2 to identify the microstructures for cleavage fracture nucleation. Micrographs were taken of each slice of the sectioned notch. The area of interest was the regions surrounding the notch root because this region was the most stressed due to the presence of the notch. As the plate steel was tested in the rolling and transverse directions (L and T), micrographs were taken from the slices in both the rolling and transverse direction. Examples of those micrographs are shown in the following figures. In this work the different microstructures for cleavage fracture nucleation, the size of particles nucleating cleavage fracture, their position with respect to the notch root and, the size and orientation of microcracks were measured in the fractography analysis. Figure 3.55 shows distribution of microcracks found in front of the notch root at room test temperature in the rolling direction. Figure 3.55 clearly shows the crack tip and the critical event prior to fracture propagation, which is the nucleation of microcracks of critical size. In order to identify the microstructures that nucleated those microvoids and microcracks, micrographs with higher magnification were taken.

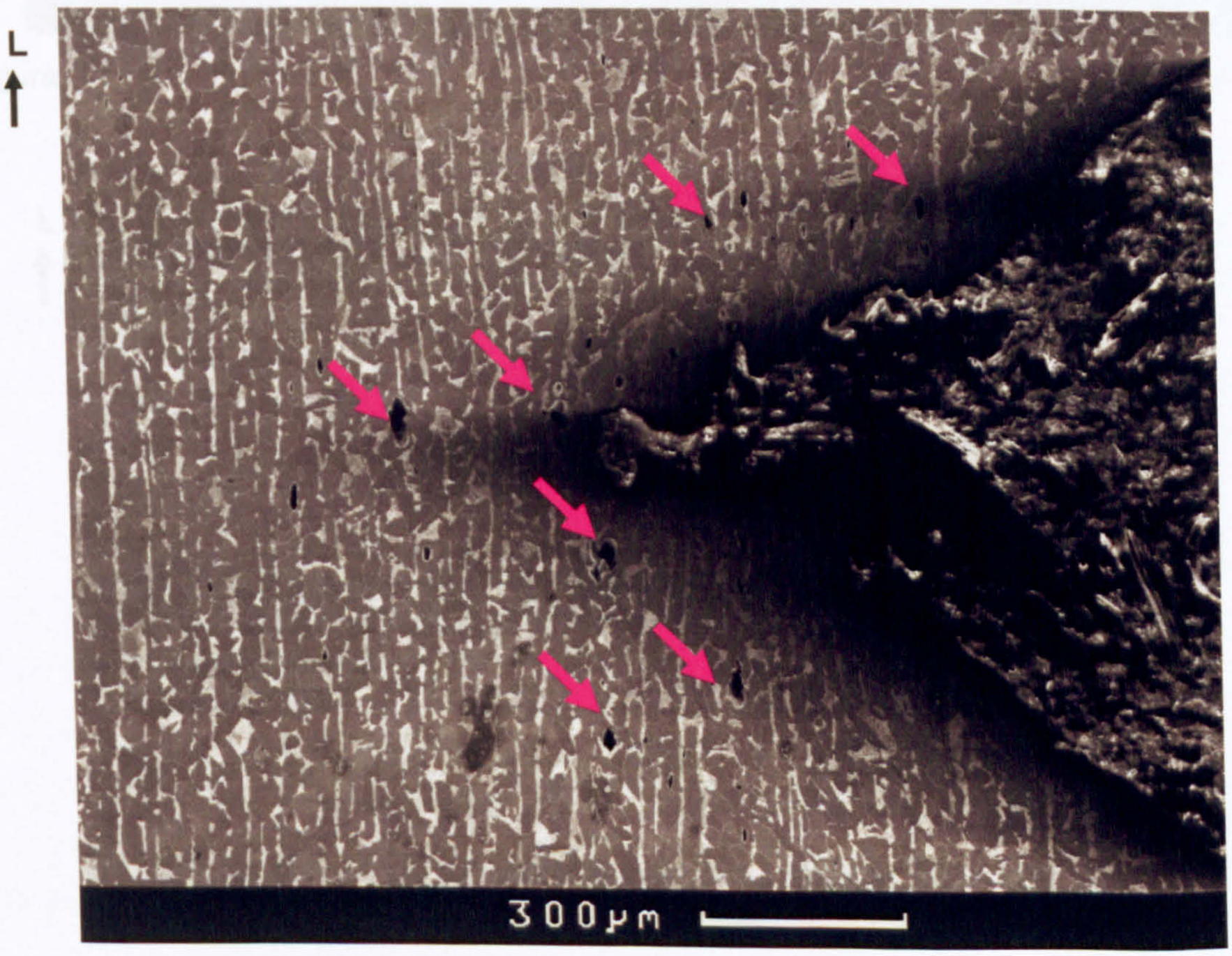

Figure 3.55 – Distribution of microcracks taken from slice 3 in RD at +25ºC.

Figure 3.56 shows a micrograph taken at $210X$ in a region close to the notch root for a test temperature of +25°C. Figure 3.56 shows that the bigger cracks were nucleated in the pearlite microstructure and pearlite boundary as marked by arrows in figure 3.56. Figure 3.57 shows a micrograph taken at $950X$ and $80\mu m$ from the notch root of slice 1, it can be seen that those microcracks were nucleated from the pearlite microstructure.

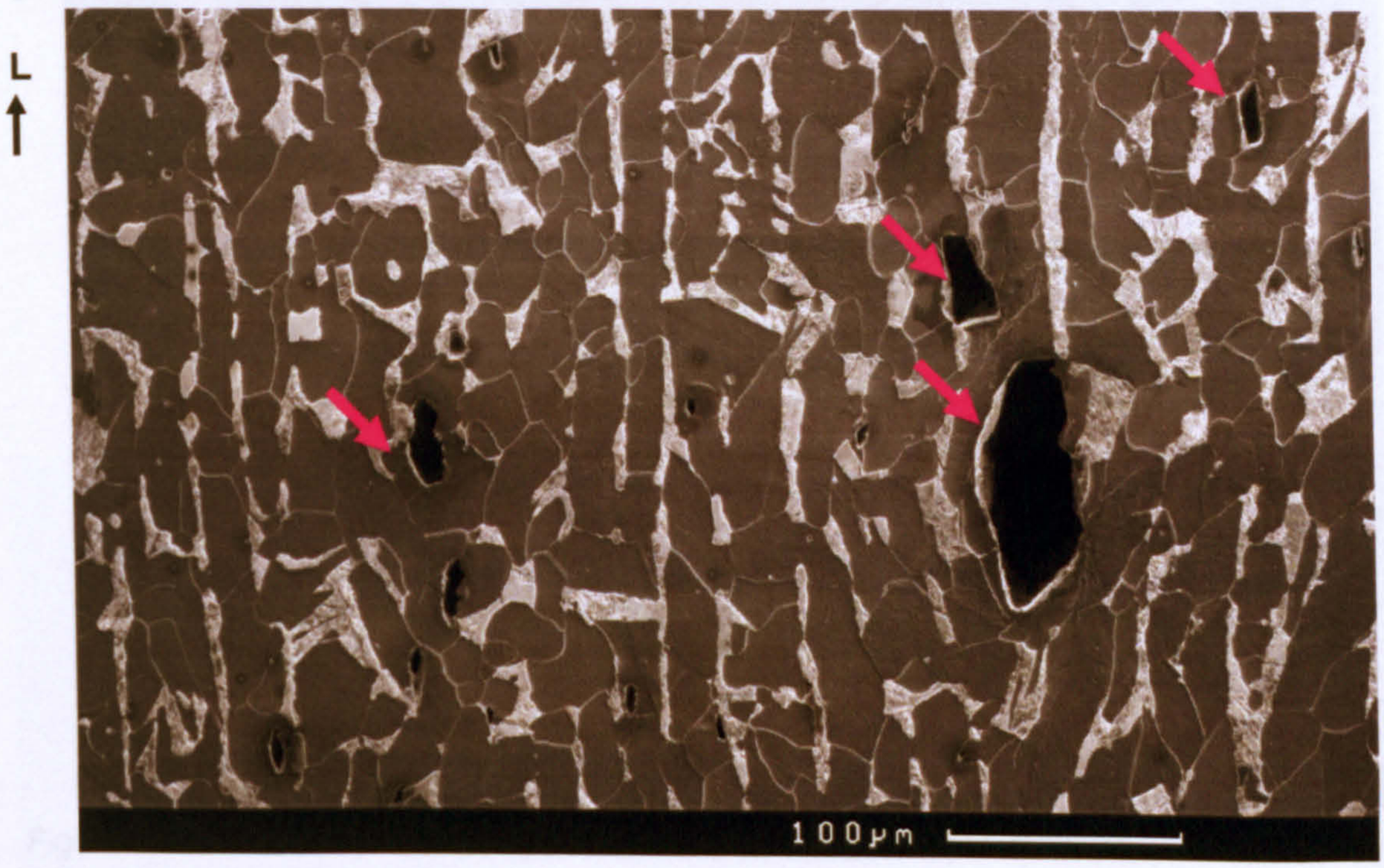

Figure 3.56 – Micrograph taken at $210X$ from slice 2, close to the notch root in RD at +25ºC.

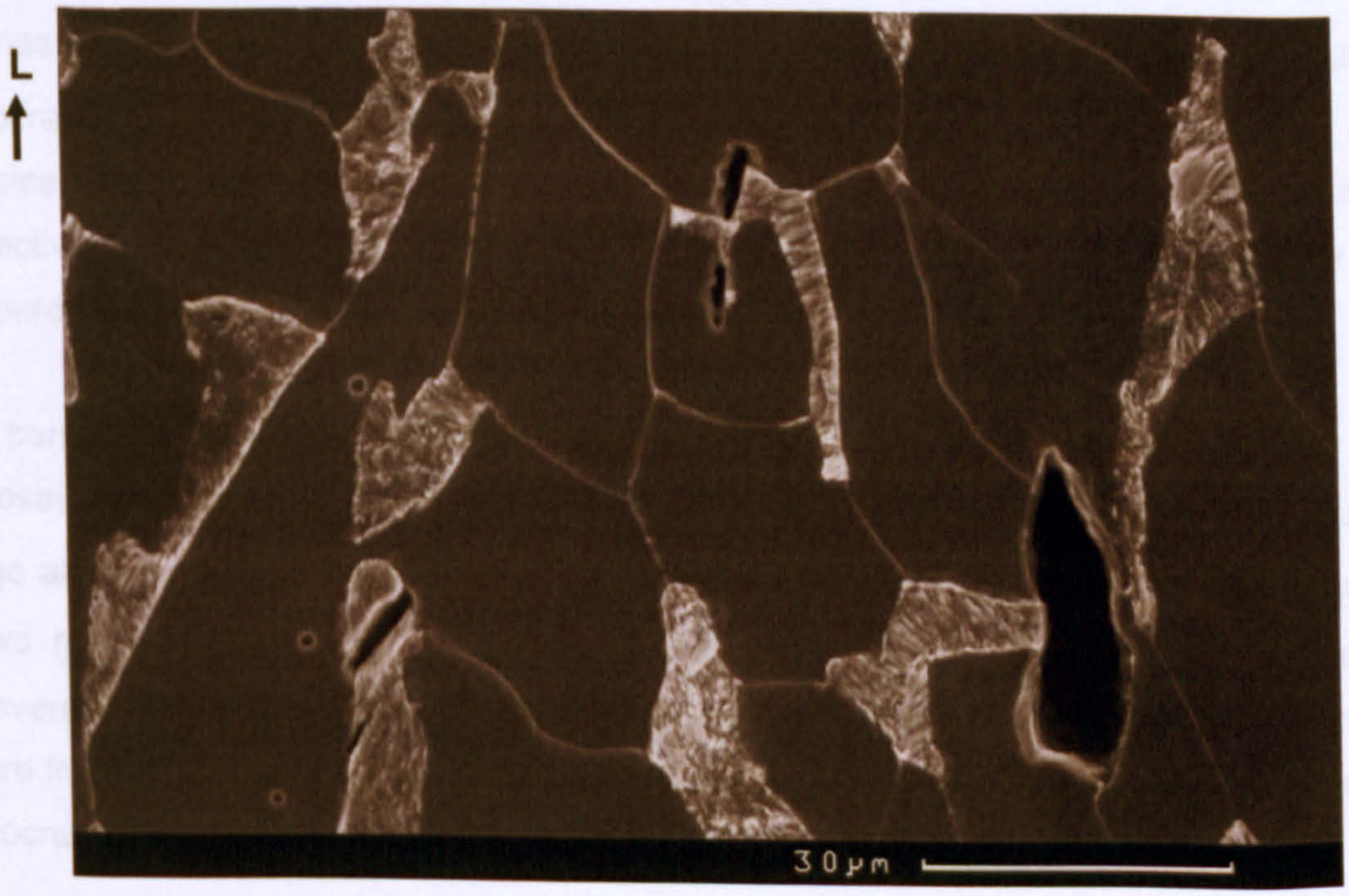

Figure 3.57 – Micrograph taken at $950X$ from slice 1, close to notch root in RD at +25ºC.

To identify the microstructures for nucleating the microcracks, micrographs of visible particles were taken, figure 3.58 shows examples of particles distributed in the matrix of the material, this figure was taken at a magnification of $2560X$ and at $100\mu m$ from the notch root.

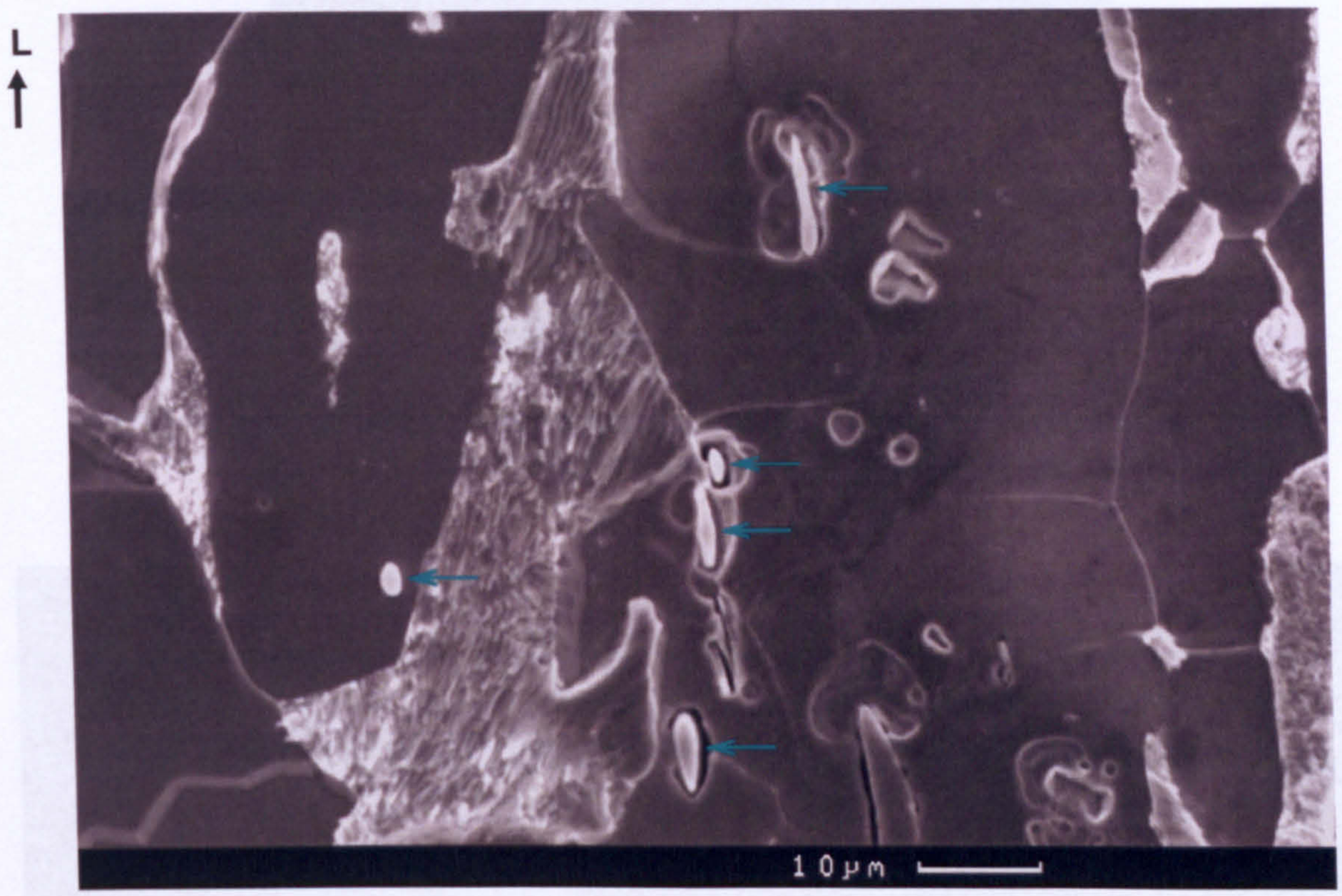

Figure 3.58 – Particles nucleating microcracks taken at $2560X$ from slice 2 in RD at +25°C.

The size of particles in figure 3.58 is in the range of 2.85 μm to 10 μm of length with a thickness of around 2.8 μm. It is clearly shown that the distribution of particles nucleating microcracks in figure 3.58 was found mainly in the ferrite matrix. But the analysis of such particles performed in section 3.6.6 and 3.6.7 for the rolling and transverse direction respectively will show that the size and number of microcracks found in the ferrite matrix is small compared with that of the pearlite microstructure.

The particle in figure 3.59 was found in a microcrack nucleated inside the lamellar pearlite microstructure in the rolling direction of the plate steel. The size of the particle is 5.25 μm. This image also shows how the particle was separated from the matrix of the material. Figure 3.60 shows microcracks of slice 3 in front of the notch root at room test temperature in the transverse direction of the plate steel. This image clearly shows the crack tip and the event before fracture propagation. For a clear identification of the microstructures that nucleated those microcracks, micrographs with higher magnification were taken.

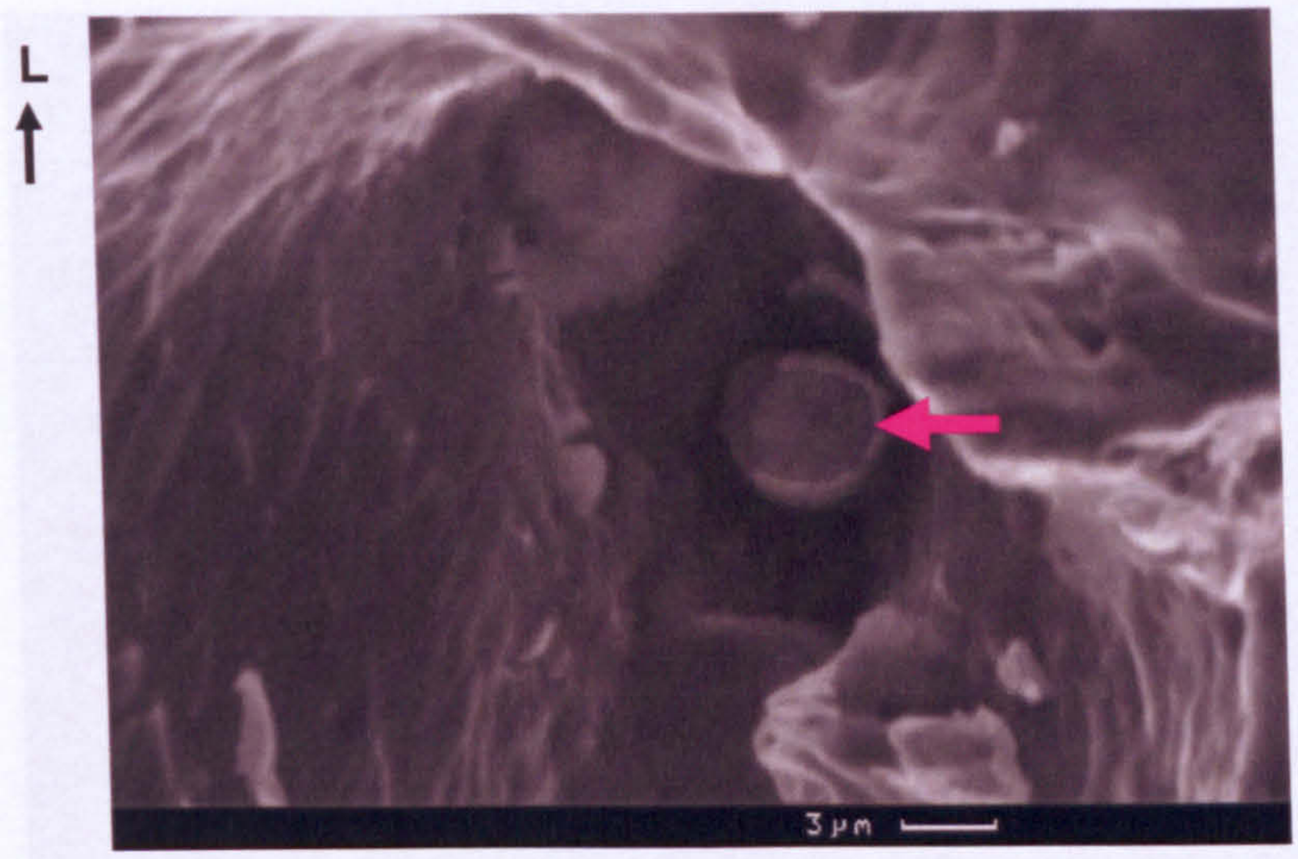

Figure 3.59 – Micrograph taken at $3160X$ inside the lamellar pearlite microstructure in RD at +25°C.

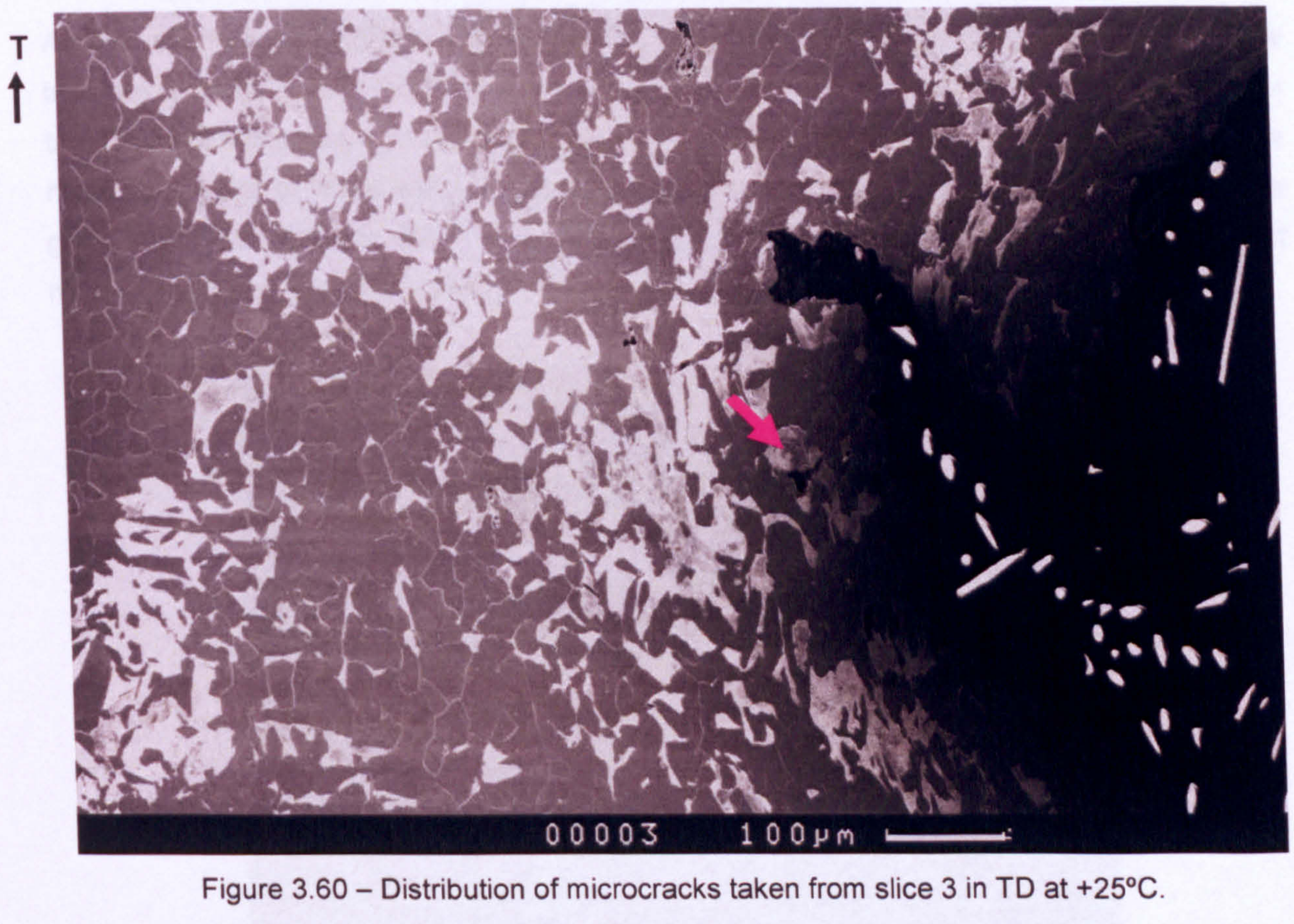

Figure 3.60 – Distribution of microcracks taken from slice 3 in TD at +25°C.

Figure 3.61 shows the microcrack of figure 3.60 marked by the arrow, the microcrack of figure 3.61 clearly shows that this microcrack was nucleated in a pearlite colony and grew through ferrite grains. The image also shows how the pearlite microstructure was broken. The microcrack marked with a red arrow shows another microcrack nucleated in another land of pearlite. The microcrack marked with the blue arrow shows how a microcrack is being nucleated in the lamellar microstructure of a land of pearlite.

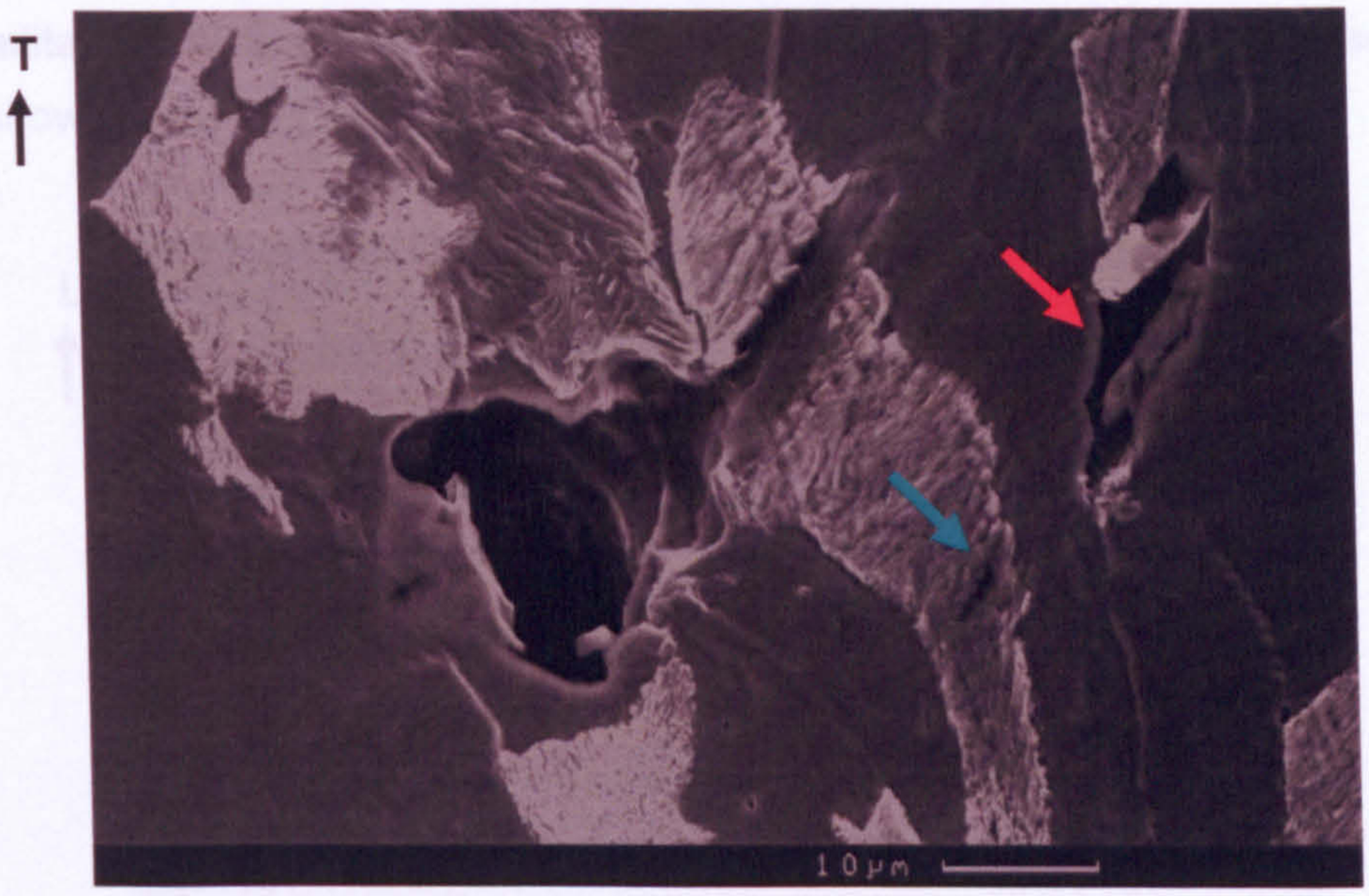

Figure 3.61 – Micrograph taken at $2000X$ of slice 4 in TD at +25°C.

Another example of distribution of microcracks nucleated in the lamellar pearlite microstructure in a region close to the crack tip is shown in figure 3.62. The micrograph was taken in the transverse direction of the plate steel. This micrograph shows a population of microcracks in the notch root. Most of these were nucleated by the lamellar pearlite microstructure. This image gives very clear evidence about how microcracks are developed in the notch region and that most of them were created in the lands of pearlite.

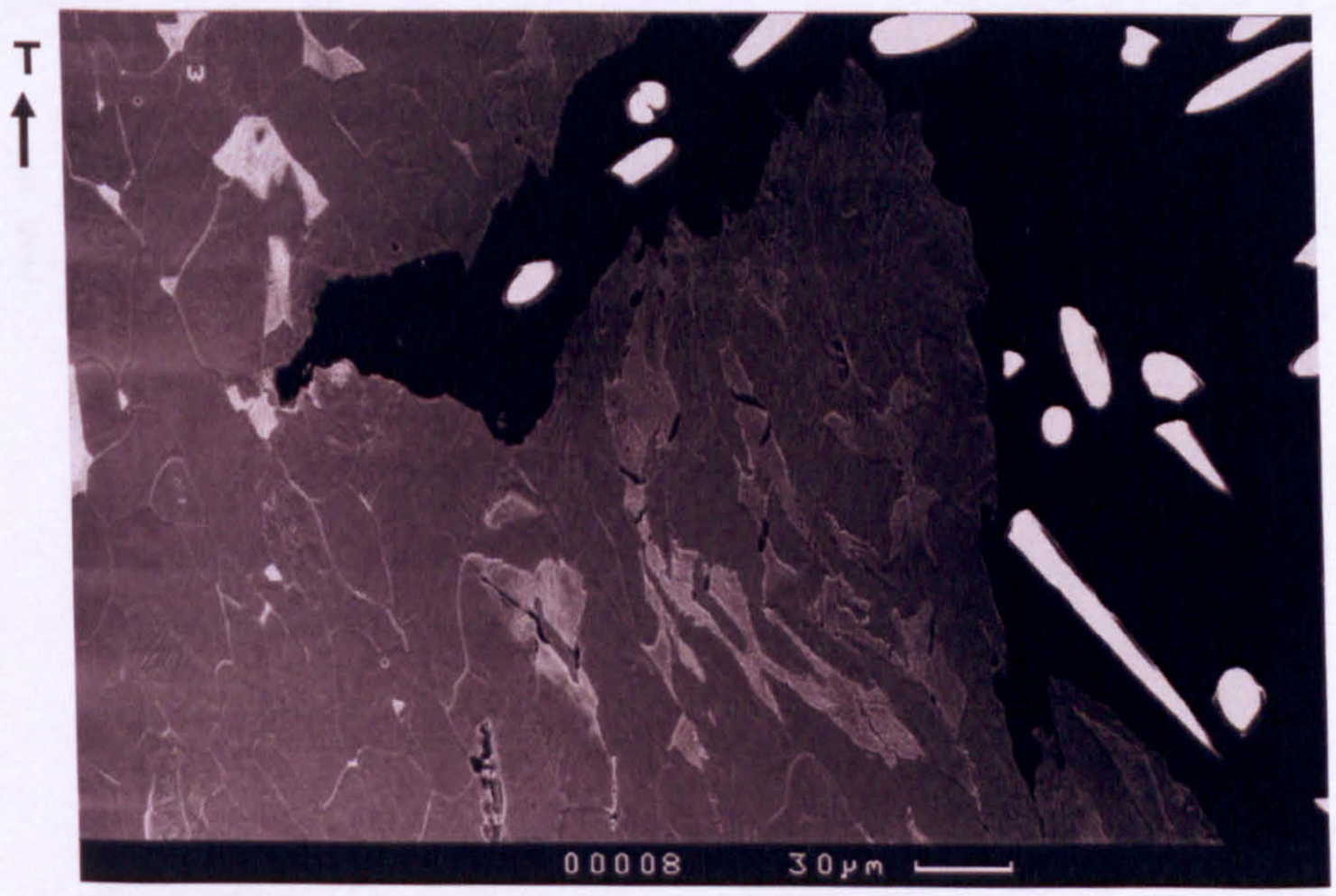

Figure 3.62 – Micrograph taken at $300X$ from slice 2 in TD at +25°C.

The following micrographs show examples of microcracks taken from the specimens tested at 0°C for the rolling and transverse directions of the plate steel. Micrograph 3.63 clearly shows a

land of pearlite. In this image the lamellar pearlite microstructure nucleated those microcracks as clearly shown in the picture.

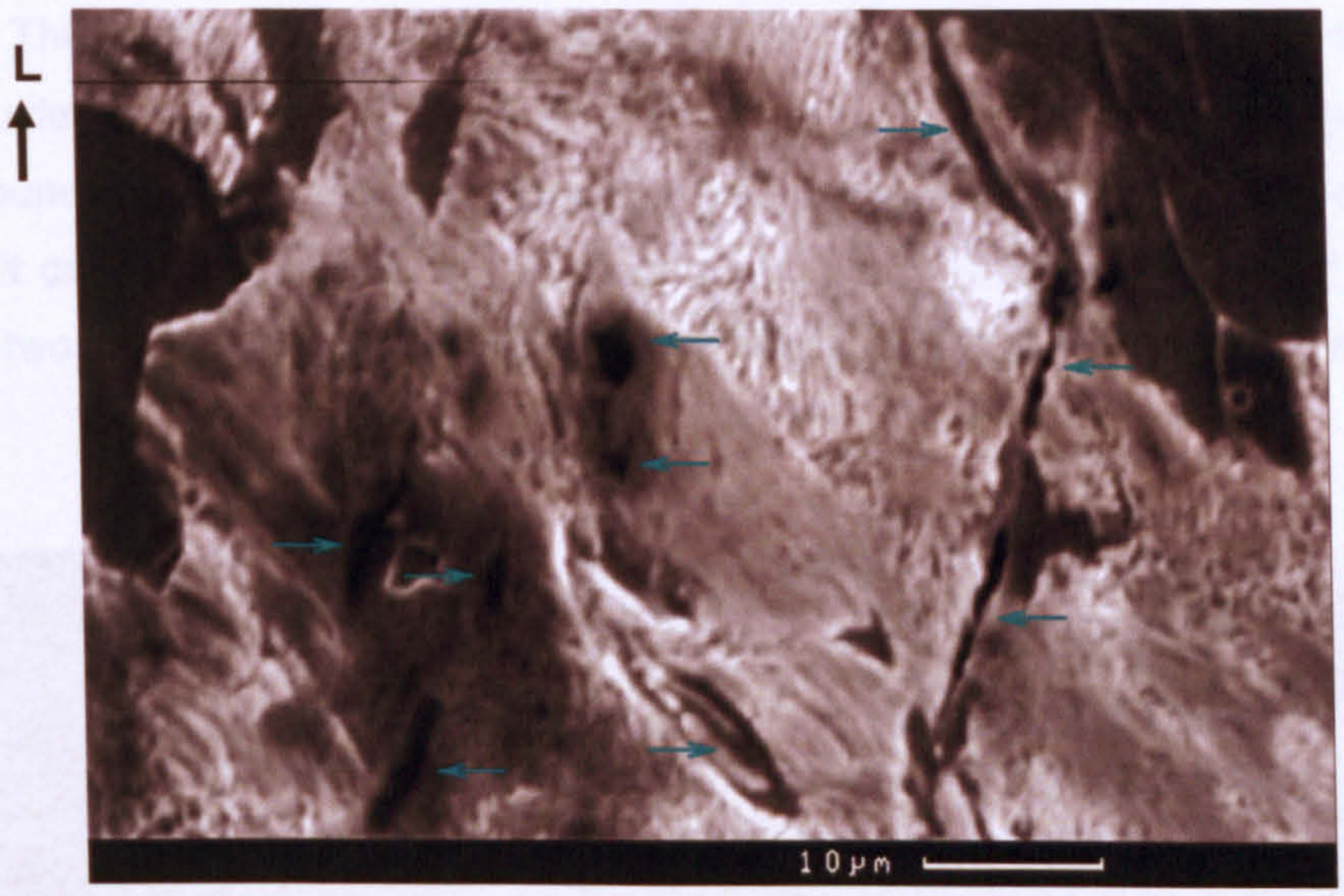

Figure 3.63 – Micrograph taken at $1650X$ from slice 3 in RD at 0ºC.

Micrograph 3.64 shows the crack tip of slice 3 of a 4PB double–notch specimen tested at 0ºC. This micrograph shows that the crack tip is located in a land of pearlite, this land is broken. The blue arrows of image 3.64 show as well a broken pearlite colony, this suggest that the crack initiated from this land of pearlite. This image gives very clear evidence that the nucleation for cleavage fracture initiation occurred mainly inside the lamellar pearlite microstructure.

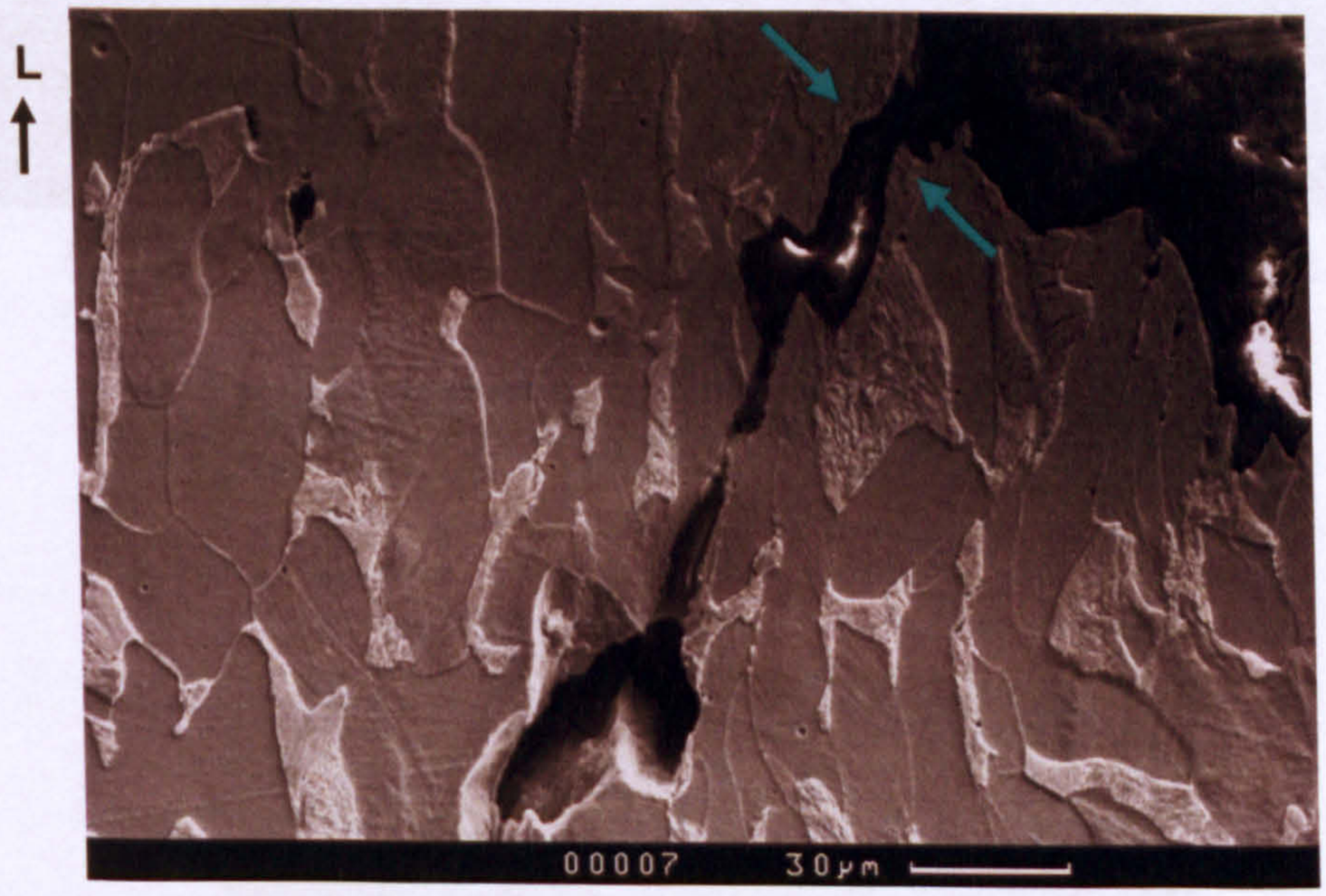

Figure 3.64 – Micrograph taken at $1000X$ from slice 3 in RD at 0ºC.

The next two micrographs were taken in the transverse direction of the plate steel at a test temperature of 0ºC. Image 3.65 shows the crack tip, in this image we can clearly see lands of

pearlite with microcracks. Most of the microcracks were nucleated inside the lamellar microstructure of pearlite and were stopped by the boundary of the ferrite grains. The microcracks are marked with blue arrows. In front of the crack tip it can be seen more microcracks. This clearly shows the fracture process of a crack and how the lands of pearlite break and nucleate microcracks. Another microcrack, which was nucleated by an inclusion in the ferrite boundary and/or the boundary of pearlite, is shown by the green arrow. From the micrograph, it can be concluded that most of the microcracks were nucleated by the lands of pearlite with two different micromechanisms, the lamellar microstructure of pearlite and pearlite boundary.

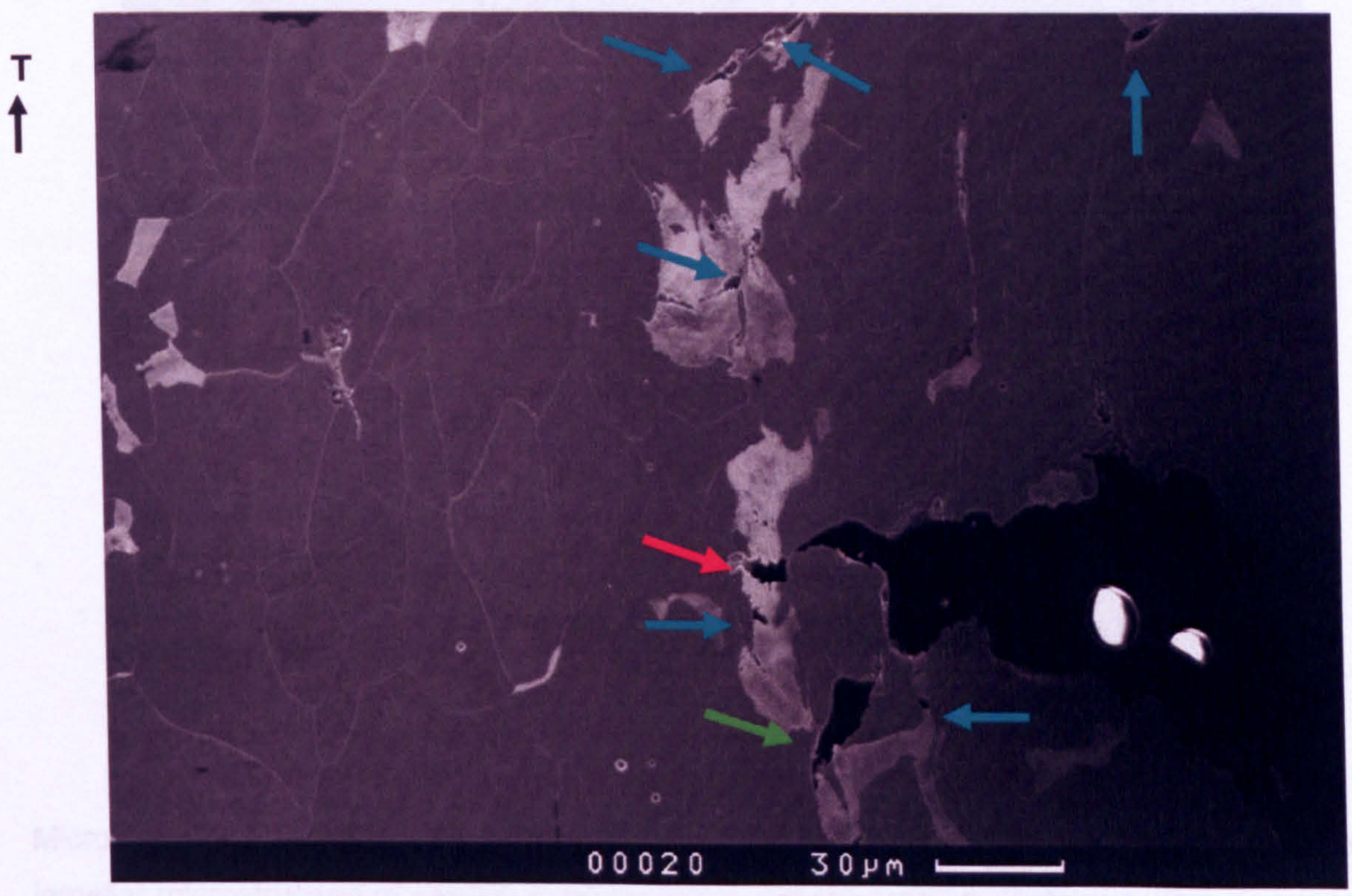

Figure 3.65 – Micrograph taken at $1000X$ from slice 3 in TD at 0ºC.

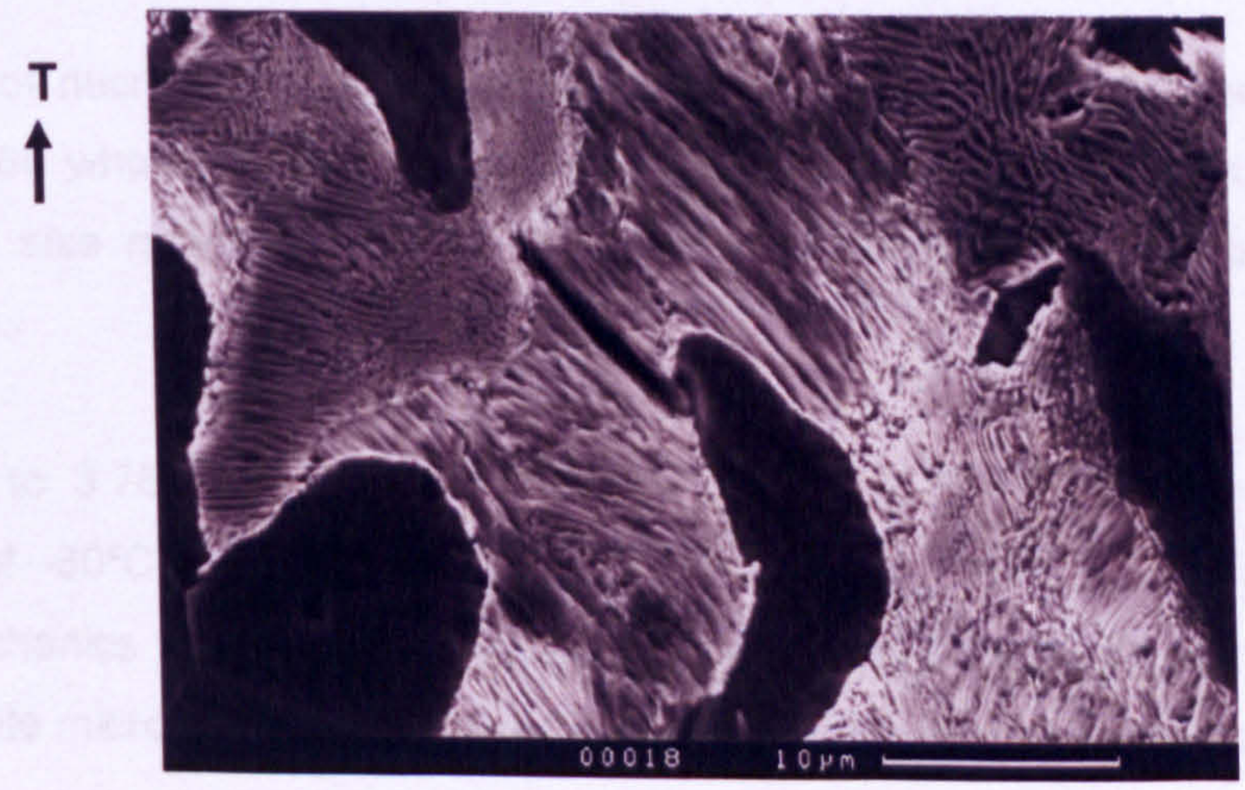

Figure 3.66 – Micrograph taken at $2500X$ from slice 3 in TD at 0ºC.

Micrograph 3.66 shows a close view of a microcrack nucleated inside the lamellar microstructure of pearlite for the transverse direction of the plate steel. This microcrack did not cross the width of the land of pearlite. This microcrack was taken in a region of about $50\mu m$ from the notch root. Examples of micrographs taken from the surviving notch at a test temperature of –60ºC in the rolling direction of the plate steel are shown in figures 3.67 and 3.68.

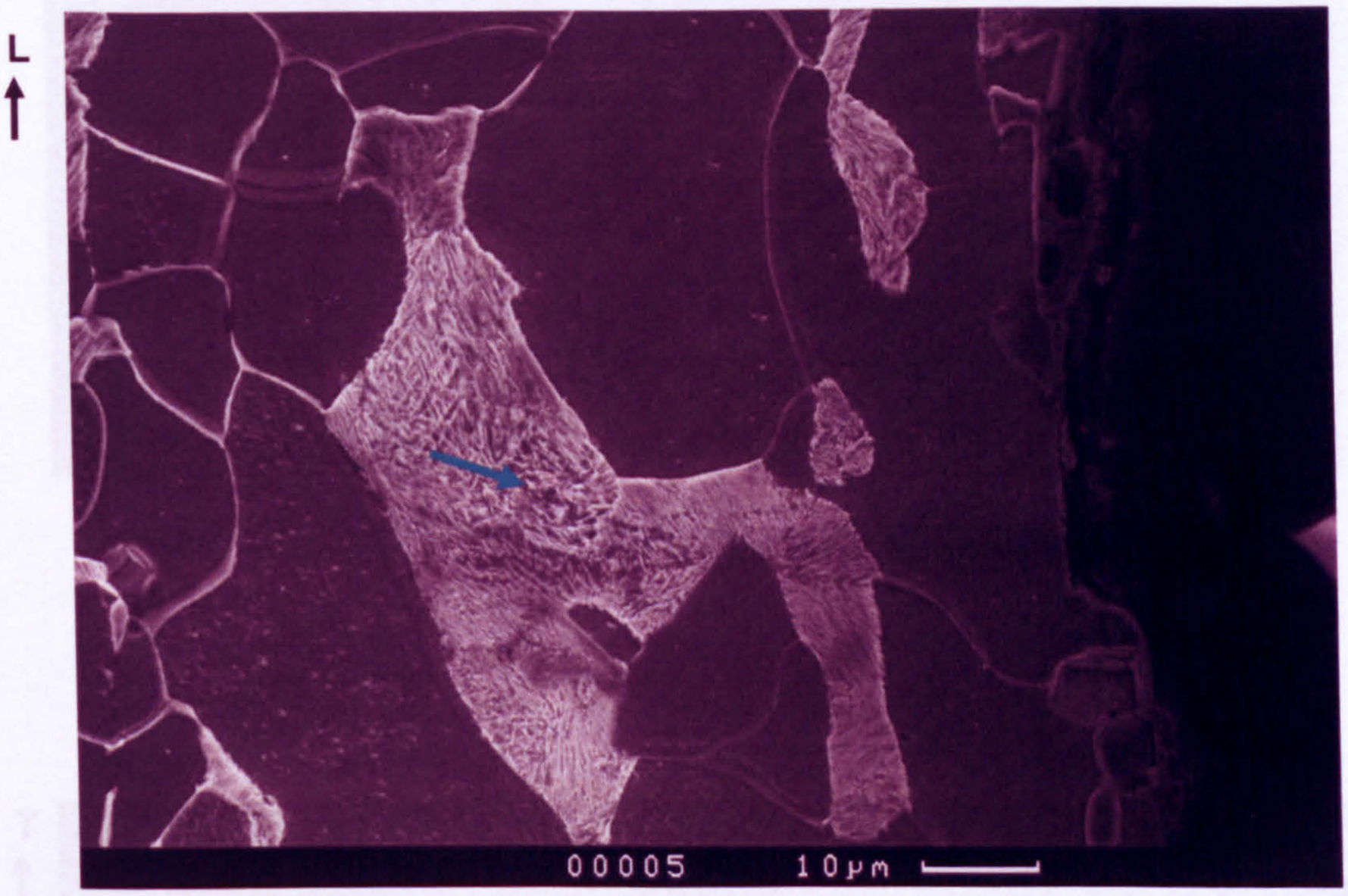

Figure 3.67 – Micrograph taken at $2500X$ from slice 3 in RD at –60ºC.

Micrograph 3.68 shows a region in the centre of a land of pearlite where separation of the lamellar microstructure of pearlite is taking place, consequently microcracks were developed. In this micrograph the initiation occurred at 3 grains from the notch root.

A close view of micrograph 3.67 gives better visualization of this process. This is shown in micrograph 3.68 where the blue arrows show points of initiation of microcracks. Microcracks with a critical size may run and join the others to create a microcrack inside the pearlite microstructure.

Figures 3.69 to 3.76 correspond to micrographs taken from the surviving notch at a test temperature of –60ºC in the transverse direction of the plate steel. These figures show that only two micromechanics for the development of microcracks were found, they are cracking in the lamellar pearlite microstructure and in the boundary of the pearlite microstructure.

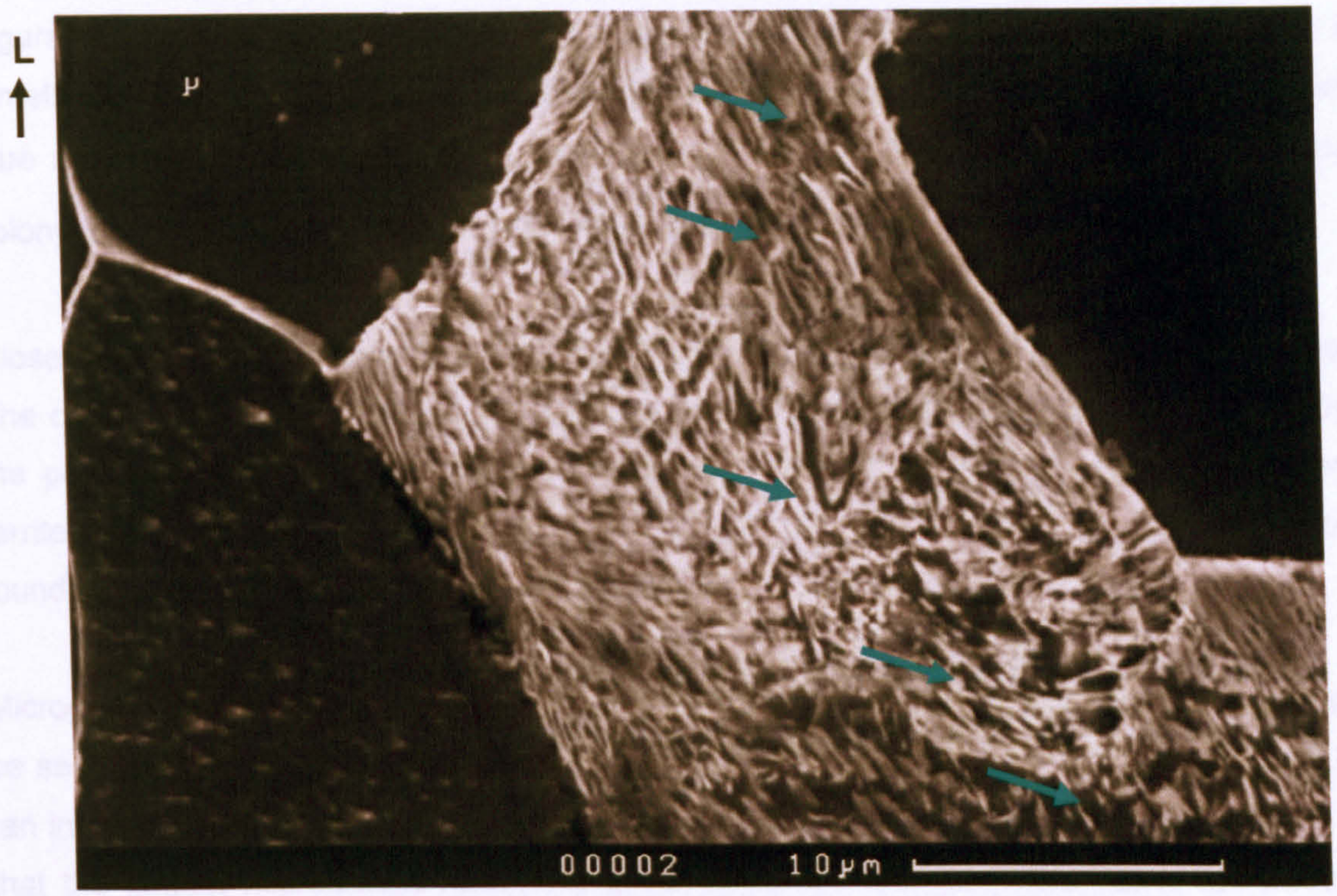

Figure 3.68 – Micrograph taken at $3500X$ from slice 3 in RD at –60ºC.

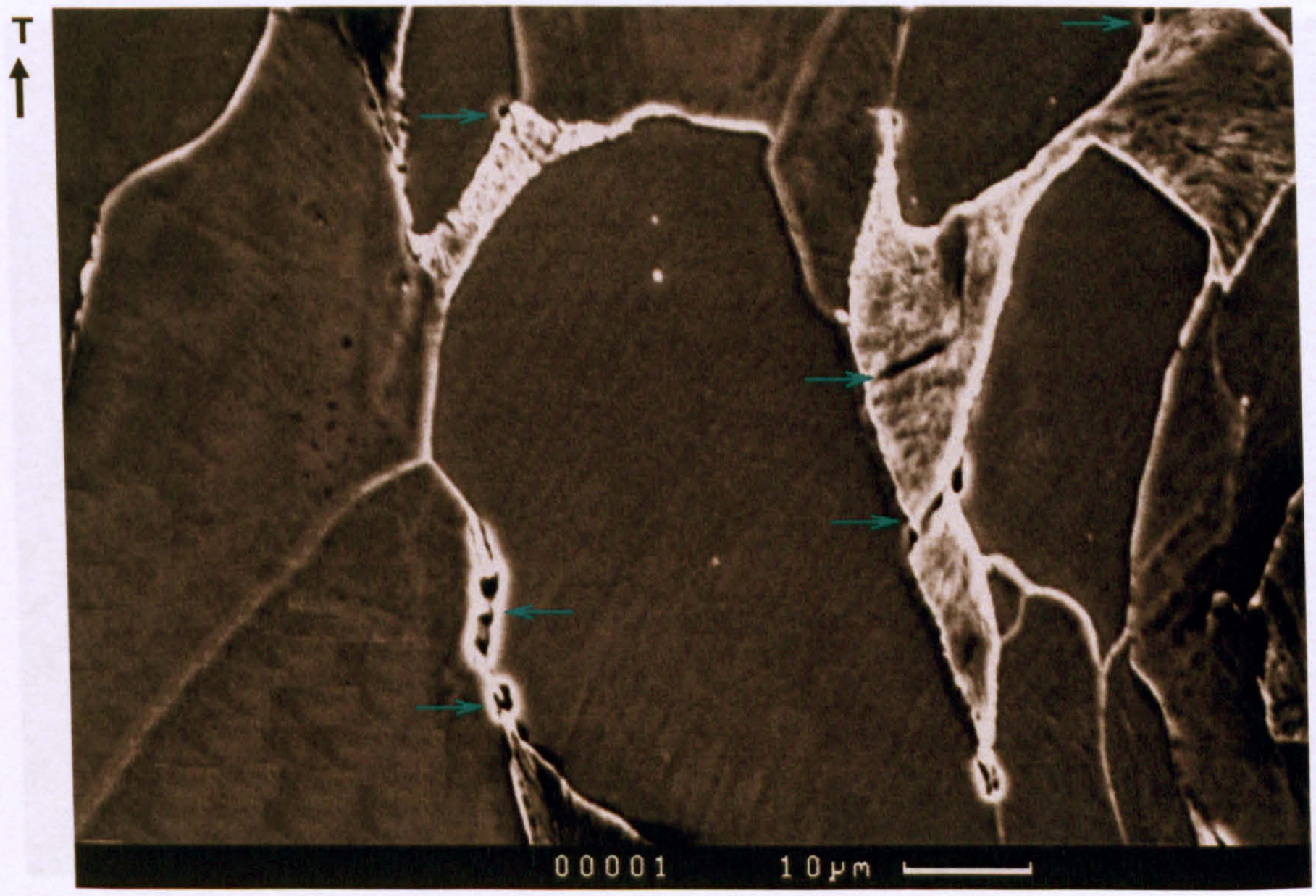

Figure 3.69 – Micrograph taken at $2500X$ from slice 2 in TD at –60ºC.

Figure 3.70 clearly shows the two micromechanisms for cleavage fracture nucleation in the lamellar pearlite and in the pearlite boundary. In this image, the microcracks are marked with blue arrows. In this particular slice, a microcrack of about $210\mu m$ was found in a pearlite colony, the distance of the tip of this microcrack to the notch root was $184\mu m$.

Close examinations revealed that this crack nucleated in the lamellar microstructure of pearlite. The crack grew through the land of pearlite, reached the pearlite boundary and grew through the pearlite–ferrite grain boundary. Once the tip reached an apparently highly mis–oriented ferrite grain (as the one showed in figure 3.70) the crack was arrested. More microcracks were found closer to the notch root as those marked by blue arrows.

Micrograph 3.71 shows the origin of the microcrack of figure 3.70. From these two images it can be seen that the microcrack was nucleated in the point marked by the arrow in figure 3.71 and ran in both directions, to the notch root and to the opposite side. This microcrack clearly shows that the largest microcracks nucleated by lands of pearlite, the microcracks ran through the pearlite microstructure. Figure 3.72 shows a close view inside the microcrack where a microcrack was arrested by a highly mis–oriented grain. In this figure MnS particles were found inside the microcrack, the particle is marked by a blue arrow.

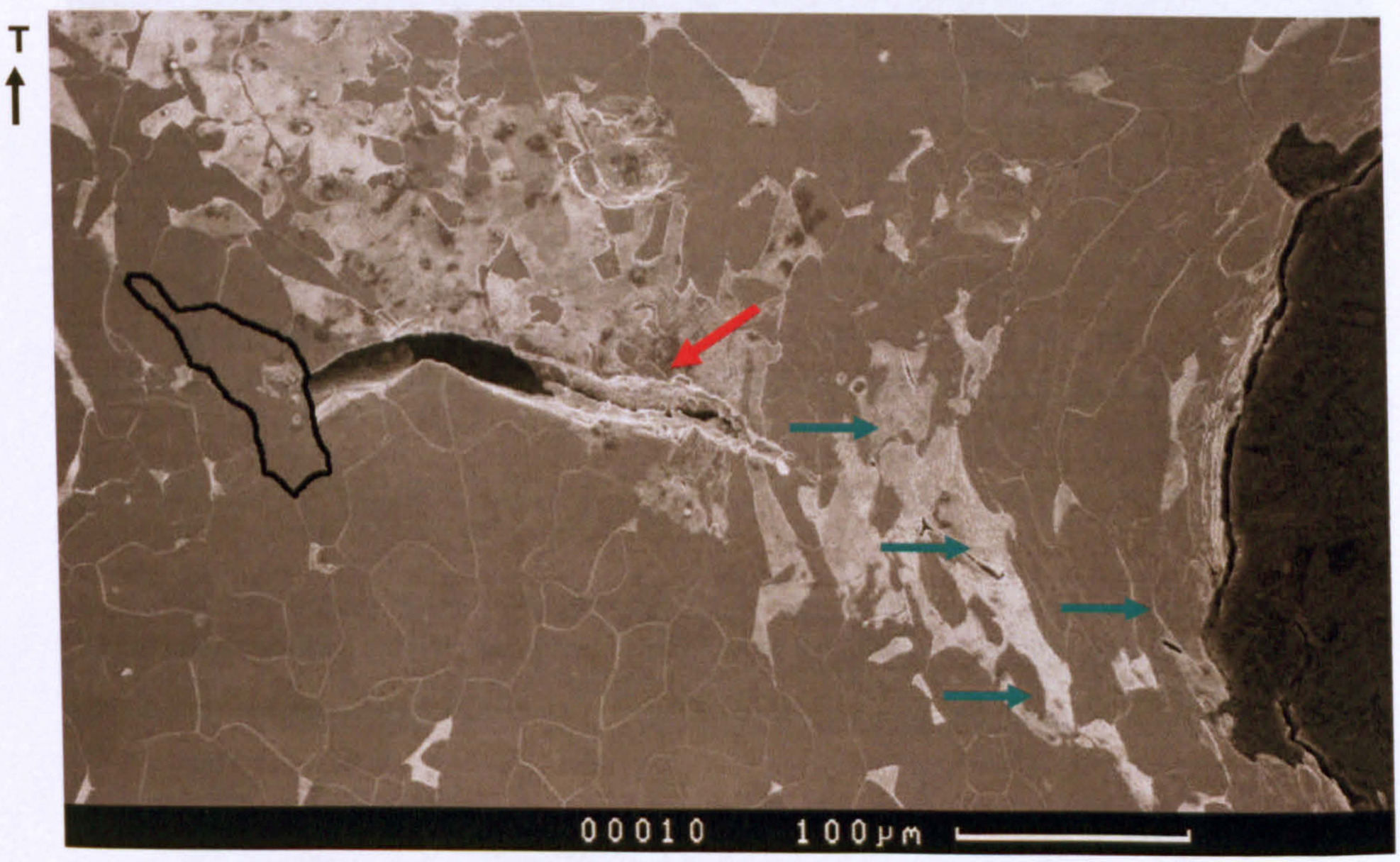

Figure 3.70 – Micrograph taken at $350X$ from slice 3 in TD at –60°C.

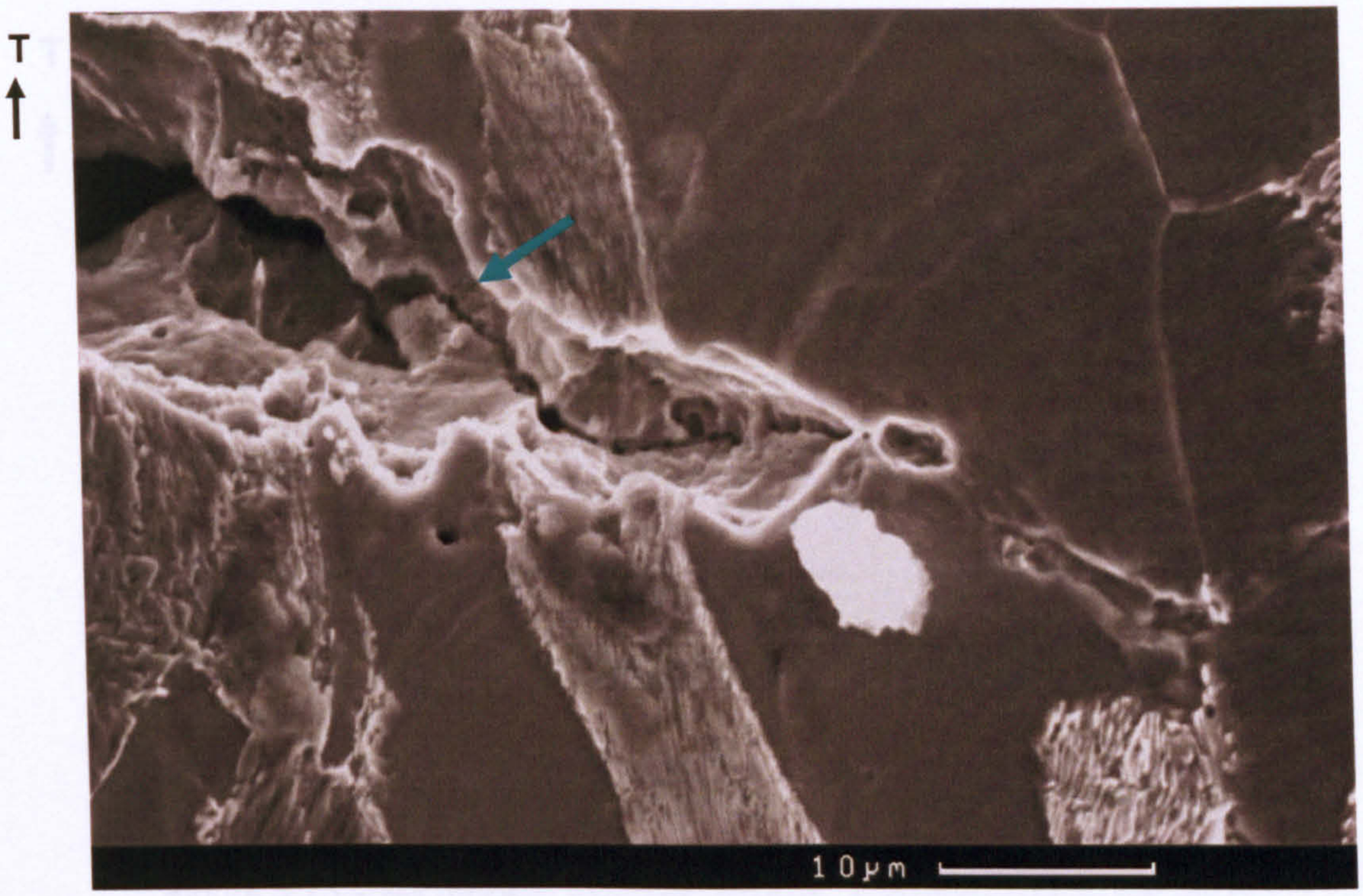

Figure 3.71 – Micrograph taken at $3500X$ from the origin of the crack of figure 5.27 in TD at –60°.

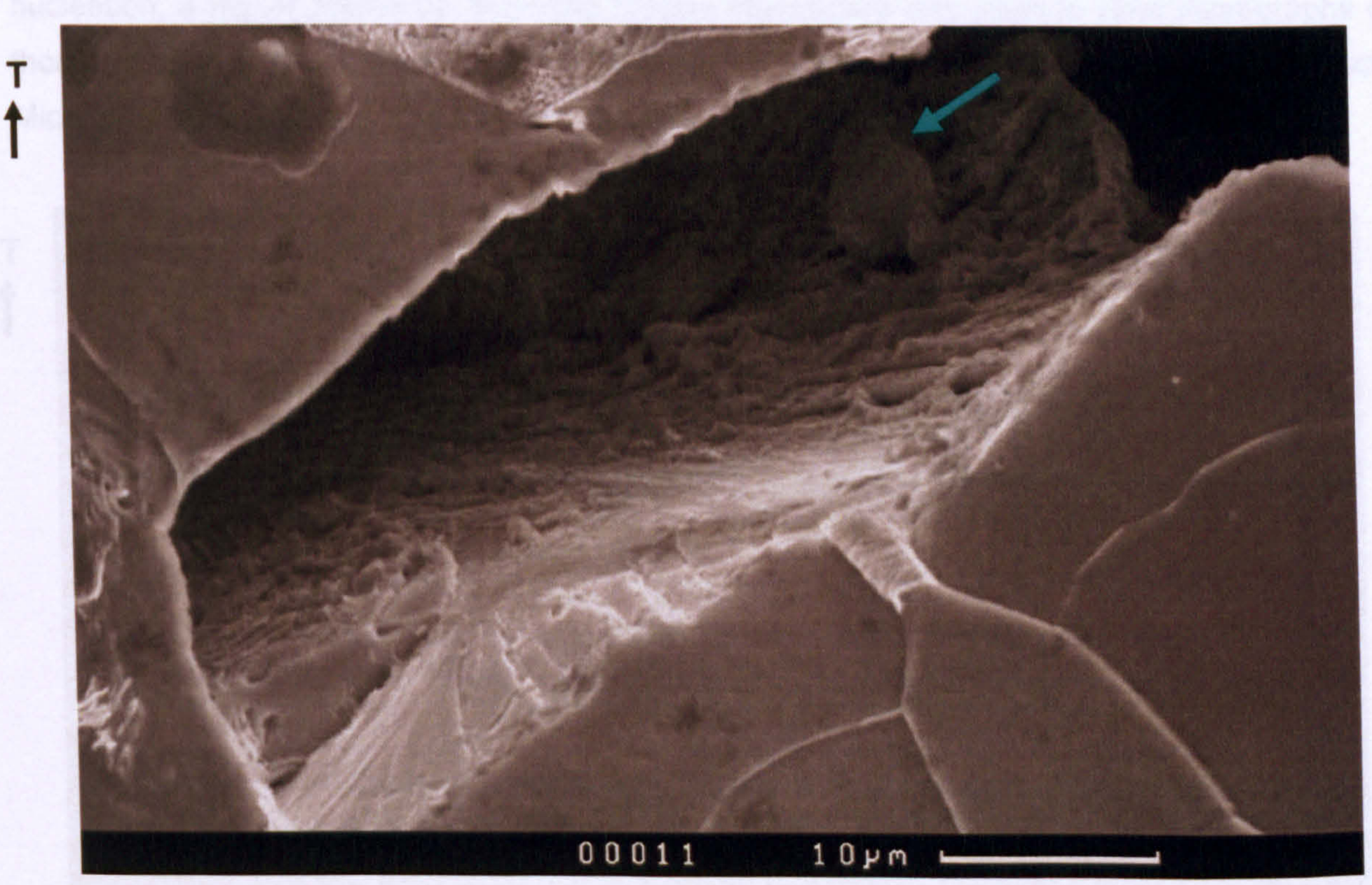

Figure 3.72 – Close view of the crack of figure 3.70 taken at $3500X$ in TD at –60°C.

Micrograph 3.73 shows particles inside the microcrack nucleated by the pearlite microstructure, the microcrack ran only in the land of pearlite and did not run through the ferrite grains.

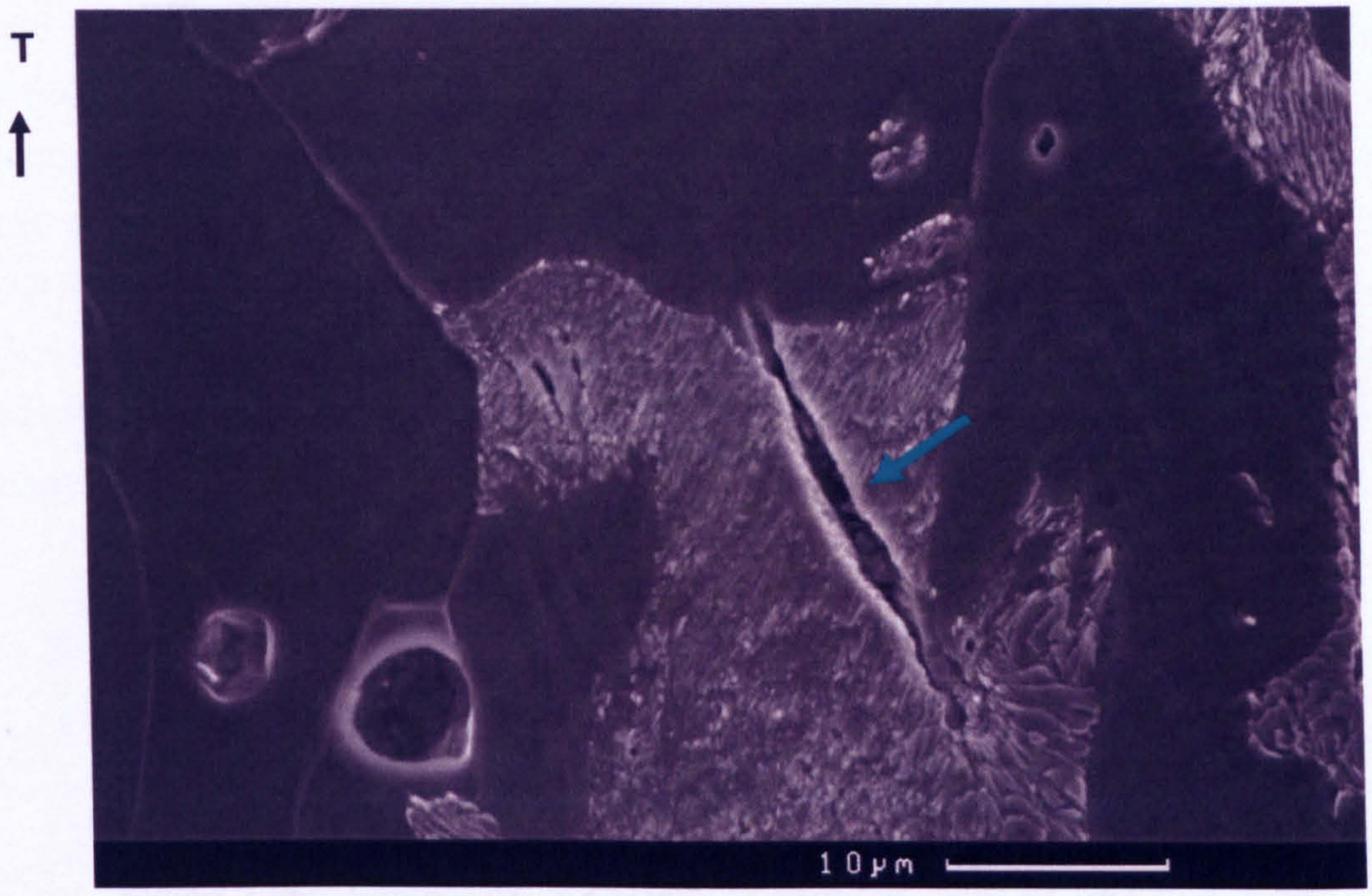

Figure 3.73 – Micrograph taken at $3500X$ from slice 3 in TD at –60ºC.

In order to have a better visualization of the particles responsible for cleavage fracture nucleation, a higher resolution Scanning Electro Microscope was used to take micrographs of those particles. Figure 3.74 shows an example of broken particles nucleating a microcrack. Micrographs with higher magnification are shown in figures 3.75 and 3.76.

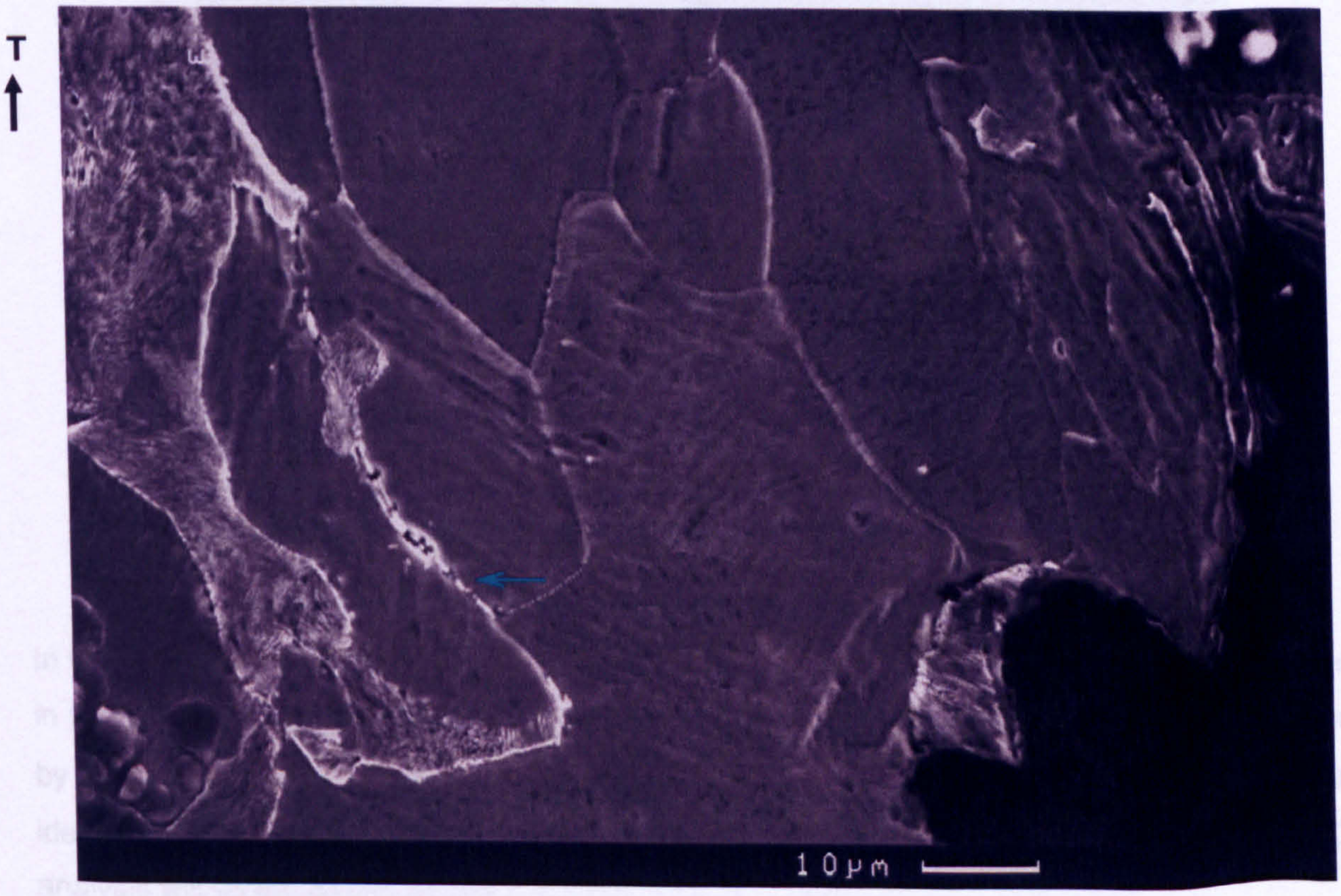

Figure 3.74 – Micrograph taken at $3000X$ from slice 3 in TD at –60ºC.

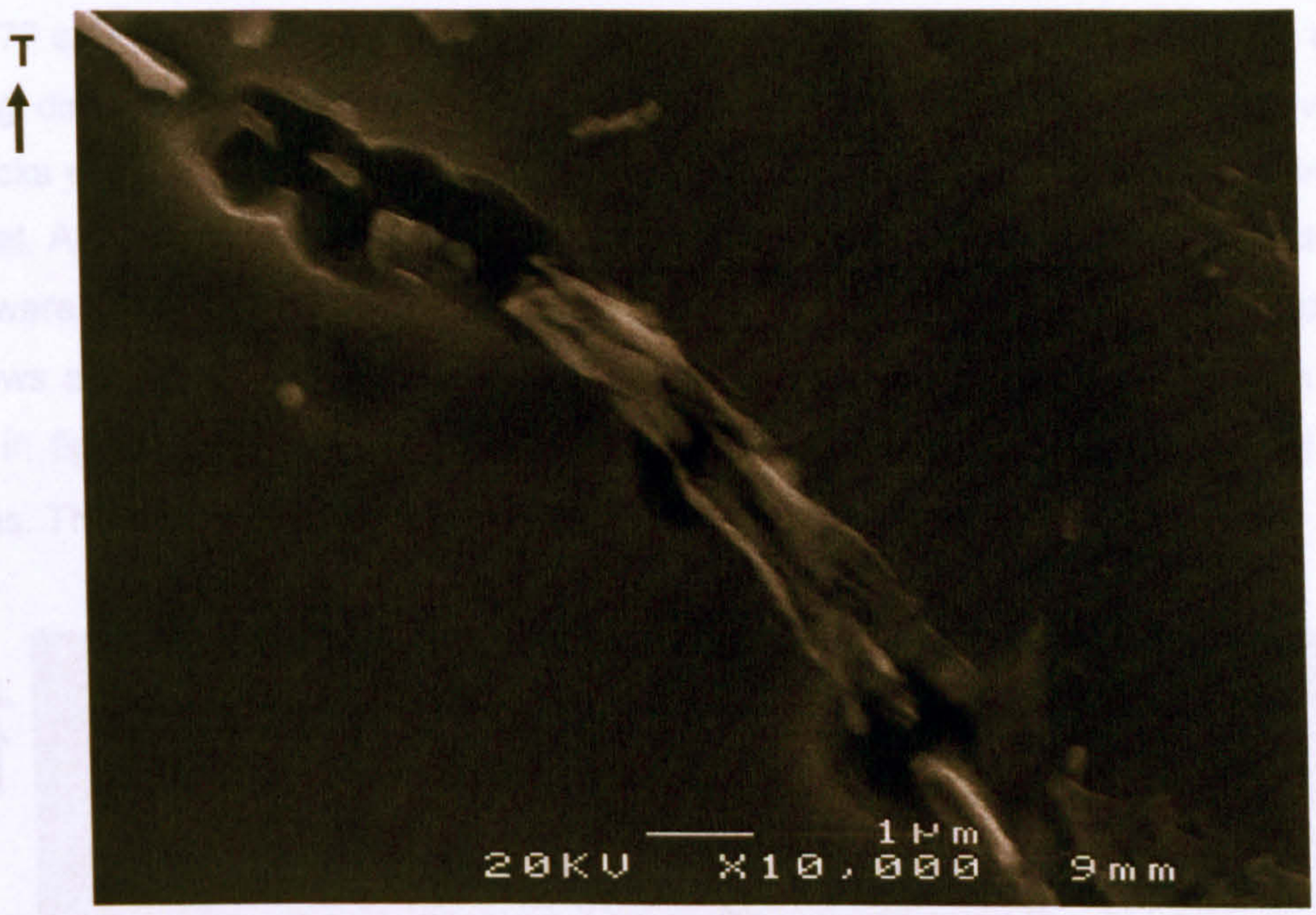

Figure 3.75 – Close view of figure 5.32 taken at $10000X$ in TD at –60ºC.

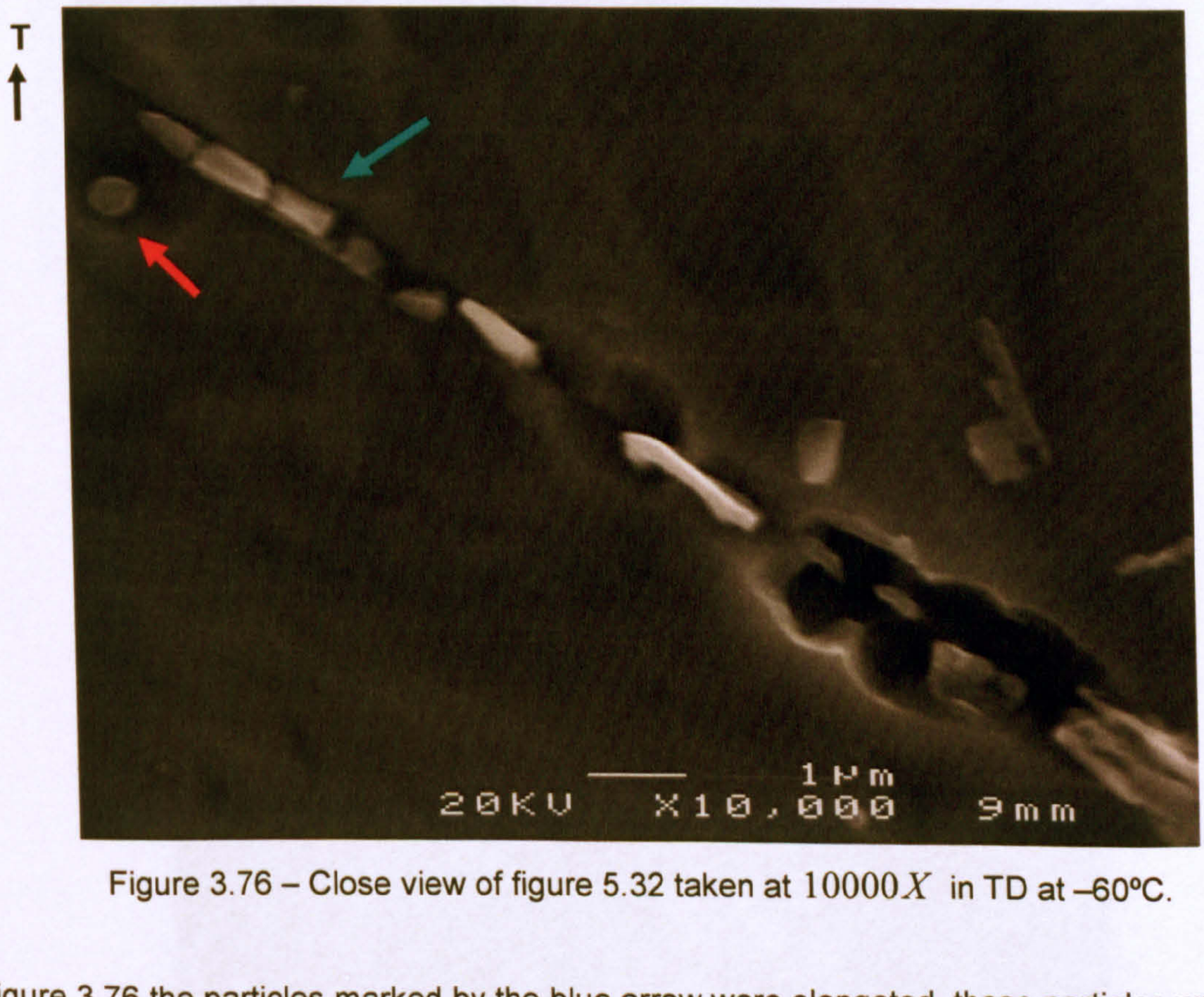

Figure 3.76 – Close view of figure 5.32 taken at $10000X$ in TD at –60ºC.

In figure 3.76 the particles marked by the blue arrow were elongated, these particles were found in the pearlite and ferrite grains boundary as clearly shown in figure 3.75. The particle marked by the red arrow is characteristic of MnS particles (section 3.6.5). But in order to clearly identify the chemical composition of those particles, an EDS analysis was done, the EDS analysis will be explained in section 3.6.5.

Figure 3.77 shows a distribution of microcracks in front of the notch root of slice 2 at –196ºC in the rolling direction. For this test temperature the same mechanisms for the development of microcracks were observed as those in previous test temperatures for the rolling direction of the plate steel. At this test temperature, microcracks were found very far from the notch root. Some of them were found very close to the edge opposite the notch root (at about 8.45 mm). Figure 3.78 shows a close view of the region marked by the red arrow of figure 3.77. The microcracks showed in figure 3.78 were nucleated by a combination of ferrite boundary and ferrite grain inclusions. These microcracks are located at about 12 grains from the notch root.

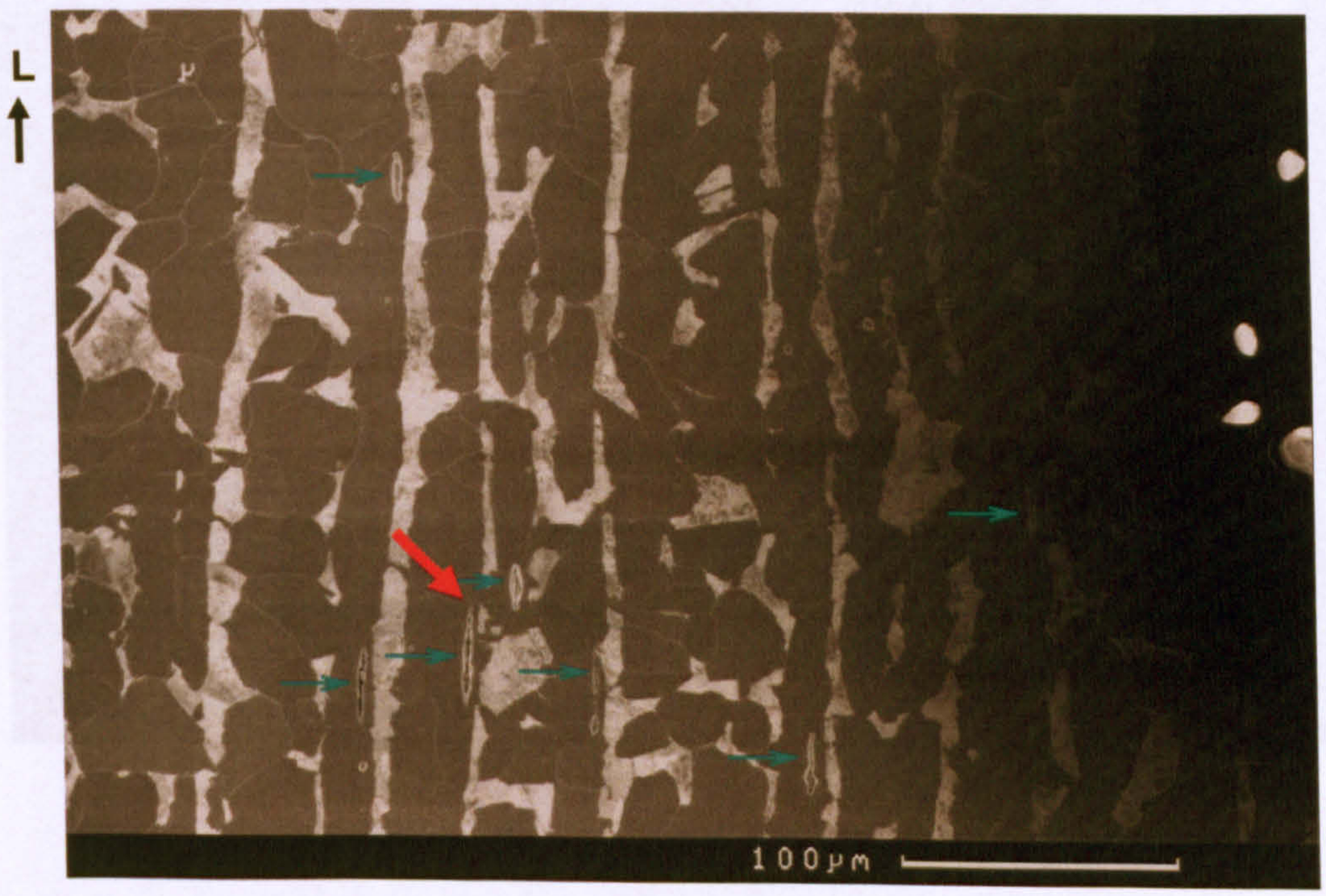

Figure 3.77 – Micrograph taken at 250X of slice 2 in RD at –196ºC).

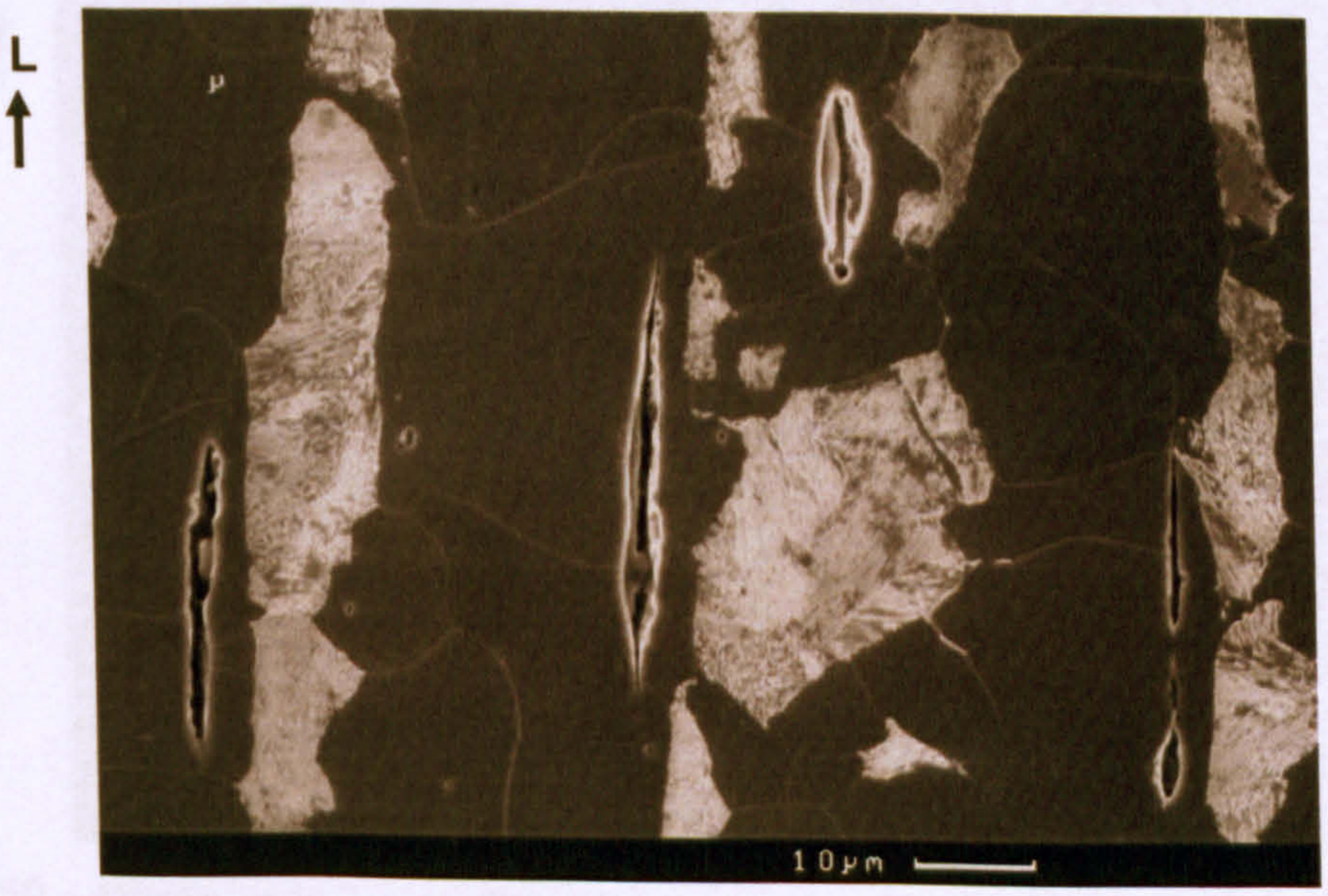

Figure 3.78 – Details of micrograph 5.34 taken at 2500X of slice 2 in RD at –196ºC.

The following micrograph (figure 3.79) was taken from slice number 5 at 200 μm from the notch root, the notch root of the following figures is oriented as that shown in figure 3.77. In this micrograph the lamellar pearlite cleavage micromechanism is marked by blue arrows and the pearlite boundary micromechanism is marked by the red arrow. Other examples of these two micromechanisms for cleavage fracture nucleation are those shown in micrograph 3.80.

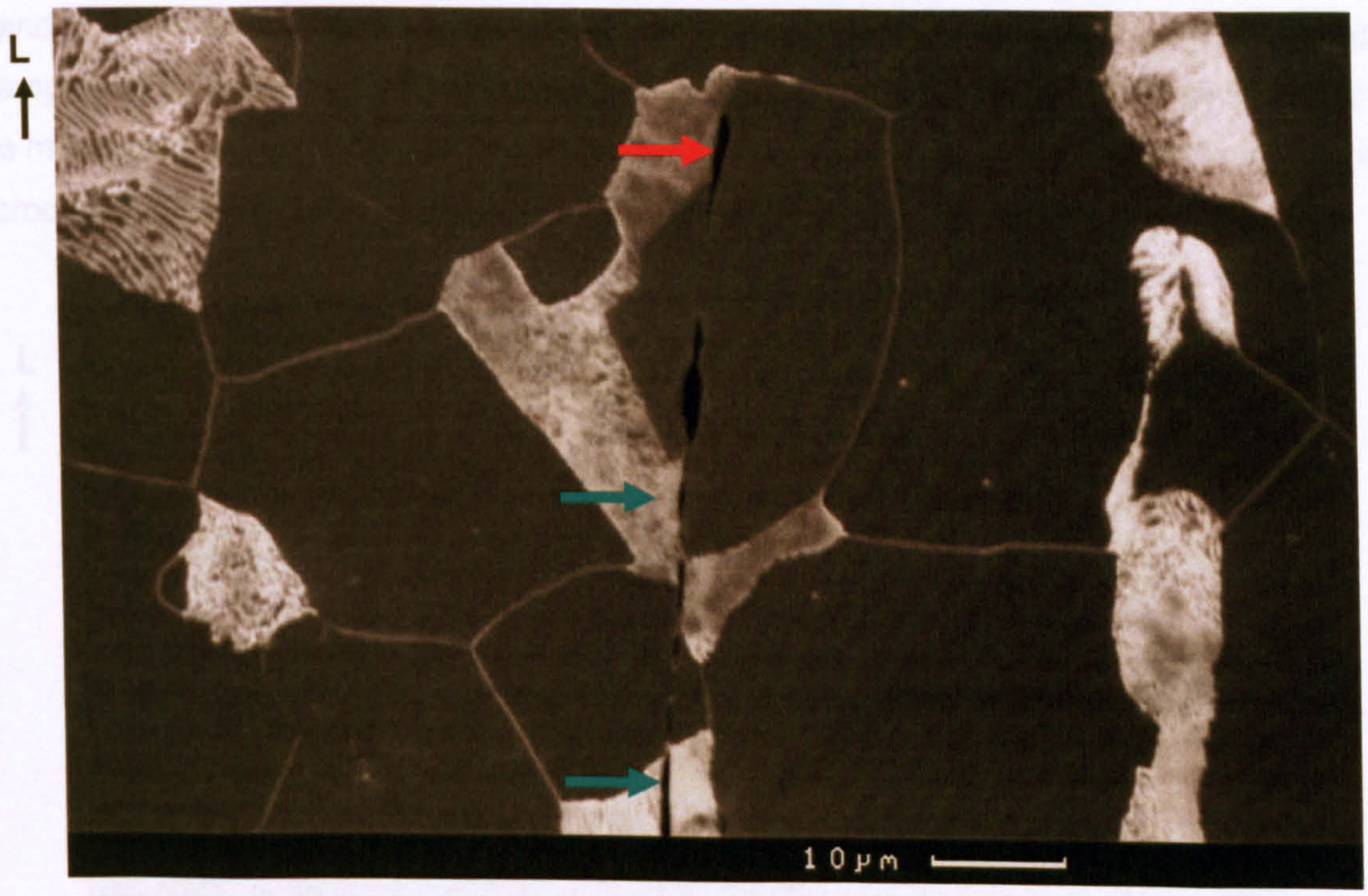

Figure 3.79 – Micrograph taken at 1200X of slice 5 in RD at –196°C.

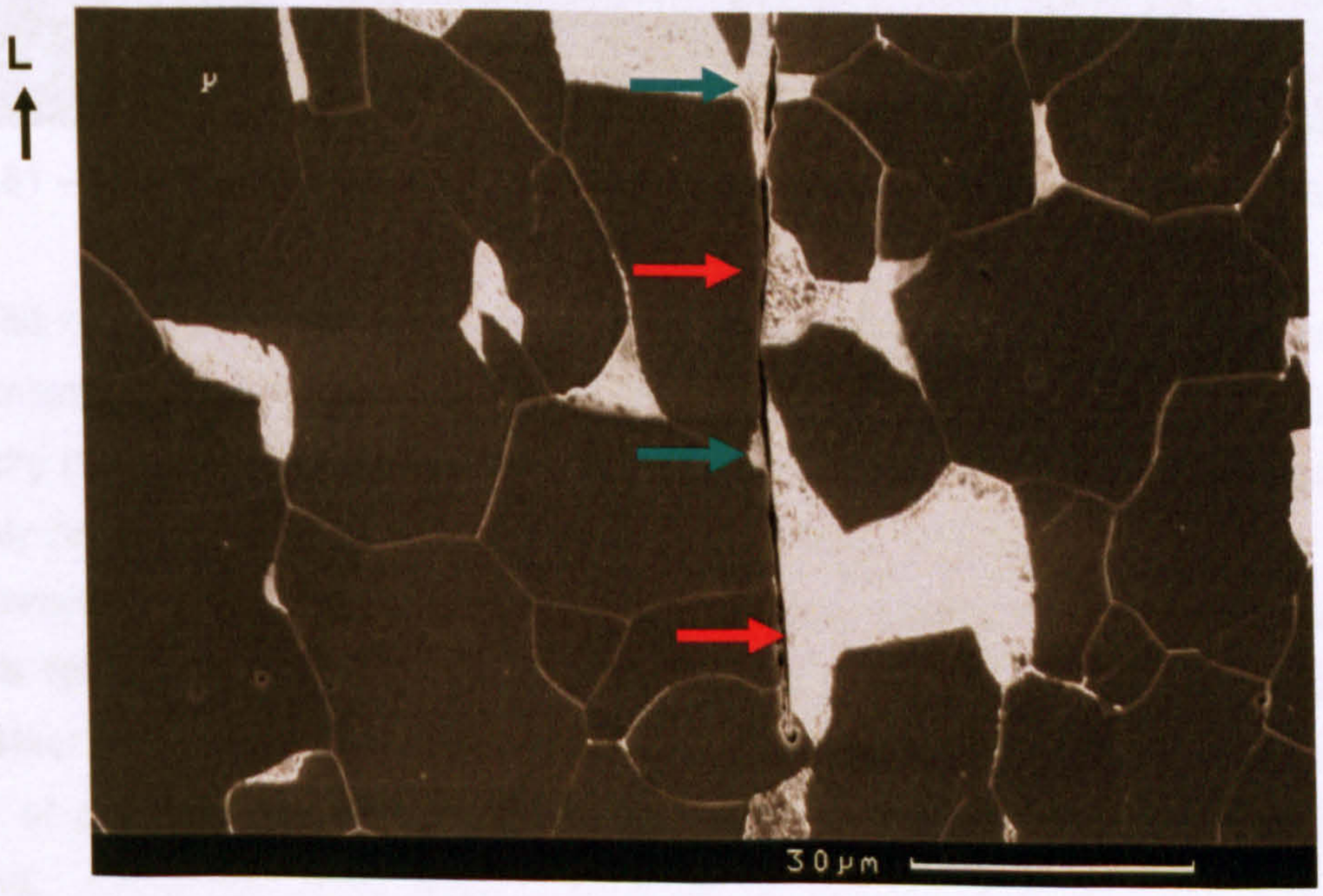

Figure 3.80 – Micrograph taken at 900X of slice 1, 150µm from the notch root in RD at –196°C.

Figure 3.80 show microcracks with two micromechanisms, the lamellar microstructure of pearlite and pearlite boundary. Both microcracks almost join to form a single microcrack, it can be seen that they run mainly through the boundary of both microstructures. Micrograph 3.81 was taken at 800 μm from the notch root. This distance represents more than 40 ferrite grain diameter. The two bigger microcracks run mainly through the boundary of ferrite grains, these microcracks are marked with blue arrows. The red arrow of figure 3.82 shows a microcrack nucleated inside a land of pearlite, the green arrows show the nucleation of microcracks inside ferrite grains. Examples of microcracks found very far from the notch root are shown in figures 3.82 and 3.83. The microcrack in figure 3.82 was found at 5.5 mm from the notch root, this figure shows clearly microcracks nucleated by the lamellar pearlite microstructure and ferrite grains.

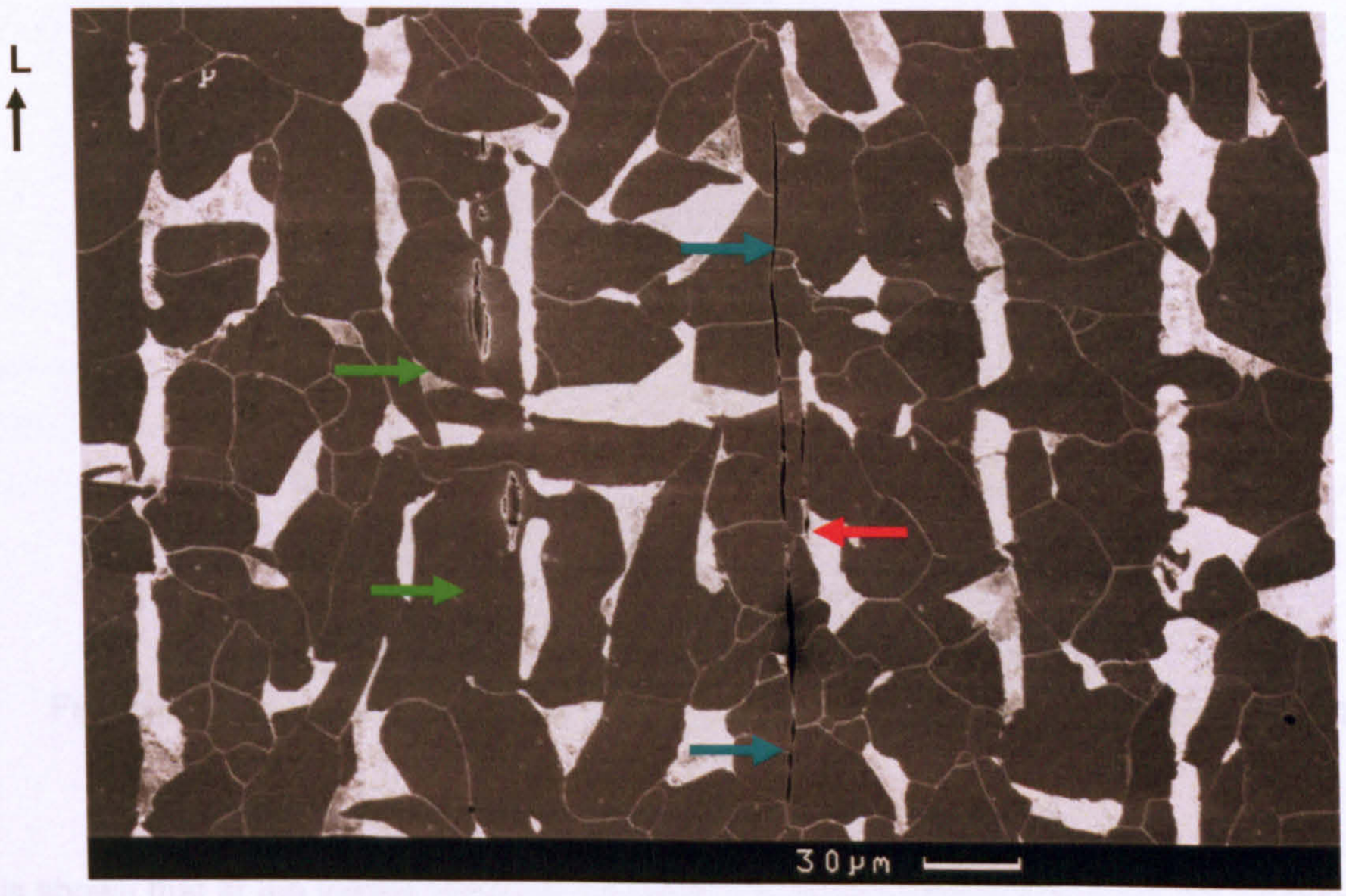

Figure 3.81 – Micrograph taken at 300X, of slice 5, 800µm from the notch root in RD at –196ºC.

Figure 3.83 shows an example of a microcrack found at 6.5 mm from the notch root. From the last two micrographs we see that microcracks were found in a position very far from the notch root. Mudry (Mudry, 1987) proposed that microcracks are created as soon as plasticity begins, conversely no microcracks exist out of the plastic zone (notch root region). This criterion has been extensively used for many local approach models. Experimental results in a wide variety of models for cleavage fracture support this hypothesis (Wang and Chen, 1999), but in the present steel at –196ºC microcracks were found very far from the notch root. In order to identify the kind of particles that nucleated the microcracks of this section, an EDS analysis was performed.

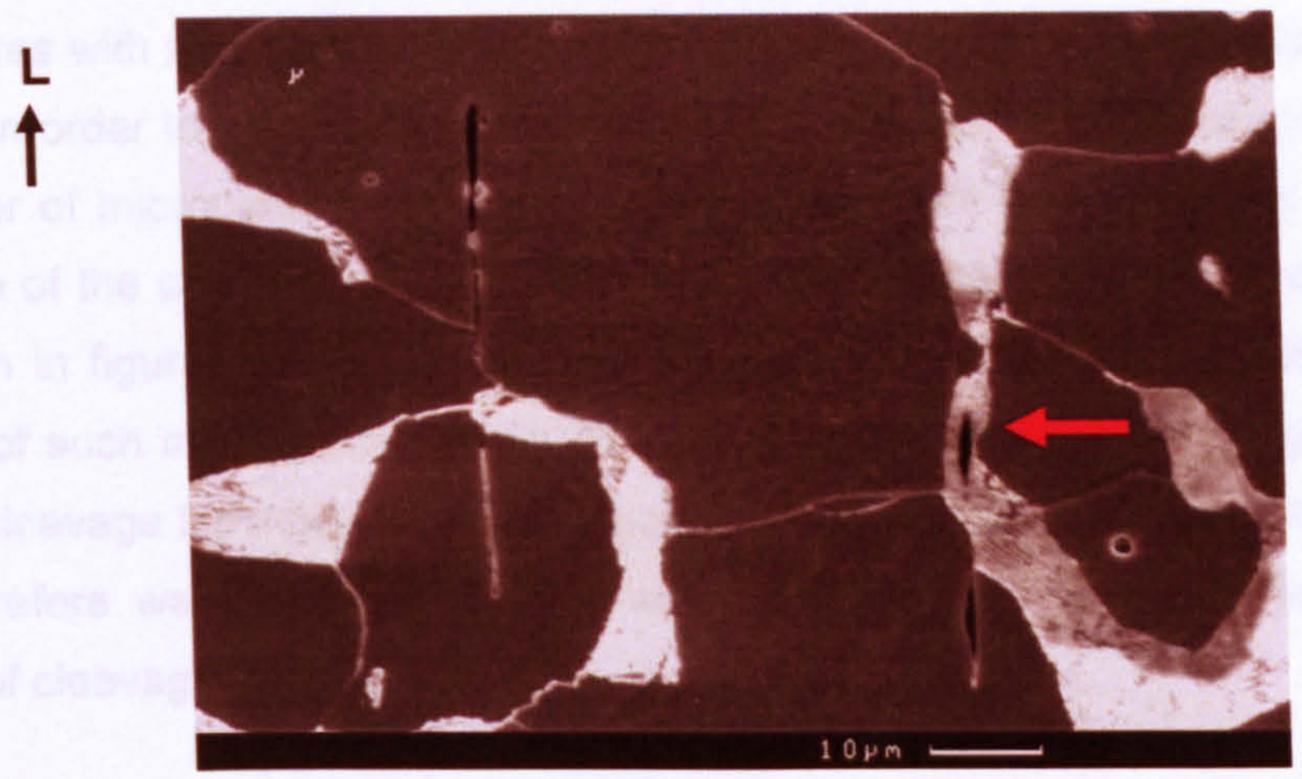

Figure 3.82 – Micrograph taken at 1300X of slice 5, 5.5 mm from the notch root in RD at –196°C.

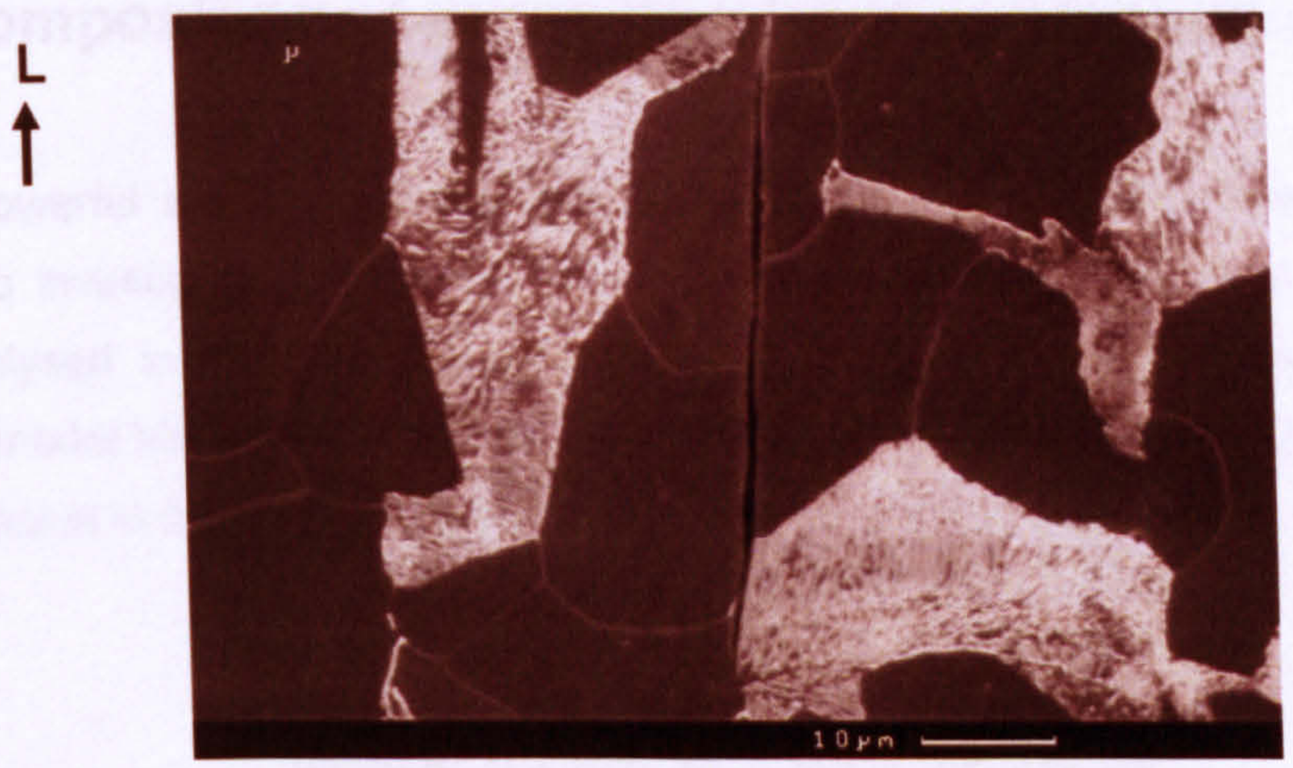

Figure 3.83 – Micrograph taken at 1300X of slice 2, 6.5 mm from the notch root in RD at –196°C.

It is shown that at the lowest temperature (–196°C), most of the microcracks are oriented in the direction of the maximum principal stress σ_1, therefore at very low temperature where all the conditions for cleavage fracture are met, the microcracks will be oriented in the direction of σ_1 as discussed in section 2.3.

The present section showed that the analysis of the microstructures nucleating cleavage was done on a large number of microcracks for each test temperature. Ideally the identification of the microstructures initiating cleavage is done on the examination of the fracture surfaces of toughness specimens tested at very low temperatures by tracing back the river patterns created on the cleavage facets. But due to the nature of the microstructures of the present steel, they were not clearly identified with the typical method. From the examples of lands of cleavage of figures 3.26, 3.27, 3.28, 3.102, 3.103, 5.19, 5.20, it can be seen that there was no clear evidence of the microstructures initiating cleavage. Therefore it was proposed to identify such

microstructures with metallographic analysis of the surviving notches of four point double–notch bend tests. In order to validate this method, we formulated the following hypothesis: due to the large number of microcracks analyzed in each direction of the plate steel (sections 3.6.6 and 3.6.7), some of the analyzed microstructures have truly nucleated microcracks, as for example those shown in figures 3.58, 3.73, 3.74, 3.75 and 3.76. If we calculate the mean size of the distribution of such microstructures we find that this value falls in the range of size of particles nucleating cleavage for mild steels reported in literature (the analysis has been done in section 5.8.6). Therefore we can conclude that we have identified the real microstructures for the nucleation of cleavage fracture.

3.6.5 EDS analysis for the identification of the chemical composition of microstructures nucleating cleavage.

EDS is a powerful tool for microanalysis of elemental constituents. The EDS analysis was performed to investigate the chemical constituent of the micro features nucleating cleavage fracture analysed in previous section. To perform the EDS analysis a Scanning Electron CAMSCAN model MK2 Microscope was used. The EDS analysis of the particles that nucleated fracture is shown in figures 3.84 to 3.91.

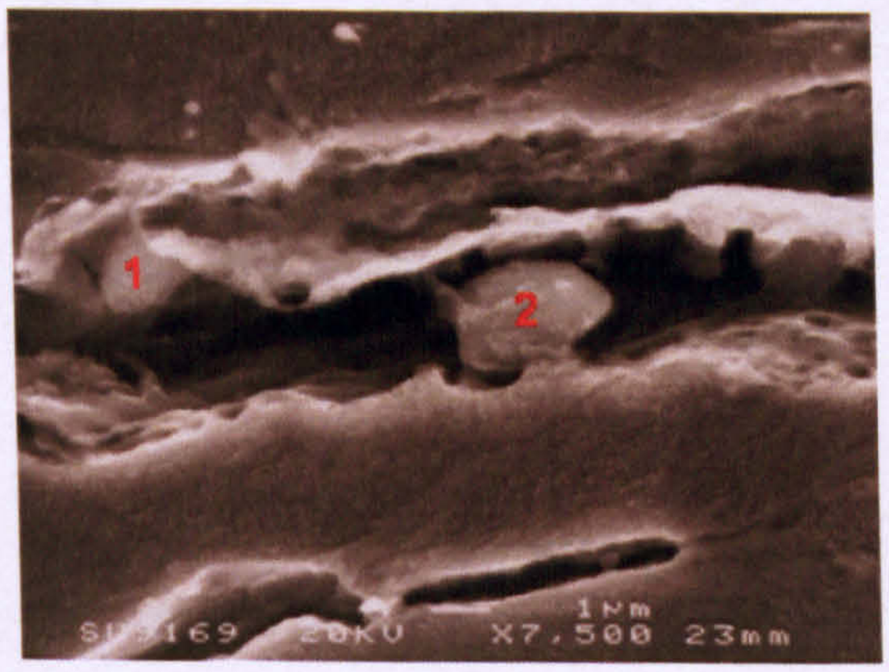

Figure 3.84 – EDS analysis of particles found in the ferrite–ferrite microstructure.

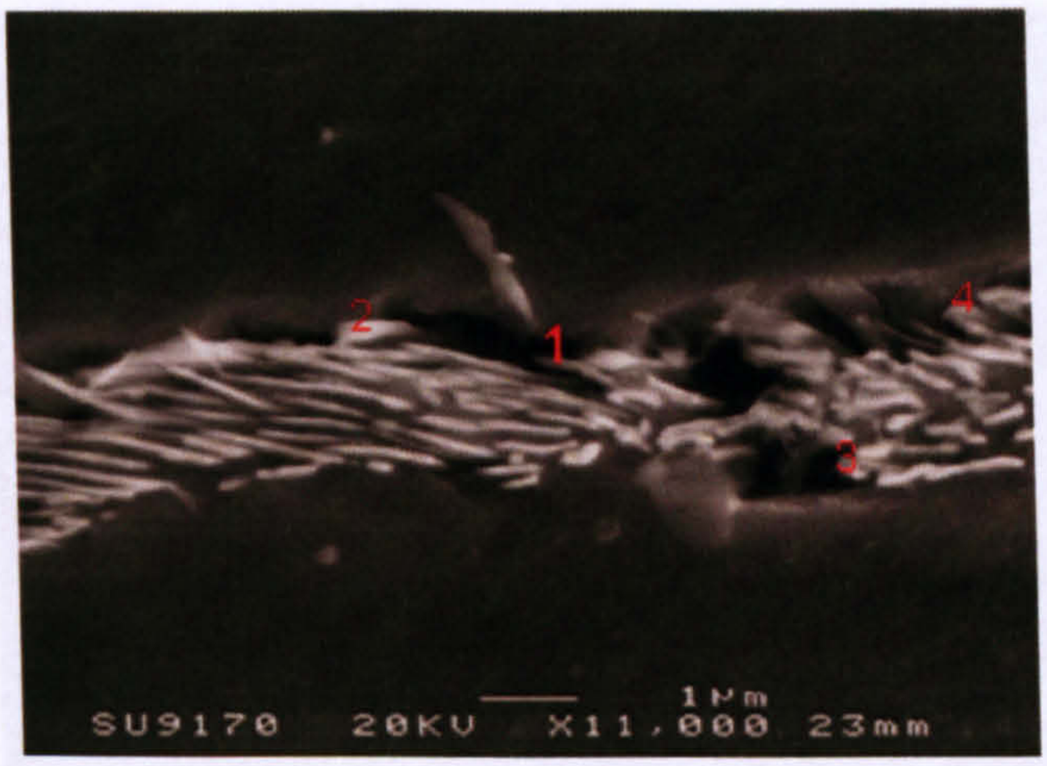

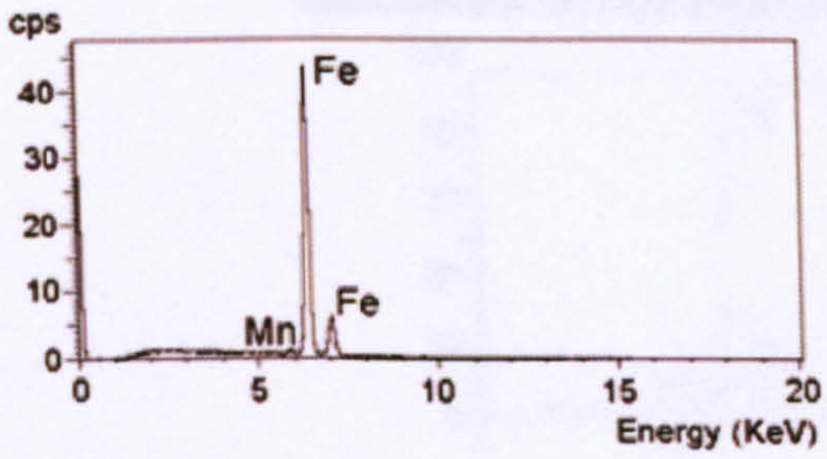

Particles 1 and 2

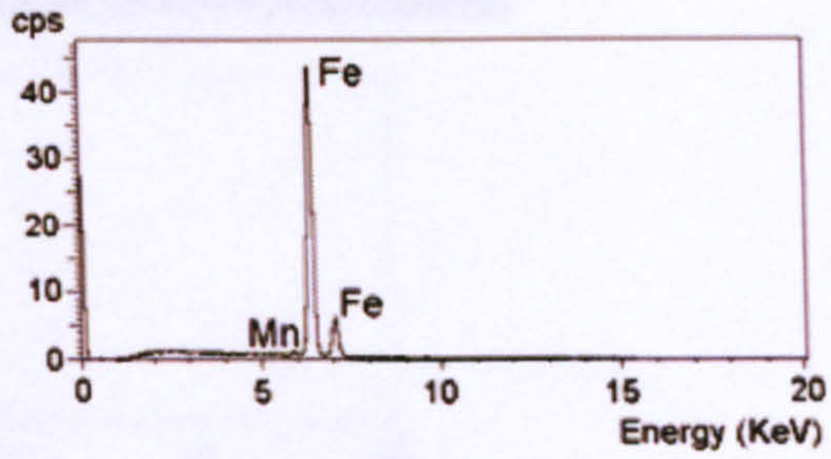

Particles 3 and 4

Figure 3.85 – EDS analysis of particles found in the lamellar pearlite microstructure.

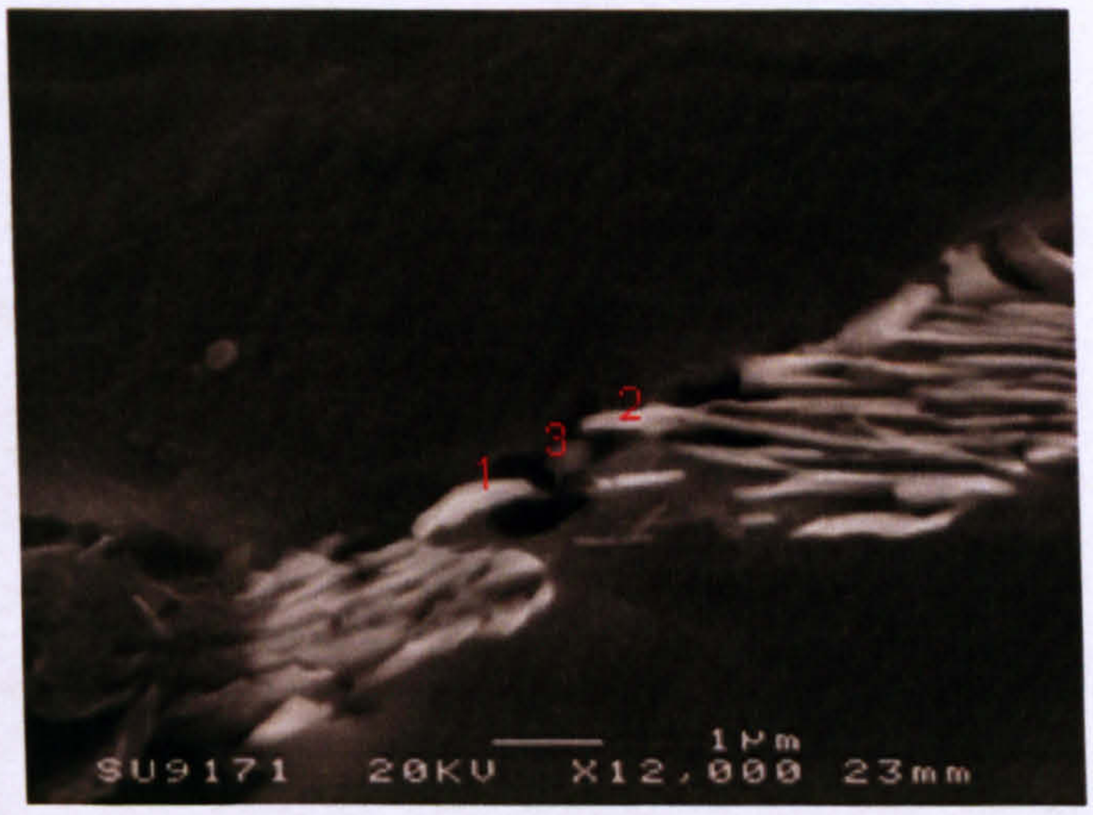

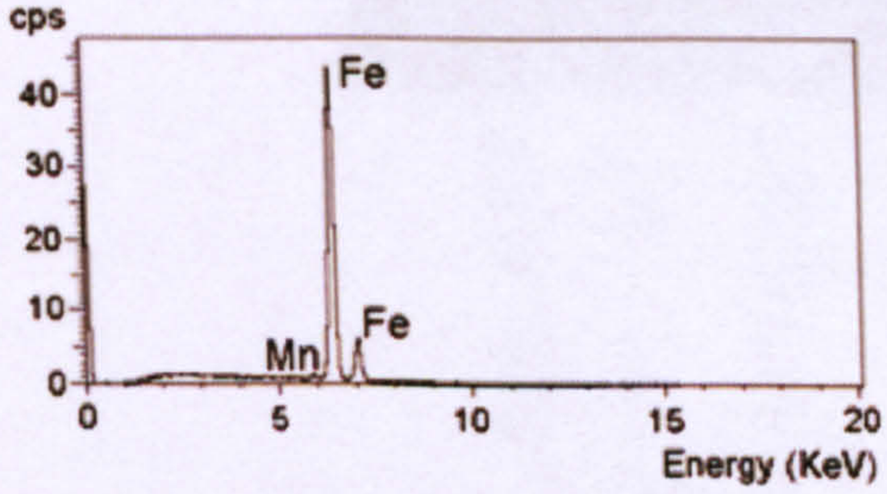

Particles 1 and 2

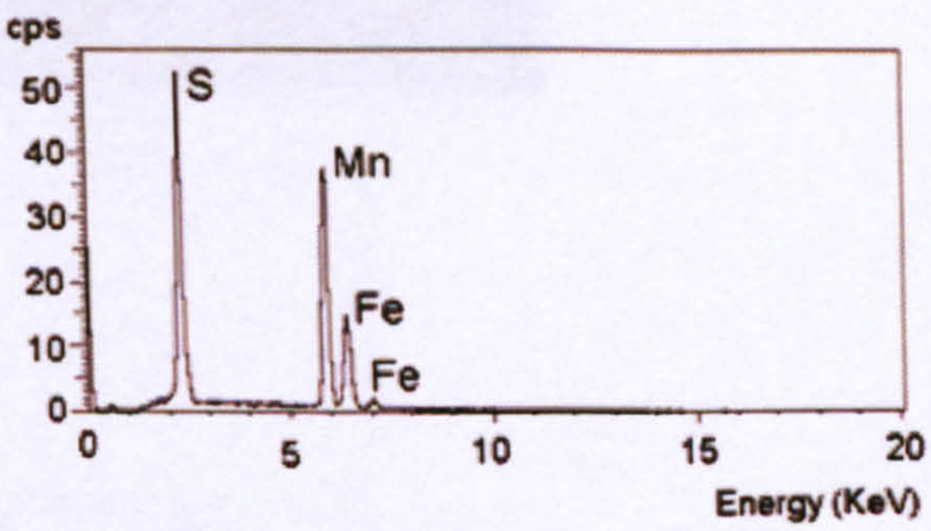

Particle 3

Figure 3.86 – EDS analysis of particles found in the lamellar pearlite microstructure.

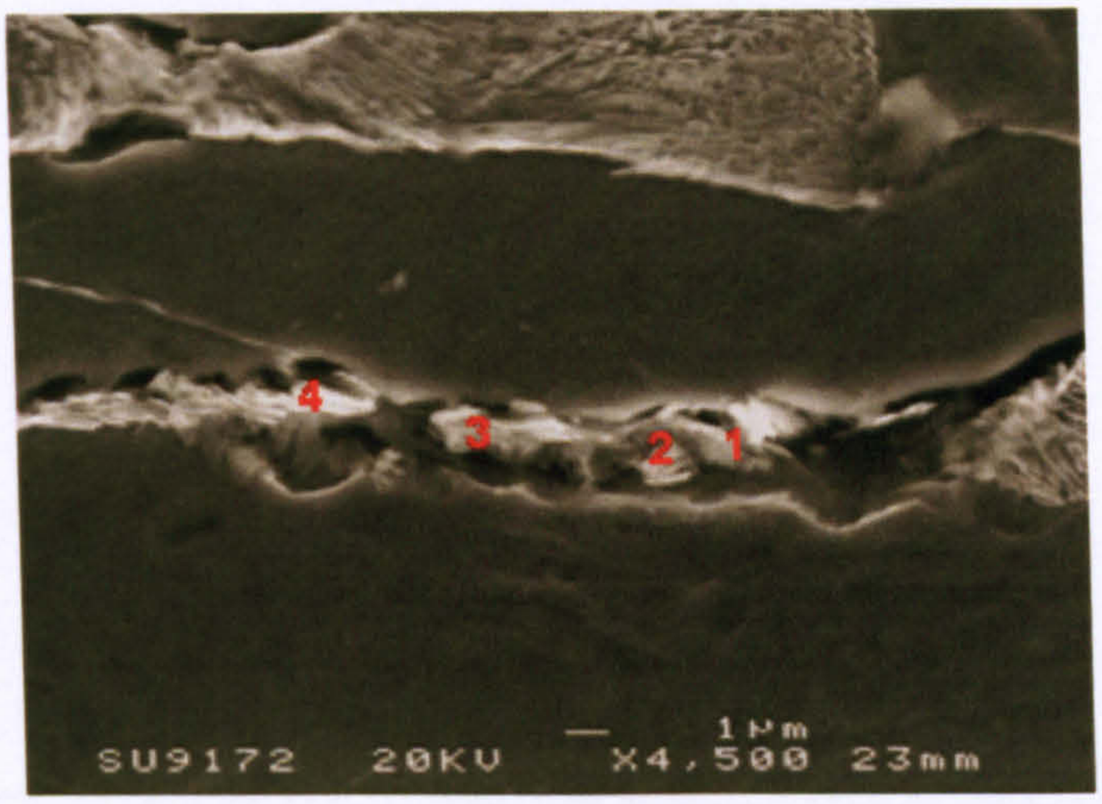

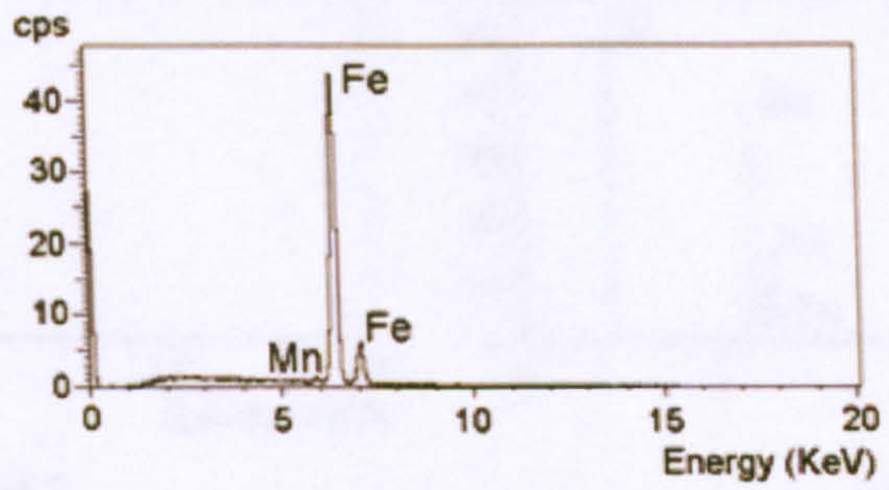

Particles 1, 2, 3 and 4

Figure 3.87 – EDS analysis of particles found in the lamellar pearlite microstructure.

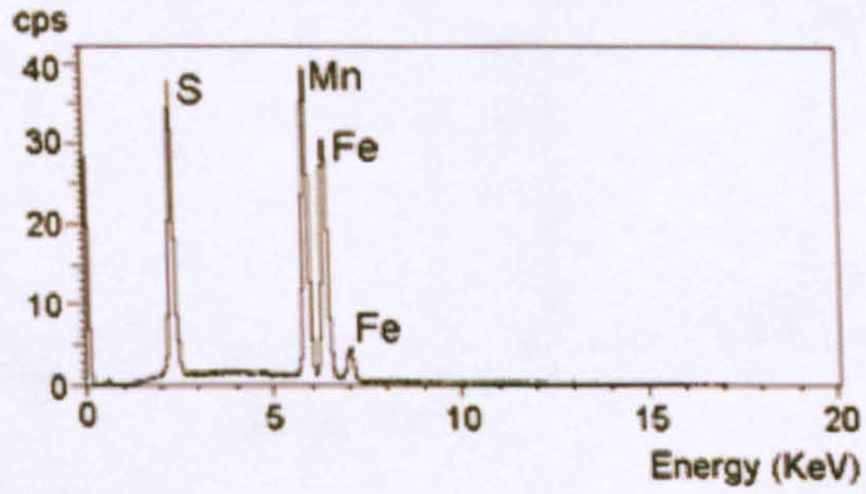

Particle 1

Figure 3.88 – EDS analysis of particles found in pearlite–ferrite boundary microstructure.

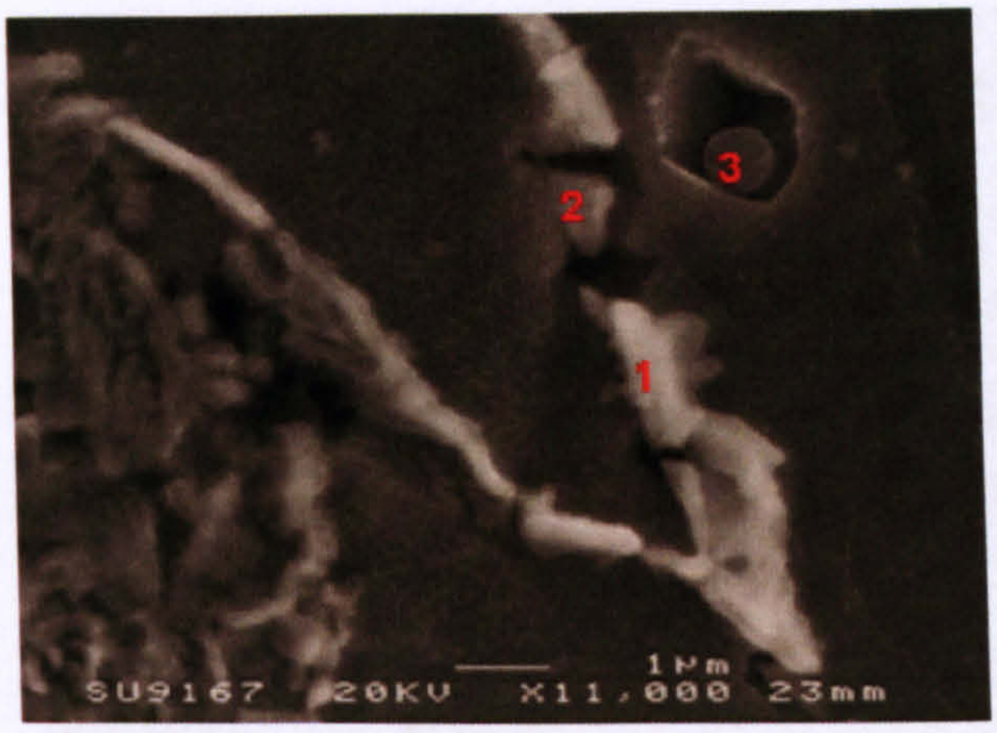

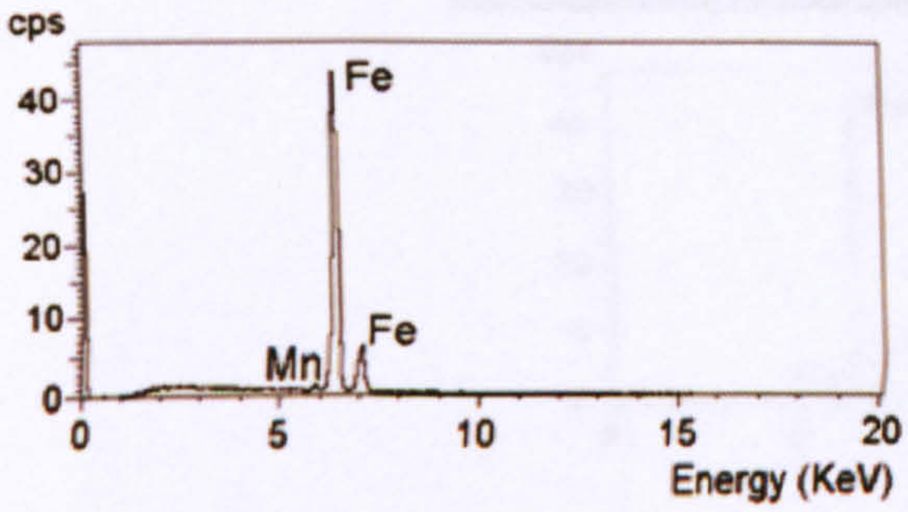

Particles 1 and 2

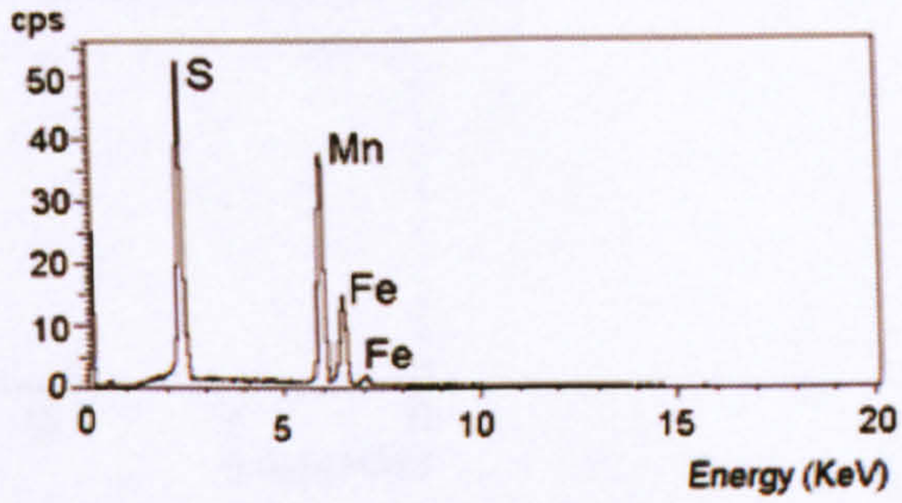

Particle 3

Figure 3.89 – EDS analysis of particles found in ferrite–ferrite (2), ferrite inclusions (3), lamellar microstructure of pearlite (1).

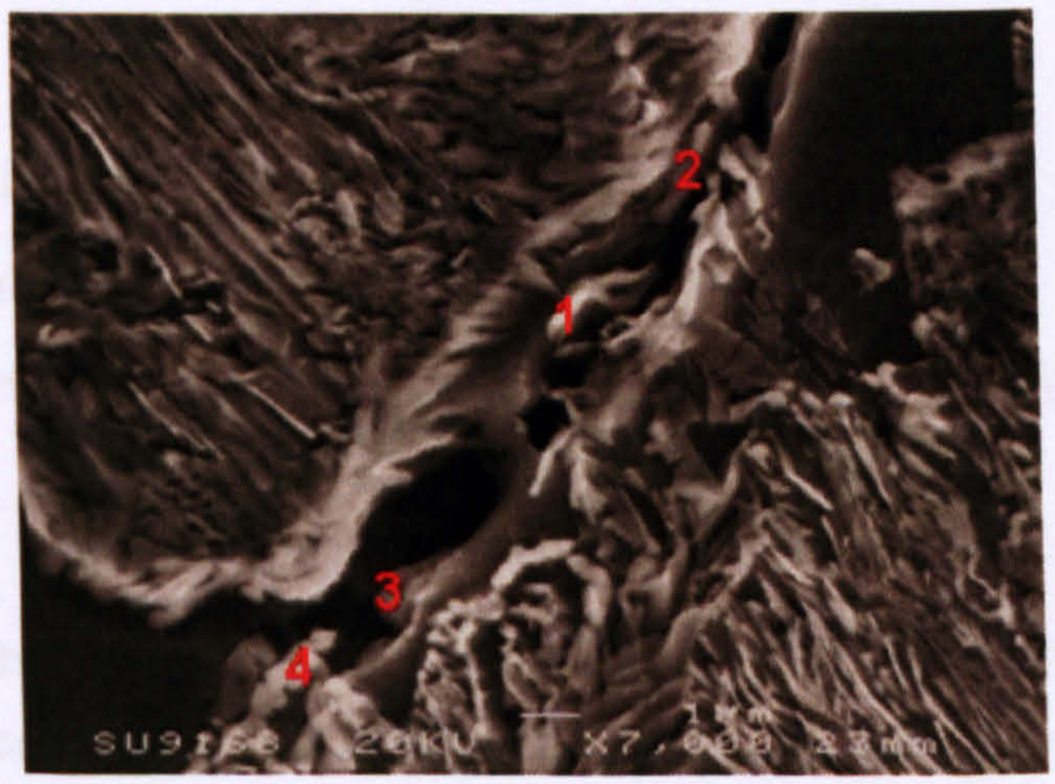

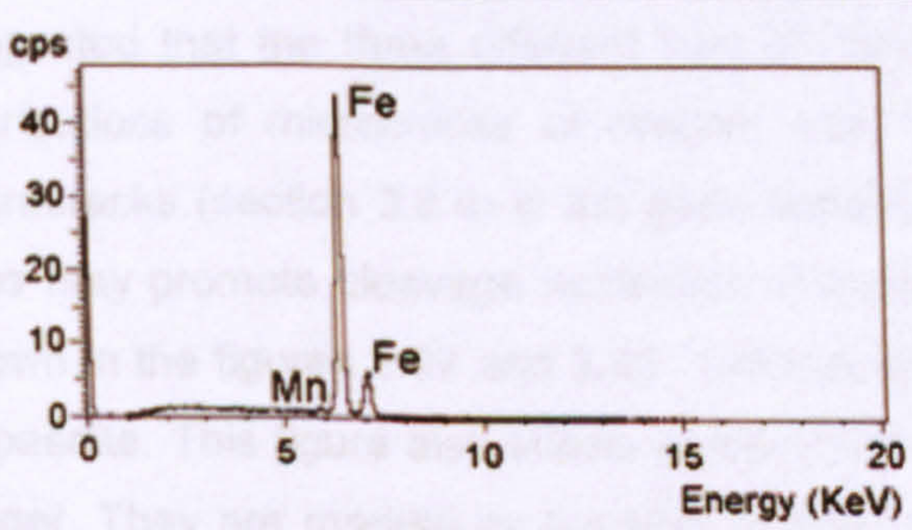

Particles 1 and 2

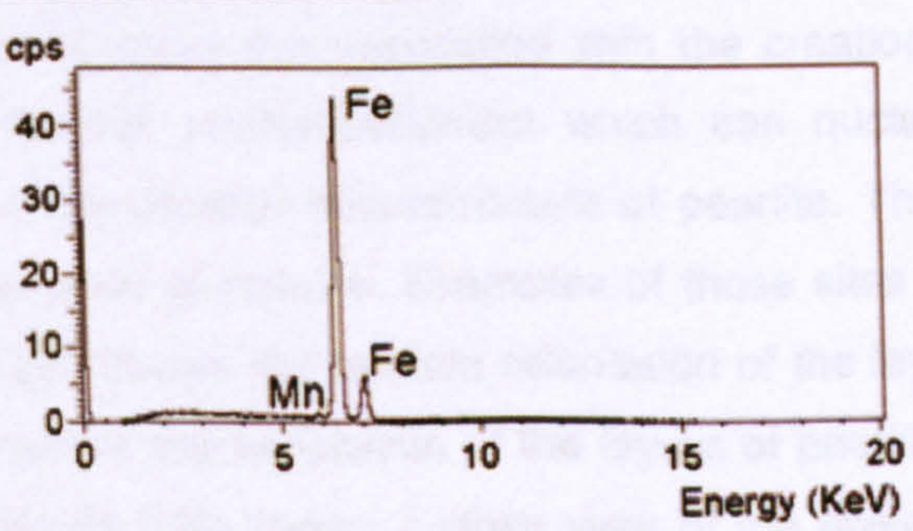

Particle 3 and 4

Figure 3.90 – EDS analysis of particles found in the lamellar pearlite microstructure.

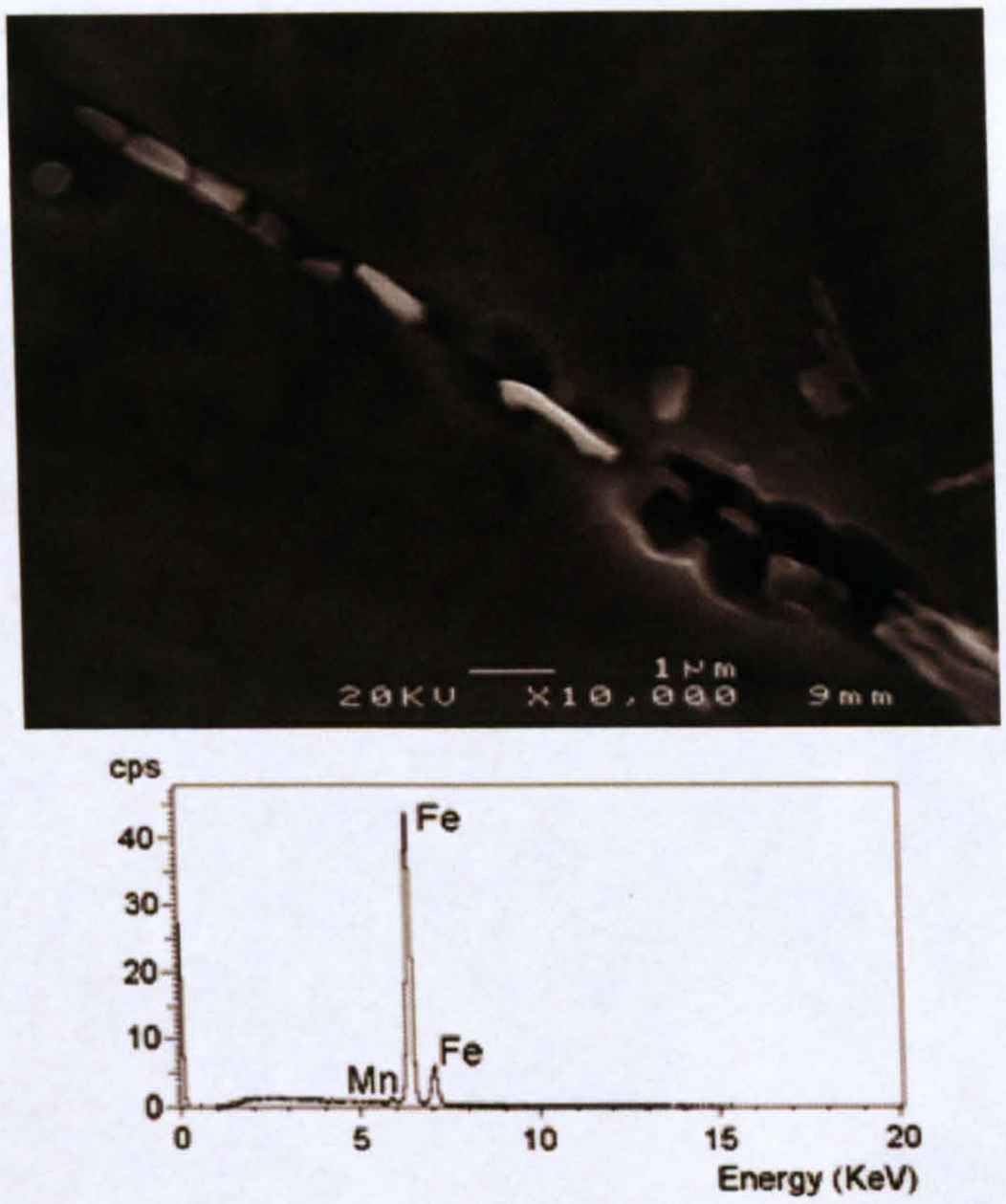

Figure 3.91 – EDS analysis of particles found in ferrite grains and the lamellar microstructure of pearlite.

From the EDS analysis, it was identified 3 different kind of particles nucleating cleavage, they are:

- MnS particles with small amount of iron (Fe);
- Iron particles (Fe) with small amount of (Mn)
- Particles with about the same percent of sulphide (S), manganese (Mn) and iron (Fe).

It can be seen that the three different kinds of microstructures, found experimentally, contain the same constituent but with different percent of chemical composition, therefore it can be suggested that the three different kind of microstructures are associated with the creation of distributions of microcracks of random size. Another micromechanism which can nucleate microcracks (section 3.6.4) is the gaps between the lamellar microstructure of pearlite. These sites may promote cleavage nucleation in some lands of pearlite. Examples of those sites are shown in the figures 3.92 and 3.93. The first image shows the random orientation of the layers of pearlite. This figure also shows some points where the separation of the layers of pearlite is bigger. They are marked by the blue arrows. Figure 3.93 shows a close view of the layers of

pearlite. The thickness of the lamellar microstructure of pearlite is about $180nm$. This size is similar with the particles of figure 3.91.

Figure 3.92 – Colony of pearlite microstructure showing the random orientation of groups of layers of pearlite.

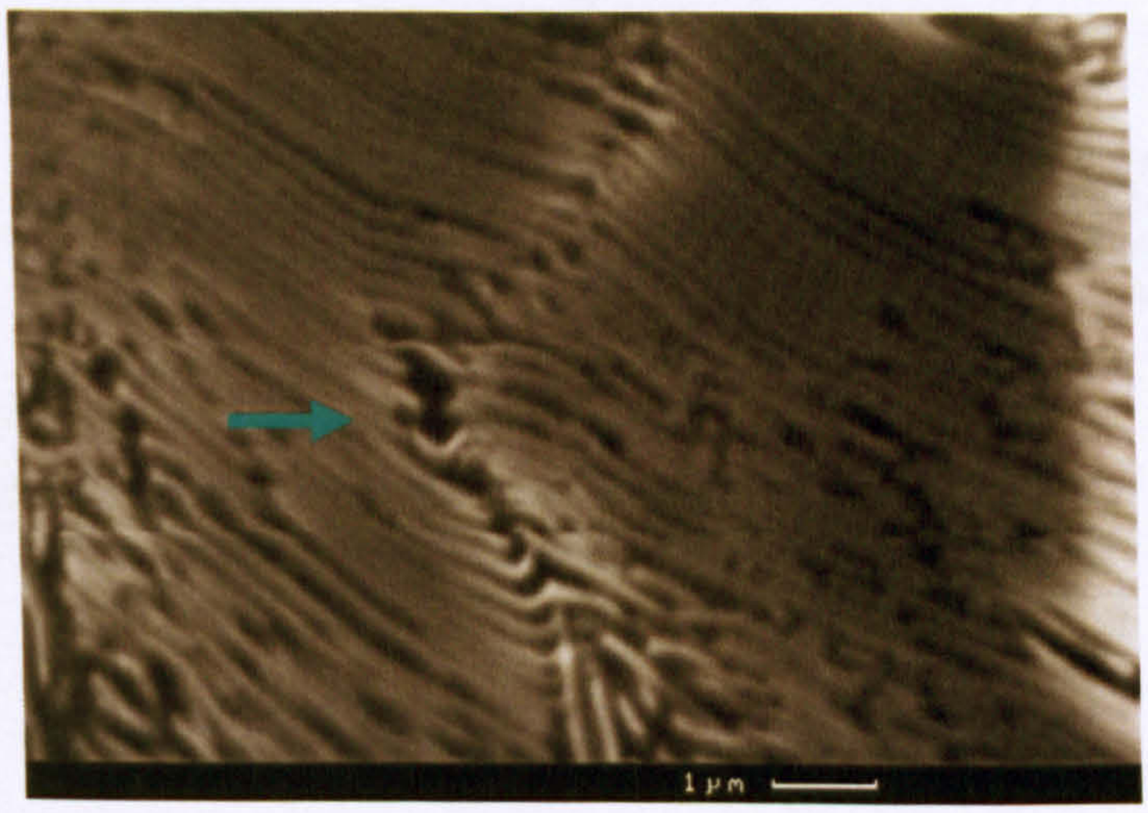

Figure 3.93 – Lamellar pearlite microstructure in a ferritic steel.

Hausild (Hausild et al., 2004) performed a fractography analysis of cleavage fracture initiation microstructures in the ductile–brittle transition temperature region of a A508 C1.3 steel on broken Charpy surfaces. The authors showed that no carbides were found at the origin of cleavage. The authors found particles and clusters of MnS. They also suggested that slip, grain boundary and multi–initiation were potential initiation points for cleavage nucleating. In the

steel under study we observe that MnS particles nucleate cleavage fracture along with the lamellar microstructure of pearlite. It can be concluded that the EDS analysis was very useful to correctly identify the cleavage microstructures for the steel under analysis as these microstructures will be used in further simulations.

3.6.6 Analysis of the distribution of microcracks in the rolling direction of the plate steel.

The schematic distributions of microcracks for each test temperature of the four different microstructures for cleavage fracture nucleation; pearlite boundary, the lamellar pearlite microstructure, ferrite grain inclusions and ferrite grain boundary are shown in the following graphs. In these graphs we can observe that the pearlite boundary micro features extended farther away from the notch root than the other microstructures, except at –196ºC where microcracks nucleated by ferrite inclusions and the lamellar pearlite nucleated microcracks very far from the notch root as seen in figure 3.97. The distribution of microcracks in the surrounding region of the notch root for the following range of temperatures: +25ºC, 0ºC, –60ºC and –196ºC are shown in figure 3.94, 3.95, 3.96 and 3.97 respectively. The distributions of microcracks were plotted on the same scale in order to compare the distributions for the different temperatures.

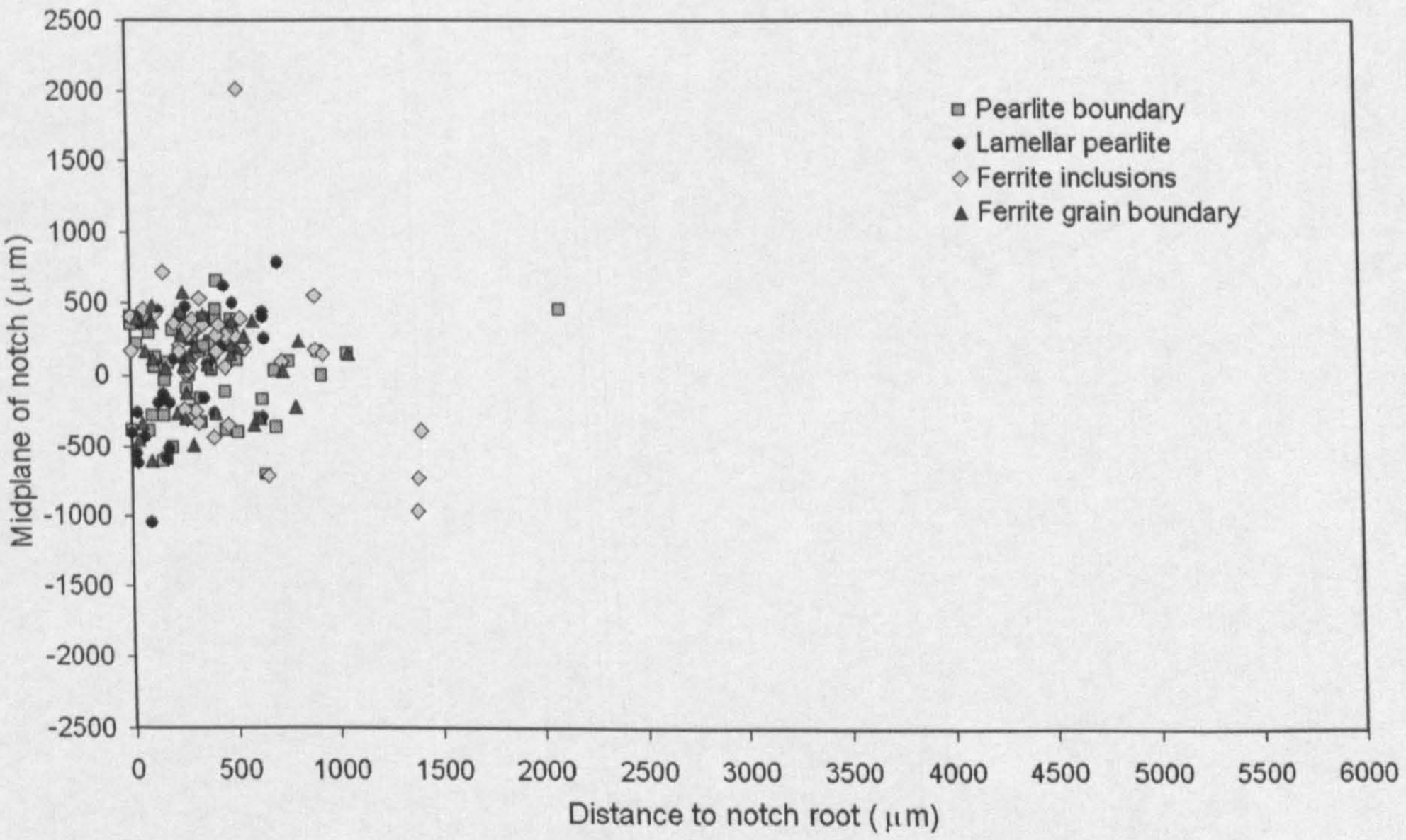

Figure 3.94 – Microcracks distributed ahead of the notch root at test temperature of +25ºC, in the rolling direction of the plate steel.

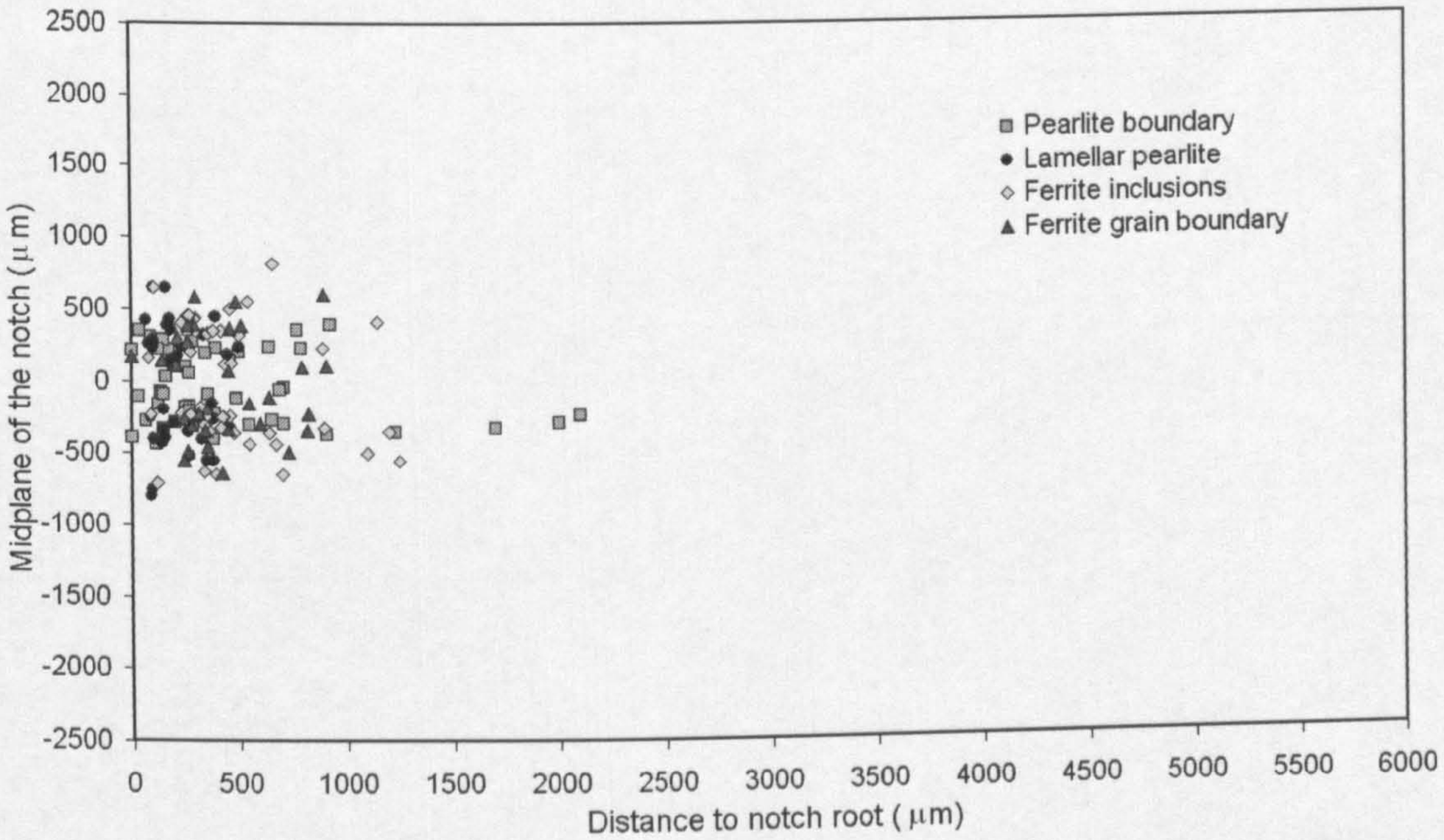

Figure 3.95 – Microcracks distributed ahead of the notch root at test temperature of 0ºC, in the rolling direction of the plate steel.

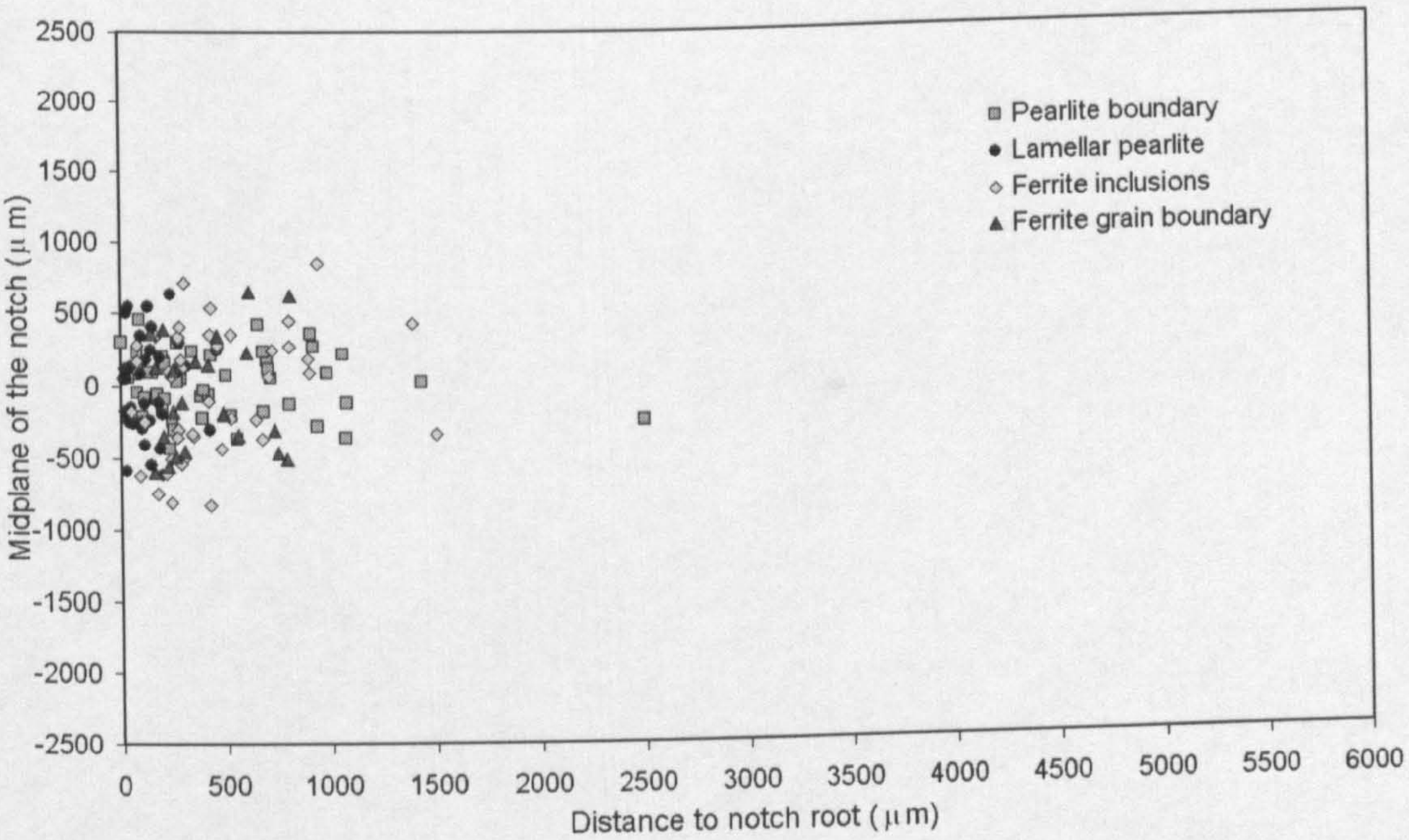

Figure 3.96 – Microcracks distributed ahead of the notch root at test temperature of –60ºC, in the rolling direction of the plate steel.

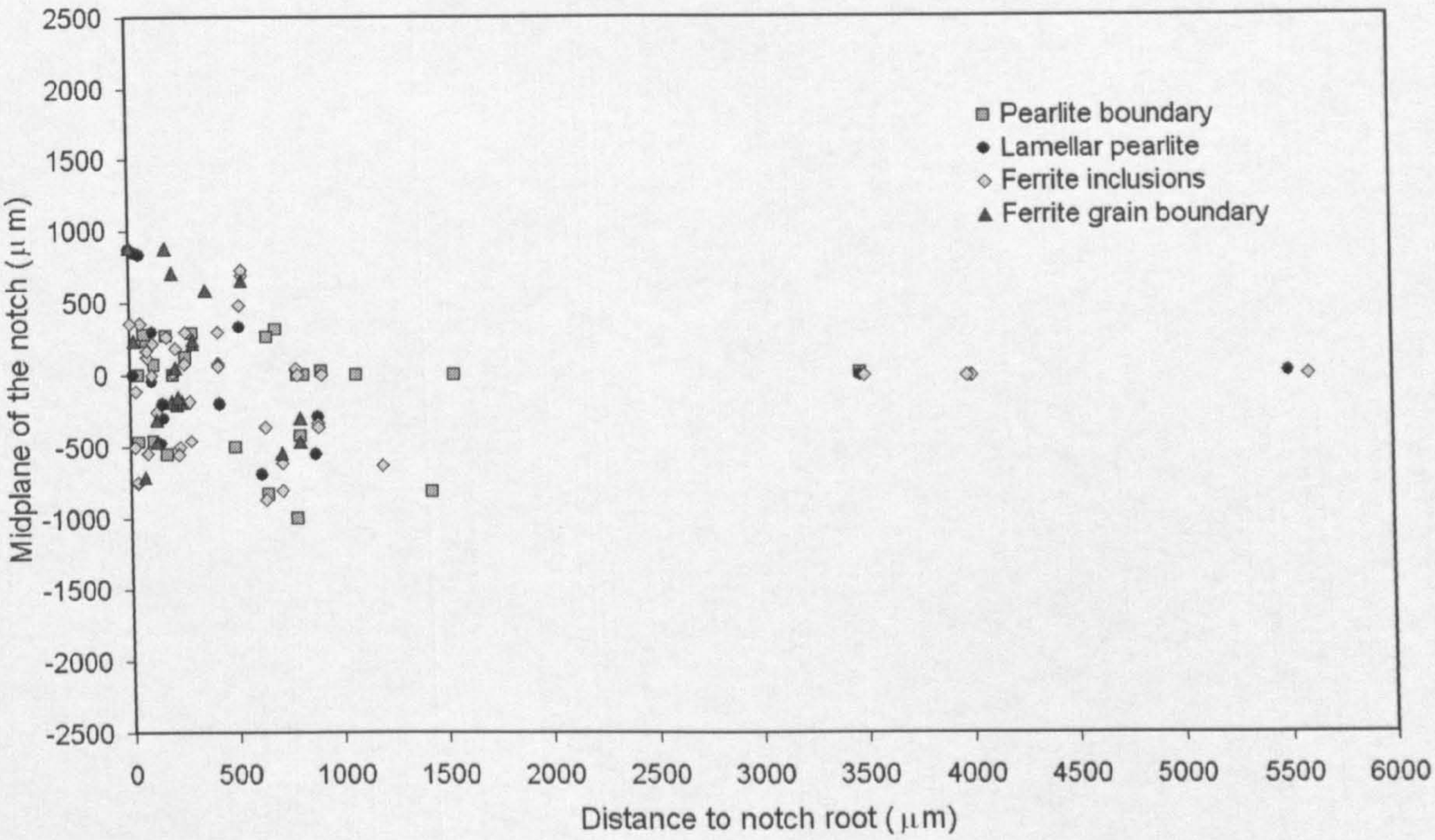

Figure 3.97 – Microcracks distributed ahead of the notch root at test temperature of –196ºC, in the rolling direction of the plate steel.

From the above graphs we observe that the four micromechanisms for the development of microcracks were developed at all temperatures. At +25ºC the pearlite boundary and ferrite grain inclusions microstructures extended farther away than the other two micromechanisms. But the microstructures that nucleated the longest and widest microcracks are the lamellar microstructure of pearlite and pearlite boundary as shown in graph 3.98. For lower temperatures, there was found a competition between the four microstructures for nucleating cleavage fracture as shown in graphs 3.95, 3.96 and 3.97. At 0ºC the microstructures that nucleated the farthest microcracks was the pearlite boundary followed by the ferrite grain inclusions; these two microstructures also nucleated the widest and longest microcracks as shown figure 3.99. At a test temperature of –60º the farthest microcrack was nucleated at a pearlite boundary, but a competition between all the microstructures was found, with the exception of ferrite grain boundary, for the nucleation of the widest and longest microcracks as shown in figure 3.100.

Finally for –196ºC it can be seen in figure 3.97 that the farthest microcracks were nucleated by ferrite grain inclusions. But in the higher density region of the distribution, the pearlite boundary microstructure nucleated the farthest microcracks. At this test temperature, the widest microcrack was nucleated by pearlite boundary but the longest microcracks were nucleated by ferrite grain inclusions and by the lamellar microstructure of pearlite. Close observations of the distribution of microcracks from figures 3.94, 3.95, 3.96 and 3.97 showed that at a distance of around $1mm$ from the notch root, the highest population density of microcracks nucleated by

all microstructures was developed for all test temperatures. This distance included the largest and widest microcracks (microcracks of critical size). This distance can be considered as the critical cleavage nucleation region for notch specimens for the steel under analysis. But a region of around $2\,mm$ from the notch root includes all microcracks for +25°C, 0°C and –60°C. For –196°C, microcracks were found at a distance very close to the edge opposite to the notch root. But as shown in figure 3.97 only a few microcracks were found at a distance beyond $2\,mm$ from the notch root. It can be concluded that the region of $2\,mm$ from the notch root can be considered as the distance that covers the cleavage fracture initiation points for all test temperatures of Grade A plate steel for the rolling direction.

It can be concluded that the distance of $2\,mm$ from the notch root covers the majority of cleavage initiation points. This distance can be defined in finite element models to compute the distribution of stresses and strains in the notch region in order to analyze cleavage toughness parameters as the local cleavage fracture stress. This distance of $2\,mm$ has been extensively used to compute the distribution of stress and strain ahead of the notch root in notched specimens loaded in bending for the development of statistical models for cleavage fracture (Wang and Chen, 1999, Wang et al., 2003a, Wang et al., 2005a, Wang et al., 2004a, Wang et al., 2003b, Bordet et al., 2004, Wu and Knott, 2004, Wang and Chen, 2000). From the present analysis, it can be concluded that the fracture nucleation region for Grade A ship plate steel was measured with metallographic analysis. The computing of the distribution of stresses and strains must be done in this region which can be considered as the nucleation region. This region showed the conditions of microcracks density prior to fracture. It is clearly shown that due to the distribution of initiation points with respect to the notch root, we will have a distribution of the cleavage fracture toughness parameter σ_F because this parameter is based on the distance of the microcracks with respect to the notch root. The number of microcracks nucleated by each microstructure and for all tested temperatures is shown in table 3.4. In this table it can be seen that the number of microcracks decreases with test temperature. It is well known that as the temperature decreases, the strain needed to create microcracks decrease with test temperature. Therefore less number of microcracks will be developed in less volume of strained material. At +25°C the pearlite boundary is the dominant microstructure which nucleated 37% of the total of microcracks. At 0°C this mechanism nucleated 30.6% of the total of microcracks. For test temperature of –60°C the same microstructure was the dominant one which nucleated 32.6% of the total of microcracks. But at –196°C the ferrite grain inclusions microstructure was the dominant one which nucleated 41.3% of the total of microcracks. But, as mentioned above, the widest microcracks found at this temperature were nucleated by the pearlite boundary microstructure. The longest microcracks were nucleated by ferrite grain inclusions. This suggest that for all test temperatures, in the rolling direction, the dominant cleavage fracture nucleation microstructures are pearlite boundary and ferrite grain inclusions.

Table 3.4 – Number of microcracks per fracture initiation microstructure in RD.

Temperature	Pearlite boundary	Lamellar pearlite	Ferrite inclusions	Ferrite grain boundary	Total of microcracks
+25ºC	70 (37%)	37 (19.5%)	46 (24%)	37 (19.5%)	190
0ºC	49 (30.6%)	35 (21.9%)	45 (28.1%)	31 (19.4%)	160
–60ºC	51 (32.1%)	37 (23.3%)	47 (29.5)	24 (15.1%)	159
–196ºC	27 (23.7%)	20 (17.5)	47 (41.3%)	20 (17.5%)	114

Although the number of microcracks may suggest which microstructure dominates for each test temperature, the size of microcracks must be taken into account in order to define properly the dominant microstructure for fracture propagation. So in order to investigate which microstructure nucleated the widest and largest microcracks at each test temperature, the width against length of the distribution of microcracks was plotted to identify the microstructure that nucleated microcracks of a critical size. The graphs are shown in the following figures. In these figures the same scale was used in all test temperatures to visualize the variation of the size of microcracks with respect to test temperature.

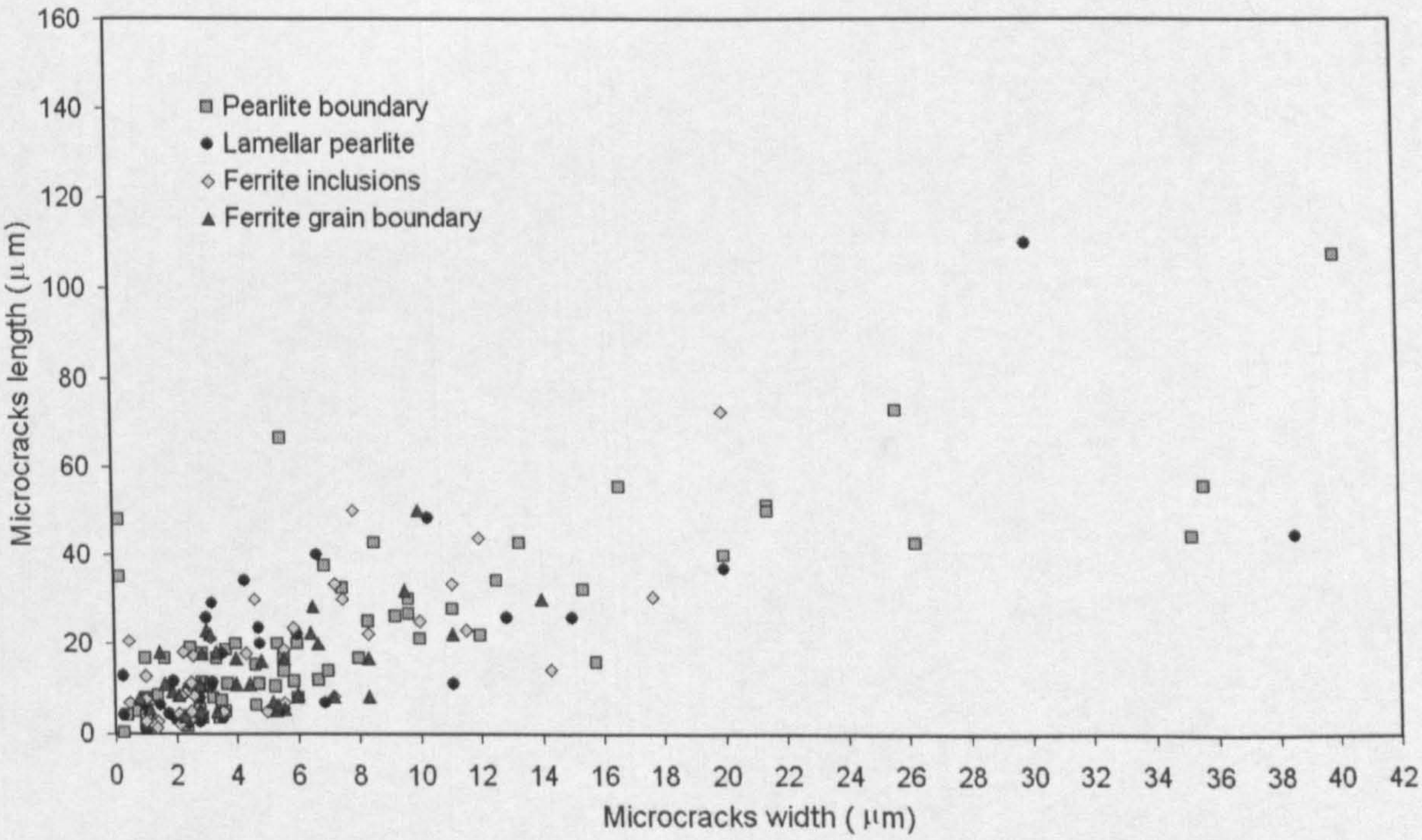

Figure 3.98 – Distribution of microcracks width vs length at test temperature of +25ºC, in the rolling direction of the plate steel.

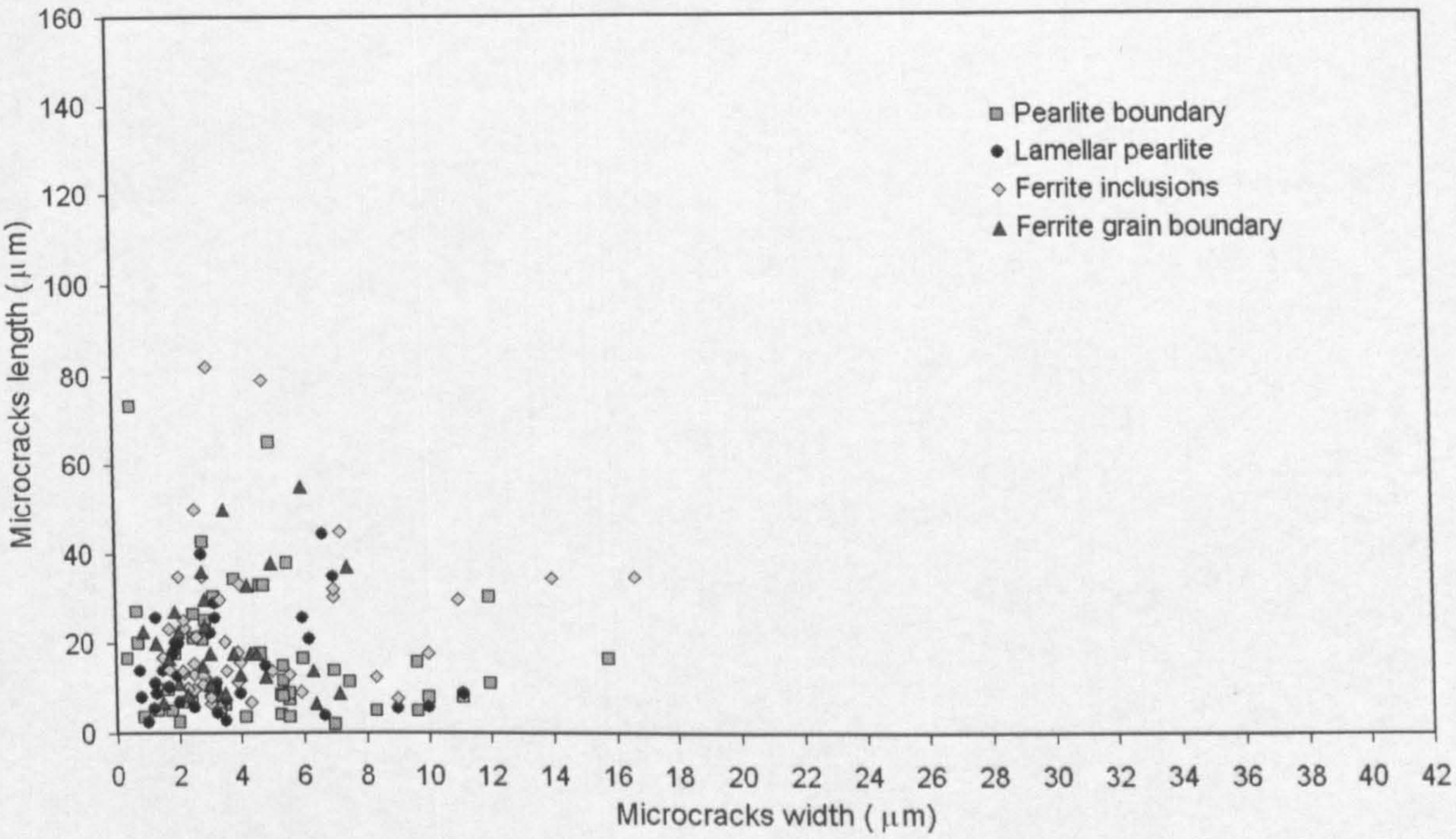

Figure 3.99 – Distribution of microcracks width vs microcracks length at test temperature of 0ºC, in the rolling direction of the plate steel.

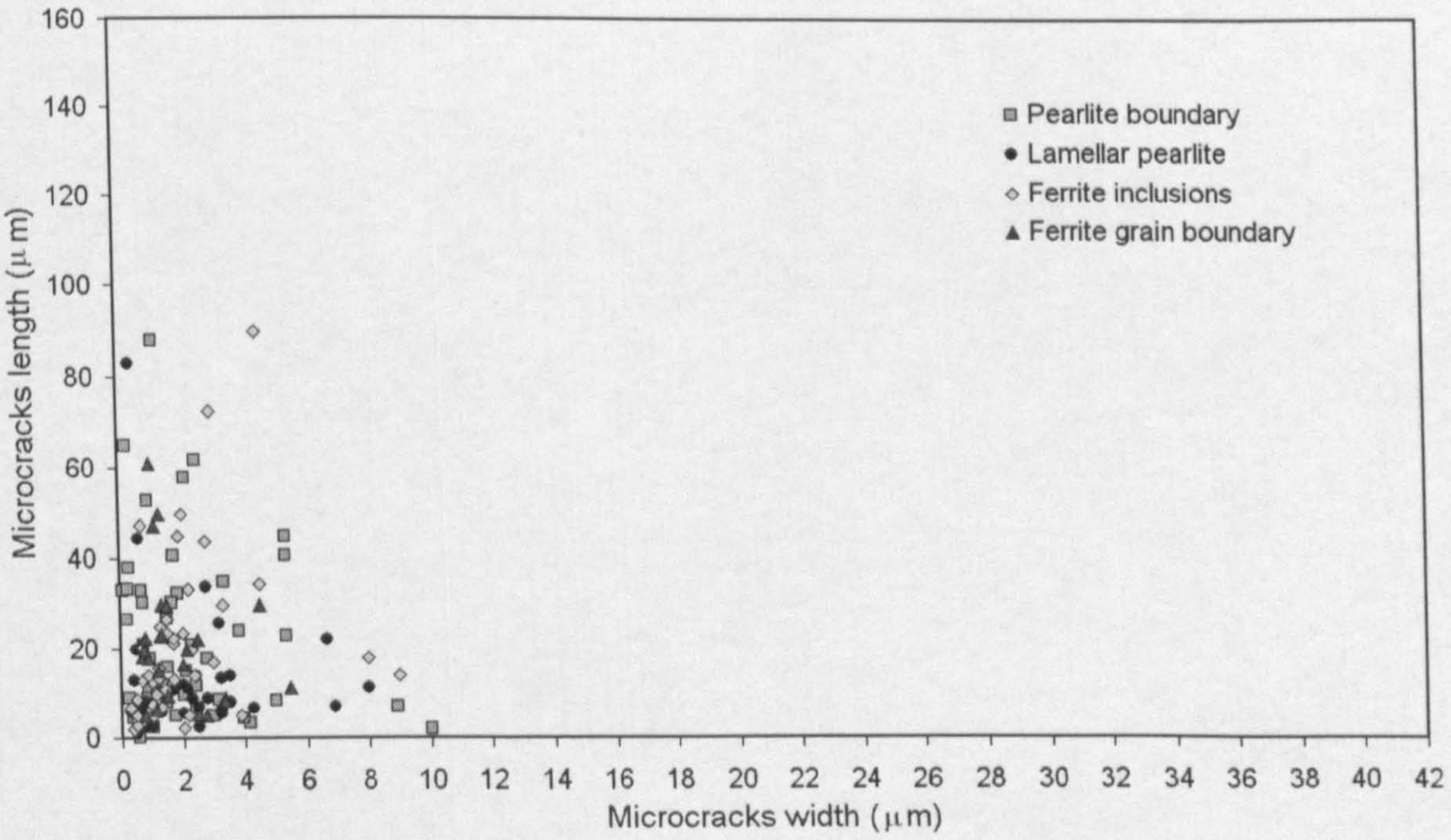

Figure 3.100 – Distribution of microcracks width vs microcracks length at –60ºC test temperature, in the rolling direction of the plate steel.

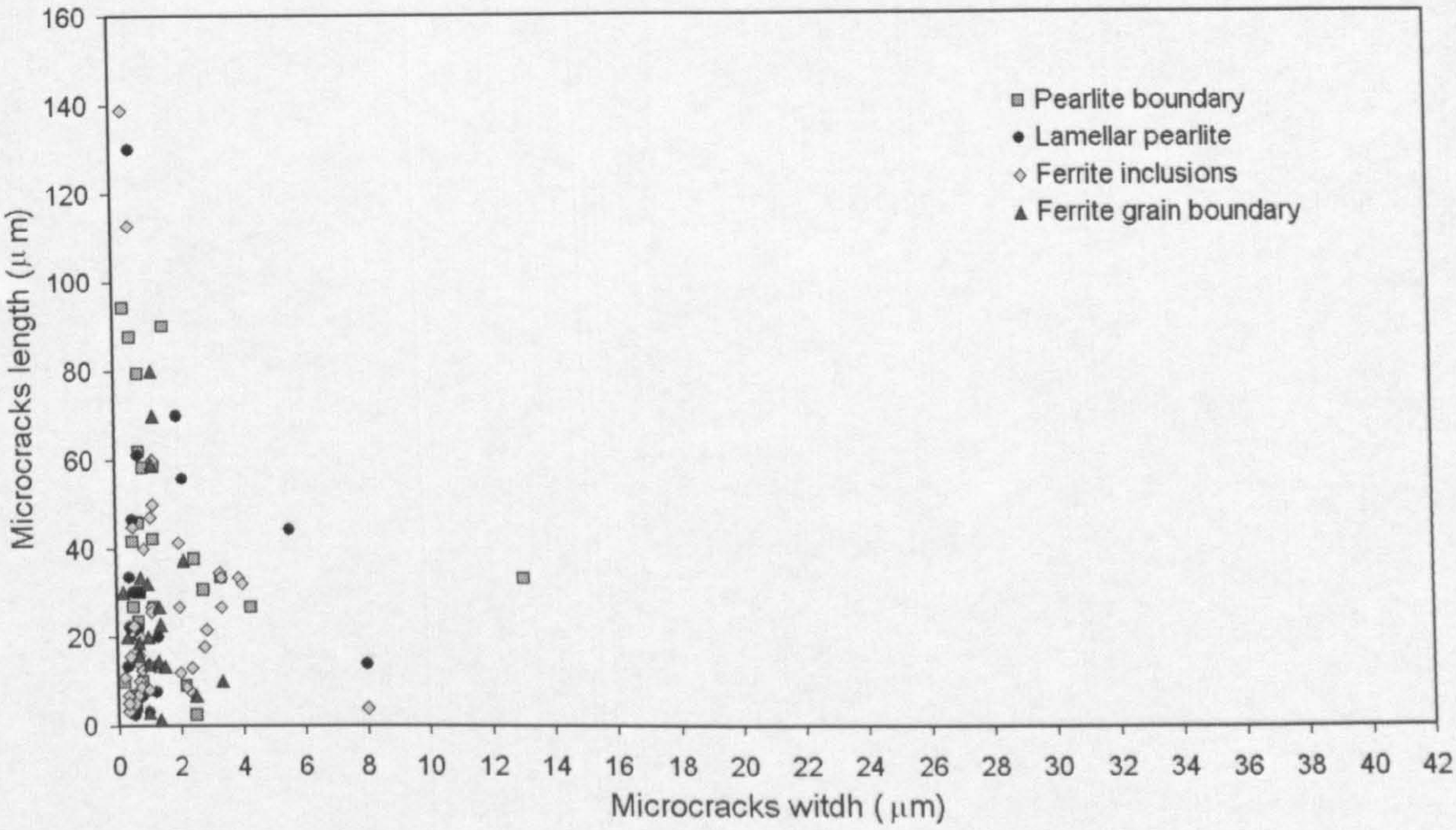

Figure 3.101 – Distribution of microcracks width vs length for –196°C test temperature, in the rolling direction of the plate steel.

Figure 3.98 shows the length against width of the microcracks at room temperature. In this graph it can be seen that the widest and longest microcracks were developed by the lamellar microstructure of pearlite and pearlite boundary micromechanisms. This analysis suggests that the lamellar and pearlite boundary microstructures are the dominant for the nucleation of microcracks of critical size. At 0°C, it was found that competition of the pearlite boundary micro features and ferrite grain inclusions dominate at this test temperature. These two microstructures nucleated the widest and longest microcracks. From this analysis we can see that there was a change of dominant mechanism for microcracks nucleation at lower temperatures. At –60°C, it was found that a competition of three microstructures nucleated the longest and widest microcracks. They are: pearlite boundary, lamellar pearlite and ferrite grain inclusions. At –196°C it was found that the lamellar pearlite and pearlite boundary nucleated the widest microcracks along with the ferrite grain inclusions. From this analysis, we see clearly that in the rolling direction of the plate steel, there is a competition of three microstructures for the nucleation of microcracks of critical size, they are: pearlite boundary, lamellar pearlite and ferrite grain inclusions.

This analysis gave clearer explanation for the identification of the microstructures that nucleated microcracks of critical size. Therefore it can be seen that it is more important to analyze the microstructures that nucleated the widest and longest microcracks prior to failure than the analysis of the number of microcracks (table 3.4) for the identification of the microstructures initiating cleavage fracture.

Microscopic examinations of the surfaces of broken Charpy specimens revealed a high distribution of MnS particles in the matrix of the material for specimens tested at room temperature. Figure 3.102 shows the different micromechanisms for cleavage fracture nucleation. In this figure the region marked with a dashed line corresponds to a colony of pearlite. The pearlite colony was identified based on the fact that in pearlite colonies very small microvoids are nucleated as those shown in figures 3.27 and 3.104 as explained in section 3.4.2. The red arrow shows the origin of cleavage fracture in a land of pearlite. In this figure large microvoids nucleated by inclusions can be seen as marked by the blue arrows, and large dimples, as marked with green arrows. The four microstructures for fracture initiation were developed in this micrograph, but it is quite difficult to identify them clearly in fracture surfaces of broken specimens taken at low magnification. In order to show clearly those microstructures in fracture surfaces of Charpy specimens, micrographs with higher magnification were taken. The different micromechanisms developed in fracture surfaces of broken Charpy specimens are shown in figures 3.102, 103, 3.104 3.105 and 3.106.

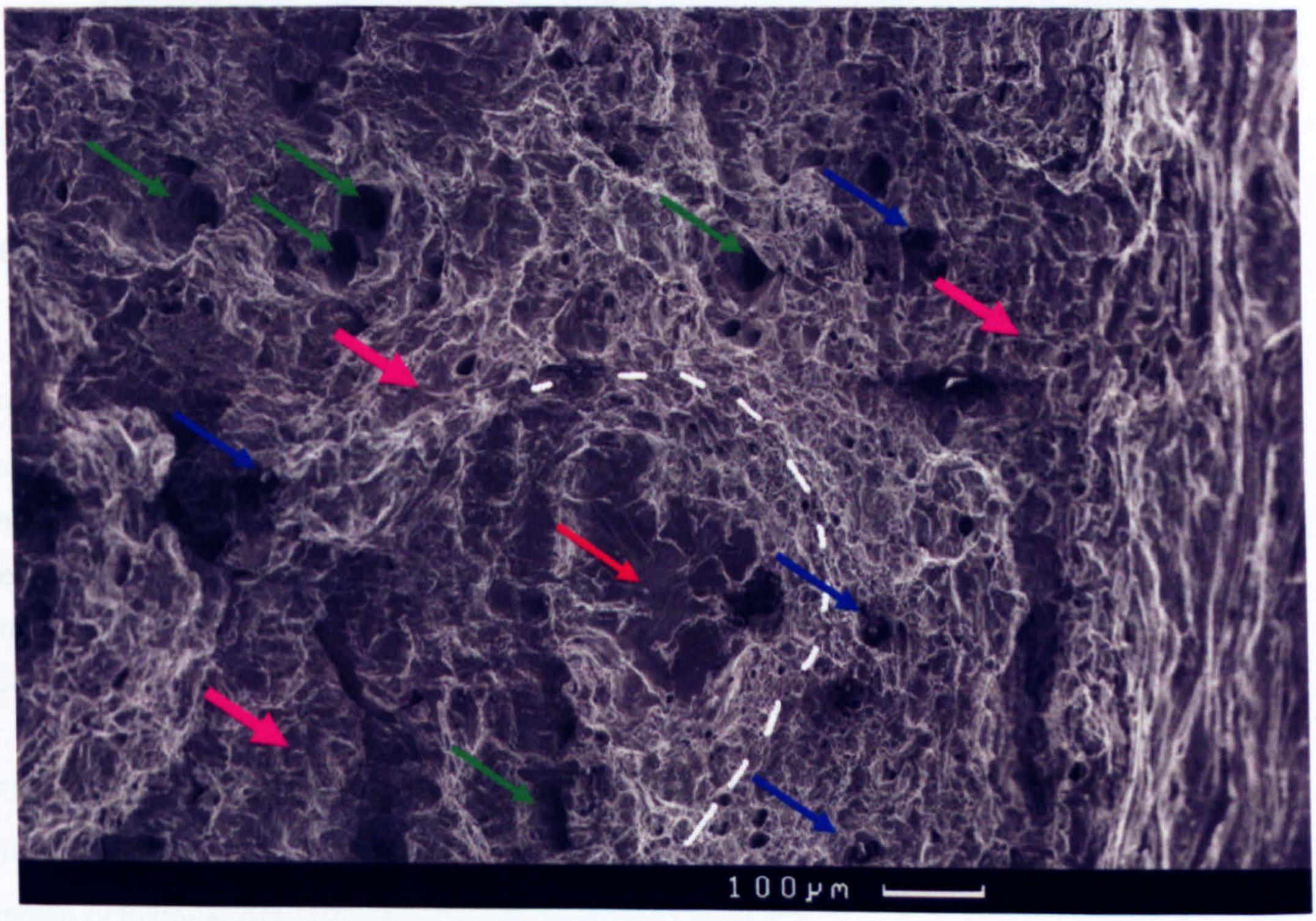

Figure 3.102 – Different microstructures for fracture initiation, the red arrow shows the lamellar pearlite, blue and green arrows show the ferrite grains inclusions.

Figure 3.102 shows apparently the pearlite boundary micromechanics for the initiation of cleavage and the origin of cleavage, in this figure the boundary of the pearlite is marked by a dashed line. Even when this figure gives an insight of the fact that a microcrack was initiated in

a pearlite boundary, as the pearlite microstructure is surrounding the microcrack, the SEM analysis of the sections of the surviving notches of four point double–notch bend specimens gave better views of the pearlite microstructure associated with the development of cleavage.

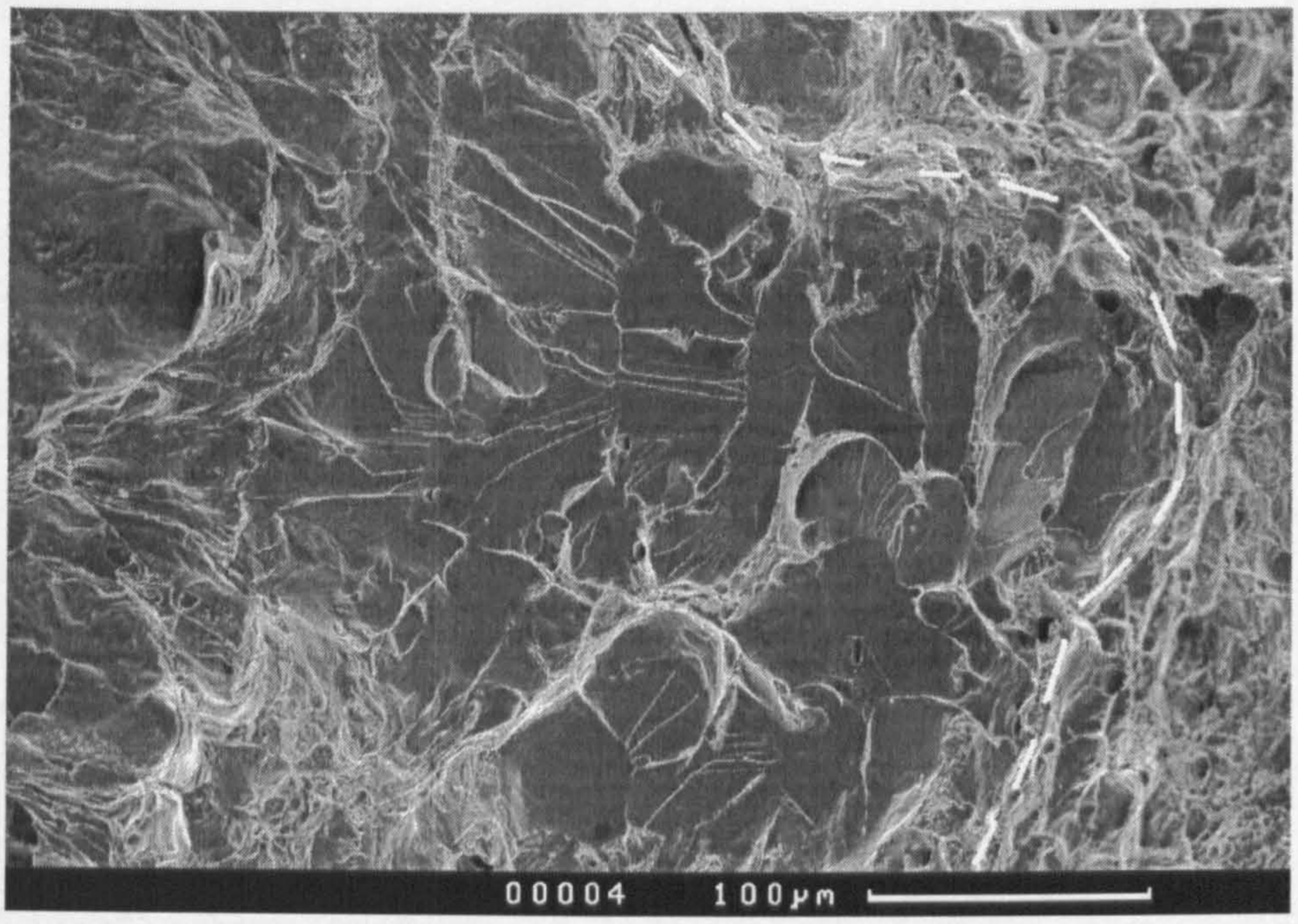

Figure 3.103 – Pearlite boundary micromechanism nucleating which nucleated a microcrack in the fracture surface of a Charpy specimen tested at room temperature.

Figure 3.104 shows a micrograph taken in a colony of pearlite. In this image it can be seen some SMn particles, they are marked with blue arrows. The same type of particles was found in the analysis performed in section 3.6.4 in 4PB double–notch specimens tested at room temperature. From the present results it can be seen that there exist transferability of the micromechanisms for cleavage fracture identified with 4PB double–notch specimens and with Charpy tests.

Figure 3.105 shows clearly the ferrite grain SMn inclusions. These particles nucleated microvoids. The size of micrograph 3.105 is $222\times148\,\mu m$, this means that a relatively small region of material contains a high distribution of inclusions.

The ferrite grain boundary micromechanics is more difficult to identify in fracture surfaces of Charpy specimens. This can be identified clearly by the analysis of the sectioned slices of 4PB double–notch specimens (section 3.6.4). Figure 3.106 shows an example of this micromechanics. The red arrow shows the separation of ferrite grains.

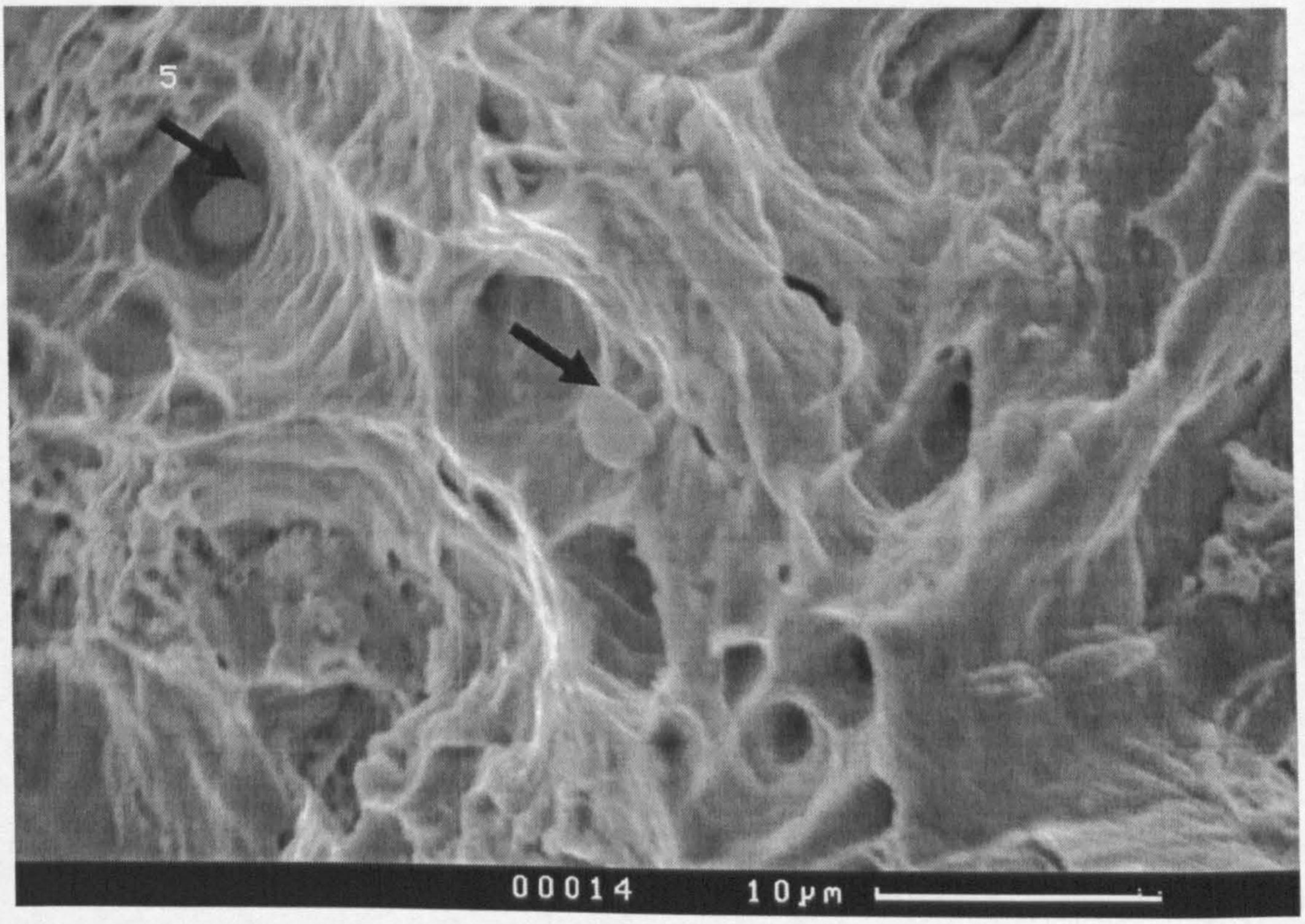

Figure 3.104 – Region of a pearlite colony in a fracture surface of a Charpy specimen tested at room temperature.

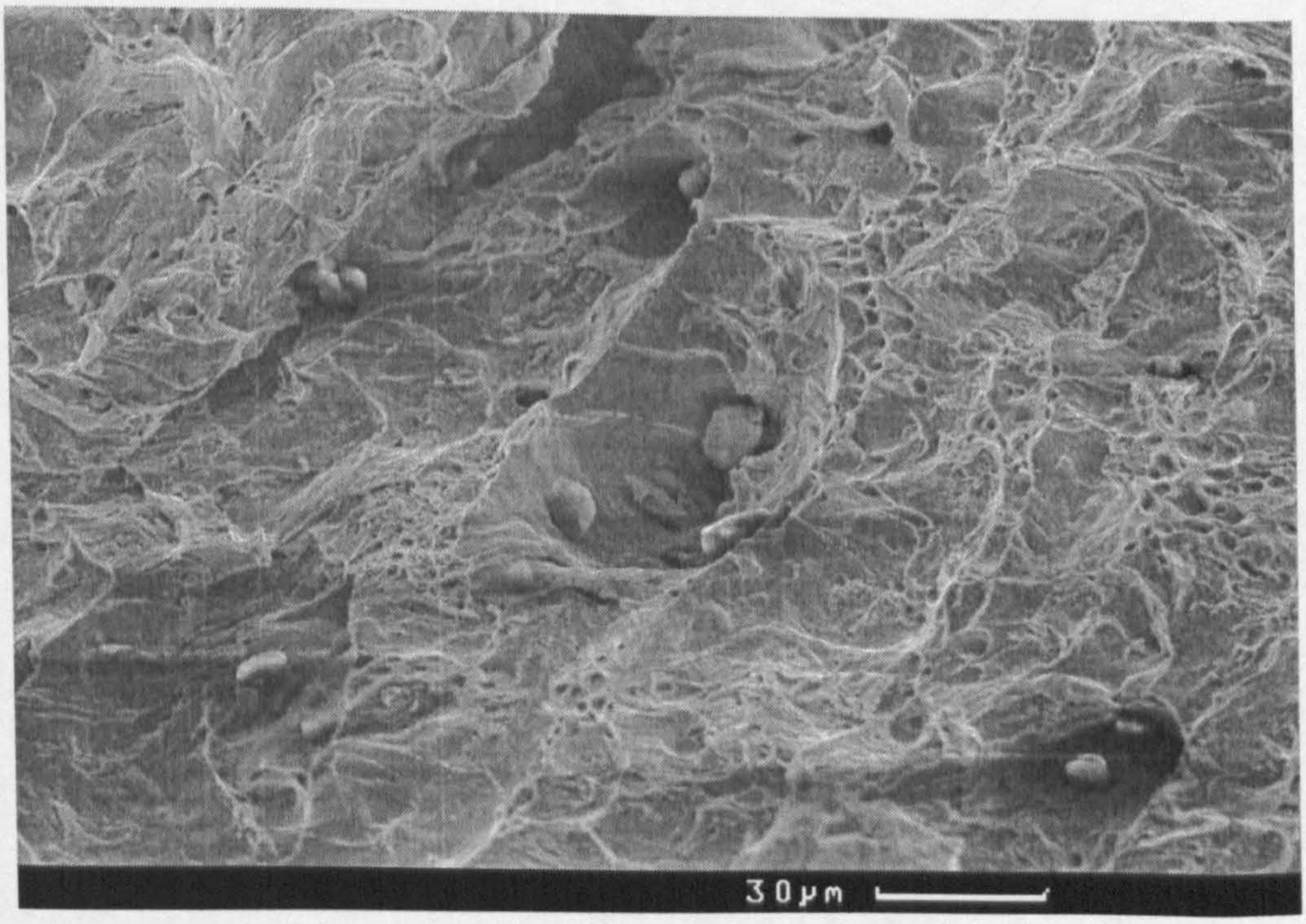

Figure 3.105 – Ferrite inclusions distributed in the matrix of the material.

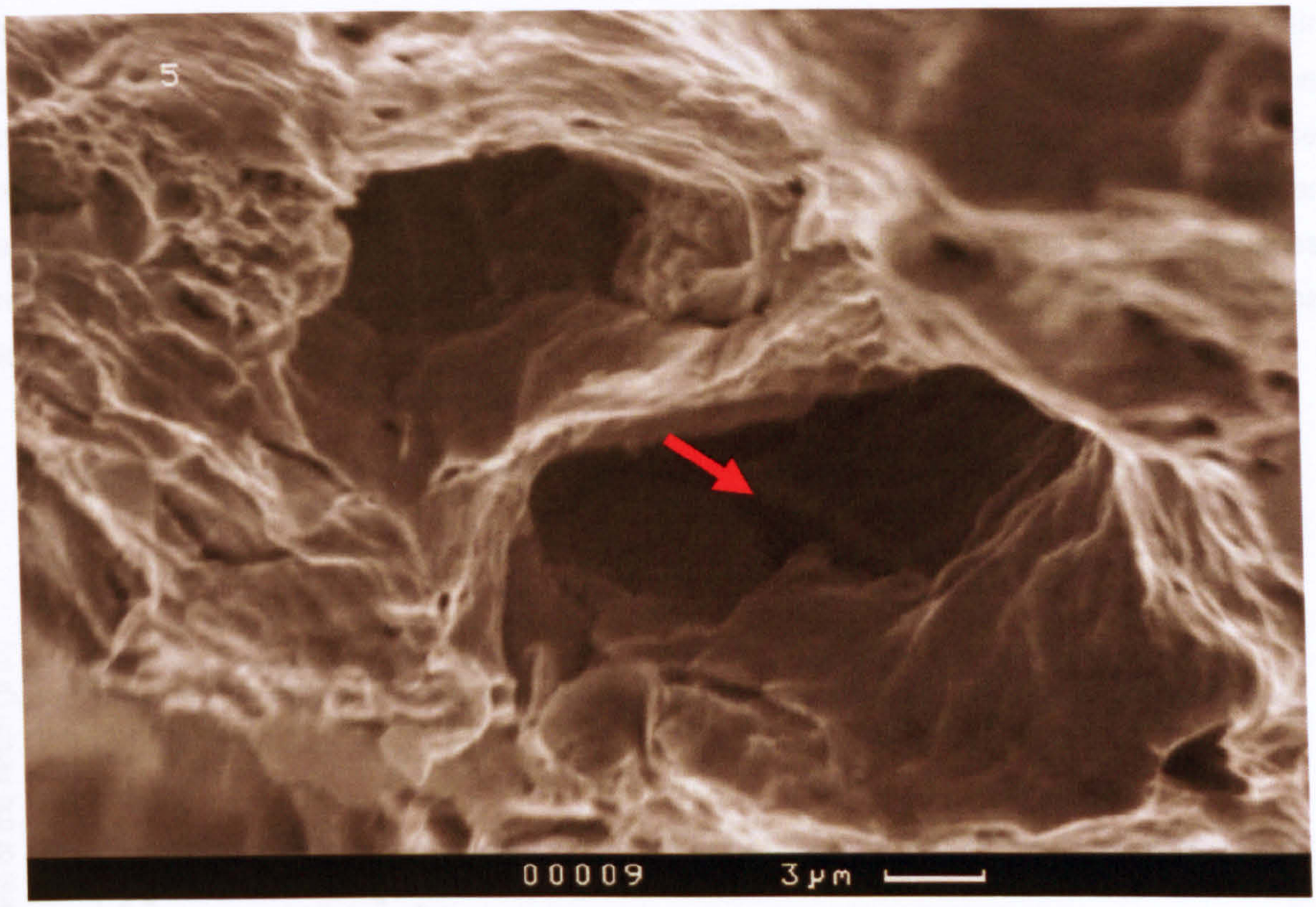

Figure 3.106 – Ferrite grain boundary micromechanism.

From the present analysis it can be seen that the micro features identified in Charpy surfaces correlated with the micro features identified in the surviving notches of 4PB double notch specimens. Therefore transferability of the identified microstructures in section 3.6.4 for Charpy tests exists. Consequently these microstructures can be implemented in the subroutine of the CAFE model to simulate the transition ductile–brittle of the material under analysis and to simulate the initiation points for cleavage fracture in the present work.

3.6.7 Analysis of the distribution of microcracks in the transverse direction of the plate steel.

The schematic distribution of microcracks for each test temperature and the different microstructures for cleavage initiation micromechanism is shown in the following graphs for the transverse direction of the plate steel. In these figures we can observe that some micromechanisms extended farther away than others. The analysis for the identification of the microstructures nucleating cleavage fracture was done at three temperatures: +25ºC, 0ºC and –60ºC. The explanation for testing at these temperatures will be done at the end of the present section.

The distributions of microcracks were plotted on the same scale in order to visualize their distribution with respect to the notch root for each test temperature. Figure 3.107 shows the distribution of microcracks in front of the notch root at test temperature of +25ºC for the transverse direction of the plate steel. At this test temperature the pearlite boundary, lamellar pearlite and ferrite grain inclusions microstructures nucleated microcracks at similar distances from the notch root with exception of a microcrack nucleated by the ferrite grains inclusions which was nucleated farther away than the other two microstructures.

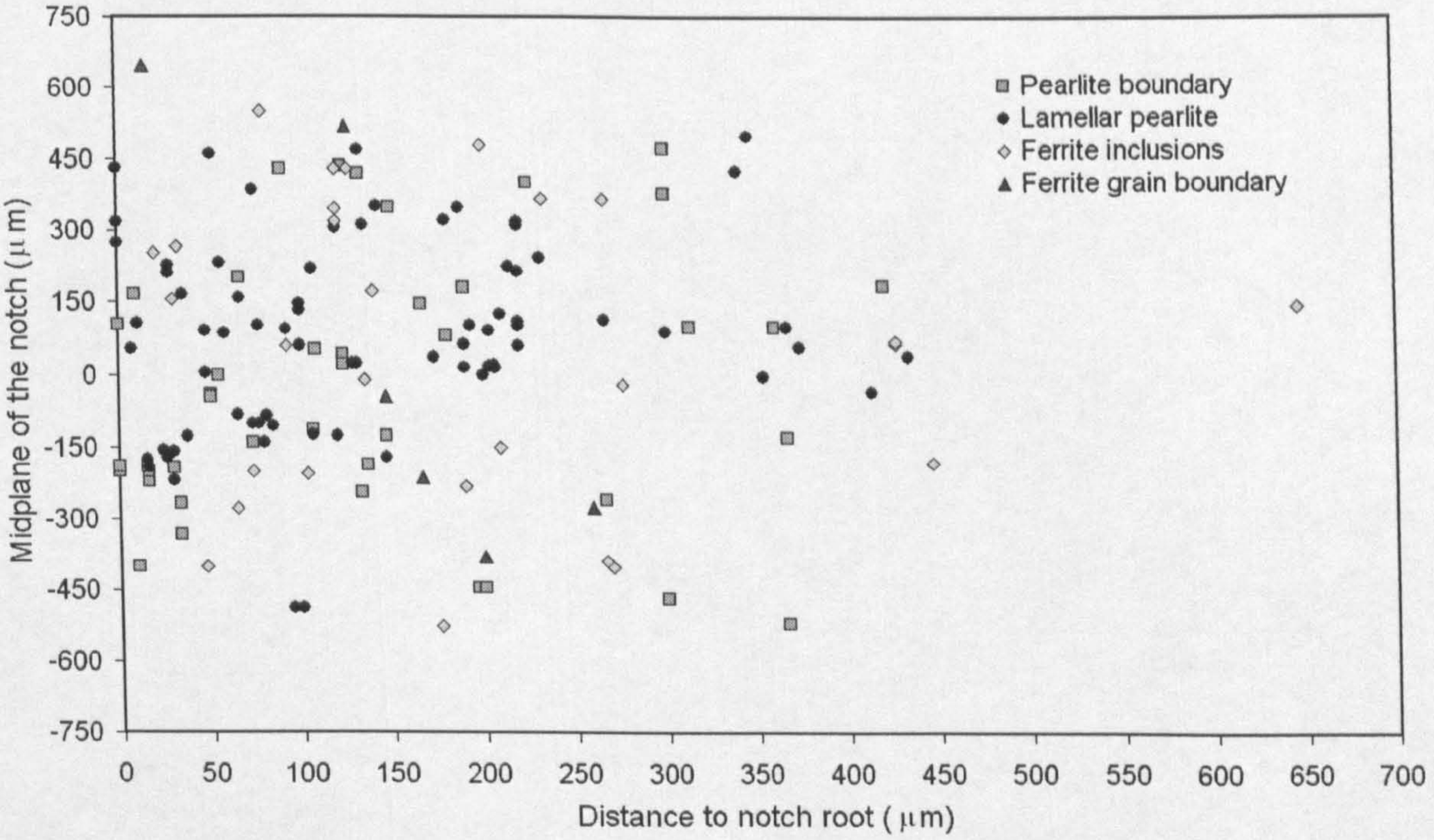

Figure 3.107 – Microcracks distribution in the transverse direction of the plate steel at test temperature of +25ºC.

The ferrite grain boundary microstructures nucleated only a few microcracks. For this test temperature it can be seen that there exist a competition between three main microstructures for the nucleation of microcracks.

Figure 3.108 shows the distribution of microcracks in front of the notch root at test temperature of 0ºC. From this graph, it can be seen that the distribution of microcracks is very similar to that of room temperature but with a decrease of the distance from the notch root in the $+y$ and $-y$ axis. The same three microstructures as for the previous test temperature dominate the nucleation of microcracks. As for +25ºC, at the 0ºC there exists a competition between the three microstructures for the nucleation of microcracks.

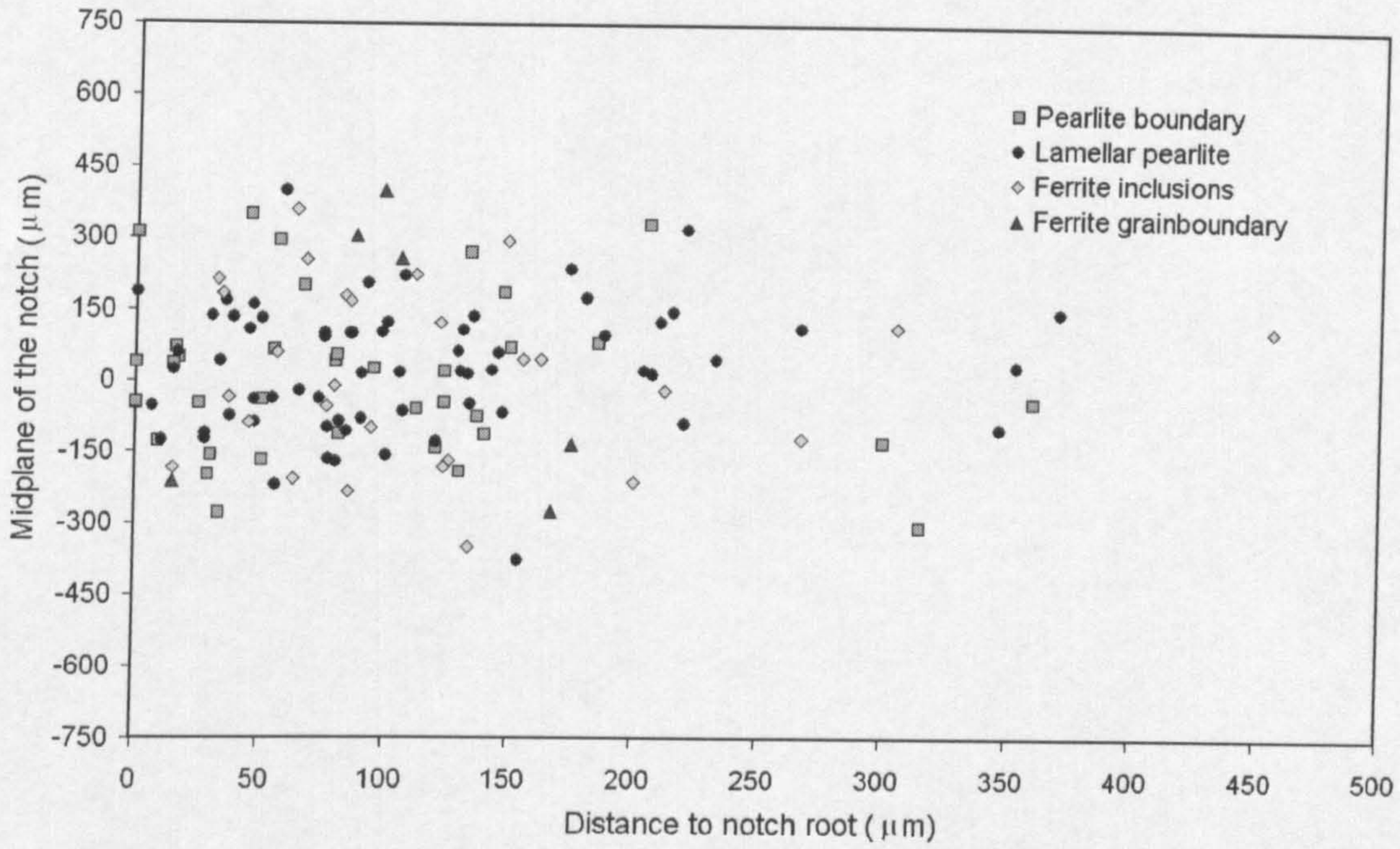

Figure 3.108 – Microcracks distribution in the transverse direction of the plate steel at test temperature of 0ºC.

The distribution of microcracks at –60ºC is shown in figure 3.109, where 100% of brightness was observed in the fracture surfaces of Charpy specimens, for this test temperature it was found that only two microstructures for nucleation of microcracks remained as shown in figure 3.109. They are the lamellar pearlite microstructure and the boundary of pearlite colonies. Contrary to the rolling direction of the plate steel, where the four microstructures for cleavage fracture nucleated microcracks at all test temperatures (section 3.6.6). In the transverse direction of the plate steel, at –60ºC, the two microstructures for cleavage fracture initiation had similar distributions.

The number of microcracks for each microstructure was different. The lamellar pearlite microstructure nucleated 58.7% of the total of microcracks. The pearlite boundary micromechanism nucleated only 41.3% of microcracks. This suggests that the dominant microstructure for cleavage fracture nucleation is the lamellar pearlite microstructure.

It is important to notice that at lower temperatures the distance of nucleation of microcrack decreased significantly, at –60ºC this cleavage fracture nucleation distance is about 220 μm extended ahead of the notch root, which is about half of the distance for room temperature test.

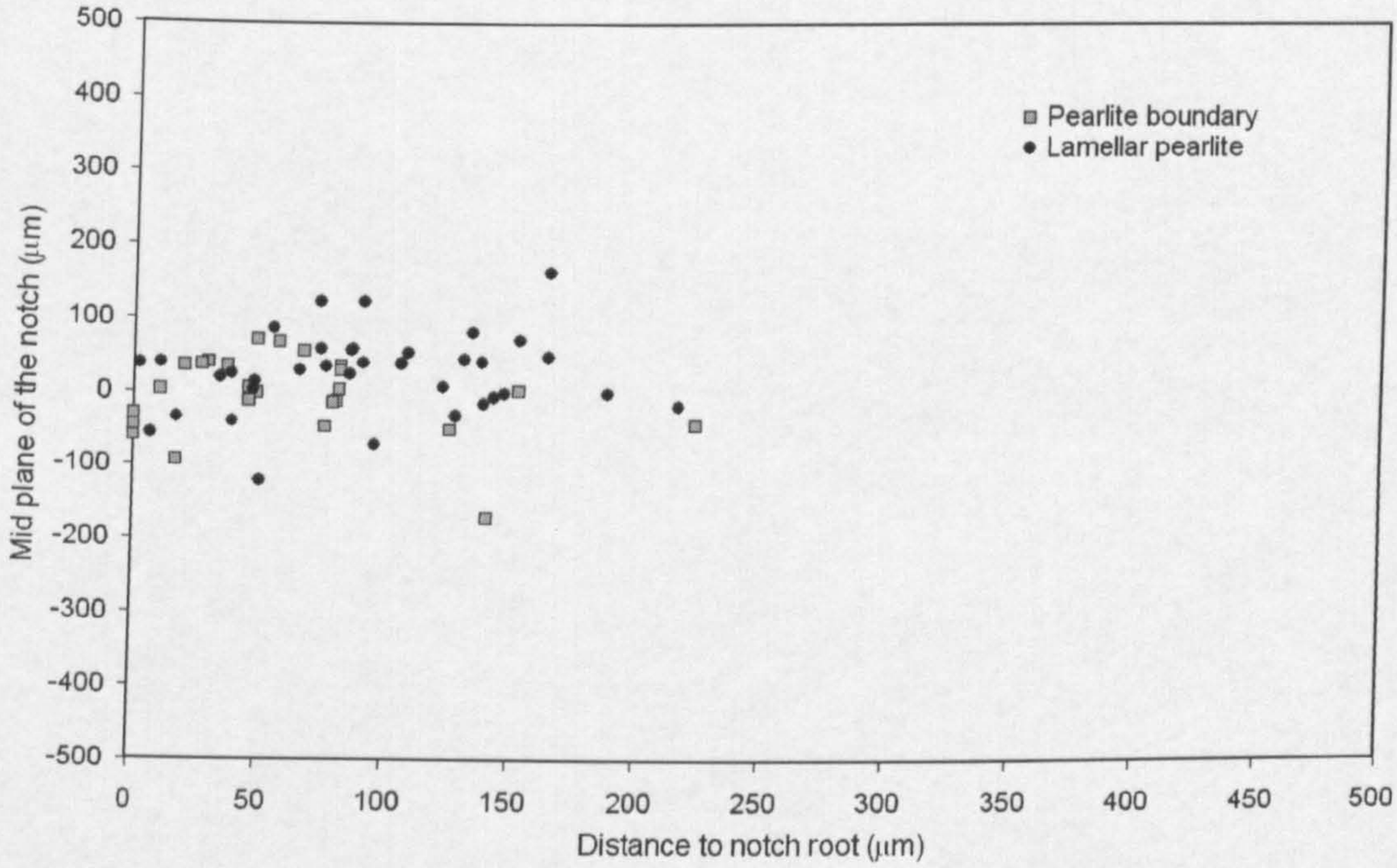

Figure 3.109 – Microcracks distribution, in the transverse direction of the plate steel at test temperature of –60ºC.

The number of microcracks for each micromechanism and each test temperature is shown in table 3.5. This table shows that at room temperature the number of microcracks was higher and decreased with decrease of test temperature. At –60ºC the number of microcracks decreased about 60%. It is very important as well to notice that the higher number of microcracks, at all test temperatures, were nucleated by the lamellar pearlite microstructure. This suggests that the dominant micromechanism for the transverse direction of the plate steel in each test temperature is the lamellar pearlite microstructure.

Table 3.5 – Number of microcracks per fracture initiation microstructure TD.

Temperature	Pearlite boundary	Lamellar pearlite	Ferrite inclusions	Ferrite grain boundary	Total of microcracks
+25ºC	42 (27.5%)	77 (50.3%)	28 (18.3%)	6 (3.9%)	153
0ºC	37 (27.2%)	65 (47.8%)	28 (20.6%)	6 (4.4%)	136
–60ºC	26 (41.3%)	37 (58.7%)			63

The present analysis showed that the microcracks found at –60°C lay substantially on a line ahead of the notch and they were more evenly distributed at higher temperatures. This effect

was observed only in the transverse direction of the plate steel were the pearlite microstructure is distributed randomly in the ferrite matrix and is the weakest link for the nucleation of microcracks of critical size. The lands of pearlite of critical size which lay on the fracture propagation path nucleated microcracks in a smaller plastic region. Therefore the region containing the distribution of microcracks, in the transverse direction, is smaller at –60°C than that at the same temperature in the rolling direction. This is due to the anisotropy properties of the material. In order to investigate which microstructure nucleated the wider and larger microcracks, the length against width of those microcracks were plotted. The results are shown in graphs 3.110, 3.111 and 3.112 for +25ºC, 0ºC and –60ºC respectively.

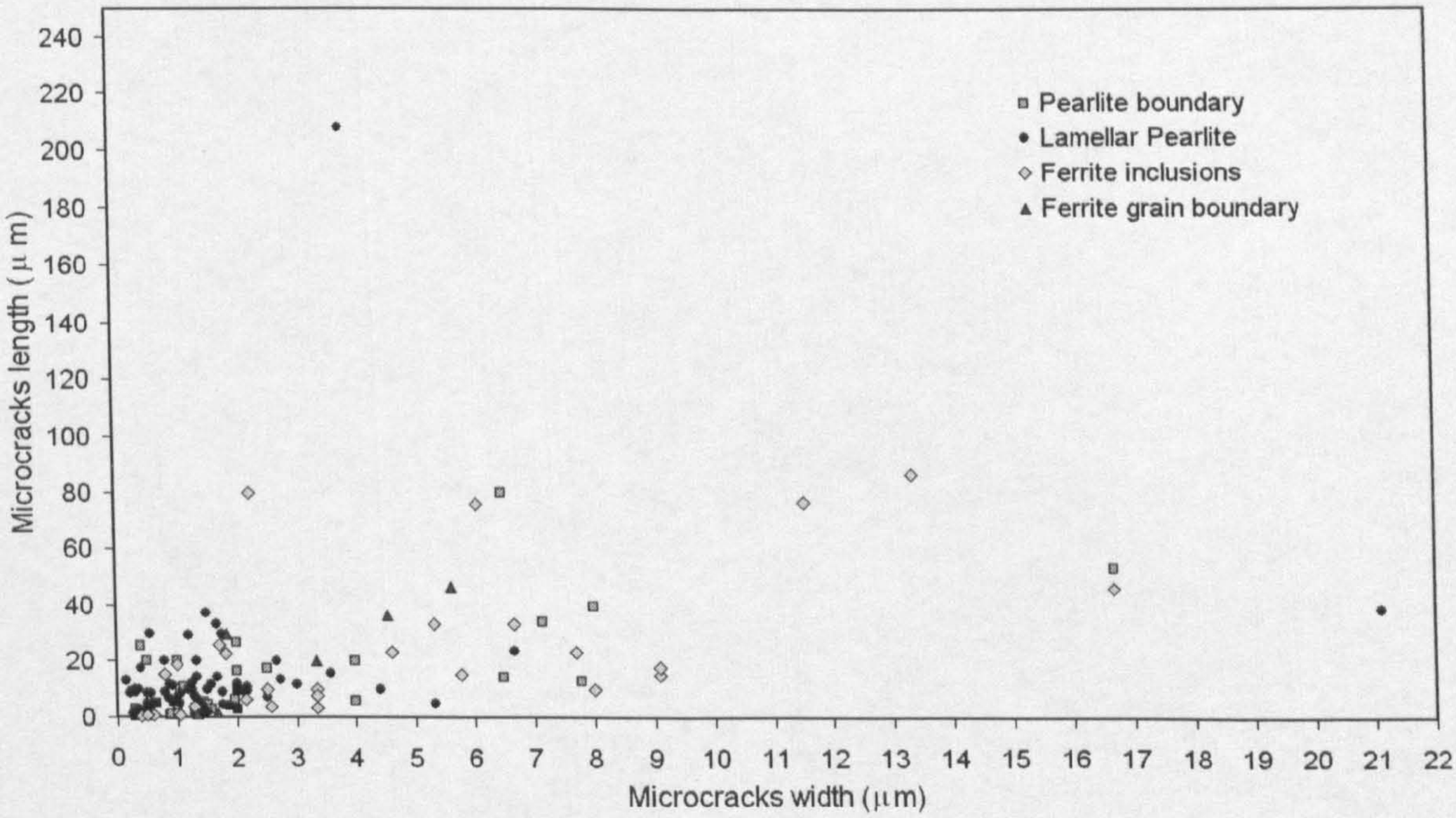

Figure 3.110 – Plot of the width vs length of microcracks at +25ºC in the transverse direction of the plate steel.

In figure 3.110 we can see that the longest and widest microcrack at test temperature of +25ºC was developed by the lamellar pearlite microstructure. The size of the longest microcrack has a length of 207 μm and the widest microcrack has a width of 21 μm. The pearlite boundary and ferrite grains inclusions nucleated wide microcracks as well but the length of those microcracks is less than 50% of the longest microcrack nucleated by the lamellar pearlite microstructure. The ferrite grains boundary micro features did not nucleate microcracks of significant size. Based on the present analysis it can be seen that the dominant microstructure for the creation of microcracks of critical size at +25ºC is the lamellar pearlite.

Figure 3.111 shows the plot of width against length of microcracks at 0ºC. In this graph we observe four microstructures for the initiation of fracture, as at room temperature. The lamellar pearlite microstructure nucleated the longest and widest microcrack. From this figure it can be

seen that, as at room temperature, the lamellar pearlite micromechanism is the dominant microstructure for the nucleation of the largest microcracks.

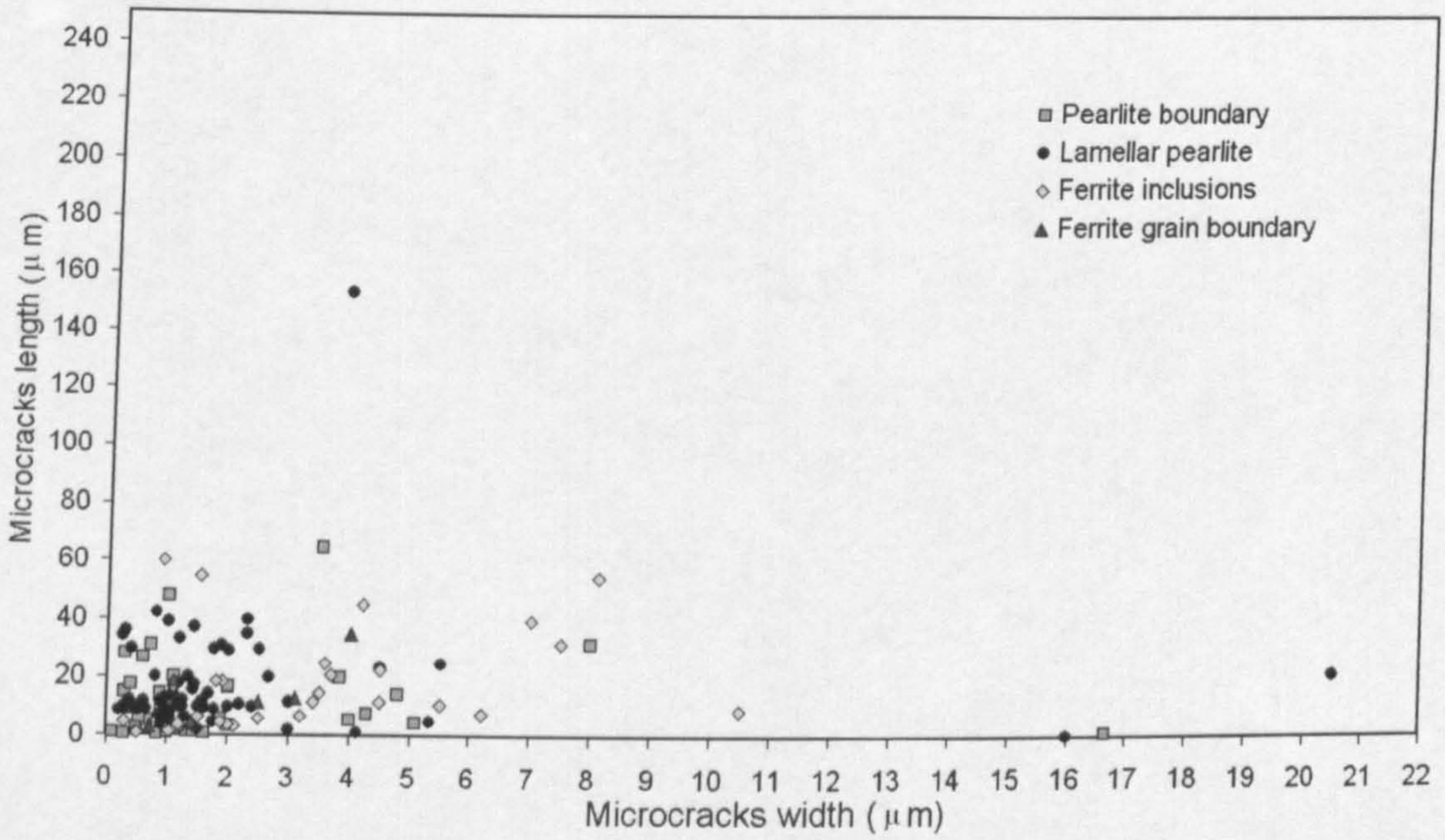

Figure 3.111 – Plot of the width vs length of microcracks at 0ºC in the transverse direction of the plate steel.

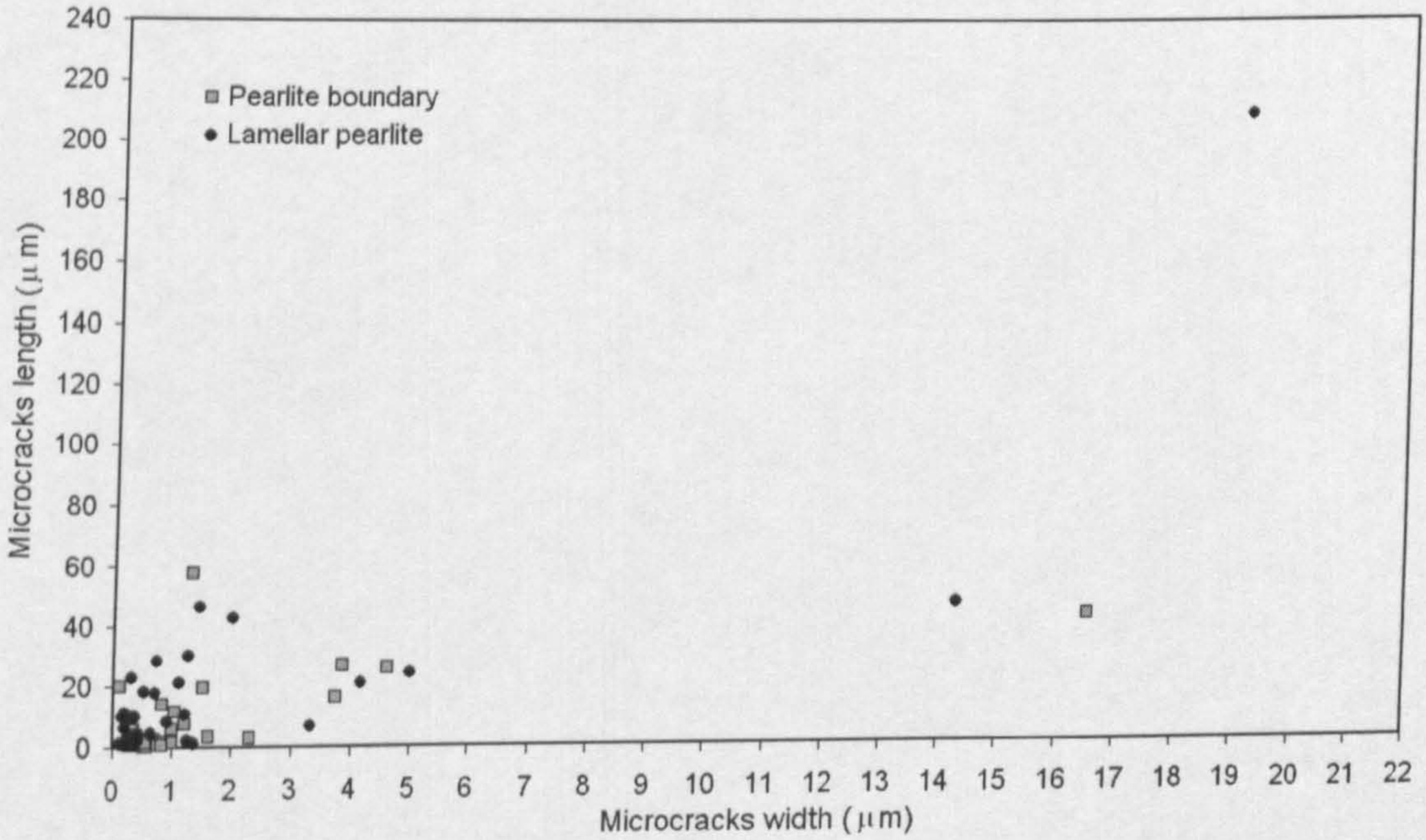

Figure 3.112 – Plot of the width vs length of microcracks at –60ºC in the transverse direction of the plate steel.

At a test temperature of –60°C, the plot of width against length was shown in figure 3.112. In this figure we can see that the longest and widest microcrack was developed by the lamellar pearlite microstructure. The longest microcrack has a length of 210 μm and the width of this microcrack was 16.5 μm. The present analysis shows that there is a competition of both microstructures for the nucleation of microcracks with length smaller that 60 μm, but the lamellar pearlite microstructure nucleates the longest and widest microcracks. This supports the proposal that the lamellar pearlite microstructure can be considered the dominant one for the nucleation of cleavage fracture in the transverse direction of a Grade A ship plate steel. As mentioned before, at this temperature we have the sufficient conditions for cleavage fracture to occur. This suggests that at any lower temperature that –60°C the same micromechanisms will be developed for the initiation of cleavage fracture.

Based on the results of figures 3.107, 3.108 and 3.109 and on the results of sections 3.6.6 and 3.6.7 it can be concluded that the microstructures for cleavage fracture initiation are different for the rolling and transverse direction of Grade A ship plate steel. It can be concluded as well that in the rolling direction of the plate steel there is a competition between four different microstructures for the nucleation of cleavage fracture, and they remain in the transition region of the curve. But for the transverse direction only the lamellar pearlite microstructure and the pearlite boundary microstructures can initiate cleavage fracture, therefore in the present analysis we have observed the nucleation of microcracks at each test temperature. Now it is essential to define in the formation of microcracks, if the critical event is the nucleation or the propagation of microcracks.

Nucleation depends solely on the local stresses at the tip of a slip or twin band and therefore on the effective shear stress (equivalent to the difference between the applied shear stress and that opposing dislocation motion) acting on a band, but is unaffected by a superimposed stress. (Smith, 1968). Growth is influenced by both the applied load and the localized stresses due to the inhomogeneous plastic deformation, and it is this the difference between the nucleation and growth processes that enables the critical event in the cleavage process to be determined (Smith, 1968).

Based on these definitions, it can be concluded that the critical event in the brittle fracture process is cleavage crack growth. Cottrell and Smith (Cottrell, 1948, Smith, 1968) states that the critical event in the formation of a microcrack is its growth and not its nucleation. In the analysis of cleavage fracture initiation microstructures in the present work, we analyzed the critical conditions prior to fracture propagation. This means that a high distribution of microcracks was created prior to the critical event which is the propagation of these microcracks. Therefore different microstructures can lead to microcracks propagation in the

present steel; microcracks subjected to the highest level of stresses and/or microcracks of critical size.

Simulation of fracture propagation in engineering structures with the finite element method has been the issue of much attention in last years because of the nature of metals. The important features in cleavage fracture modelling, for example the effect of grain size, the different microstructures for cleavage fracture initiation, the temperature, etc., should be implemented in models and be explainable provided that the model is sufficiently realistic. The grain size and the micro features distributed in the matrix of metals have a strong influence on the fracture properties of materials.

The aim of the present section was to analyze the microstructures for cleavage fracture nucleation in order to incorporate the micro features nucleating cleavage in finite element models. Therefore finite element simulations must include the real micro features that nucleate cleavage. In the present work, they are incorporated via the CAFE model (Chapter V). It can be seen that there is an agreement between the hypothesized microstructures for cleavage fracture and experimental work. In order to show that the proposed CAFE model is capable to simulate distributions of microcracks for the range of temperatures mentioned above, the experimentally measured distributions of microcracks are needed to validate the proposed model. The explanation about how the micro features nucleating cleavage fracture were incorporated in CAFE model is showed in chapter V.

3.7 Conclusions.

In the present section it can be seen that the microstructures for cleavage fracture initiation are different for the rolling and transverse directions. In the rolling direction, four microstructures for cleavage fracture nucleation were found at all test temperatures. But for the transverse direction, on the lower shelf, only two microstructures for cleavage fracture nucleation were found. It was found as well that there exists a competition between all the cleavage fracture microstructures for the nucleation of microcracks. As one of the purposes of the present research project is to simulate the distribution of cleavage fracture initiation points, it is very important to include in the model all four microstructures for cleavage fracture initiation found experimentally. The present work also showed that there exists transferability for the nucleation of microcracks from quasi static tests (four point double notch bend specimens) to high strain rate tests (impact Charpy tests) as the same microstructures for the nucleation of microcracks was found in the rolling direction of the plate steel.

For finite element simulation, the hardening curves of the steel are needed. These curves were obtained in the present section from room to very low temperatures. Notch tensile tests were performed as well in this chapter to measure damage model parameters of the constitutive Rousselier ductile damage model used in the CAFE model to simulate the ductile part in the model.

It can be concluded that extensive experimental work was carried out in order to measure the mechanical properties of the material and to obtain the damage model parameters. This relevant data will be used in the following sections of this work for numerical simulation. New findings were found as well in the present research work, which contribute to the field of knowledge.

3.8 References.

ASM INTERNATIONAL (1987) Modes of Fracture. *Metals Handbook Ninth Edition, Volume 12 Fractography*, 12-71.

AYVAR, S. S., HASHEMI, S. H., HOWARD, I. C. & YATES, J. R. (2006) An experimental and finite element study of the ductile tearing characteristics of high-toughness gas pipeline steel. *Preceeding of the international congress on fracture hold by the University of Southampton*, 259.

BOGDAN, W., JASON, P. P. & ROBERT, H. D. J. (2006) Temperature dependence of Weibull stress parameters: Studies using the Euro-material. *Engineering Fracture Mechanics,* 73, 1046-1069.

BORDET, S. R., KARSTENSEN, A. D., KNOWLES, D. M. & WIESNER, C. S. (2004) A new statistical local criterion for cleavage fracture in steel. Part II: application to an offshore structural steel. *Engineering Fracture Mechanics,* 72, 453-474.

BORDET, S. R., KARSTENSEN, A. D., KNOWLES, D. M. & WIESNER, C. S. (2005) A new statistical local criterion for cleavage fracture in steel. Part I: model presentation. *Engineering Fracture Mechanics,* 72, 435-452.

BRITISH STEEL LIMITED SWINDEN TECHNOLOGY CENTRE HEALTH AND SAFETY EXECUTIVE (2000-2001) Offshore Technology Report OTO-2000 001.

BRITISH STEEL PLC FOR THE HEALTH AND SAFETY EXECUTIVE (1997) Literature Review of the Fracture Properties of Grade A Ship Plate: OTH 95 489.

CHEN, J. H., HU, S. H. & WANG, G. Z. (2001) Mechanism of detrimental effects of carbon content on cleavage fracture toughness of low-alloy steel. *Metallurgical and Materials Transactions,* 32A, 1081-1091.

CHEN, J. H., LI, Z. & WANG, G. Z. (2003) Effect of tensile prestrain on the notch toughness of low-alloy steel. *Metallurgical and materials transactions* 34-4.

CHEN, J. H., WANG, G. Z., YANG, C., MA, H. & L., S. (1997) Advances in the mechanism of cleavage fracture of low alloy steel at low temperature: Part I: critical event. *International Journal of Fracture,* 83, 105-120.

COTTRELL, A. H. (1948) Dislocation theory of yielding and strain aging of iron. *Proc. Phys. Soc.*, LXII, 49-62.

CURRY, D. A. (1981) A micromechanistic approach to the warm pre-stressing of ferritic steels. *international Journal of Fracture,* 17, 335-343.

DOWLING NORMAN, E. (2007) Mechanical behavior od materials, Third Edition. *Pearson, Prentice Hall*, 89.

EN ISO 14556:200 BRITISH STANDARDS (1987) Method for Precision Determination of Charpy V-Notched Impact energy for Metals. BS131-6.

GRIFFITHS, J. R. & OWEN, D. R. J. (1971) An elastic-plastic stress analysis for a nothed bar in plane strain bending. *J. Mech. Physics Solids,* 19, 419-431.

HASHEMI, S. H., HOWARD, I. C., YATES, J. R. & ANDREWS, R. M. (2004) Micro-mechanical damage modeling of notched bar testing of modern line pipe steel. *in ECF15. Advance fracture mechanics for life and safety assesments. EMAS Publications, Stockholm, Sweden.*

HAUSILD, P., BERDIN, C. & BOMPARD, P. (2004) Prediction of cleavage fracture ofr a low-alloy steel in the ductile-to-brittle transition temperature range. *Materials Science and Engineering,* 391-A, 188-197.

KNOTT, J. F. (1973) Fundamentals of fracture mechanics *Butterworths, London.*

LLOYDS REGISTER OF SHIPPING Marine Classification Society. 1-11 Neville Road, Croydon Surrey, UK.

MATERIALS LABORATORY, E. S. N. R., CROYDON, CR0 2DS (1997) Investigation of Toughness Properties of Grade A Ship Plate. 97-3353.

MICRO-MEASUREMENT DIVISION Precision Strain Gages, Measurements Group, Notrh Carolina.

MUDRY, F. (1987) A local approach to cleavage fracture. *Nuclear Engineering and Design,* 105, 65-76.

SHTERENLIKHT, A., HASHEMI, S. H., YATES, J. R., HOWARD, I., C. & ANDREWS, R. M. (2005) Assessment of an instrumented Charpy impact machine. *International Journal of Fracture,* 132, 81-97.

SMITH, E. (1968) Cleavage fracture in mild steel. *The International Journal of Fracture Mechanics,* 4, 131-145.

STRNADEL, B. & HAUSILD, P. (2008) Statistical scatter in the fracture toughness and Charpy impact energy of pearlitic steel. *Materials Science and Engineering,* A - 486, 208-214.

TRANSPORTATION SAFETY BOARD OF CANADA (2002) Marine Investigation Report, Report Number M02L0021, Hull Fracture Bulk Carrier Lake Carling Gulf of St. Lawrence, Quebec.

WANG, G. Z. & CHEN, J. H. (1999) Effect of notch geometry on the local cleavage fracture stress. *Fatigue Fract. Engng Mater. Struct.,* 22, 849-858.

WANG, G. Z. & CHEN, J. H. (2000) A statistical model for cleavage fracture in notched specimens of C-Mn steel. *Fatigue Fract Engng Mater Struct,* 24, 451-459.

WANG, G. Z., LIU, Y. G. & CHEN, J. H. (2003a) Investigation of fracture initiation in notched specimens of a C-Mn steel with carbides and inclusions. *Materials Science and Engineering,* A369, 181-191.

WANG, G. Z., LIU, Y. G. & CHEN, J. H. (2004a) Investigation of cleavage fracture initiation in notched specimens of a C-Mn steel with carbides and inclusions. *Materials Science and Engineering,* A369, 181-191.

WANG, G. Z., REN, X. C. & CHEN, J. H. (2004b) Effects of loading rate on fracture behavior of low-alloy steel with different grain sizes. *Metallurgical and materials transactions,* 35A, 1775-1778.

WANG, G. Z., WANG, J. G. & CHEN, J. H. (2003b) Effects of geometery of notched specimens on the local cleavage fracture stress of C-Mn steel.

WANG, G. Z., WANG, J. G. & CHEN, J. H. (2003c) Effects of geometry of notched specimens on the local cleavage fracture stress σf C-Mn steel. *Engineering Fracture Mechanics,* 70, 2499-2512.

WANG, G. Z., WANG, Y. L. & CHEN, J. H. (2005a) Effects of loading rate on the local cleavage fracture stress in notched specimens *Engineering Fracure Mechanics,* 72, 675-689.

WANG, G. Z., WANG, Y. L. & CHEN, J. H. (2005b) Effects of loading rate on the local cleavage fracture stress σf in notched specimens. *Engineering Fracture Mechanics,* 72, 675-689.

WILLIAM, F. H. (2005) Mechanical behavior of materials. *Cambridge University Press,* p62.

WILLIAN, K., SZAROLETTA & NANCY, L. D. (2002) Four point bending: A New Look. *Preceeding of the 2002 American Society for Engineering Education annual Conference and Exposition Copyright 2002, American Society for Engineering and Education.*

WU, S. J. & KNOTT, J. F. (2004) On the statistical analysis of local fracture stresses in notched bars. *Journal of the Mechanics and Physics of Solids,* 52, 907-924.

XIANGQIAO, Y. & WEISHENG, L. (1993) Research into fracture behavior of mild steel in Charpy v-notch impact test. *International Journal of Fracture,* 59, R75-R79.

YOUNG-ROC IM, B.-J. L., YONG JUN OH, JUN HWA HONG, HU-CHUL LEE (2004) Effect of microstructure on the cleavage fracture strength of low carbon Mn-Ni-Mo bainitic steels. *Journal of Nuclear Materials,* 324, 33-40.

Chapter IV

Micromechanical modelling and calibration of damage model parameters

The present chapter shows the micromechanical damage modelling of smooth and notch tensile tests with different constraint level for calibration of Gurson's damage model parameters. Finite element simulations of Charpy tests are also shown in the present section. The results showed that the true stress-strain curve of Grade A plate steel was measured appropriately as it agrees well with the experimentally obtained stress-strain curve. Transferability between smooth and notch tensile tests with different constraint level was obtained, but q_2 parameter had to be modified from 0.85 to 0.80 to correlate numerical data with experimental work. This shows that not complete transferability of Gurson's damage model parameters for quasi static and high strain rates tests was obtained

4.1 Micro–mechanical computer modelling of tensile tests.

As already mentioned in the literature review, the Gurson and Rousselier damage model are some of the most used ductile damage models for modelling fracture propagation. In the present section, the Gurson–Tvergaard–Needleman (GTN) model, which incorporates ductile damage theory, was chosen for modelling because the model for isotropic materials has been incorporated into the ABAQUS Finite Element Program (ABAQUS 6.5, 2004) and its use is straightforward. The model reads typically the yield potential of the equations discussed in section 2.2.4. As explained in previous sections, the model allows the interaction between the elastic–plastic stress and strain field and the softening effects due to ductile damage and crack growth.

Finite element simulations of smooth and notch tensile tests have been done mainly to calibrate Gurson's damage model parameters and to investigate transferability of damage parameters between quasi static tensile tests with different constraint level and Charpy tests. The tensile tests were simulated with the finite element program ABAQUS Explicit (ABAQUS 6.5, 2004) because in ABAQUS Explicit, the element deletion technique is provided. So damage and/or dead elements are removed from the analysis where the failure criterion is locally reached, this simulates crack propagation through the microstructure. Element deletion can be visualized as the crack propagation path in a finite element model. These properties of ABAQUS Explicit were vital for the choice of this program for finite element simulation of fracture initiation and propagation.

As shown in section 2.2.4, the GTN model requires seven material constants which must be calibrated during the simulation process to be characterized as material damage model parameters. The parameters are: q_1, q_2, q_3, f_o, f_c, f_f and L_c. The initial void volume fraction, was estimated using the Franklin's formula (Franklin, 1969). The use of Franklin's formula (equation 2.12, section 2.2.4) resulted in an initial void volume fraction value of $f_o = 7.8218^{-4}$ for Grade A plate steel with MnS inclusions. This value is assumed to be the initial void volume fraction of the test material. But in order to correlate experimental vs numerical simulation data, the initial void volume fraction had to be fitted by trial and error.

The best fitted value for tensile tests in the present work is $f_o = 0.001$. It can be seen that the initial void volume fraction obtained with Franklin's formula is very different from the fitted value which resulted in a better correlation of experimental against numerical data. Bernaur and Hashemi found the same trend (Bernaur and Brocks, 2001, Hashemi et al., 2004). Due to time constraint no further research work about this was done.

The relative density (ratio of solid volume to total volume of material), was calculated with equation (2.15, section 2.2.4) which gave a value of $r = 0.9979$. Typical values of q parameters, as proposed by Tvergaard (Tvergaard, 1981) and explained in section 2.2.4 are: $q_1 = 1.5,\ q_2 = 1,\ q_3 = 2.25$ for ferritic steels, these values were used to start the finite element simulations.

The critical mesh size, L_c, and the final void volume fraction were determined by a trial and error procedure until the model response matched the experimental data in each set of test samples. This parameter can be measured on fracture surfaces of broken specimens; this is the distance between the large void spacing. L_c can be as well calculated by trial an error. The value of L_c is in the range of distance between large microvoids as shown in figure 3.102 (section 3.6.6). As mentioned above, the damage parameter q_2 and the initial void volume fraction f_o, were tuned for better correlation with experimental data.

4.1.1 Calibration and transferability of micro–mechanical damage parameters with smooth tensile tests.

Following the recommendations of Bernaur and Brocks (Bernaur and Brocks, 2001) for the calibration of damage model parameters with tensile test data. The authors found that the load against elongation of tensile tests data is not a suitable measure for adjusting numerical with experimental data in order to determine damage parameters of the damage models. The reduction of diameter is a much more reliable quantity for this task (load against diametral contraction). Based on this research work, the experimentally measured load–diametral contraction data were used for the calibration of material damage parameters.

Due to symmetry, only one quarter of the tensile bars was simulated. For this purpose a 3D finite element model was created using C3D8R 8–node reduced integration finite elements. The model consisted of 10647 finite elements and 12034 nodes. The experimentally measured mechanical properties of the plate steel, reported in tables 3.3 and 3.3 for the rolling and transverse direction respectively and the true stress–strain curves for rolling direction (figure 3.6) and transverse direction (figure 3.7), determined by uniaxial tension, were included in the finite element model to account for strain hardening. Figure 4.1 shows the finite element model of the smooth tensile test and the zone where the damage model was applied.

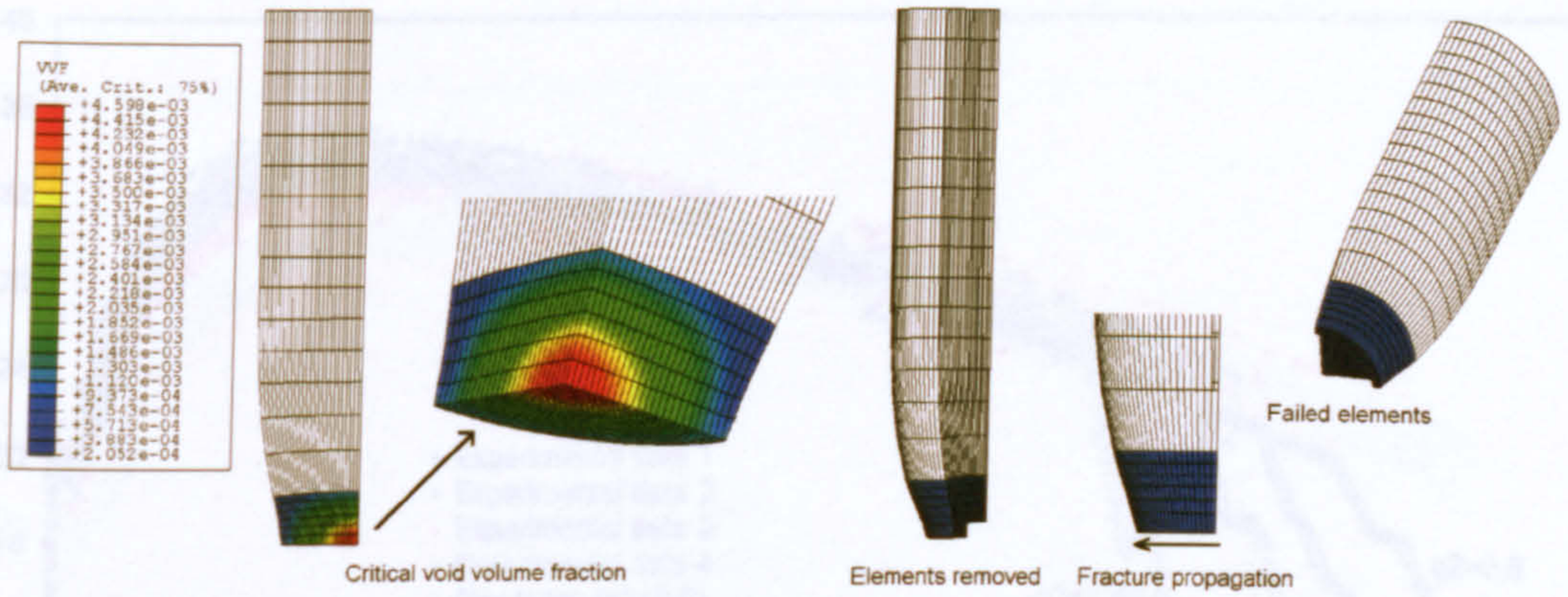

Figure 4.1 – 3D simulation of a quarter of a smooth tensile test

In Gurson's model, fracture starts when the void volume fraction reaches a critical value (as shown in figure 4.1) which simulates the state when the cavities link. This process is simulated in the finite element by the elimination of the damage elements to model the fracture propagation path. Figure 4.1 shows the critical void volume fraction (the red region in the centre of the specimen) and the elements removed in the centre of the smooth tensile bars due to the high triaxiality. From the FE analysis, it was found that the model was not sensitive to q_3 variation. However the model is strongly sensitive to the variation of q_1 and q_2 parameters. The higher the values of q_1 and q_2 the sooner the failure occurred. This is shown in figures 4.2 and 4.3 for the set of plain bar tests. A similar trend was observed in notched tensile bars.

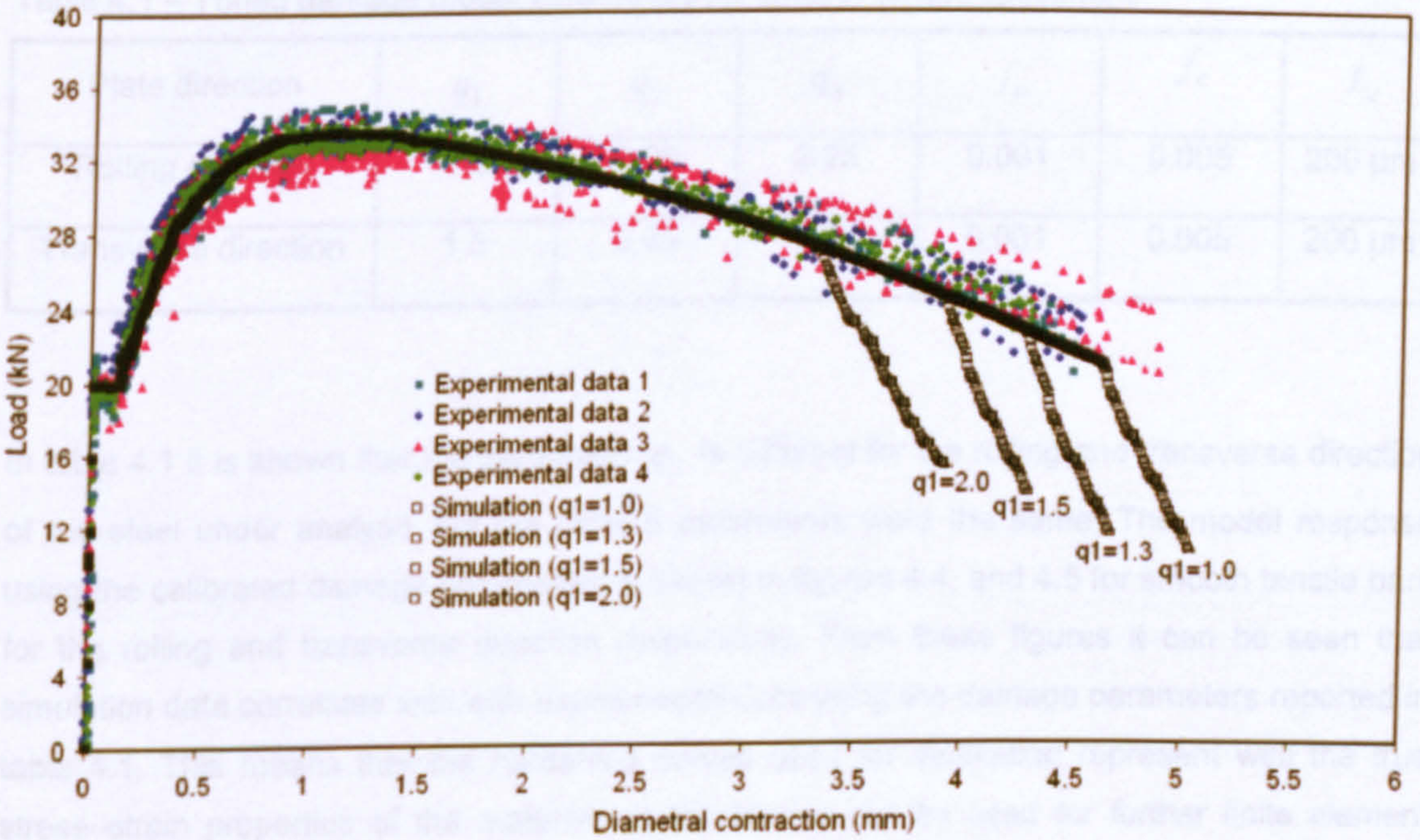

Figure 4.2 – Influence of the variation of q_1 Gurson's damage model parameter, with ($q_2 = 0.85$), in the rolling direction with smooth tensile tests.

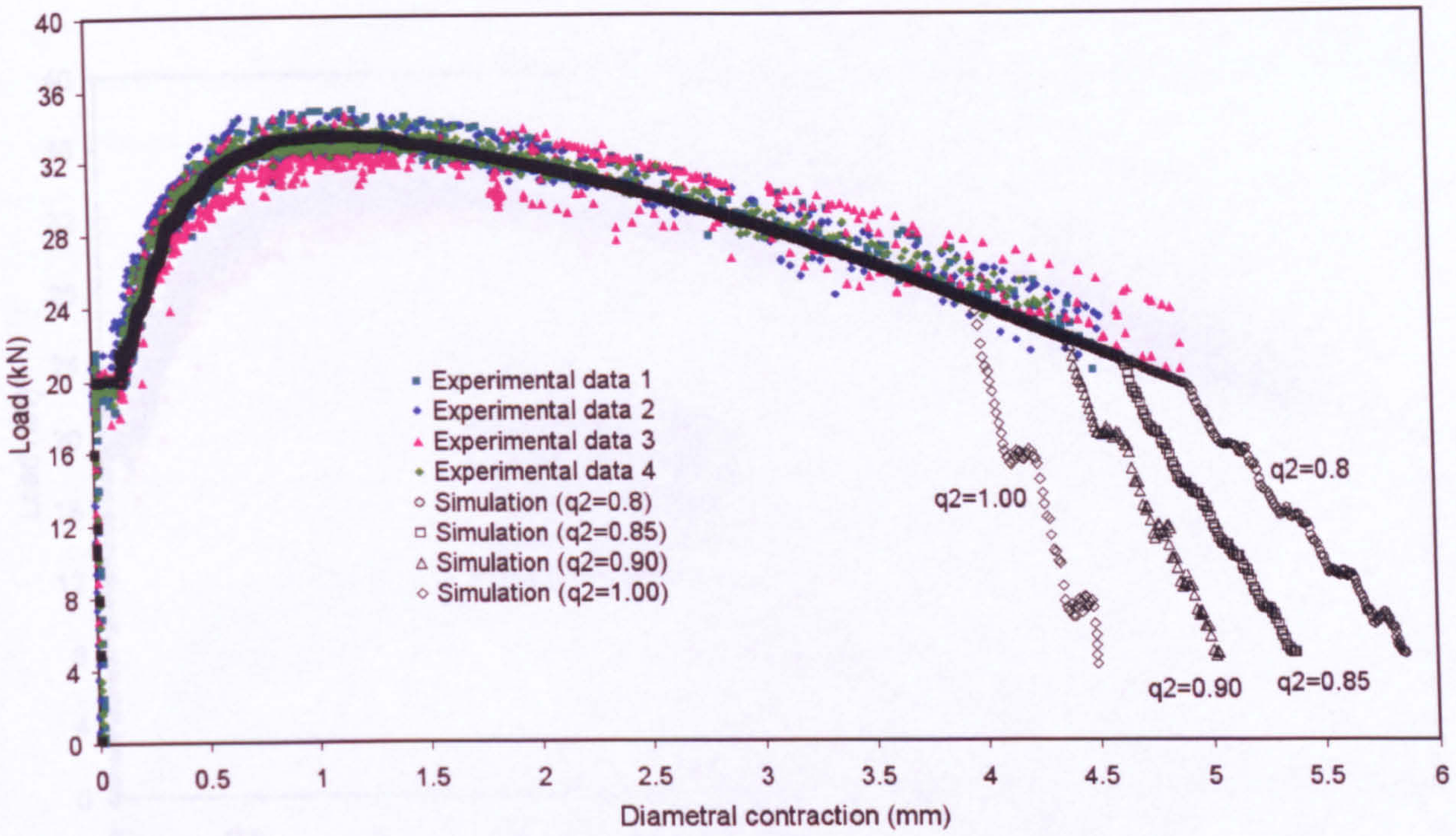

Figure 4.3 – Influence of the variation of q_2 Gurson's damage model parameter, with $(q_1 = 1.5)$, in the rolling direction with smooth tensile tests.

The tuning of the damage parameters was performed by comparison of experimental and computational load against diametral contraction data. The best tuned damage parameters are reported in Table 4.1 for the rolling and transverse directions of the plate steel.

Table 4.1 – Tuned damage model parameters for smooth tensile specimens.

Plate direction	q_1	q_2	q_3	f_o	f_c	L_c
Rolling direction	1.5	0.85	2.25	0.001	0.005	200 μm
Transverse direction	1.5	0.95	2.25	0.001	0.005	200 μm

In table 4.1 it is shown that the parameter q_2 is different for the rolling and transverse direction of the steel under analysis but the other 5 parameters were the same. The model response using the calibrated damage parameters is shown in figures 4.4, and 4.5 for smooth tensile bars for the rolling and transverse direction respectively. From these figures it can be seen that simulation data correlates well with experimental data using the damage parameters reported in table 4.1. This means that the hardening curves used for simulation represent well the true stress–strain properties of the material, so the curves can be used for further finite element simulations to characterize the toughness properties of the material.

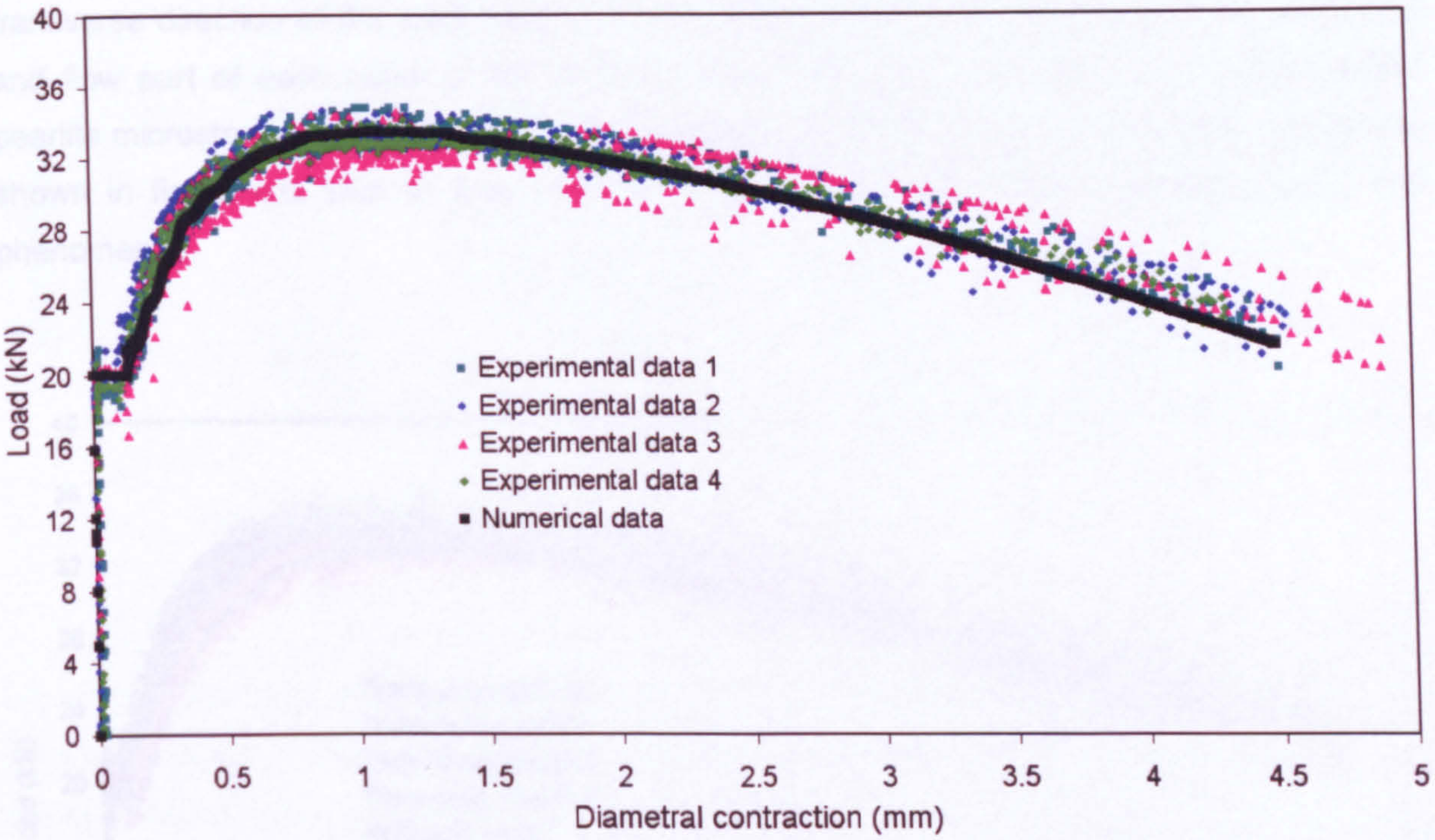

Figure 4.4 – Experimental vs numerical data of smooth tensile specimens in the rolling direction of the plate material.

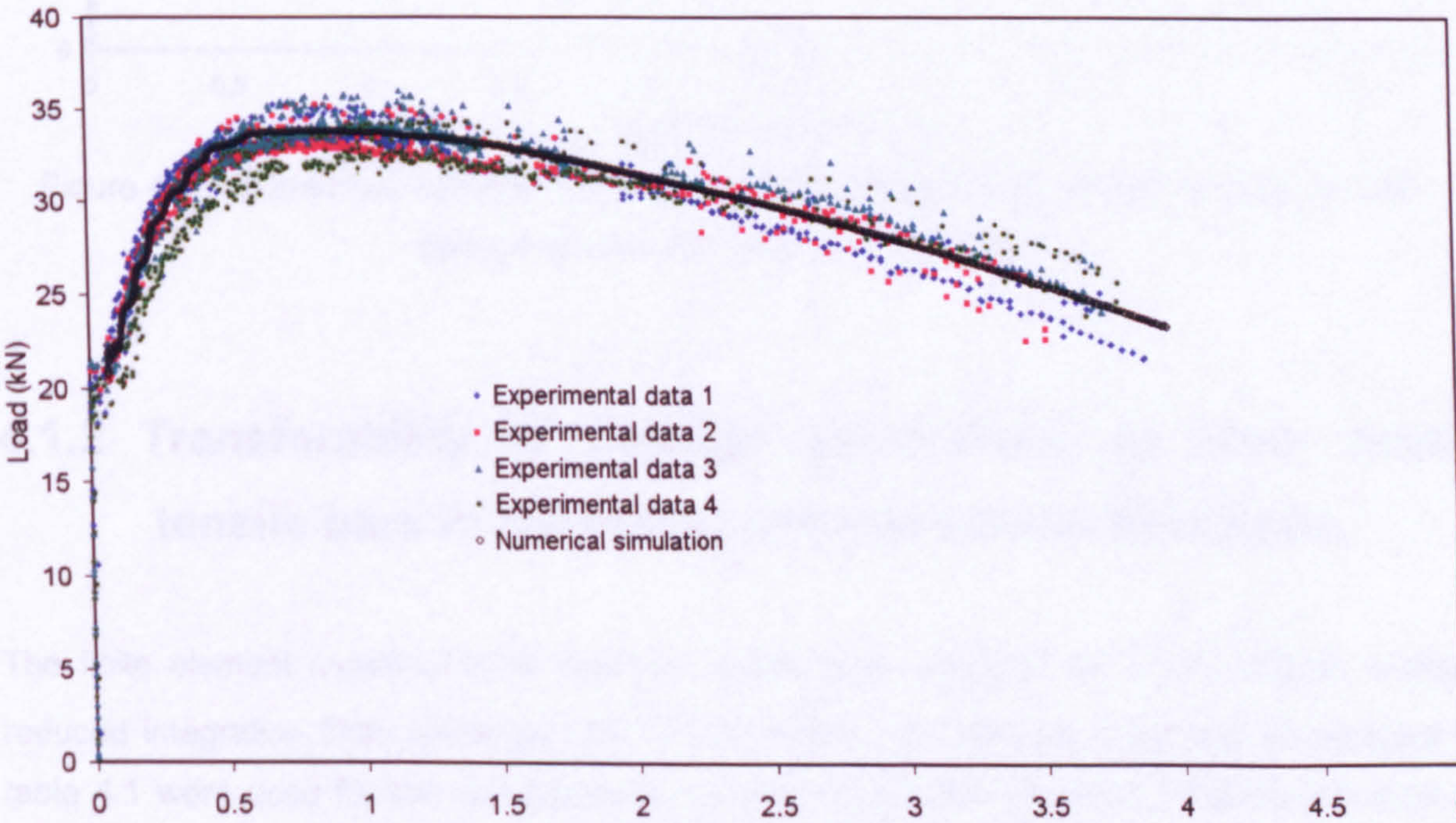

Figure 4.5 – Experimental vs numerical data of smooth tensile specimens in the transverse direction of plate material.

Figure 4.6 shows the effect of experimental vs numerical data of tensile tests in the rolling and transverse direction of the plate steel, the figure clearly shows the difference in the hardening and flow part of each curve of the material. The difference of orientation of the ferrite and pearlite microstructures for the rolling and transverse direction has strong influence on the data shown in figure 4.6. Due to time constraints, no further investigation was done about this phenomenon.

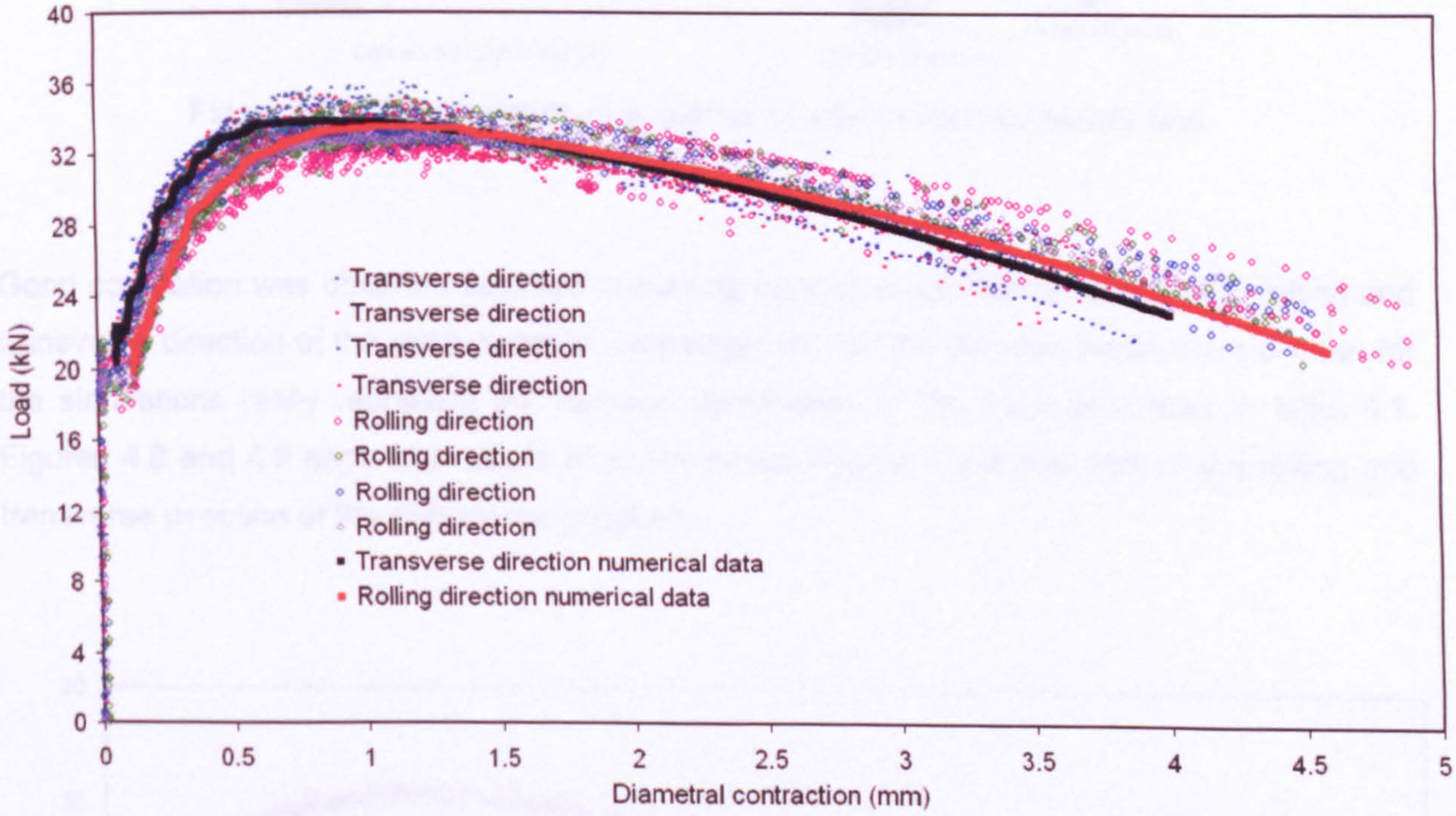

Figure 4.6 – Correlation between experimental and numerical data of tensile tests for both transverse direction and rolling direction.

4.1.2 Transferability of damage parameters on 6mm notch tensile bars in the rolling and transverse directions.

The finite element model of 6mm notched tensile tests consisted of 9776 C3D8R 8–node reduced integration finite elements and 11124 nodes. The calibrated damage parameters of table 4.1 were used for the simulations in the present section. Figure 4.7 shows the zone to which the damage model was applied. In this figure the damage elements were removed from the analysis.

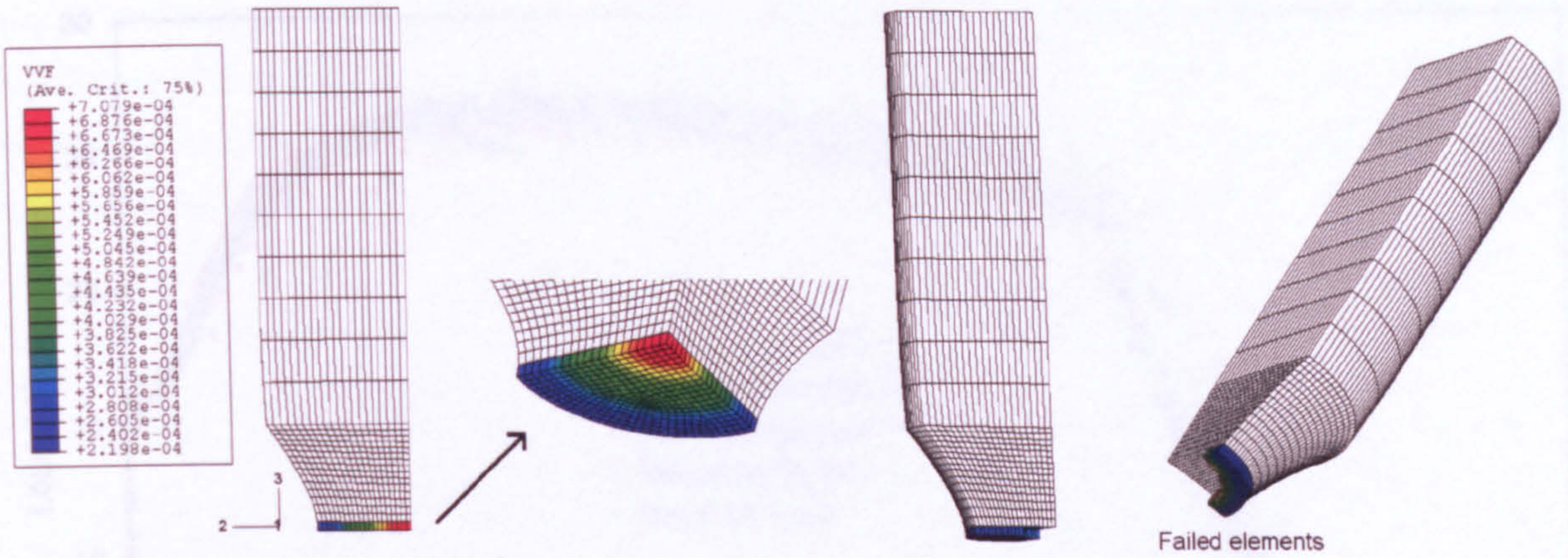

Figure 4.7 – 3D simulation of a quarter of a 6mm notched tensile test.

Good correlation was obtained between numerical against experimental data for the rolling and transverse direction of the plate material. This suggests that the damage parameters chosen for the simulations really represent the damage parameters of the steel described in table 4.1. Figures 4.8 and 4.9 show the results of experimental against numerical data in the rolling and transverse direction of the material respectively.

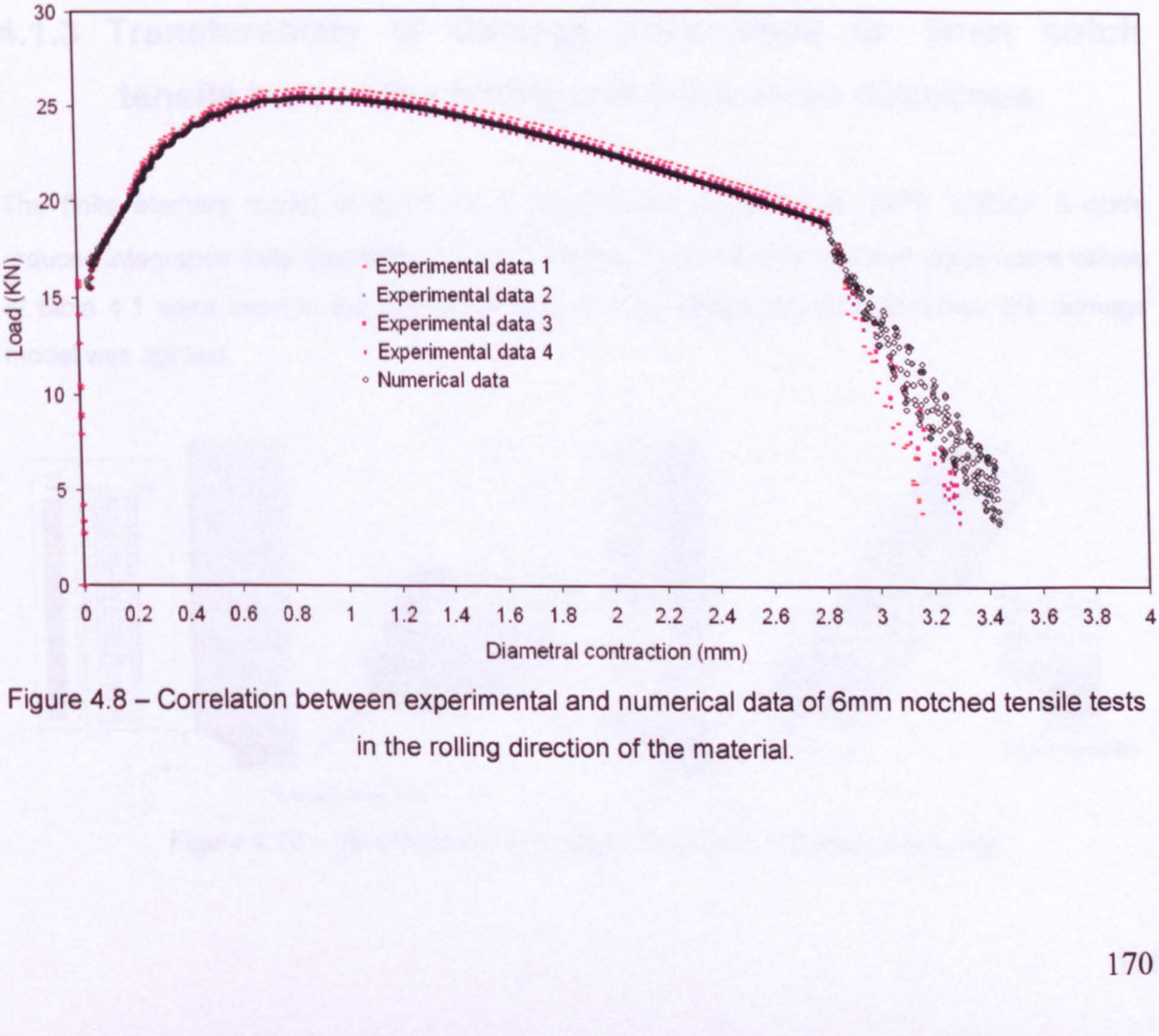

Figure 4.8 – Correlation between experimental and numerical data of 6mm notched tensile tests in the rolling direction of the material.

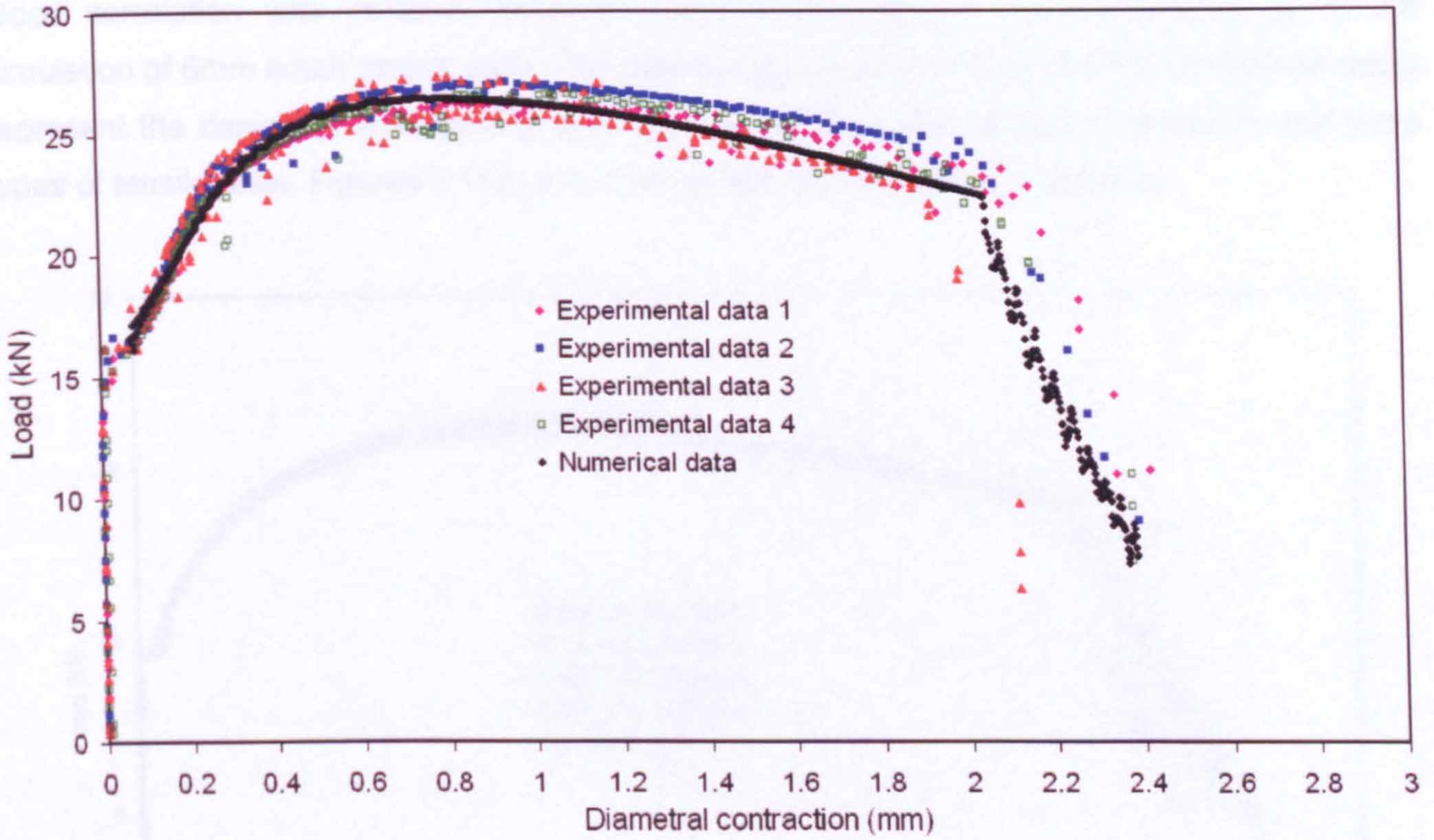

Figure 4.9 – Correlation between experimental and numerical data of 6mm notched tensile tests in the transverse direction of the material.

4.1.3 Transferability of damage parameters on 2mm notch tensile bars in the rolling and transverse directions.

The finite element model of 2mm notch tensile tests consisted of 7020 C3D8R 8–node reduced integration finite elements and 8115 nodes. The calibrated damage parameters values of table 4.1 were used in the simulation. Figure 4.10 shows the zone to which the damage model was applied.

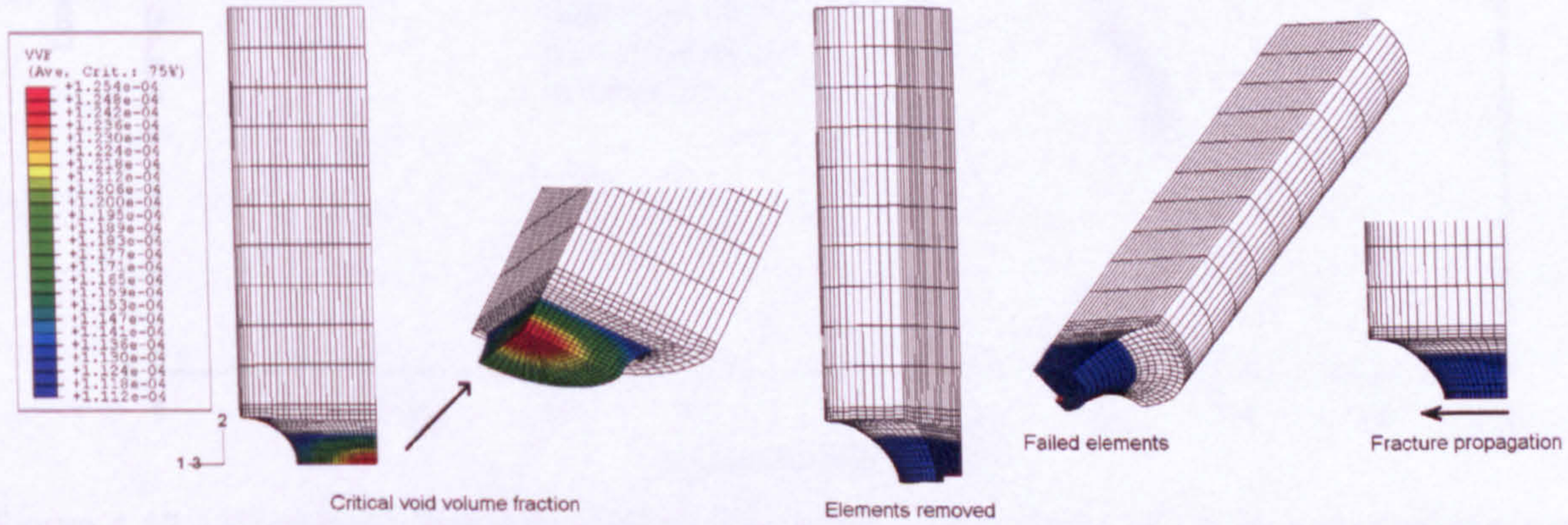

Figure 4.10 – 3D simulation of a quarter of a 2mm notched tensile test.

Good correlation was obtained between experimental against numerical data, as in the simulation of 6mm notch tensile tests. The damage parameters chosen for the simulations really represent the damage parameters of the steel as good correlation was obtained for the three types of tensile tests. Figures 4.11and 4.12 show the results of the simulations.

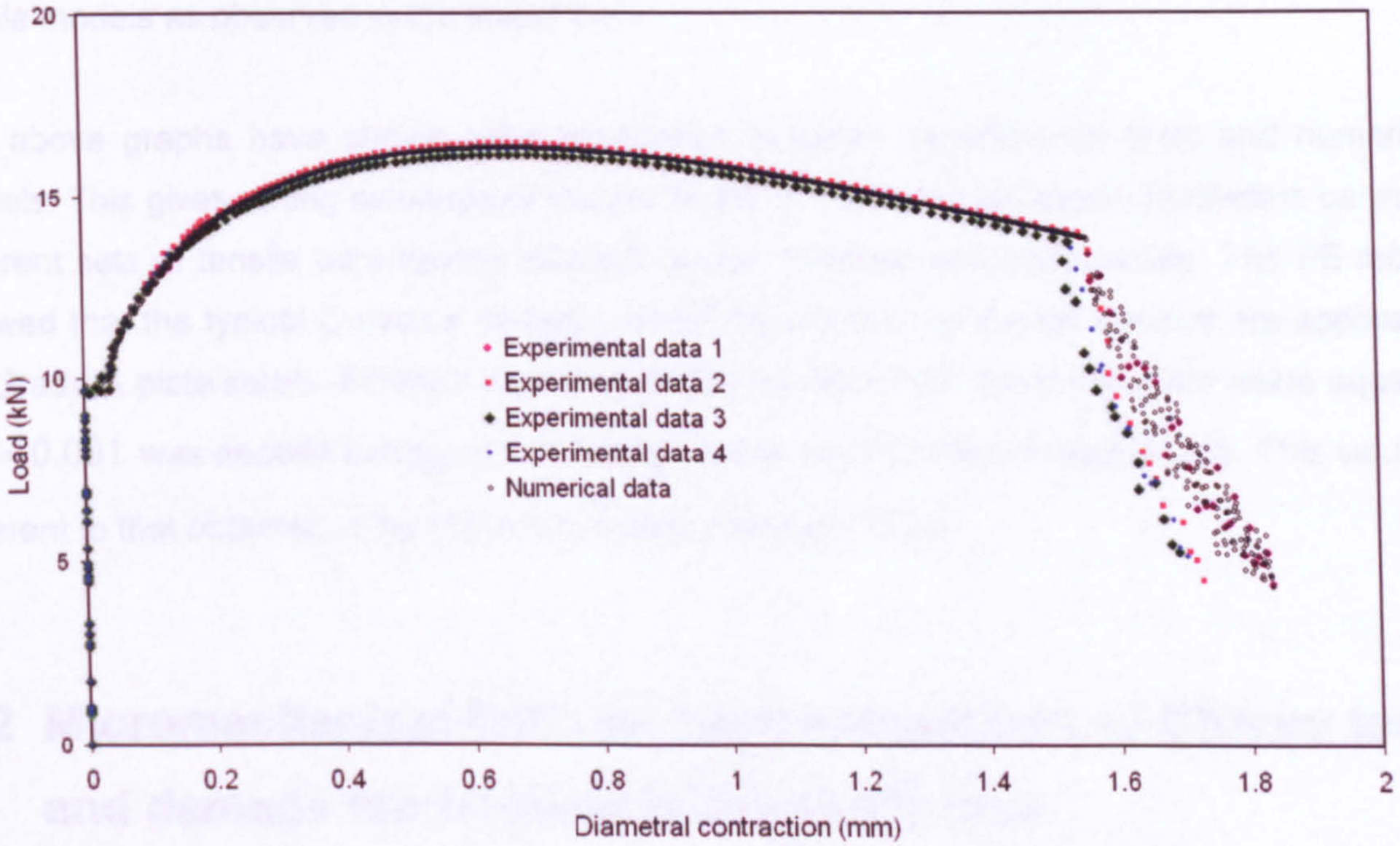

Figure 4.11 – Correlation between experimental and numerical data of notch tensile tests with a notch radio of 2mm in rolling direction of the plate steel.

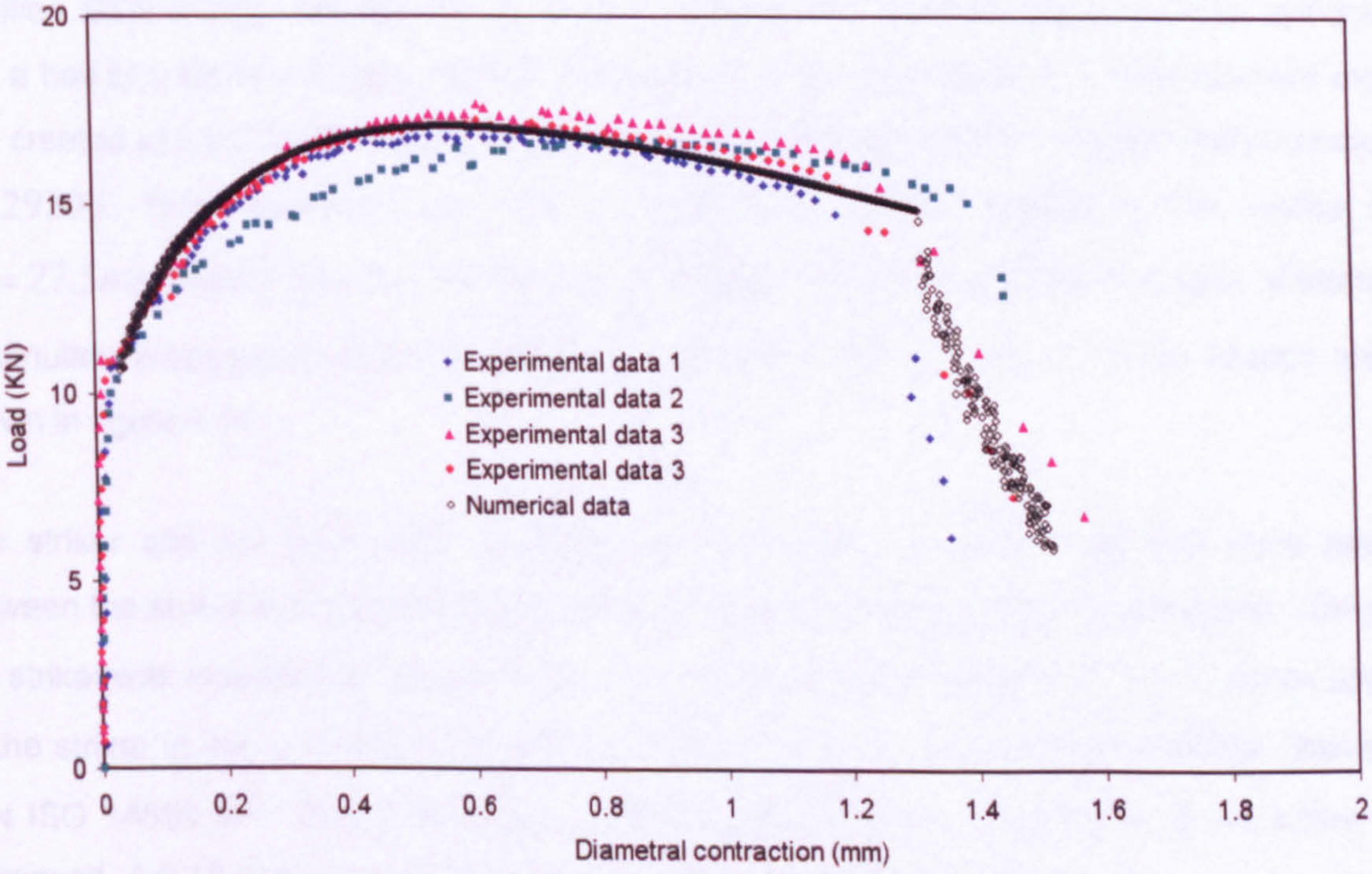

Figure 4.12 – Correlation between experimental and numerical data of notched tensile tests with a notch radio of 2mm in the transverse direction of the plate steel.

It can be seen that micro–mechanical model was able to effectively simulate the fracture of all tensile specimens having different geometries and constraint levels. From the finite element models of the tensile bars of figures 4.1, 4.7 and 4.10 it is clearly shown that the stress localization occurred in the centre of each tensile bars. Fracture propagation occurred from the centre of the specimens where the stress triaxiality is higher and propagated to the edge of the tensile models as observed in the tested bars.

The above graphs have shown good agreement between experimental tests and numerical models. This gives strong evidence of transferability of the damage model parameters between different sets of tensile bars having different gauge diameter and notch acuity. The FE model showed that the typical Gurson's damage model parameters for ductile fracture are applicable for Grade A plate steels. Finally it was shown that a critical void volume fraction value equal to $f_c = 0.001$ was needed to trigger the damage at the centre of tensile specimens. This value is different to that obtained using Franklin's model (Franklin, 1969).

4.2 Micromechanical finite element simulations of Charpy tests and damage model parameters calibration.

The finite element program ABAQUS Explicit 6.5 (ABAQUS 6.5, 2004) was used to simulate the Charpy tests. The finite element simulation was carried out, as in previous sections, with the modified GTN ductile damage theory at room temperature (section 2.2.4). Due to symmetry, only a half of a Charpy impact test was simulated. For this purpose a $3D$ finite element model was created using C3D8R 8–node reduced integration finite elements. The 3D model consisted of 29290 finite elements and 32964 nodes. All nodes located in the centre line $(y = 27.5mm \text{ plane})$ were constrained in y direction. The mesh size for the zone of interests to simulate propagation path was $0.20mm$. The finite element model of the Charpy test is shown in figure 4.13.

The striker and the anvil were modelled as rigid bodies. Contact conditions were applied between the striker and specimen and between the anvil and specimen. Only the first $20mm$ of the striker was modelled as shown in Fig. 4.13. An initial impact velocity of $5.5m/s$ was applied to the striker in the x direction. In order to apply the $19kg$, as specified by British Standards (EN ISO 14556:200 British Standards, 1987), by the hammer, the density of the striker was increased. A 0.15 friction coefficient was adopted for all contact surfaces.

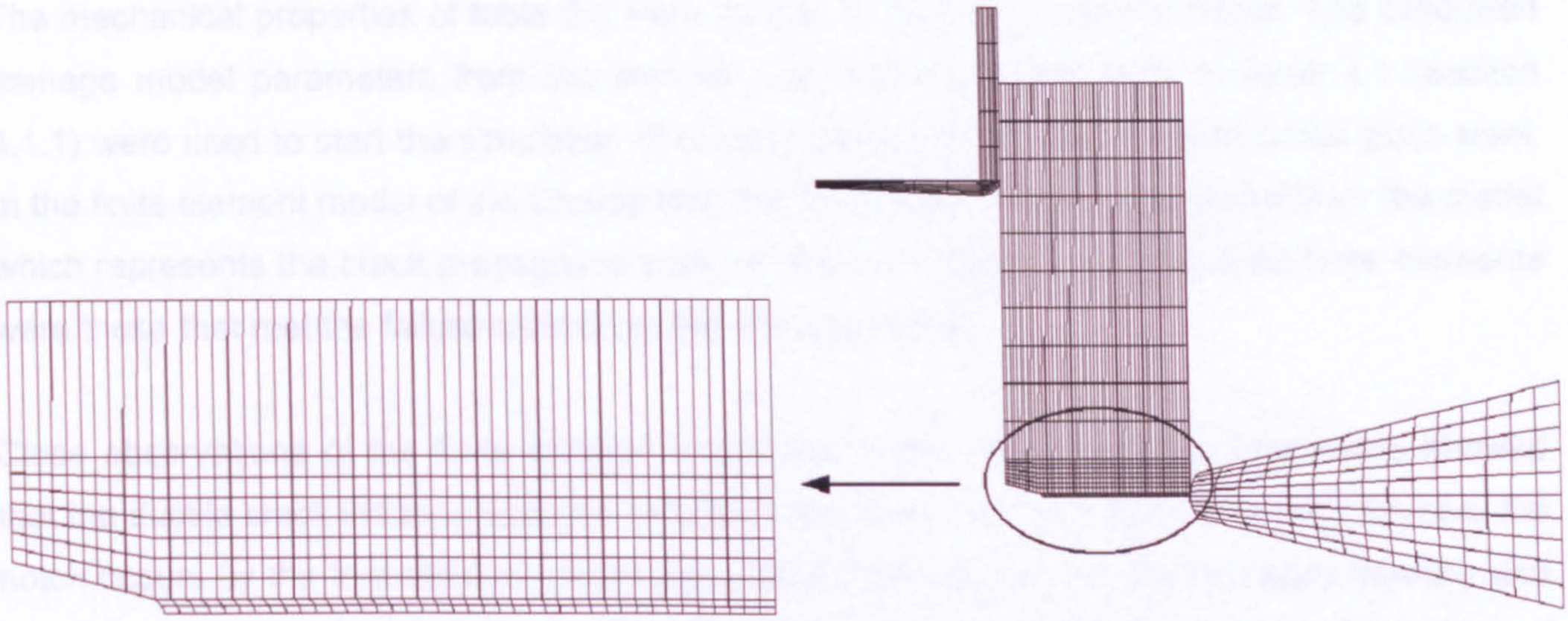

Figure 4.13 – 3D finite element model of a half of a Charpy test.

The contact pressure between hammer and specimen was output from the finite element model. This data was plotted against the hammer displacement. This was done by the definition of a reference node for the striker, so the contact pressure between specimen–striker and the displacement is transferred to the reference node.

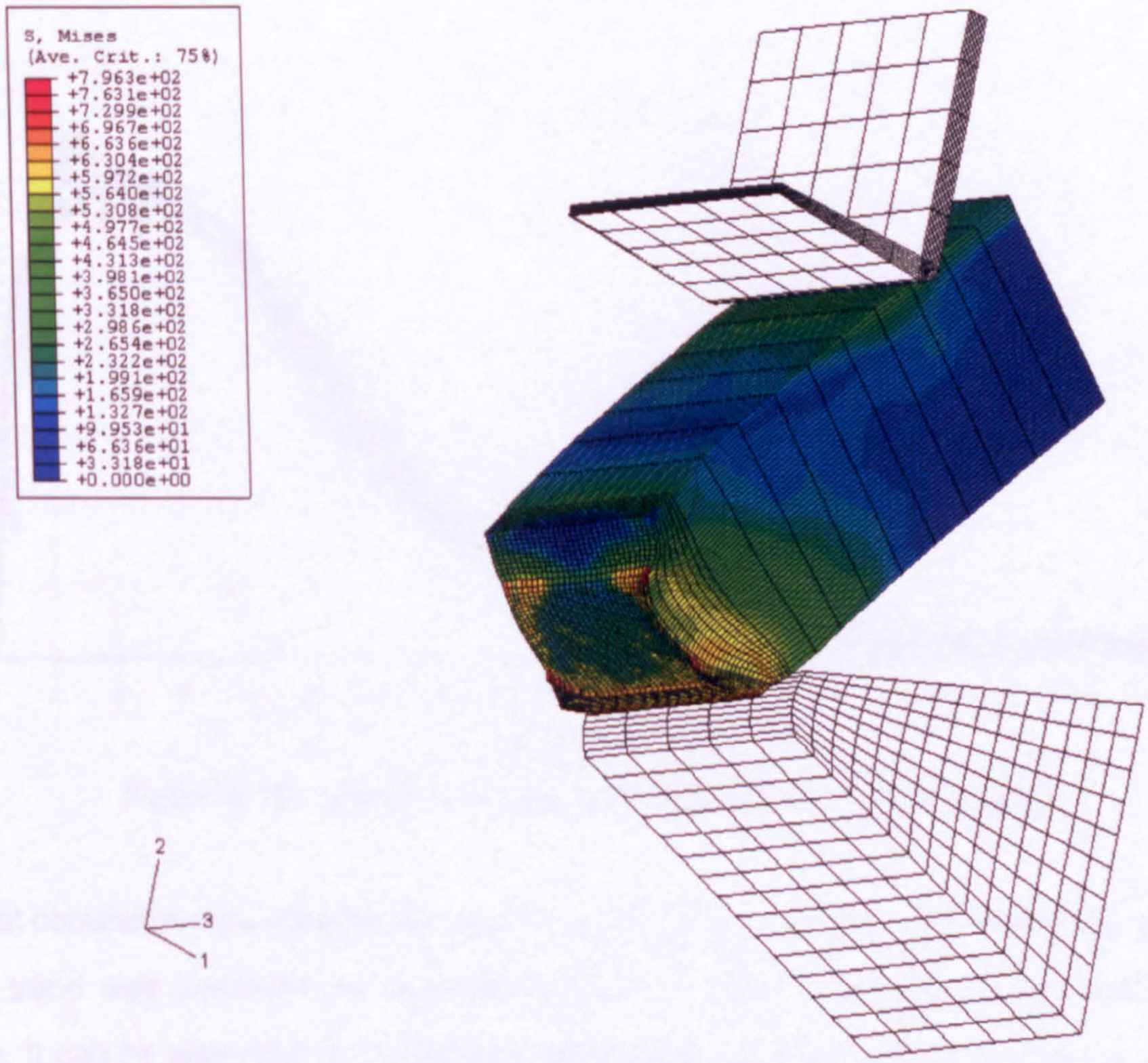

Figure 4.14 – Charpy finite element model.

The mechanical properties of table 3.2 were applied to the finite element model. The calibrated damage model parameters from the smooth and notched tensile tests of table 4.1 (section 4.1.1) were used to start the simulation of Charpy tests in the rolling direction of the plate steel. In the finite element model of the Charpy test, the failed elements were removed from the model which represents the crack propagation path, as shown in figure 4.14. The dead finite elements were those that met the failure criterion in the damage model.

Close observations of the finite element model and of the broken Charpy specimens showed that the ductile crack initiation appears parallel to the notch root and that crack initiation from the notch occurs by the formation of microvoids (figure 3.26, section 3.4.2). It spreads laterally and reaches the lateral surfaces by the formation of lips as shown in figure 4.14. The principal measurement of the Charpy test is the energy absorbed in fracturing the specimen. Figure 4.15 shows numerical vs experimental data. It can be seen that the model reproduced the fracture propagation region very well.

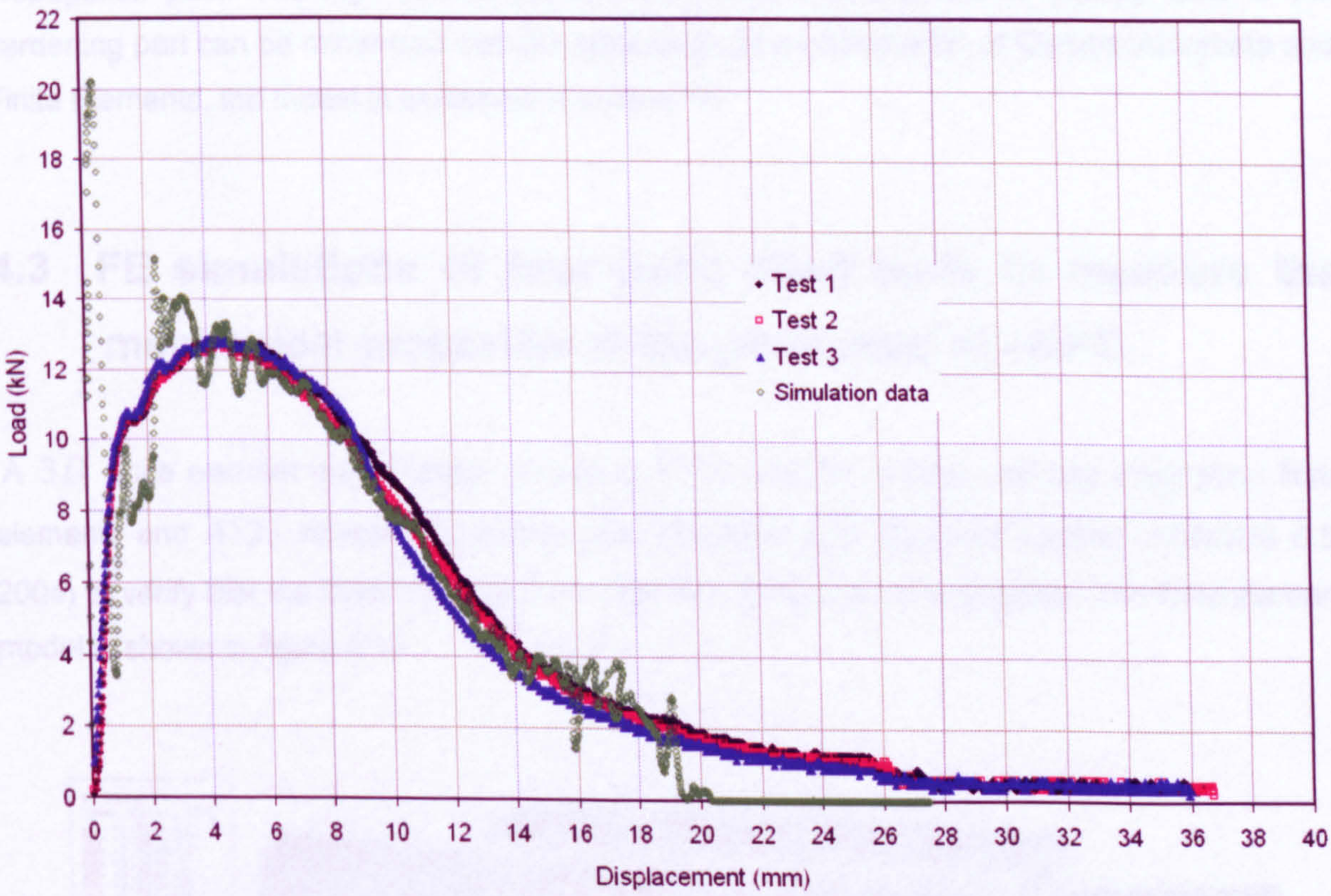

Figure 4.15 – Simulation vs experimental data of a Charpy tests.

The best correlation was obtained by modifying the q_2 parameter of GTN model to $q_2 = 0.8$, a similar trend was observed by Hashemi (Hashemi, 2004). The other 5 parameters do not change. It can be seen that q_2 parameter suffers only a variation of 0.05 which is close to the fitted value of 0.85 reported in table 4.1. From the present analysis and from literature review

(Hashemi, 2004) it can be seen that there exist transferability of Gurson's damage model parameters for tensile, quasi static, tests with different constraint level and for different kind of toughness specimens tested in quasi static conditions. But for high strain rate tests, the damage model parameter q_2 needs to be fitted to a smaller value in order to obtain correlation with experimental data.

The present finite element results of Charpy tests showed high oscillations in the hardening part of experimental data, this effect has been also reported elsewhere (Rossoll et al., 1998, Hashemi et al., 2004, Tronskar et al., 2001, Serizawa et al., 2001), these oscillations may be due to the fact that only 20mm of the striker was simulated and to the probably ductile failure induced by σ – waves applied at the moment of impact. Due to time constraint no further work about the inducing σ – waves was done in the present research work. It can be seen that at displacement equal to $19\,mm$, there was a drop of load as showed in figure 4.15, this drop of numerical data may be due to the accumulation of damage in the finite elements located in the propagation path. The high oscillations of finite element simulations of Charpy tests in the hardening part can be minimized with the application of a combination of Cellular Automata and Finite Elements, the model is explained in chapter VI.

4.3 FE simulations of four point bend tests to measure the mechanical properties of the plate steel at –60°C.

A $3D$ finite element model which consist of 4753 C3D8R 8–node reduced integration finite elements and 4133 nodes was created and simulated with ABAQUS Explicit (ABAQUS 6.5, 2004) to verify that the fitted stress–strain curve for –60°C was done properly. The finite element model is shown in figure 4.16.

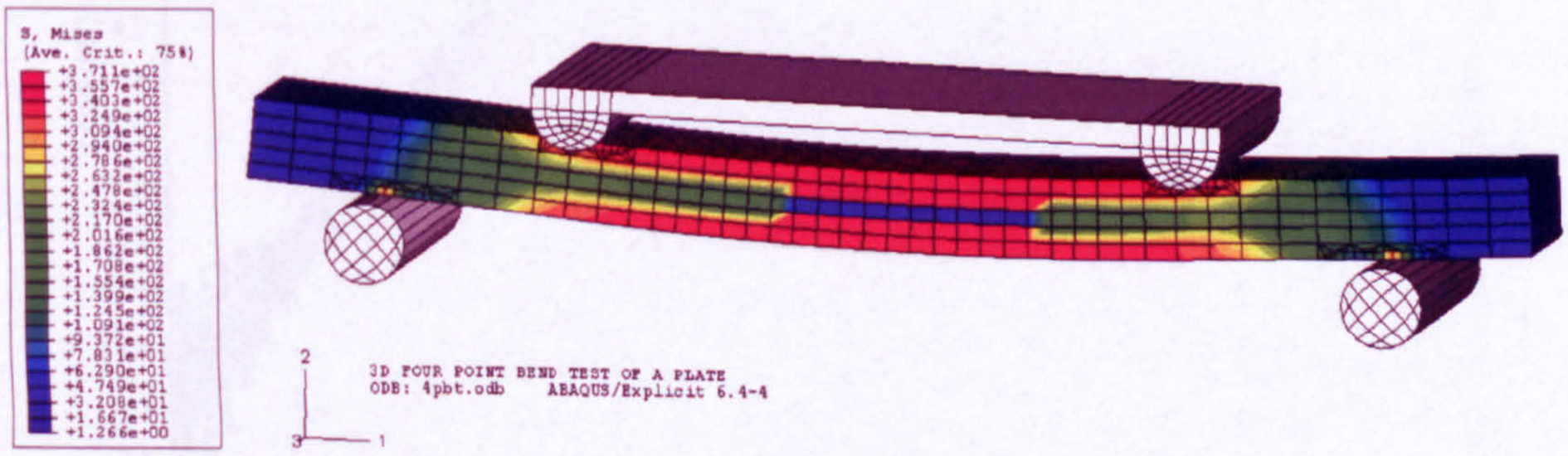

Figure 4.16 – 3D simulation of four point bend test.

The three sets of data measured experimentally, load–deflection, load–microstrain (in tension), load–microstrain (in compression) will be obtained numerically and plotted versus the experimentally measured data. Figure 4.17 shows results of simulation against experimental data of load–deflection. Figure 4.18 shows the load–microstrain measured with strain gauges loaded to tension. Figure 4.19 shows the load–microstrain measured with the strain gauges loaded in compression.

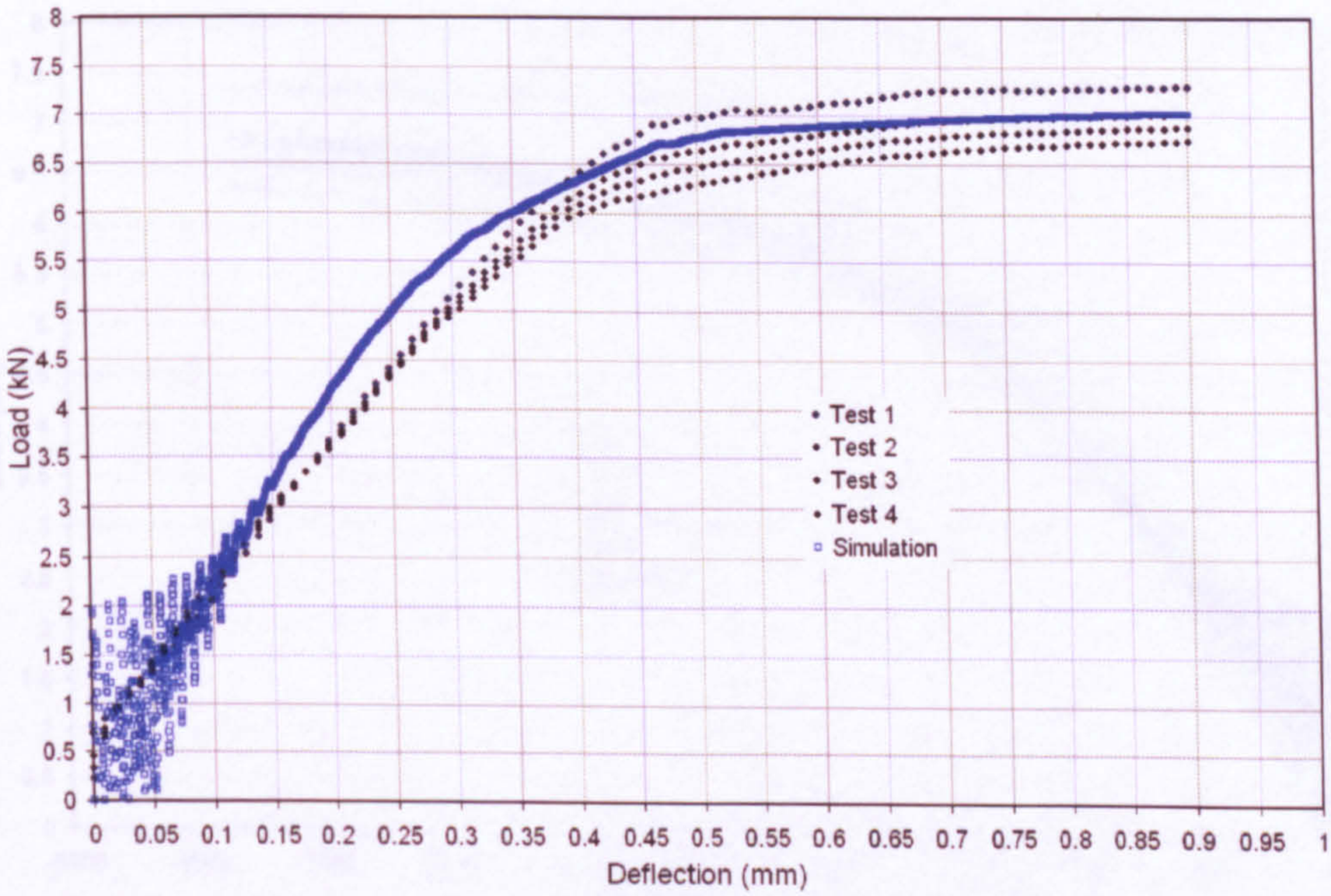

Figure 4.17 – Simulation vs experimental data for σ_y values.

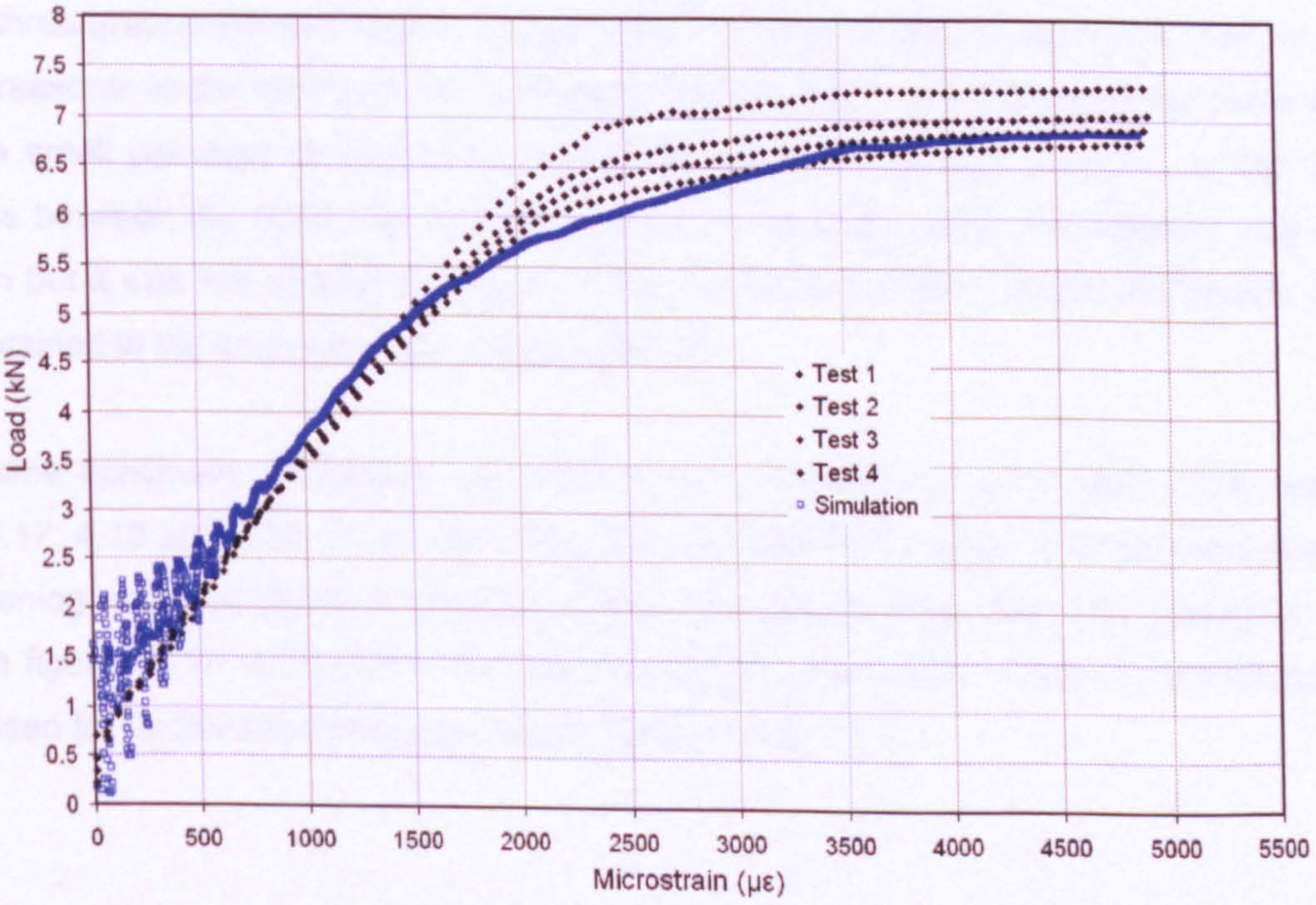

Figure 4.18 – Simulation vs experimental data of load–microstrain in tension.

The finite element length in the surfaces of the centre of the model is $1\,mm$, the size of the strain gauges that is used for measurement purposes (size of the zone covered by the resistance) was $8\,mm$. So from 8 finite elements located in the middle of the specimen in both surfaces, the logarithmic strains were obtained from the finite element model and plotted versus the experimental data.

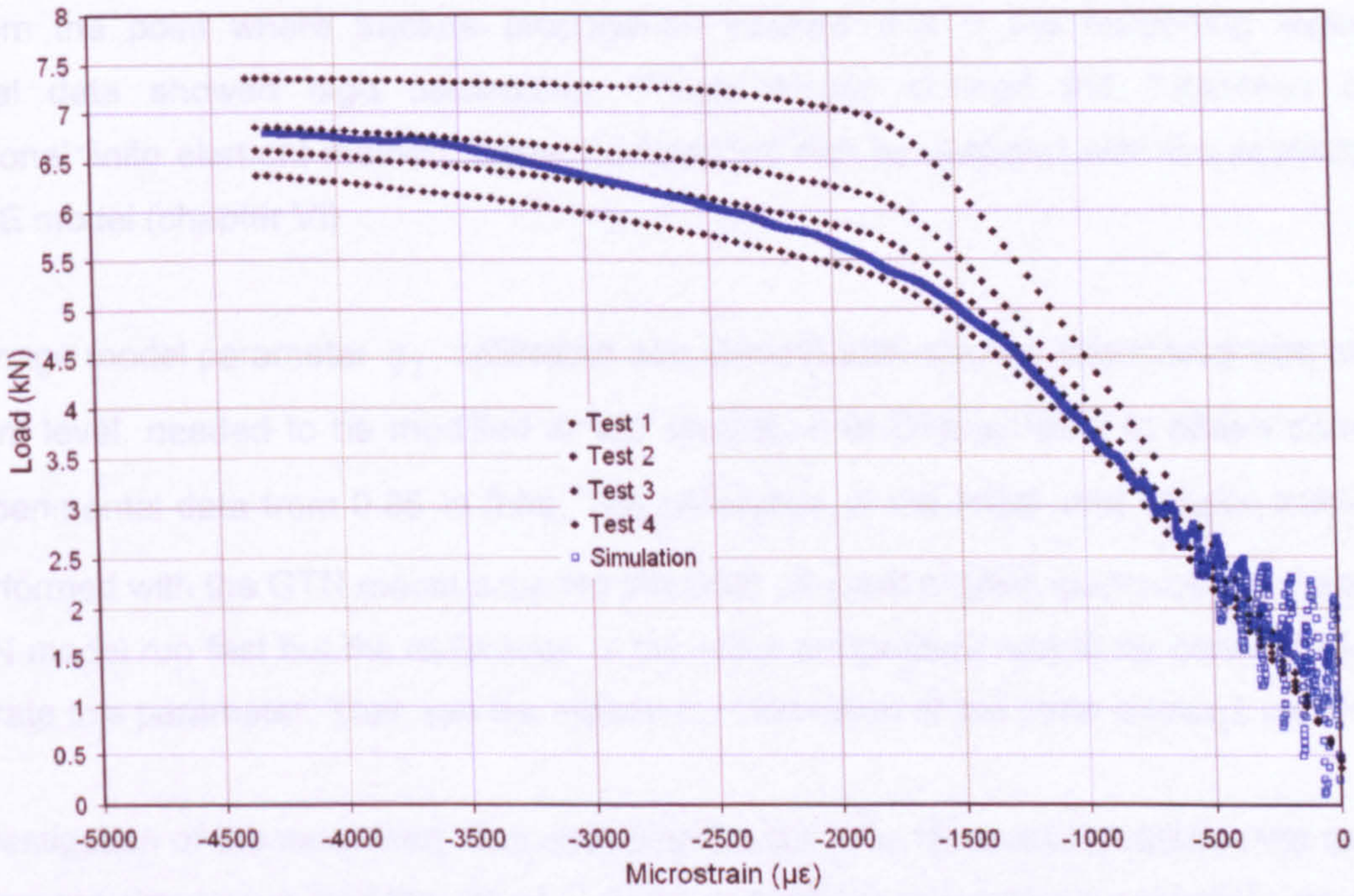

Figure 4.19 – Simulation vs experimental data of load–microstrain compression.

The last three graphs showed scatter of load from 0 to about 2.5kN. This scatter may be due to different reasons: to the sliding of the specimens with respect to the pins, because there was no applied a small pre–load to minimize such effect before the loading process, to the contact conditions between the specimen and the pins because temperature was applied only on the specimen but it was not applied to the pins. These effects probably caused the scatter in data points obtained in the analysis of the present section.

Due to time constraint no further research on this phenomenon took place. The results of figures 4.17, 4.18 and 4.19, it can be shown that the application of the method developed to fit the hardening curve for –60ºC was done properly, the experimental data was simulated well as shown in figures 4.17, 4.18 and 4.19, with very good correlations. This means that the curve can be used for further simulations for test temperature of –60ºC.

4.4 Conclusions.

The finite element simulation results of smooth and notch tensile tests showed that the true stress–strain curve properly simulates the load–diametral contraction of tensile tests. Once simulation of experimental against numerical data correlation was obtained, the hardening curves can be used for further finite element simulations. The hardening curves were applied to simulate a Charpy test which properly reproduced the data obtained with instrumented Charpy tests from the point where fracture propagation initiates, but in the hardening region the numerical data showed high oscillations. These results showed the limitations of the conventional finite element method. Better correlations can be obtained with the application of the CAFE model (chapter VI)

The damage model parameter q_2, calibrated with smooth and notched specimens with different constraint level, needed to be modified in the simulation of Charpy tests to obtain correlation with experimental data from 0.85 to 0.80. The calibration of the initial void volume fraction f_0 was performed with the GTN model because the finite element models incorporating damage by the GTN model run fast but the calibration of the other parameters had to be done first in order to calibrate this parameter. That was the reason for calibration of the other damage parameters.

The investigation of the measured, true stress–strain curve to reproduce experimental data with finite element simulations and the effect of fitting damage parameters on numerical results was done in this section. It was shown as well that the finite element model of tensile tests in the rolling direction of the plate steel was able to simulate the Lüders bands region as shown in figures 4.2, 4.3 and 4.4. But because the objective of the present research work is not investigating this phenomenon, no further investigation about this was done.

4.5 References.

ABAQUS 6.5 (2004) Analysis User's Manual, Finite Elemente Simulation Program (ABAQUS version 6.5.).

BERNAUR, G. & BROCKS, W. (2001) Micro-mechanical modelling of ductile damage and tearing - results of an European numerical round robin. *Fatigue Fract Engng Mater Struct,* 25, 363-384.

EN ISO 14556:200 BRITISH STANDARDS (1987) Method for Precision Determination of Charpy V-Notched Impact energy for Metals. BS131-6.

FRANKLIN, A. G. (1969) Comparison between a Quantitave Microscopic and Chemical Methods for Assessment of Nonmetallic Inclusions. *J. Iron and Steel Institute,* 207, 181-186.

HASHEMI, S. H. (2004) Assessment of the fracure bahaviour of high grade steel for gas pipelines. *A thesis submited for the degree of Doctor of Philosophy, Department of Mechanial Engineering, The University of Sheffield.*

HASHEMI, S. H., HOWARD, I. C., YATES, J. R. & ANDREWS, R. M. (2004) Micro-mechanical damage modeling of notched bar testing of modern line pipe steel. *in ECF15. Advance fracture mechanics for life and safety assesments. EMAS Publications, Stockholm, Sweden.*

ROSSOLL, A., BERDIN, C., FORGET, P., PRIOUL, C. & MARINI, B. (1998) Mechanical aspects of the Charpy impact test. *Nuclear Engineering and Design,* 188, 217-229.

SERIZAWA, H., WU, Z. & MURAKAWA, H. (2001) Computational analysis of Charpy impact test using interface elements. *Trans. JWRI,* 30, 97-102.

TRONSKAR, J. P., MANNAN, M. A. & LAI, M. O. (2001) Measurement of fracture initiation toughness and crack resistance in instrumented Charpy impact loading. *Engineering fracture mechanics,* 69, 321-338.

TVERGAARD, V. (1981) Influence of voids on shear band instabilities under plane strain conditions *International Journal of Fracture,* Vol.17, 381-388.

Chapter V

The cellular automata finite element model for ductile and cleavage fracture simulation

Cellular automata are arrays of cells created inside the structure of finite elements, each of these cells contain a finite state machine. The resulting construct is a physical space filled with cells which represent a material volume. The cells go from their current state to some next state. The combination of Cellular Automata and Finite Elements resulted in the development of the CAFE model. The number of cellular automata arrays is unlimited, the variables included in cellular arrays is also unlimited. Cellular Automata can accommodate as many cells as needed and any physical property of engineering materials can be defined. This makes the CAFE model a powerful tool for fracture propagation simulation of ductile and brittle fracture and for the simulation of the ductile–brittle transition.

5.1 Implementation of CAFE model and the definition of micro physical features of metals into the model.

In the present work, a continuation of the development of the CAFE model for fracture initiation and propagation simulation proposed by Shterenlikht (Shterenlikht, 2003) has been done. The model was realized via the user material subroutine VUMAT, programmed in FORTRAN 90 and linked to ABAQUS Explicit 6.5 Finite Element code (Karlssonn and Sorensen, 2001). The program utilizes explicit dynamic integration of the equations of motion. The reduced integration 8–node single integration finite elements C3D8R (ABAQUS 6.4, 2003) were used to mesh the damage zone chosen to apply the model. C3D8R elements have only one integration point. The explicit dynamic version of the Abaqus code was chosen because of the element removal feature which is not available in Abaqus/Standard. The removal of dead finite elements from the mesh is necessary in large deformation analysis. Otherwise the dead elements, which have the highest strains, might turn inside out; the solution will terminate in this case.

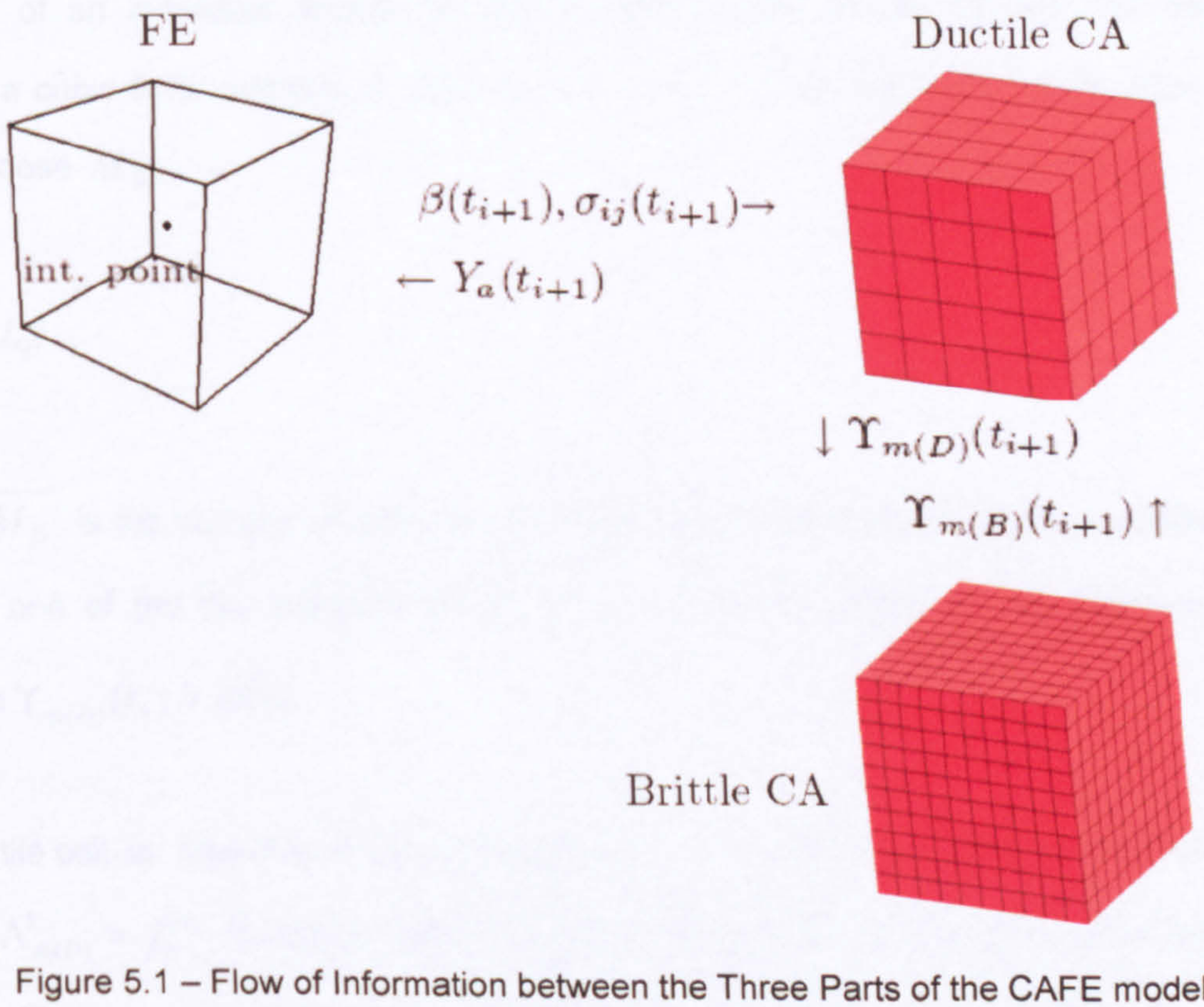

Figure 5.1 – Flow of Information between the Three Parts of the CAFE model.

The flow of information between the three parts of the CAFE model is shown in figure 5.1. It can be seen that the CAFE model has three independent size scales: the finite elements size, the ductile cells size and the brittle cells size. In CAFE model, the constitutive ductile Rousselier model integration is performed at finite element integration points. The damage variable $\beta(t_{i+1})$

is distributed in the ductile CA array. Only the solution–dependent state variables are returned to the FE from the ductile CA array, as the new macro stress tensor, $\sigma_{ij}(t_{i+1})$ is calculated already at the FE as shown in figure 5.1. The critical value of the damage variable is a randomly assigned cell property, $\Lambda^1_{m(D)} = \beta^m_F$. So β^m_F is used in equation 5.2 (section 5.2) for the CAFE model. The functionality of the CAFE model has been explained elsewhere (Shterenlikht, 2003), but the author of the present work considers that it is important to explain in this work how the model works. Therefore in the present section the explanation of how the model was developed and coded to simulate fracture initiation and propagation is presented.

5.2 The ductile CA array.

As mentioned before (section 2.6.2), the ductile CA cells are related to the ductile damage cells. Therefore the total number of cells of the ductile CA array, M_D, are chosen as a result the linear size of an individual ductile CA cell is close to the ductile damage cell size, L_D. Assuming a cubic finite element of size $L_{FE} \times L_{FE} \times L_{FE}$, then the following equation can be used to choose M_D:

$$\frac{L_{FE}}{\sqrt[3]{M_D}} = L_D \qquad 5.1$$

where $\sqrt[3]{M_D}$ is the number of cells per dimension of a cubic ductile CA. Each ductile cell m can take one of the two possible states, $\Upsilon_{m(D)}$: $alive$ or $dead$. In the beginning of the simulation $\Upsilon_{m(D)}(t_o) = \text{alive}$.

Each ductile cell m has only one cell property $(N_D = 1)$, this is the value of initial void volume fraction, $\Lambda^1_{m(D)} = f_o^m$. A random number generator is used to generate the initial void volume fraction f_o^m for each cell at the beginning of the simulation. This is done with a Weibull distribution via the shape and scale parameters values of the experimentally measured distribution of microvoids (section 5.8.2). The incorporation of the distribution of f_o instead of using the mean value is because of the fact that in order to simulate the typical scatter of Charpy data in the transition region, we need to introduce random values of this parameter in the ductile cells. Therefore in each run of the CAFE model, the model will sample different

values of f_o, consequently scatter in data points will be obtained. Otherwise with the definition of the mean value of f_o, scatter would not be possible, this is because in each run of the model, the model will sample always the same values of f_o distributed uniformly in the model. Each ductile cell m carries only one state variable, $Q_D = 1$. This is the current value of the damage parameter $\Gamma^1_{m(D)}(t_i) = \beta_m(t_i)$. In the present work the same critical threshold value of the damage variable β_F is used for all ductile cells. In the ductile CA array the state of each cell m is determined by the following criterion:

$$\Upsilon_{m(D)}(t_{i+1}) = \begin{cases} alive & \text{if} \quad \beta_m(t_{i+1}) < \beta_F \\ \\ dead & \text{otherwise} \end{cases} \qquad 5.2$$

5.3 The brittle CA array.

Similarly to the ductile CA array, the brittle damage cell size, L_B, and the total number of brittle CA cells is calculated as follows:

$$\frac{L_{FE}}{\sqrt[3]{M_B}} = L_B \qquad 5.3$$

where $\sqrt[3]{M_B}$ is the number of cells per dimension of a cubic brittle CA. As explained in before, a brittle damage cell is 10 to 20 times larger than the mean (or median) grain size. Ideally a brittle cell size has to be related to the grain size, or to the facets size of broken grains or to the size of facets composed of various grains with small misorientation angle (section 5.8.5.1). However for steels with small grain sizes this will lead to extremely high numbers of brittle cells per CA, so a compromise approach is proposed. The brittle cell size is chosen with equation 5.3. However a randomly generated ferrite grain size and pearlite lands size value is assigned to the brittle cells on the fracture stress equations (equations 5.6 and 5.7) therefore random values of σ_F are distributed in the brittle CA array. The pseudorandom generator is based on experimentally determined Weibull distribution analysis of the microstructure.

Brittle cracks typically initiate from hard particles in ferrite–pearlite steels; usually a grain boundary carbide, large inclusions e.g. MnS, the lamellar pearlite microstructure (composed of

a mixture of ferrite and cementite) and pearlite boundary (section 3.6.4). For the purpose of modelling we formulate the following necessary conditions for brittle crack initiation at a particular cell, contrary to the original model for the brittle part where only cells with adjacent grain boundary carbide can initiate brittle fracture (Shterenlikht, 2003). The microstructures nucleating cleavage fracture in the rolling direction (section 3.6.6) and transverse direction (section 3.6.7) are different. In the present work the investigation is focused in the rolling direction of the plate steel, therefore the cleavage nucleation microstructures in the rolling direction will be incorporated in the model, they are:

- Lamellar pearlite microstructure.
- Pearlite boundary.
- Ferrite grains inclusions.
- Ferrite grain boundary particles (carbides).

These four microstructures for cleavage fracture will be implemented into the CAFE model via the fracture stress distributions assigned to the brittle CA arrays of each microstructure as proposed by Shterenlikht (Shterenlikht, 2003). The percentage of each microstructure is shown in table 5.1. In this table we see that the pearlite microstructure corresponds to 24% of the total of the microstructure and 76% corresponds to the ferrite matrix (the procedures to measure each microstructure are explained in sections 5.8.3 and 5.8.4 for the ferrite and pearlite microstructures respectively).

As shown experimentally in section 3.6.4, each microstructure has two different mechanisms for the nucleation of cleavage fracture, consequently two different microstructures for the nucleation of cleavage fracture has to be defined for each microstructure. Therefore the brittle CA array must be divided, according to experimental data, in 76% of the microstructure to account for cleavage fracture on ferrite grains with ferrite grains inclusions and ferrite grain boundary carbides; and 24% of the microstructure to account for cleavage fracture on pearlite with the lamellar pearlite microstructure and pearlite boundary.

Table 5.1 – Percent of microstructure in the matrix of the plate steel

% of ferrite	% of pearlite
76%	24%

Accordingly a special state of the brittle CA cells is created for each microstructure. For the ferrite microstructure: *alive with a grain boundary carbide* or simply $aliveFC$ and *alive with an inter–hard particle* or simply $aliveFI$. For the pearlite microstructure: *alive with a pearlite land*

boundary carbide (the pearlite microstructure is composed on ferrite and cementite which is hard and can be considered as carbides) $alivePC$, and finally *alive with an inter–particle* or simply $alivePI$, therefore only brittle cells with the following states:

$$\Upsilon_{m(d)}(t_o) = aliveFC$$

$$\Upsilon_{m(d)}(t_o) = aliveFI$$

$$\Upsilon_{m(d)}(t_o) = alivePC$$

$$\Upsilon_{m(d)}(t_o) = alivePI$$

can initiate a brittle crack. Now we have to synchronize both CA arrays for coupling the ductile and brittle fracture processes. All ductile failures must be reflected into the brittle CA array. However a distinction must be made between the brittle cells failed due to the brittle failure mode, and those which were made dead artificially (the mapped ductile cells over the brittle CA array) to synchronise the integrity of both CA arrays. A special state of brittle CA cells is created, dead in the ductile CA array or simply $deadD$. Finally the state $deadB$ is reserved for the brittle CA cells which fail when the brittle failure criterion is satisfied. Thus for each microstructure (ferrite and pearlite), each brittle cell can take one of the five possible states.

Ferrite; $\Upsilon_{m(B)}$: $alive$, $aliveFC$, $aliveFI$, $deadB$ or $deadD$.

Pearlite; $\Upsilon_{m(B)}$: $alive$, $alivePC$, $alivePI$, $deadB$ or $deadD$.

In the beginning of the simulation, for the ferrite microstructure, $\Upsilon_{u(B)}(t_o) = aliveFC$, $\Upsilon_{v(B)}(t_o) = aliveFI$ and $\Upsilon_{w(B)}(t_o) = alive$, $u = 1...U$, $v = 1...V$, and $w = 1...W$, so $U + V + W = M_B$. Then the fraction of brittle cells which have a grain boundary carbide and inclusion is:

$$\eta = \frac{U + V}{M_B} \qquad 5.4$$

The same condition is applied to the pearlite microstructure. In the beginning of the simulation, $\Upsilon_{u(B)}(t_o) = alivePC$, $\Upsilon_{v(B)}(t_o) = alivePI$ and $\Upsilon_{w(B)}(t_o) = alive$, $u = 1...U$, $v = 1...V$, and $w = 1...W$, so $U + V + W = M_B$.

In the present CAFE model, a random number generator is used to assign the initial state to cells. Each brittle cell m has two cell properties $(N_B = 2)$: the fracture stress, $\Lambda^1_{m(B)} = \sigma^m_F$, and the grain orientation angle, $\Lambda^2_{m(B)} = \alpha^m$. Therefore a distribution of grain orientation angles between two grains is assigned to the brittle CA array with a random number generator based on Weibull distribution analysis of experimental data (section 5.8.5). Accordingly if l is a grain (brittle cell) adjacent to grain m (brittle cell) then $\left|\alpha^m - \alpha^l\right|$ is a difference between the orientation of grains m and l.

Temperature dependence of the misorientation threshold, θ_F was introduced to the model in order to improve the ductile–brittle transition simulation as suggested by Shterenlikht (Shterenlikht, 2003). Although there is little experimental evidence that θ_F is temperature–sensitive because usually misorientation analysis is performed on fracture surfaces obtained at the lower shelf temperatures (Bhattacharjee and Davies, 2002, Bhattacharjee et al., 2003), the incorporation of temperature dependence of the misorientation threshold was applied to the model as shown in figure 5.2.

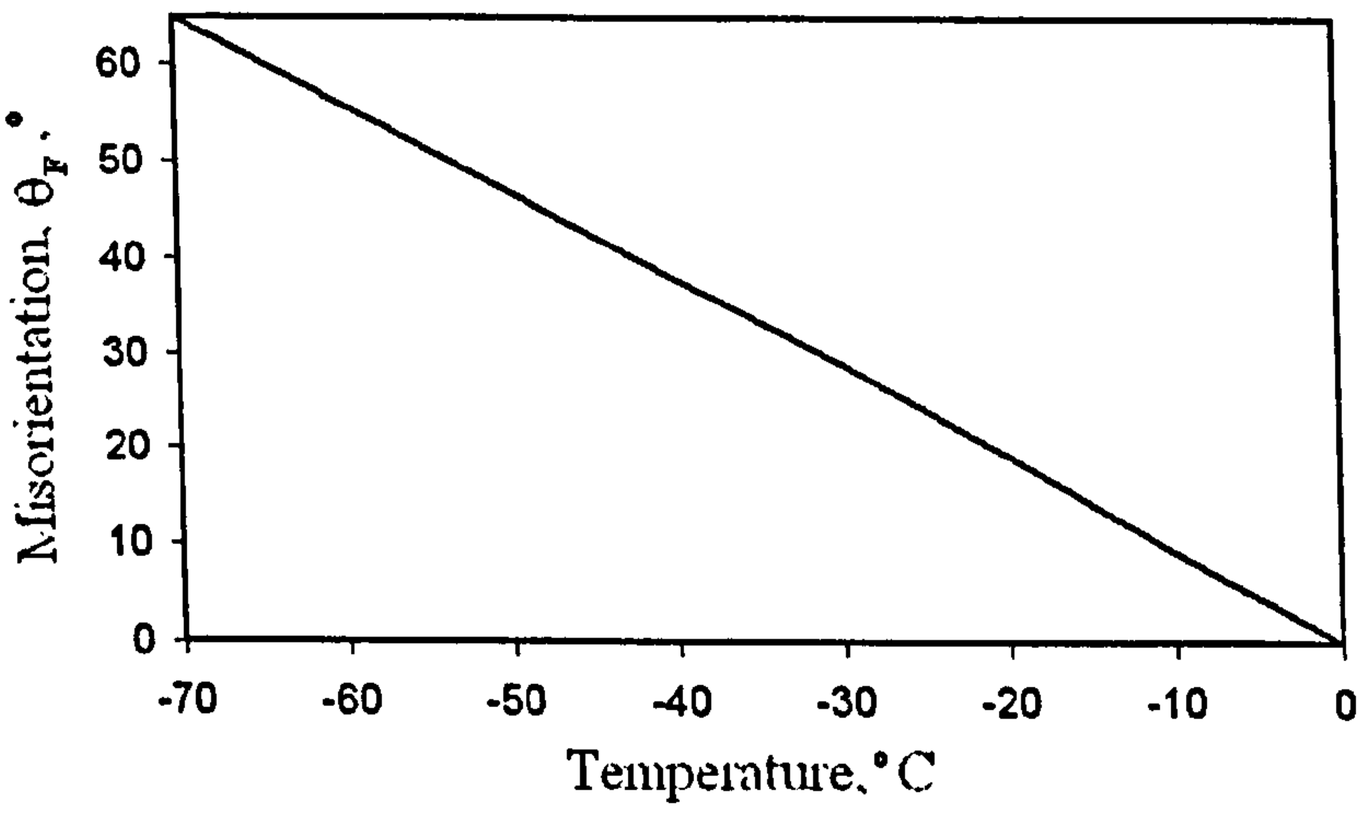

Figure 5.2 – The misorientation threshold, θ_F (°).

As explained before, the fracture stress of a cell is linked to the size of the grain that this cell embodies. Smith (Smith, 1966a, Smith, 1966b) derived an equation to compute the fracture stress (σ_F) of a carbide interface (equation 2.38 of section 2.3.1):

$$\sigma_F^{cf} = \sqrt{\frac{\pi E \gamma_{cf}}{(1-\nu^2)d_c}} \qquad 5.5$$

where σ_F^{cf} is the fracture stress of a carbide–ferrite interface, γ_{cf} is the effective surface energy of a carbide–ferrite interface, d_c is the carbide size, E is the elasticity modulus and ν is the Poisson's ratio. Based on Smith's analysis, Lin (Lin et al., 1987) obtained a similar equation for the fracture stress of a ferrite–ferrite interface (equation 2.39 of section 2.3.2):

$$\sigma_F^{ff} = \sqrt{\frac{\pi E \gamma_{ff}}{(1-\nu^2) d_g}} \qquad 5.6$$

where σ_F^{ff} is the fracture stress of a ferrite–ferrite interface, γ_{ff} is the effective surface energy of a ferrite–ferrite interface, d_g is the ferrite grain size.

Equation 5.6 can be used to calculate the fracture stress for lands of pearlite $\left(\sigma_F^{PP}\right)$ by using the value of pearlite lands size and the effective fracture surface energy of the particles found in the lamellar pearlite microstructure:

$$\sigma_F^{pp} = \sqrt{\frac{\pi E \gamma_{pp}}{(1-\nu^2) d_p}} \qquad 5.7$$

where σ_F^{pp} is the fracture stresses of pearlite–pearlite interface, γ_{pp} is the effective surface energy of pearlite–pearlite interface, d_p is the pearlite land size. Equation 5.5 can be used to calculate the fracture stress of a carbide interface in the boundary of lands of pearlite:

$$\sigma_F^{pf} = \sqrt{\frac{\pi E \gamma_{pf}}{(1-\nu^2) d_{pf}}} \qquad 5.8$$

where σ_F^{pf} is the fracture stress of a carbide interface of lands of pearlite, γ_{pf} is the effective surface energy of the carbide interface of lands of pearlite, d_{pf} is the carbide size at the interface of the boundary of lands of pearlite. It is clearly shown that the application of equations 5.6, 5.7 and 5.8 will result in different distributions of fracture stresses $\left(\sigma_F\right)$ for the same material as the size of the microstructures for cleavage fracture nucleation are different.

A random number generator is used to generate a ferrite grain size d_g based on the analysis of grain size distribution. The pearlite lands size d_p is generated with a random number generator based on the analysis of pearlite size distribution. Random number generators are used as well to generate the effective fracture surface energy (γ) which is calculated based on the size of the micro features initiating cleavage fracture of each microstructure. Then a fracture stress is assigned to each cell based on the generated microstructure. It can be seen that in the present model we have introduced the distribution of the physical variables in σ_F equations, rather than the mean value. Then a random value of fracture stress is assigned to each cell based on the generated microstructure and particles size. Each brittle cell m carries only one state variable $Q_B = 1$, this is the current value of the maximum principal stress, $\Gamma^1_{m(B)}(t_i) = \sigma_I^m$.

As assumed experimentally and based on literature review (section 2.3.4), a high–angle misorientation grain boundary can inhibit or even arrest microcrack growth (Hohava et al., 2002, Bhattacharjee and Davies, 2002, Bhattacharjee et al., 2003). Again we simplify this idea and formulate the following necessary condition for crack propagation. A crack will propagate from one brittle CA cell, m, to another, l, if the misorientation angle for these two cells, defined as the absolute value of the difference of their orientation angles, $\left|\alpha^m - \alpha^l\right|$, is less than a misorientation threshold, θ_F. It is assumed that θ_F is a material property. The value of the maximum misorientation angle equal to $\theta_F = 65°$ was used in the present CAFE model (section 5.8.5). The distribution of misorientation angles was analysed experimentally with a Weibull distribution and a random number generator was used to distribute them in each brittle CA cell *m*. Finally the following simple propagation criterion is used which must be satisfied in all cases. A brittle cell m will become dead at time t_{i+1} if the maximum principal stress, $\sigma_I^m(t_i)$, is greater than or equal to the fracture stress of this cell, σ_F^m. This criterion is identical to that of Folch (Folch, 1997). Thus the state of each cell m is determined by the following criterion:

$$\Upsilon_{m(B)}(t_{i+1}) = \begin{cases} deadB & \text{if: } \sigma_I^m(t_i) \geq \sigma_F^m \wedge \{(\Upsilon_{m(B)}(t_i) = alivC \vee \\ & ([\Upsilon^m_{l(B)}(t_i) = deadB \vee \Upsilon^m_{l(B)}(t_i) = deadD] \wedge \\ & \left|\alpha^m - \alpha^l\right| < \theta_F\} \\ \Upsilon_{m(B)}(t_i) & \text{otherwise} \end{cases} \quad 5.9$$

The present section showed that it has been introduced to the model four different cleavage fracture nucleation microstructures which were found experimentally (section 3.6.4). The microstructures have been incorporated in the brittle CA array for the nucleation of microcracks in the notch region of notched specimens. This was done by dividing the total brittle CA array to account for 76% of the total cells for the ferrite grains and 24% for the pearlite lands (equations 5.6 and 5.7). Because each microstructure has two mechanisms for the nucleation of microcracks, the particles found in the boundary of each microstructure were introduced via equations 5.6 and 5.8.

5.4 The FE part of the CAFE model.

Each material point has three solution–dependent variables (Shterenlikht, 2003); $A = 3$. They are the state $\Upsilon_1(t_i)$, the integrity $\Upsilon_2(t_i)$ and the fraction of brittle phase $\Upsilon_3(t_i)$. As follows from equation 2.51 (section 2.6.2), the FE state variables depend on the states of the brittle and ductile CA cells:

the number of brittle CA cells with $\Upsilon_{m(B)}(t_i) = deadB$:

$$X^B_{(B)}(t_i) = \sum_{m=1}^{M_B} m \quad \forall m : \Upsilon_{m(B)}(t_i) = deadB \tag{5.10}$$

the number of brittle CA cells with $\Upsilon_{m(B)}(t_i) = deadD$:

$$X^D_{(B)}(t_i) = \sum_{m=1}^{M_B} m \quad \forall m : \Upsilon_{m(B)}(t_i) = deadD \tag{5.11}$$

the total number of dead brittle CA cells:

$$X_{(D)}(t_i) = X^B_{(B)}(t_i) + X^D_{(B)}(t_i) \tag{5.12}$$

and the number of dead ductile CA cells:

$$X_{(D)}(t_i) = \sum_{m=1}^{M_D} m \quad \forall m : \Upsilon_{m(D)}(t_i) = dead \tag{5.13}$$

are calculated. The FE state variables are calculated according to the following three equations:

$$\mathrm{Y}_1(t_i) = \begin{cases} dead & \text{if} \quad \mathrm{Y}_2(t_i) \le 0 \\ alive & \text{otherwise} \end{cases} \qquad 5.14$$

$$\mathrm{Y}_2(t_i) = 1 - \frac{X_{(D)}(t_i)}{X_{(D)}^{\max}} - \frac{X_{(B)}^{B}(t_i)}{X_{(B)}^{\max}} \qquad 5.15$$

$$\mathrm{Y}_3(t_i) = \frac{X_{(B)}^{B}(t_i)}{X_{(B)}(t_i)} \qquad 5.16$$

where $X_{(D)}^{\max}$ and $X_{(B)}^{\max}$ are the maximum numbers of dead cells allowed in the ductile and the brittle CA arrays respectively. If the number of dead cells in any array exceeds its maximum then a crack (or ductile void linkage) is assumed to propagate across the whole of the finite element. The load–bearing capacity of this finite element is then considered zero and the element is removed from the mesh.

$\mathrm{Y}_1 \in [alive, \mathrm{dead}]$; $\mathrm{Y}_2 \in [-1...1]$; $\mathrm{Y}_3 \in [0...1]$, in the beginning of the analysis $\mathrm{Y}_1(t_0) = alive$, $\mathrm{Y}_2(t_0) = 1$ and $\mathrm{Y}_3(t_0) = 0$, for all finite elements of the CAFE model. When a finite element fails $\mathrm{Y}_1(t_f) = dead$ and $\mathrm{Y}_2(t_f) = 0$, where t_f is the time of failure.

5.5 Steps showing how the CAFE model works.

From the analysis described in section 2.6.2 and in previous sections of the present chapter, it can be seen that only the ductile CA array is used to calculate material constitutive response, but the brittle CA array is used only to assess the onset of brittle fracture at each cell. Therefore, before the brittle CA cells can be processed to decide if any of them have died in a time increment, the material response has to be calculated via the ductile CA array as clearly shown un figure 5.1. Because of the complexity of the model, in this section the author explains how the CAFE model works, the sequence of operations that are performed at each time increment on each FE and the corresponding two CA arrays, ductile and brittle, of the CAFE model. Each step explains the operations performed at cellular and finite element level. In the model some operations are performed at finite element level and the cells arrays use those values to calculate other parameters at that level and vice versa.

5.5.1 Step 1.

The stress at time t_{i+1} at each FE integration point, $\sigma_{ij}(t_{i+1})$, and the value of the damage variable, $\beta_m(t_{i+1})$, are given by the ABAQUS solver to the VUMAT subroutine.

5.5.2 Step 2.

The maximum principal stress, $\sigma_I(t_i)$, and its direction cosines, $d_k(t_i)$, are calculated from the stress tensor at increment time t_i, $\sigma_{ij}(t_i)$.

5.5.3 Step 3.

The damage variable increment tensor at each ductile CA cell m at time t_{i+1}, $\beta_m(t_{i+1})$ is calculated. The following criteria are used:

$$\forall\, m : \beta_m(t_{i+1}) = \beta(t_{i+1}) \qquad 5.17$$

$$\forall\, m : \ \Upsilon_{m(D)}(t_i) = dead : \qquad 5.18$$

$$\text{If } d_k^l \cdot d_k(t_i) \approx 1 \quad \text{then} \quad \beta_l(t_{i+1}) = c_D \cdot \beta(t_{i+1}) \qquad 5.19$$

where $c_D > 1$, is the concentration factor for the ductile CA array, in the present work a value of $c_D = 1.5$ was used, d_k^l are the direction cosines of the line connecting the centres of cells m and l Shterenlikht (Shterenlikht, 2003).

The condition of equation 5.18 means that if there is a dead ductile cell then all neighbouring cells which lie on or near the plane perpendicular to the direction of the maximum principal stress in the element will receive a concentration factor. This condition reflects the strain concentration in material surrounding a microvoid. The sign $(\approx)$ rather than $(=)$ is used in

equation 5.19 because there are only 13 pairs of neighbouring cell with unique combinations of d_k^l (Shterenlikht, 2003). So it is very unlikely that $d_k^l \cdot d_k(t_i) = 1$.

5.5.4 Step 4.

The state of each ductile cell m at time t_{i+1}, $\Upsilon_{m(D)}(t_{i+1})$, is obtained according to equation 5.2, this equation has the form:

$$\Upsilon_{m(D)}(t_{i+1}) = \begin{cases} alive & \text{if } \beta_{\mathrm{m}}(t_{i+1}) < \beta_F \\ \\ dead & \text{otherwise} \end{cases} \qquad 5.20$$

5.5.5 Step 5.

All dead ductile CA cells are mapped over the brittle CA array. A mapping function, $\mathbb{M}_{D\to B}$, distributes the array of ductile CA cell states, $\Upsilon_{m(D)}(t_{i+1})$, across the brittle CA array. Since both CA arrays occupy the same physical space, any change in one array is reflected in the other array. The result is the "synchronisation" array of the brittle CA cell states, $\Upsilon_{m(BD)}(t_{i+1})$.

$$\Upsilon_{m(BD)}(t_{i+1}) = \mathbb{M}_{D\to B}(\Upsilon_{\overline{m}(D)}(t_{i+1})) \qquad 5.21$$

The subscript BD means that each brittle cell m has the state of the ductile cell occupying the same physical space. The subscript $\overline{m}$ instead of the usual m is used in the right part of equation 5.21 because $M_B \neq M_D$, so $\overline{m} = 1...M_D$ and $m = 1...M_B$.

The space of states $\Upsilon_{m(BD)}$ is the same as of $\Upsilon_{m(D)}$, either $dead$ or $alive$. The $\Upsilon_{m(BD)}(t_{i+1}) = dead$ means that there is a ductile void in the physical space associated with brittle cell m. Consequently the state of brittle cell m is changed to $deadD$ in the brittle CA array. To acknowledge this fact this is expressed by equation 5.22.

$$\Upsilon_{m(B)}(t_{i+1}) = \begin{cases} deadD & \text{if: } \Upsilon_{m(BD)}(t_{i+1}) = dead \ \wedge \\ & (\Upsilon_{m(B)}(t_i) = alive \ \vee \\ & \Upsilon_{m(B)}(t_i) = aliveC) \\ \Upsilon_{m(B)}(t_i) & \text{otherwise} \end{cases} \qquad 5.22$$

The work of mapping function $\mathbb{M}_{D\to B}$ is illustrated in figure 5.3a and 5.3b. Figure 5.3a shows a two–dimensional slice of $\Upsilon_{m(D)}(t_{i+1})$. Dead cells have grey colour and the white ones are alive cells. Figure 5.3b shows a two–dimensional slice of $\Upsilon_{m(BD)}(t_{i+1})$. It is easy to see that the locations of groups of grey cells in $\Upsilon_{m(BD)}(t_{i+1})$ are very close to locations of grey cells in $\Upsilon_{m(D)}(t_{i+1})$.

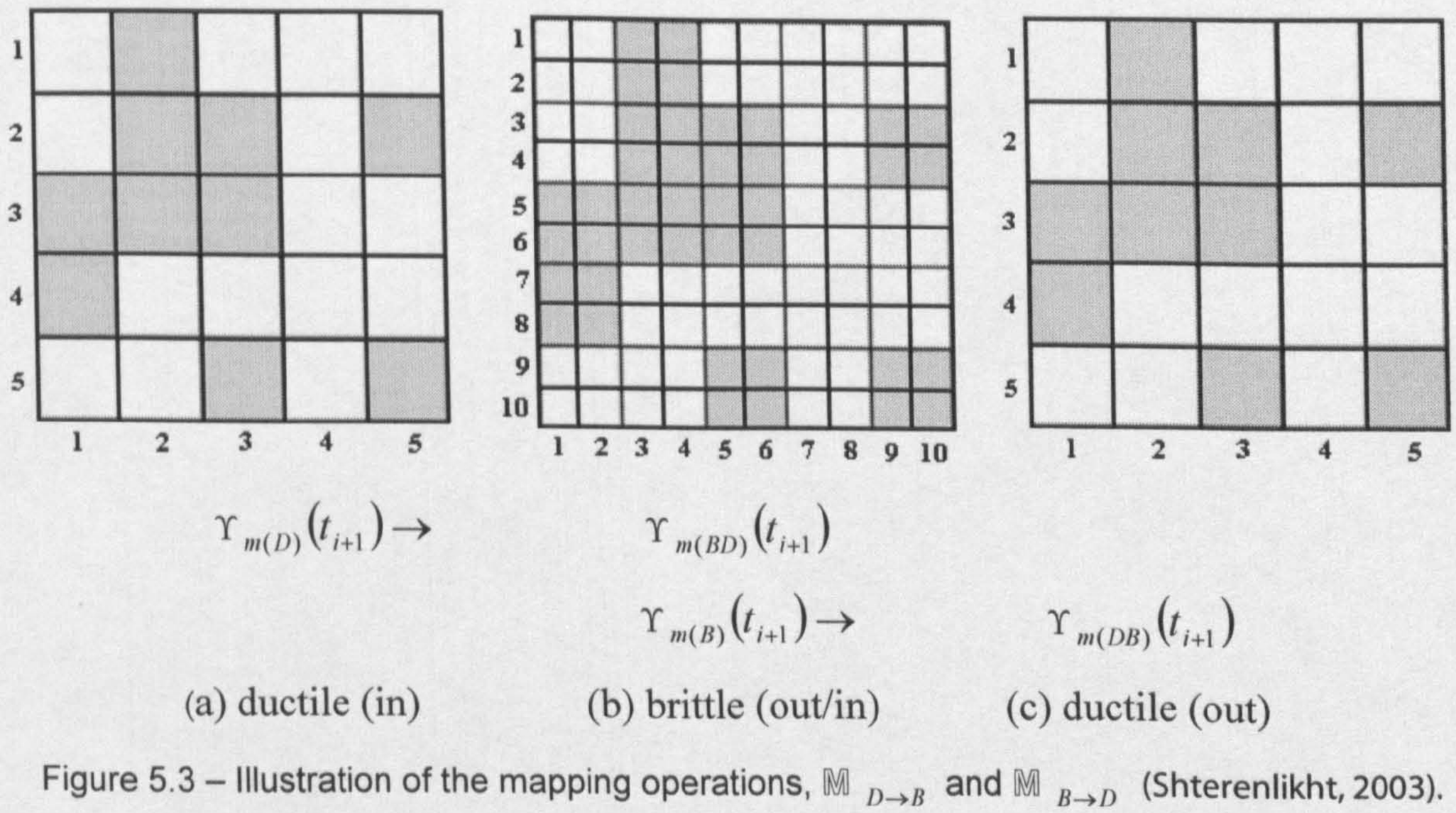

$\Upsilon_{m(D)}(t_{i+1}) \to$ $\Upsilon_{m(BD)}(t_{i+1})$ $\Upsilon_{m(B)}(t_{i+1}) \to$ $\Upsilon_{m(DB)}(t_{i+1})$

(a) ductile (in) (b) brittle (out/in) (c) ductile (out)

Figure 5.3 – Illustration of the mapping operations, $\mathbb{M}_{D\to B}$ and $\mathbb{M}_{B\to D}$ (Shterenlikht, 2003).

Because of the discrete nature of the CA space, the dead cells in $\Upsilon_{m(BD)}(t_{i+1})$ will occupy exactly the same physical space as the dead cells in $\Upsilon_{m(D)}(t_{i+1})$ only if the number of cells per

linear brittle CA dimension, $\sqrt[3]{M_B}$, is divisible by the number of cells per linear ductile CA dimensions, $\sqrt[3]{M_D}$:

$$\mathrm{mod}\sqrt[3]{\frac{M_B}{M_D}} = 0 \qquad 5.23$$

In the example shown in figure 5.2a and 5.2b $\sqrt[3]{M_B = 10}$ and $\sqrt[3]{M_D} = 5$, so the condition of equation 5.23 does not hold. Therefore the location of dead (grey) cells in physical space $\Upsilon_{m(D)}(t_{i+1})$ and in $\Upsilon_{m(BD)}(t_{i+1})$ are close to each other, but not identical.

5.5.6 Step 6.

This step is the brittle CA analogue for the ductile CA. The maximum principal stress in each brittle CA cell m at time t_{i+1}, $\sigma_I^m(t_{i+1})$, is calculated. The following criteria are used:

$$\forall\, m \quad \sigma_I^m(t_i) = \sigma_I(t_i) \qquad 5.24$$

$$\forall\, m : \Upsilon_{m(B)}(t_i) = deadB : \text{ if } d_k^I \cdot d_k(t_i) \approx 1 \text{ then } \sigma_I^I(t_i) = c_B \cdot \sigma_I(t_i) \qquad 5.25$$

$$\forall\, m : \Upsilon_{m(B)}(t_i) = deadD : \text{ if } d_k^I \cdot d_k(t_i) \approx 1 \text{ then } \sigma_I^I(t_i) = c_D \cdot \sigma_I(t_i) \qquad 5.26$$

where c_B is the concentration factor for the brittle CA array, in the present work a value of $c_B = 11$ was used. The meaning of equation 5.25 and 5.26 for the brittle CA array is similar to that of equation 5.19 for the ductile CA array (step 3).

5.5.7 Step 7.

This step is the brittle CA analogue for the ductile CA (step 4). The state of each brittle cell m at time t_{i+1}, $\Upsilon_{m(B)}(t_{i+1})$, is obtained according to equation 5.9. This equation has the form:

$$\Upsilon_{m(B)}(t_{i+1}) = \begin{cases} deadB & \text{if: } \sigma_I^m(t_i) \geq \sigma_F^m \ \wedge \ \{(\Upsilon_{m(B)}(t_i) = alivC \\ & ([\Upsilon_{I(B)}^m(t_i) = deadB \ \vee \ \Upsilon_{I(B)}^m(t_i) = deadD] \ \wedge \\ & |\alpha^m - \alpha^I| < \theta_F\} \\ \Upsilon_{m(B)}(t_i) & \text{otherwise} \end{cases} \quad 5.27$$

5.5.8 Step 8.

This step is the brittle CA analogue for the ductile CA (step 5). All dead brittle CA cells are reflected into the ductile CA array. A special mapping function, $\mathbb{M}_{B\to D}$ distributes the array of brittle CA cell states, $\Upsilon_{m(B)}(t_{i+1})$, across the ductile CA array. The result is the synchronisation array of the ductile CA cell states, $\Upsilon_{m(DB)}(t_{i+1})$.

$$\Upsilon_{\bar{m}(DB)}(t_{i+1}) = \mathbb{M}_{B\to D}(\Upsilon_{m(B)}(t_{i+1})) \quad 5.28$$

The subscript "DB" means that each ductile cell $\bar{m}$ has the state of the brittle cell occupying the same physical space. The subscript $\bar{m}$ instead of the usual m is used in the left part of equation 5.28 because $M_B \neq M_D$, so $\bar{m} = 1...M_D$ and $m = 1...M_B$. This change of notation is used in equation 5.28 and 5.21.

The space of states $\Upsilon_{m(DB)}$ is the same as $\Upsilon_{m(D)}$, either $dead$ or $alive$. The $\Upsilon_{m(DB)}(t_{i+1}) = dead$ means that there is a brittle cell crack in the physical space associated with ductile cell m. So the state of ductile cell m is changed to $dead$ to acknowledge this fact. This is expressed by the following equation:

$$\Upsilon_{m(D)}(t_{i+1}) = \begin{cases} dead & \text{if } \Upsilon_{m(DB)}(t_{i+1}) = dead \ \wedge \ \Upsilon_{m(D)}(t_i) = alive \\ \Upsilon_{m(D)}(t_i) & \text{otherwise} \end{cases} \quad 5.29$$

Contrary to the brittle CA array, no special cell states are created in the ductile CA array to distinguish between the dead ductile cells due to the ductile failure mode and those made dead artificially for synchronization (equation 5.22 and 5.29). Therefore the percentage of brittle phase can only be calculated via the brittle CA array.

The process of mapping function $\mathbb{M}_{B\to D}$ is illustrated in figure 5.3b and 5.3c. It is important to note that although each of the two mapping functions $\mathbb{M}_{D\to B}$ and $\mathbb{M}_{B\to D}$, reflects the state of one CA array onto the state of another CA array only approximately, mapping errors do not accumulate. As shown in figure 5.3 the sequential application of both mapping operations produces a cell state array identical to the initial one. It is easy to see that the figures 5.3a and 5.3c are identical. Therefore this property of mapping function can be written literally as follows:

$$\Upsilon_{m(D)}(t_{i+1}) = \mathbb{M}_{B\to D}\left(\mathbb{M}_{D\to B}(\Upsilon_{m(D)}(t_{i+1}))\right) \qquad 5.30$$

5.5.9 Step 9.

The FE solution–dependent variables at time t_{i+1}, $\mathrm{Y}_k(t_{i+1})$, are calculated according to equations 5.14, 5.15 and 5.16, these equations have the form:

$$\mathrm{Y}_1(t_i) = \begin{cases} dead & \text{if} \quad \mathrm{Y}_2(t_i) \le 0 \\ alive & \text{otherwise} \end{cases} \qquad 5.31$$

$$\mathrm{Y}_2(t_i) = 1 - \frac{X_{(D)}(t_i)}{X_{(D)}^{\max}} - \frac{X_{(B)}^{B}(t_i)}{X_{(B)}^{\max}} \qquad 5.32$$

$$\mathrm{Y}_3(t_i) = \frac{X_{(B)}^{B}(t_i)}{X_{(B)}(t_i)} \qquad 5.33$$

5.5.10 Step 10.

The solution–dependent variables at time t_{i+1}, $\mathrm{Y}_k(t_{i+1})$, are returned by the VUMAT subroutine to the ABAQUS solver. This step completes the cycle.

The flow diagram of the present CAFE model is explained in appendix A, from this diagram it can be seen that some parameters are calculated at the finite element level and used as input values into the CA arrays. This condition is used instead of calculating such parameters at cellular level, this makes the model faster as the number of finite elements is small compared to the number of cells.

From the last sections, it can be seen that the coupling of the ductile and the brittle fracture process is through the state of the cells of each CA array. From equations 2.49 (section 2.6.2) it can be seen that the full transfer rule for the ductile CA array depends of the ductile transition rule, the state of a cell m and the neighbouring cells at time t_i, the cell properties of the cell m and the neighbouring cells, the state variable of the cell m and finally on the state of cell m will depend on the state of a group of S corresponding cells of the brittle CA array as shown in figure 5.3. For the case of the full transfer rule for the brittle CA array, from equation 2.50 (section 2.6.2) it can be seen that the full transfer rule depends of the brittle transition rule, the state of a cell m and the neighbouring cells at time t_i, the cell properties of the cell m and the neighbouring cells, the state variable of the cell m and finally on the state of cell m will depend on the state of a group of S corresponding cells of the ductile CA array as shown in figure 5.3.

From equations 2.49 and 2.50 it can be seen that cell s belongs to the group of S cell of one CA array, the states of which will have an influence on cell m of the other CA array. It can be seen that S depends on the total number of cells in each CA array. Therefore the cell states in the ductile CA array are affected by the states of cells in the brittle CA array and vice versa. This to ensure that any change in material integrity, no matter what fracture mechanism caused it, is accounted for in both CA arrays.

Because of the fact that both CA arrays occupy the same physical space, then in order to visualize the cells that died when the condition for nucleating microvoids or microcracks are met, three different colours were assigned to the CA arrays. Blue for the all the alive cells, green for the cells that died in the ductile regime and red for the cells that died in the brittle regime. Therefore the simulation of the ductile–brittle transition is by the automatically generation of dead ductile and brittle cells in each run of the CAFE model. The percent of brittle phase is in function of the test temperature. The temperature dependence was introduced via the power hardening law (Shterenlikht, 2003) in the CAFE model.

5.6 Properties of the CAFE model.

In the present CAFE model, finite elements with a single integration point (C3D8R) have been used. Therefore there are no stress or strain gradients across the finite elements. Mapping procedures such as triangulation (Das, 2002) is not need to be applied to decide which CA cells fall under the influence of a particular integration point. Care must be taken to ensure that finite element sizes are appropriate for regions of high strain gradients as the accuracy of a single integration point finite element is inevitably not as good as that of a finite element with several integration points.

Neither rotation nor deformations of finite elements are assigned to the corresponding CA arrays. Consequently the fracture propagation path will be visualised in the initial finite element configuration, as will be shown in chapter VI.

5.7 Application of CAFE model on ductile and cleavage fracture.

The application of the CAFE model for the simulation of cleavage fracture involves many stages and the fitting of microstructural parameters of the material under study. In the original model, Shterenlikht (Shterenlikht, 2003) suggested a fitting procedure to obtain such microstructural ductile and brittle fracture parameters. In the present work the fitting procedure was attempted but the model did not reproduce the experimental work properly. This may be due to the different distributions of the micro parameters introduced in the original model which are the parameters of a TMCR steel. Therefore a combination of the microstructural parameters of the TMCR steel with the mechanical properties of the Grade A plate steel is not correct. Consequently the fitting procedure did not reproduce the experimental data of the plate steel. So the author of the present project proposed to make a quantification analysis of the microstructural parameters of the steel under analysis in order to introduce to the model parameters proper of Grade A plate steel for a better simulation. The next sections shows the parameters introduced to the model and how they were analyzed.

5.8 Input parameters.

The ductile cell size for CAFE simulations was taken as $0.1mm$, this size is based on the spacing between larger dimples associated with larger precipitates and/or inclusions.

Accordingly the brittle cell size was taken as $0.05mm$, this size is based on the cleavage facet size. These values are the half of size of Shterenlikht model (Shterenlikht, 2003) for a TMCR steel, where the grain size of the TMCR steel was in a range from 5 to 10μm. Ideally brittle cells size must be related to the cleavage facets size or in other words to the effective grain size. If we use the mean grain size value for Grade A plate steel which is $19.5\mu m$ and a finite element size of $1mm^3$ we will have 132651 brittle cells accommodated in each finite element. So the resulted number of cells per finite element will be very high and the run time will increase significantly, so in the present work we used a brittle cell size of $50\mu m$. The finite element size in the damage zone was chosen to be around $0.5mm$ for all the finite elements. This will result in the definition of 125 ductile and 1000 brittle CA cells associated with each finite element in the damage zone of Charpy and four point double–notch bend tests.

5.8.1 Rousselier damage model parameters D, σ_1 and β_F.

Fischer (Fischer et al., 1995) described a methodology to calculate the damage parameter D based on a simple post–processing procedure using the results of an incremental elastic–plastic analysis without taking damage into account explicitly but using a critical strain parameter in the damage indicator D. The damage indicator parameter D, can be calculated by the integration of equation 5.34 (Fischer et al., 1995),

$$\dot{D} = \dot{D}\left(D,\ \sigma_m / \sigma_{eq},\ \varepsilon_{pv},\ \dot{\varepsilon}_{pv} \right) \qquad 5.34$$

where ε_{pv} is the equivalent plastic strain, σ_m is the mean stress, σ_{eq} is the equivalent von Mises stress. In a post–processing procedure, σ_m, σ_{eq}, and ε_{pv} can be taken directly from the stress analysis at each load increment. It can be seen from equation 5.34 that the damage parameter D is based on the stress triaxiality and the critical plastic strain. The damage indicator does not influence the elastic–plastic analysis which means that a "perfect" structure is investigated in the stress analysis. Therefore, this indicator can only be used to indicate the start of a microcrack. After calibration, the damage parameter indicator D, can be used for approximately indicating the onset of a local macrocrack in a structure. This parameter controls the stable propagation of a crack (section 6.1).

Experimentally, the calibration is performed by inspecting the central neck region of tensile specimens with no local stress gradient (smooth tensile tests). Rousselier's damage parameter falls between 1.5 and 2, (Rousselier, 1986), for an Mn–Ni–Mo low alloy steel for PWR vessels (A508 Cl 3) steel. (Tvergaard, 1981) obtained more realistic deformation at fracture with a value of 3 rather than 2. In an European program for simulation with different damage models (Bernaur and Brocks, 2001), some authors used a damage parameter equal to $D = 2$ (Bernaur and Brocks, 2001). In this work a value between 1.5 and 3 will be used for D to analyze the effect of this parameter in matching the experimental data. The different results with variation of parameter D will show the effect of this parameter on numerical simulations. The results are shown in section 6.1. The Rousselier damage parameter, σ_1, is related to the tearing resistance of the matrix material. σ_1 is approximately equal to the mean flow stress of the material multiplied by a factor of $2/3$ (Rousselier, 1986, Rousselier, 1981). More exactly, it is given by the initiation of ductile fracture in the centre of notched tensile specimens. For the rolling and transverse direction, the damage parameter σ_1 was calibrated with notch tensile tests with different constraint levels. In the present work, two different constraint levels were used in the notch tensile tests. The geometry of the notch tensile specimens was shown in section 3.2. In this section the damage model parameter σ_1 was calibrated for the rolling and transverse directions of the plate steel. Figure 5.4 and 5.5 show the plot of notch tensile tests with two different constraint levels for rolling and transverse direction of the plate steel. These figures also show the position where σ_1 is measured.

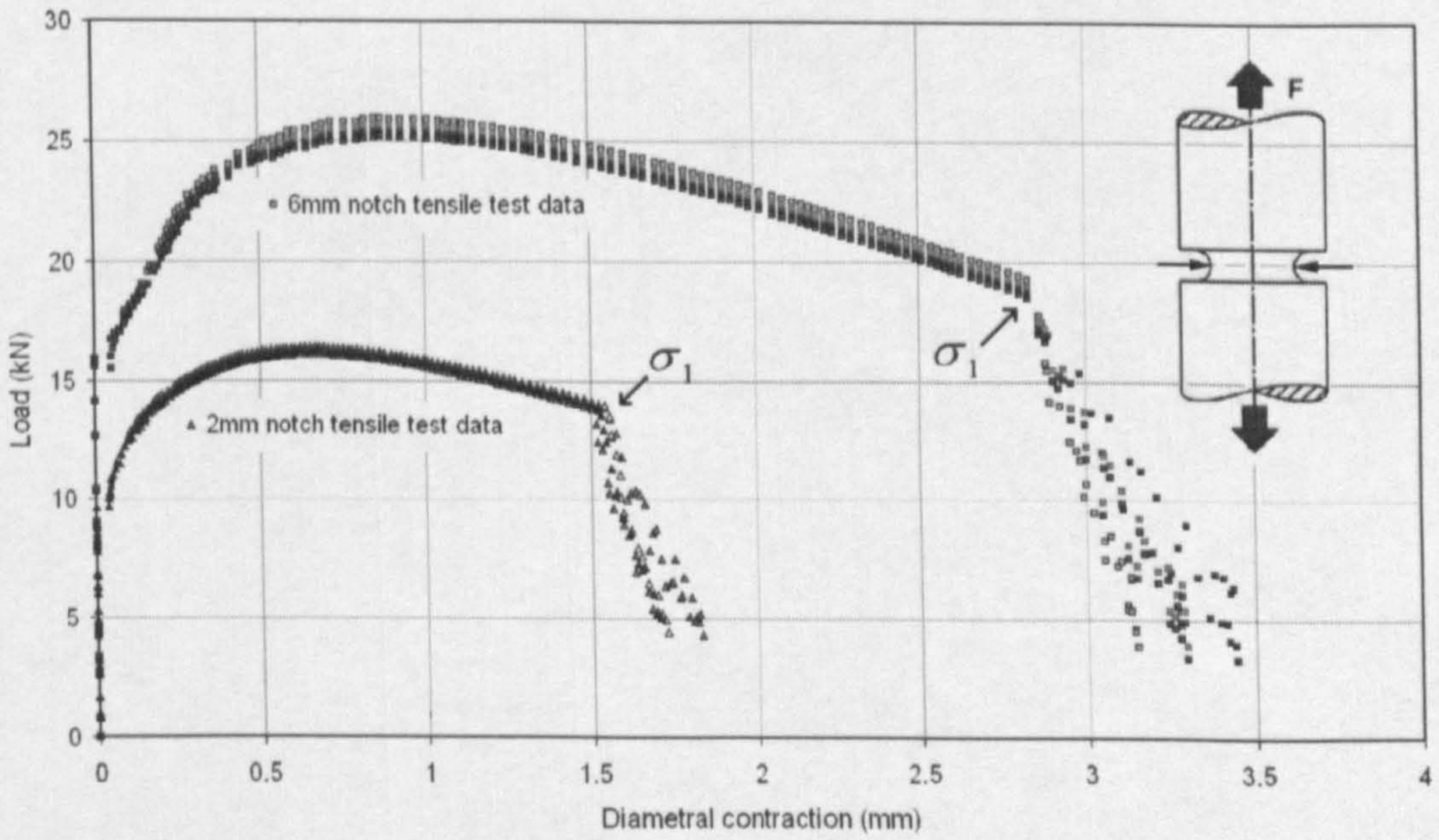

Figure 5.4 – Rousselier damage model parameter σ_1 in the rolling direction.

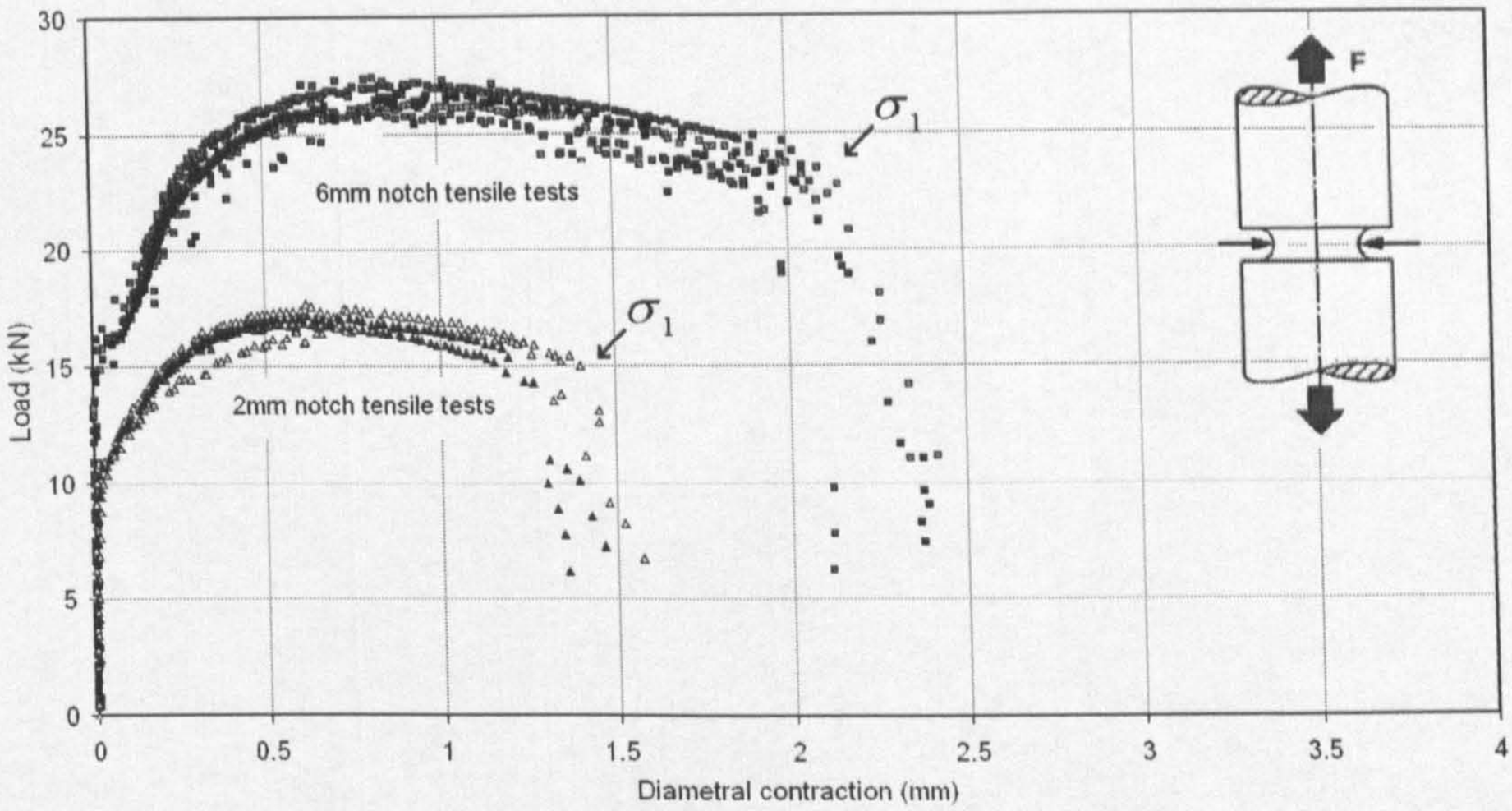

Figure 5.5 – Rousselier damage model parameter σ_1 in the transverse direction.

The experimental values of σ_1 are reported in tables 5.2 and 5.3 for rolling and transverse direction respectively. From these tables we can see that σ_1 values are higher in the rolling direction than those in the transverse direction. The fracture stress values of smooth tensile tests were also calculated and reported in tables 5.2 and 5.3 in order to make a comparison with those values measured using notch tensile specimens.

Table 5.2 – Rousselier damage parameter σ_1 in the rolling direction of the plate steel.

Test No.	Smooth tensile tests	6mm notch tensile tests	2mm notch tensile tests
Test 1	$\sigma_1 = 914MPa$	$\sigma_1 = 917MPa$	$\sigma_1 = 876MPa$
Test 2	$\sigma_1 = 916MPa$	$\sigma_1 = 893.5MPa$	$\sigma_1 = 898MPa$
Test 3	$\sigma_1 = 1059MPa$	$\sigma_1 = 905MPa$	$\sigma_1 = 867MPa$
Test 4	$\sigma_1 = 989MPa$	$\sigma_1 = 882MPa$	$\sigma_1 = 891MPa$
Average	$\sigma_1 = 969.5MPa$ (std=69MPa)	$\sigma_1 = 899.2MPa$ (std=15MPa)	$\sigma_1 = 883MPa$ (std=14MPa)

From table 5.2 it can be seen that the damage parameter σ_1 for the notch tensile specimens has less variation than for smooth tensile specimens. The standard deviation is very similar for the two sets of notch tensile specimens. Notch tensile tests are recommended for the calibration of the damage parameters of the Rousselier damage model (Bernaur and Brocks, 2001). This

variation was less pronounced in the transverse direction of the plate steel as clearly shown in table 5.3 where the standard deviation for smooth tensile tests is almost similar for notch tensile tests with a notch radius of 2mm, but the mean of smooth tensile tests was very different than that of notch tensile tests. From the results of tables 5.2 and 5.3, the values of $\sigma_1 = 890MPa$ and $\sigma_1 = 830MPa$ were chosen for the rolling and transverse direction but this parameter may be adjusted to obtain correlation with experimental data. σ_1 parameter is generally considered a material constant. In the present steel this parameter has shown some scatter, the level of scatter is different in each direction of the plate steel. The σ_1 parameter is generally calibrated with round notched tensile specimens for the Rousselier damage model as suggested by Batisse and Bernaur (Batisse et al., 1987, Bernaur and Brocks, 2001).

Table 5.3 – Rousselier damage parameter σ_1 in the transverse direction of the plate steel.

Test No.	Smooth tensile tests	6mm notch tensile tests	2mm notch tensile tests
Test 1	$\sigma_1 = 733MPa$	$\sigma_1 = 848MPa$	$\sigma_1 = 812MPa$
Test 2	$\sigma_1 = 781MPa$	$\sigma_1 = 862MPa$	$\sigma_1 = 821MPa$
Test 3	$\sigma_1 = 772MPa$	$\sigma_1 = 788MPa$	$\sigma_1 = 901MPa$
Test 4	$\sigma_1 = 847MPa$	$\sigma_1 = 818MPa$	$\sigma_1 = 826MPa$
Average	$\sigma_1 = 783MPa$ (std=47MPa)	$\sigma_1 = 829MPa$ (std=33MPa)	$\sigma_1 = 840MPa$ (std=41MPa)

The critical value of the damage variable, β_F, was distributed across the ductile CA cell using a normal distribution function. The median value applied to the model is $\bar{\beta}_F = 8$ with a standard deviation equal to $STD(\beta_F) = 1.2$. The median value $\bar{\beta}_F$ was based on the best fitted critical damage variable obtained in section 6.4.

5.8.2 Weibull analysis of the distribution of void volume fraction.

The analysis of the distribution of void volume fraction was performed by microscopic examination of fracture surfaces of tensile and Charpy specimens tested at room temperature in regions of pure ductile fracture. To perform the analysis, a Scanning Electron CAMSCAN model

MK2 Microscope was used. A set of three micrographs of broken surfaces of tensile tests and Charpy broken surfaces were analysed. Figure 5.6 shows a fracture surface of a tensile specimen and how the distance between voids was characterized. The void volume fraction is generally related to the distance between large voids nucleated by the debonding of MnS inclusions distributed randomly in fracture surfaces of Charpy and/or tensile specimens. Micrographs of broken surfaces of tensile specimens were taken from regions very close to the centre of the broken surfaces, as the severe stress triaxiality occurred in the centre of tensile specimens, and fracture propagation occurred from the centre of tensile specimens to the edge. So in this region we obtain information on the critical void volume fraction where fracture propagation occurs. The measurement between the distances of microvoids is shown clearly in figure 5.6.

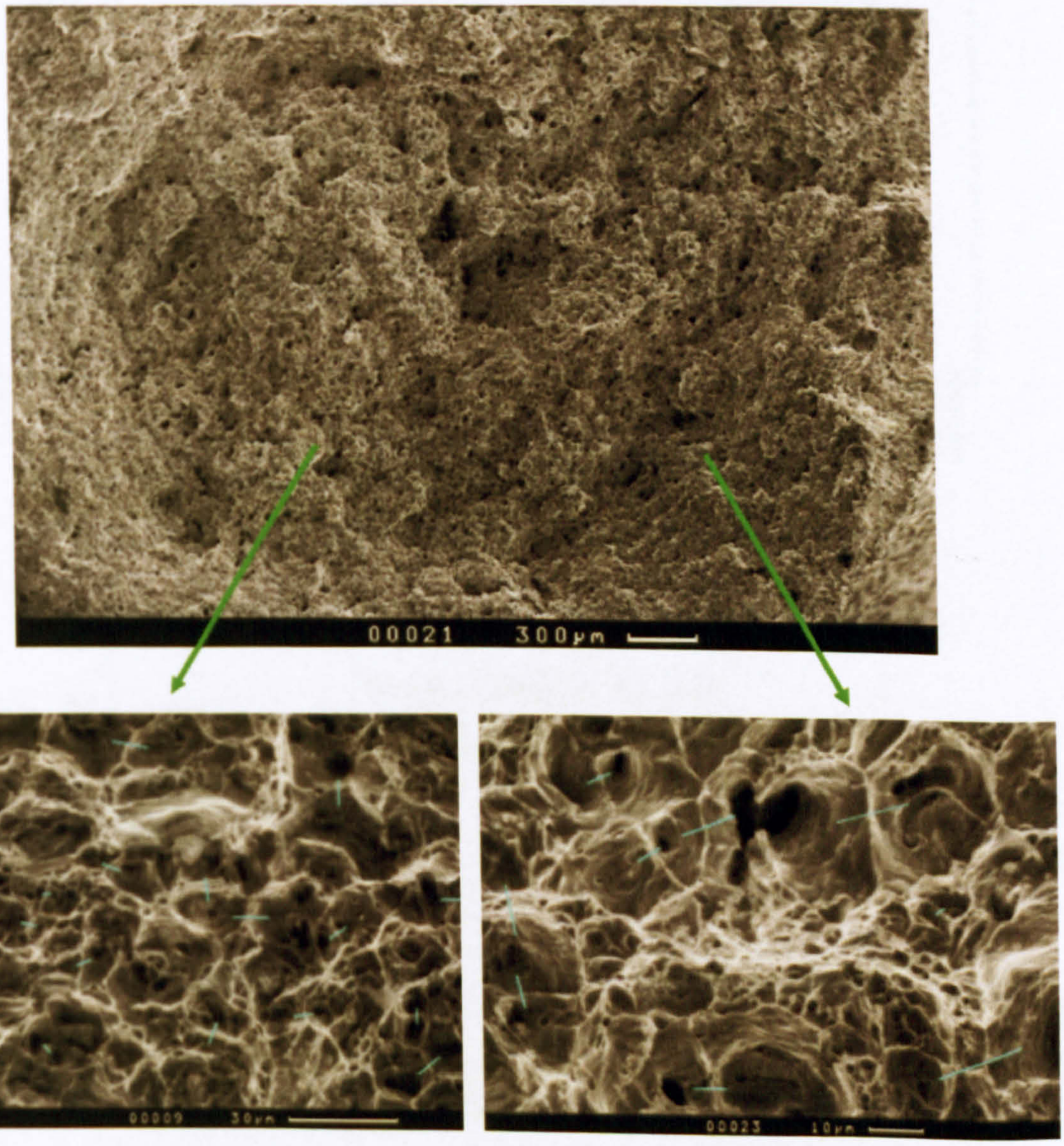

Figure 5.6 – Micrographs showing the how the void volume fraction was analysed.

Figure 5.7 shows the distribution of the distance between large voids. The void volume fraction distribution was analyzed with Weibull distribution analysis. The program @RISK (@RISK for Excel, 2007) was used to perform such analysis. Figure 5.8 shows the fit curve (green line) to experimental data. This line represents a Weibull function from which the Weibull parameters are calculated. The obtained Weibull parameters calculated with @RISK are shown in figure 5.8. Those parameters will be used to introduce the distribution of void volume fraction into the ductile part of the CAFE model via random number generators.

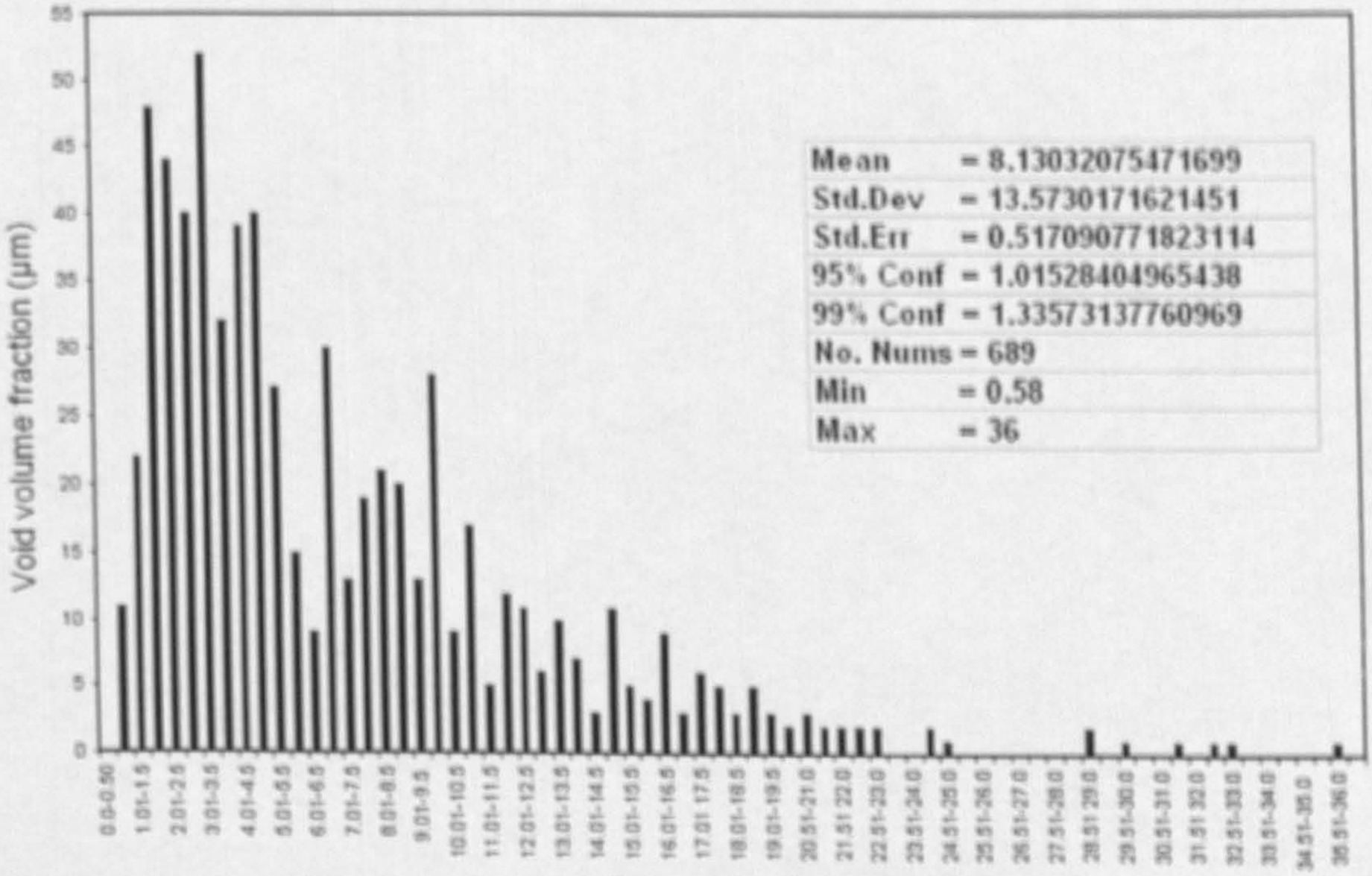

Figure 5.7 – Void volume fraction distributions.

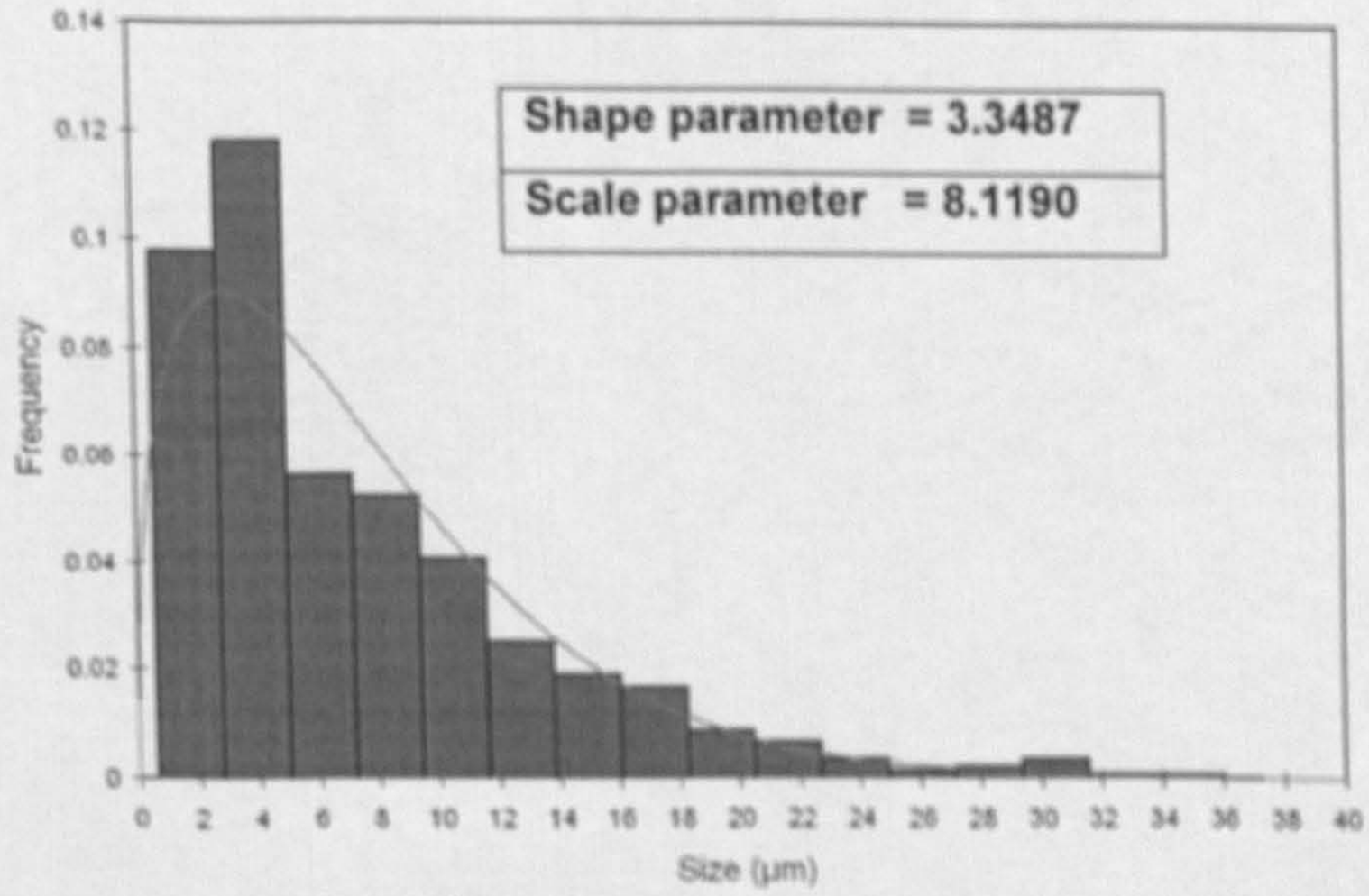

Figure 5.8 – Weibull distribution fit performed.

In order to make a comparison of the Weibull parameters calculated with @RISK with other program, the author calculated those parameters with Excel (Office XP). In this program, the maximum likelihood estimation procedure was used to estimate the Weibull parameters by performing a simple linear regression. With this method we can obtain that parameters by fitting a straight line as shown in figure 5.9. The values of the shape and scale parameters are also shown in this figure. The Weibull parameters calculated with both methods are very similar, both methods gave good results, so each of the results can be used as input parameters for the ductile part of the CAFE model.

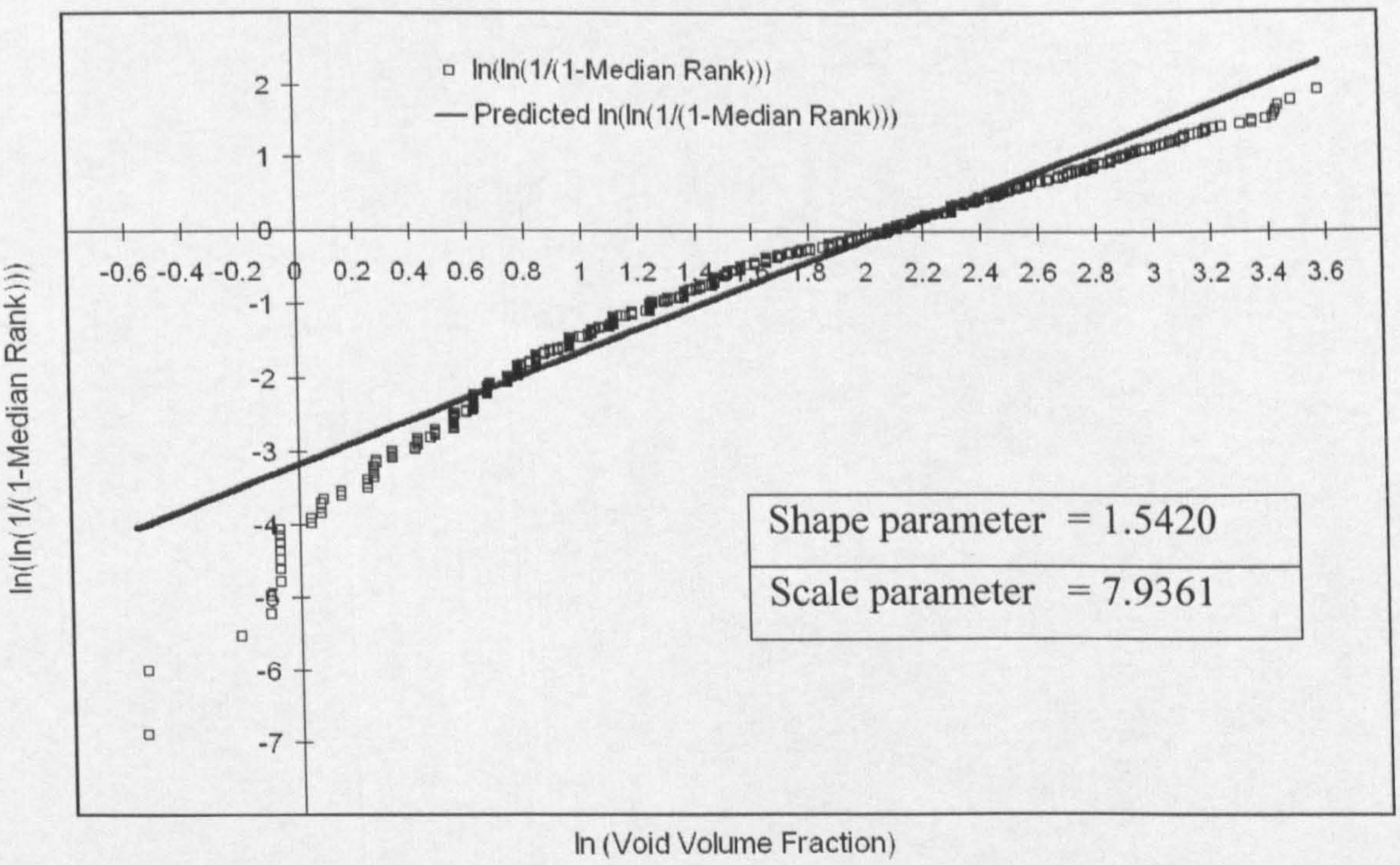

Figure 5.9 – Line fit plot used to calculate Weibull parameters with Excel.

5.8.3 Weibull analysis of the distribution of microstructure.

It is well established (Wu et al., 2005) that for hot–rolled or normalized ferrite–pearlite microstructures that the yield stress σ_y, the critical local fracture stress σ_F and the Charpy impact transition temperature are a linear function of the mean grain size of polygonal ferrite. The empirical equations, however, can only be applied to materials regarded as uniform homogeneous, such as normalized steels, which have a single size distribution of ferrite grains together with small and finely distributed carbides. But for non–homogeneous materials, such as steels with duplex ferrite structure seen in thermomechanically control rolled steels, the average grain size parameters does not properly represent the real microstructure (Davis and Strangwood, 2002) and therefore cannot be used to predict cleavage fracture stress and ITT.

Therefore the distribution of grain size of the present steel was analyzed and introduced into the CAFE model. Four samples were cut in the through thickness of the plate material in the rolling direction of the plate steel. These four sections are schematically marked by the letter a, b, c and d in figure 5.10, the plate thickness of $20\,mm$. This was done to take into account the variation of grain size through the thickness of the plate, for a better characterization of grain size in CAFE simulations.

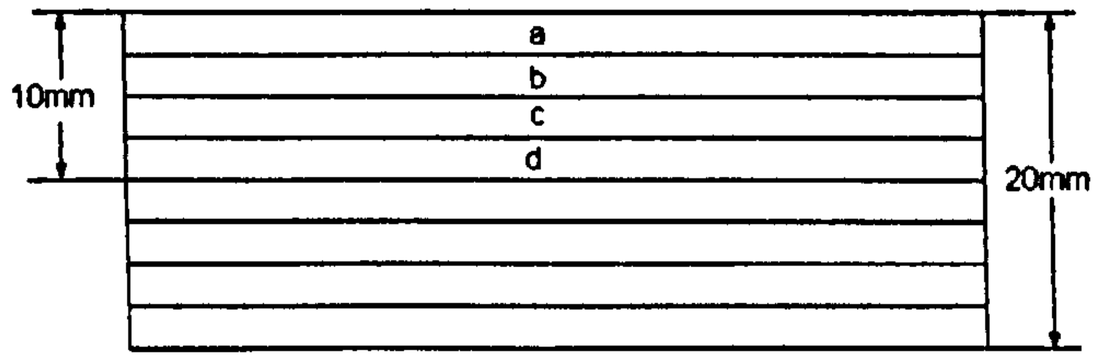

Figure 5.10 – Schematic representation in the through thickness of the plate steel of the positions from where samples were taken to analyze the grain size.

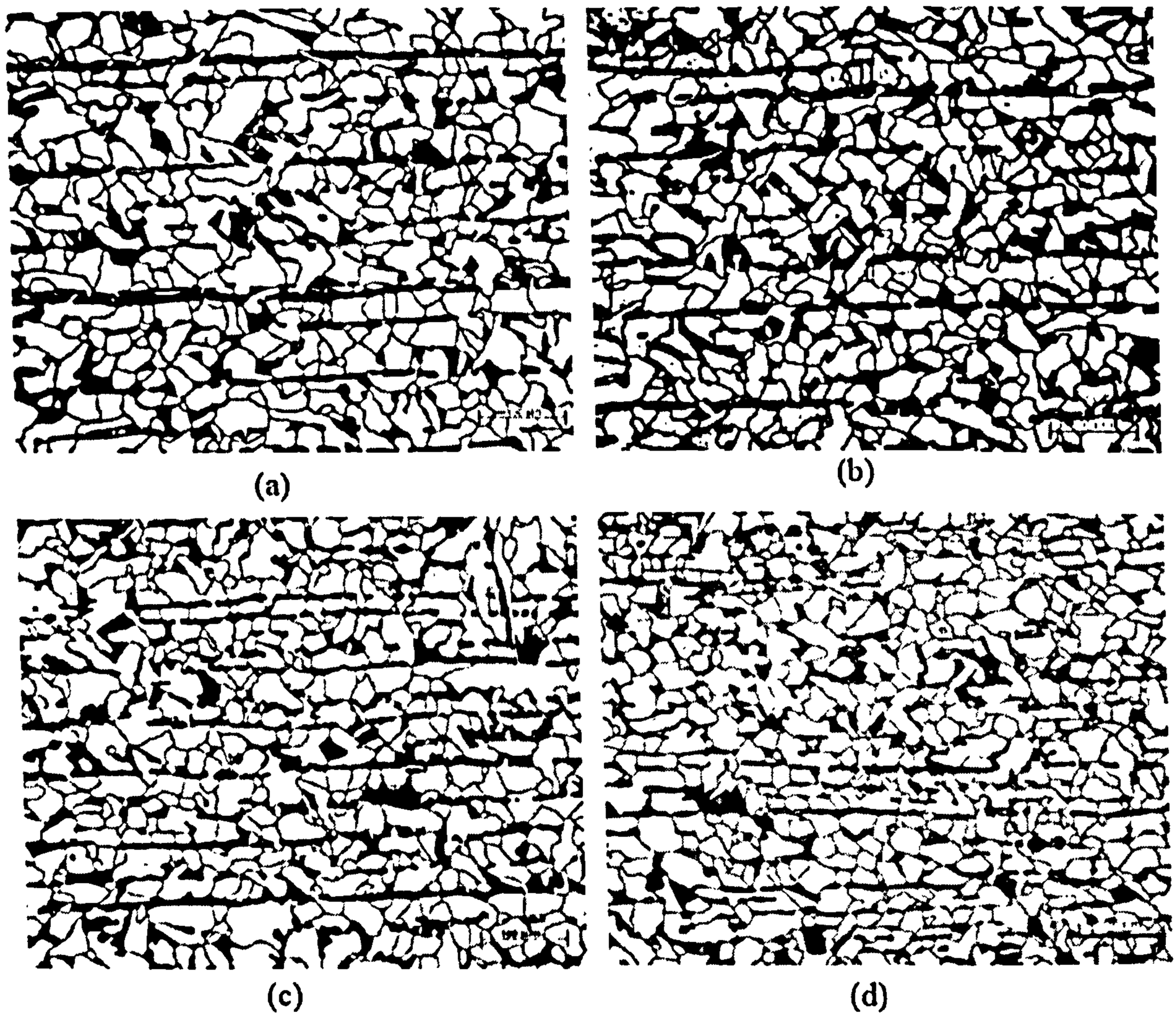

Figure 5.11 – Microstructure of Grade A plate steel showing the difference of grain size through the plate thickness showed schematically in figure 5.10.

The samples were mounted in bakelite, polished and etched with a mixture of nital at 5% and picral to reveal the pearlite microstructure. An optic microscope was used to take the images of the microstructure. The micrographs were taken with a magnification of $20X$. Figure 5.11 shows the typical microstructure of Grade A ship plate steels of each section of the plate marked in figure 5.10. This figure clearly shows the variation of grain size through the thickness of the plate. The analysis showed that the mean grain size in each figure is different.

The micrographs clearly show bands of pearlite in the matrix of ferrite which follow the rolling direction of the plate steel. The thickness of pearlite bands varies according to the variation of grain size in the through thickness. For small grains the thickness of the pearlite bands are smaller. The grains close to the surface of plate are smaller. In order to perform grain size analysis, the four images of figure 5.11 were put together in a single picture and analysed as one image. The resulting image is shown in figure 5.12; in this figure we eliminated many grains of the side of the figure because they apparently did not represent complete grains. This was done in order to perform a better measurement o grain size. The statistical analysis of grain size was performed with the Image Analysis and Measurement Program SigmaScan Pro version 5.0 (SigmaScan Pro Version 5.0, 2005).

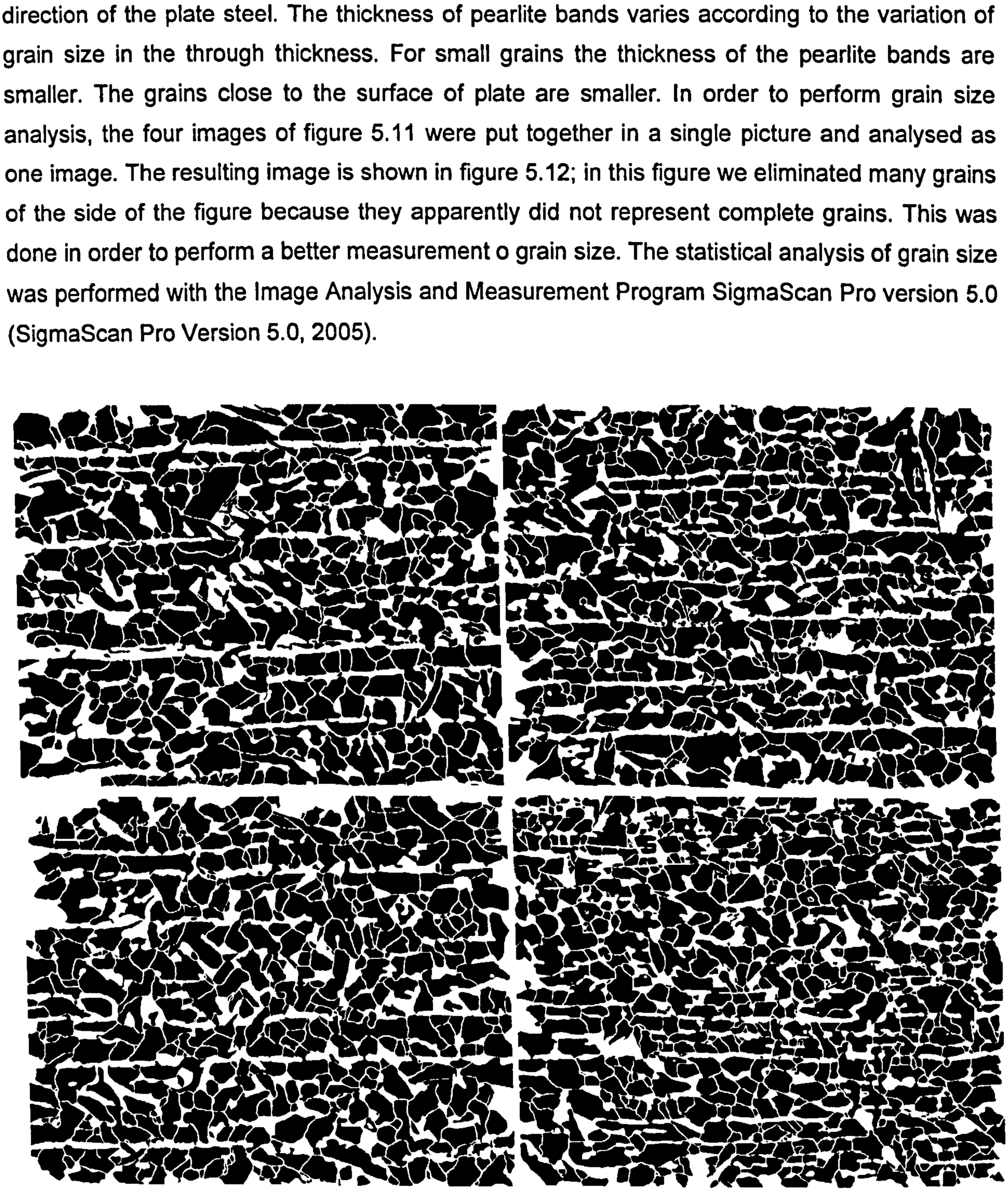

Figure 5.12 – Microstructure of Grade A ship plate steel.

In figure 5.12 the grains are represented by black lands. This was done to give a clear definition of each grain to the program. The analysis of the distribution of grain size is shown in figure 5.13. A total of 2239 grains were counted. Statistical analysis showed that the mean grain size is $19.5\mu m$. It can be seen that the grain size is relatively small, but the toughness properties of this material, as mentioned before, are quite limited. This may suggest that the grain size is not the only parameter that can control the toughness properties of this kind of steels. Humphreys (Humphreys, 1997) reported ASTM grain size of the order of 7.5 to $10\mu m$ for 40 plates of Grade A ship plate steel. In the present case, the mean of grain size is $19.5\mu m$, which is about twice as large as that reported by Humphreys. The distribution of grain size was analysed with Weibull distribution analysis. The results are shown in figure 5.13. In this work it is suggested that the toughness properties of the material under study is more related to the distribution of the size of pearlite lands rather than to ferrite grains size as will be shown later in this work.

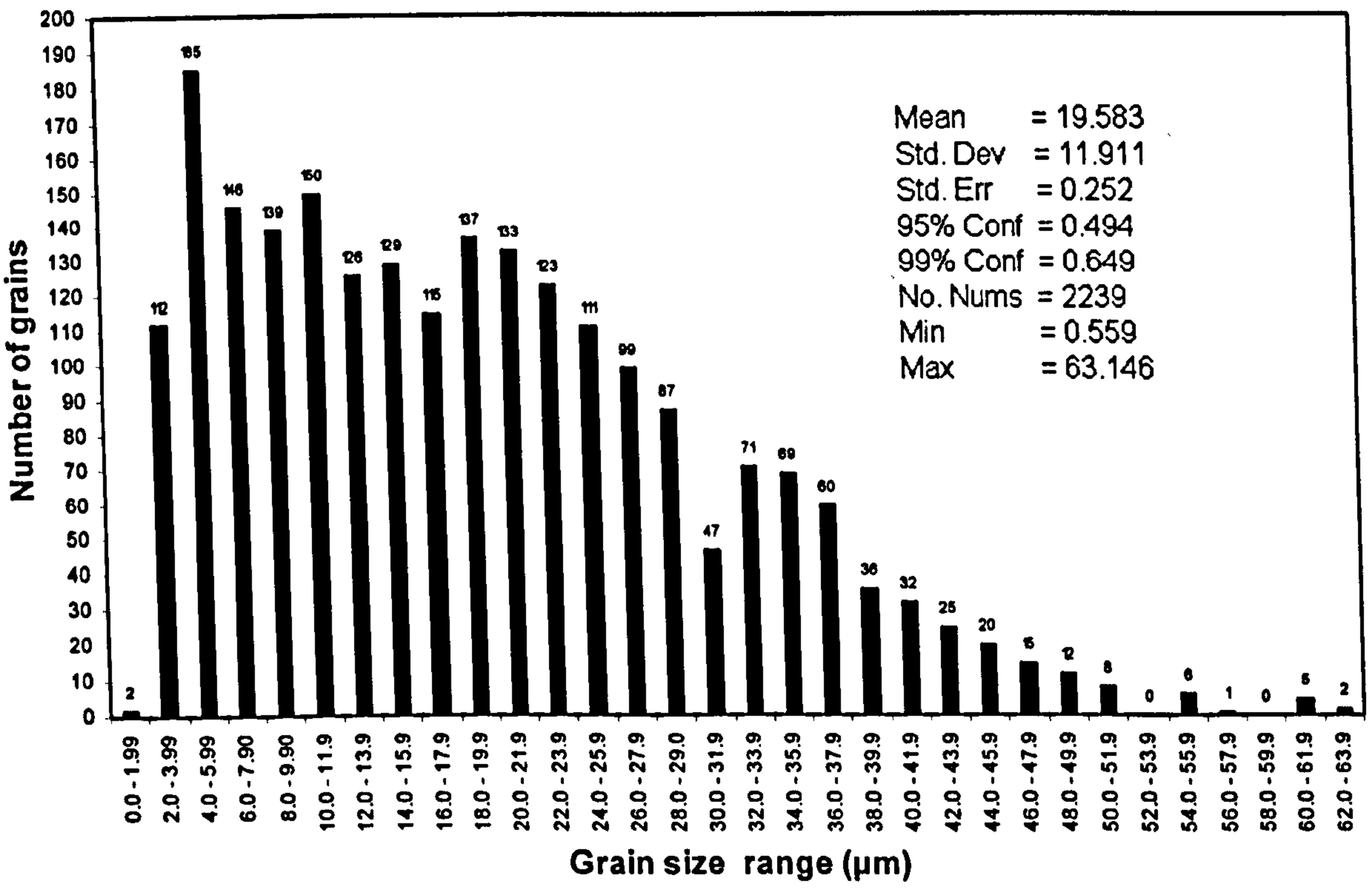

Figure 5.13 – Grain size distributions in terms of Ferret diameter.

The distribution of grain size was analysed in terms of the ferret diameter. In this distribution it was found grains from very small to large grains. The range of the smallest grains are from $0.55\mu m$ to $2\mu m$, the largest grain was about $63\mu m$. The analysis was done with the program @RISK Industrial Version (@RISK for Excel, 2007) and with the program Excel. Figure 5.14 shows the fit of the distribution to calculate the Weibull parameters. The values of the Weibull parameters, the shape and scale parameter values are also shown in this figure.

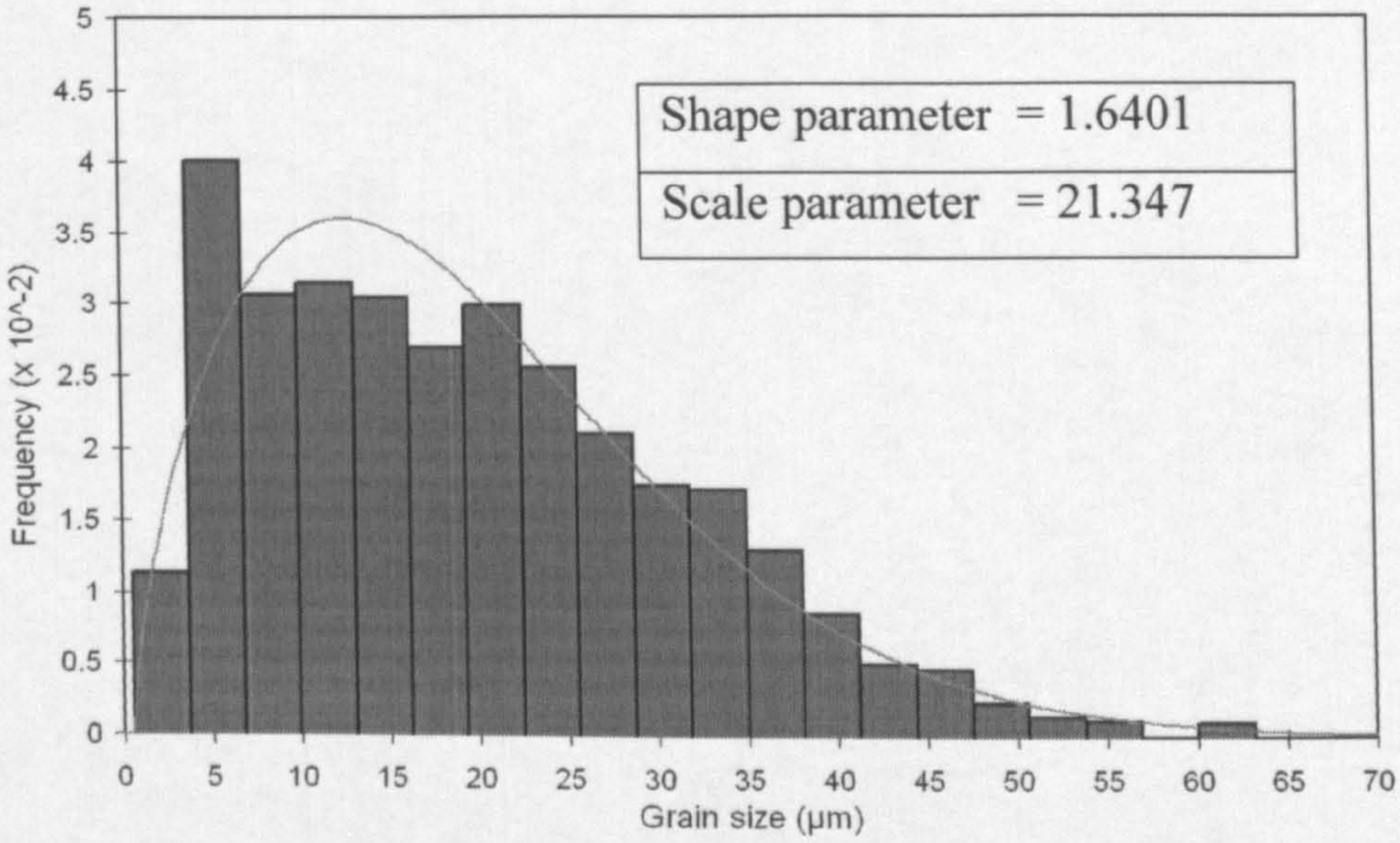

Figure 5.14 – Weibull distribution fit performed with @Risk.

In order to make a comparison of the Weibull parameters calculated with @RISK with other program, the author calculated those parameters with Excel. In Excel, the maximum likelihood estimation procedure was used to estimate the Weibull parameters by performing a simple linear regression. One can obtain the parameters by fitting a straight line as shown in figure 5.15. The shape and scale Weibull parameters are also shown in this figure.

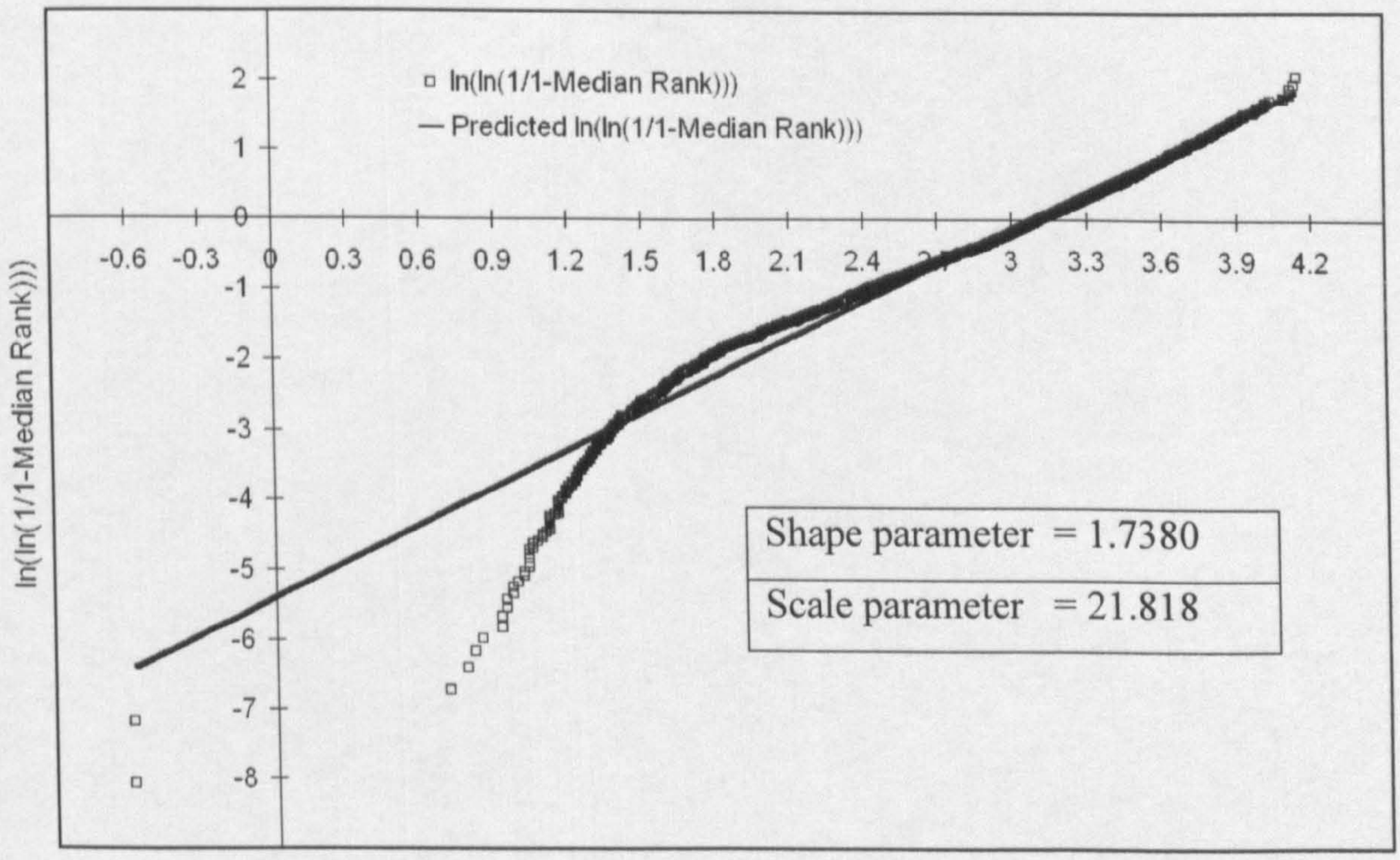

Figure 5.15 – Line fit plot used to calculate Weibull parameters.

It can be seen that the Weibull parameters calculated with both methods described above are very similar, both of them gave good results. The results obtained with @Risk will be used in the CAFE model because this program fitted better the experimental data.

5.8.4 Weibull analysis of the distribution of pearlite microstructure.

An analysis of the distribution of the pearlite microstructure took place in order to identify the pearlite length size of these colonies in the microstructure. Figure 5.16 shows typical distribution of pearlite lands in ferrite matrix. From figure 5.16 we found that some pearlite lands have a length up to $145\mu m$. The thickness of pearlite varies in the through thickness of the plate steel. The thickness is bigger in the middle of the plate. Figure 5.17 shows the distribution analysis of pearlite lands, the mean size of pearlite lands is about $34\mu m$. The statistical analysis was performed with the Image Analysis and Measurement Program SigmaScan Pro version 5.0 (SigmaScan Pro Version 5.0, 2005).

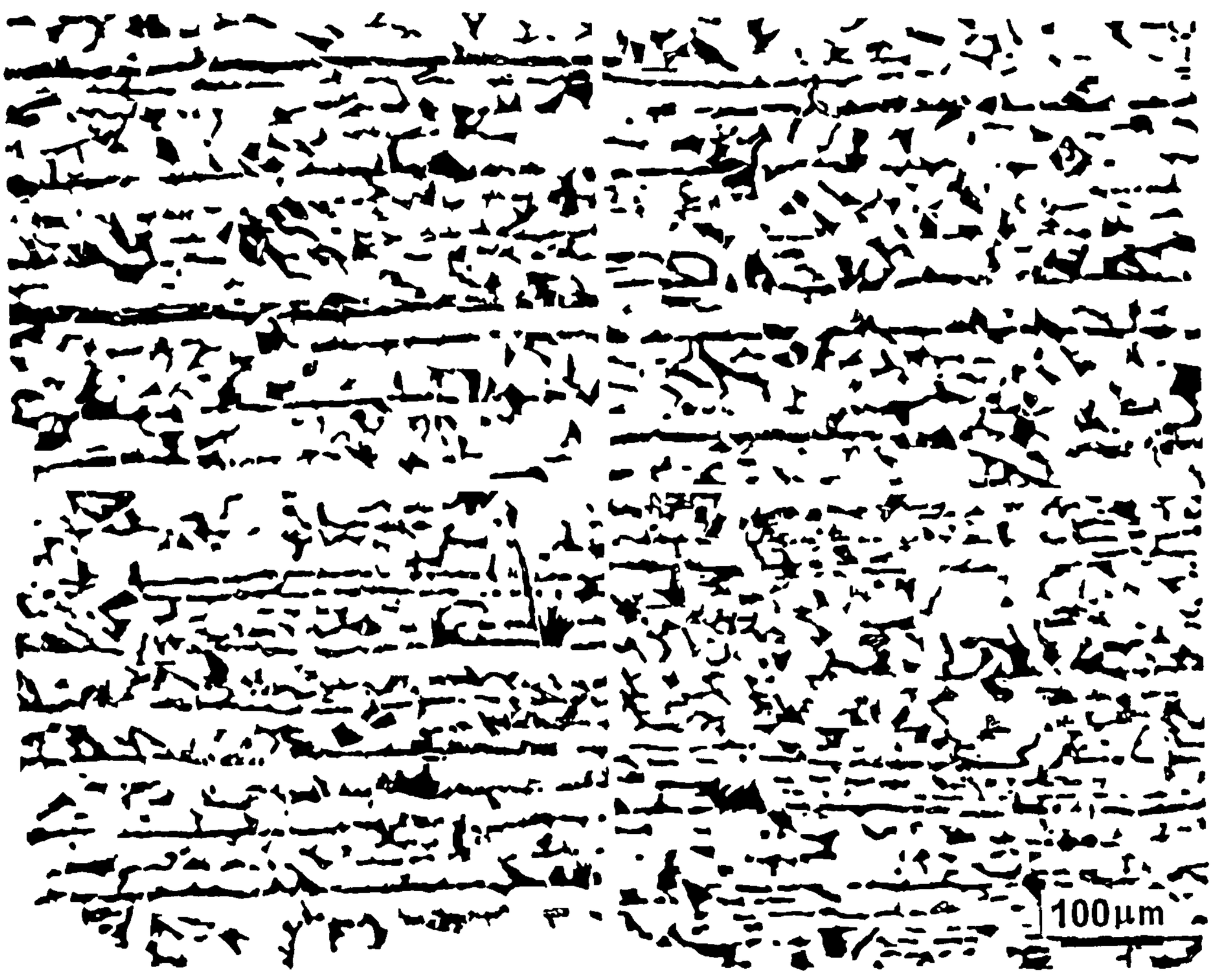

Figure 5.16 – Distribution of pearlite microstructure of Grade A ship plate steel.

As in previous microstructural analysis, the statistical analysis was performed with @RISK and Exel. The data was analyzed with Weibull distribution analysis. The Weibull parameters were calculated with @RISK, the values of those parameters are: shape parameter = 2.115 and scale parameter = 37.363. Figure 5.18 shows the fit line in experimental data which represent the Weibull distribution function where the program Exel was used to fit this curve. The shape and scale parameters obtained are also shown in figure 5.18.

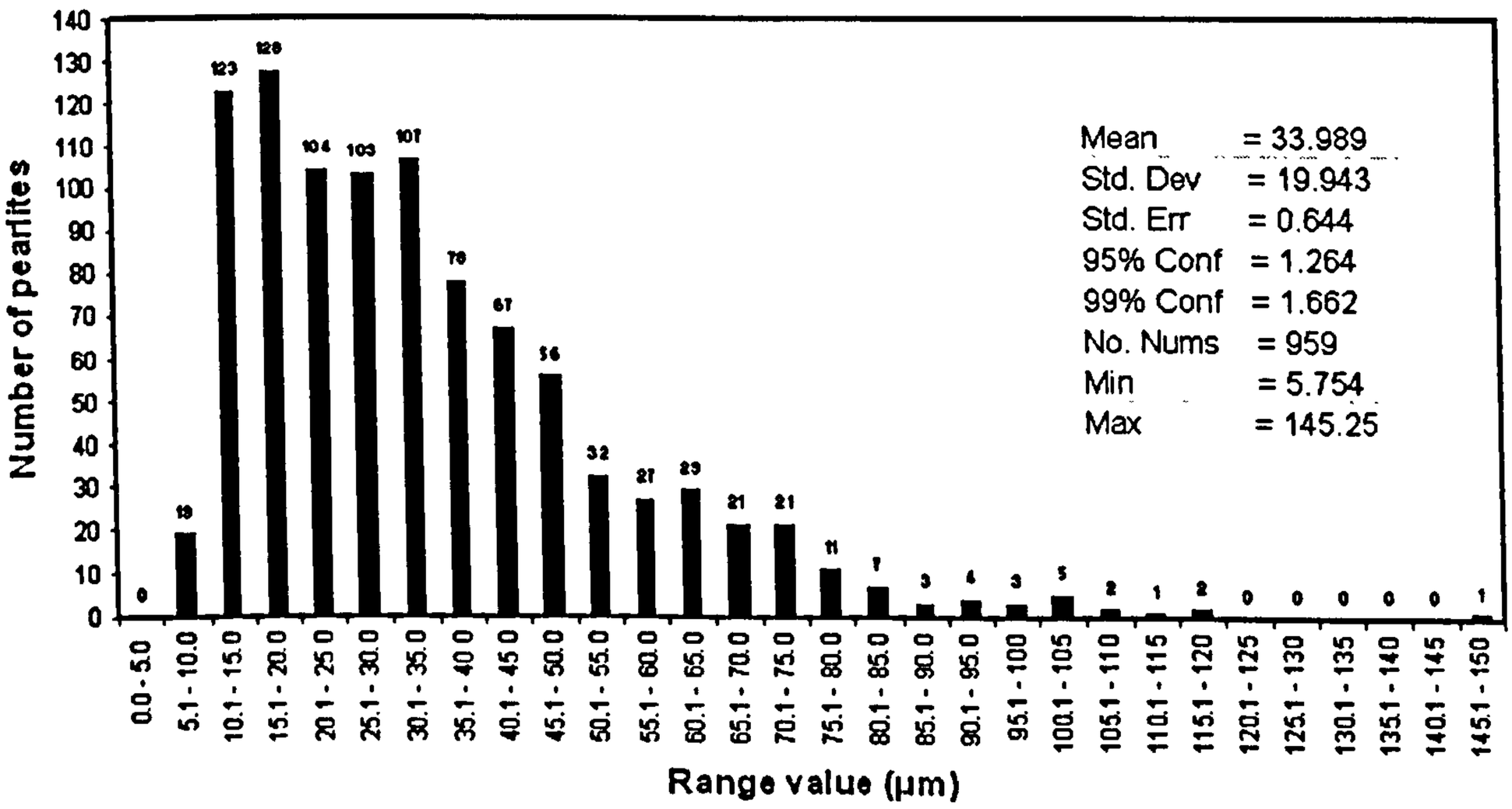

Figure 5.17– Distribution of the length of the pearlite microstructure.

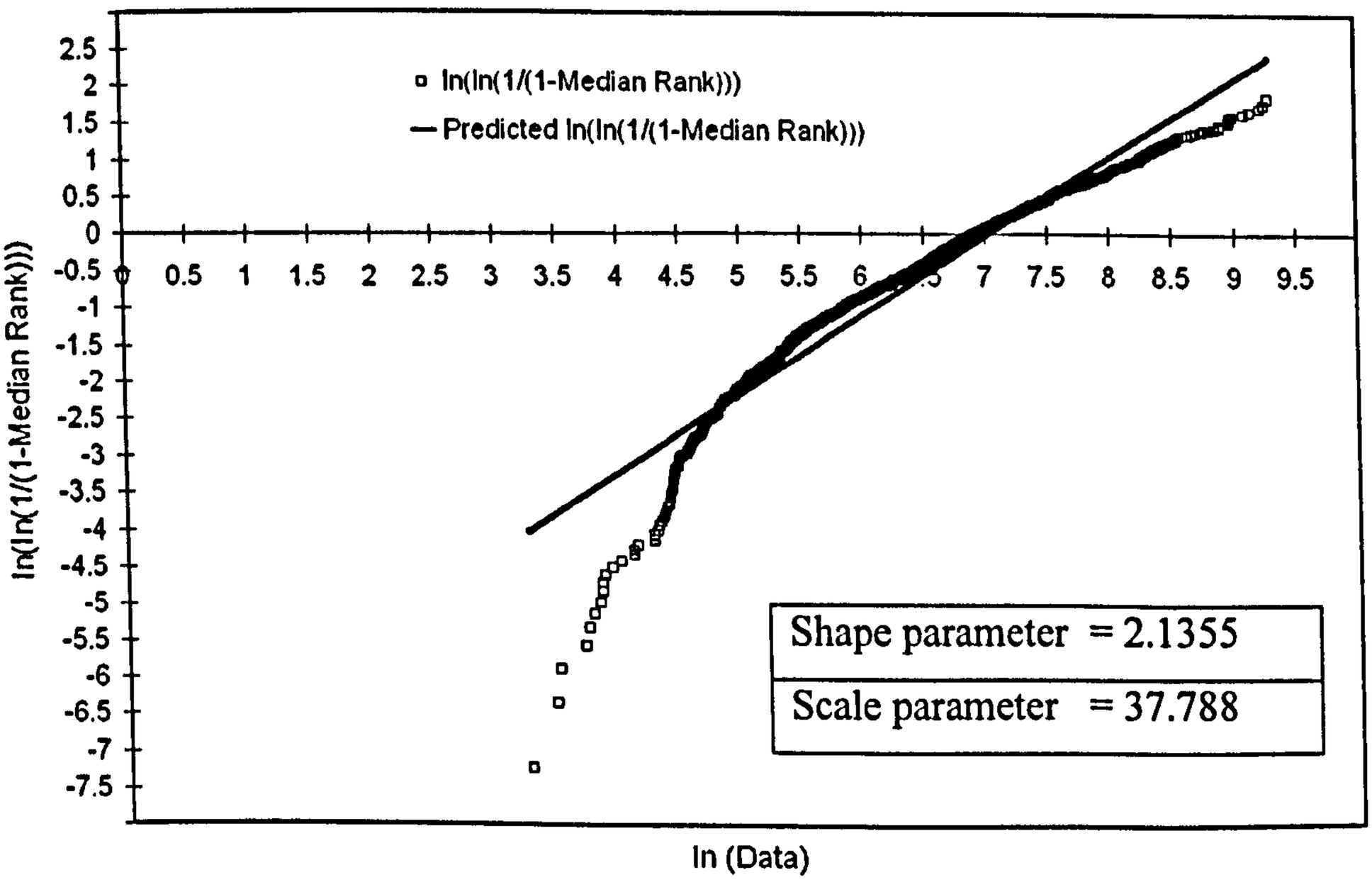

Figure 5.18 – Line fit plot used to calculate Weibull parameters.

5.8.5 Weibull analysis of the distribution of misorientation of grains in terms of cleavage facets orientation.

The misorientation angle of grains in steels plays a vital role in the propagation of cleavage fracture and in the fracture surface appearance. High misorientation angles along with large cleavage facets affect the fracture toughness and the ductile–brittle transition temperature of steels. For ferritic steels it has been identified that the twist misorientation across a high misorientation angle has a more profound effect on cleavage fracture resistance than the tilt misorientation. Detailed observations and measurements over random selections of small and large misorientation angles may lead to a quantitative model for the resistance of cleavage fracture. Due to time constrain, this idea will be explored in a near future. In this analysis it was found that high misorientation angles offer greater resistance to fracture propagation in the ductile brittle transition of steels. The effect of misorientation angle of grains in terms of microcrack propagation and microcracks nucleation is also discussed in the present section.

Kim (Kim et al., 2000), showed a distribution of misorientation angles where large number of boundaries fall into two ranges of misorientation angles; the ranges were below 10° and between 50° and 60° in a bainitc steel. He also showed that a crack front may ignore grain boundary angles smaller than 15°. Below this angle single large facets accommodated multiple grains, they also found that the facet size matches a defined "effective grain size" which is defined on the basis of grain boundary misorientation. The criterion in deciding the effective grain size can be defined by the ability of its boundary to act as the barrier to the deformation or crack propagation, and its ability can be explained in relation with the misorientation at the boundaries. When boundary between two adjacent packets has low misorientation, the deformation or crack is expected to easily transmit across the boundary, and in these cases, the two packets can be regarded as a single grain. They also found that low angle boundary has a low misorientation. Hence, these boundaries are expected to have low resistance to the transmission of deformation. They also summarized that the fracture direction is maintained within a packet regardless of the existence of lath. This result indicates that the lath or cell boundaries do not act as effective barrier to the crack propagation. Thus the unit of the optical microstructure analysis may not match the real microstructural unit experienced by a crack, when fracture propagation is in progress. Figure 5.19 shows the optical microstructure of Grade A plate steel. This image shows apparently some high mis–oriented grains. The red arrows show large grains and the blue ones show small grains. But this optical view obviously does not truly show the real misorientation of grains. The distribution of misorientation angles between grain boundaries is generally quantified using EBSD patterns (Randle, 1990, Cizek et al., 2006). But due to the time that this kind of analysis takes, in the present work the misorientation was characterized in terms of the misorientation of the cleavage facets.

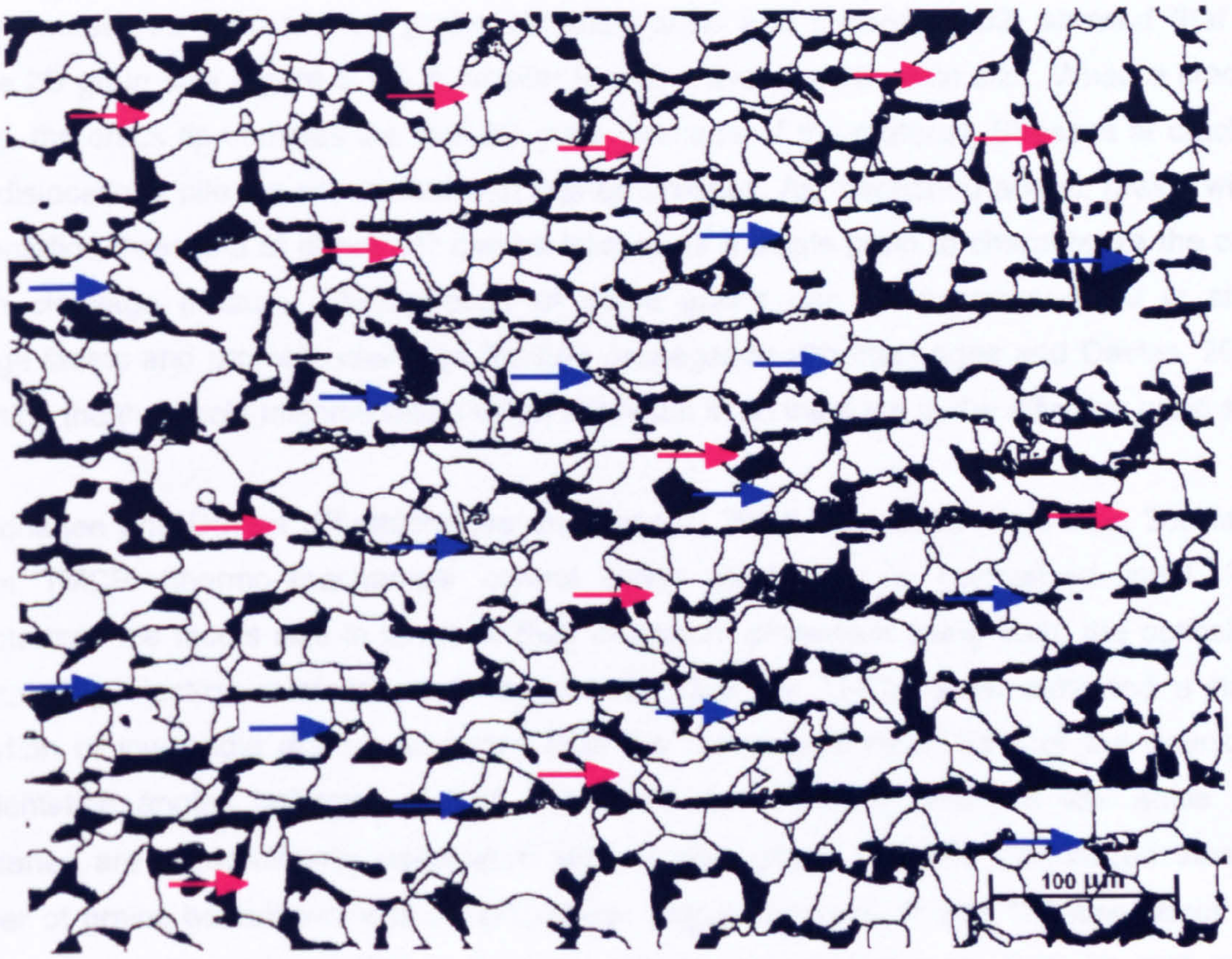

Figure 5.19 – Microstructure of Grade A ship plate steel, ferrite grains with lands of pearlite.

The temperature selected for the analysis of misorientation angle in terms of the misorientation of cleavage facets were –60º and –196º. The first temperature was chosen due to the fact that at this temperature the fracture surfaces of Charpy specimens were totally brittle and the second temperature is the lower shelf of the transition temperature and all the necessary conditions for cleavage fracture are satisfied. This figure also shows a distribution of both small and large grains. It can be shown that some grains apparently are mis–oriented with respect to their neighbours as their length is oriented *certain angle* with respect to the length of the other grains. The red arrows show some examples of grains with apparently large misorientation. Fractography analysis was carried out on the fracture surfaces of both, four point double–notch bend specimens and Charpy specimens with a Scanning Electron CAMSCAN model MK2 Microscope.

5.8.5.1 Definition of misorientation of cleavage facets.

The cleavage facets size and its misorientation angle represent the microstructural unit that a crack front experiences in metals. A comparison of the traditional optically measured grain size from 2D surfaces (figure 5.19) which is generally characterized with metallographic analysis and the distribution of the facets size, which can be considered real 3D surfaces due the fact that

they are measured from broken grains (Bhattacharjee and Davies, 2002) showed that the average 2D grain size (figure 5.19) is smaller than the average 3D grain size. When a crack is growing, the crack tip samples the real 3D grain structure of the material. Stresses at crack tip cause dislocations pile–up associated with higher stresses. As mentioned above, grains with a misorientation threshold of about 15° can be treated as a single grain to characterize the crack front in cleavage fracture. Then groups of those grains can be accommodated in single cleavage facets and promote cleavage fracture propagation (Bhattacharjee and Davies, 2002). Increasing the threshold misorientation value will result in an increase in the effective grain size.

Bhattacharjee and Davies (Bhattacharjee and Davies, 2002) measured more than 300 facets from a TMCR (thermo–mechanical control rolled steel) and a normalized steel. They characterized the facets size in terms of their maximum dimension using both, the optical and the scanning electron microscope. They showed that the TMCR steel exhibited a higher proportion of low angle grain boundaries than the normalized steel. 63% of the grains had misorientation angles between 3° and 10°. They demonstrated that the low angle grain boundaries are predominantly associated with smaller grains. For the normalized steel the number of grains boundaries with misorientation angles between 3° and 10° was about 15%. Their analysis also showed that grains with misorientation angles as high as 12° can be accommodated in a single cleavage facet. This led to the conclusion that single cleavage facets can be made up of several grains in both steels. In the present analysis, micrographs were taken from different areas of broken Charpy and 4PBT fracture surfaces of specimens tested at –196°C. The misorientation angle of the cleavage facets (grain misorientation) was characterized in terms of the misorientation of the largest size of each facet created by the broken of grains with respect to largest size of its neighbour facets, the angle between the orientation of two facets was measured. Careful attention was paid into the definition of cleavage facets as twins generated in the grains, when the deformation of grains during the loading process takes place, can create confusion for the definition of the orientation, the boundary and size of facets, In order to identify correctly cleavage facet boundaries and size, the cleavage planes that occurred in the grains helped to minimize the errors when identifying the cleavage facets. Figure 5.20 shows an example of how the cleavage facets orientation was characterized. The red lines represent the size of the cleavage facets and their orientation in terms of their maximum dimension. This picture also shows a distribution of large and small facets distributed randomly on fracture surfaces of Charpy specimen tested at –196°C. The misorientation of each facet with respect to its neighbours was measured, and the size of each facet was measured as well. This was to analyze how the sizes of grains affected the fracture propagation direction and the roughness of the fracture surfaces and consequently the fracture toughness of the material. Large cleavage facets were found in this material on Charpy surfaces, some of them were located close to the notch root. Figure 5.21 shows some examples of those large cleavage facets.

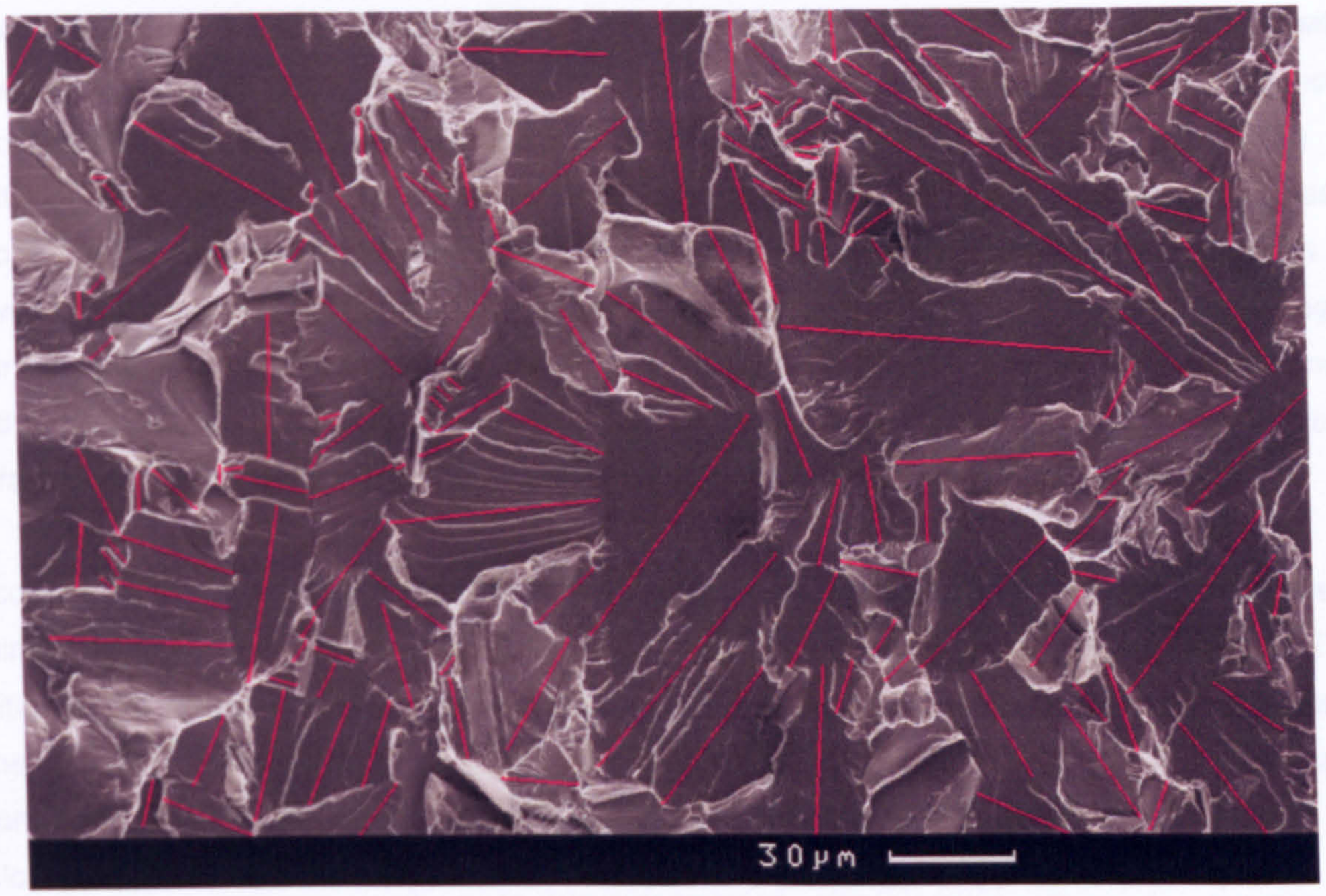

Figure 5.20 – Orientation definitions of cleavage facets, test temperature of –196°C.

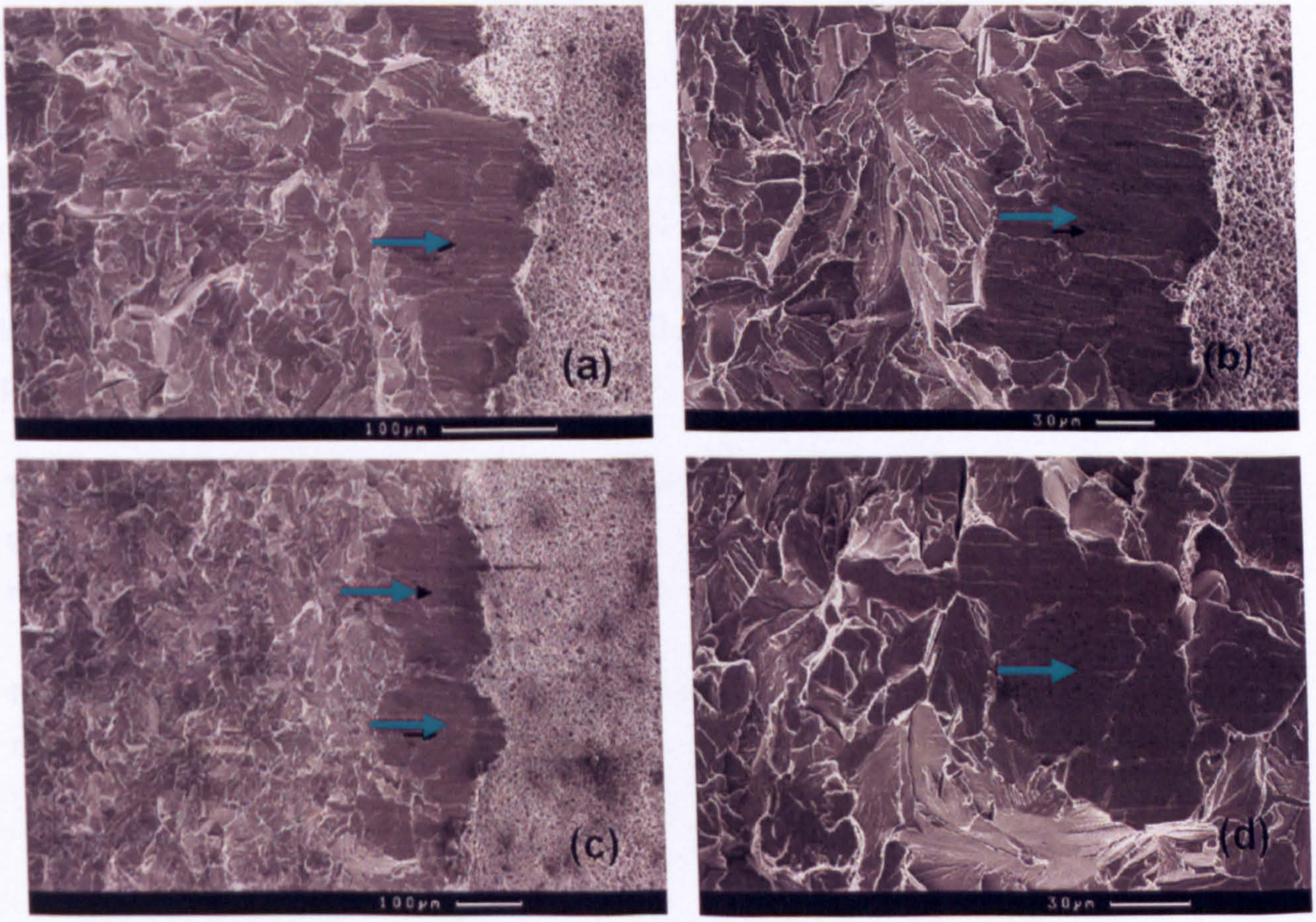

Figure 5.21 – Large cleavage facets composed of several grains developed in fracture surfaces of Charpy specimens tested at room temperature.

Close analysis showed that those large cleavage facets were composed of groups of grains with small misorientation and different grain sizes. As mentioned above, grains with low misorientation angles are generally associated with small grain size (Wu and Davis, 2004). A similar dependence of grain boundary misorientation angle related to small grains size has been reported in the literature (Muirhead, 2001). This trend was also found in the present analysis. It is well known that the lath and cell boundaries are low angle boundaries, and the low angle boundary has low misorientation. Hence, these boundaries are expected to have low resistance to the transmission of deformation. Results from examining Charpy impact brittle fracture surfaces will result in examination of the effect of misorientation on crack propagation.

According to the misorientation angle between the crystallographic directions of two adjacent grains, the grain boundaries can be divided in low–angle and high–angle boundaries. The limiting angle of misorientation between the low–angle and high–angle boundaries is typically considered to be in the range from 10º to 15º (Humphreys and Hatherly, 2004). The low–angle boundaries, where the angle between the grains is low, may be regarded as arrays of dislocations, the simplest form of the low–angle boundaries is so called symmetrical tilt boundary, which is illustrated in figure 2.3a (section2.3.4). The number of dislocations involved in the boundary and the total energy of the boundary increase with increasing the misorientation angle.

In the present work we separated grain boundaries by the extent of the misorientation between the two grains. In the present work, we postulated that angle grain boundaries are those with a misorientation less than 15º, but this property can vary depending of the material, from 15º to 10°º (Humphreys and Hatherly, 2004). In this analysis another characterization was found. This is the misorientation between small and large cleavage facets. These special boundaries have particular orientation of a high misorientation angle.

The measurements were characterized in three different groups of cleavage facets size, small–small cleavage facets size and their misorientation, small–large cleavage facets size and their misorientation and large–large cleavage facets size and their misorientation.

Figures 5.22, shows the histograms of the misorientation angles measured from cleavage facets of broken surfaces of Charpy specimens.

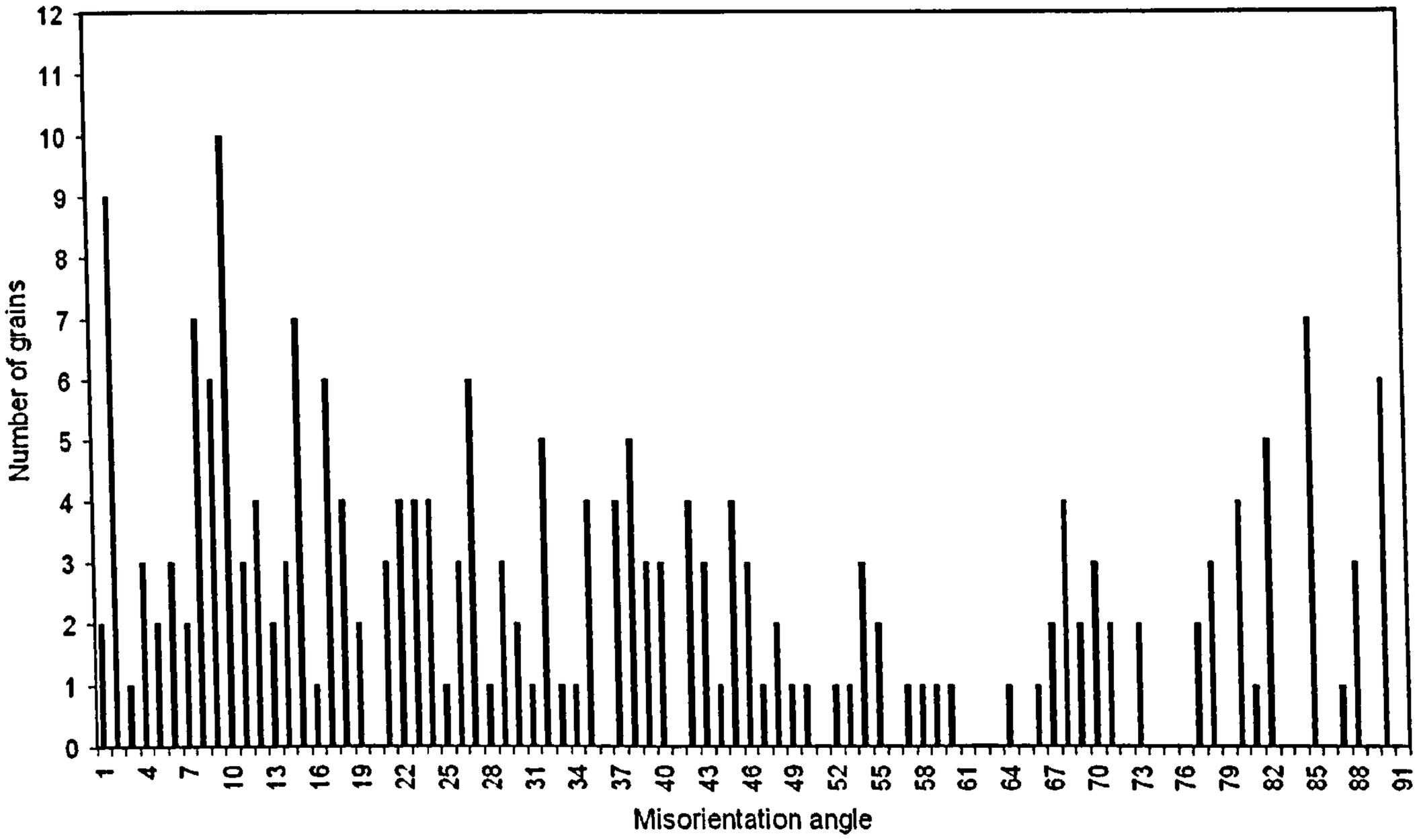

Figure 5.22 – Histogram of misorientation angle of grains for a test temperature of –196°C.

The following figures show the plot of misorientation angles against cleavage facets size of broken Charpy specimens tested at –196°C.

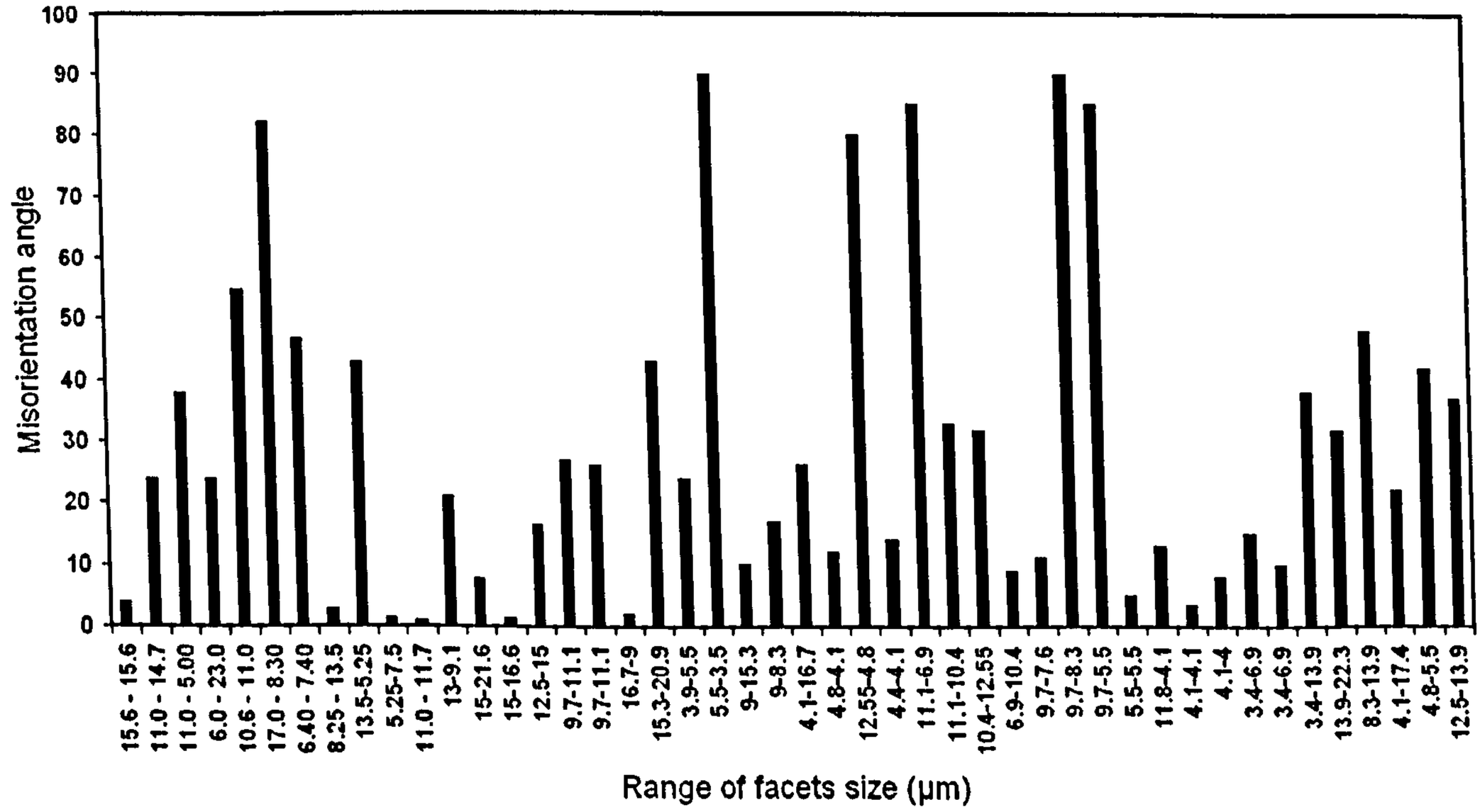

Figure 5.23 – Histogram of misorientation angle between small–small grains for a test temperature of –196°C.

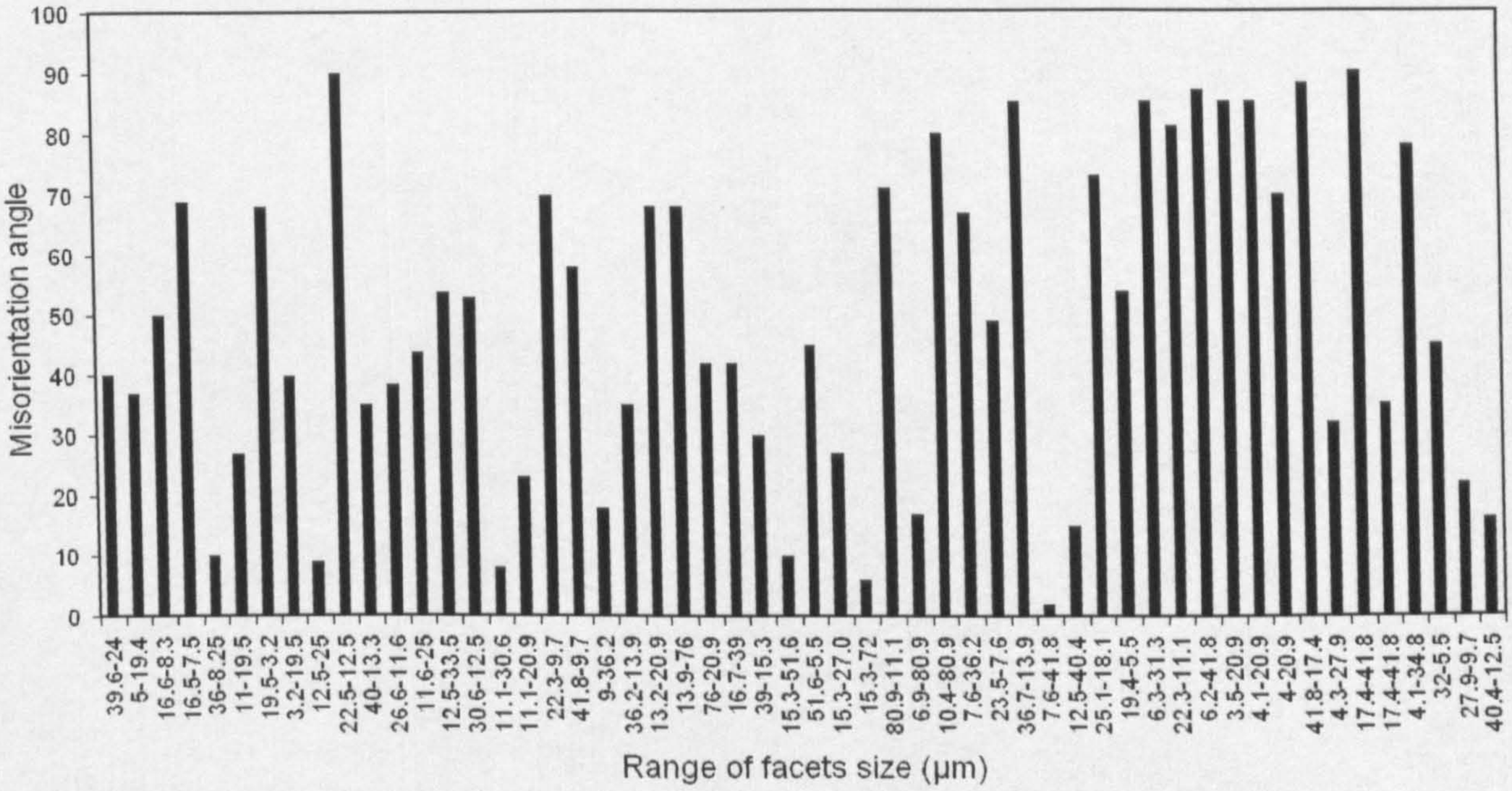

Figure 5.24 – Histogram of misorientation angle between small–large grains for test temperature of –196ºC.

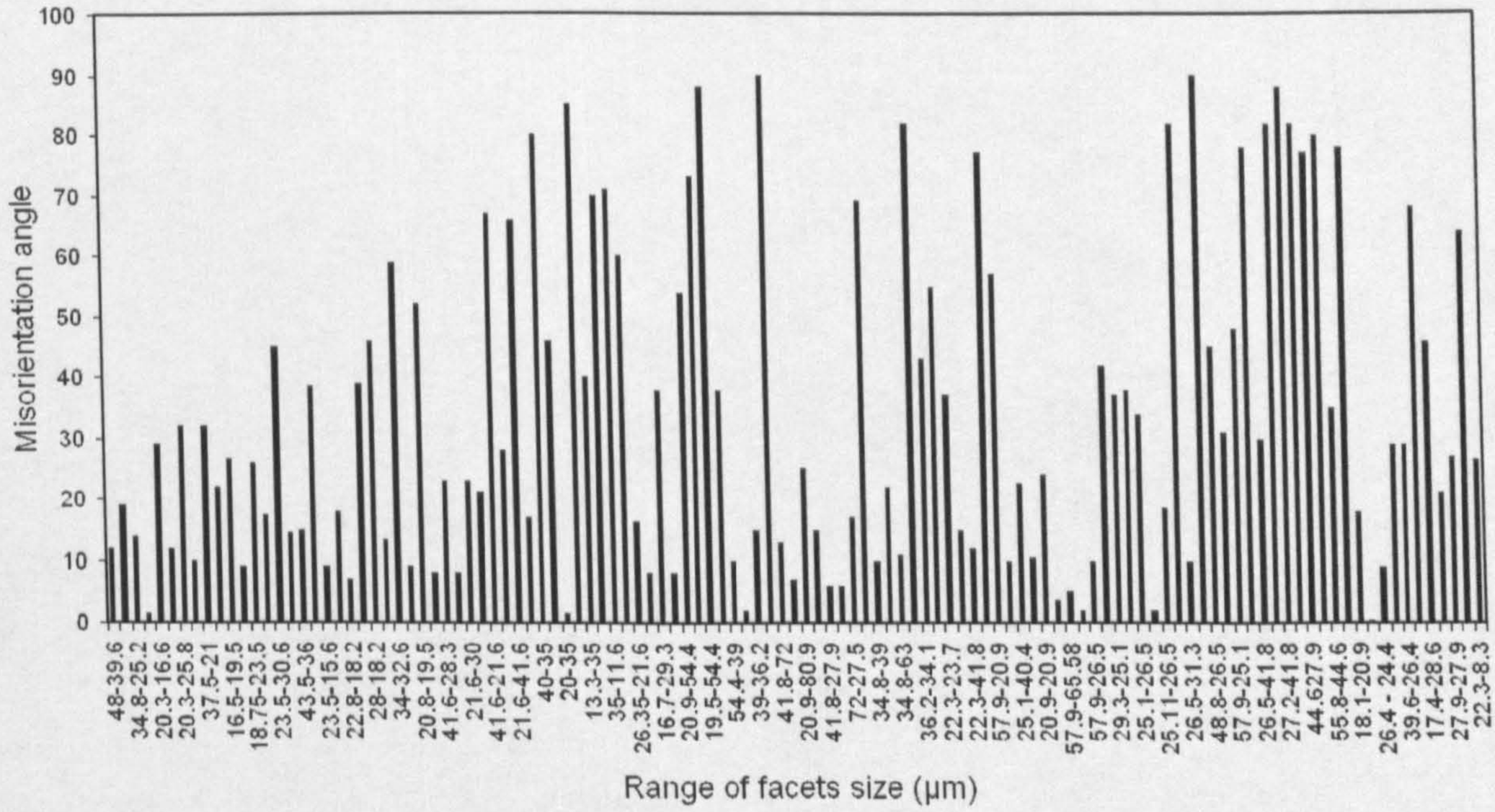

Figure 5.25 – Histogram of misorientation angle between large–large grains for a test temperature of –196ºC.

Shashwat and Sommatch (Shashwat and Sommath, 2006) found that the misorientation angle distribution fall in a range from 5º to 65º for a high strength low alloy ferritic steel (HSLA 50 grade). In present study the misorientation distribution in terms of cleavage facets for Grade A plate steel falls in a range of 1º to 90º. In the present work we separated the misorientation angle of grains in three groups from 0º to 15º, from 15.1º to 45º and from 45.1º to 90º. The results were expressed in percent (%), they are shown in table 5.4.

Table 5.4 – Misorientation angle results.

Facets size	Misorientation angle 0º – 15º (%)	Misorientation angle 15º – 45º (%)	Misorientation angle 45º – 90º (%)
Small – small	45.0	35	20
Small – large	12.9	38.7	48.4
Large – large	32.7	40.1	27.2

From above analysis, and based on the results on literature (Humphreys and Hatherly, 2004), it can be seen that grains with up to about 15º misorientation angle can be accommodated in single facets. As shown in figure 5.21, single facets of the order of $560\mu m$ were created in broken Charpy surfaces, they must have been created by grains with misorientation angle equal or less than 15º. This suggest that the crack front can break groups of grains with low misorientation angle forming single facets, then 15º can be used in the characterization of the effective grain size for the present steel. In other words, the grain size distribution obtained from metallographic observations is not the one a crack encounters in steels. The cracks actually experience a larger mean "effective" grain size, and this is the one measured by the analysis of cleavage facets where broken grains gives a more realistic measurement of grain size.

From table 5.4 it is also clearly shown that the percentage of small–small facets with a misorientation equal or less than 15º is high (about 45%). Therefore a high percentage of small–small facets can be accommodated in single facets creating or be part of large facets. The misorientation of cleavage facets with a range from 15.1º to 45º can create single facets, and the misorientation of cleavage facets with a range from 45.1º to 90º may deviate the propagation path of a crack or even arrest such a crack.

For the case of small–large facets size, it can be seen that the highest percentage falls in cleavage facets with misorientation in the range from 45.1º to 90º. In this range some small facets were created apart from the large facets and some were part of the same cleavage facets. From table 5.4 we can see that a low percent of this classification of facet misorientation had a misorientation angle equal or less than 15º which can be accommodated in single cleavage facets. The percentage of the remaining range, (15.1º to 45º), is relatively high and create single cleavage facets.

Finally for the classification of large–large cleavage facets, it can be seen that the percentage of those facets with a range of misorientation from 0º to 15º is 32.7% and is therefore relatively high. Therefore this percentage of large–large grains can be accommodated in single cleavage

facets and create facets in the order of 625 μm as those of figure 5.21. The percentage for the misorientation range between 15.1º and 45º is 40.1%. This means that high percentage of grains can create single cleavage facets, but small percentage (27.2%) of large grains has the ability to deviate and/or arrest potential running microcracks.

From this analysis it can be seen that the misorientation of grains has a strong influence on fracture propagation. High mis–oriented grains can stop or even arrest running microcracks. Figure 5.26 shows an example of the effect of high misorientation angle of large grains in the propagation of a microcrack. In this figure the crack found a highly mis–oriented grain. This grain boundary is almost perpendicular to the fracture propagation direction (see figure 3.70), the grain arrested the microcrack of figure 5.26a. Figure 5.26b shows evidence of slip created in the cleavaged ferrite grain. This slip is the results of dislocations formed in the ferrite grains. It is interesting to observe that due to the high–misoriented grain, the fracture path did deviate the cleavage propagation direction to an angle which depends on the size and misorientation of the grain. It is important to observe that this microcrack was created by a land of pearlite microstructure positioned close to the notch root. Figure 5.26c shows the effect of high misorientation angles in the surface appearance, the crack was deviated by an angle θ with respect to the plane YX.

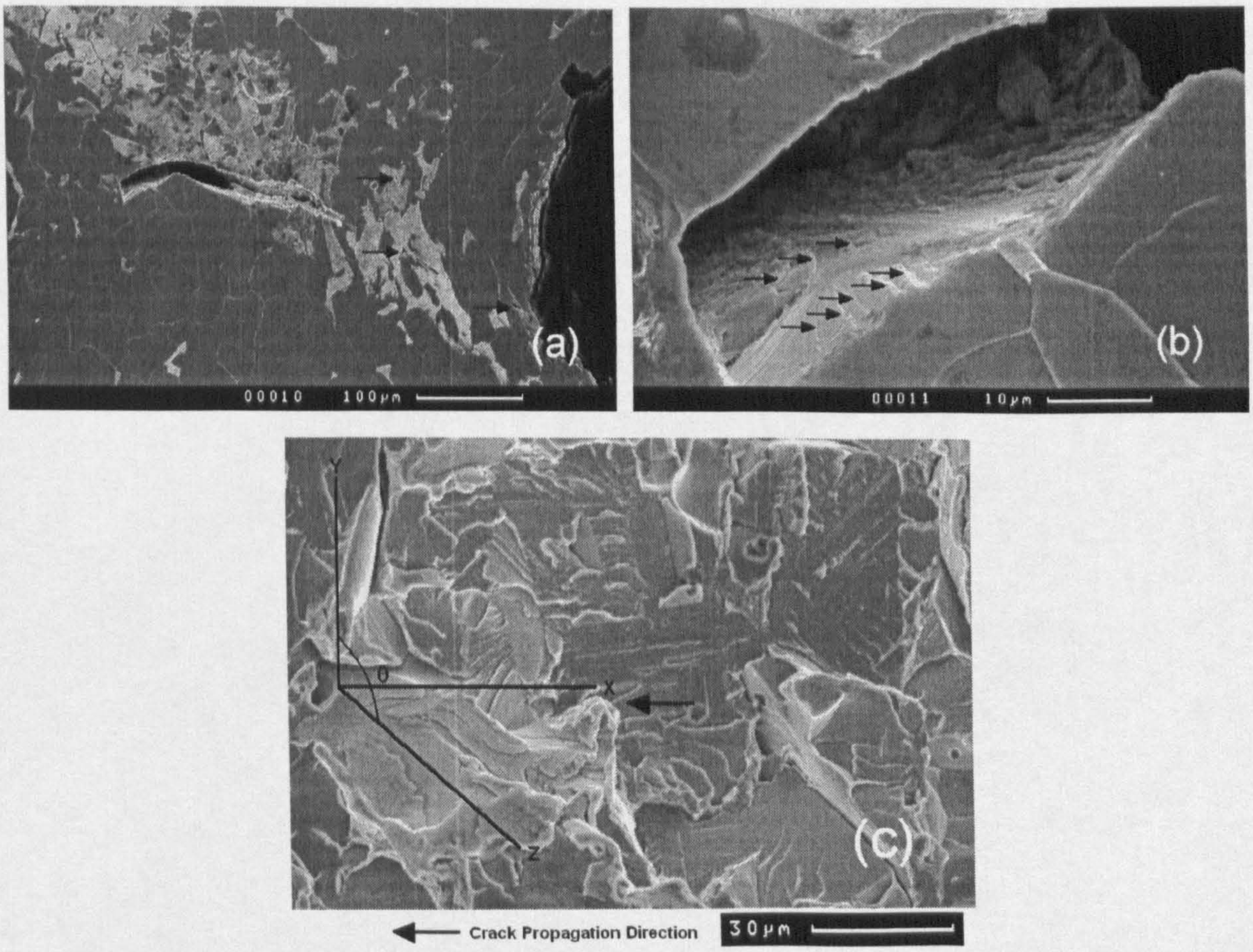

Figure 5.26 – A microcrack arrested by a high mis–oriented grain.

Based on results of Kim, Bhattacharjee and Davies (Kim et al., 2000, Bhattacharjee and Davies, 2002), who showed the possibility to define an effective grain size on the basis of misorientation angles by identifying a threshold misorientation angle below which grain boundaries are discounted, neighbouring grains with boundaries angles below the threshold value would be considered as one effective grain from the perspective of misorientation (and hence by the crack front). The effect of high misorientation angle of large grains was discussed in this section of the present work, as the purpose of the present work is to include in the CAFE model the distribution of the misorientation angle of the present steel under analysis. The distribution of misorientation angle of figure 5.22 was analysed with Weibull distribution analysis. Figure 5.27 shows the fitted line on experimental data used to compute the Weibull analysis and consequently the value of shape and scale Weibull parameters.

According to equation 2.38 (section 2.3.1), the fracture stress of a ferrite–ferrite interface is inversely related to the grain size, so the fine grain region will represent a significant obstacle to an advancing crack. There is some experimental evidence in support of this idea (Malik et al., 1996, Jang et al., 2003). There is also some experimental evidence that a high–angle misorientation boundary can act as a crack arrester or at least retard or inhibit the crack propagation (Zikry and Kao, 1996). Nohava (Nohava et al., 2002) reported crack arrest in A508 Class 3 steels at grain boundaries with 55° and 60° misorientation angles. In this work it has been shown evidences of crack arrest for grains with orientation in the range from 65° to 90°.

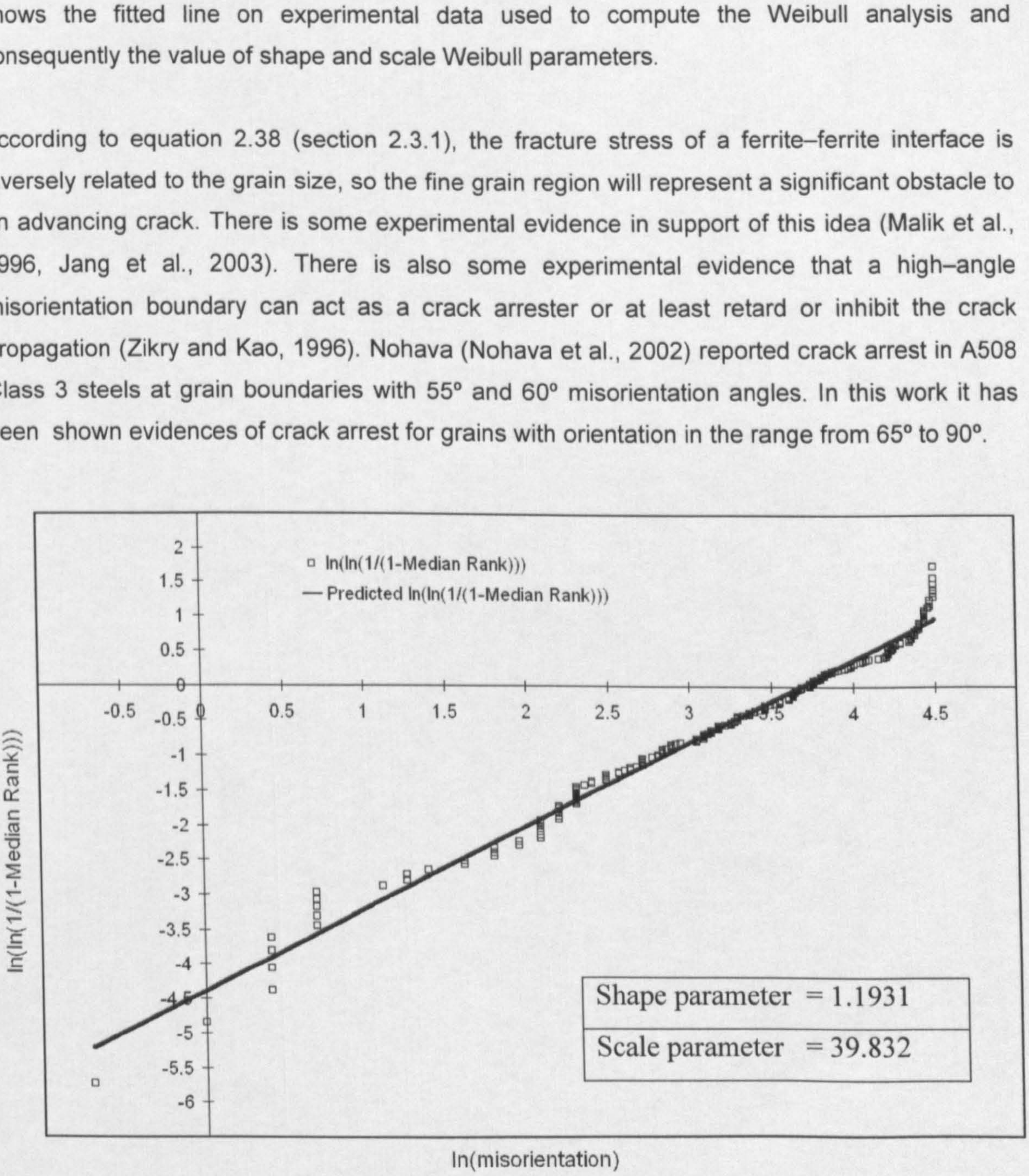

Figure 5.27 – Line fit plot used to calculate Weibull parameters.

The shape and scale parameters of the misorientation angles were programmed in the CAFE model to generate statistical values of the misorientation angles for each brittle cell in each simulation. From the present work, it can be concluded that the creation of large facets size is related to the low misorientation angle of groups of grains. It was found as well that low misoriented grains promote cleavage fracture. Grains with low misorientation are the critical ones that do not oppose resistance for cleavage propagation. It was shown as well from the present analysis that a grain highly mis–oriented was able to arrest a microcrack of about 210 μm. This means that high mis–oriented grains can arrest microcracks of critical length in a ferritic steel. The critical angle for the creation of single cleavage facets composed of single or many grains is 15º which can be considered as the angle of the effective grain. In this steel the percent of grains with a orientation smaller that 15º is 30%. In other words, this represents a high percentage of the total of grains to create large cleavage facets composed with various grains. 38% of grains have misorientation between 15º and 45º. 32% of the totals of grains have a misorientation between 45º and 90º but in this classification only a small percentage of grains have a misorientation higher than 65º which has the ability to arrest potential microcracks. If it is considered that the crack front ignores the low angle boundaries and goes through groups of such grains treating them as a single effective grain size, then the effective grain size observed by the crack front is larger than the 3D grain size. An analysis of the cleavage faces sizes was carried out as well in order to define the optimum size of brittle cells in the CAFE model. As explained in section 5.3, the cell size of the brittle cells arrays must be related to the cleavage facets size created when grains break. Figure 5.28 shows the histogram of cleavage facets size.

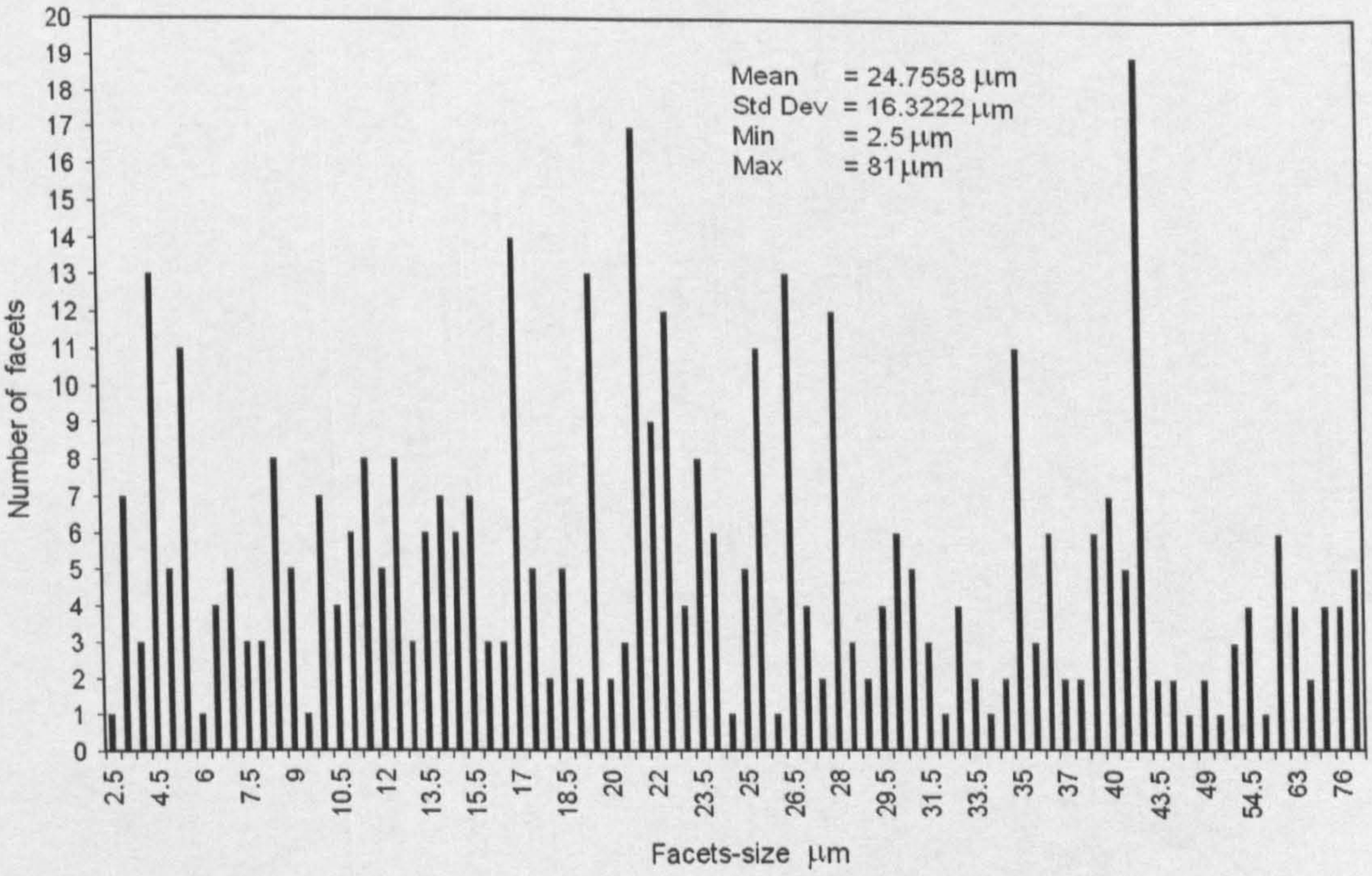

Figure 5.28 – Histogram of cleavage facet sizes for test temperature of –196ºC.

The present analysis also showed that the mean of the cleavage facets size obtained experimentally is $24.7\mu m$. If we make a comparison with the mean value of grain size measured with an optical microscope (section 5.8.3) which is $19.5\mu m$ we observe a variation of about 11% with respect to the 2D grain size measured on figure 5.12. Therefore the 3D grain size measured from cleavage facets is 1.26 times larger that that measured with the optical technique. Brittle fracture process is therefore likely to be more closely related to the 3D grain size. Gladman (Gladman, 1997) has shown that the 3D grain diameter size is about 1.61 times larger than for 2D optically measured grain size if the grain shape is assumed to be tetrakaidecahedral for TMCR steels and 1.05 times larger for normalized steels. These two factors can be used to convert the measured 2D grain size into 3D real grain size. Therefore in the present work, instead of introducing the 2D optically measured grain size in the CAFE model, it was introduced the 3D grain size which will result in the real definition of the grain size.

It can be seen that the analyses performed in the present section were very useful because the real 3D grain size and the distribution of the mis–orientation angle of ferrite grains were measured experimentally with very good results.

5.8.6 Weibull analysis of the distribution of particles nucleating cleavage and the fracture surface energy γ.

Most statistical and probabilistic models for cleavage fracture account generally for only one microstructure for cleavage fracture simulation and modelling. Most of them take into account grain boundary carbides as the cleavage initiation fracture mechanism (Beremin, 1983, Bernauer et al., 1999, Bordet et al., 2005, Chen et al., 1997, Wang and Chen, 2000, Wang and Chen, 1999, Wang et al., 2003, Godse and Gurland, 1989, Groom and Knott, 1975, Hahn et al., 1960, Kaechele and Tetelman, 1969, Tetelman et al., 1968, Wallin, 1991). As explained before, in the present work the author has identified four cleavage fracture microstructures for cleavage fracture in the rolling direction of the plate steel and two microstructures for the transverse direction.

The experimental analysis for the identification of the micro features for nucleating fracture using SEM analysis has been done in section 3.6.4. In the present section, the distributions of such micro features and the analysis to measure the distributions of the effective fracture surface energy γ for the micromechanisms mentioned above will be shown. Those microstructures are: ferrite grain boundary microstructures, ferrite grain inclusions, lamellar pearlite and pearlite boundary. Examples of particles responsible for nucleating microcracks are

shown in section 3.6.5 in the EDS analysis. The histograms of the size (thickness) of those micro features are shown in figures 5.29, 5.30 and 5.31.

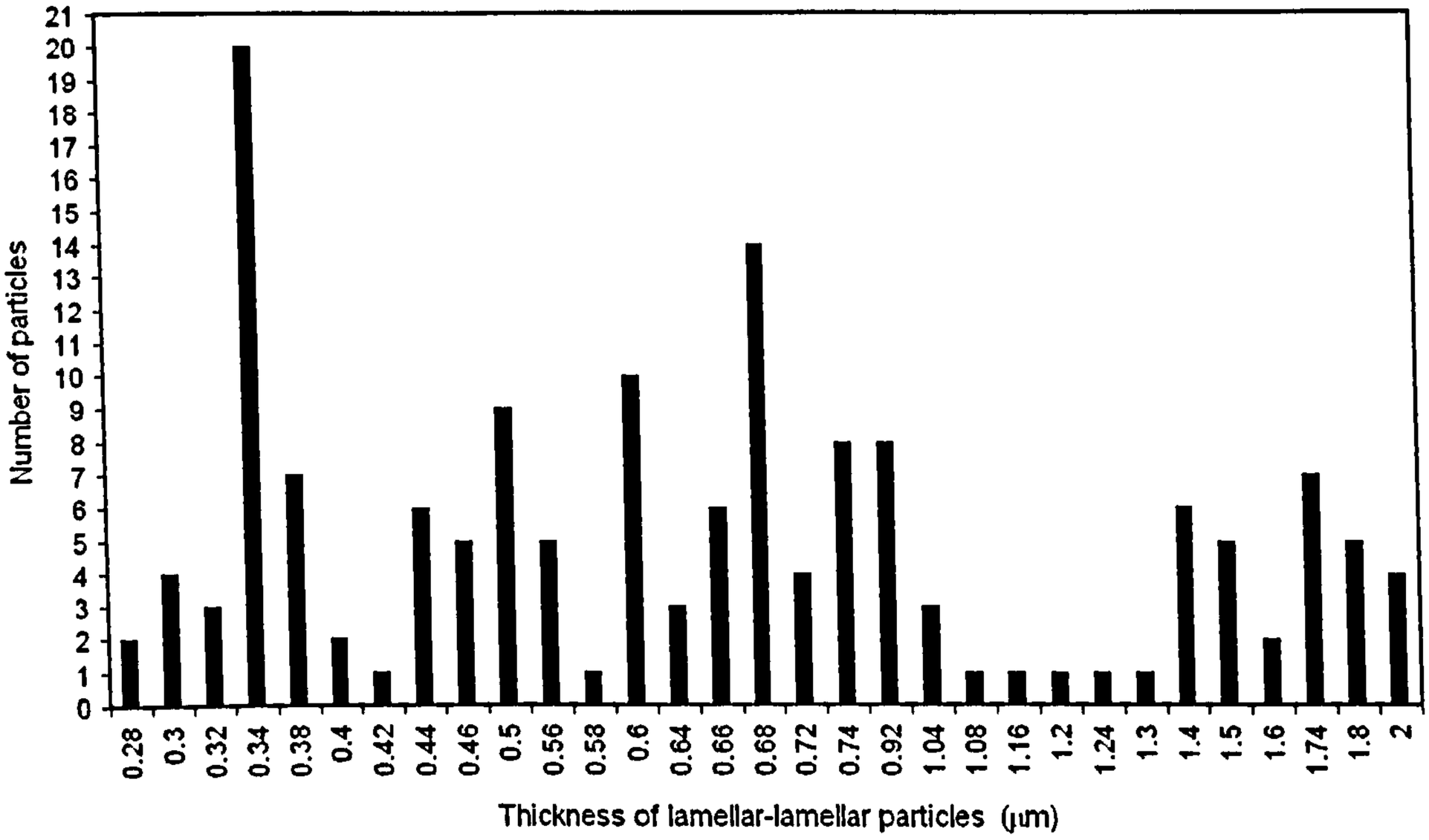

Figure 5.29 – Distribution of the thickness of particles found in the lamellar microstructure of pearlite from 25°C to –196°C.

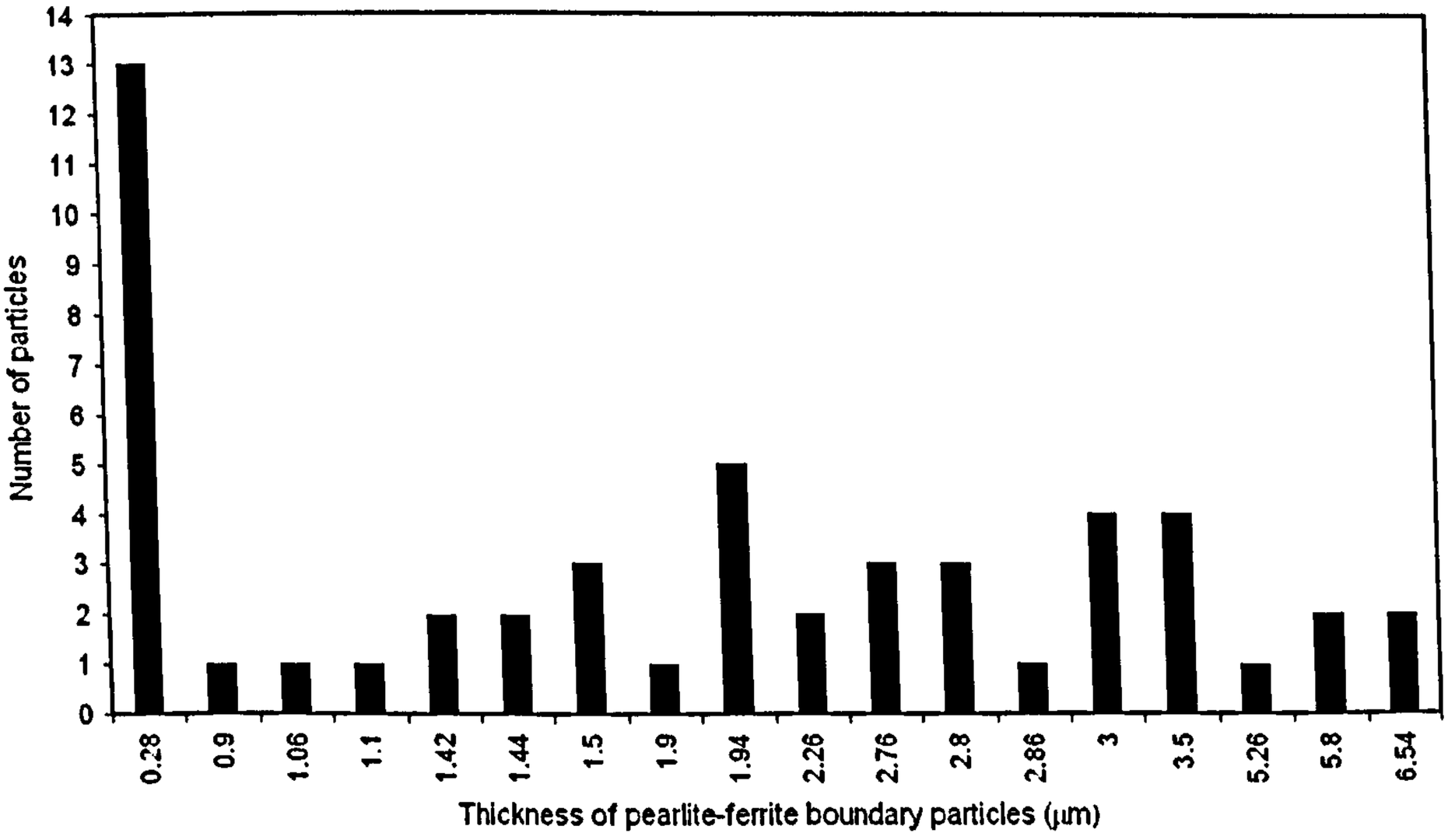

Figure 5.30 – Distribution of the thickness of particles found in pearlite–ferrite boundary interface from 25°C to –196°C.

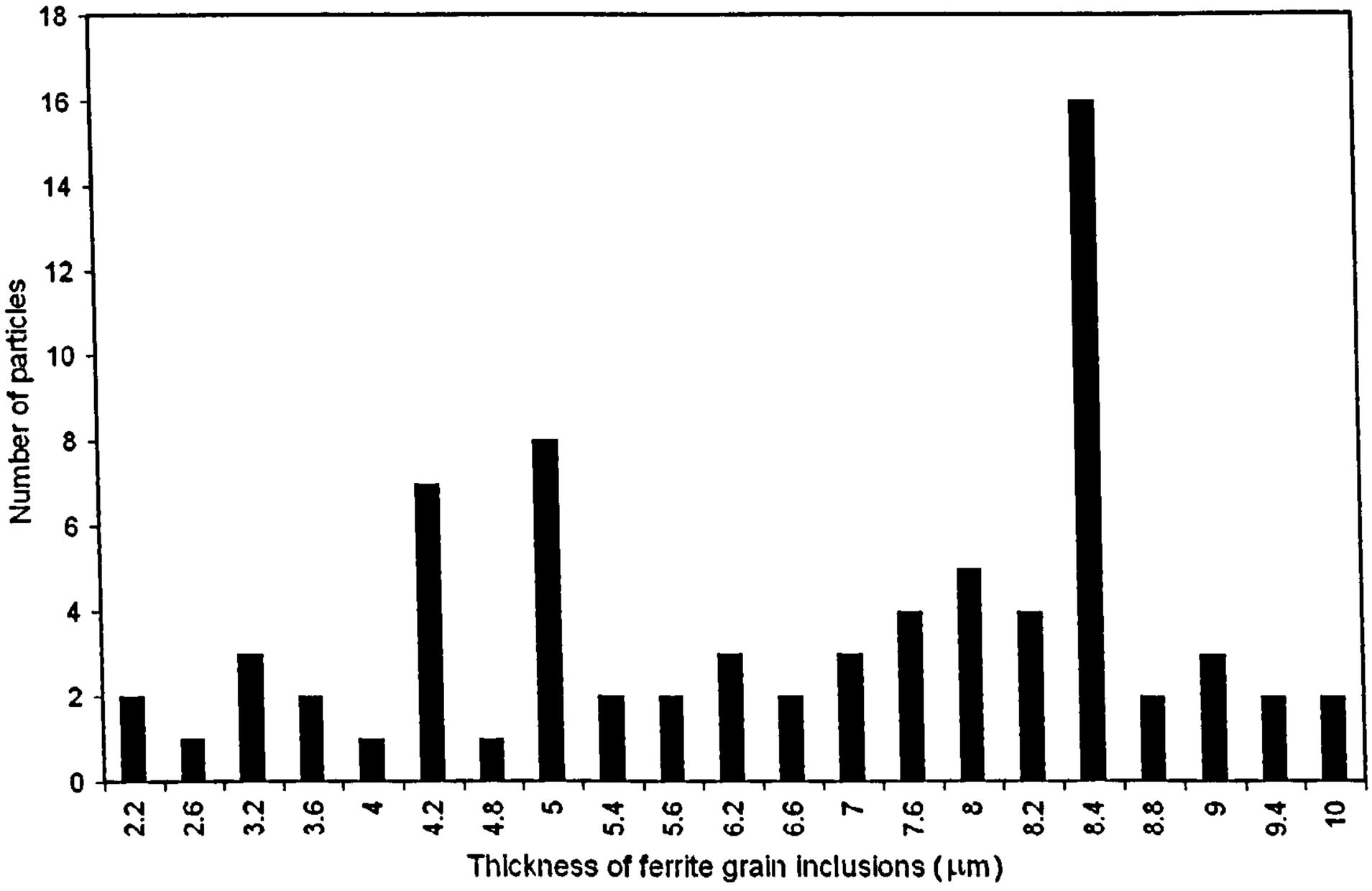

Figure 5.31 – Distribution of the thickness of ferrite grain inclusions found from 25°C to –196°C

Few particles nucleating microcracks in ferrite grain boundary were found in the analysis, and the size of those particles fall in the range of the distribution of particles of figure 5.29, therefore the same distribution of the thickness of particles of figure 5.29 was used for the ferrite grain boundary cleavage microstructure.

The energy of a surface is closely related to its surface free energy, defined as the work that can be obtained from the destruction of unit area of a surface. The analysis to obtain the distribution of the effective fracture surface energy γ for each mechanism is based on the distribution of the thickness of particles that nucleated microcracks. By applying the modified Griffith equation as interpreted by Curry and Knott (Curry and Knott, 1978, Curry and Knott, 1979), cleavage fracture initiated at inclusions occurs at a critical local fracture stress, σ_F (section 2.3.1) given by:

$$\sigma_F = \left[\frac{\pi E \gamma_p}{(1-\nu^2)d_c}\right]^{1/2} \qquad 5.35$$

Using the modified equation of Griffith (Tanguy et al., 2003), given by:

$$d_c = \frac{4E\gamma_c}{\pi(1-\upsilon^2)(\sigma_{I_p}^{\max})^2} \qquad 5.36$$

Where d_c is the size of the particles. With the measured values of particles initiating cleavage fracture it is possible to calculate the effective fracture surface energy with values of the particles size by applying the modified Griffith equation as interpreted by Curry and Knott (Curry and Knott, 1978, Curry and Knott, 1979). Cleavage fracture initiated at inclusions occurring at a critical local fracture stress σ_F.

$$\gamma = \frac{d_c \pi (1-\nu^2)(\sigma_{I_p}^{\max})^2}{4E} \qquad 5.37$$

The effective fracture surface energy was calculated using equation 5.37 for each microstructure. To calculate the maximum principal stresses of equation 5.37, a 3D finite element model of four point double–notch bend test was created. Due to symmetry, only a quarter of the model was simulated. The 3D finite element model is shown in figure 5.32. This picture also shows a close view of the notch root.

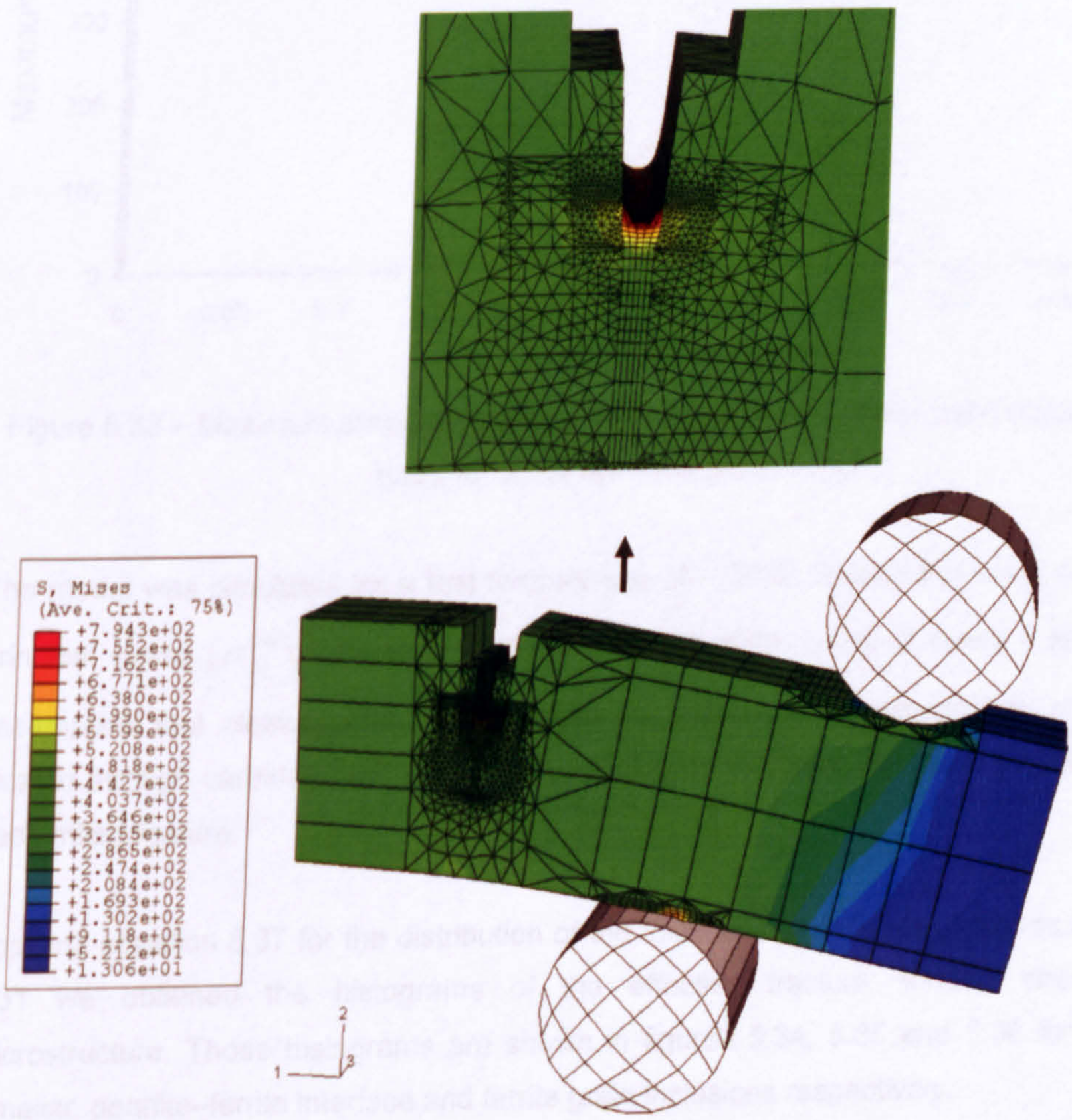

Figure 5.32 – 3D finite element model of blunt four point double–notch test.

The finite element model consisted of 43543 C3D8R and C3D4 reduced integration finite elements. A refinement was done in the notch region, the size of those finite elements were about 50 μm. The following graph (figure 5.33) shows the distribution of the maximum principal stress of a distance of 2 mm from the notch root.

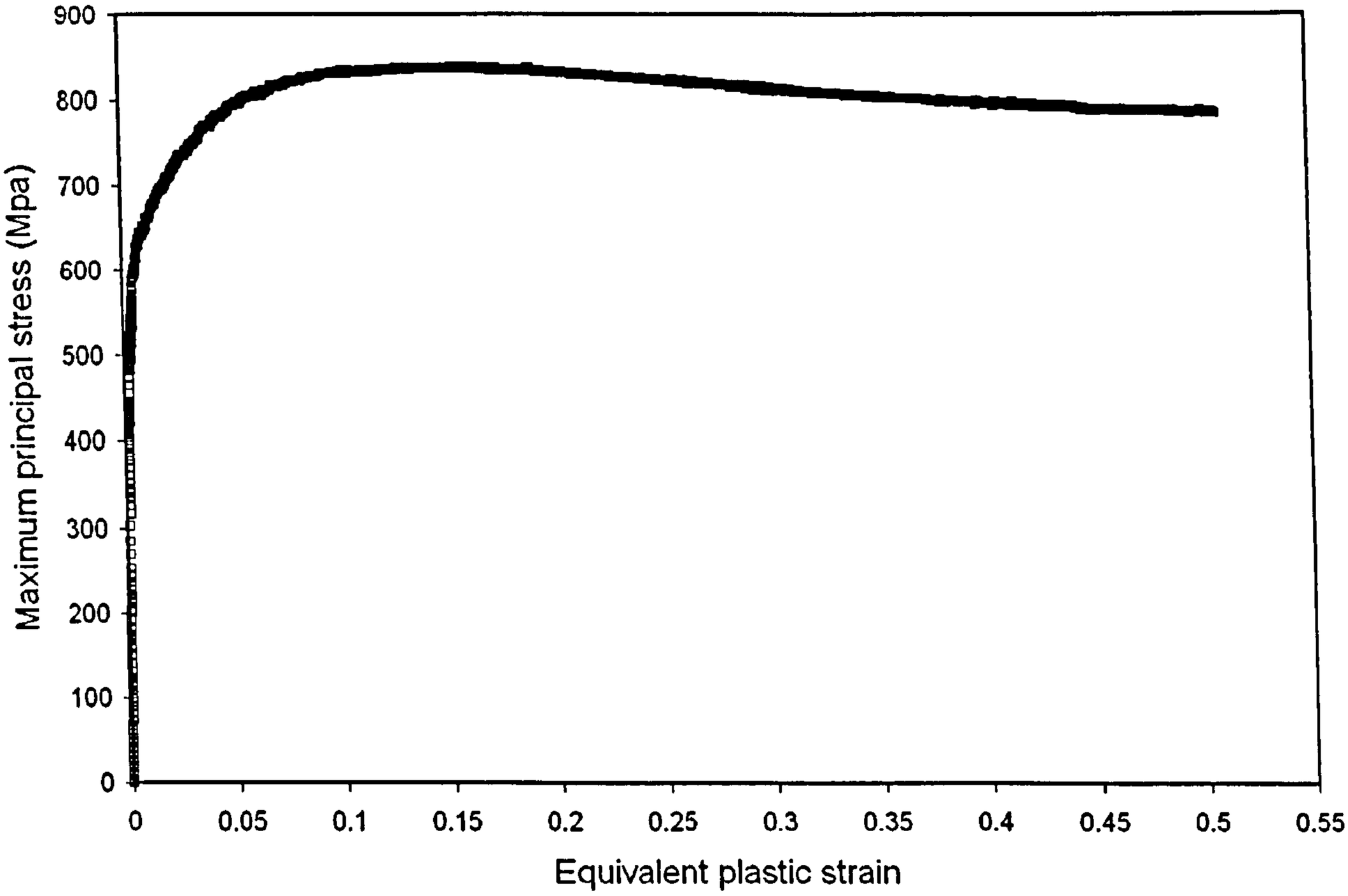

Figure 5.33 – Maximum principal stresses in the notch region of four point double–notch bend tests, for a test temperature of –196°C.

The model was simulated for a test temperature of –196°C. Taking the value of the maximum principal stress (σ_{pl}^{max}) calculated with the finite element model of figure 5.32, and with the assumption that cleavage fracture is stress controlled by the propagation of a microcrack located through carbides thickness, it was possible to calculate the fracture surface energy for each micro feature.

Applying equation 5.37 for the distribution of the thickness of particles of figures 5.29, 5.30 and 5.31 we obtained the histograms of the effective fracture surface energy for each microstructure. Those histograms are shown in figures 5.34, 5.35 and 5.36 for the lamellar–lamellar, pearlite–ferrite interface and ferrite grain inclusions respectively.

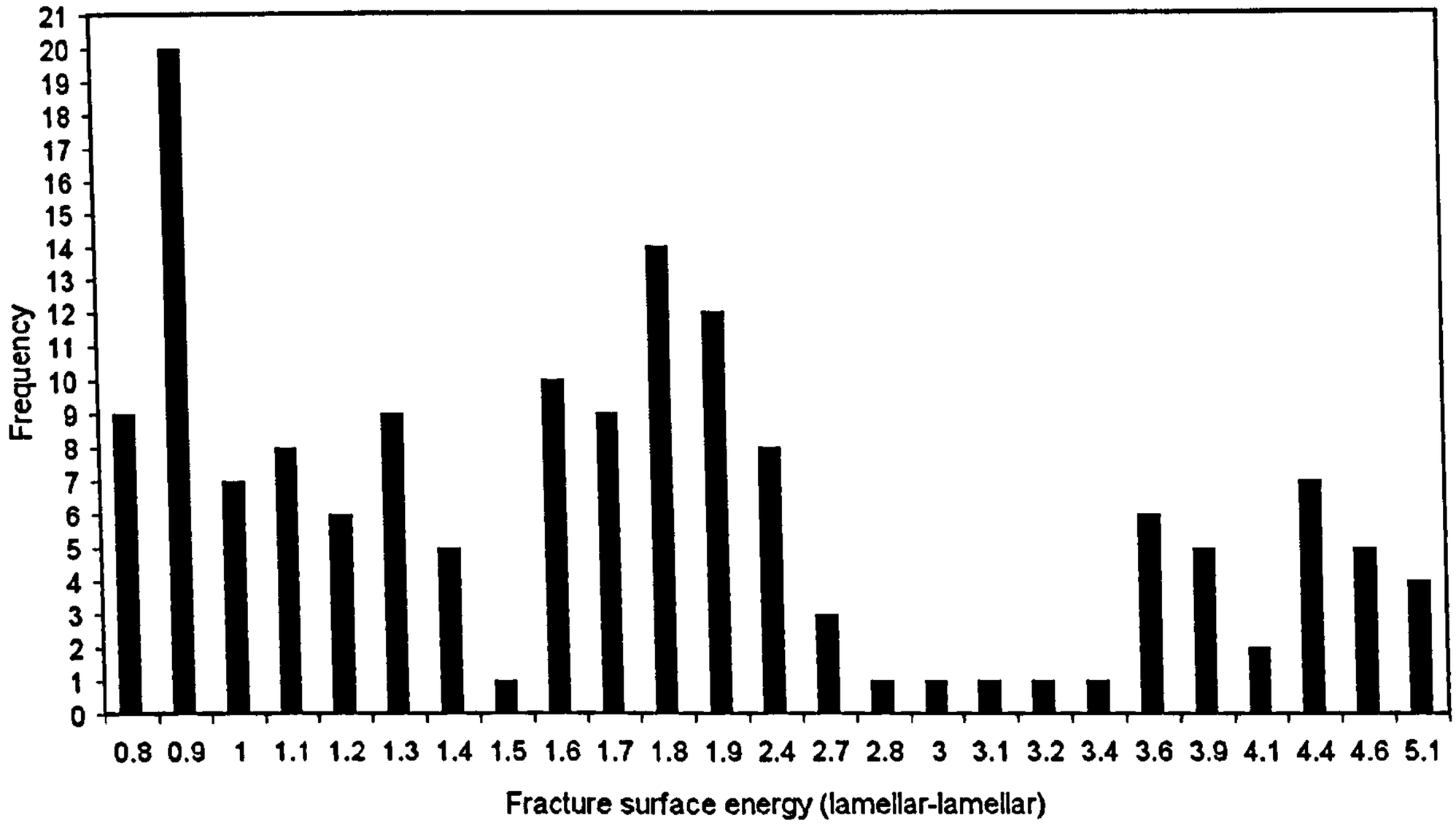

Figure 5.34 – Distribution of the fracture surface energy for particles found in the lamellar microstructure in the next range of temperatures, from 25°C to –196°C.

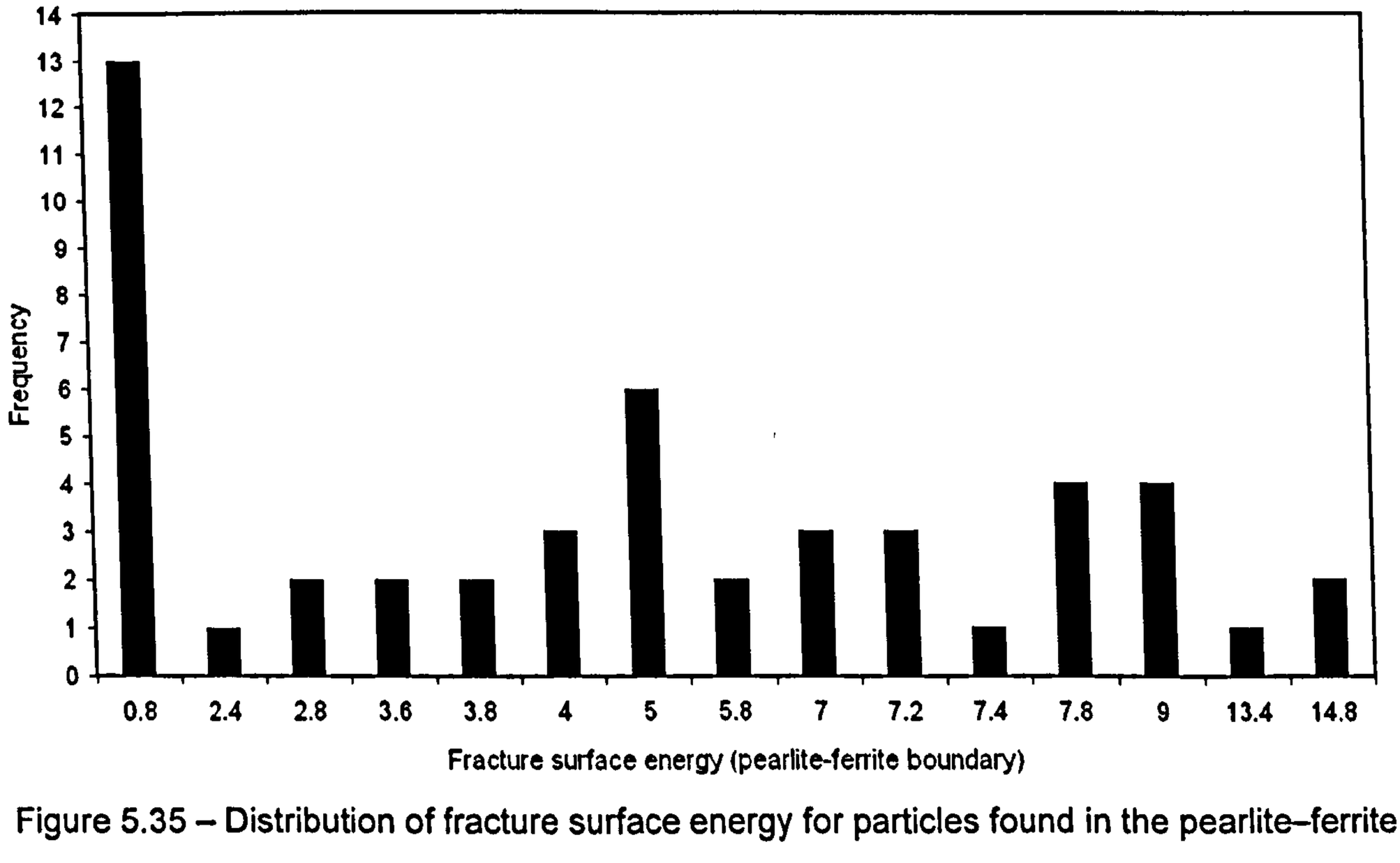

Figure 5.35 – Distribution of fracture surface energy for particles found in the pearlite–ferrite boundary interface in the next range of temperatures, from 25°C to –196°C.

If we take into account the mean size of the particles, we obtain a fracture surface energy of $\gamma^{p-f} = 5.387 Jm^{-2}$ for the pearlite–ferrite boundary interface and $\gamma^{pp} = 1.977 Jm^{-2}$ for the lamellar microstructure of pearlite. We can see that the effective surface energy for the lamellar pearlite microstructure decreased by about 63% due to the reduction of particles inside the pearlite and to the larger size of pearlite colonies compared to grain sizes. Wu and Knott (Wu

and Knott, 2004) reported cleavage–initiating inclusions in the highly stressed test volume for a pressure weld metal in the range from 2.2 μm to 2.5 μm for a degraded and an as–received microalloyed steel with effective fracture surface energy values of $\gamma_p = 6.5 Jm^{-2}$ and $\gamma_p = 8.0 Jm^{-2}$ respectively. Tanguy (Tanguy et al., 2003) measured a value of the effective fracture surface energy equal to $\gamma_p = 7.0 Jm^{-2}$ for an SA 508 steel with the cracked carbides in the boundary of ferrite grains . We can see that the values of the effective surface energy for the pearlite–ferrite interface is very similar to that obtained by Wu, Davies, Knott and Tanguy (Wu and Davis, 2004, Wu and Knott, 2004, Tanguy et al., 2003), but the effective surface energy for the lamellar micro features is different and small compared with that of SA 508 and the microalloyed steels. The distribution of the fracture surface energy for the ferrite grain inclusions is shown in figure 5.36.

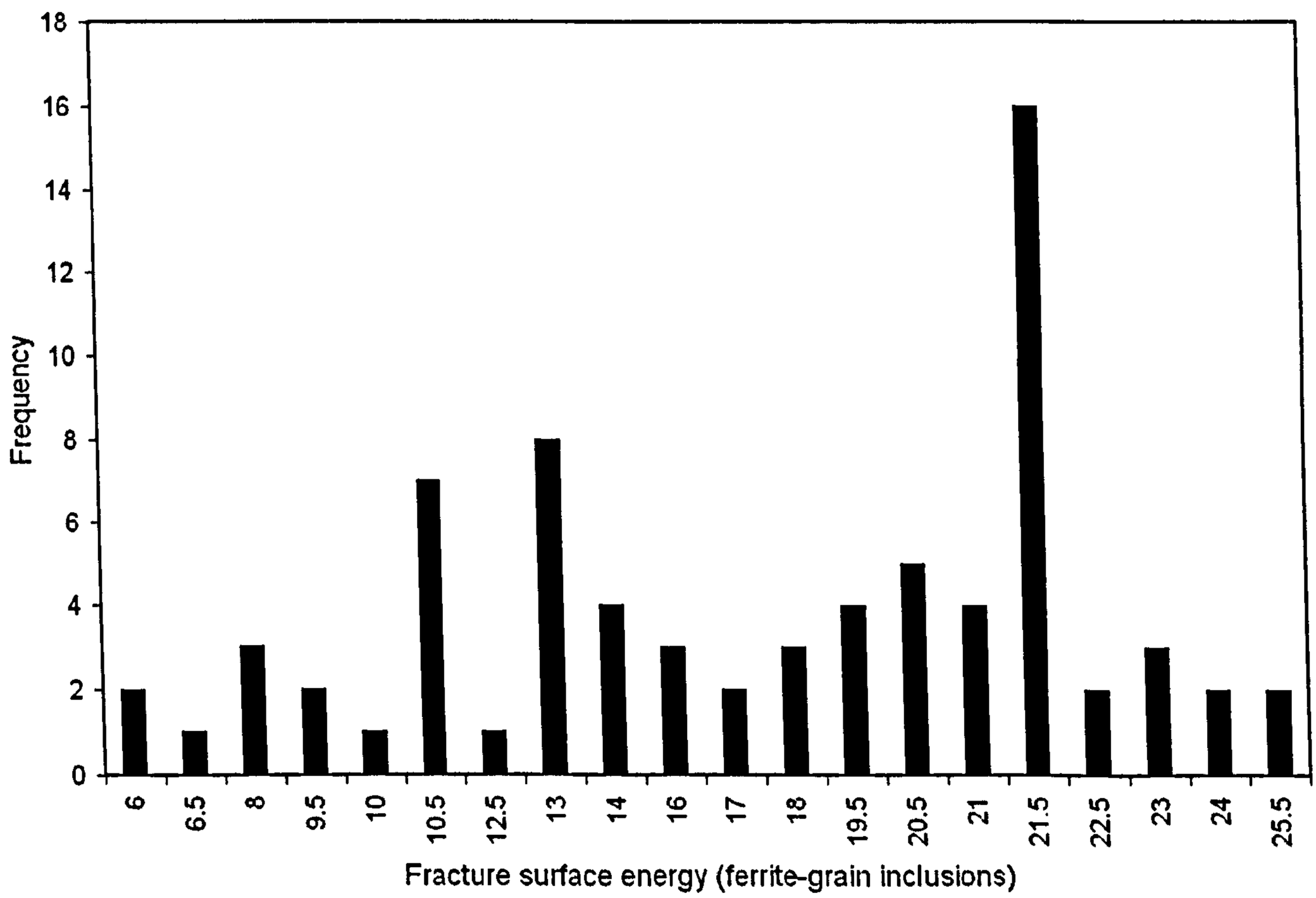

Figure 5.36 – Distribution of fracture surface energy for ferrite grain inclusions in the next range of temperatures, from 25°C to –196°C.

The mean value of the fracture surface energy of the ferrite–grain inclusions is: $\gamma^{ff} = 16.7 J/m^2$. The measured value for the ferrite–grain inclusions is very close to the value reported by Knott (Knott, 1977) for ferrite grain inclusions which was $\gamma_p = 14 J/m^2$. This result suggests that the distribution of the fracture surface energy for the ferrite–grain microstructure

correlate with values reported in the literature. The above results have shown that the measured fracture surface energy values reported in this research work are in the range of those reported in the literature.

The mean values of the particles can be considered as the critical particles size for cleavage fracture as they initiated cleavage. But real structures have particles of random size distributed in the matrix of the material (section 3.6.4). When the structure is subjected to load, the regions subjected to the highest level of stresses and strain, which contain distributions of particles of random size, will develop a distribution of microcracks nucleated by particles of critical size or by particles subjected to the highest level of stress. When fracture propagation occurs, the crack tip may encounter regions of microcracks generated by small particles subjected to the highest level of stress and/or regions of material with particles of critical size. From the present analysis it can be seen that the distribution of the fracture surface energy γ for each microstructure in the local fracture stress equations σ_F (equations 5.5 to 5.8, section 5.3) represents better the real observations of the distribution of particles nucleating cleavage fracture (particles of different size). In order to distribute the effective fracture surface energy of each microstructure in the fracture stress equations, σ_F, the data were analyzed with Weibull distribution analysis. The shape and scale parameters of the fracture surface energy for each micro feature are reported in Table 5.5.

Table 5.5. Weibull analysis of the fracture surface energy.

Weibull parameters	Pearlite–ferrite microstructure	Lamellar–lamellar microstructure	Ferrite Grain inclusions	Ferrite Grain Boundary
Shape Parameter	1.065 Jm^{-2}	2.018 Jm^{-2}	3.190 Jm^{-2}	2.018 Jm^{-2}
Scale Parameter	5.967 Jm^{-2}	2.219 Jm^{-2}	18.771 Jm^{-2}	2.219 Jm^{-2}

Random number generators using the shape and scale parameters of Weibull distributions distribute the effective fracture surface energy γ of each micro feature in the brittle cells array. The implementation of the distribution of each microstructure in the CAFE model simulates better the real nature of the steel as in real structures we have a distribution of the size of those particles distributed in the matrix of the material. The random number generator will generate random values of the effective surface energy into the local fracture stress (σ_F) which will be distributed in the brittle cells arrays (section 5.3). The Weibull analysis was performed with Excel where the maximum likelihood estimation procedure was used to estimate the Weibull

parameters by performing a simple linear regression function. It can be seen that instead of assigning to the CAFE model a mean value of the effective fracture stress surface energy, a distribution of fracture surface energy of the cleavage particles will give better results for the simulation of the scatter of Charpy energy values.

5.8.7 Fracture stress histograms.

The fracture stress histograms, σ_F, for each microstructure, ferrite grains and pearlite lands were assigned to the brittle CA cells based on Weibull distribution functions, using the values of the effective fracture surface energy for each microstructure and the grain size histograms. The fracture stress, σ_F, histograms were calculated using Lin equations for each microstructure (Lin et al., 1987) as described in section 2.3.1. The resulting histograms of the generated brittle CA cell fracture stress for each microstructure are shown in figure 5.37. Therefore we can generate the fracture stress values using the grain size histograms of each microstructure and the mean value of the fracture surface energy, γ, of each microstructure (figure 5.37). But the power of the CAFE model allows the user to implement the distribution of both, the fracture surface energy, γ, and the distribution of each microstructure into the fracture stress equations, σ_F, (section 5.3) instead of the definition of just the mean value of the effective fracture surface energy γ and the distribution of grain size as shown in figure 5.37. This will result in a better definition of the fracture stress histograms, σ_F, assigned to the brittle CA cells as in real materials the crack tip and/or the most loaded regions may encounter cleavage particles of different sizes.

From the histograms of figure 5.37, it can be seen that as the ferrite grains are smaller in size than pearlite lands (section 5.8.3 and 5.8.4) the distribution of fracture stress for pearlite lands are smaller which means that the pearlite lands can withstand smaller fracture stresses, σ_F, than the ferrite microstructure. Results of the simulation of transitional ductile–brittle (Shterenlikht, 2003) has shown that the whole of the grain size, and here the size of pearlite lands are necessary for a proper simulation of the transitional fracture behaviour as it allows the CAFE model to pick up combination of the microstructure of different size and assign to the brittle CA cells a distribution of fracture stress values, σ_F. If all grains have the same grain size, or only the mean grain size is used for simulation, then no transitional behaviour is possible, as the model will show that all cells fail in either ductile or brittle mode, depending on the simulation temperature.

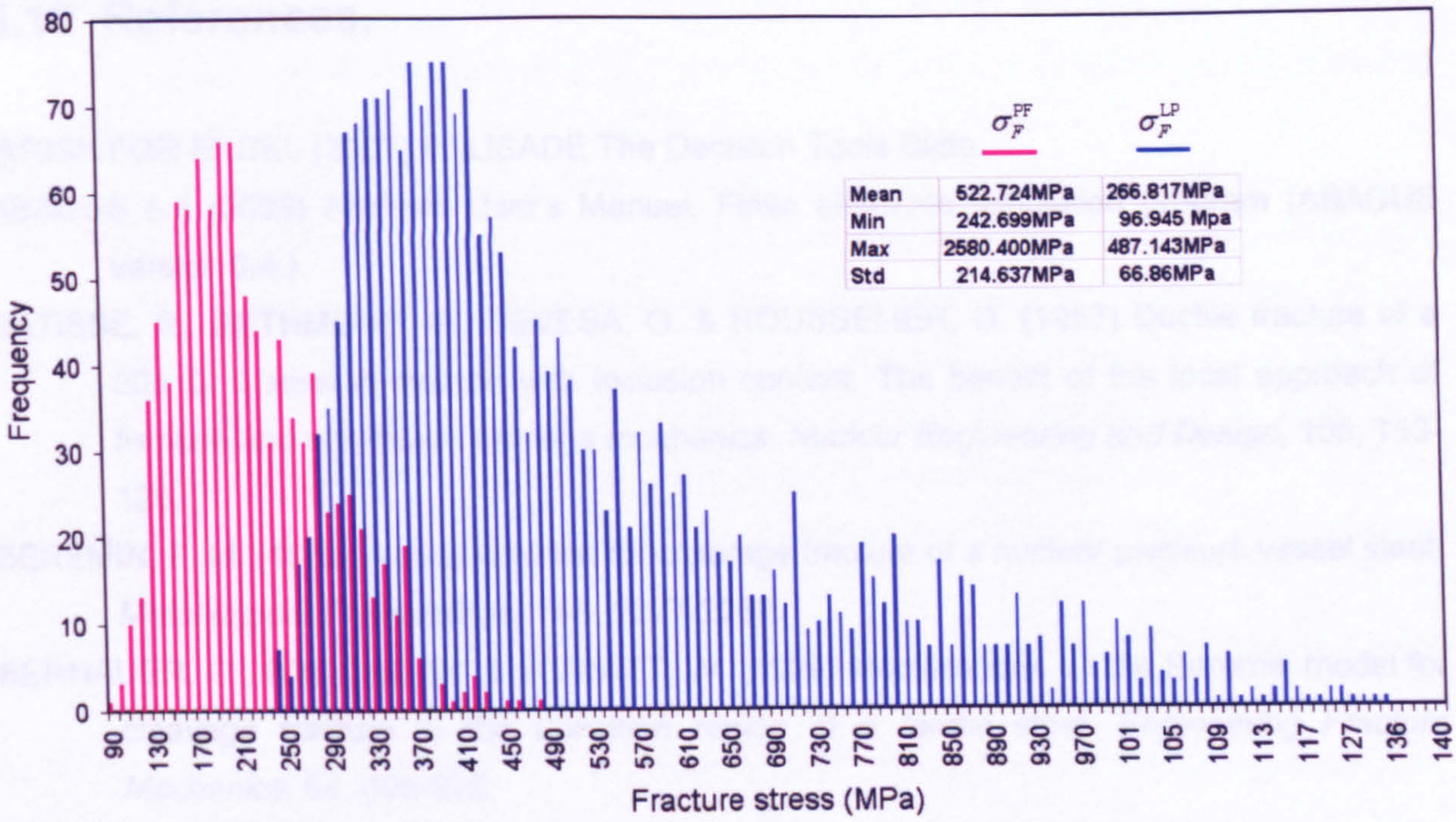

Figure 5.37 – Distribution of fracture stresses of ferrite grains and pearlite lands.

5.9 Conclusions.

In the present chapter, it has been explained how the CAFE model works to simulate fracture initiation and propagation and how the physical parameters of steels were incorporated in the model. As explained in this chapter, the physical parameters of material were introduced with random number generators to the ductile and brittle cells arrays. This means that each ductile or brittle cell will have a different value of model parameters. Consequently the total array of cells will have random values of physical model parameters then in each run of the model, the model will assign random values of the parameters to the most loaded region, and consequently the model may find weak regions of material which promote fracture nucleation and consequently the promotion of fracture propagation. In other runs the model may find strong regions of the material and some potential microcracks may arrest in this region. The resulting toughness values will be higher in this case. This suggests that the model is capable to simulate the typical scatter in terms of Charpy impact energy values in the transitional region ductile–brittle of the steel under analysis.

5.10 References.

@RISK FOR EXCEL (2007) PALISADE The Decision Tools Suite.

ABAQUS 6.4 (2003) Analysis User's Manual, Finite elemente simulation program (ABAQUS version 6.4.).

BATISSE, R., BETHMONT, G., DEVESA, G. & ROUSSELIER, G. (1987) Ductile fracture of a 508 Cl 3 steel in relation with inclusion content: The benefit of the local approach of fracture and continuum damage mechanics. *Nuclear Engineering and Design,* 105, 113-120.

BEREMIN, F. M. (1983) A local criterion for cleavage fracture of a nuclear pressure vessel steel. *Metallurgical Transactions,* 14A, 2277-2287.

BERNAUER, G., BROCKS, W. & SCHMITT, W. (1999) Modifications on the Beremin model for cleavage fracture in the transition region of a ferritic steel. *Engineering Fracture Mechanics,* 64, 305-325.

BERNAUR, G. & BROCKS, W. (2001) Micro-mechanical modelling of ductile damage and tearing - results of an European numerical round robin. *Fatigue Fract Engng Mater Struct,* 25, 363-384.

BHATTACHARJEE, D. & DAVIES, C. L. (2002) Influence of processing history on mesotexture and microstructure-toughness relationship in controll-rolled and normalised steel. *Scripta Materialia*, 825-831.

BHATTACHARJEE, D. C., DAVIS, C. L. & KNOTT, J. F. (2003) Predictability of Charpy impact toughness in thermomechanically controll rolled (TMCR) microalloyed steels. *Ironmarking and Steelmaking,* 30, 249-255.

BORDET, S. R., KARSTENSEN, A. D., KNOWLES, D. M. & WIESNER, C. S. (2005) A new statistical local criterion for cleavage fracture in steel. Part I: model presentation. *Engineering Fracture Mechanics,* 72, 435-452.

CHEN, J. H., WANG, G. Z., YANG, C., MA, H. & ZHU, L. (1997) Advances in the mechanism of cleavage fracture of low alloy steel at low temperature. Part III. Local fracture stress: σf. *Int. J. Fract.,* 83, 139-157.

CIZEK, P., WYNNE, B. P. & RAINFORTH, W. M. (2006) EBSD investigation of the microstructure and texture characteristics of hot deformed duplex stainless steel. *Journal of Microscopy,* 222, 85-96.

CURRY, D. A. & KNOTT, J. F. (1978) Effects of microstructure on cleavage fracture stress in steel. *Metal Sci.,* 12, 511-514.

CURRY, D. A. & KNOTT, J. F. (1979) Effect of microstructure on cleavage fracture toughness of quenched and tempered steels. *Metall. Sci*, 341-345.

DAS, S. (2002) The effect of boundary conditions and material data representation on the simulation of deformation during hot rolling. *Department of Engineering Materials, University of Sheffield, Ph. D. Thesis.*

DAVIS, C. L. & STRANGWOOD, M. (2002) *J. Mater. Sci,* 37, 1083-1090.

FISCHER, F. D., KOLEDNIK, O., SHAN, G. X. & RAMMERSTORFER, F. G. (1995) A note on calibration of ductile failure damage indicators. *International Journal of Fracture,* 73.

FOLCH, L. C. A. (1997) Application of the local damage mechanics approach to transition temperature behaviour in steels. *PhD thesis, University of Manchester Institute of Science and Technology, Department of Civil and Structural Engineering.*

GLADMAN, T. (1997) The physical metalluergy of microalloyed steels. *London, the Institute of Materials* 154.

GODSE, R. & GURLAND, J. (1989) A statistical mode for low temperature cleavage fracture in mild steel. *Acta Metall,* 37, 541-548.

GROOM, J. D. G. & KNOTT, J. F. (1975) Cleavage fracture in prestrained mild steel. *Metal Sci.,* 9, 390-400.

HAHN, G. T., OWEN, W. S., ABERBACH, B. L. & COHEN, M. (1960) Micromechanism of brittle fracture in a low-carbon steel. *Welding Journal,* 3, 367-376.

HOHAVA, J., HAUSILD, M., KARLIK, M. & BOMPARD, P. (2002) Electron backscattering difraction analysis of secondary cleavage cracks in a reactor pressure vessel steel. *Materials Characterization,* 43, 211-217.

HUMPHREYS, A. O. (1997) Management sumary. Investigation of toughness properties of Grade A ship plate. *Materials Laboratory, Engineering Services, 1 Neville Road, Croydon, CR0 2DS, Materials Department.*

HUMPHREYS, F. J. & HATHERLY, M. (2004) Recrystallisation and related annealing phenomena. *Second edition. Elsevier Ltd., Oxford, UK,* 628.

JANG, J. L., LEE, B. W., JU, J. B., KWON, D. & KIM, W. S. (2003) "Experimental analysis of the practical LBZ effects on the brittle fracture performance of cryogenic steel HAZs with respect to crack arrest toughness near fusion line". *Engineering Fracure Mechanics,* 70(10), 1245-1257.

KAECHELE, L. E. & TETELMAN, A. S. (1969) A statistical investigation of microcrack formation. *Acta Metall,* 17, 463-475.

KARLSSONN & SORENSEN (2001) Abaqus Theory Manual. *Inc., Providence, Rhode Island, USA.*

KIM, M.-C., YONG, J. O. & JUNG, H. H. (2000) Characterization of boundaries and determination of effective grain size in Mn-Mo-Ni low alloy steel from the view of misorientation. *Scripta Materialia,* 43, 205-211.

KNOTT, J. F. (1977) Micromechanisms of Fracture and the Fracture Toughness of Engineering Alloys. *Fracture 1977, ICF4, Waterloo Canada, June 1977,* 1, 61-91.

LIN, T., EVANS, A. G. & RITCHIE, R. O. (1987) Stochastic modeling of the independent roles of particle size and grain size in transgranular cleavage fracture. *Metalluergical Transactions,* 18(4), 641-651.

MALIK, L., PESSEGODA, B. A., GRAVILLE, B. A. & TYSON, W. R. (1996) Crack arrest toughness of a heat-affected zone containing local brittle zones. *Journal of Offshore Mechanics and Artic Engineering, Transactions of the ASME,* 118, 292-200.

MUIRHEAD, J. J. (2001) The morphological characterization of grains and grain boundaries. *PhD thesis, Sheffield Hallam University.*

NOHAVA, J., HAUSILD, J. P., KARLÍK, M. & BOMPARD, P. (2002) Electron backscatering diffraction analysis of secondary cleavage cracks in a reactor pressure vessel steel. *Materials Characterization,* 49 (3), 211-217.

RANDLE, V. (1990) Representation of grain misorientations (mesotexture) in Rodrigues-Frank space. *Proc. R. Soc. Lond. A.,* 431, 61-69.

ROUSSELIER, G. (1981) Finite deformation constitutive relations including ductile fracture damage. *In: Three Dimensional Constitutive Relations and Ductile Fracture (Edited by S. Nemat-Nasser). Amsterdam North-Holland*, 331-355.

ROUSSELIER, G. (1986) Ductile fracture models and their potential in local approach of fracture. *Nuclear Engineering and Design,* 105, 97-111.

SHASHWAT, S. & SOMMATH, G. (2006) Modelling cyclic ratcheting based fatigue life of HSLA steels using crystal plasticity FEM simulations and experiments. *International Journal of Fatigue*, 1690-1704.

SHTERENLIKHT, A. (2003) 3D CAFE modelling of transitional ductile-brittle fracture in steels. *Ph.D Thesis, Department of Mechanical Engineering, University of Sheffield.*

SIGMASCAN PRO VERSION 5.0 (2005) Image Analysis and Measurement Program.

SMITH, E. (1966a) The formation of a cleavage crack in a crystalline solid - I. *Acta Metallurgica,* 14, 985-989.

SMITH, E. (1966b) The formation of a cleavage crack in a crystallinesolid - II. *Acta Metallurgica,* 14, 991-996.

TANGUY, B., BESSON, J. & PINEAU, A. (2003) Comment on Effect of carbide distribution on the fracture toughness in the transition temperature region of a SA 508 steel. *Scripta Materialia,* 49, 191-197.

TETELMAN, A. S., WILSHAW, T. R. & RAU JR, C. A. (1968) The critical tensile stress criterion for cleavage. *international Journal of Fracture,* 4, 147-157.

TVERGAARD, V. (1981) Influence of voids on shear band instabilities under plane strain conditions *International Journal of Fracture,* Vol.17, 381-388.

WALLIN, K. (1991) Statistical modelling of fracture in the ductile-to-brittle transition region. *in J. G. Blauel and K. H. Schwalbe, eds, "Defect Assessment in Components - Fundamentals and Applications, ESIS/EGF9, Mechanical Engineering Publications, London*, 415-445.

WANG, G. Z. & CHEN, J. H. (1999) Effect of notch geometry on the local cleavage fracture stress. *Fatigue Fract. Engng Mater. Struct.*, 22, 849-858.

WANG, G. Z. & CHEN, J. H. (2000) A statistical model for cleavage fracture in notched specimens of C-Mn steel. *Fatigue Fract Engng Mater Struct,* 24, 451-459.

WANG, G. Z., WANG, J. G. & CHEN, J. H. (2003) Effects of geometry of notched specimens on the local cleavage fracture stress σf C-Mn steel. *Engineering Fracture Mechanics,* 70, 2499-2512.

WU, S. J. & DAVIS, C. L. (2004) Investigation of the microstructure and mesotexture formed during thermomechanical controlled rolling in microalloyed steels. *Journal of Microscopy,* 213, 262-272.

WU, S. J., DAVIS, C. L., SHTERENLIKHT, A. & HOWARD, I. C. (2005) Modeling the ductile-brittle transition behavior in thermomechanically controlled rolled steels. *Metallurgical and Materials Transactions A,* 36A, 989-997.

WU, S. J. & KNOTT, J. F. (2004) On the statistical analysis of local fracture stresses in notched bars. *Journal of the Mechanics and Physics of Solids,* 52, 907-924.

ZIKRY, M. A. & KAO, M. (1996) Inelastic microstructural failure mechanisms in crystalline materials with high angle grain boundaries. *Journal of the Mechanics and Physics of Solids,* 44(11), 1765-1798.

Chapter VI

Simulation of microcracks and the ductile-brittle transition with the CAFE model

The results of the application of the CAFE model are given in this section. These results are given at cellular and macro level. Figures showing the CA arrays created inside the structure of finite elements, in the damage zone simulated with the CAFE model, are presented in this chapter. To make this possible, EnSight Gold Version 7.0 was used. The power of the model to simulate the distribution of cleavage initiation points and the ductile-brittle transition is presented as well. Good correlation between numerical against experimental data is shown at micro-cellular and macro levels.

6.1 Sensitivity analysis of Rousselier's damage parameter D with Charpy data and CAFE simulations.

Rousselier's damage model parameter D was fitted with the original Charpy CAFE model (Shterenlikht, 2003). The 3D finite element model of the Charpy test is shown in figure 6.1, the damage part of the model consisted of 900 C3D8R 8–node and 1322 C3D6 6–node single integration finite elements. The model has in total 2222 finite elements. The number of nodes were 2807. The anvils and the hammer were simulated as rigid bodies, contact conditions were applied between the specimen, anvils and hammer. In this model, the density of the hammer was increased up to reach the $19.5kg$ of the standard hammer (EN ISO 14556:200 British Standards, 1987). This parameter controls the rate of damage and must be tuned with numerical solutions. The true stress–strain data in the rolling direction of the plate steel (figure 3.6) and the mechanical properties of table 3.2 (chapter 3) were applied to the simulation of Charpy tests. The following simulations show the results of the simulation performed at room temperature.

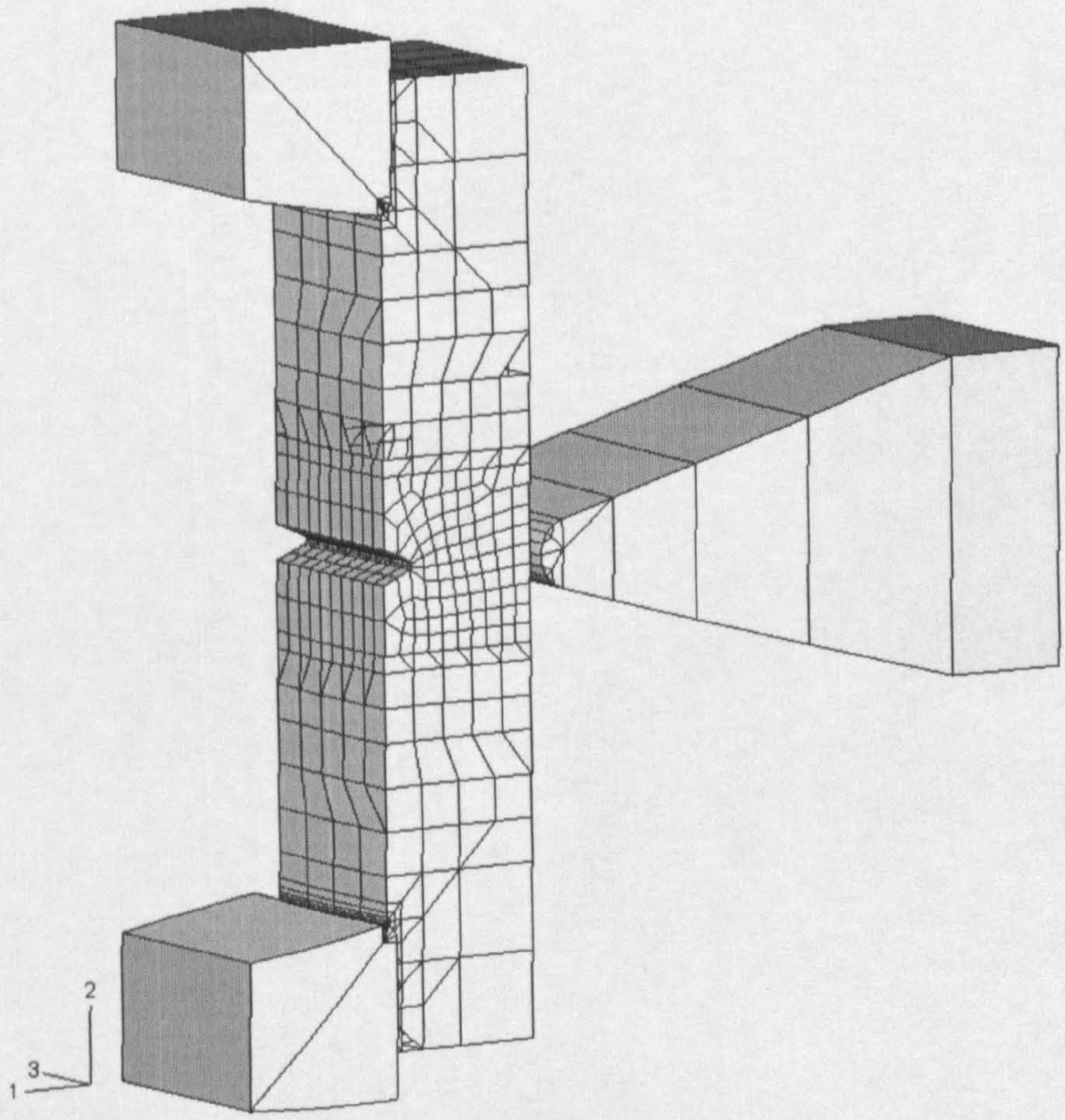

Figure 6.1 – 3D Charpy finite element model used in CAFE simulations.

Figure 6.2 shows the CA array on the damage zone of the original model of a Charpy impact test where the CAFE model was applied. In this figure the green cells correspond to the ductile fracture process and the red ones to the brittle part. In this figure it can be seen that some points of cleavage fracture were developed in the region in front of the notch root. These cleavage fracture initiation points correlate with those regions of cleavage fracture found in broken Charpy surfaces tested at room temperature (figure 3.25, section 3.4.2).

Figure 6.3 shows a $3D$ view of the CA arrays of the original CAFE model (Shterenlikht, 2003). This image also shows some points of cleavage initiation points. The simulation was performed only at room test temperature because the model was a constitutive ductile damage model and it does not incorporated temperature dependence.

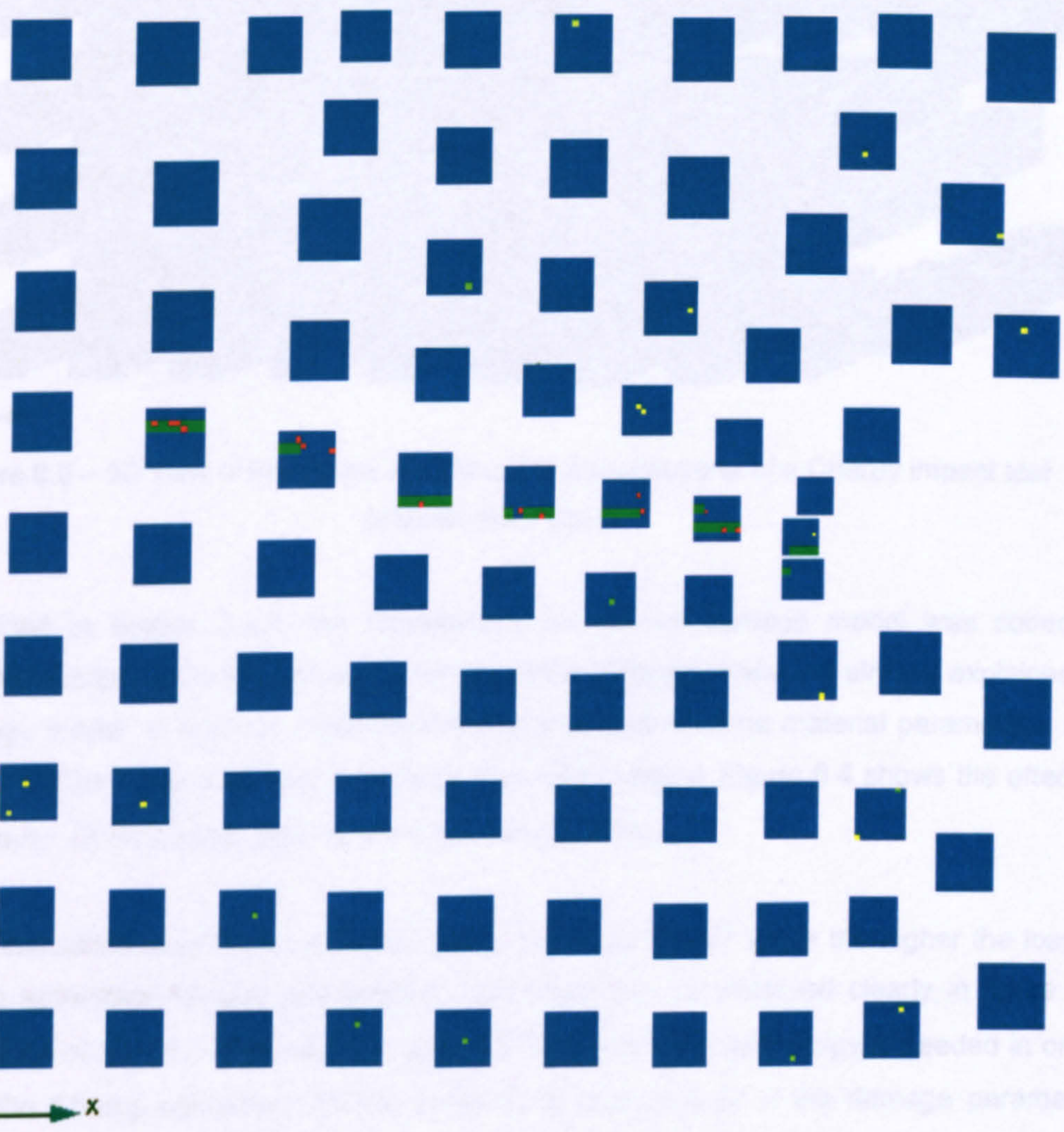

Figure 6.2 – 2D view of the arrays of cells of the damage zone of a Charpy impact test.

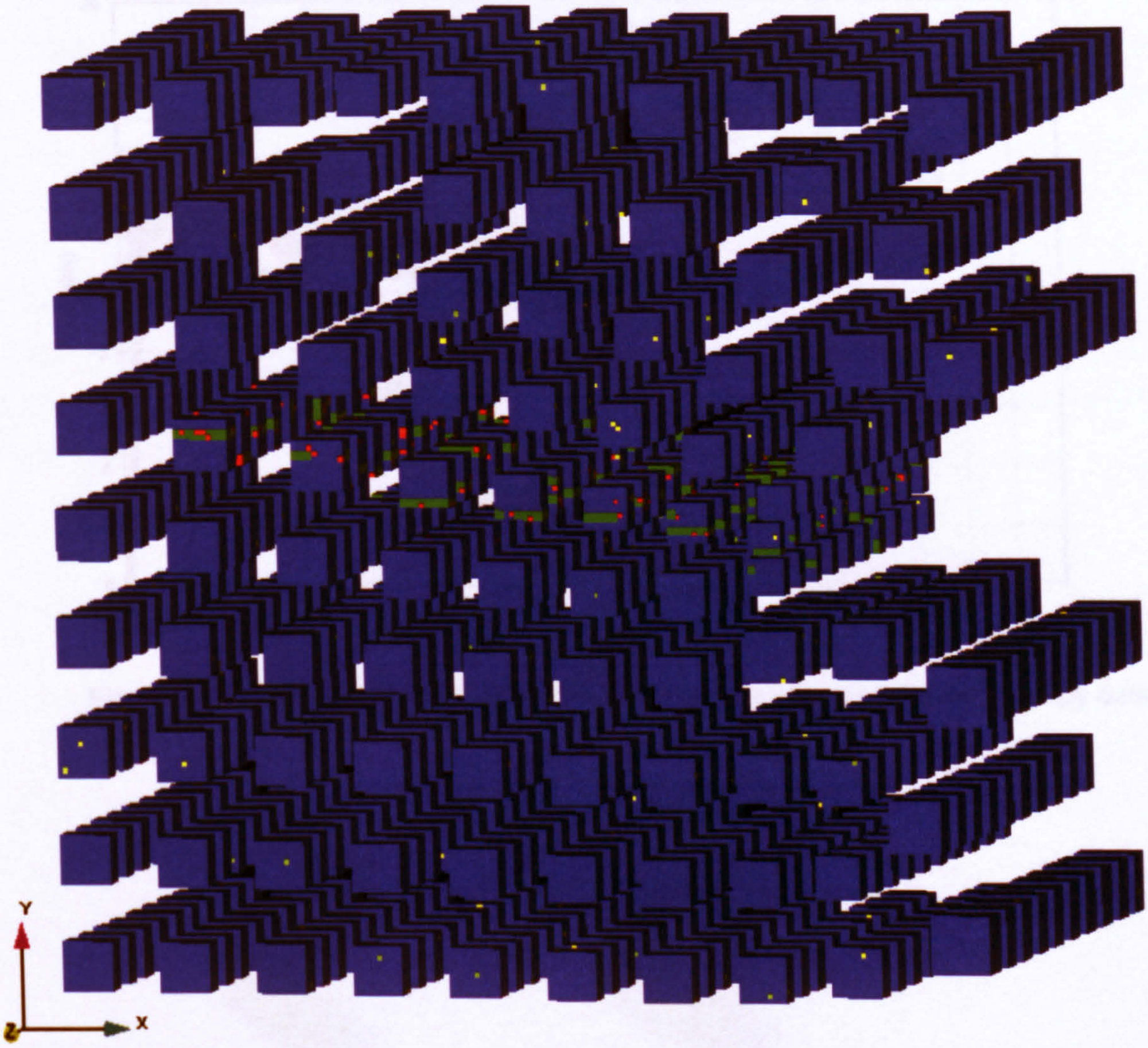

Figure 6.3 – 3D view of the arrays of cells of the damage zone of a Charpy impact test (Shterenlikht, 2003).

As explained in section 2.2.5, the Rousselier's constitutive damage model was coded to simulate the ductile part in the Cellular Automata Finite Element model. As already explained, in this damage model, in order to make the damage variables become material parameters, one needs to calibrate those parameters for each particular material. Figure 6.4 shows the effect of the parameter D on Charpy data for room test temperature.

From the simulation results we can observe that the lower the D value the higher the load is needed to accelerate fracture propagation. This effect can be observed clearly in figure 6.5 where a value of $D = 1.5$ promoted the arrest of the crack and high energy is needed in order to break the Charpy specimen. On the other hand, high values of the damage parameter, $D = 3$, promotes fracture propagation as shown in figures 6.4 and 6.5. Figure 6.5 shows the failed elements.

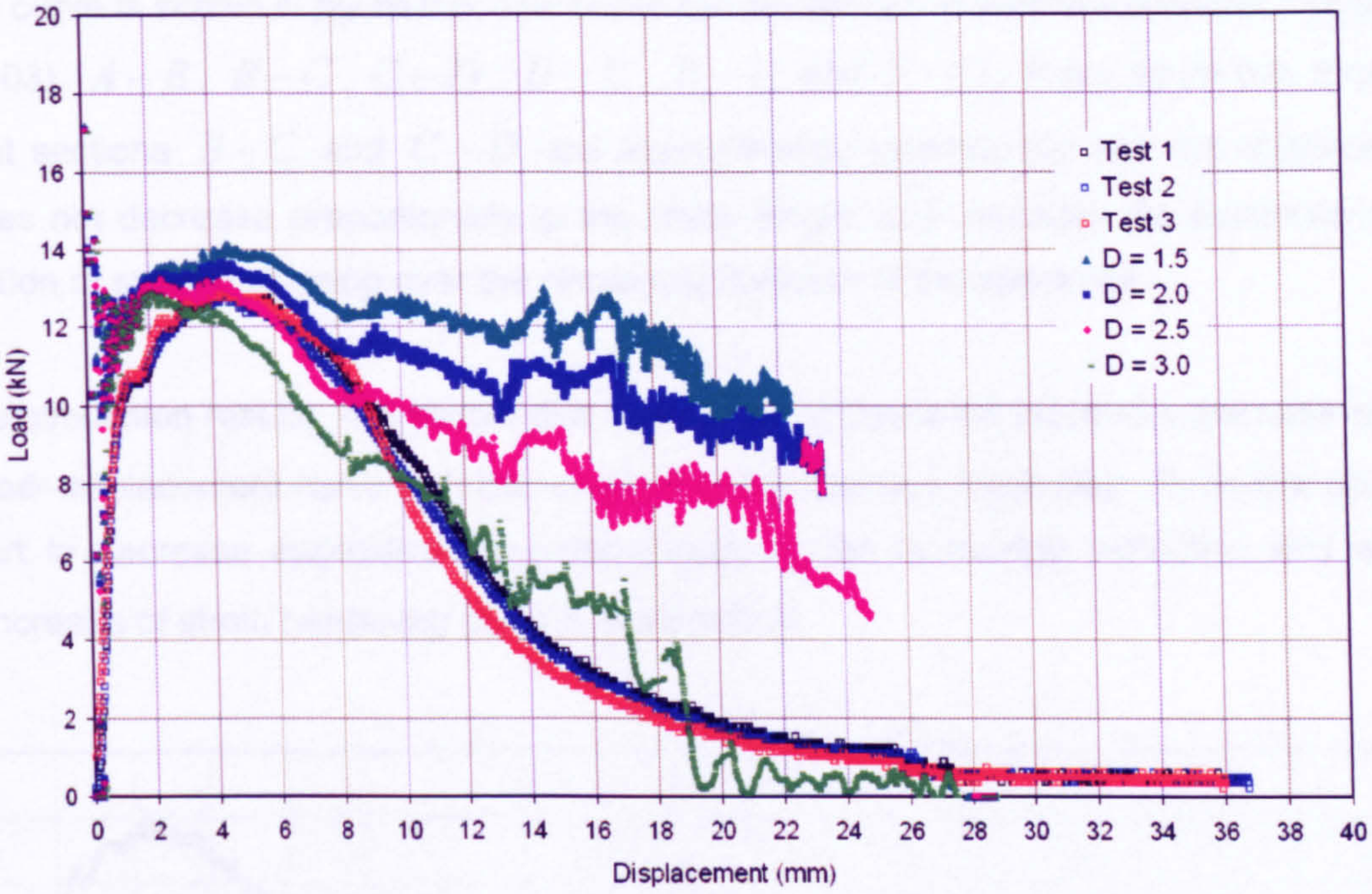

Figure 6.4 – Calibration of the Rousselier parameter D on instrumented Charpy data.

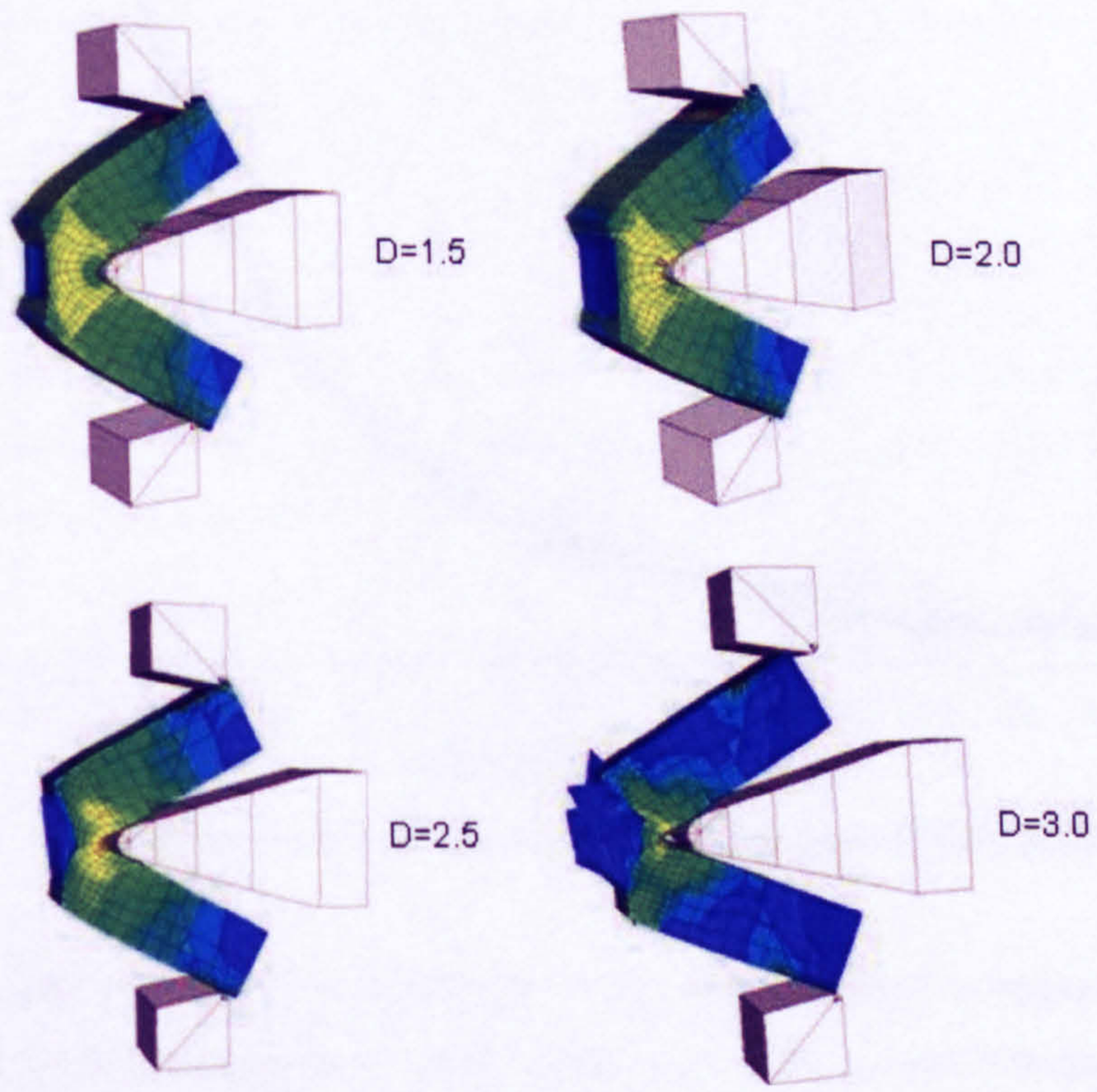

Figure 6.5 – Effect of the Rousselier parameter D on Charpy tests simulations.

In graph 6.4 it is shown that with a value of $D = 3$, correlation between numerical against experimental was obtained. Therefore these values will be used in the CAFE model in further simulations. In order to explain the physical meaning of the material parameter D and its effect in Charpy data, the load–displacement curve of instrumented Charpy tests was used (section

3.4). The curve is shown in figure 6.6. The curve can be divided in different sections (Vodopivec et al., 2003), $A-B$, $B-C$, $C-D$, $D-E$, $E-F$ and $F-G$. From figure 6.6, it can be seen that sections $B-C$ and $C-D$ are approximately symmetrical and the displacement force does not decrease proportionally to the crack length, this indicates the existence of the continuation of strain hardening over the remaining ligament of the specimen.

From the simulation results, it is shown that in point D of figure 6.6 there is a dramatic change in the load–displacement curve with the variation of the damage parameter D. In this point the load start to decrease approximately proportionally to the increasing deflection and without further increase of strain hardening down to the point E.

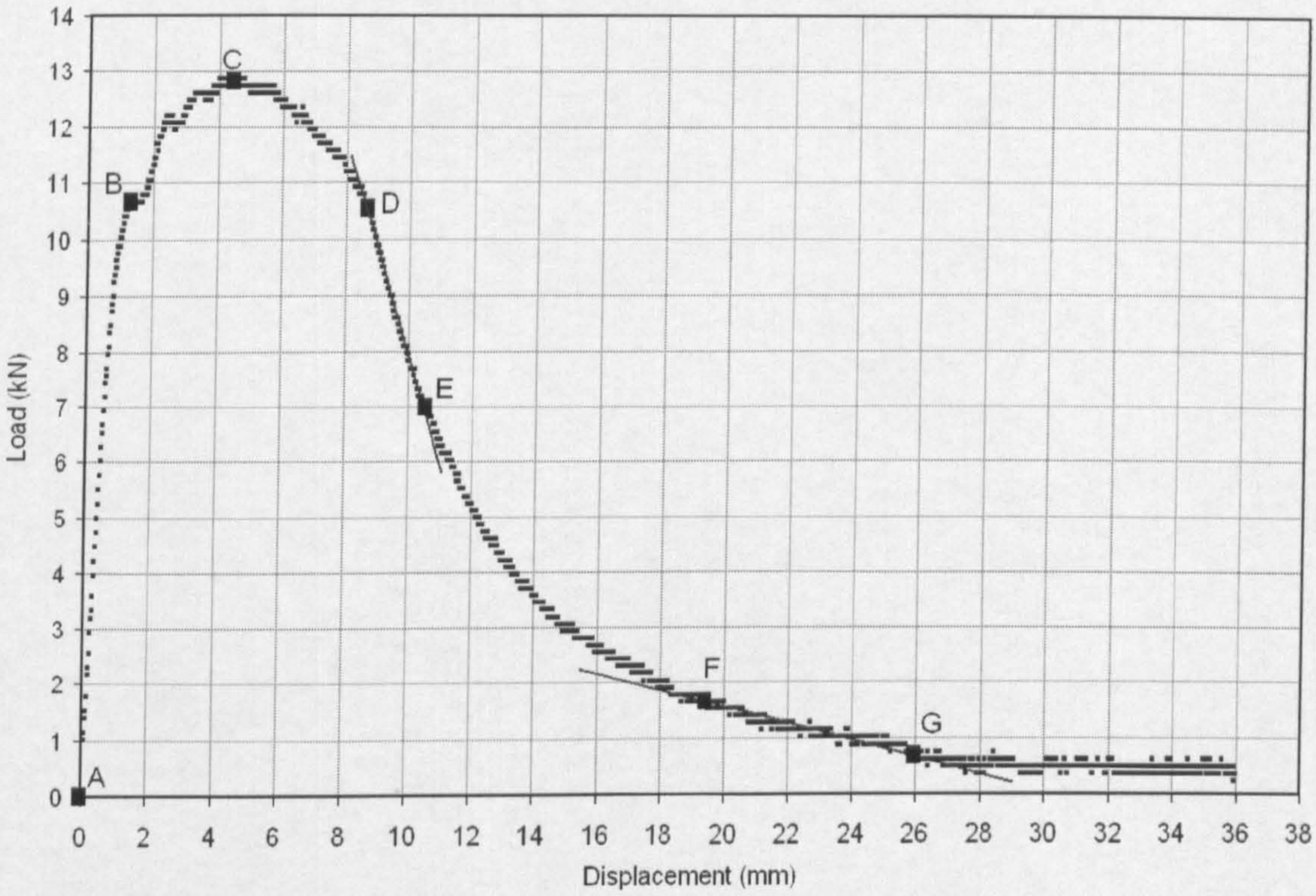

Figure 6.6 – Instrumented Charpy impact tests and fracture identification points.

In figure 6.6, the load increases proportionally to the displacement in region $A-B$ where elastic deformation occurs. Plastic deformation starts from point B and the displacement force increases then up to the maximum load in point C. From point C, the load decreases first in a non–linear way with increasing displacements up to point D. Fracture propagation initiates in point C. Afterwards the load continues to decrease approximately proportionally to the displacement to the inflection point E. From point E to point F the load decreased with non proportionality to the displacement. Section $F-G$ showed proportionality. It is clearly shown

that the displacement starts to increase faster from point E with lower load. In figure 6.6 we also see a decrease of load needed for fracture propagation in part $C-D$. Based on these observations we can suggest that in terms of Charpy test data, that the material parameter, D, controls the load needed for fracture propagation and consequently the crack arrest properties of the metal. From the above results it can be seen that the parameter D has strong influence on the output in Charpy simulations data and it is very important to calibrate properly such parameter with experimental data. After calibration, the damage parameter indicator, D, can be used for approximately indicating the onset of a local macrocrack in a structure and this parameter controls the stable propagation of a crack. Therefore this parameter is an indicator of the start of a microcrack.

6.2 Sensitivity analysis of Rousselier's damage parameter σ_1 with Charpy data and CAFE simulations.

As explained in previous sections, the material damage model parameter σ_1 is related to the tearing resistance of the matrix material. Figure 6.7 shows the effect of the variation of this material parameter. In this curve we can observe that in the rolling direction of the plate steel, the best value which simulates the Charpy experimental data is in the range of $\sigma_1 = 800MPa$ to $\sigma_1 = 1000MPa$ (table 5.2, section 5.8.1). The mean of σ_1 is about $\sigma_1 = 900MPa$. A value of $\sigma_1 = 900MPa$ used in the CAFE model gave the best correlation with experimental data (figure 6.7). Therefore this value will be used in further simulations.

From figure 6.7 it is shown that low σ_1 values leads to a drop in the energy absorbed by specimens. It is interesting to observe that this parameter does not increase in any way the toughness properties of the material. Even with a value of $\sigma_1 = 1500MPa$, there was no variation in the curve after the parameter σ_1 was calibrated for a particular material. Interestingly this value can control only the rapid fracture propagation part of Charpy data (from point B to G in figure 6.6) as shown by the finite element models in figure 6.8. From these figures we can conclude that lower values of σ_1 promotes rapid or low fracture propagation from point B to F. High values of σ_1 promotes high distortion in failed elements as shown in figure 7.6 for a value of $\sigma_1 = 1500MPa$.

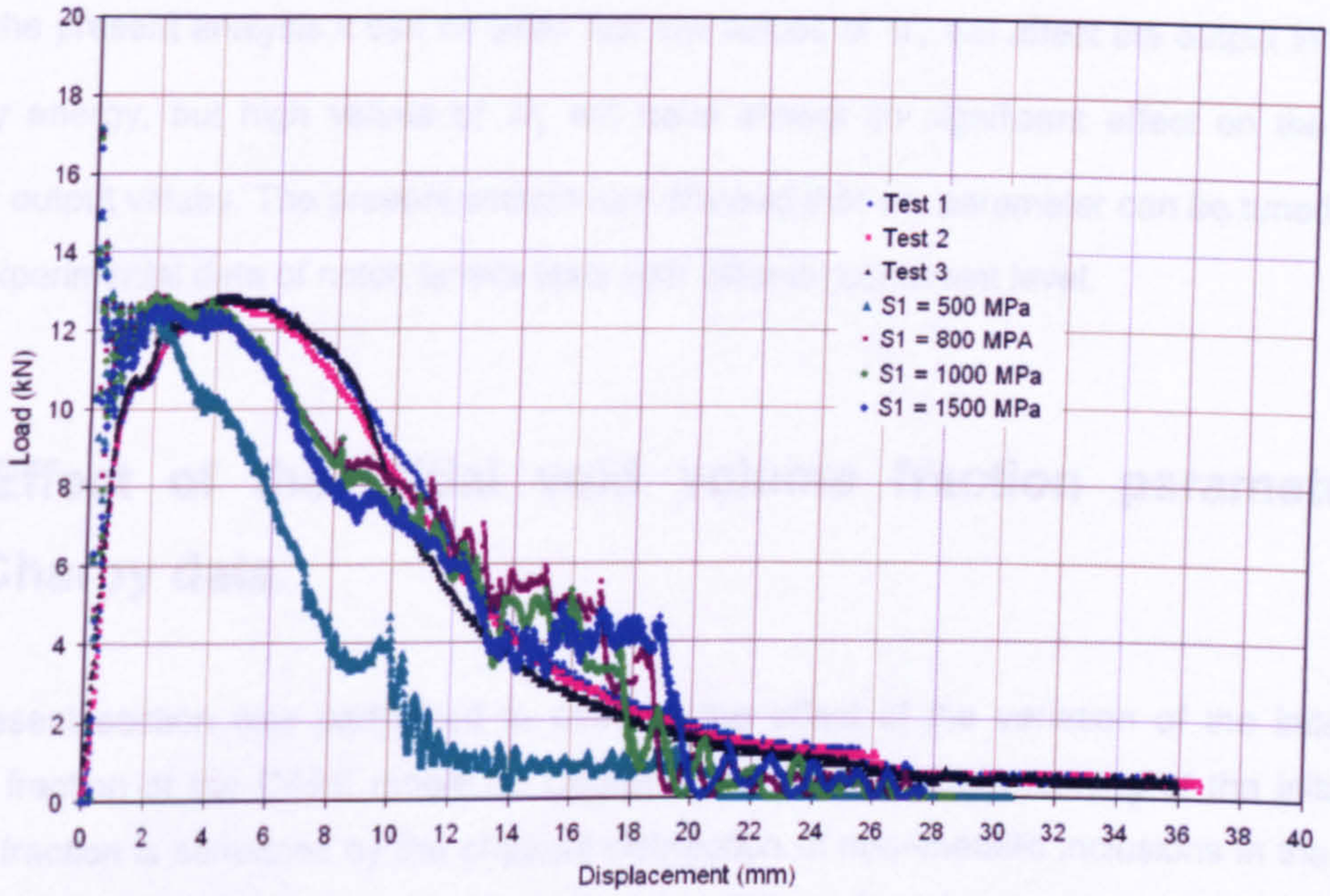

Figure 6.7 – Calibration of the Rousselier parameter σ_1 on instrumented Charpy data.

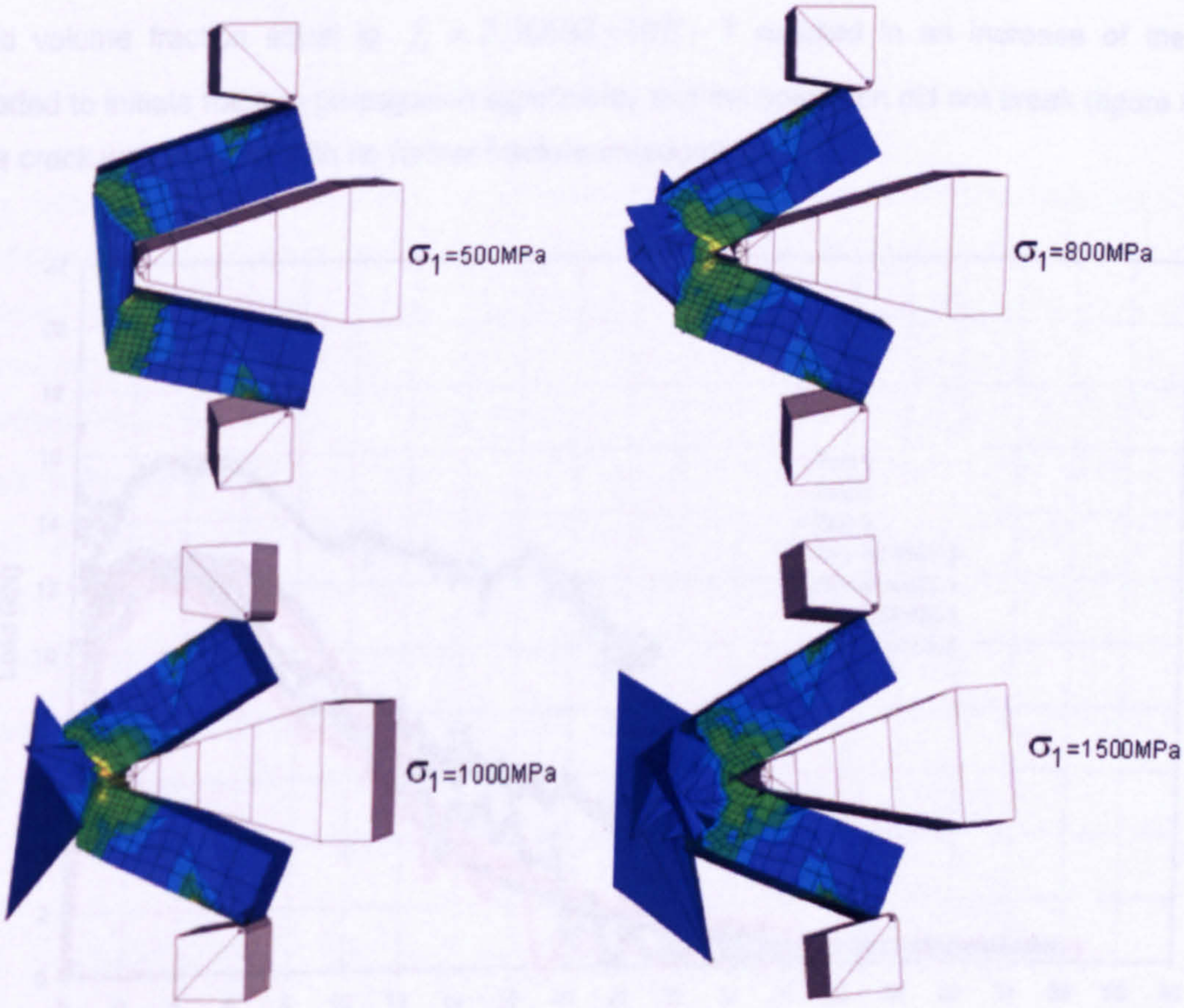

Figure 6.8 – Effect of the Rousselier parameter σ_1 on Charpy tests simulations.

From the present analysis it can be seen that low values of σ_1 will affect the output in terms of Charpy energy, but high values of σ_1 will have almost no significant effect on the Charpy energy output values. The present section also showed that σ_1 parameter can be tuned directly from experimental data of notch tensile tests with different constraint level.

6.3 Effect of the initial void volume fraction parameter in Charpy data.

The present section was performed to observe the effect of the variation of the initial void volume fraction of the CAFE model on Charpy data. The physical meaning of the initial void volume fraction is simulated by the physical distribution of non–metallic inclusions in the matrix of the material. In figure 6.9 we observe that small initial void volume fraction will make the steel very tough and consequently will retard fracture initiation and propagation for steels as higher loads will be needed for fracture nucleation. This can be shown clearly in figure 6.9, an initial void volume fraction equal to $f_0 = 2.06608 \times 10E-3$ resulted in an increase of the load needed to initiate fracture propagation significantly and the specimen did not break (figure 6.10). The crack was arrested with no further fracture propagation.

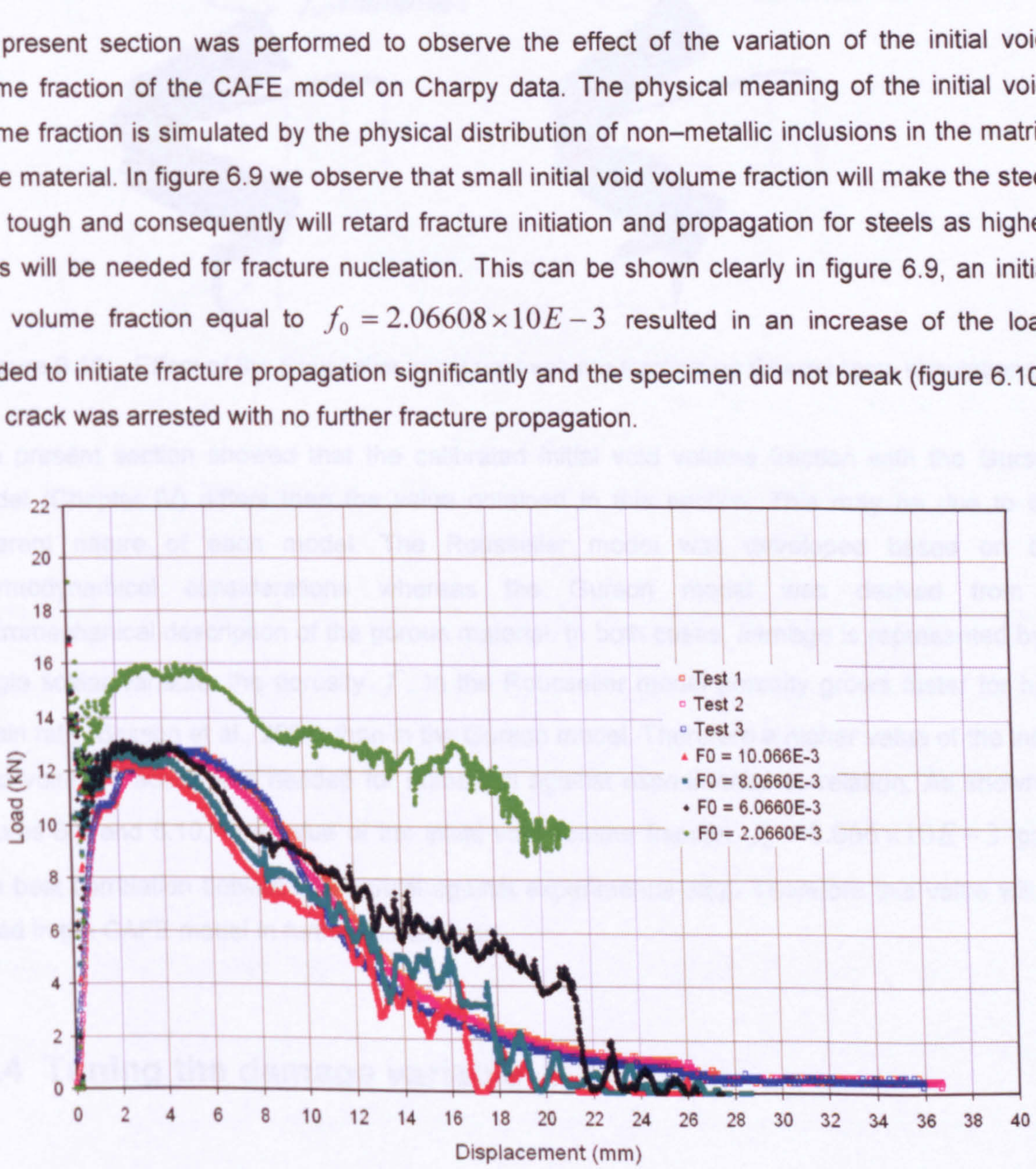

Figure 6.9 – Calibration of the initial void volume fraction on instrumented Charpy data.

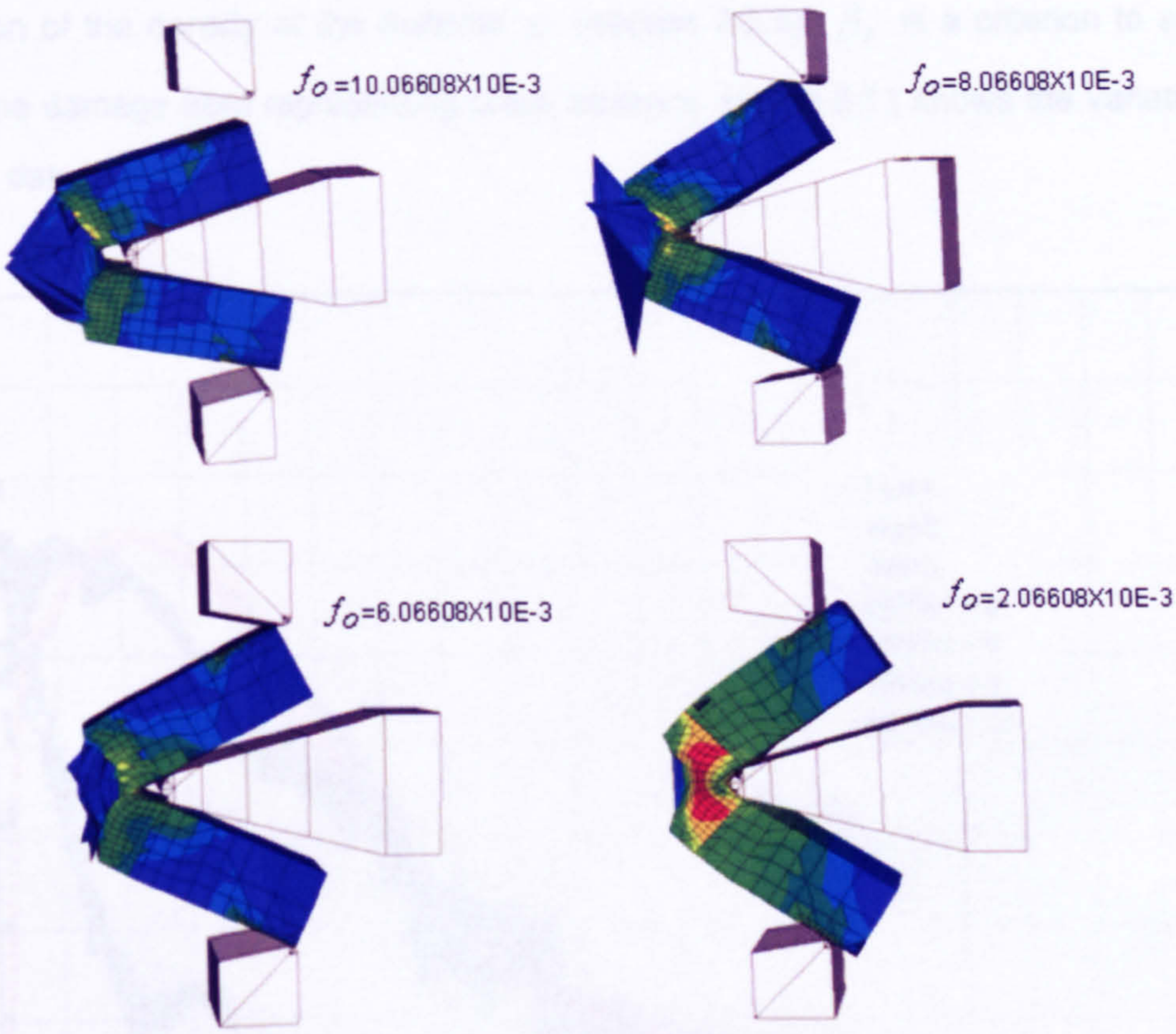

Figure 6.10 – Effect of the Rousselier initial void volume fraction on Charpy tests simulations.

The present section showed that the calibrated initial void volume fraction with the Gurson model (Chapter IV) differs than the value obtained in this section. This may be due to the different nature of each model. The Rousselier model was developed based on the thermodynamical considerations whereas the Gurson model was derived from a micromechanical description of the porous material. In both cases, damage is represented by a single scalar variable: the porosity f. In the Rousselier model porosity grows faster for high strain rate (Besson et al., 2001) than in the Gurson model. Therefore a higher value of the initial void volume fraction was needed for numerical against experimental correlation. As shown in figures 6.9 and 6.10. The value of the initial void volume fraction $f_0 = 8.066 \times 10E-3$ gave the best correlation between numerical against experimental data. Therefore this value will be used in the CAFE model in further simulations.

6.4 Tuning the damage variable β_F.

The critical value of the damage variable β_F is used as a criterion to advance the crack (Li et al., 1994). Therefore this parameter is closely related to the void growth ratio as this parameter

is a function of the density of the material ρ (section 2.2.5). β_F is a criterion to specify the extent of the damage front representing crack advance. Figure 6.11 shows the variation of β_F on Charpy data.

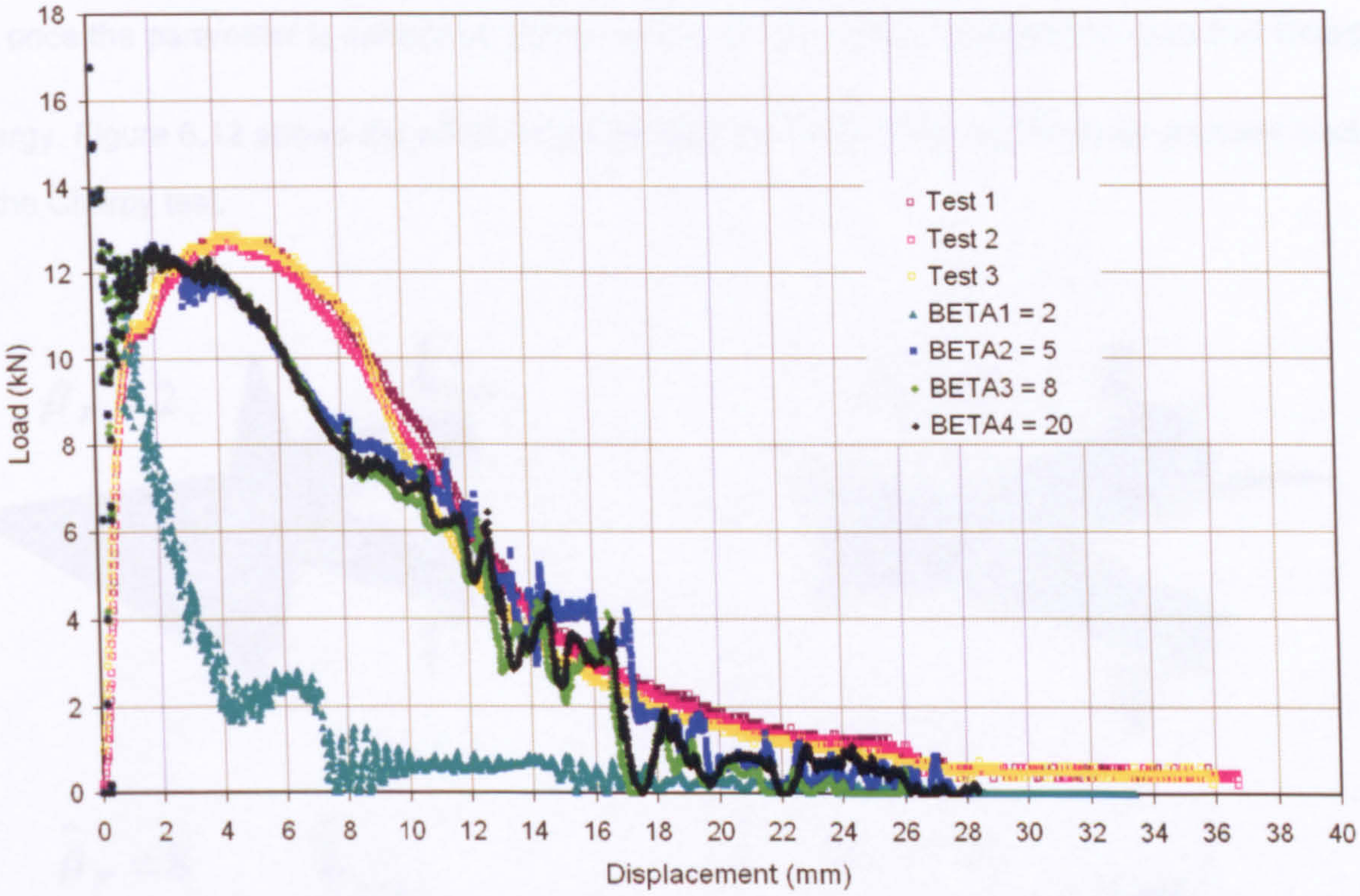

Figure 6.11 – Calibration of the critical value of the damage variable β_F.

From figure 6.11 we can see that very low values of $\bar{\beta}_F$ promotes rapid loss of load bearing capacity of the finite elements. A value of $\bar{\beta}_F = 5$ gave good agreement of numerical simulations with experimental data. A value of $\bar{\beta}_F = 8$ gave a good correlation with experimental data as well, therefore either of these two values can be used for further simulations. But a value of $\bar{\beta}_F = 8$ will be used in the CAFE model for further simulations because this value gave better results on figure 6.12 than with a value of $\beta_F = 5$. The distortion in the failed elements with a value of $\bar{\beta}_F = 8$ is not as high as that with a value of $\bar{\beta}_F = 5$. It can be seen in figure 6.11 that at displacement of 16mm there was needed a higher load to break the specimen and the specimen did not break totally. Therefore a value $\bar{\beta}_F = 8$ will be used in following simulations. Similar values are reported in literature (Shterenlikht and

Howard, 2006, Li et al., 1994). It can be seen as well that higher values of $\bar{\beta}_F$ has almost no effect on the output data as shown in figure 6.11. From the present results it can be seen that small values of the damage variable $\bar{\beta}_F$ will affect considerably the output of Charpy energy but once the parameter is calibrated, higher values of $\bar{\beta}_F$ does not affect the output of Charpy energy. Figure 6.12 shows the effect of the damage parameter $\bar{\beta}_F$ on the finite element model of the Charpy test.

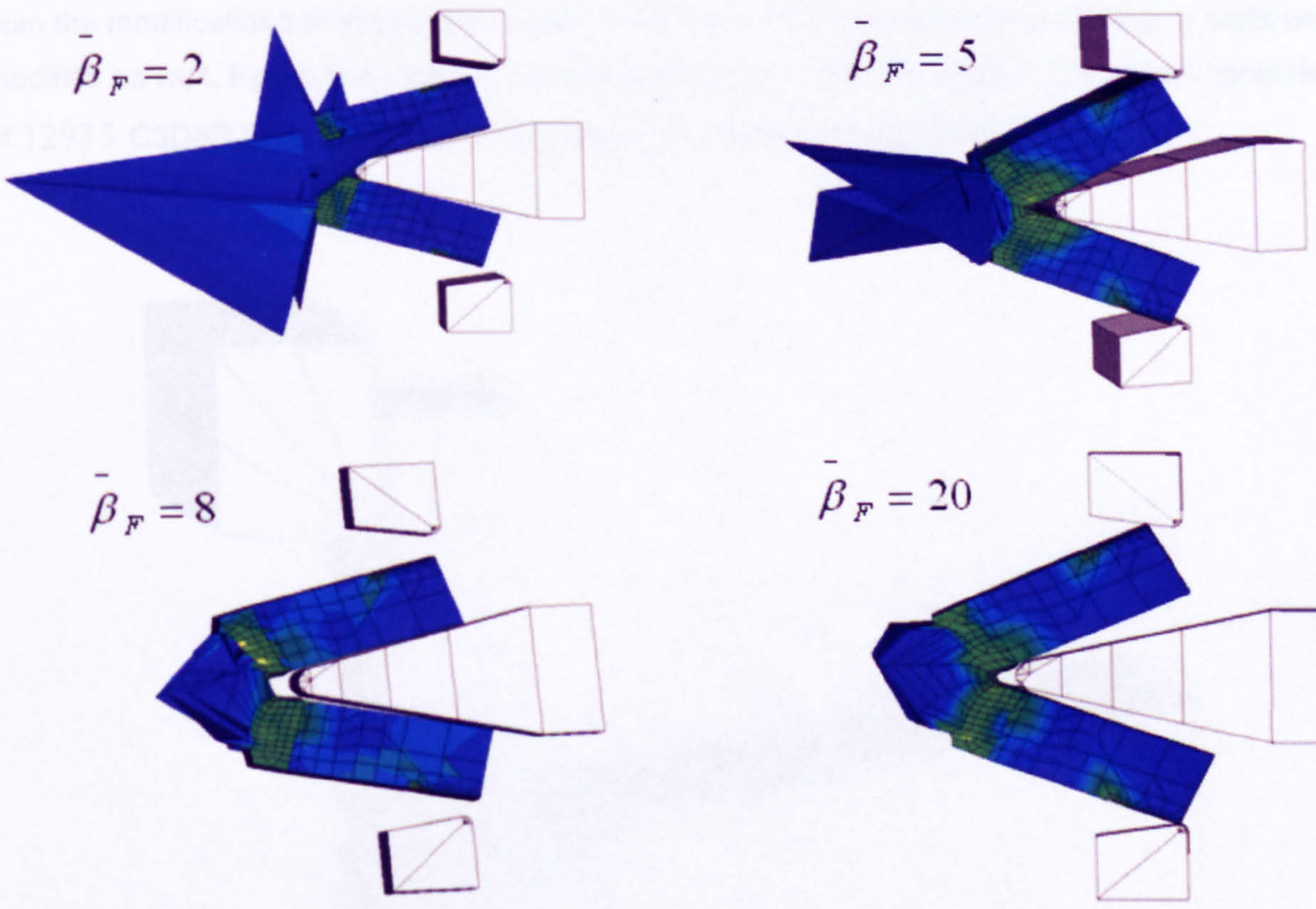

Figure 6.12 – Calibration of the critical value of the damage variable β_F.

Figure 6.12 shows how very low values of $\bar{\beta}_F$ will result on a rapid loss bearing capacity of finite elements and consequently the absorbed Charpy impact energy will be very small. In the sensitivity analysis, it has been shown that in figures 6.5, 6.8, 6.10 and 6.12 the failed elements distorted highly when the Rousselier damage model parameters were fitted to accelerate fracture initiation and propagation. This phenomenon did not occurred on the finite element simulations that reproduced properly the experimental data as no further distortion on the failed finite elements occurred. This may suggest that as the specimens failed very quickly, further applied load tend to distort highly the failed elements as those shown in figures 6.5, 6.8, 6.10

and 6.12. Those highly distorted dead finite elements, once deleted, show the fracture propagation path and do not affect in any way the numerical results.

6.5 The modified CAFE model.

As shown in previous section, the calibration of the damage model parameters of the CAFE model was performed with the original finite element model (Shterenlikht, 2003, Wu et al., 2005, Shterenlikht et al., 2005). The mesh size of each finite element in the damage zone was about $1mm^3$. In the present work in order to obtain better correlation with experimental data, apart from the modifications of the original CAFE model, the finite element model of Charpy tests was modified as well. Figure 6.13 shows the new Charpy finite element model. The model consisted of 12935 C3D8R 8–node reduced integration finite elements and 7488 nodes.

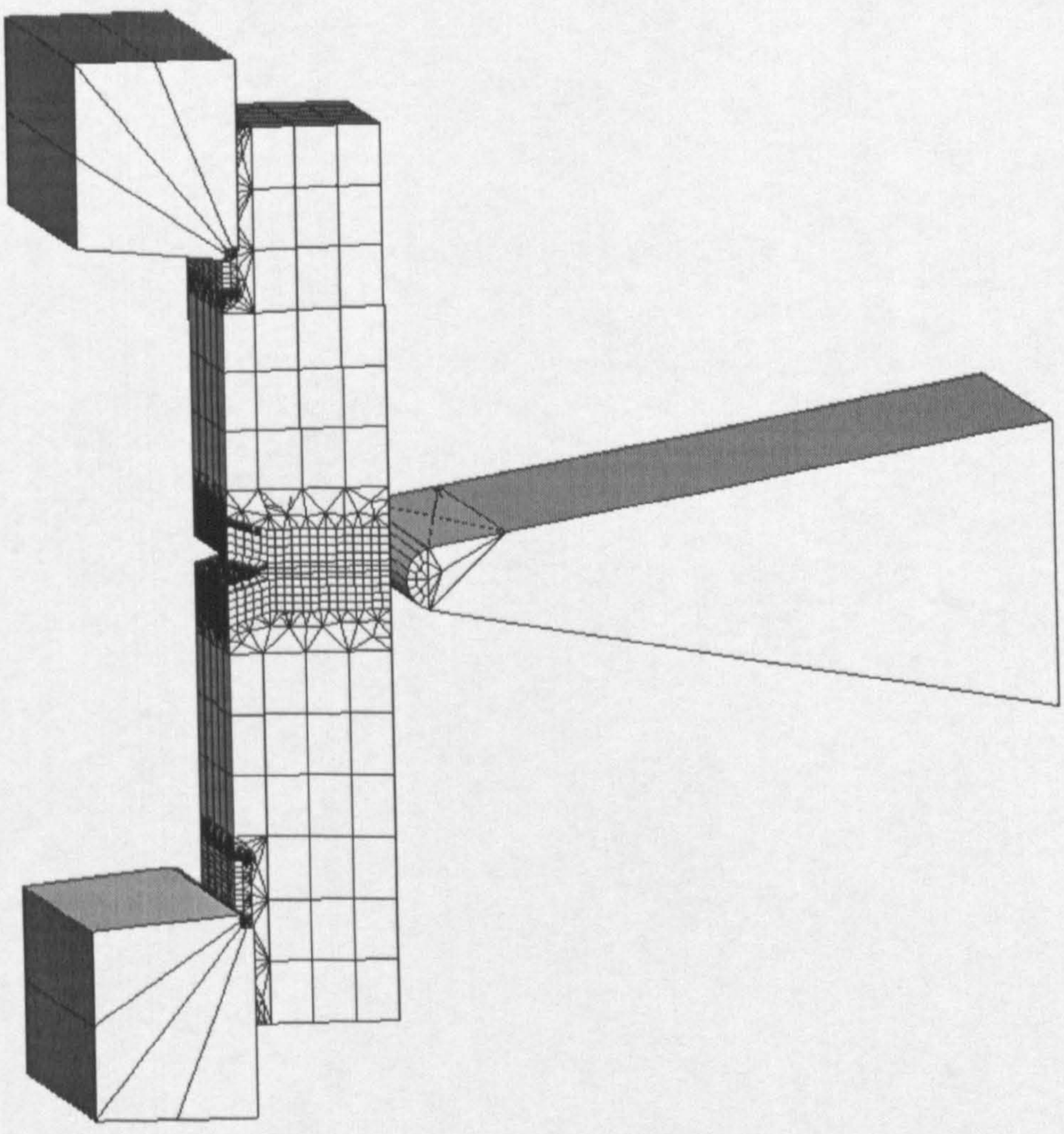

Figure 6.13 – The new finite element model used for Charpy CAFE simulations.

The damage zone consisted of 2100 C3D8R 8–node reduced integration finite elements (HKS, 2004) as shown in figure 6.13. The finite elements in the damage zone are $0.5mm \times 0.5mm \times 0.5mm$ cubic elements. Slightly smaller finite elements were used near the root of the notch, so $5 \times 5 \times 5$ ductile cell $(M_D = 125)$ and $10 \times 10 \times 10$ brittle cell $(M_B = 1000)$ CA arrays were created for each finite element in the damage zone. Thus the ductile damage cell size is $L_D \approx 0.5/5 = 0.1mm$ and the brittle damage cell is about $L_B \approx 0.5/10 = 0.05mm$.

The CAFE model will therefore have 262500 ductile and 2100000 brittle CA cells. In this model the finite elements were created parallel to the fracture propagation path in order to simulate better the fracture propagation path in the Charpy model. A close view of the new finite element mesh created in the damage zone where the CAFE model was applied is shown in figure 6.14. From this picture we can see a better finite element mesh than the original one of the CAFE model. Along with the modifications proposed in the previous chapter of this research work, better correlation between experimental and numerical data can be obtained. The visualization of the cells arrays of the damage region was done with the visualization program EnSight Gold version 7.1. The cells array of the damage zone are shown in figure 6.15.

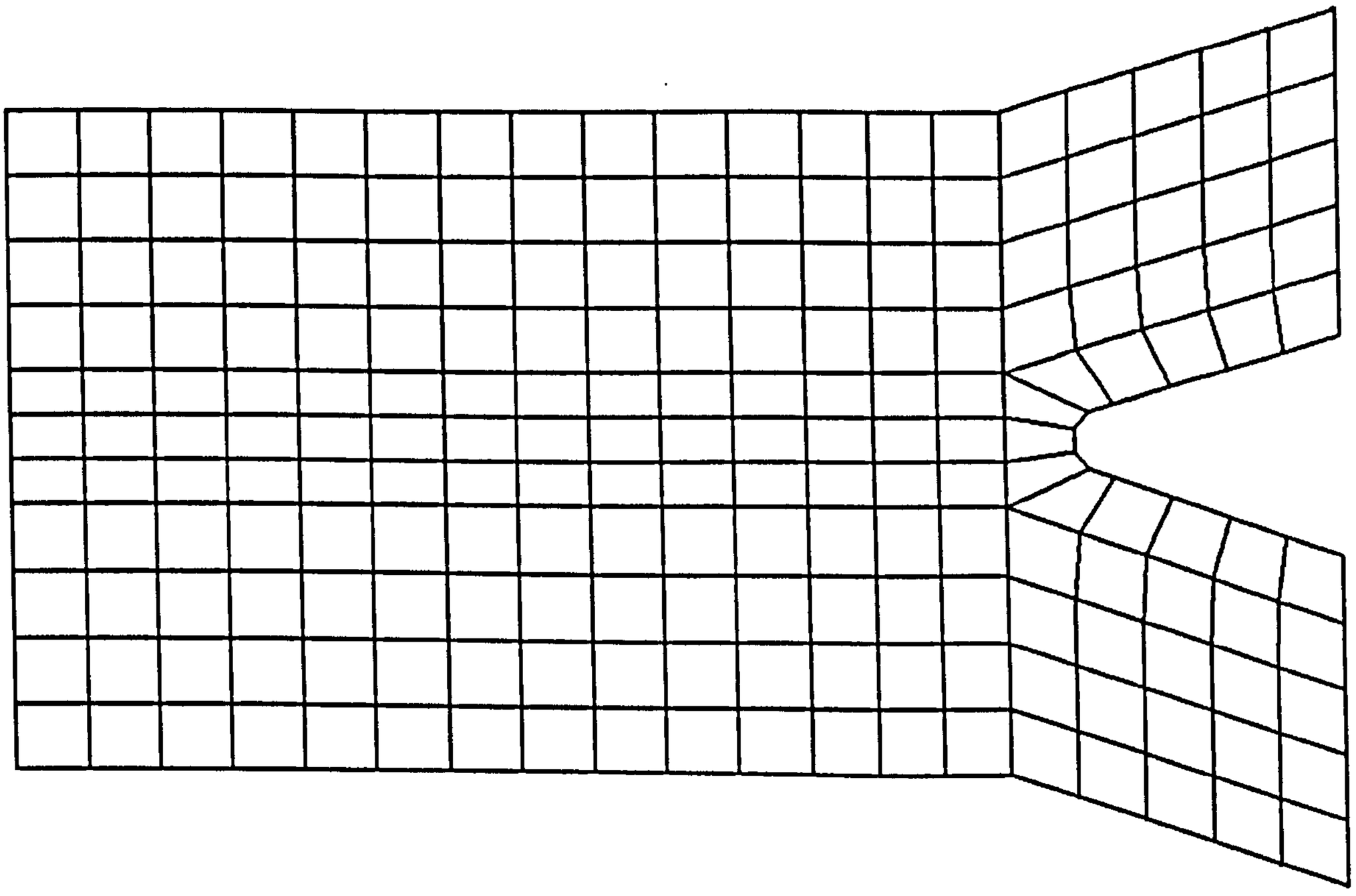

Figure 6.14 – The new finite element model used for Charpy CAFE simulations.

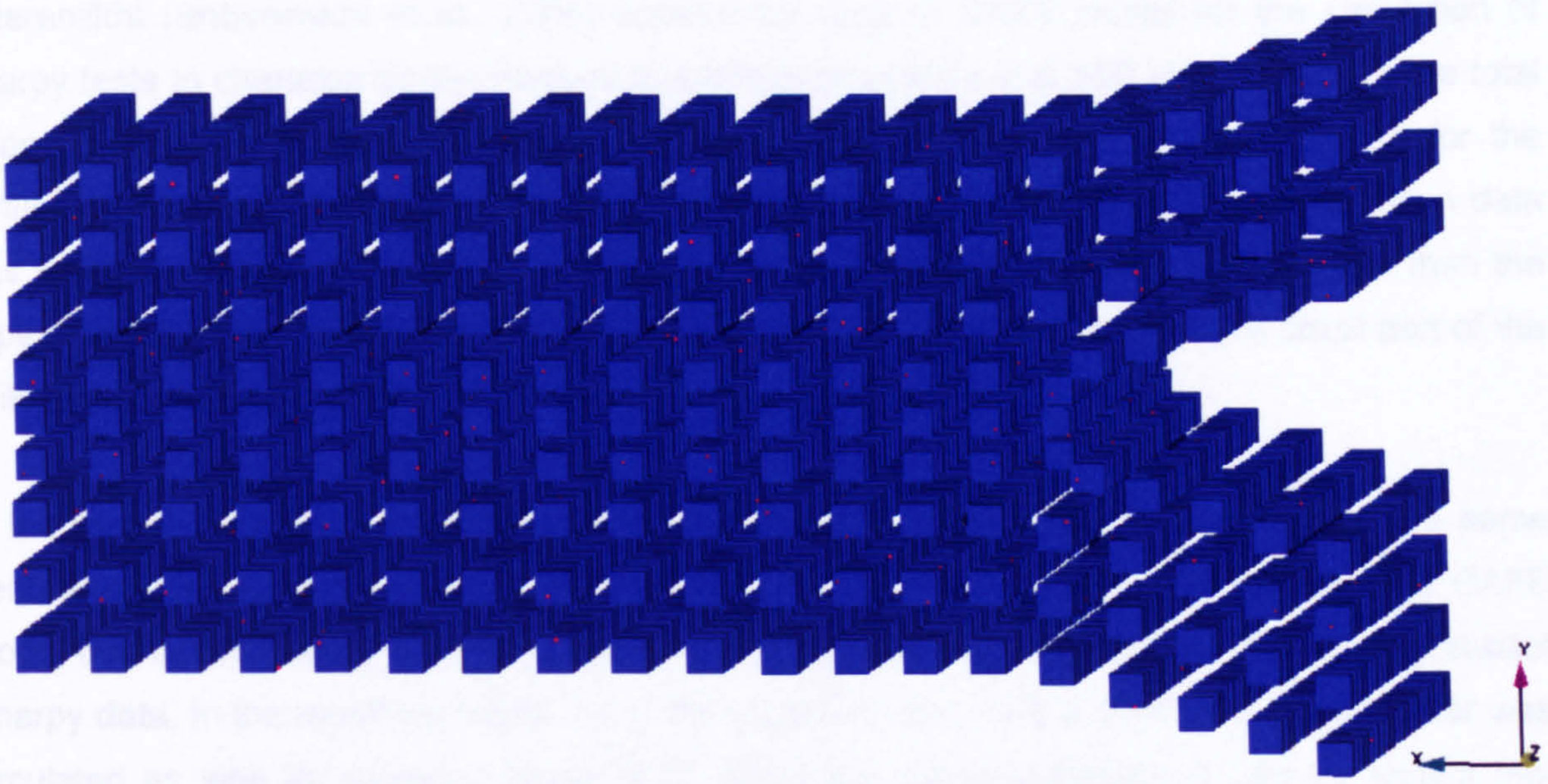

Figure 6.15 – 3D view of the arrays of cells of the damage zone of a the new model of the Charpy impact test.

The numerical vs experimental correlation with the already calibrated damage model parameters applied to the new Charpy CAFE model is shown in graph 6.16. From this graph, we can see that a much better correlation was obtained. This is essentially shown in the hardening part of the load–displacement curve of Charpy data computed in figures 6.4, 6.7, 6.9, and 6.11 with the previous model.

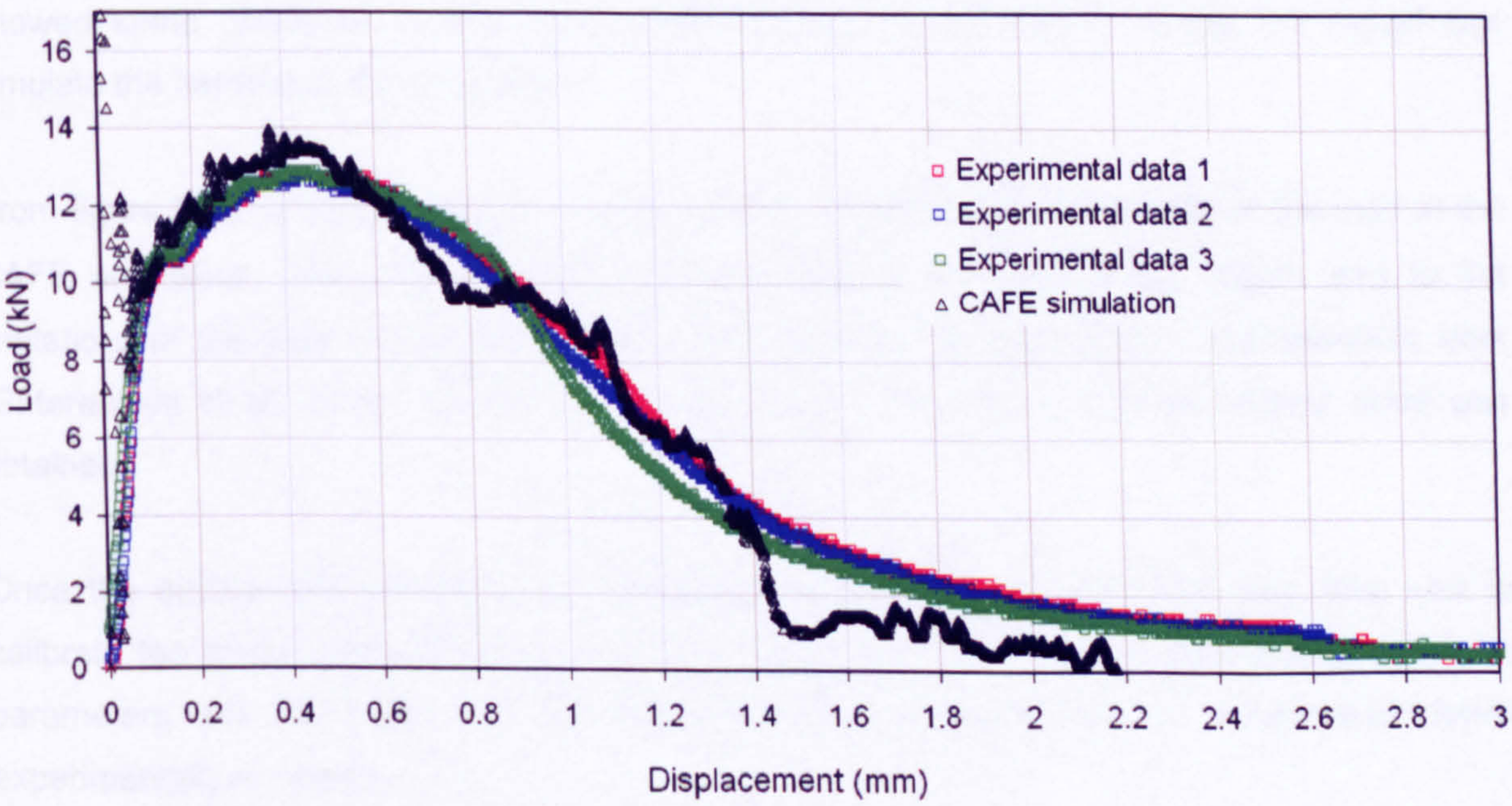

Figure 6.16 – The new finite element model used for Charpy CAFE simulations.

Shterenlikht (Shterenlikht et al., 2005) applied the original CAFE model for the simulation of Charpy tests to characterize the fracture toughness properties of a X80 steel. Although the total Charpy impact energy was obtained, the numerical results showed poor correlation for the simulation of the load–displacement curve of Charpy data. The Charpy CAFE simulation data was stiffer than the experiment and the simulated load peak was narrower and higher than the experimental curve. The authors attributed this difference to the fact that only a small part of the striker was simulated and this may have caused such effects.

In the present research work and with the application of the original CAFE model, the same trend was obtained as shown in figures 6.4, 6.7, 6.9, and 6.11, but with the modified CAFE model this inconsistency was corrected as the model simulated better the experimental impact Charpy data. In the modified model, as in the original model, only a small part of the striker was simulated as well as shown in figure 6.13. From the present analysis it can be shown that simulating only a small part of the striker does not affect the numerical output data.

The finite element simulation performed in section 4.2 with Gurson's damage model (Gurson, 1977a, Gurson, 1977b) showed very good correlation in the fracture propagation region of Charpy data. But in the plastic deformation or hardening region (where the load increases parabolically to the deflection) high oscillations were obtained. Many pure finite element simulations of impact Charpy tests, are not able to reproduce properly the hardening part of the Charpy tests, although they reproduce the region from where fracture propagation initiates to the end of the tests. As shown in section 4.2, they show high oscillations in the hardening region of experimental data (Serizawa et al., 2001, Eberle et al., 2001). Although simulation results showed some oscillation in the elastic region of the present CAFE model, the model can simulate the hardening region properly.

From figure 6.16, at displacement equal to $1.4\,mm$, the model shows a drop of the load in the CAFE simulation. This may be due to accumulation of damage in this region and to the limitations of the finite element model. This drop of data was also shown in Shterenlikht work (Shterenlikht et al., 2005), but as in the present case, the impact Charpy energy value was obtained.

Once the ductile damage model parameters were calibrated properly, the next step was to calibrate the model parameters of the brittle part of the CAFE model. The calibration of the parameters will be done with the simulation of the distribution of microcracks found experimentally en section 3.6.4.

6.6 Application of CAFE model on 4PB double–notch specimens to simulate distributions of microcracks.

As mentioned long before, one of the main aims of the present project is to apply the modified CAFE model to simulate the distribution of cleavage fracture initiation points in the plastic zone of notched specimens. In the present research work, $3D$ finite element simulations of four point double–notch bend specimens were done. Figure 6.17 shows the $3D$ finite element model. This figure also shows a close view of the notch root where the CAFE model was applied. The other parts of the model were simulated with finite elements without any damage. The model consisted of 6886 C3D8R 8–node reduced integration finite elements and 3049 nodes.

The damage zone consisted of 627 8–node reduced integration finite elements. In the present simulations, the CAFE model was applied only on a region of 2mm ahead of the notch root. Due to symmetry, only a quarter of 4PB double–notch specimens was simulated. The load was applied through the pins which were simulated as rigid bodies. Subsequently contact conditions were applied between the pins and the surface which would be in contact with those pins.

As already explained in previous sections, as the finite elements are used only to represent the structural part of the model, all the material data is moved from the finite elements to the underlying arrays of cellular automata. The arrays of cells have a microstructural significant size. The finite element mesh is constructed to represent the overall shape change of the specimen adequately. This means that it is possible to construct large finite elements in the notch region of 4PB double–notch bend specimen to reduce the number of finite elements in the damage zone and stresses and strains are performed at cellular level. The ductile cells size is $100\mu m^3$ and the brittle cells size is $50\mu m^3$, the same as for the Charpy test simulation.

The cell arrangement generated in the damage zone is shown in figures 6.18 and 6.19 for 2D and 3D respectively. As in the Charpy model, it can be seen that the cells arrays are accommodated according to finite element size. Then smaller finite elements will contain smaller cell size arrays. Therefore it is very important to generate finite elements of similar size in order to make the finite element model accommodate the cell arrays with almost the same size. From figure 6.18 it can see that the generated cells array have similar size. In the notch region, it can be seen as well that the finite elements have similar size. The damage zone consists of 637 C3D8R single integration finite elements (HKS, 2004). The finite elements in this region are shown in figure 6.17.

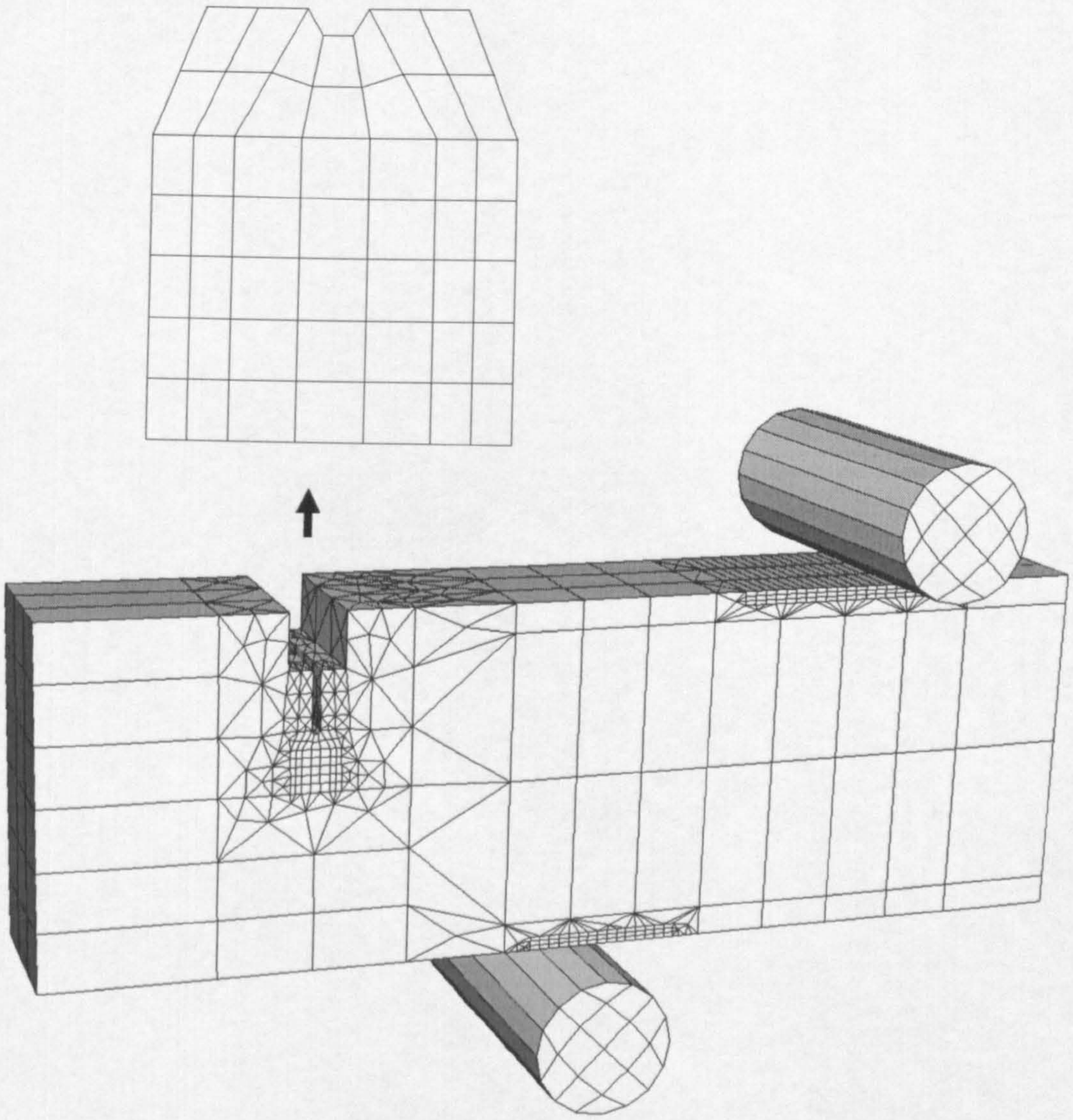

Figure 6.17 – CAFE model of a blunt notch four point double–notch bend test.

They finite elements are almost $0.28mm \times 0.28mm \times 0.28mm$ cubic elements, but slightly smaller elements were used near the root of the notch root. $5 \times 5 \times 5$ ductile cell $\left(M_D = 125\right)$ and $10 \times 10 \times 10$ brittle cell $\left(M_B = 1000\right)$ CA arrays were created for each finite element of the damage zone. Thus the ductile damage cell size is about $L_D \approx 0.28/5 = 0.05mm$ and the brittle damage cell size is abut $L_B \approx 0.28/10 = 0.028mm$. The CAFE model will therefore have 79625 ductile and 637000 brittle CA cells. The visualization of the cells arrays was done with the visualization program EnSight Gold version 7.1.

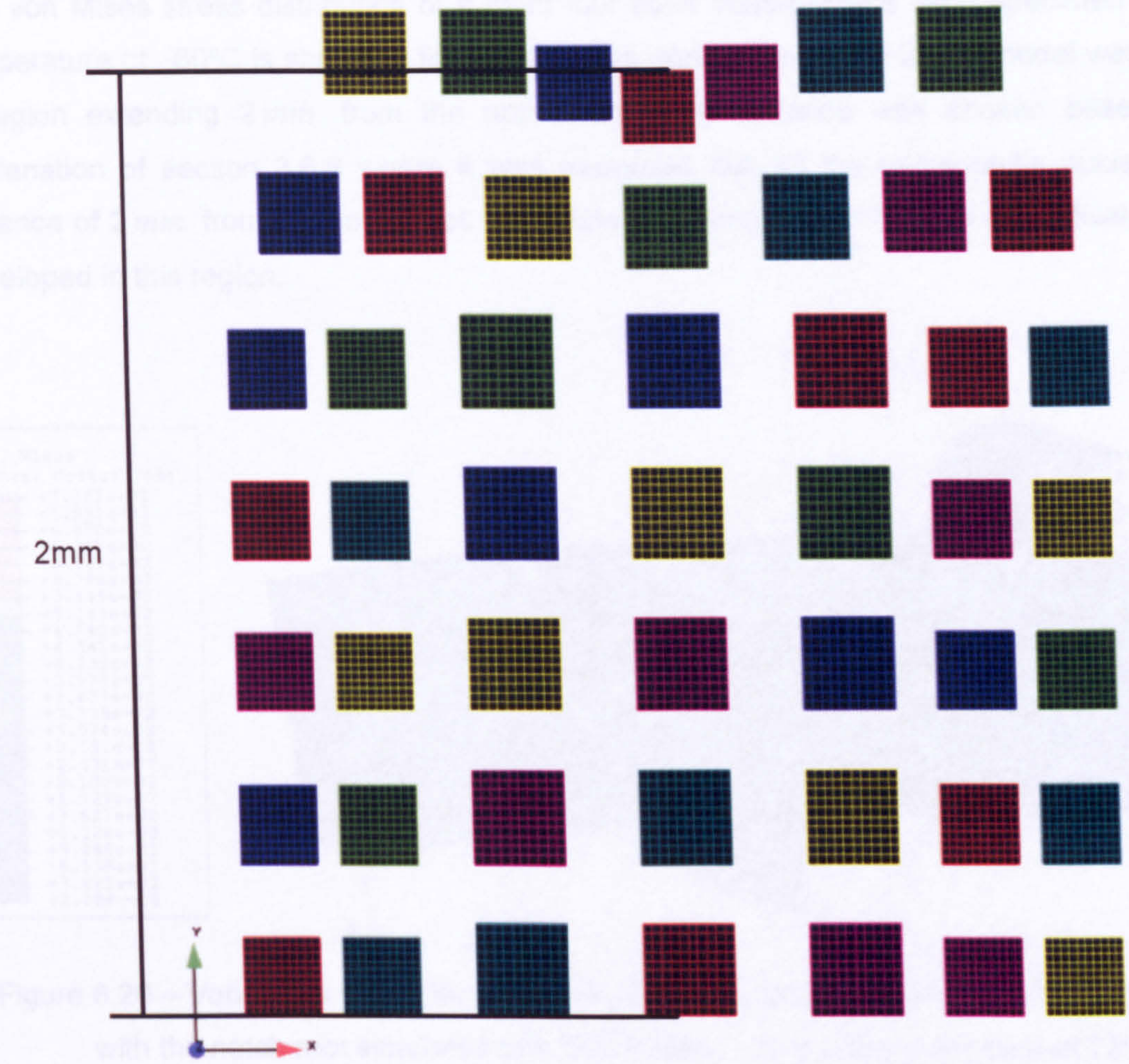

Figure 6.18 – 2D view of cells arrays of the region simulated with CAFE model.

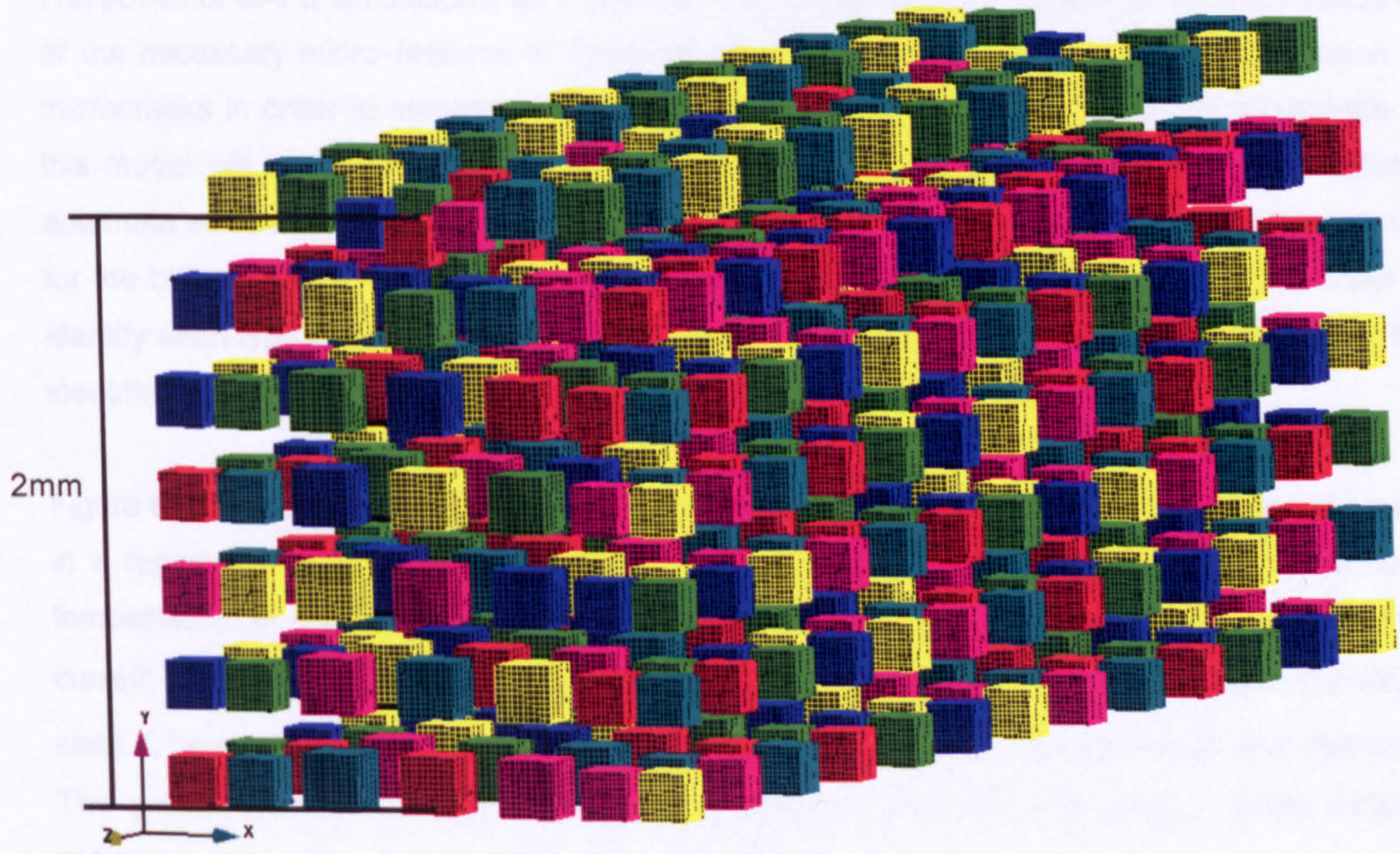

Figure 6.19 – 3D view of cells arrays of the region simulated with CAFE model.

The von Mises stress distribution of a blunt four point double–notch bend specimen for a test temperature of –60°C is shown in figure 6.20. The application of the CAFE model was done on a region extending $2\,mm$ from the notch root. This distance was chosen based on the explanation of section 3.6.6 where it was explained that all the microcracks nucleated in a distance of $2\,mm$ from the notch root. Therefore all the conditions prior to the critical event are developed in this region.

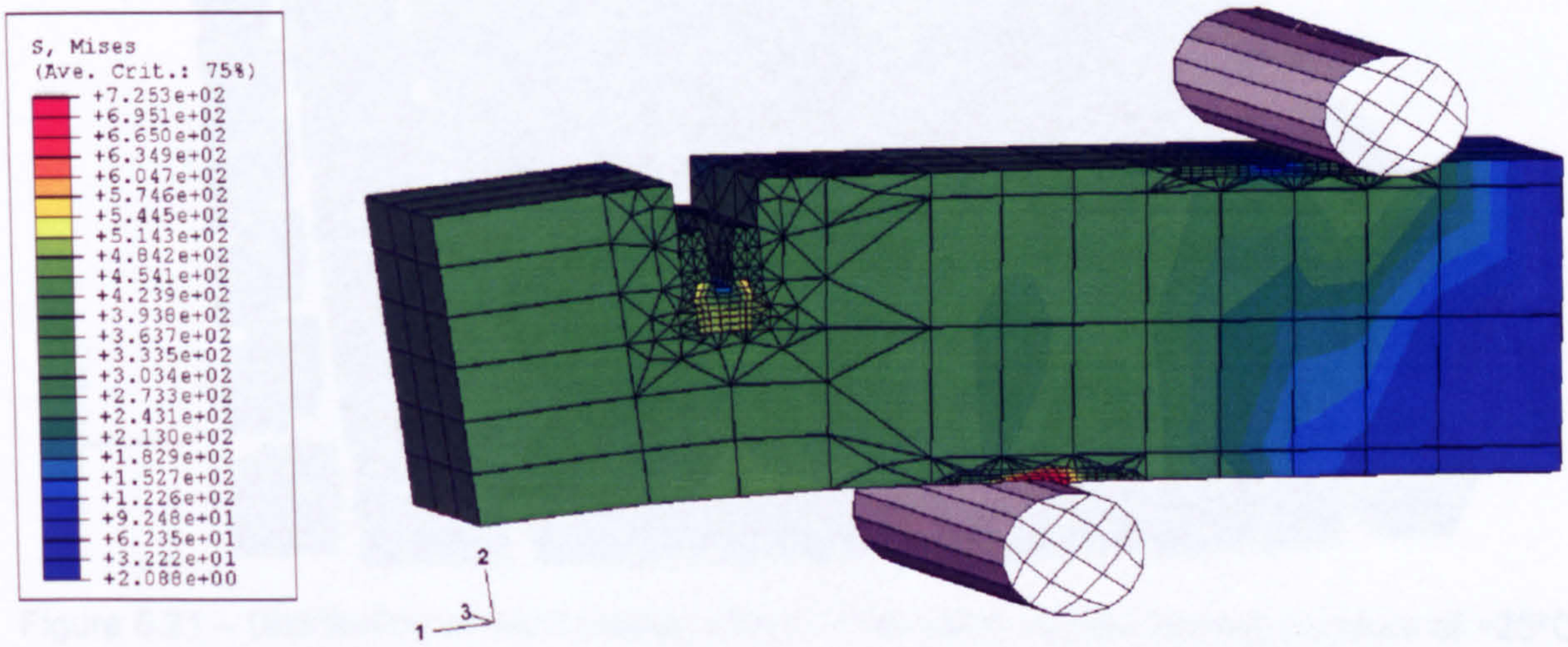

Figure 6.20 – Von Mises stress distribution of blunt four point double–notch bend specimens with the notch root simulated with CAFE model for a test temperature of 25°C.

The power of CAFE simulations, as explained in previous sections, allows the implementation of all the necessary micro–features of materials which play an important role in the nucleation of microcracks in order to simulate real microstructures. In the present section the advantage of this model will be shown, especially at cellular level. As explained in Chapter V, two cellular automata arrays were created; one to account for the ductile fracture process and the other one for the brittle fracture. Consequently two colours of cells were defined in the model in order to identify each type of fracture, the green to identify the initiation of ductile fracture and red for the identification of cleavage fracture initiation.

Figure 6.21 shows a close view of an example of the two generated ductile and brittle cell arrays in a region surrounding the notch root of a 4PB double–notch specimen simulated at room temperature. In Chapter V it was explained that the cells have the capability to go from their current state to some other state. In the present work, they go from the *alive* state to the *dead* state. The cells that *died* in the ductile and brittle fracture type are the green and red ones. The green and red cell cells simulate the distribution of ductile and brittle fracture initiation region.

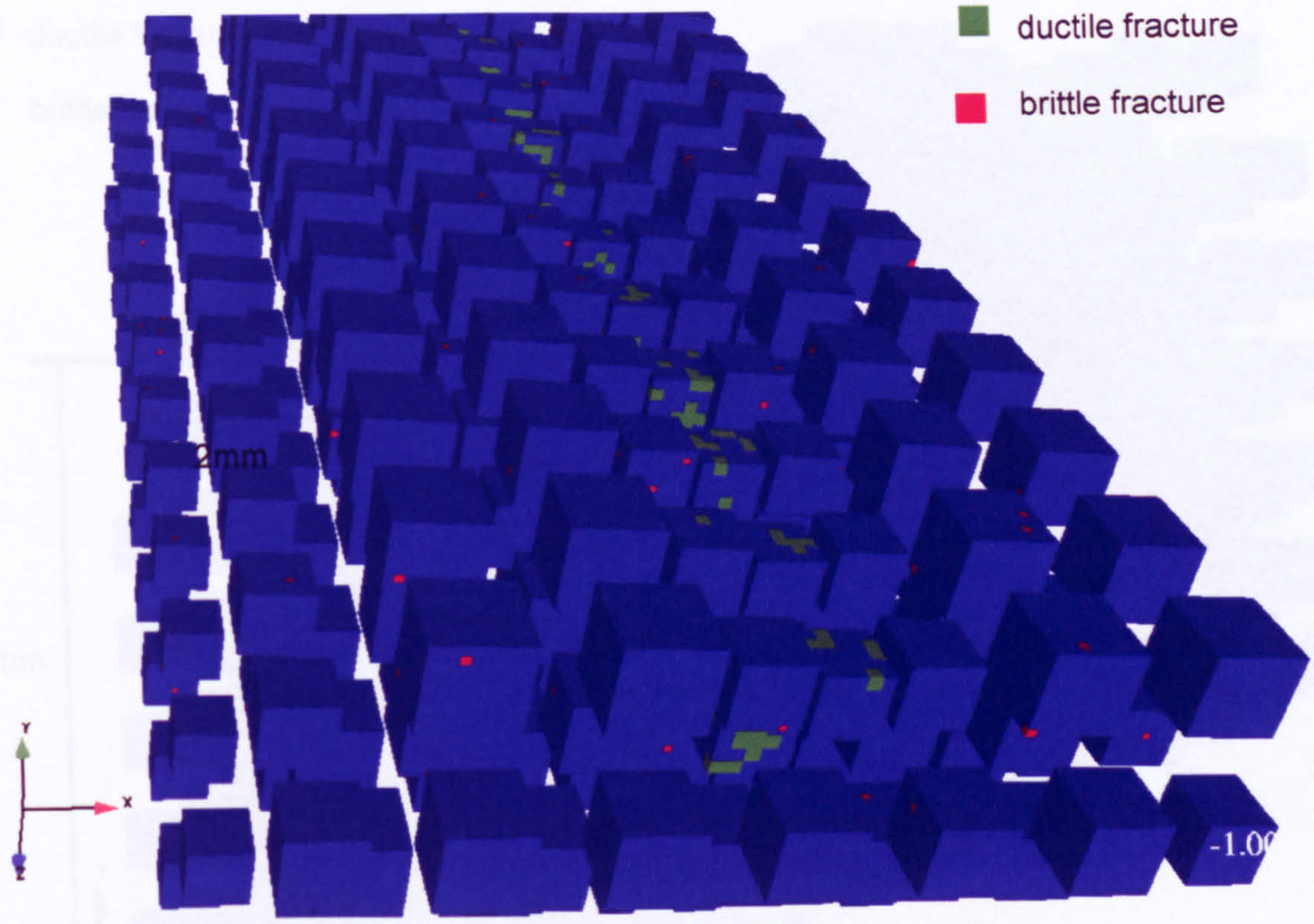

Figure 6.21 – Distribution of microcracks in front of the notch root for test temperature of +25ºC in blunt four point double–notch bend tests simulated with the CAFE model, the applied load was 41.5kN.

Figure 6.22 shows a 3D view of the CA arrays created in the damage zone of four point double–notch bend specimens simulated with the modified CAFE model for a test temperature of 0ºC. In this figure it can be seen some red cells. They represent the distribution of cleavage fracture initiation points distributed in the notch region.

From the results in the analyses performed in section 3.6.6, it can be seen that the experimentally measured distribution of the position of microcracks were simulated well with the modified CAFE model at micro–cellular level as the distribution of the position of cleavage fracture initiation points are located in the position surrounding the notch region as shown in figure 6.22.

In figure 6.22 it is shown as well that most of the microcracks nucleated around 1 mm extending from the notch root at test temperature of 0°C. The density nucleation sites were consistent with experimental results for a test temperature of 0°C. It was found as well some microcracks extending up to a distance of 2 mm .

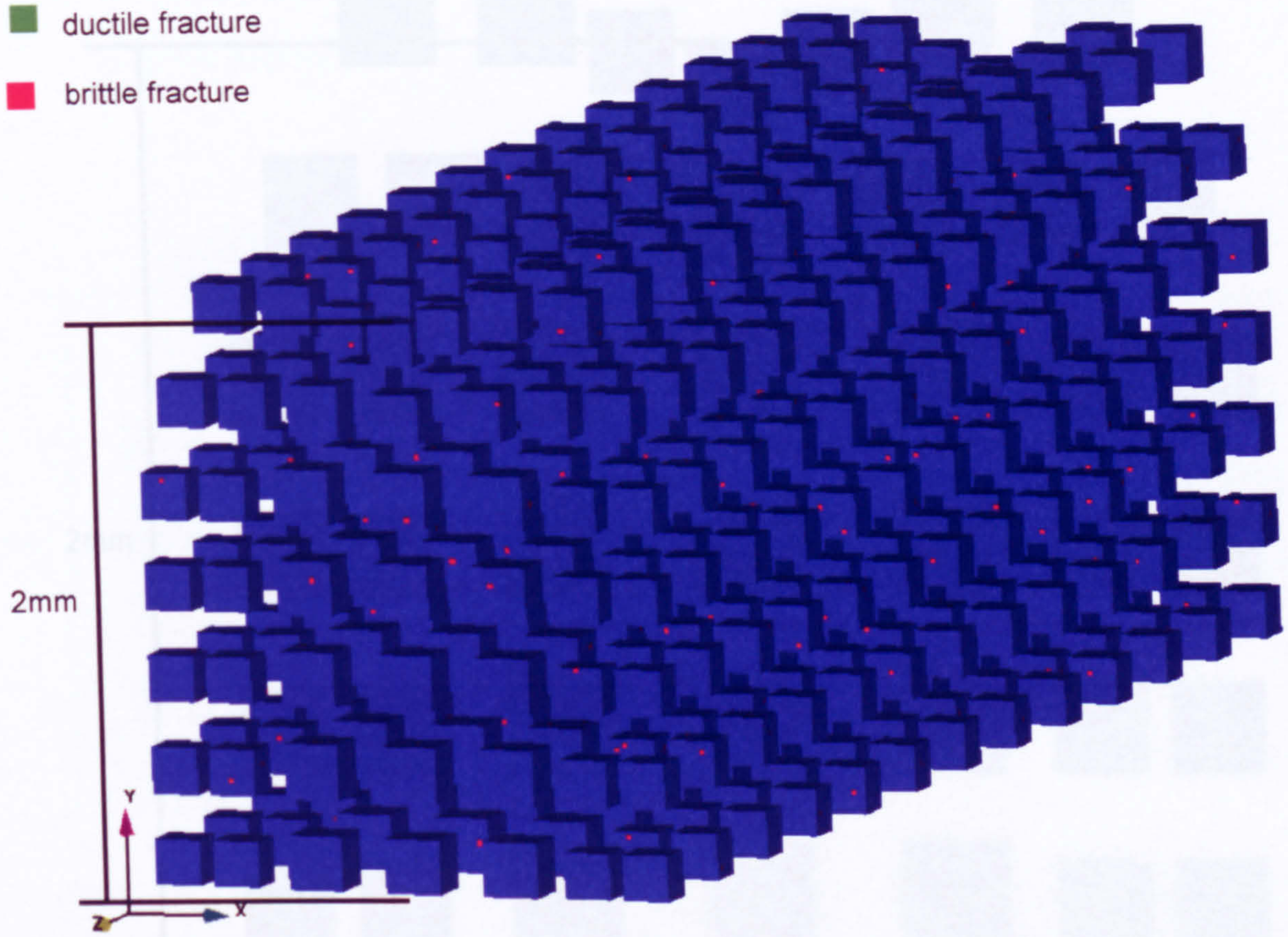

Figure 6.22 – Distribution of microcracks in the notch region of a blunt four point double–notch bend tests simulated with CAFE model for a test temperature of 0°C, the applied load was 36kN.

In order to show more clearly that the CAFE model has the capability to simulate properly the cleavage fracture initiation points at the temperatures proposed in the present work, figure 6.23 shows the distribution of the initiation points for a test temperature of –60°C in a 2D view. In this image it is shown clearly that the CAFE model simulates appropriately the distribution of cleavage fracture initiation points as the higher density of initiation points was located at a distance of about 1 mm extending from the notch root.

Experimentally (section 3.6.6) it was found that the majority of cleavage initiation points nucleated at around 1 mm from the notch root, the CAFE simulations results for this test temperature showed that the distribution of cleavage fracture initiation points correlates with those analyzed experimentally in section 3.6.6 for this test temperature, the correlation in terms of distribution of initiation points is shown in figure 6.25.

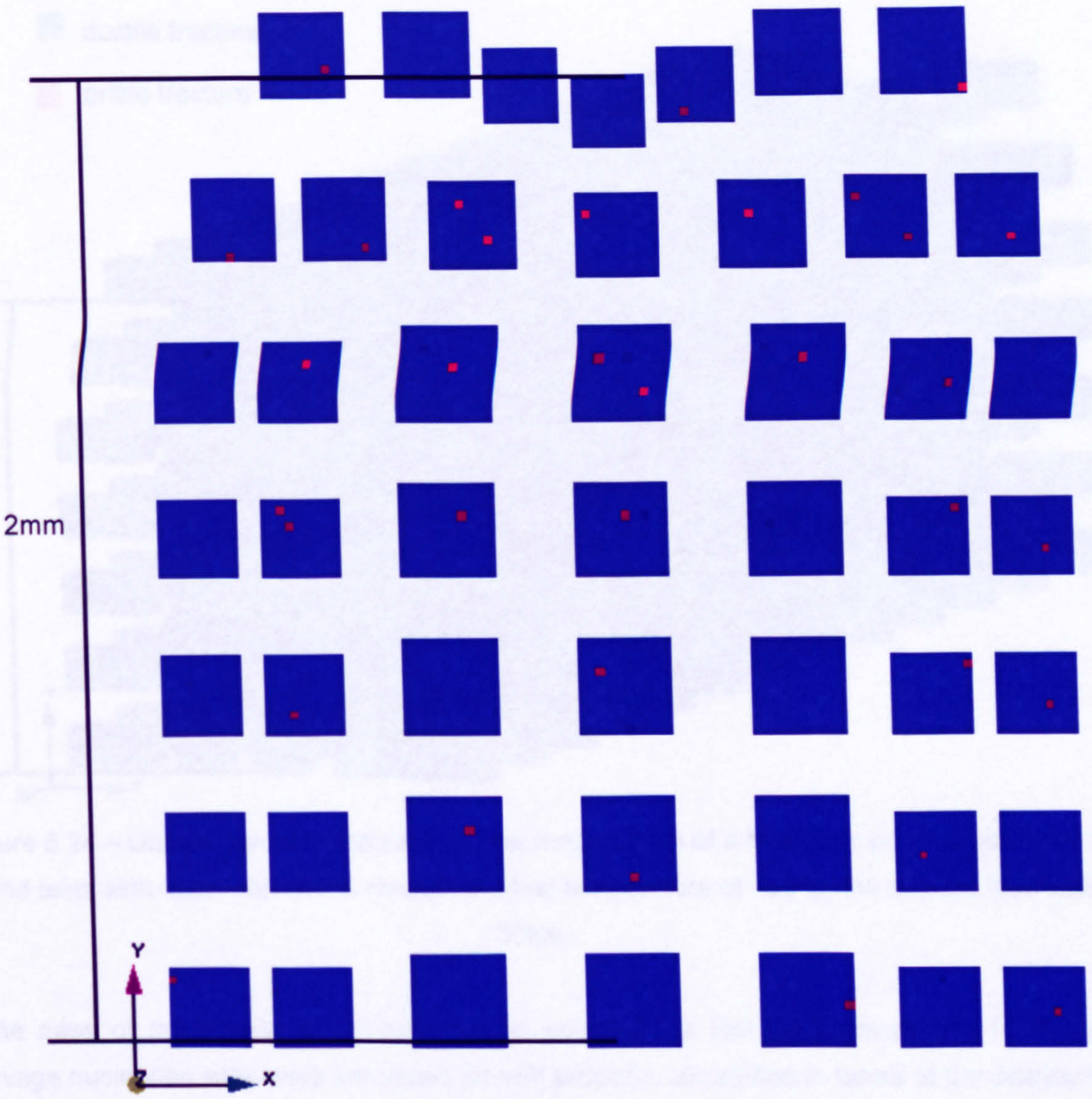

Figure 6.23 – Distribution of microcracks in the notch region of a blunt four point double–notch bend tests simulated with CAFE model for a test temperature of –60ºC in the rolling direction of the plate steel.

Figure 6.24 shows a 3D view of the population of cleavage fracture initiation points for the temperature of –60ºC. In this image it can be seen that the distribution of initiation points were successfully reproduced. This 3D view shows a better visualization of the distribution of initiation points in the through thickness of the plate steel; the microcrack population was simulated appropriately. In the experimental analysis, the cleavage fracture initiation points were identified on the surfaces of each slice of the sectioned surviving notch of blunt four point double–notch bend tests, but in the through thickness of each slice there must be more microcracks in the surrounding region of the notch root. With CAFE simulations we can obtain the distribution of the initiation points throughout the thickness of the specimen as clearly shown in figure 6.24.

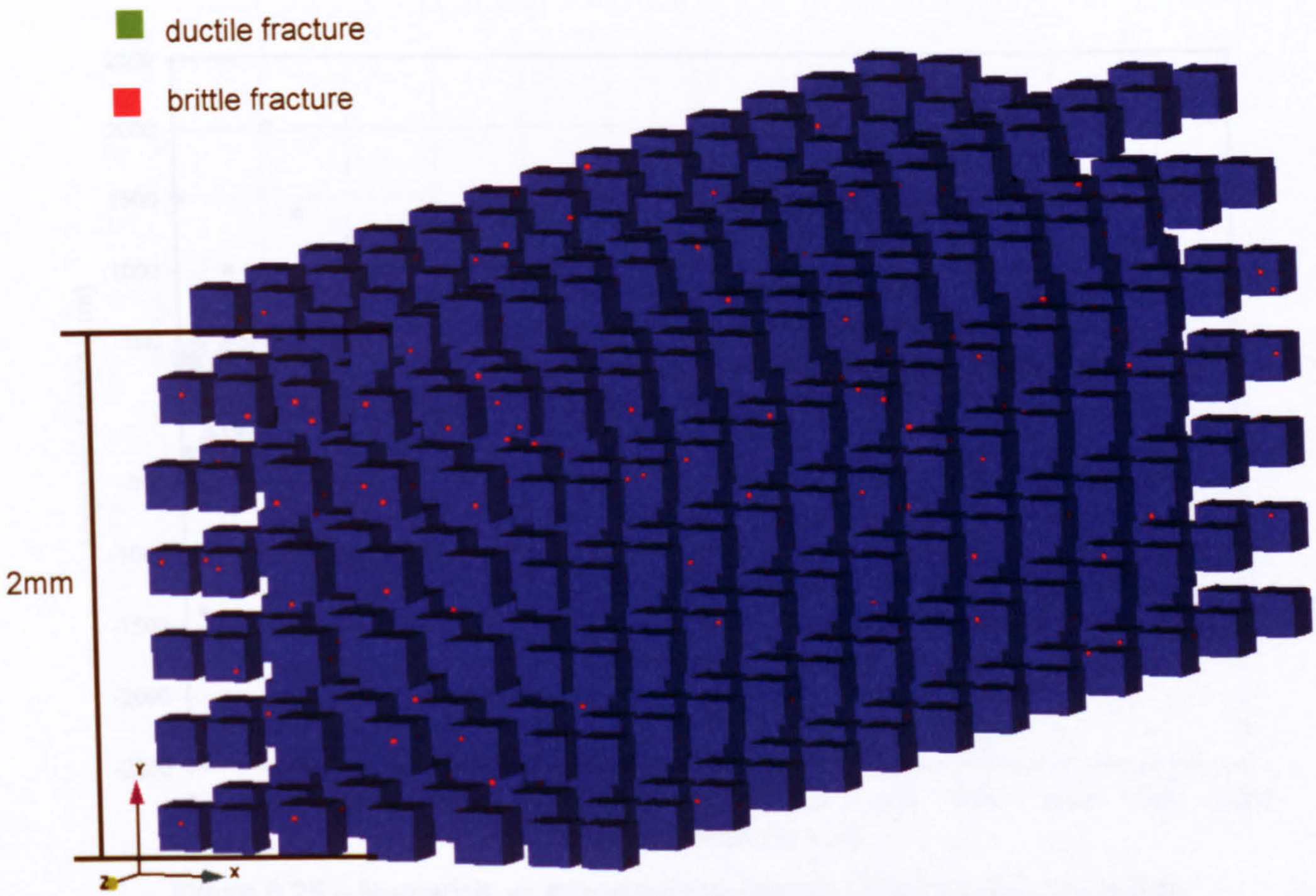

Figure 6.24 – Distribution of microcracks in the notch region of a blunt four point double–notch bend tests simulated with CAFÉ model for a test temperature of –60°C, the applied load was 30kN.

In the case of the simulation of the initiation points for a test temperature of –196°C, the cleavage nucleation sites were simulated as well properly, correlation in terms of the distribution of cleavage fracture nucleation points was obtained. The figures presented in this section have shown the potential of the CAFE model to simulate the distribution of initiation points for ductile and brittle fracture. But in order to show that the CAFE model properly simulated the distribution of cleavage fracture initiation points, the distribution of cleavage fracture initiation points obtained at cellular level were plotted against distribution of cleavage initiation points measured experimentally.

The following graphs show correlations between experimental and numerical distributions of cleavage initiation sites simulated numerically with the CAFE model for +25°C, 0°C, –60°C and –196°C at micro–cellular level. The distributions of cleavage initiation were obtained with the program EnSight Gold version 7.0.

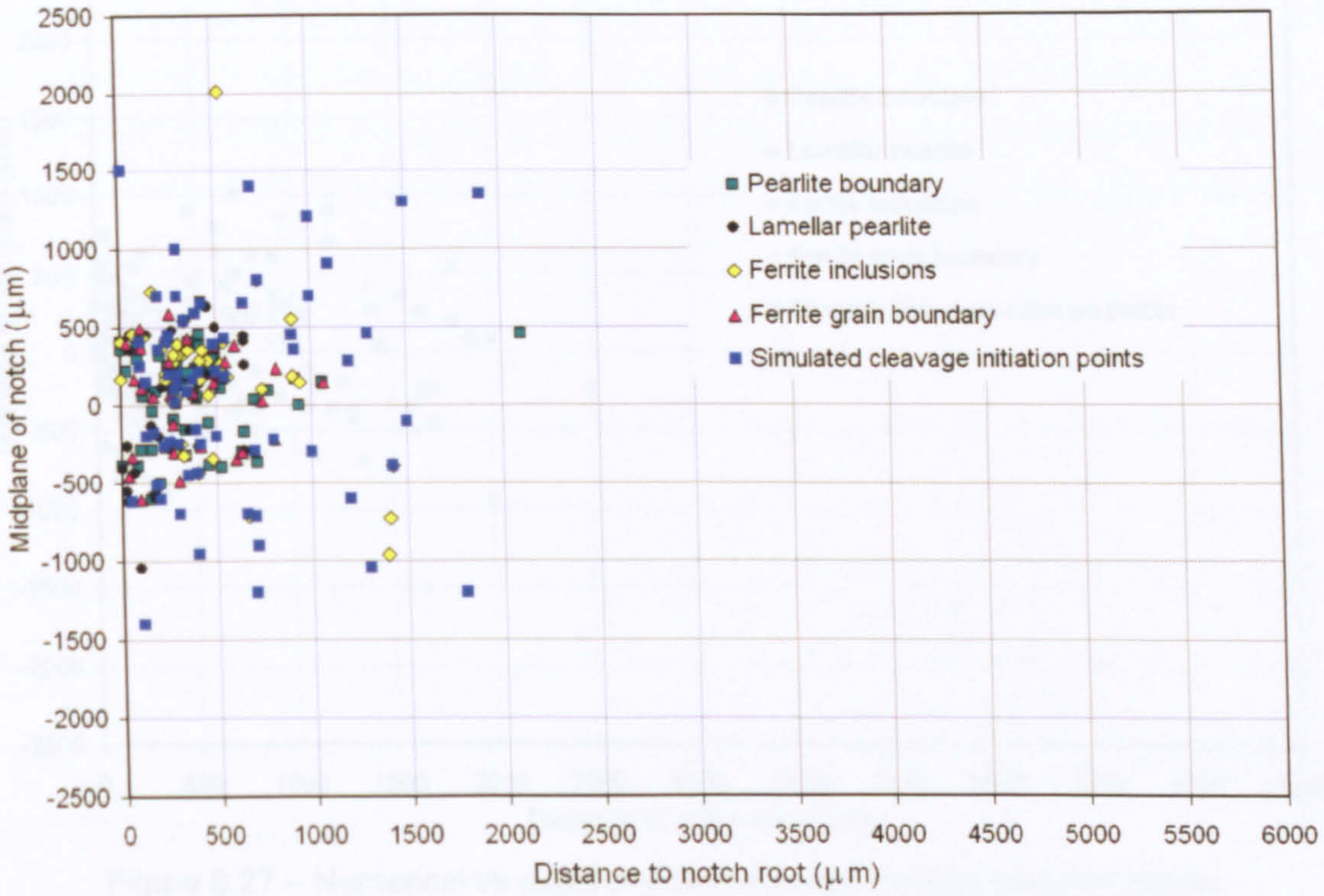

Figure 6.25 – Numerical vs experimental cleavage fracture initiation points for test temperature of 25°C.

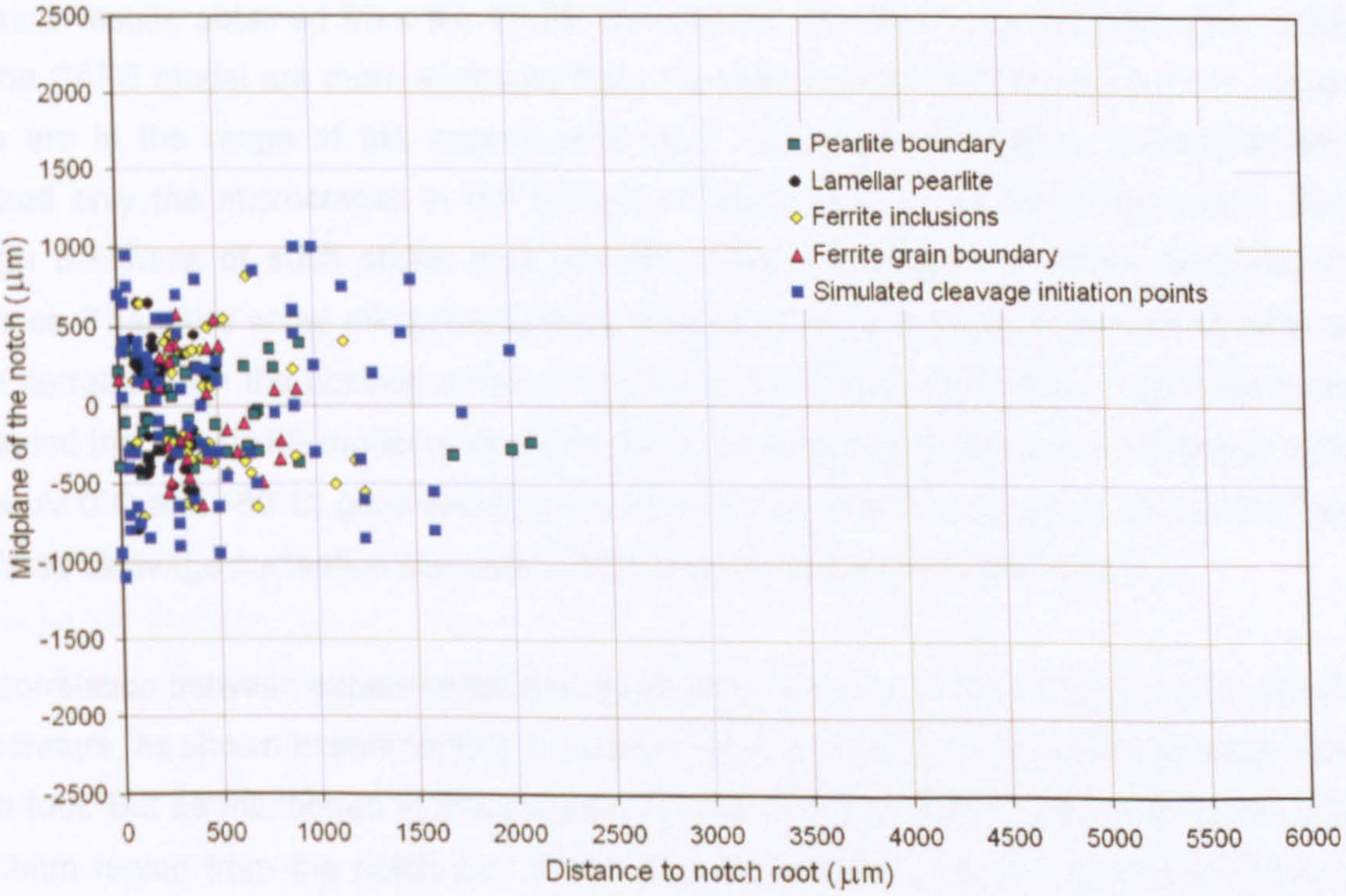

Figure 6.26 – Numerical vs experimental cleavage fracture initiation points for test temperature of 0°C.

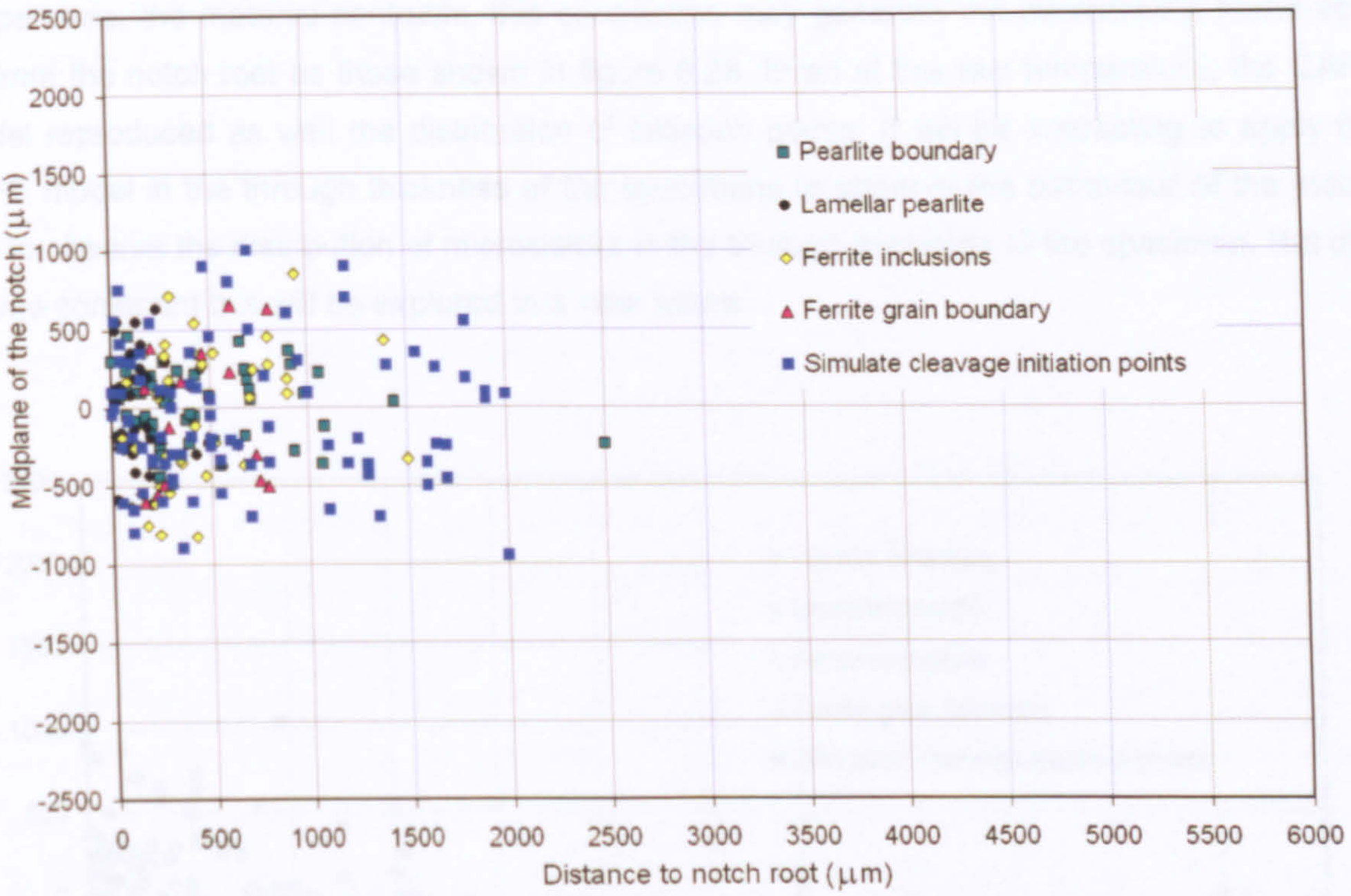

Figure 6.27 – Numerical vs experimental cleavage fracture initiation points for test temperature of –60°C.

Figures 6.25, 6.27 and 6.38 show how the distributions of microcracks were simulated properly. The distributions of microcracks measured experimentally were reproduced well with the numerical results obtained from the CAFE simulations. At +25°C, the initiation sites obtained with the CAFE model are more scattered than the experimental data points, but the numerical points are in the range of the experimental data. As mentioned before, experimentally we analyzed only the microcracks in the surface of each slice of the sectioned notch. But the through thickness of such slices must contain more microcracks in some sections of the thickness. Therefore some microcracks must be located in the through thickness of such slices which correlate with the position of the microcracks simulated numerically. Therefore it can be concluded that the CAFE model is very suitable to simulate the distribution of cleavage initiation points. At 0°C and –60°C, good results were obtained as shown in figures 6.26 and 6.27 as the simulated cleavage nucleation sites are in the range of the experimental results.

The correlation between experimental and results for –196°C is shown in graph 6.28. At this test temperature, as shown experimentally in section 3.6.6, microcracks nucleated far away from the notch root. But as mentioned in this section, the CAFE model was applied to simulate only the first 2mm region from the notch root and it was not applied in all the thickness of four point double–notch bend specimen. In order to apply the CAFE model in the through thickness of the specimens, we have to create a very large amount numbers of ductile and brittle cells, consequently the time to run the model will be increased considerably. At liquid nitrogen

temperature, the material contracts, this contraction may generate the microcracks found very far from the notch root as those shown in figure 6.28. Even at this test temperature, the CAFE model reproduced as well the distribution of initiation points. It will be interesting to apply the CAFE model in the through thickness of the specimens to observe the behaviour of the model and to observe the distribution of microcracks in the through thickness of the specimen. But due to time constraint this will be explored in a near future.

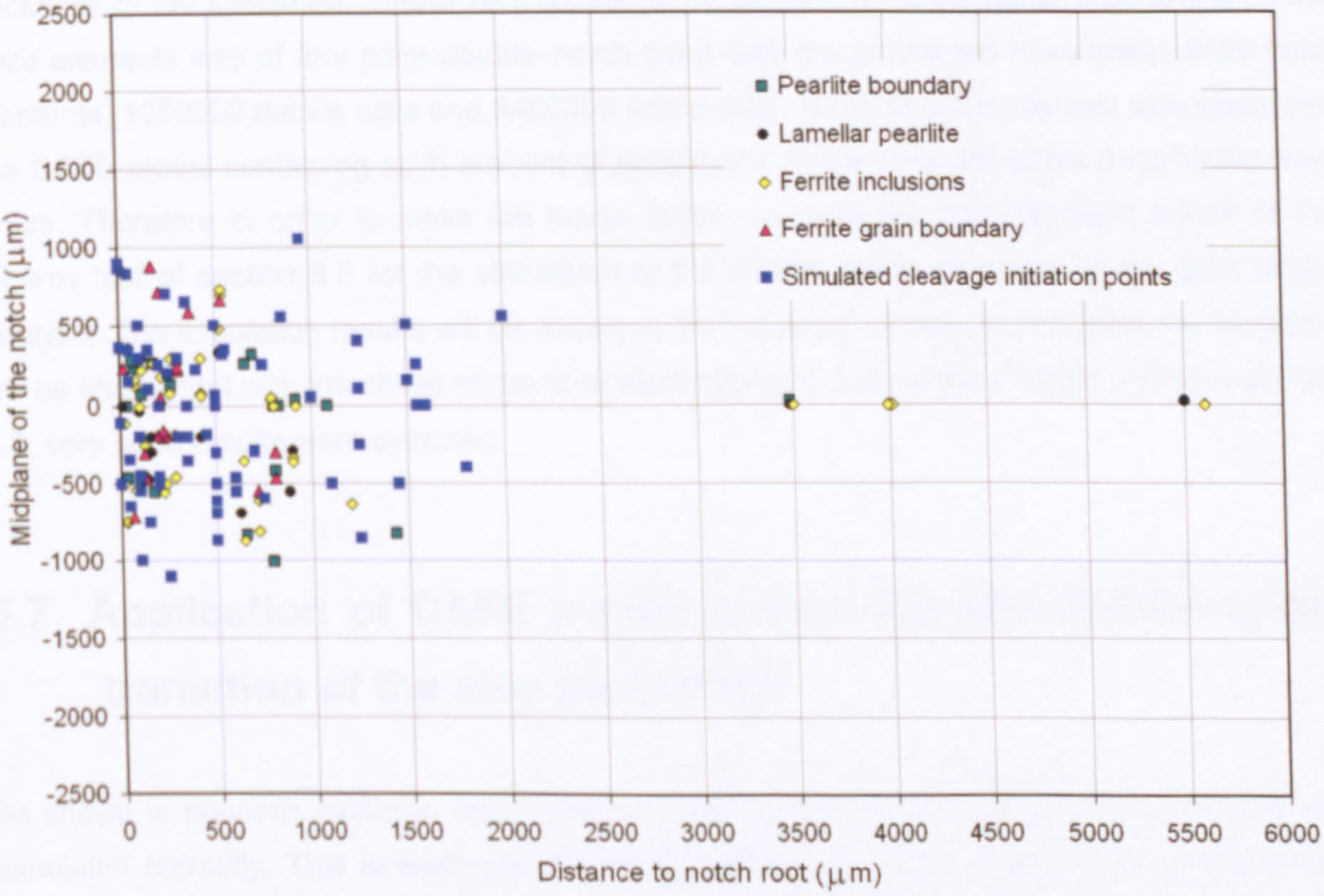

Figure 6.28 – Numerical vs experimental cleavage fracture initiation points for test temperature of –196ºC.

The last four graphs showed that the CAFE model simulated well the cleavage fracture initiation points and the numerical data fall in the range and/or the distribution of the experimentally measured cleavage fracture initiation points for all the microstructures. From these graphs it can be concluded that correlation in terms of the distribution of cleavage fracture initiation points at the four test temperatures, has been obtained in the present research work.

From the Charpy finite element model simulated with the CAFE model (section 6.5) and the four point double–notch bend model of the present section simulated with the CAFE model, it can be seen that the size of the finite elements simulated with the CAFE model is different in each model. The size of the finite elements of the damage zone of four point double–notch bend

specimens are about the half of the finite elements of the damage zone of the Charpy model, consequently the ductile and the brittle cells size are also different.

In the simulation of four point double–notch bend specimens, the size of brittle cells was about 28μm. This size of brittle cells was chosen in order to relate the brittle cells size with the grain size of the steel under analysis. As shown above, in the simulation of four point double–notch bend tests, the CAFE model was applied only on a region of 2mm extending ahead of the notch root. But in the simulation of Charpy tests, the CAFE model was applied in the through thickness of the specimen. Therefore if a Charpy model with finite elements size similar to the finite elements size of four point double–notch bend test, the model will have about 8400 finite elements, 1050000 ductile cells and 8400000 brittle cells. A run of a Charpy test simulated with the CAFE model containing such amount of ductile and brittle cells will takes days rather than hours. Therefore in order to make the model faster we used the finite element model of the Charpy test of section 6.5 for the simulation of the ductile–brittle transition of the steel under analysis. The simulation results will be shown in the following section. In the following section it will be shown that with the chose of the finite elements size used in the Charpy model of section 6.5, very good results were obtained.

6.7 Application of CAFE model to simulate the ductile–brittle transition of the ship plate steel.

As shown in previous sections, the ductile and the brittle part of the steel under analysis was simulated correctly. This is evidenced by the simulation of impact Charpy tests in the ductile regime. For the brittle part, the distribution of the cleavage fracture initiation sites were simulated properly as compared to experimental data. This means that the subroutine was coded properly and the implementation of the cleavage microstructures was done correctly. The calibration of the damage model parameters was done correctly as well. Now the next step is to apply the modified CAFE model to simulate the ductile–brittle transition in terms of Charpy impact energy values at any test temperature in the transition region of the steel plate.

As explained in Chapter V, the model has the capability to simulate the typical scatter in terms of Charpy impact energy values observed experimentally in the transition region as random values of damage model parameters were distributed in the ductile and brittle CA arrays. Accordingly in each simulation, the CAFE model internally tests different values of the damage model parameters. This will result in scatter in Charpy energy values for each run of the model. The ductile–brittle transition of the present steel simulated with the modified CAFE model is shown in figure 6.29. From this graph it can be seen that the modified CAFE model simulated

the typical scatter of Charpy energy values in the transition region, the simulated results fall in the range of experimental data.

At 100% of cleavage, the simulated results were quite high in comparison with experimental work. This difference is probably caused by the fact that fracture cannot cross the finite element boundary due to the limitations of the ABAQUS code. The information given to the VUMAT subroutine is limited, no finite element number, either external, given by the user, or internal, used in the solver stiffness matrix, is given to VUMAT. This means that it is not possible to establish which finite elements are being processed in this call to the subroutine. Consequently it is not possible to find the neighbouring finite elements from VUMAT. Thus fracture must reinitiate in each finite element in the fracture propagation path. As fracture propagation requires less energy than initiation, this limitation is likely to result in over–estimated energy values, as seen in figure 6.29.

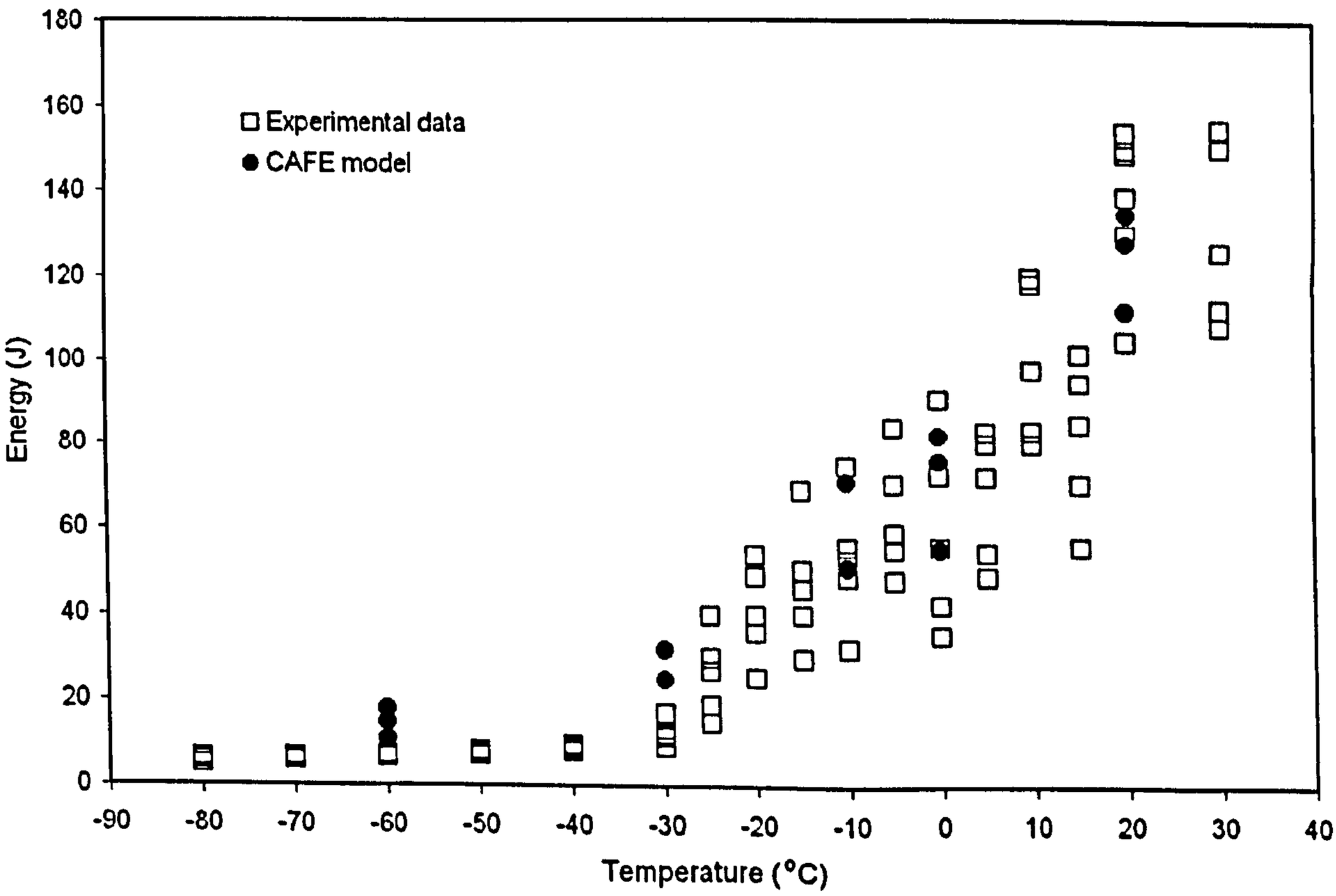

Figure 6.29 – CAFE simulation of the Charpy impact energy values.

The Rousselier continuous ductile damage model, used in this work, can only account for volumetric void growth. But an additional principle has to be applied to estimate the onset of shear instability of ductile cells. The possibility of including an appropriate shear localisation model into the present CAFE structure was not explored due to time constraint, but research work in this line will be explored in a near future. From the presented results it was clearly

shown that the CAFE model was suitable for the simulation of cleavage initiation and fracture propagation in a Grade A ship plate steel. It can be concluded that the CAFE model is capable of simulating ductile and brittle fracture initiation and propagation in the transition region.

6.8 Conclusions.

In the present chapter it is very important to simulate the ductile and the brittle fracture part of the CAFE model properly. In the brittle part, the cleavage fracture initiation points were simulated at all test temperatures in the surviving notch of blunt four point double–notch bend tests. This means that the model parameters of the brittle part were coded properly as the model was capable to reproduce the experimentally measured distribution of cleavage fracture initiation points. It is important to mention that the model simulated properly in terms of distribution the experimental cleavage fracture nucleation points. Because only the surfaces of the sectioned notch were analyzed with the SEM, in the through thickness of each section there must be microcracks from which their coordinates will correlate with the position of the simulated position of microcracks.

The ductile part of the CAFE model was simulated properly as well because the model was capable to reproduce the instrumented Charpy tests data (load–displacement). This gives clear evidence that the model and the damage parameters were calibrated properly in the ductile region of the CAFE model. From these results it can be seen that once the model was calibrated, the model was able to simulate the ductile and the brittle part correctly. After numerical against experimental data correlation was obtained, the model was able to simulate the ductile–brittle transition of the steel under analysis.

6.9 References.

BESSON, J., STEGLICH, D. & BROCKS, W. (2001) Modeling of crack growth in round bars and plane strain specimens. *International Journal of Solids.*, 38, 8259-8284.

EBERLE, A., KLINGBEIL, D. & SCHICKER, J. (2001) The calculation of dynamic J-curves from 2D and 3D finite element analysis of a Charpy tests using a rate-dependent damage model. *European Structural Integrity Society ESIS, Charpy Centenay Conference*, 2, 777-785.

EN ISO 14556:200 BRITISH STANDARDS (1987) Method for Precision Determination of Charpy V-Notched Impact energy for Metals. BS131-6.

GURSON, A. L. (1977a) Continuum theory of ductile rupture by void nucleation and growtn: Part I - Yield criteria and flow rules for porous ductile media. *Eng. Mat. Tech.*, Vol. 99, 2-15.

GURSON, A. L. (1977b) Porous rigid-plastic materials containing rigid inclusions: Part II - Yield function, plastic potential and void nucleation. *D. M. R. Taplin, ed., Proceedings of the international conference of fracture. Vol 2A, Pergamon Press*, 357-364.

HKS (2004) ABAQUS Theory Manual, Version 6.5.

LI, Z. H., BILBY, B. A. & HOWARD, I. C. (1994) A study of the internal parameters of ductile damage theory. *Fatigue Fract Engng Mater Struct*, 17, 1075-1087.

SERIZAWA, H., WU, Z. & MURAKAWA, H. (2001) Computational analysis of Charpy impact tests using interface elements. *Trans. JWRI*, 30, 97102.

SHTERENLIKHT, A. (2003) 3D CAFE modelling of transitional ductile-brittle fracture in steels. *Ph.D Thesis, Department of Mechanical Engineering, University of Sheffield.*

SHTERENLIKHT, A., HASHEMI, S. H., YATES, J. R., HOWARD, I., C. & ANDREWS, R. M. (2005) Assessment of an instrumented Charpy impact machine. *International Journal of Fracture*, 132, 81-97.

SHTERENLIKHT, A. & HOWARD, I. C. (2006) The CAFE model of fracture - application to a TMCR steel. *Fatigue Fract Engng Mater Struct*, 29, 770-787.

VODOPIVEC, F., ARZENSEK, B., KMETIC, D. & VOJVODIC-TUMA, J. (2003) In the Charpy Fracturing Process. *MATERIALI IN TEHNOLOGIJE*, 37, 317-326.

WU, S. J., DAVIS, C. L., SHTERENLIKHT, A. & HOWARD, I. C. (2005) Modeling the ductile-brittle transition behavior in thermomechanically controlled rolled steels. *Metallurgical and Materials Transactions A*, 36A, 989-997.

Chapter VIII

Discussion

The present chapter describes the discussion of the work developed in the present research project. The chapter also shows the achievements with CAFE modelling and the points where research work is still needed in order to improve the performance of the CAFE model to simulate cleavage initiation and the ductile-brittle transition in steels. Some suggestions about the use of Grade A ship plate steel for the construction of merchant ships are also described in this chapter.

7.1 Cleavage fracture microstructures.

It has been shown in this research work, that four triggering cleavage fracture microstructures are present in a Grade A plate steel contrary to the statement that cleavage nucleation is dominated by grain boundary cracked carbides. Recent work reported in literature showed that in some steels, cleavage can be triggered by different micro features but the present steel showed a competition of four microstructures for nucleation of cleavage fracture. This confirm the hypothesis (section 2.8) that due to the ferrite–pearlite microstructure of the steel under analysis a competition of different microstructures for the nucleation of cleavage fracture could exist in the present steel. The experimental results of sections 3.6.4, 3.6.6 and 3.6.7 support the hypothesis. It was showed as well that those microstructures have a strong influence on the toughness properties of the steel under analysis. The experimental work carried out to investigate the micro features nucleating cleavage fracture proved to be very effective because it led to identify that cleavage fracture occurred from +25°C to –196°C in the plate steel. It was found as well that the microstructures for cleavage fracture are different in the rolling and transverse directions of the plate steel: four cleavage fracture nucleation microstructures created microcracks from +25°C to –196°C in the rolling direction. But in the transverse direction at –60°C, with 100% of cleavage fracture, only two microstructures nucleated microcracks, the other two microstructures occurring at higher temperatures. This is due to the different orientation and distribution of pearlite in the matrix material in the rolling and transverse directions, as explained in sections 3.6.6 and 3.6.7.

In Grade A plate steel, it was found that, in the rolling direction, most microcracks, nucleated by all microstructures and at all test temperatures, occurred at a distance of about 1*mm* from the notch root. This region included the largest and widest microcracks developed by each microstructure. But a region of about 2*mm* from the notch root included most of the microcracks for the following test temperatures: +25°C, 0°C, –60°C and –196°C. It was found as well that at –196°C, microcracks were found at a distance beyond 2*mm*, some of them where found very close to the edge opposite to the notch root (section 3.6.6). Therefore it was concluded that the distance of 2*mm* from the notch root can be considered as the region that includes most cleavage fracture initiation for all test temperatures of Grade A plate steel in the rolling direction. But in the transverse direction the microcracks nucleation region is different. The farthest microcrack was found at around 650 μm for a test temperature of +25°C, but at 100% of cleavage fracture (–60°C), the farthest microcracks were found at about 230 μm from the notch root (section 3.6.7). The fractography analysis also showed that the largest microcrack (a microcrack with a length of 210 μm) was found in the transverse direction of the plate steel at a test temperature of –60°C. This analysis revealed that in the rolling direction, the cleavage nucleation region is similar for all test temperatures, but in the transverse direction this region

decreases with test temperatures. This may suggest that if the maximum principal stresses are parallel to the transverse direction of the plate steel then the largest microcracks will be developed inside the steel. Therefore navy structures may consider this in the construction of merchant ships to avoid that the highest level of stresses and strain do not occur in the transverse direction of the plate steel.

As described in section 2.7, one of the main objectives of the present research project was to incorporate the micro features nucleating cleavage fracture, found experimentally with the fractography analysis performed in section 3.6.4 into the CAFE model. This aimed to introduce the real microstructures of materials in the micromechanical model for better modelling of mechanical behaviour of materials and to physically base the input parameters of the model. It can be seen that the analysis for the identification of competition of different micro features triggering cleavage in a Grade A plate steel has contributed to the field of knowledge because it has been analyzed the real microstructures that nucleate cleavage instead of assuming that grain boundary cracked carbides initiate cleavage in the ferritic–pearlitic steel analyzed. The incorporation of those micro features has been successfully incorporated in the CAFE model for cleavage modelling of the steel under analysis. The following section will discuss technical points about the implemented CAFE model.

7.2 Improvement of CAFE simulations and validations.

The single integration 8–node brick C3D8R finite elements were used to mesh the damage region of Charpy and four point double–notch bend tests simulated with the CAFE model. This type of finite elements are the only 8–node finite element allowed in ABAQUS Explicit (ABAQUS 6.5, 2004). However, if 8–noded finite elements with more than one integration points would be available in ABAQUS, additional modelling possibilities could have been included in the model: the macro strain gradients could have been fed to the CA arrays by modifying the algorithm that redistributes the strain across the cells, this will allow for better simulation of local strain and stress gradients.

The model was primarily designed to model fracture propagation, therefore the size of the smallest modelling entity (CA arrays) was chosen equal to that of the fracture propagation steps of ductile and brittle fracture. However the model formalism allows for the use of much smaller entities, like the micro features nucleating fracture, for explicit simulation of crack initiation. In this case, the smallest modelling entities have to be chosen on the basis of crack initiation micromechanisms, which were based on real micro features of the material. In cleavage fracture, they are usually grain boundary cracked carbides, non–metallic inclusions, the lamellar

microstructure of pearlite, etc. Consequently a much more thorough modelling of the fracture initiation can be achieved if the CAFE model has cells size of carbides, inclusions and the thickness of the lamellar microstructures of pearlite. In principle this can be done in two main ways:

The first way is to create brittle cells with size equal to the different cleavage fracture microstructures (carbide size, inclusions size, lamellar thickness of pearlite). This approach was explored by Das (Das et al., 2001, Das, 2002, Das et al., 2003), he created brittle cells with size equal to that of a typical carbide in a steel. His results showed very good correlation between the prediction of oxide cracking during hot rolling and the experimental observations of the quality of the slab surface after rolling. But for the creation of four distributions of brittle cells with size related to each cleavage fracture microstructure, extensive research work is needed because the creation of those arrays of smaller cells size than the two main CA arrays distributed randomly is very complicated. This approach is easier when the microstructure for cleavage fracture is related to only one, for example grain boundary carbides, because a third level of CA arrays is created only around grain boundaries. But the implementation of four microstructures by using CA arrays for each of the cleavage microstructures: $aliveFC$, $aliveFI$, $alivePC$ and $alivePI$ is more complicated and extensive research work is needed. A detailed simulation of fracture initialisation according to this approach is strongly recommended for future work.

The second approach is to create layers of CA only for $aliveFC$, $aliveFI$, $alivePC$ and $alivePI$ brittle cells. These additional layers can be used for detailed modelling of stress fields at each cleavage fracture microstructure (grain boundary, ferrite grain inclusions, pearlite boundary and lamellar pearlite). Moreover, this approach allows for three or more CA arrays with independent cell sizes by dividing the brittle CA array to account for each of the cleavage microstructures. The present approach gave good results. From the present analysis it has been shown that the highest level of details in the CAFE model can be used where it is really required.

At present, little work has explored the incorporation of different micro features for cleavage fracture nucleation, but none has introduced statistical distributions of microstructures nucleating cleavage fracture in a Cellular Automata Finite Element model. This shows the novelty of the present research work. The power of the CAFE model for simulation of fracture initiation and propagation showed that the model can deal with the proposal of the present research work. The results of the pictures in Chapter VI showed that the present CAFE model is very suitable for modelling the ductile–brittle transition in steels, and the model allows the user to implement different microstructures for cleavage fracture. This model is also very suitable to

simulate the distribution of cleavage fracture initiation points observed experimentally in section 3.6.4. The model can also predict realistic transitional behaviour, including the levels of scatter in terms of the total energy absorbed in the impact Charpy tests (figure 6.29).

From the numerical and experimental results, it is interesting to observe that at the lower shelf of the transition curve, the data is smoother than at the upper shelf. This may be due to the temperature dependence of yield stress σ_y and the hardening exponent n. They are the main parameters resulting in the ductile–brittle transition, but probably the yield stress and the hardening exponent are not main ones. Therefore the temperature dependence of σ_y and n were not enough to simulate the ductile–brittle transition. The difference between the yield stresses at the upper and lower shelf temperatures is relatively small: at 25°C, $\sigma_y = 260MPa$; and at –60°C, $\sigma_y = 330MPa$. The hardening exponents for each temperature are 0.2 and 0.13 respectively. From these values it can be seen that due to the relatively low difference in those values for each test temperature it has been necessary to include other parameters dependence on temperature related to the microstructure to improve the numerical results in the simulation of the ductile–brittle transition.

Temperature dependence of the misorientation threshold, θ_F, was introduced in the CAFE model in order to improve the results for the simulation of the ductile–brittle transition. Even when there is little experimental evidence that θ_F is temperature–sensitive, because usually misorientation analysis is performed on fracture surfaces obtained at lower shelf temperatures to characterize fracture (Bhattacharjee and Davies, 2002, Bhattacharjee et al., 2003), this idea improved the numerical results.

Particular attention was drawn as well towards the microstructure distribution. As shown in sections 5.8.3 and 5.8.4, the microstructure of the steel consists of ferrite and pearlite. The strategy of applying different random number generators to simulate each microstructure histograms was included into the model through the fracture stress histogram as suggested by Shterenlikht (Shterenlikht, 2003). This improved as well the CAFE results.

And finally, as mentioned in section 5.8.5, it was shown that instead of introducing the distribution of 2D optically measured grain size in the model, the distribution of the real 3D grain size, analyzed with the measurement of cleavage facets, was distributed in the brittle CA arrays. Because the 3D grain size is 1.26 times larger than the 2D grain size, therefore the definition of the 2D grain size will result in an overestimation of numerical results.

7.3 Suggestions about the use of Grade A plate steel for the construction of hulls of merchant ships.

Because of the high proportion of pearlite microstructure and micro features promoting cleavage fracture in the rolling and transverse directions of the plate steel, the steel is susceptible to cleavage from room to liquid nitrogen test temperatures. In the rolling direction of the plate steels, as the temperature decreases, there is a competition of the microstructures for the nucleation of cleavage fracture with a noticeable change of the micromechanisms for cleavage fracture at lower test temperatures. At 0°C the longest and widest microcracks were nucleated by the pearlite boundary and ferrite grain inclusions, but the other two microstructures compete as well for the nucleation of microcracks of considerable size. At –60°C, the pearlite boundary, ferrite grain inclusions and the lamellar pearlite microstructure nucleated the longest and widest microcracks. From these results it can be seen than for this test temperature, the competition of these microstructures for the nucleation of microcracks of critical size is very similar. Finally at –196°C, where all the conditions for cleavage fracture are met, the longest microcracks were nucleated by the ferrite grain inclusions and the lamellar pearlite microstructure. These two microstructures also nucleated microcracks with critical width, but it was found that the widest microcrack was nucleated by pearlite boundary microstructure. The results showed that in the present steel, there is a competition between the four microstructures for the nucleation of microcracks of critical size, and because of the fact that some microstructures have less influence on the nucleation of microcracks of critical size, the possibility for such microstructures to nucleate microcracks of critical size exists. Therefore it can be concluded that the pearlite microstructure has high influence on the toughness properties of the steel because the largest and widest microcracks have been created by this microstructure.

The work showed that Grade A ship plate steel is very sensitive to the nucleation of microcracks by different microstructures; even at room temperature the steel can fail by cleavage. This was shown in figures 3.25, 3.26 and 3.27 where lands of cleavage were found on the fracture surfaces of Charpy specimens tested at room temperature. This implies that engineering structures built with Grade A plate steel may have distributions of microcracks in the most loaded regions and they can lead to the development of macro cracks as the plastic regions contain high population of microcracks. The fractography analysis also revealed that small colonies of pearlite microstructure did not nucleate microcracks in any test temperature, this suggest that only pearlite colonies with a critical size can nucleate microcracks.

7.4 References.

ABAQUS 6.5 (2004) Analysis User's Manual, Finite Elemente Simulation Program (ABAQUS version 6.5.).

BHATTACHARJEE, D. & DAVIES, C. L. (2002) Influence of processing history on mesotexture and microstructure-toughness relationship in controll-rolled and normalised steel. *Scripta Materialia*, 825-831.

BHATTACHARJEE, D. C., DAVIS, C. L. & KNOTT, J. F. (2003) Predictability of Charpy impact toughness in thermomechanically controll rolled (TMCR) microalloyed steels. *Ironmarking and Steelmaking*, 30, 249-255.

DAS, S. (2002) The effect of boundary conditions and material data representation on the simulation of deformation during hot rolling. *Department of Engineering Materials, University of Sheffield, Ph. D. Thesis.*

DAS, S., PALMIERE, E. J. & HOWARD, I. C. (2001) CAFE: A new approach to the modelling of multipass hot rolling. *in "Proceedings of Modelling of Metal Rolling Processes Symposium 11 - Through Modelling", The Institute of Materials, London*, 33-40.

DAS, S., PALMIRE, E. J. & HOWARD, I. C. (2003) CAFE: a tool for modelling thermomechanical processes. *in E. J. Palmire, M. Mahfouf and C. Pinna, eds, "Thermomechanical Processing: Mechanics, Microstructural and Control, Proceeding of the International Conference, Sheffield, 23-26 June, 2002" IMMPETUS, BBR Solutions, Chesterfield, UK*, 296-301.

SHTERENLIKHT, A. (2003) 3D CAFE modelling of transitional ductile-brittle fracture in steels. *Ph.D Thesis, Department of Mechanical Engineering, University of Sheffield.*

Conclusions

From the present research work it can be concluded that with the use of four point double–notch bend specimens it was possible to identify the microstructures associated with cleavage fracture in a Grade A ship plate steel. The analysis resulted in the identification of four different microstructures associated with the development of microcracks in the notch region of the surviving notch of the double–notch bend specimens which was subjected to the critical conditions prior to failure. In the steel analyzed in the present research work, were found microcracks associated with micro features inside ferrite grains and pearlite colonies and microcracks associated with micro features found in the boundary of ferrite grains and the colonies of pearlite.

During the analysis of the different microstructures associated with the distribution of microcracks, it was suggested that due to the high amount of microcracks counted, some of micro features found in those microcracks really nucleated microcracks. The size of those particles correlated with the size of particles reported in the literature. This suggests that the different distributions of particles found experimentally with the fractography can cleave the microstructure and create microcracks. The hypothesis that due to the composition of pearlite and ferrite of the Grade A plate steel, a possibility of finding four different potential microstructures for the nucleation of microcracks could exist was proved.

The statistical distributions of the different microstructures for the development of microcracks were analyzed with Weibull analysis and were incorporated in the CAFE model via the distribution of the fracture stress histograms of the ferrite grains and pearlite lands into the brittle CA array. For the ductile fracture process, it was incorporated in the CAFE model a distribution of the experimentally measured distribution of the distance between microvoids characteristic of ferritic steels.

The results of the simulation of microcracks in the notch region of the surviving notches of four point double–notch bend specimens showed that the CAFE model was coded properly as the model was able to simulate distributions of microcracks nucleated by the different microstructures for different test temperatures. The distribution of the microcracks agrees with the experimentally measured distributions of microcracks at cellular–micro level. The new CAFE model showed that it was able to reproduce the load–displacement curve of a Charpy test better than the previous CAFE model. After calibration of the ductile and the brittle parts the model, it was used to simulate the ductile–brittle transition of the steel under analysis with very good results. Finally, from the results showed in the present research work, it can be seen that the work is original as there has been not found in the literature simulations of microcracks at micro

level with the use of the cellular automata technique coupled to the finite element method. This shows the novelty of the present research project.

Future work

1. In finite element models, fracture has to reinitiate in each finite element during fracture propagation, and because of the fact that fracture initiation requires more energy than propagation, this limitation may result in over estimation of Charpy energy values. This limitation can be improved by defining the numbers of neighbouring finite elements using material point coordinates which can be given to the VUMAT subroutine in order to define in the subroutine which finite elements are being processed. Then VUMAT will know which finite elements are being processed consequently additional information can be given to the subroutine about which finite elements are located in the region of fracture initiation and propagation. Therefore an additional criterion taking into account this information can be implemented in the subroutine to improve the output results. However, this idea requires research work and is computationally expensive as the full deformation history must be traced for each finite element in the damage zone. Therefore research work in about this idea is recommended for the future.

2. The constitutive Rousselier ductile damage model, used in the present work, can only account for volumetric growth of microvoids but an additional criterion must be applied to estimate the onset of shear instability of ductile damage cells. The possibility of including an appropriate shear localisation model into the CAFE model was not explored due to time constraints. Research work about the additional criterion of including shear instability in the Rousselier damage model is recommended for future work.

3. Many model parameters require proper tuning before good correlation with experimental data is achieved. The maximum number of dead cells allowed in the ductile and brittle CA arrays affects considerably the model performance. In this work the values for these parameters were based on estimates and on some data fitting. This can be done by a detailed understanding of the fracture process at the micro-scale in order to give a metallurgical meaning to those values. The effect of θ_F on the transition temperature range, the link between c_D and c_B in the upper and lower shelf of Charpy energy values were not investigated in detail. This was due to time constraint, but it would be interesting to investigate in greater detail the influence of the those parameters in various simulations of the CAFE model and investigate their metallurgical meaning in the transition region.

4. To the date, the CAFE model has not been applied in the simulation of pre–cracked laboratory specimens with through–thickness cracks as compact specimens, single edge notched bend specimens, modified double–cantilever beam, DCB specimens, etc. Therefore research work in this direction is recommended in a near future in order to observe the behaviour of the present model on fractured structures. But it is strongly recommended to perform first research work in the previous points before exploring this point in order to improve the performance of the model before exploring its application in fracture structures.

5. The modelling of fatigue with the CAFE model is also recommended as future work. This in order to study the behaviour of the model on this kind of simulations and to identify which numerical subroutines need to be modified for proper simulation of fatigue with the CAFE model.

Finally, it can be concluded that the hypothesis proposed in this work was proved satisfactory, the project has contributed to the field of knowledge as new findings and new techniques for modelling cleavage nucleation with the CAFE model were successfully achieved. The work also showed the areas where research work is still needed in order to improve the performance of the CAFE model and for better understanding of cleavage fracture.

Appendix A

ABAQUS SOLVER

CELL States

Step 9

The finite elemen solution-dependen variables at time t_{i+1} are calculated a ccoding to next equations:

$$Y_1(t_i) = \begin{cases} dead & \text{if } Y_2(t_i) \le 0 \\ alive & \text{otherwise} \end{cases}$$

$$Y_2(t_i) = \frac{X_{(D)}(t_i)}{X_{(D)}^{max}} - \frac{X_{(B)}^{b}(t_i)}{X_{(B)}^{max}}$$

$$Y_3(t_i) = \frac{X_{(B)}^{b}(t_i)}{X_{(B)}(t_i)}$$

FINITE ELEMENT INTEGRATION POINTS

Rousselier continuous ductile damage model applied at FE level

Step 1

$\sigma_{ij}^{m}(t_{i+1})$ and $\beta_m(t_{i+1})$

Are obtained via the solutions of equations of the Rousselier continuous ductile damage model

Step 2

From the stress tensor, $\sigma_{ij}(t_i)$ at integration points, the maximum principal stress and its direction cosines are obtained.

$\sigma_I(t_i)$

$d_k(t_i)$

Step 3

$\beta_m(t_{i+1})$ is calculated and distributed at each ductile CA cell m. The following criteria is used:

$$T_{m(D)}(t_i) = dead$$

$\beta_m(t_{i+1})$

If

$d_k^1 \cdot d_k(t_i) \approx 1$

Then

No

Step 10

The FE stress tensor and solution-dependent variables at incremente time t_{i+1} are returned by the VUMAT subroutine to the ABAQUS solver

$\sigma_{ij}(t_{i+1})$

$Y_k(t_{i+1})$

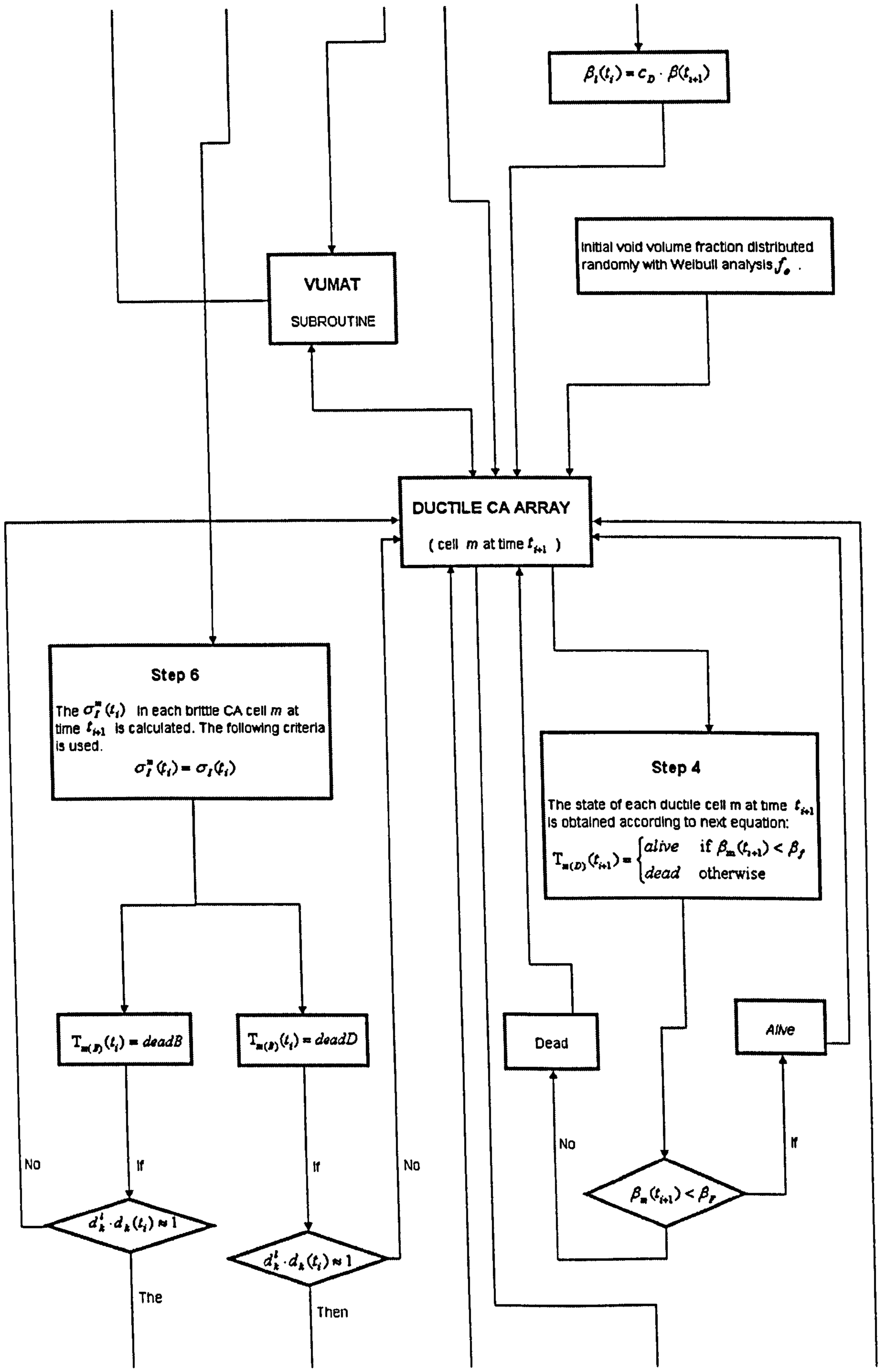
$\beta_i(t_i) = c_D \cdot \beta(t_{i+1})$
VUMAT
SUBROUTINE
Initial void volume fraction distributed randomly with Weibull analysis f_o .
DUCTILE CA ARRAY
(cell m at time t_{i+1})
Step 6
The $\sigma_I^m(t_i)$ in each brittle CA cell m at time t_{i+1} is calculated. The following criteria is used.
$\sigma_I^m(t_i) = \sigma_I(t_i)$
$T_{m(B)}(t_i) = deadB$
$T_{m(B)}(t_i) = deadD$
No
If
$d_k^i \cdot d_k(t_i) \approx 1$
The
If
No
$d_k^i \cdot d_k(t_i) \approx 1$
Then
Step 4
The state of each ductile cell m at time t_{i+1} is obtained according to next equation:
$T_{m(D)}(t_{i+1}) = \begin{cases} alive & \text{if } \beta_m(t_{i+1}) < \beta_f \\ dead & \text{otherwise} \end{cases}$
Dead
Alive
No
If
$\beta_m(t_{i+1}) < \beta_f$

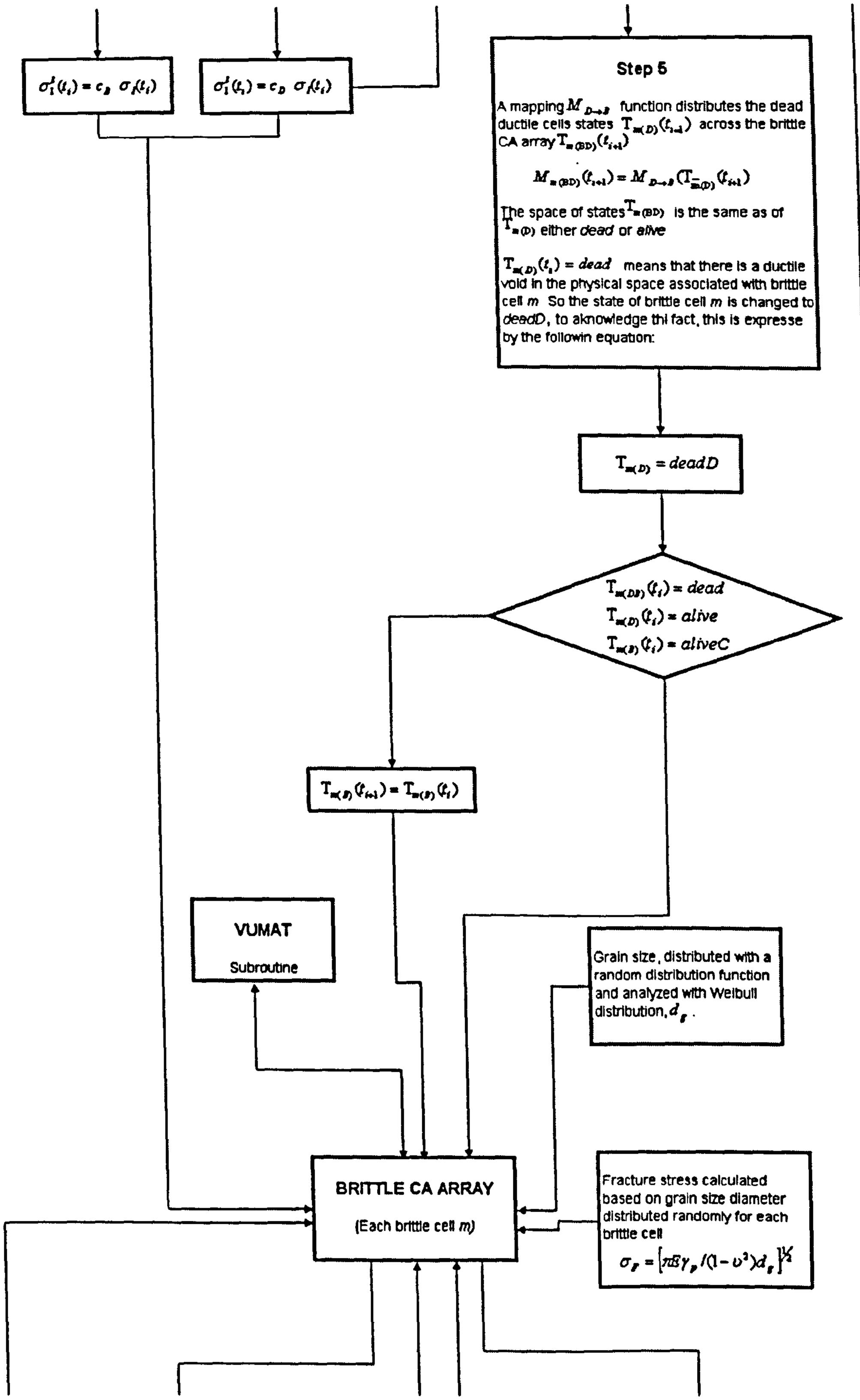
$\sigma_1^d(t_i) = c_B\ \sigma_f(t_i)$
$\sigma_1^d(t_i) = c_D\ \sigma_f(t_i)$
Step 5
A mapping $M_{D\to B}$ function distributes the dead ductile cells states $T_{m(D)}(t_{i+1})$ across the brittle CA array $T_{m(BD)}(t_{i+1})$
$M_{m(BD)}(t_{i+1}) = M_{D\to B}(T_{m(D)}(t_{i+1})$
The space of states $T_{m(BD)}$ is the same as of $T_{m(D)}$ either *dead* or *alive*
$T_{m(D)}(t_i) = dead$ means that there is a ductile void in the physical space associated with brittle cell m So the state of brittle cell m is changed to *deadD*, to aknowledge thi fact, this is expresse by the followin equation:
$T_{m(D)} = deadD$
$T_{m(DB)}(t_i) = dead$
$T_{m(D)}(t_i) = alive$
$T_{m(B)}(t_i) = aliveC$
$T_{m(B)}(t_{i+1}) = T_{m(B)}(t_i)$
VUMAT
Subroutine
Grain size, distributed with a random distribution function and analyzed with Weibull distribution, d_g .
BRITTLE CA ARRAY
(Each brittle cell *m)*
Fracture stress calculated based on grain size diameter distributed randomly for each brittle cell
$\sigma_f = \left[\pi E \gamma_p / (1-\upsilon^2) d_g\right]^{1/2}$

Step 7

This step is the brittle CA analogue for the ductile CA.

Five states in the brittle CA array are assigned at the begining of the simulation.

alive - *cell state*
aliveFC - alive ferrite cells with a grain boundary carbide
aliveFI - alive ferrite with inter carbide
alivePC - alive pearlite wht a grain boundary carbide
alivePI - alive pearlite with inter carbide
deadB - when the brittle failure criterion is satisfied
deadD - when a condition is satisfied in the ductile CA array.

$T_{m(B)}(t_{i+1}) = deadB$

$T_{m(B)}(t_{i+1}) = T_{m(B)}(t_i)$

$T_{m(B)}(t_i) = ahveC$
$T_{m(B)}(t_i) = ahvelC$
$T^{m}_{I(B)}(t_i) = deadB$
$T^{m}_{I(B)}(t_i) = deadD$

Each brittle cell m has two cell properties ($N_B = 2$), these are the fracture stress and the grain orientation angle:

$$\Lambda^1_{m(B)} = \sigma^m_f \quad \text{and} \quad \Lambda^2_{m(B)} = \alpha^m$$

A brittle cell m will become dead at time if the next criterion is satisfied:

$$\sigma^m_I(t_i) \geq \sigma^m_f$$

A crack will propagate from one brittle cell m to another l, if the misorientation angle for these two cells is less than a misorientation threshold.

$$|\alpha^m - \alpha^l| \leq \theta_T$$

Step 8

This step is the brttle analogue for the ductile CA.

All dead brittle CA cells are reflected into the ductile CA array. A mapping fuction, $M_{B \to D}$ distributes the array of brittle CA cell states, $T_{m(DB)}(t_{i+1})$ across the ductile CA array.The result is a synchronisation array of the ductile CA cell states, $T_{m(DB)}(t_{i+1})$.

$$T_{m(DB)}(t_{i+1}) = M_{B \to D}(T_{m(B)}(t_{i+1}))$$

The space of states of $T_{m(DB)}$ is the same as of either *dead* or *alive* $T_{m(D)}$

$T_{m(DB)}(t_{i+1}) = dead$, means that there is a brittle crack in the physical space associeted with ductile cell m, so the state of ductile cell m is changed to *dead*. to acknowledge this fact, this can be expressed by the following equation.

$T_{m(D)}(t_{i+1}) = dead$

If

$T_{m(DB)}(t_{i+1}) = dead$
$T_{m(D)}(t_i) = alive$

Alive

Dead

$T_{m(D)}(t_{i+1}) = T_{m(D)}(t_i)$